The Auroral Dynamic Duo: Spatial, Spectral and Temporal Trends of Jupiter's Northern and Southern X-ray Aurorae

William Dunn

A thesis submitted to UCL for the degree of

Doctor of Philosophy

Mullard Space Science Laboratory

Department of Space and Climate Physics

University College London

8th March 2018

I, William Dunn, confirm that the work presented in this thesis is my own. Where information has been derived from other sources, I confirm that this has been indicated in the thesis.

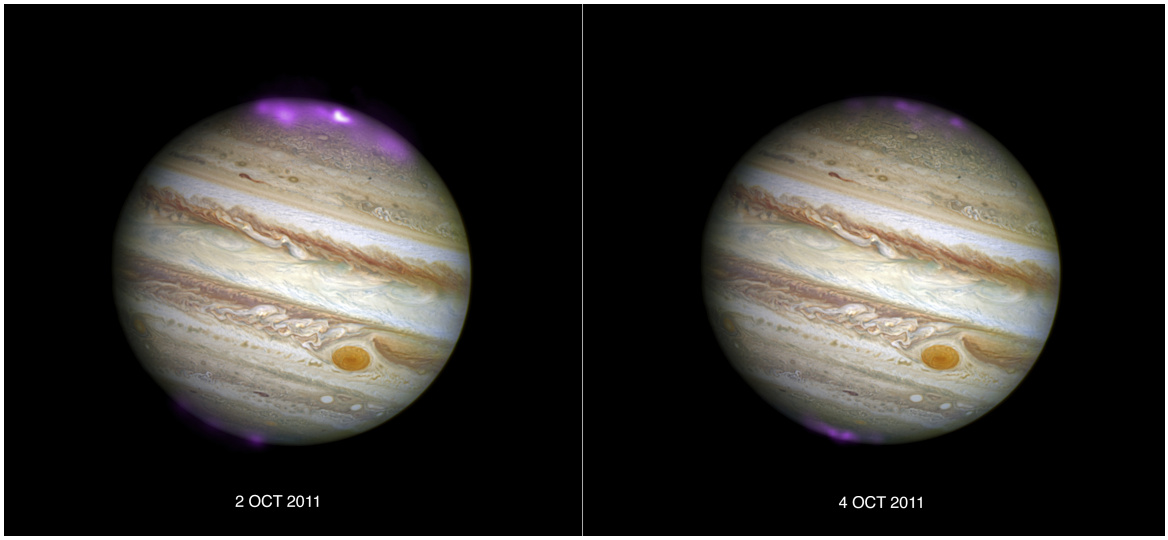

Figure 1: Chandra images of Jupiter's X-ray Aurora overlaid on a Hubble Space Telescope optical image of the planet. An Interplanetary Coronal Mass Ejection is predicted to have impacted the planet on October 2, 2011 and to have passed the planet by 4 October 2011. Jupiter's X-ray aurora exhibits a variety of changing characteristics between these two observations (Chapter 2). Image credit: NASA

"We had the sky, up there, all speckled with stars, and we used to lay on our backs and look up at them, and discuss about whether they was made, or only just happened- Jim he allowed they was made, but I allowed they happened; I judged it would have took too long to make so many. "

— Mark Twain, *The Adventures of Huckleberry Finn*

"What better basis for education than the appreciation of nature in all her terrible glory. Why, the very foundation of science and medicine lies in a preoccupation with natural forms. Their workings; their shapes... The very marvel that moves men's hearts. "

— Alan Moore

"Look again at that dot. That's here. That's home. That's us. On it everyone you love, everyone you know, everyone you ever heard of, every human being who ever was, lived out their lives. The aggregate of our joy and suffering, thousands of confident religions, ideologies, and economic doctrines, every hunter and forager, every hero and coward, every creator and destroyer of civilization, every king and peasant, every young couple in love, every mother and father, hopeful child, inventor and explorer, every teacher of morals, every corrupt politician, every "superstar," every "supreme leader," every saint and sinner in the history of our species lived there–on a mote of dust suspended in a sunbeam.
The Earth is a very small stage in a vast cosmic arena. Think of the rivers of blood spilled by all those generals and emperors so that, in glory and triumph, they could become the momentary masters of a fraction of a dot. Think of the endless cruelties visited by the inhabitants of one corner of this pixel on the scarcely distinguishable inhabitants of some other corner, how frequent their misunderstandings, how eager they are to kill one another, how fervent their hatreds.
Our posturings, our imagined self-importance, the delusion that we have some privileged position in the Universe, are challenged by this point of pale light. Our planet is a lonely speck in the great enveloping cosmic dark. In our obscurity, in all this vastness, there is no hint that help will come from elsewhere to save us from ourselves.
The Earth is the only world known so far to harbor life. There is nowhere else, at least in the near future, to which our species could migrate. Visit, yes. Settle, not yet. Like it or not, for the moment the Earth is where we make our stand.
It has been said that astronomy is a humbling and character-building experience. There is perhaps no better demonstration of the folly of human conceits than this distant image of our tiny world. To me, it underscores our responsibility to deal more kindly with one another, and to preserve and cherish the pale blue dot, the only home we've ever known."

— Carl Sagan, *Pale Blue Dot*

Abstract

Jupiter's soft X-ray aurora is concentrated into a bright and dynamic hot spot that is dominated by charge exchange from precipitating high charge-state ions (e.g. Gladstone et al. (2002); Cravens et al. (2003); Elsner et al. (2005)). These highly energetic planetary emissions exhibit pulsations over timescales of 10s of minutes. In one observation these pulsations were found to have a very regular periodic pulsation timescale of 45 minutes (Gladstone et al. 2002), but in all subsequent observations the timescale for pulsations was found to be irregular (e.g. Elsner et al. (2005); Branduardi-Raymont et al. (2004)). Surrounding this pulsating soft X-ray (< 2 keV) spot, there is a transient auroral oval of hard X-rays (> 2 keV) produced by precipitating electrons that also produce the co-located UV main oval (e.g. Branduardi-Raymont et al. (2007a, 2008)). The hot spot's magnetic field lines have been suggested to map beyond 30 Jupiter Radii (R_J) to Jupiter's outer magnetosphere and possibly to the Jovian cusp (Pallier and Prangé 2001). This led Bunce et al. (2004) to propose that Jupiter's X-ray aurora was produced by the influence of dayside reconnection on the current systems at the magnetopause and therefore by the interaction between the solar wind and Jupiter's magnetosphere.

In this thesis, we analyse the spatial, spectral and temporal characteristics of Jupiter's X-ray aurora from Chandra and XMM-Newton observation campaigns during 2007, 2011 and 2016. By applying the latest magnetosphere model mapping (Vogt et al. 2011, 2015), we identify that Jupiter's X-ray hot spot may originate from regions along the pre-noon to dusk magnetopause and that the hard X-rays mostly map to the middle magnetosphere, with a slight dawn preference. Our mapping for the hot spot supports previous suggestions that one may expect a solar wind relationship to the emissions.

Indeed, we find that during solar wind density enhancements and magnetic field rotations from Interplanetary Coronal Mass Ejections and Corotating Interaction Regions, the Jovian soft X-ray aurora brightens, expands, changes spectral populations and exhibits pulsations on quicker timescales. The hard X-ray aurora also brightens during solar wind compressions, but behaves independently of the soft X-ray emissions. During 4 (of 5) observed solar wind compressions, Jupiter's X-ray aurora pulses with a characteristic regular period of 9-13 minute. During solar wind rarefactions, the aurora dims and exhibits longer time-scale pulsations.

It is unlikely that the X-ray aurora exists in isolation from other well-studied Jovian auroral wavebands, so we compare the X-ray aurora with radio, IR and UV emissions. We find that non-Io decametric radio emission bursts associated with solar wind compressions (e.g. Hess et al. 2014) occur during X-ray brightening. We note connections between the IR methane layer hot spot and the co-located X-ray hot spot, which may suggest that deeply penetrating ions producing the near-instantaneous X-ray emissions subsequently heat the stratosphere (e.g. through secondary electrons or subsequent photon emissions). We find (for limited available UV comparisons) that when UV dusk polar arcs form, the X-ray hot spot also brightens in a similar region. The normally transient hard X-ray emissions are observed to brighten and occur co-located with UV dusk polar arcs and UV dawn storms.

Perhaps our most surprising result is that during some observations the Northern and Southern X-ray hot spots appear to behave independently of one another. Brightening in each hot spot is not correlated and a regular 9-11 minute pulsation period in the South (observed by both Chandra and XMM-Newton) is not also observed in the North, which exhibits more complex, irregular pulsations. The two hot spots both map to the noon-magnetopause, but the Northern hot spot also maps along the dusk flank. We propose a few possible explanations:

1. The North and South X-ray hot spots are produced by cusp processes in-line or slightly adapted (non-sub-solar or high-latitude reconnection) from

Bunce et al. (2004).

2. In addition to the cusp, the Northern aurora also maps to the dusk sector, which may be associated with tail reconnection. The viewing geometry may prevent this from being observed in the South. The combination of cusp and tail pulsations would produce a more complex lightcurve for the North, while for the South the observed lightcurve would be more regular because it only consists of pulsed transits to the noon magnetopause. This would also exhibit a solar wind relationship. Large-scale tail reconnection can be triggered by magnetospheric compressions. Associated X-ray emissions would therefore 'switch on' with solar wind compressions, causing the observed X-ray brightening and 'expanded hot spot' (actually constituting two sources in the North: tail and cusp).

3. Kelvin Helmholtz Instabilities (KHI) that form in the pre-noon sector (e.g. Ma et al. (2015)), and grow along the dusk flank, generate field line resonances. The characteristic period associated with these resonances depends on the field line length. For regions further from noon, this would produce increasingly long timescales, which would explain the more complex Northern lightcurve. This can also generate intermittent reconnection and uni-directional currents (through field line twisting) which may explain differing hemispheric brightnesses. The scales of the KHI depend on the magnetic field strength, density and velocity of the plasmas on either side of the magnetopause and thus vary with solar wind conditions.

4. Alternative wave-particle interactions that propagate to different altitudes for each pole might also be responsible.

While deciphering between these mechanisms is beyond the scope of this thesis, we close by proposing future investigations that may identify the mechanism/s responsible for producing the high-energy precipitation that generates Jupiter's enigmatic X-ray aurora.

Contents

List of Figures

List of Tables

Chapter 1

Introduction

1.1 Combining Distinct Paradigms

> *"Scientists that use different paradigms exist in literally different worlds, epistemology being such an integral component of reality."*
> — Kim Stanley Robinson, *Green Mars*

This thesis presents a series of observations of Jupiter's X-ray aurora during varying solar wind conditions. To begin to interpret the spectral, spatial and temporal signatures associated with Jupiter's X-ray emissions it is important to first build familiarity with the diverse and otherwise distinct overarching fields contained within the topic:

- X-rays and Their Emission and Absorption Processes
- X-ray Emissions from Jupiter
- The Solar Wind - Jupiter's Surrounding Plasma Environment
- The Jovian Magnetosphere - Structures and Dynamics
- Jupiter's Multi-Waveband Aurora

Having built this background, we finish the introduction by discussing previous ideas for how these topics combine to provide Jupiter with the acceleration and particle fluxes needed to produce the observed X-ray Aurora. We then introduce the X-ray observatory instrumentation that is utilised throughout the thesis to study the X-ray emissions.

1.2 X-rays and Their Emission and Absorption Processes

1.2.1 The Discovery of X-rays

> *"I feel a sadness on me, that's how the Irish people say it. In their language you can't say "I am sad" or "I am happy". They understood what we English long forgot. We're not our sadness, we're not our happiness or our pain but our language hypnotises us and traps us in little labelled boxes.... Reality is all about language."*
>
> — Grant Morrison, *The Invisibles*

> *"We evidently lack the word for an object like this... It is authentically a new thing on the face of the world."*
>
> — Phillip K Dick, *The Man in the High Castle*

On November 8th 1895, following a correspondence with Nikola Tesla, Röntgen identified a puzzling new phenomena that shared properties with both light and cosmic rays, but did not possess all of the properties of either known phenomena. It was detectable on photographic film, as expected for light, and also produced sufficient ionisation for electroscope discharge, as expected for cosmic rays. However, unlike for cosmic rays, it did not respond to electric or magnetic fields as a charged particle was expected to, and, unlike for visible light, lenses and prisms would not deviate this new phenomenon. This collection of contradictions led the true nature of the phenomenon to remain unknown for two decades and led to its identification as X-radiation.

Two decades after its discovery, by diffracting X-radiation through crystal lattices, Von Laue and the Braggs (in 1912 and 1913) discovered that X-rays were transverse waves. This forever connected X-rays to the other wavebands in the electromagnetic spectrum. For photons with energies 1 eV or less, departures from wave theory are barely noticeable, however, X-rays have energies greater than 0.1 keV so their behaviour is often more particle-like (Culhane and Sanford 1981).

While astronomers had to await the dawn of the space age in the 1940s to use X-rays to explore the Universe, X-rays were becoming progressively integral as a tool to probe the physical world. Their application and study led to groundbreaking discoveries in a wide variety of fields. Possibly the

most notable of these was the use of X-ray diffraction to discover DNA by Watson, Crick, Franklin and Wilkins. The diverse array of work that utilised X-rays meant that the physical processes, applications and instrumentation associated with the phenomena were becoming well-documented by the time humanity ventured into Earth's upper atmosphere and X-ray astronomy became possible.

This application of and contribution to laboratory physics is a consistent component of the planetary X-ray story and particularly Jupiter's X-rays. We leave many X-ray absorption and emission mechanisms undiscussed because they involve energy regimes irrelevant for Jupiter. The Jovian X-ray emission processes are: Bremsstrahlung continuum emissions, Charge Exchange Line emissions, Fluorescence line emissions, In/Elastic Scattering emissions and possibly synchrotron power law emissions.

1.2.1.1 Bremsstrahlung

First identified by Nikola Tesla in the late 1800s, Bremsstrahlung was placed into its modern context by Carl Anderson in 1930, when he found that relativistic electrons lost kinetic energy by emitting radiation.

Bremsstrahlung (from braking (bremsen) radiation (strahlung)) is emitted when a charged particle is accelerated/decelerated by the electrostatic field of another charged particle. To adhere to energy conservation, the kinetic energy of the decelerating charged particle is converted to emitted photons. This produces continuum emission for which the frequency of the peak intensity depends on the extent of the particle deceleration.

The intensity, I of bremsstrahlung emission at a given frequency, ω, is expressed as:

$$I(\omega) = \frac{e^2}{3\pi\varepsilon_0 c^3}[|a_{\parallel}(\omega)|^2 + |a_{\perp}(\omega)|^2] \tag{1.1}$$

where e is the charge of an electron, ε_0 is the permittivity of free space, c is the speed of light, and $a_{\parallel}$ and $a_{\perp}$ are the particle acceleration in its rest frame parallel with and perpendicular to the direction of motion, respectively.

Since the acceleration or deceleration of the electron in each direction depends on the electric field, E, that it experiences, this can be expressed by:

$$a_{||}(\omega) = \dot{v}_x(\omega) = \frac{1}{(2\pi)^{\frac{1}{2}}} \int_{-\infty}^{\infty} -\frac{eE_x}{m_e} dt = \frac{1}{(2\pi)^{\frac{1}{2}}} \int_{-\infty}^{\infty} \frac{\gamma Z e^2 v t}{4\pi\epsilon_0 m_e (b^2 + \gamma^2 v^2 t^2)^{\frac{3}{2}}} exp(i\omega t) dt \tag{1.2}$$

$$a_{\perp}(\omega) = \dot{v}_z(\omega) = \frac{1}{(2\pi)^{\frac{1}{2}}} \int_{-\infty}^{\infty} -\frac{eE_z}{m_e} dt = \frac{1}{(2\pi)^{\frac{1}{2}}} \int_{-\infty}^{\infty} \frac{\gamma Z e^2 b}{4\pi\epsilon_0 m_e (b^2 + \gamma^2 v^2 t^2)^{\frac{3}{2}}} exp(i\omega t) dt \tag{1.3}$$

where Ze is the charge of the nucleus, m_e is the electron mass, v is the radiation-emitting electron's velocity, b is the collision parameter and where

$$\gamma = \frac{1}{\sqrt{1 - \frac{v^2}{c^2}}} \tag{1.4}$$

Letting $x = \frac{\gamma v t}{b}$ more clearly highlights distinctions between the parallel and perpendicular accelerations:

$$\dot{v}_x(\omega) = \frac{1}{(2\pi)^{\frac{1}{2}}} \frac{Ze^2}{4\pi\epsilon_0 m_e} \frac{1}{\gamma b v} \int_{-\infty}^{\infty} \frac{x}{(1 + x^2)^{\frac{3}{2}}} exp\left(i \frac{\omega b}{\gamma v} x\right) dx \tag{1.5}$$

$$\dot{v}_z(\omega) = \frac{1}{(2\pi)^{\frac{1}{2}}} \frac{Ze^2}{4\pi\epsilon_0 m_e} \frac{1}{b v} \int_{-\infty}^{\infty} \frac{1}{(1 + x^2)^{\frac{3}{2}}} exp\left(i \frac{\omega b}{\gamma v} x\right) dx \tag{1.6}$$

so that the expression for $\dot{v}_x(\omega)$ is distinguished from that for $\dot{v}_z(\omega)$ by the division by γ and by the presence of x in the denominator of the integral. These integrals can be expressed through modified Bessel functions of the 0th (K_0) and 1st order (K_1) respectively (Longair (2011) and references therein), so that:

$$\dot{v}_x(\omega) = \frac{1}{(2\pi)^{\frac{1}{2}}} \frac{Ze^2}{4\pi\epsilon_0 m_e} \frac{1}{\gamma b v} 2i \frac{\omega b}{\gamma v} K_0\left(\frac{\omega b}{\gamma v}\right) \tag{1.7}$$

$$\dot{v}_z(\omega) = \frac{1}{(2\pi)^{\frac{1}{2}}} \frac{Ze^2}{4\pi\epsilon_0 m_e} \frac{1}{b v} 2 \frac{\omega b}{\gamma v} K_1\left(\frac{\omega b}{\gamma v}\right) \tag{1.8}$$

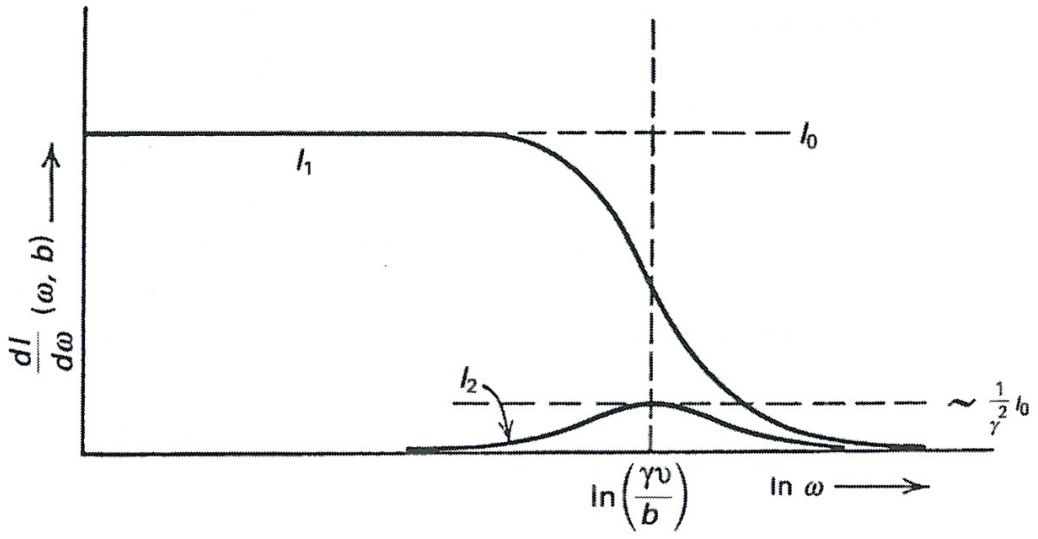

Figure 1.1: Figure from Jackson (1999): The spectrum of bremsstrahlung radiation from the acceleration components perpendicular (I_1) and parallel to the direction of motion (I_2). This shows that the emitted spectrum has a larger proportion from the perpendicular acceleration and that this becomes increasingly dominant for relativistic systems (lower values on the x-axis).

Re-writing equation 1 to include the Bessel function provides:

$$I(\omega) = \frac{Z^2 e^6 \omega^2}{24\pi^4 \varepsilon_0^3 c^3 m_e^2 v^4 \gamma^2} \left[\frac{1}{\gamma^2} K_0^2 \left(\frac{\omega b}{\gamma v} \right) + K_1^2 \left(\frac{\omega b}{\gamma v} \right) \right] \tag{1.9}$$

This reveals the interesting result that the higher intensity of the bremsstrahlung is emitted due to the perpendicular acceleration of the radiation-emitting particle. While this effect is present for non-relativistic particles, it becomes dominant for relativistic particles through two effects:

1. In the case where the electron is relativistic (i.e. $\gamma > 1$) then $\left(\frac{\omega b}{\gamma v}\right) << 1$, and $K_0\left(\frac{\omega b}{\gamma v}\right) = -ln\left(\frac{\omega b}{\gamma v}\right)$, while $K_1\left(\frac{\omega b}{\gamma v}\right) = \frac{\gamma v}{\omega b}$. Figure 1.1 shows that the contribution to the Bremsstrahlung spectrum from the 1st order modified Bessel function (I_1), associated with the perpendicular acceleration, is larger than that for the 0th order modified Bessel function (I_2), associated with the parallel acceleration. For cases where the electron has a much smaller velocity than the speed of light, then $\left(\frac{\omega b}{\gamma v}\right) >> 1$ and the parallel and perpendicular components contribute more equally.

2. If the radiation-emitting particle is relativistic then the intensity of the emission associated with the parallel direction of motion is further reduced

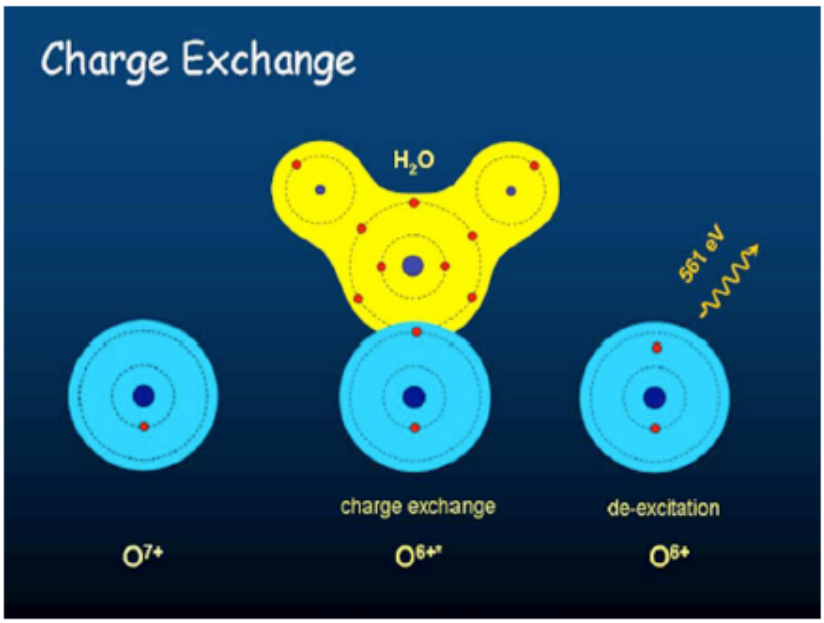

Figure 1.2: Figure from Dennerl (2009): Illustration of the Charge Exchange (CX) process for an O^{7+} solar wind ion undergoing charge transfer with a cometary coma water molecule. The O^{7+} acquires an electron in an excited state and subsequently de-excites to emit an O^{6+} X-ray spectral line.

by the extra factor of $\frac{1}{\gamma^2}$, meaning that the perpendicular component further dominates.

Given that the electrons that precipitate in the Jovian main auroral oval have energies of between 30 keV (0.3 c, γ=1.05) and 200 keV (0.7 c, γ=1.4) (e.g. Gustin et al. 2006), relativistic effects should be considered. For Jupiter, this results in viewing geometry implications that are particularly relevant when comparing the Northern and Southern auroral emissions.

1.2.1.2 Charge Exchange

The importance of Charge Exchange (sometimes called 'charge transfer') as an astrophysical X-ray generator came to the fore with the detection of X-rays from solar wind interactions with cometary neutrals (Lisse et al. 1996; Cravens 1997). Since this discovery, the application of charge exchange physics to astrophysical objects has proliferated to: planetary atmospheres, supernova remnants, star forming regions and different galactic structures (e.g Wargelin et al. (2008); Dennerl et al. (2006); Dennerl (2010)). Charge exchange is distinct from other astrophysical X-ray generation mechanisms because it not

only involves hot populations, but also permits X-rays to probe interactions with cold gases.

In charge exchange a colliding ion takes one or more electrons from a neutral atom. For high charge-state ions the electron may be captured into a high energy-level from which it subsequently de-excites to the ground state. In the transition to the ground state (possibly via a cascade of several energy levels), a sufficiently large energy difference between the initial state and ground state will generate an X-ray photon. An example Jovian charge exchange process is:

$$O^{q+} + H_2 \rightarrow O^{(q-1)+*} + H_2^+ \tag{1.10}$$

The precise energies of the X-ray photons provide signatures for specific ion species and processes. The high cross sections for charge exchange collisions have led to the detection of charge exchange lines from many solar wind ions including: O^{7+}, O^{6+}, C^{5+} and Ne^{8+} (Lisse et al. 2001; Krasnopolsky 2002).

1.2.1.3 A Brief Note on Nomenclature

Throughout this thesis, atomic charge states and accompanying spectral lines are indicated by the atom's associated letter and a subsequent roman numeral - e.g. 'O VIII'. O I is neutral oxygen and each subsequent roman numeral increment indicates a charge-state increase of one, so O II is O^+, O III is O^{++} and so on until O VIII which is O^{7+} (note O^{8+} is fully ionised and so has no electrons to produce spectral lines).

We also refer to emission lines as Heα, Lymanα (Lyα), Lyβ etc. In this case 'He' indicates helium-like transitions (charge-states where an ion only possesses two electrons) - e.g. O^{6+}, O VII. Lyman indicates hydrogen-like transitions - e.g. O^{7+}. The Greek letters indicate the number of energy levels that an electron de-excites through. α indicates a transition from n=2 to n=1, β indicates n=3 to n=1 and so on. Oxygen Lyα is therefore the line emitted when an O^{7+} (O VIII) electron relaxes from n=2 to n=1 to fill the ground-

state. For Jupiter, this is often observed following charge exchange where an electron is captured by precipitating O^{8+}.

Different transitions depend on the different orbitals occupied by electrons. This occupancy is often written in the following format :

$$nl^x \tag{1.11}$$

where n is the energy level (principal quantum number or orbital shell), l is the orbital angular momentum with s, p, d, f indicating $l = 0, 1, 2, 3$ respectively and x indicates the number of electrons in a sub-shell (up to a maximum of $2(2l + 1)$ - 2 for s, 6 for p, 10 for d and so on).

For the configuration of multiple electrons presenting different possible transitions, the state of the system can be represented by:

$$^{2S+1}L_J \tag{1.12}$$

where S is the total spin, L is the total orbital angular momentum and J is the total angular momentum (from $L + S$ to $|L - S|$) so that for $L = 1$, $S = 0, 1$ J will be 1 when S=0, and J could be 0, 1 or 2 for S = 1. This means that He-like (2 electron) 1s2p could occupy any one of four different energy states: for $S = 0$ it is ^{1}P$_1$, but for $S = 1$ it could be $^3P_0$, $^3P_1$, $^3P_2$. This produces multiple possible transitions for He-like ions, where these transitions will often take the form of triplets:

1. A resonance line where the electron transitions from an S=0 state:

$$1s2p(^1P_1) \rightarrow 1s^2(^1S_0) \tag{1.13}$$

2. An intercombination line from two distinct $S = 1$ transitions from:

$$1s2p(^3P_2) \rightarrow 1s^2(^1S_0) \tag{1.14}$$

$$1s2p(^3P_1) \rightarrow 1s^2(^1S_0) \tag{1.15}$$

3 A forbidden line:

$$1s2s(^3S_1) \rightarrow 1s^2(^1S_0) \tag{1.16}$$

Forbidden lines are not strictly forbidden. In fact, for cometary charge exchange they are the strongest Oxygen Heα emissions (Kharchenko and Dalgarno 2000; Kharchenko et al. 2003). However, the timescales for forbidden line emissions are longer than those for resonance or intercombination. For the Jovian aurora where the combination of precipitating ion velocities and high atmospheric density lead to short timescales between collisions, the forbidden line may be quenched (energy from excited oxygen is re-distributed through collisions, preventing forbidden line emission) (Kharchenko et al. 2008).

1.2.1.4 Fluorescence Lines

Fluorescence of solar X-rays is an important X-ray emission mechanism for planetary atmospheres (e.g. Earth (Grader et al. 1968), Venus and Mars(Dennerl 2002; Dennerl et al. 2002)).

During fluorescence, a photon is absorbed to either: 1) excite an electron to a higher orbital with a subsequent relaxation and re-emission of light (sometimes re-emission takes place over longer wavelengths, through a cascade) or 2) ionise an electron occupying an inner orbital, an outer orbital electron will subsequently relax into this vacant inner orbital (core hole) and emit an X-ray. In either instance, the energy of the light emitted is the difference in energy between the higher orbital and the orbital that the electron relaxes into. Case 2 particularly results in characteristic X-ray line emission, since ionising radiation leads to an electron transition to the ground state via a discrete set of common transitions.

K-shells indicate the lowest orbitals (n = 1), L is the second orbital (n=2), M the third orbital (n=3) and so on. The relaxation of an L-shell electron to a K-shell is labelled a K_α line. M to a K-shell is a K_β and so on. For Venus, for

example, the C-K_α, N-K_α and O-K_α lines were expected, but the wavelengths of the observed lines were slightly shifted because the atoms had molecular bonds as part of atmospheric CO, CO_2 or N_2 (Dennerl et al. 2002).

Instead of photon emission the Auger effect often occurs, in which electron de-excitation to the inner orbital results in the ionisation of another electron. For Jupiter's atmosphere, emission from carbon fluorescence in methane may be limited by the Auger effect, with the most prominent line at 0.284 keV with low photon yields of 0.0025 (Cravens et al. (2006) and references therein).

1.2.1.5 Thomson, Compton and Inverse Compton Scattering

While fluorescence provides the dominant X-ray emission from the atmospheres of Venus and Mars, the gas giant planets are more dependent on elastic-scattering with atmospheric hydrogen to produce the observed emissions (e.g. Maurellis et al. (2000); Cravens et al. (2006)).

Thomson scattering is the elastic scattering of electromagnetic radiation by a non-relativistic charged particle. The incident photon accelerates the charged particle in the direction of the photons electric fields oscillation. As the charged particle accelerates it re-emits radiation of the same wavelength as the initial photon, but in the direction perpendicular to its motion, thus scattering the initially incident photon in a different direction. Thomson scattering applies if the photon energy is less than the particle energy:

$$hf << mc^2 \tag{1.17}$$

where h is the Planck's constant, f is the frequency of the incident radiation, m is the mass of the charged particle and c is the speed of light.

Compton scattering describes inelastic collisions/scattering between photons and charged particles. In this scattering, the X-ray photon loses energy while the charged particle gains kinetic energy. The change in the X-ray frequency from an initial, f_i, to a final value, f_f, depends upon the change in

momentum, p, of the charged particle with mass, m:

$$hf_i + mc^2 = hf_f + \sqrt{p^2c^2 + m^2c^4} \tag{1.18}$$

Inverse Compton scattering may also be relevant for X-ray emission from the Jovian radiation belts. This occurs typically for relativistic particles, where the incident photon gains energy and the charged particle loses kinetic energy.

1.3 An X-ray History of Jupiter

1.3.1 The Discovery of Astrophysical X-rays

"History is written by the optimists."

— Michio Kaku

The capabilities and application of astrophysical X-ray observations is inextricably linked to space flight. Our atmosphere removes light with wavelengths shorter than 300 nm, which ensures that X-ray observations are not possible from the Earth's surface. We must therefore venture above the atmosphere's protective veil to explore the richness of the Universe's highest-energy domains.

In 1919, Goddard first identified the potential of rockets for researching the space environment, it wasn't until the post-war era in the late 1940s that the weapons of destruction from World War 2 could become tools for inquiry. By the end of the 1940s, photon counters were being launched on rockets and in 1949 Friedman and colleagues first detected the Sun's UV and X-ray emissions and identified that it was this emission that produced our ionosphere (Culhane and Sanford (1981) and references therein).

From 1957-1978, the use of sounding rockets proliferated with UK institutions launching 198 Skylarks (Massie and Robins 1986). In 1962, this led to the surprising discovery of two X-ray sources beyond our Solar System: the Crab Nebula and Scorpius X-1 (Giacconi et al. 1962; Bowyer et al. 1964). The Crab Nebula had been studied since its supernova observation in 1054 CE, but Scorpius X-1 presented an entirely new object (a low mass X-ray binary), the

exploration of which depended upon a waveband which Earth's atmosphere would absorb. It was this concept of a waveband range that permitted exploration of an otherwise invisible Universe that prompted construction of the first dedicated X-ray telescopes.

1.3.2 The First X-ray Telescopes

"Knowledge is a chain reaction. No thought comes from nothing."
— Petter S. Rosenlund, *The Heavy Water War*

While the foundations of X-ray astronomy were built by sounding rockets, the limited time that they spent above 120 km, meant that space-based telescopes were necessary to build a more detailed understanding of the many known astrophysical sources of X-rays.

From the establishment of NASA, in 1958, the topics discussed in this thesis were at the forefront of space exploration. Exploration of planetary magnetospheres and X-ray astronomy - initially of the Sun and then objects further afield - were pioneered by satellites such as the Orbiting Geophyiscal Observatory (OGO), the Orbiting Solar Observatory (OSO) and the Orbiting Astronomical Observatory (OAO). The successes of the X-ray instrumentation on the OSO, lead the founding director of MSSL, Robert Boyd, to actively propose the inclusion of X-ray instrumentation on OAO-3 - Copernicus.

From the launch of the first dedicated X-ray observatory, pulsating emissions became a powerful probe for the exploration of astrophysical processes. The Uhuru satellite conducted a full sky survey from 2 to 20 keV, discovering more than 150 X-ray sources. Two of these sources (Cen X-3 and Her X-1) were found to pulse with periods of a few seconds (the rotation rate of a neutron star) and to intermittently dim for a few hours, which was later discovered to be caused by the occultation of their stellar partner.

1.3.3 The Search for X-rays from Jupiter

"The truth dazzles gradually or else the world would be blind."
— Emily Dickinson

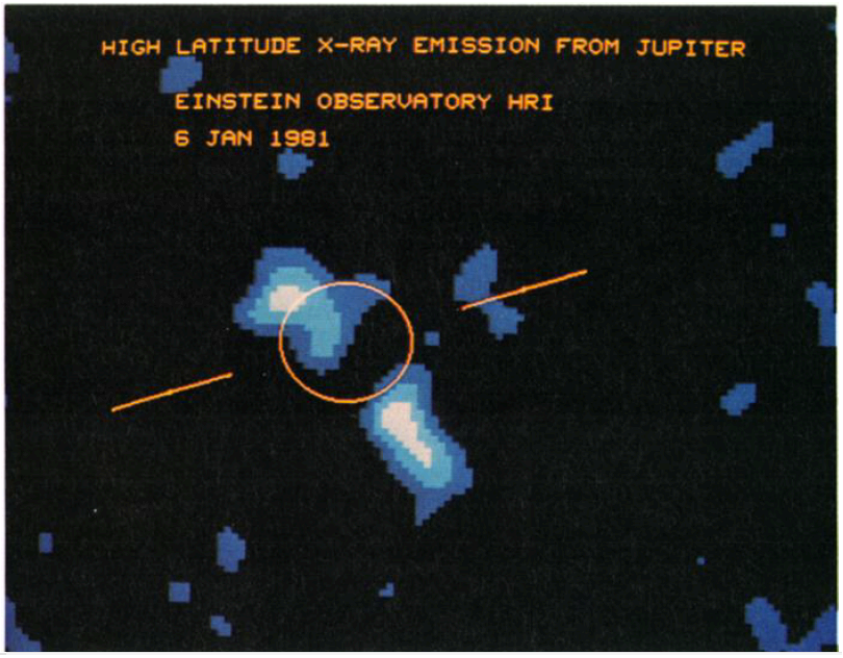

Figure 1.3: The first detection of X-rays from another planet - Jupiter's X-ray aurora as imaged by the Einstein Observatory in April 1979 and January 1981 (Metzger et al. 1983).

The search for X-ray emission from Jupiter began in 1962 by rocket (Fisher et al. 1964) and continued unsuccessfully by balloon (Edwards and McCracken 1967; Haymes et al. 1968; Hurley 1972). Expectations of bremsstrahlung X-ray emission from Earth's aurora continued to drive searches at Jupiter, with both the Copernicus (Vesecky et al. 1975) and Uhuru (Hurley 1975) satellites.

The Voyager spacecraft did not carry an X-ray detector, however, the Low Energy Charged Particle Experiment was sensitive to 14-31 keV photons and this allowed an upper limit to be placed on the Jovian X-ray emission from this band of 1.3 x 10^{-14} photons cm^{-2} s^{-1} keV^{-1} (Kirsch et al. 1981).

Finally, six months after the launch of HEAO-2 (the Einstein observatory), in April 1979, the first X-ray emissions from another planet were detected - Jupiter's X-ray aurora (Metzger et al. 1983) (see Fig. 1.3). This first observation allowed the authors to quantify the luminosity of the emissions - 4 x 10^9 W. Despite the relatively primitive spectral resolution, the instrument also allowed the authors to identify that the majority of the emission was unlikely to be produced by electron bremsstrahlung. Instead, they proposed that it was likely to be emission spectral lines from precipitating sulphur and oxygen ions with energies up to 4 MeV/nucleon. Limitations on spatial resolution

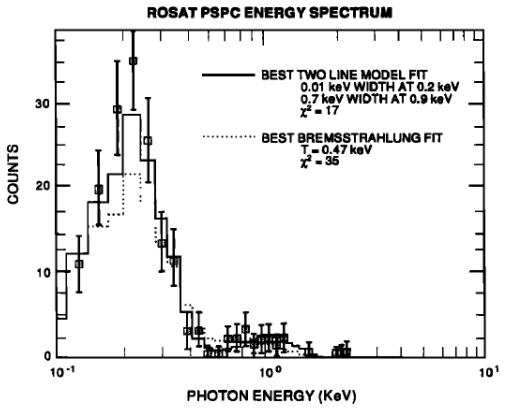

Figure 1.4: Combined ROSAT PSPC photon energy spectrum with model fits for a two spectral line model and a bremsstrahlung model (Waite et al. 1994).

Table 1.1: Table from Waite et al. (1994) showing the background subtracted net counts from the semicircular regions of integration for the Northern and Southern hemispheres for 6 short data segments over an 11h 36m window.

Start UT	Stop UT	Exposure Time	North Counts	South Counts	CML (°)
01:22:02	01:39:57	1075	14.75	4.75	91 ± 5
02:43:43	03:16:13	1950	40.28	8.28	145 ± 10
07:32:08	08:07:58	2150	19.49	6.49	321 ± 11
09:06:48	09:45:13	2305	13.87	6.87	18 ± 12
10:41:29	11:22:06	2437	22.35	5.35	76 ± 12
12:18:29	12:58:43	2414	22.44	7.44	128 ± 12

also inhibited a good understanding of the origins of the emission leading the authors to propose precipitation from the Io Plasma Torus.

Following the Einstein Observatory until the end of the 1990s, X-ray astronomy was largely dominated by small-scale complementary missions that aimed to probe differing properties of astrophysical X-ray sources. Missions like ESA's EXOSAT (1983-1986) laid the foundations for XMM-Newton, however, EXOSAT offered little directly to X-ray studies of Jupiter. Likewise, the Japanese GINGA satellite (1987-1991) lead to many important X-ray astronomy landmarks, but these are largely beyond the scope of this thesis.

1.3.4 Jovian X-ray Emissions: the ROSAT Era

Following the X-ray observations of 1981, X-ray studies of Jupiter lay dormant for a decade until April 1991, when the German Röntgen Satellite (ROSAT) presented the ideal instrument for more detailed X-ray studies of Jupiter.

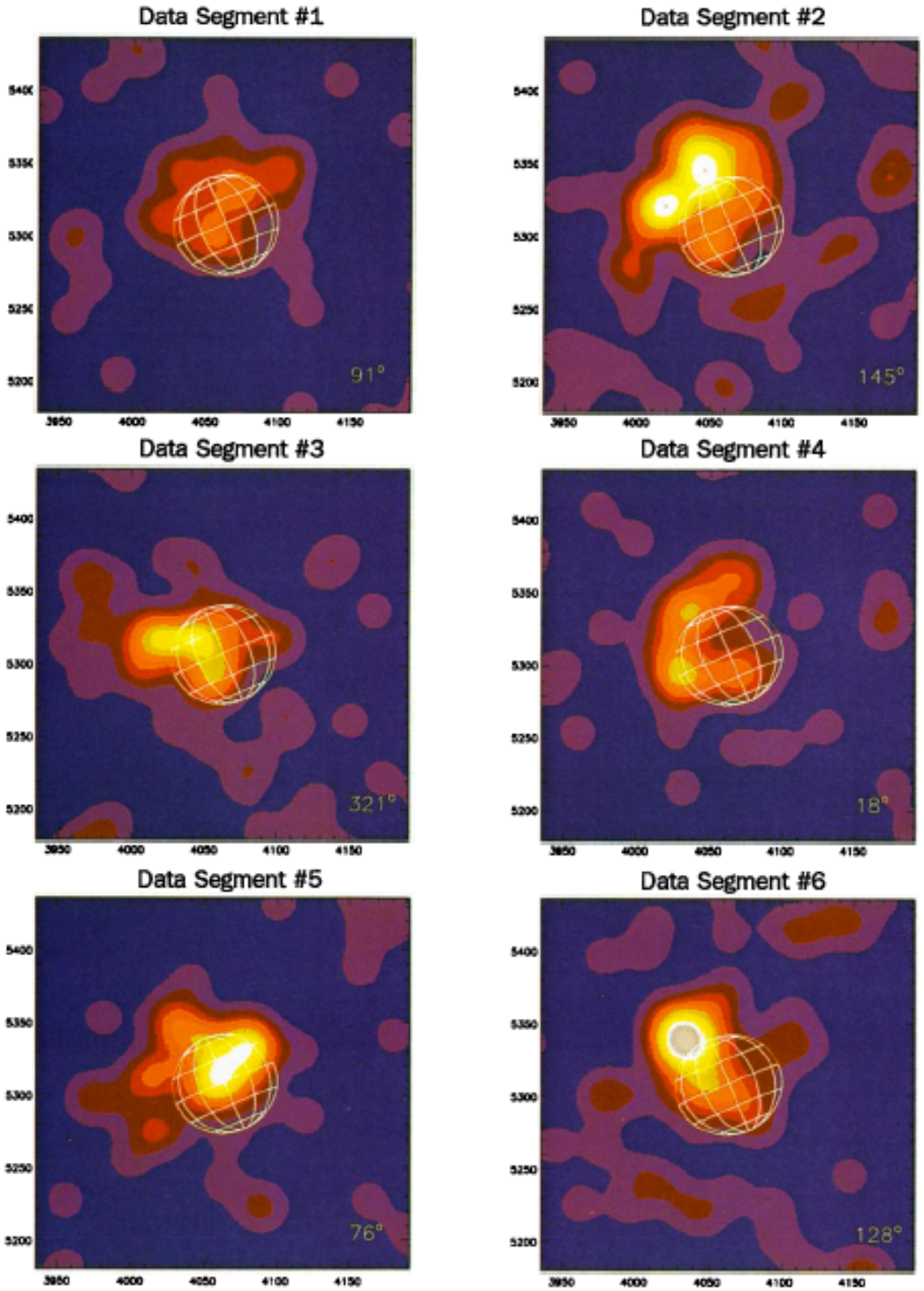

Figure 1.5: Six ROSAT HRI Images of Jupiter (shown in Table 1.1). The first evidence that Jupiter's X-ray aurora is temporally and rotationally modulated (Waite et al. 1994)).

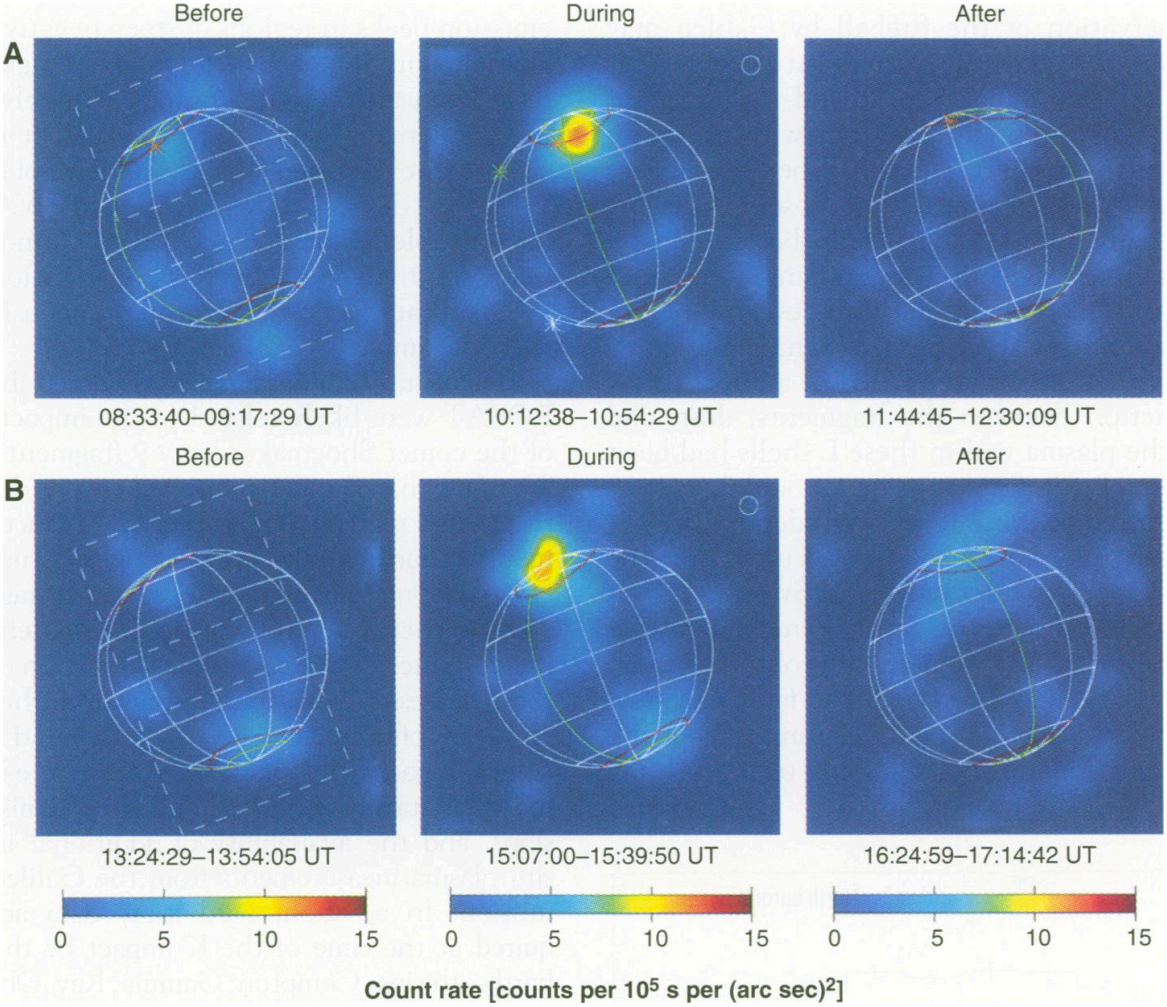

Figure 1.6: Jupiter X-ray images before, during, and after the (A) K and (B) P2 impacts from Comet Shoemaker-Levy 9. The absolute brightness scale is shown at the bottom. Contours showing the footprints of the lo plasma torus and the L = 30 R_J region are shown in red and yellow in the polar regions. The orange asterisk, when visible, shows the location of Io's Northern footprint. The green asterisk shows the magnetically conjugate region to the K impact site. The trajectory of the K fragment 3 minutes before impact are shown by a white line and asterisk, respectively. The small (3") circle in the upper right corner of the 'during' panels shows a conservative estimate for the ROSAT pointing uncertainty (Waite et al. 1995).

Waite et al. (1994) used the Position Sensitive Proportional Counter(PSPC) to confirm the earlier suggestions of Metzger et al. (1983) that the Jovian emissions were mostly produced by high charge-state ions (see Fig. 1.4) and that the energy of the emissions was between 1.3-2.1 x 10^9 W. They further used the High Resolution Imager (HRI) to take 6 ∼1000s observations over an 11 hour 36 minute window. This revealed that the X-ray aurora (like the UV aurora) was modulated by the planet's rotation (see Table 1.1 and Figure 1.5) and that there was some suggestion of a peak in the intensity around 180°. It also showed that the Northern X-ray aurora appeared to be brighter than the Southern X-ray aurora - a trend that has persisted in the following 26 years of observations.

Between the 16-22 of July 1994, the comet Shoemaker-Levy 9 crashed into Jupiter's upper atmosphere. At this time, Waite et al. (1995) observed X-ray flares in the aurora with ROSAT (see Fig. 1.6), but noted that it would be challenging for the comet to have communicated from its close radial location to the more distant regions field lines that the X-ray flares mapped to. They suggested that the interaction between dust fragments and magnetospheric plasma might be responsible.

Using the observations preceding Shoemaker-Levy 9, Waite et al. (1997), first identified Jupiter's X-ray disk emission as a distinct X-ray source from the auroral emissions. They suggested that the emission connected to regions of low surface field strength, where radiation belt particles could more easily precipitate into the loss cone (see Fig. 1.7). Gladstone et al. (1998) made further strides towards identifying the dominant source of the disk emission. They found that the emission declined from 1994-1996 (now known to be with solar cycle decline (see Fig. 1.29) and that the emission was always shifted to favour the sub-solar point, suggesting that the X-rays related to solar illumination of the Jovian disk. They connected this solar relation with heating of the thermosphere. However, they also noted that X-rays originated from low surface magnetic field strength at low latitudes and the greatest gradient in magnetic field strength at high latitudes.

In the 1990s, alongside the ROSAT observations of Jupiter, the mecha-

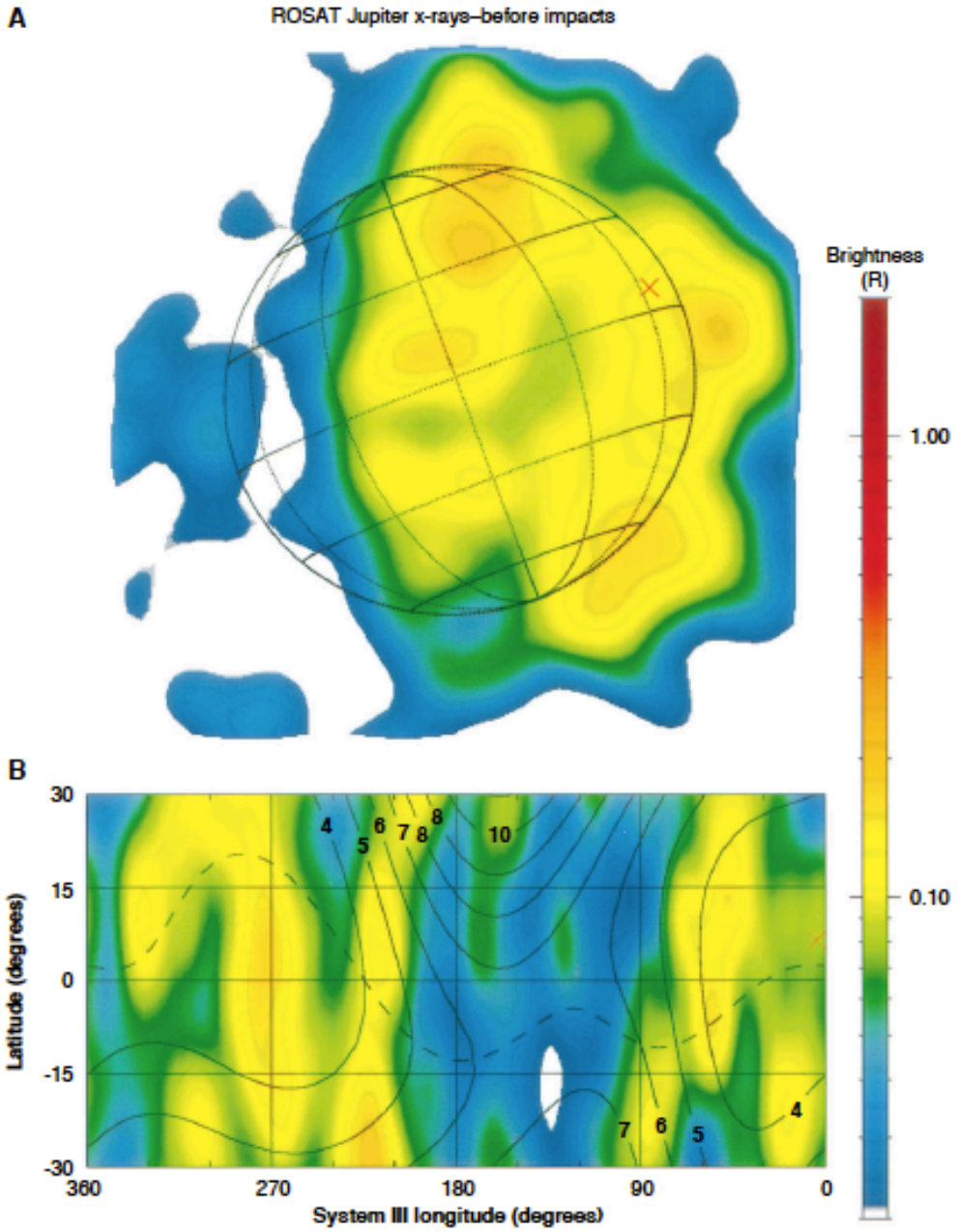

Figure 1.7: Waite et al. (1997): ROSAT HRI X-ray image of Jupiter from July 1994. Individual photons have been smoothed by the HRI point-spread function (PSF) and converted to brightness units overlaid with a Jupiter 30° latitude-longitude graticule. B) HRI x-ray map of Jupiter, produced with the data from (A) mapped into System III longitude and latitude. Contour lines show O6 model surface magnetic field strength (in gauss). The dashed line indicates the magnetic dip equator. The red 'x' marks the entry site of the Galileo probe. In both (A) and (B), false colour indicates emission brightness in Rayleighs.

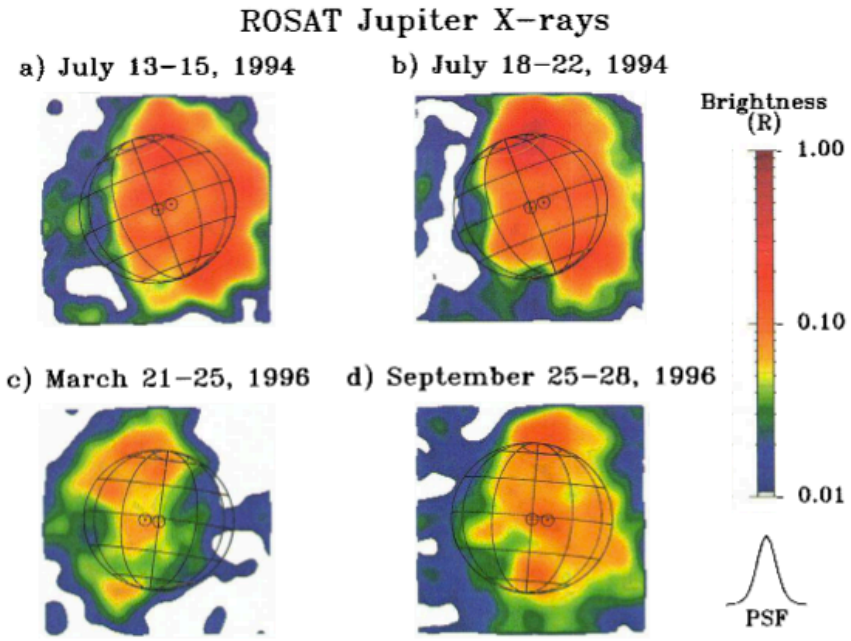

Figure 1.8: From Gladstone et al. (1998): Local time dependence of Jupiter's X-ray emission. The images show that the disk emission from Jupiter depends upon the location of the sub-solar point (circle with dot) relative to the sub-observer point (circle with cross) and that it peaks preferentially in the direction of the sub-solar point. These also show that the disk emission reduced from 1994 - 1996.

nism responsible for the ion emission of the Jovian X-rays was also correctly identified as charge exchange. (Cravens et al. 1995).

1.3.5 Jovian X-ray Emissions Post-2000

"Ultimately, the 'reality' of history is irrelevant. The train of thought it gives you is really the only concrete thing"

— Matt Kindt, *Mind MGMT*

1.3.5.1 Jupiter's X-ray Aurora

The launch of Chandra and XMM-Newton in 1999 brought a revolution in X-ray observation capabilities. These highly complementary instruments introduced significant improvements over their predecessors, with Chandra providing high spatial resolution (0.5"), XMM-Newton offering high spectral resolution (E/ΔE $\sim$ 200-800) and both providing high time resolution (<3s).

Both Chandra and XMM-Newton time-tag each X-ray photon, which, particularly for Chandra's high spatial resolution, allows X-ray emissions to

be connected with the Jovian latitude and longitudes from which they originate. Unlike for Earth, where observable surface features provide unique ways of identifying latitude-longitude coordinate locations, Jupiter's solid surface is not observable and its layers of cloud rotate around the planet at different rates. In order to apply a consistent coordinate reference frame to observations, the left-handed S3 coordinate system is often used. This coordinate system rotates with Jupiter's 9.925-hour rotation, with the 0∘ longitude line defined relative to Earth in 1965.

In December 2000, the first Chandra HRC X-ray observations of Jupiter revealed several surprising characteristics about the X-ray aurora (Gladstone et al. 2002). Jupiter's X-ray aurora was concentrated into a hot spot (see Fig. 1.9) that was fixed in S3 coordinates. Contrary to previous ideas, this meant that the soft X-ray aurora did not map to the IPT, but instead was poleward of Jupiter's main auroral oval and thus magnetically mapped beyond the middle magnetosphere. This raised new challenges in explaining the ion precipitation and introduced the possibility that the ions might precipitate directly from the solar wind. In addition, this hot spot was found to pulse with a characteristic ∼45 minute period (see Fig. 1.9). At the time, Cassini was upstream and did not detect a similar period in the solar wind, but radio bursts and in-situ particle data had detected this period before, particularly during the 1992 Ulysses fly-by (MacDowall et al. 1993).

Elsner et al. (2005) utilised Chandra's ACIS instrument to follow-up these observations in February 2003. For these observations, they found that while the aurora pulsed, the periodicity was not-regular across four observations but exhibited fluctuations between 20-60 minutes. They also found that during a coincident Hubble Space Telescope observation a UV auroral flare coincided with a brightening of the X-ray aurora (see Fig. 1.10).

In addition to the heightened spatial resolution, the new generation of X-ray telescopes brought with them a dramatic improvement in spectral resolution (up to $E/\Delta E \sim$ 200-800). Elsner et al. (2005) and Branduardi-Raymont et al. (2004) utilised this for Chandra and XMM-Newton respectively to identify the precipitating particles generating the X-ray emission. These observa-

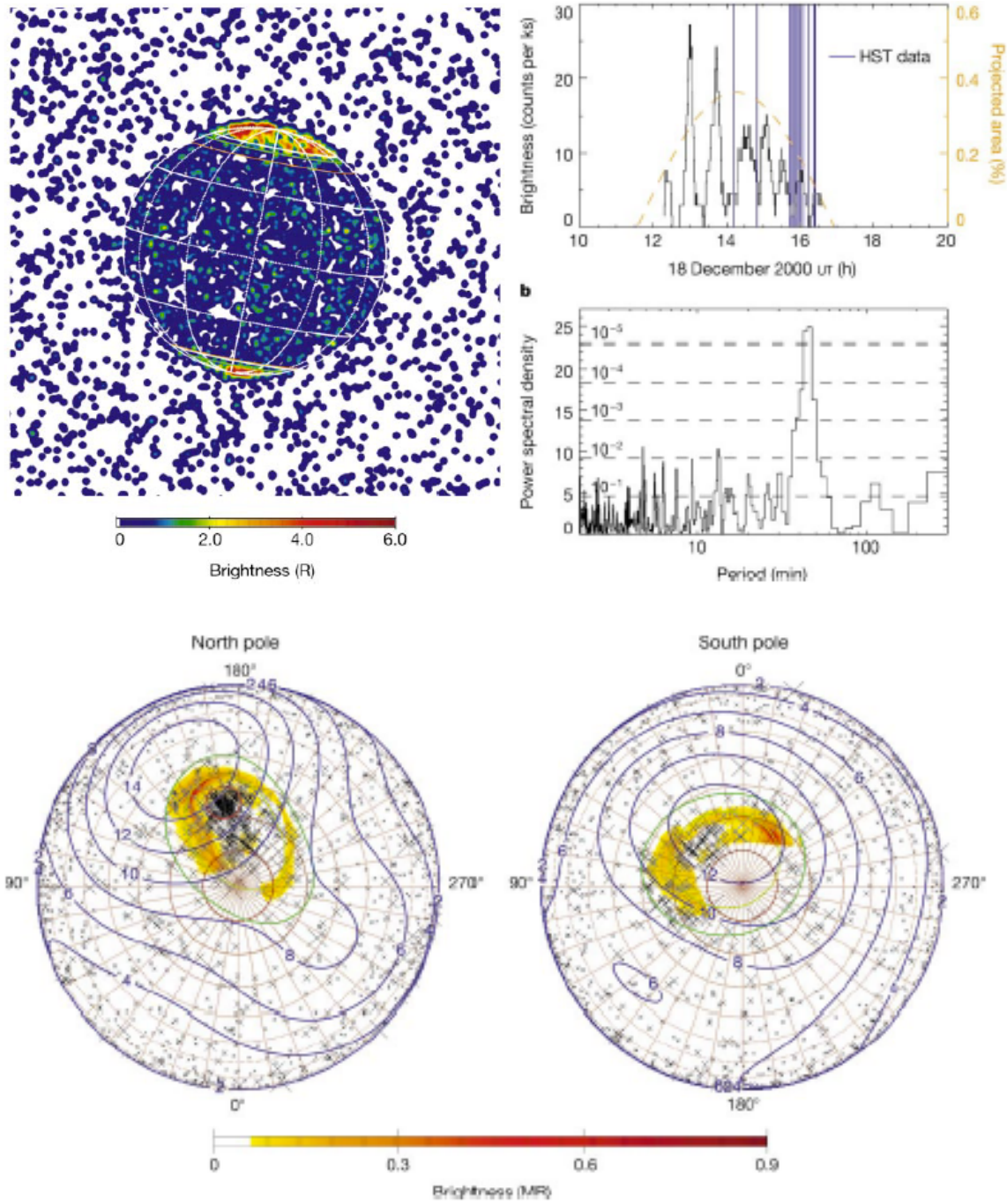

Figure 1.9: From Gladstone et al. (2002): Upper left: Chandra HRC Image of Jupiter overlaid with 30 ° by 30 ° latitude-longitude grid. Upper Right: Lightcurve and Power Spectral Density (PSD) Plots showing the characteristic 45 minute periodic pulsations. Dashed lines on the Fourier-transformed PSD show the probability of chance occurrence of the period from Leahy et al. (1983). Lower: Polar projections onto the North and South Pole of Jupiter showing the UV emission (orange) and the distribution of X-ray photons (black crosses), which are concentrated into a hot spot for the North. Contours show the VIP-4 model (Connerney et al. 1998) surface magnetic field strength in Gauss (blue) and Io's footprint (green). Lines of longitude radiate from the poles (centre) in increments of 10 °, while 10 ° increments in latitude are shown as concentric circles.

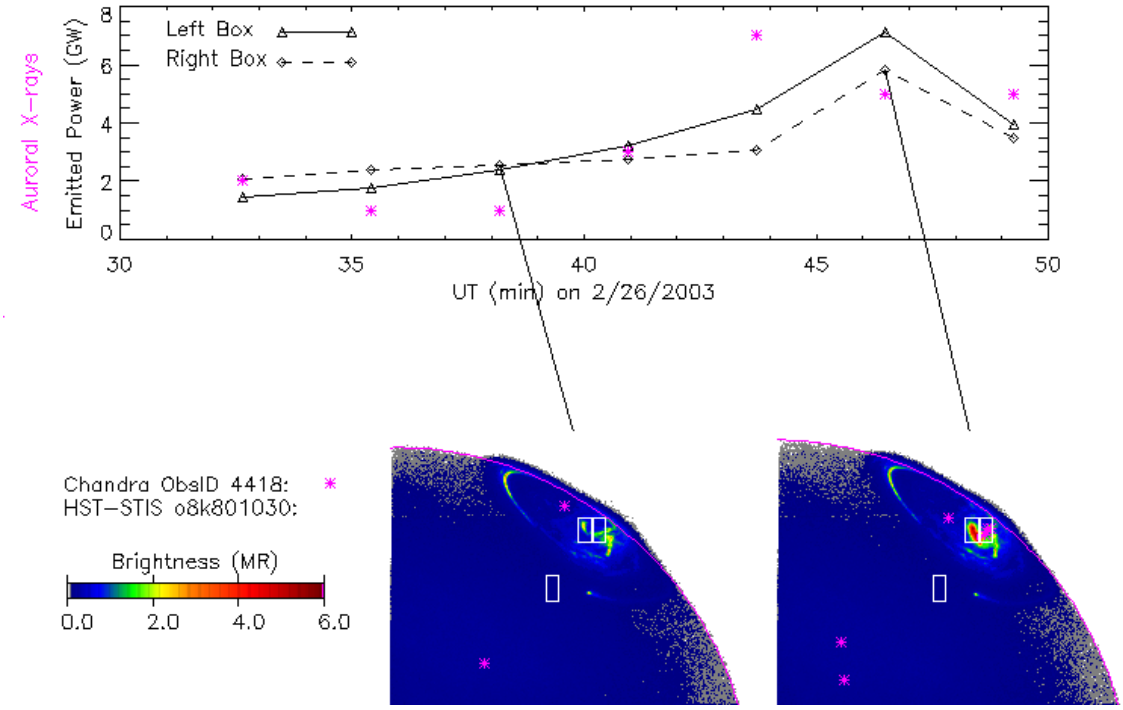

Figure 1.10: Simultaneous Chandra and Hubble Space Telescope Images of a Jovian Auroral Flare from 26 Feb 2003 (Elsner et al. 2005). Top: FUV (black) and X-ray (purple) light curves. Bottom: two HST-STIS image subframes showing an FUV flare in Jupiter's northern aurora coincident with X-ray brightening (purple crosses). The FUV light curves are for the left and right subregions of the aurora shown in the HST-STIS images, while the X-ray light curve includes the entire aurora.The average number of X ray counts per 144 s over a 2 hour span containing the flare is 1.3463.

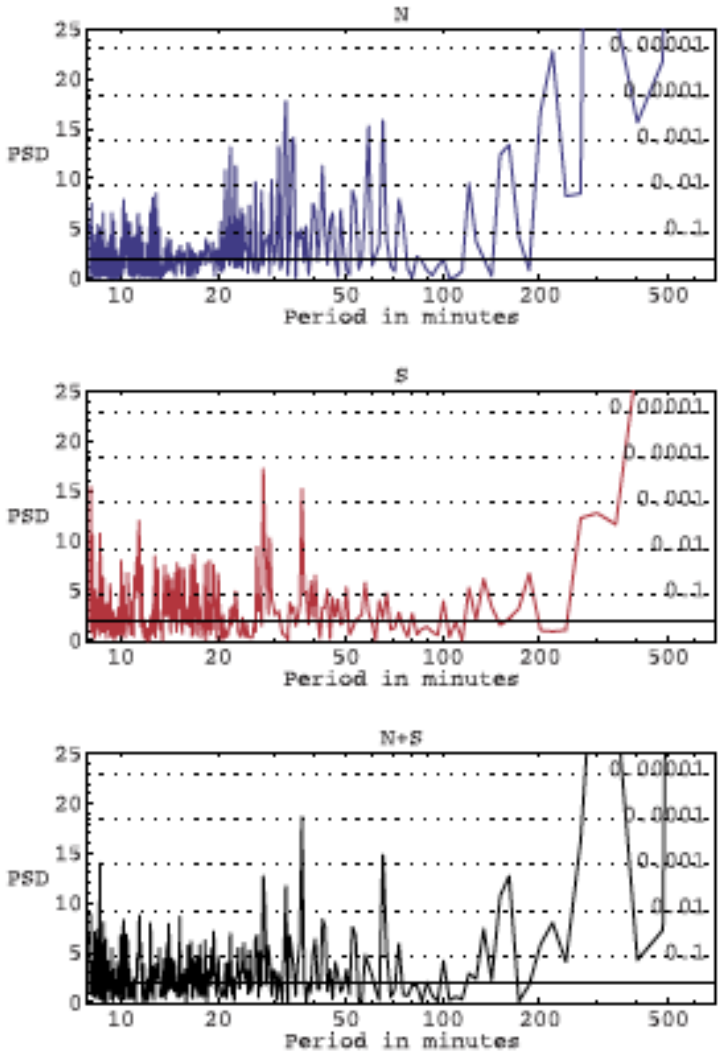

Figure 1.11: From Elsner et al. (2005): Power spectral density (PSD) versus period (in min), computed from unsmoothed 4-min binning of northern (top), southern (middle), and sum of the northern and southern (bottom) auroral zones. The solid line shows the expectation value for a steady source with Poisson statistics. The dotted lines show the single period probabilities of chance occurrence as labeled on the right.

tions confirmed high-charge state oxygen ions (e.g. precipitating $O^{7+,8+}$) were one of the key sources of the X-ray emission (e.g Fig 1.12, Table 1.3). Fitting the spectra between 0.2-0.45 keV lead to conflicting results: a fit to sulphur ions was preferred for the Chandra spectra, but a fit to Carbon lines was preferred for the XMM-Newton Epic-PN spectra. Differentiating between carbon and sulphur emissions is important since it permits us to distinguish the relative contributions of solar wind precipitation (carbon and oxygen) compared with the contribution of magnetospheric precipitation (sulphur and oxygen).

High charges states of carbon (e.g. C^{5+}) or oxygen (e.g. O^{7+}) exist in the solar wind. However, their densities are so low that MA currents would be required in order to increase their fluxes into the ionosphere to produce the observed X-ray signatures (Cravens et al. 2003; Bunce et al. 2004). In this instance, X-ray emission from solar wind precipitation should also be accompanied by high intensity UV emissions from the precipitating protons, which have solar wind densities 1000s of times larger than the high charge-state ions, but emissions of the appropriate UV intensities is very rarely observed (Cravens et al. 2003).

While producing the observed X-ray emissions from solar wind ions presents problems, producing the observed X-rays from Jupiter's magnetospheric plasma also has significant challenges. The Jovian outer magnetosphere is dominated by low charge-state ions. Typically, outer magnetosphere oxygen will have energies of 2 keV and charge states of O^{++}) (Bagenal 1994a). In order to generate the high charge states observed in the X-ray spectra (e.g. O^{7+}), these ions would need to be accelerated to energies that are sufficient to strip electrons from O^{++} when it collides into Jupiter's atmosphere. Cravens et al. (2003) suggest that ions would require an acceleration process that gave them tens of MeV of energy in order for magnetospheric plasma to produce the observed X-rays. The atmospheric and magnetospheric processes that could produce the X-ray signatures are discussed in detail in sections 1.3.6 and 1.8. Distinguishing between carbon and sulphur (or the relative contributions of each) will help to address fundamental questions about the extent to which rapidly rotating planets, such as Jupiter, are open to the solar wind and the

types of current systems and energisation that such environments produce.

Insufficient spectral resolution between 0.2-0.45 keV has thus far inhibited distinguishing between carbon and sulphur species, although it is clear that there is significant X-ray emission from spectral lines in this region. Hui et al. (2010) also attempt to differentiate the species through spectral modelling. They find that the majority of spectra are best fit with sulphur, however there are some spectra that are better fit with carbon lines. They also note that from observation-to-observation and pole-to-pole (e.g. Fig 1.13 shows pole-to-pole/observation-to-observation variation) the X-ray spectra varies significantly. Elsner et al. (2005) provide a valuable table of likely transitions above 0.299 keV, which we show here in table 1.2.

Throughout this thesis we fit spectra in a similar way to that conducted by Branduardi-Raymont et al. (2004, 2007a). We iterate fits of combinations of Gaussian lines (defined by parameters for line energy, full width half maximum and flux) along with continuum models (defined by their energy/temperature and flux). We then test the goodness of fit of these combinations of model parameters against the data with a χ^2 test:

$$\chi^2 = \sum_{i=1}^{k} \frac{(x_i - m_i)^2}{m_i} \tag{1.19}$$

where χ^2 is the goodness of fit estimator, x_i is a data value measured by Chandra or XMM-Newton and m_i indicates the model value. A $\chi^2 \sim 1$ indicates an excellent fit. χ^2 significantly larger than 1 indicates a poor match between the model and the data, while χ^2 less than 1 generally indicates that the errors are large and the model is over-fitting the data. χ^2 values of less than 1 are often measured for Jovian X-ray emissions. This is because Chandra and XMM-Newton contribute very little instrumental noise and Jupiter blocks the cosmic background noise, while the statistical errors, calculated by Poisson statistics, on the X-ray data are comparatively large.

Barbosa (1992) had previously proposed that bremsstrahlung emission associated with energetic electron precipitation was responsible for the Jovian X-ray emission. However, the studies by Metzger et al. (1983) and Waite et al.

Table 1.2: Jovian X-ray Ion Spectral Line Transitions from Elsner et al. (2005): showing possible Sulphur, Carbon, and Oxygen Transitions in the 290-900 eV Region of the Auroral Spectrum

Energy /eV	Species/Charge-state	Transition
299	CV	$1s2s \rightarrow 1s^2$
304-308	CV	$1s2p \rightarrow 1s^2$
314	SIX	$2p34d \rightarrow 2p^4$ ($^3D \rightarrow {}^3P$)
316	SXI	$2p3d \rightarrow 2p^2$
336	SX	$2p24d \rightarrow 2p^3$ ($^4P \rightarrow {}^4P$)
339-340	SXII	$3d \rightarrow 2p(^2P \rightarrow {}^2P)$
348	SXIII	$3s \rightarrow 2p$
354	CV	$1s3p \rightarrow 1s^2$
367	CVI	$2p \rightarrow 1s$
371-378	CV	$1s4p,5p \rightarrow 1s^2$
380	SXIV	$3s,3d \rightarrow 2p$
435	CVI	$3p \rightarrow 1s$
459	CVI	$4p \rightarrow 1s$
561	OVII	$1s2s \rightarrow 1s^2$ ($^3S \rightarrow {}^1S$)
568	OVII	$1s2s \rightarrow 1s^2$ ($^3P \rightarrow {}^1S$)
574	OVII	$1s2p \rightarrow 1s^2$ ($^1P \rightarrow {}^1S$)
654	OVIII	$2p \rightarrow 1s$
665	OVII	$1s3p \rightarrow 1s2$
698	OVII	$1s4p \rightarrow 1s^2$
713	OVII	$5p \rightarrow 1s$
774	OVIII	$3p \rightarrow 1s$
817	OVIII	$4p \rightarrow 1s$
836	OVIII	$5p \rightarrow 1s$

Table 1.3: Table from Branduardi-Raymont et al. (2007a) showing Best fit parameter oxygen lines in the RGS spectrum of Jupiter. [a] Wavelength of the emission line in Angstroms (fixed in the fits, except for the broad components). [b] Energy of the emission line in keV (fixed in the fits, except for the broad components). [c] Total flux in the line in units of 10^{-6} ph cm^{-2} s^{-1}. [d] FWHM width of the Gaussian model in Angstroms (fixed in the fits, except for the broad components). [e] Resonance line of the triplet. [f] Intercombination line. [g] Forbidden line.

Line	Wavelength[a]	Energy[b]	Flux[c]	FWHM[d]
OVII(r)[e]	21.602	0.574	$1.5^{+2.3}_{-1.5}$	0.1
OVII(i)[f]	21.807	0.568	$0.2^{+2.9}_{-0.2}$	0.1
OVII(f)[g]	22.101	0.561	$2.0^{+2.1}_{-1.9}$	0.1
OVIIILyα	18.97	0.654	0+0.4	0.1
OVIIILyβ	16.006	0.775	$0.5^{+0.6}_{-0.5}$	0.1
OVIIILyγ	15.176	0.817	$3.6^{+0.9}_{-0.9}$	0.1
OVIIILyδ	14.821	0.836	$0.5^{+0.8}_{-0.5}$	0.1
OVIIHeβ	18.627	0.666	$0.9^{+0.8}_{-0.9}$	0.1
OVIIHeγ	17.768	0.698	$1.1^{+0.6}_{-0.6}$	0.1
OVIIHeδ	17.396	0.713	$0.9^{0.6}_{0.6}$	0.1
OVII broad	21.8 $\pm$ 0.08	0.569 $\pm$ 0.002	$20.6^{+4.9}_{-6.7}$	$0.68^{+0.20}_{-0.15}$
OVIII broad	$19.26^{+0.14}_{-0.2}$	$0.644^{+0.006}_{-0.005}$	$6.0^{+3.1}_{-2.3}$	$0.71^{+0.34}_{-0.3}$

(1988, 1992) showed that it was not feasible for bremsstrahlung to produce all of the observed emission, since this would require 10^{15} W of electron power, which is far beyond the 10^{13} - 10^{14} W implied by UV observations. While most of the auroral X-ray photons were found to relate to charge exchange at soft energies (below 2 keV), Branduardi-Raymont et al. (2007a) found that the auroral spectra sometimes also has a hard X-ray component (above 2 keV) that is well fitted by a bremsstrahlung continuum with a temperature of 0.3 to a few 10s of keV. This hard X-ray component of the spectra was found to vary significantly over timescales of days and they note that it particularly increased during a period of heightened solar activity. At this time, the variation in the hard X-rays appeared to be independent of the soft X-ray variation. They also measured the doppler broadening of the ion charge exchange spectral lines and calculate a velocity of a few thousand km/s for the precipitating ions - in line with energies of 10s of MeV that are needed to produce the X-ray aurora (Cravens et al. 1995, 2003; Kharchenko et al. 2006, 2008; Ozak et al. 2010, 2013; Cravens and Ozak 2012)

Branduardi-Raymont et al. (2007a) also revealed another intriguing feature of the Jovian X-ray Aurora. Figure 1.13 shows that the soft X-rays (from

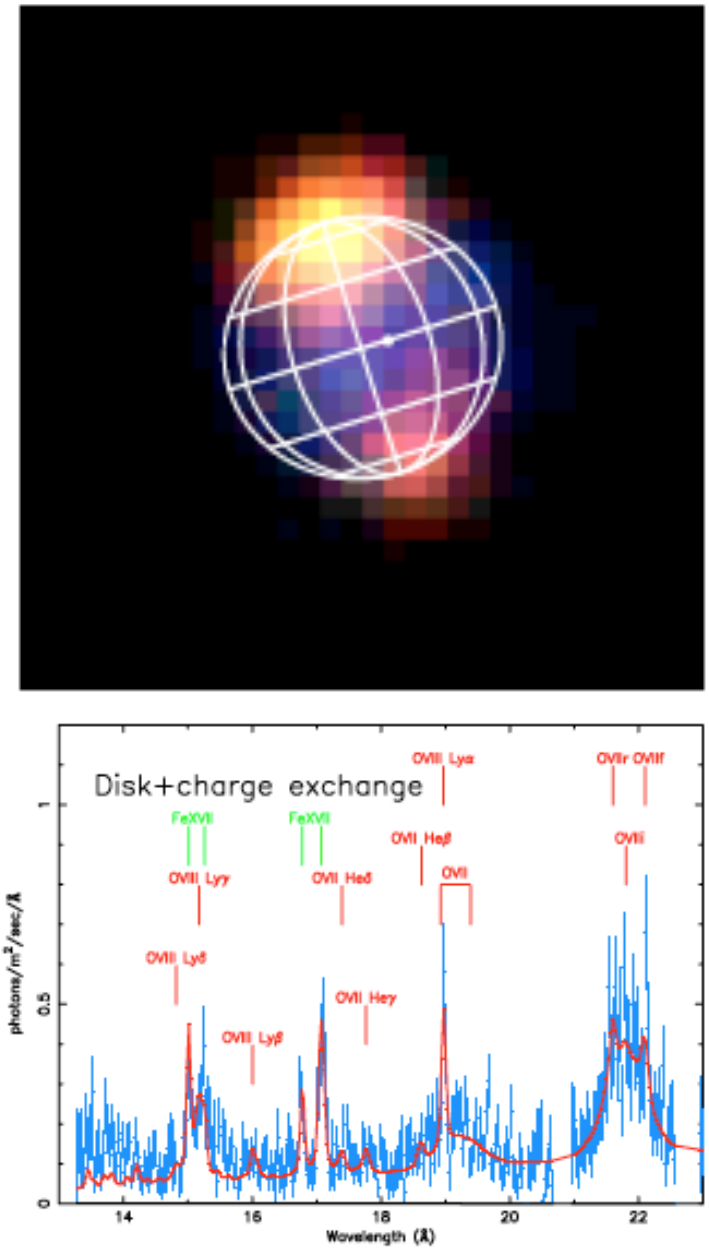

Figure 1.12: Top from Branduardi-Raymont et al. (2004): Smoothed EPIC-pn image of Jupiter (2.9 pixels); North is to the top and East to the left. Red: 0.2-0.5 keV, Green: 0.5-0.7 keV, Blue: 0.7-2.0 keV. The circular mark indicates the sub-solar point; the sub-Earth point is at the centre of the graticule. Bottom from Branduardi-Raymont et al. (2007a): Combined RGS1 and 2 spectrum of Jupiter (blue crosses) with the best fit model including both a charge exchange model to account for the aurora and a model of typical solar X-ray lines to account for the Jovian disk emission.

ion precipitation and charge exchange) are brighter in the Northern regions. This supports the findings of Waite et al. (1994) that the Northern aurora is brighter than the Southern aurora. However, these observations show that hard X-ray emission from precipitating electrons is brighter in the South (e.g. 3-5 keV and 5-10 keV emissions on Fig. 1.13). The authors explain that this is due to the preferential emission of bremsstrahlung perpendicular to the precipitation direction, so that while the auroral oval is viewed closer to the precipitation direction for the North, it is on the limb of the disk for the South. Another explanation may be an inter-hemispheric current that flows upwards from the South and downward in the North (see Chapter 3).

Following the detection of a hard X-ray component to the spectra, Branduardi-Raymont et al. (2008) utilised the Chandra ACIS and HST observation initially published in (Elsner et al. 2005) to identify the origins for this hard X-ray component of the aurora. Figure 1.14 demonstrates that the hard X-rays are generally co-located with the UV main oval and that the soft X-rays typically occur poleward of this. These hard X-rays correspond to $\sim$ 45 MW of emitted power, while the soft charge exchange X-rays account for $\sim$ 230 MW of emitted power. They note that the energies of the hard X-rays are consistent with those of the precipitating electron population producing the FUV emissions and that it is likely to be the same electron population producing the hard X-ray bremsstrahlung emission and the UV main oval.

The auroral X-ray pulsations were again not found to exhibit a regular timescale pulsation by Branduardi-Raymont et al. (2007a). However, we note that it is more challenging to identify periodic behaviour with XMM-Newton since the low spatial resolution introduces contamination from the Jovian equatorial region into the observed auroral emission. Additional noise has also been introduced by the inclusion of time intervals when the Northern (or Southern) aurora is not in view. These add challenges to tests for regular periodic behaviour.

Likewise, for Elsner et al. (2005) and Figure 1.11, it is possible that the physical process that generate the regular period may produce different time durations between each pulse. For example, changes in the scale of the Jo-

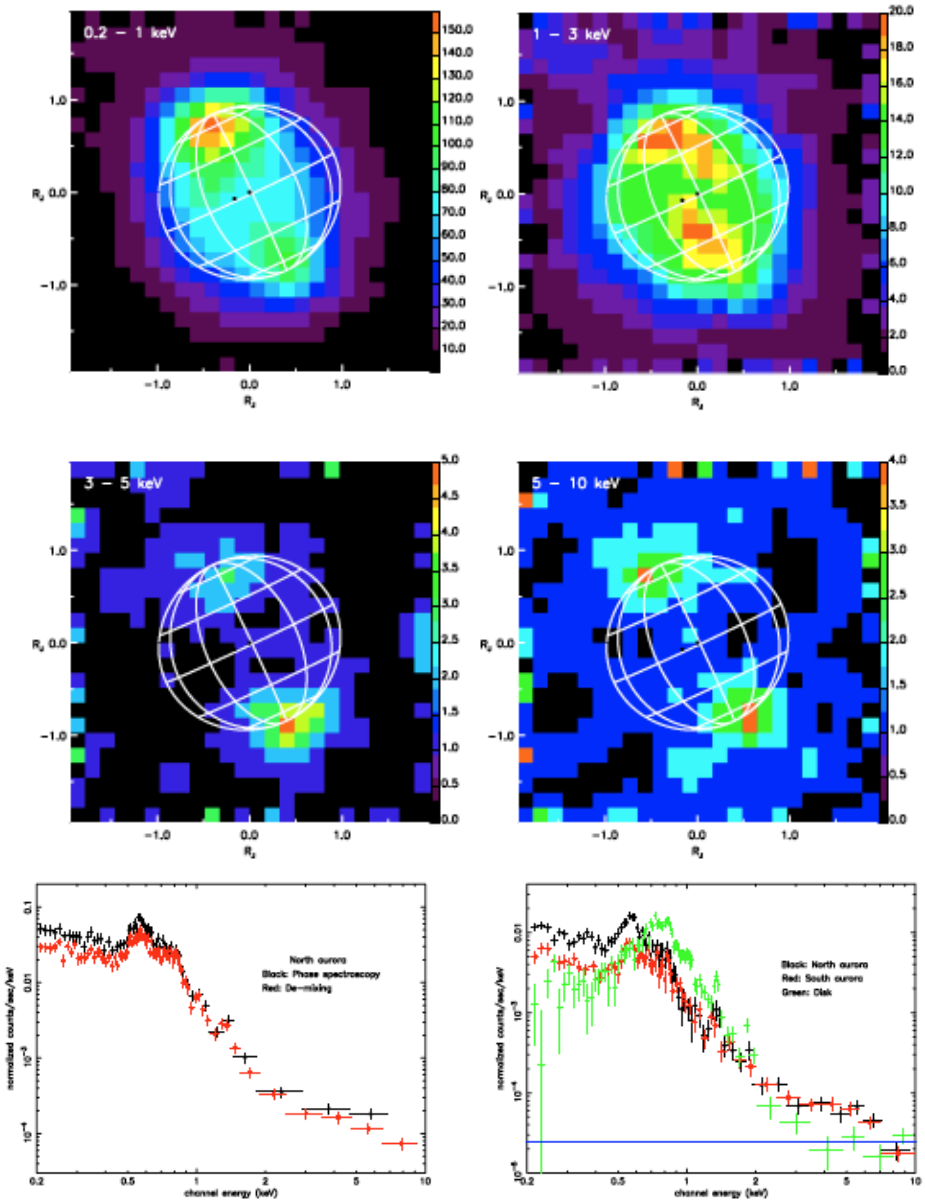

Figure 1.13: From Branduardi-Raymont et al. (2007a): Top: Smoothed XMM-Newton EPIC images of Jupiter in different bands extending to higher energies: from top left, clockwise: 0.2-1, 1-3, 5-10 and 3-5 keV. The colour scale bar is in units of EPIC counts. Lower left: Comparison of the Nov. 2003 EPIC-pn spectra of the North aurora obtained with two different extraction techniques: 'Phase spectroscopy' (black) and 'De-mixing' (red). The overall shapes of the spectra are very similar, while the flux in the de-mixed spectrum is lower, as expected. Lower right: From Branduardi-Raymont et al. (2004): Combined Nov. 2003 EPIC spectra of the North (black) and South (red) aurorae, and of the low latitude disk (green) spectrum. Differences in spectral shape between auroral and disk spectra are clear. The presence of a high energy component in the spectra of the aurorae is very evident, with a substantial excess relative to the disk emission extending to 7 keV. The horizontal blue line shows the estimated level of the EPIC particle background.

vian magnetosphere or the location of the mirror point/resonant cavity would alter the timescale between each observed pulse. Further analysis of whether the time between pulses lengthens/shortens might provide information on the nature of the driver process.

1.3.5.2 Jupiter's Equatorial X-ray Emission

Following the hints at local time dependences and a possible relationship of the equatorial emissions to magnetic field strength detected with ROSAT (Gladstone et al. 1998; Waite et al. 1997), Chandra and XMM-Newton provided new insights into the source for this 0.4-0.6 GW of X-ray emission (Branduardi-Raymont et al. 2007b).

Maurellis et al. (2000) utilised the ROSAT data to make predictions for what could be observed from the Jovian disk by Chandra. They found that in addition to the ion precipitation previously discussed, the Jovian X-ray emission from the disk was also likely to be produced by solar photons. They calculated that 90% of solar reflected emission would be from elastic scattering of solar photons by atmospheric neutrals (particularly H_2) and the other 10% would be soft X-ray emission from fluorescence of the carbon K-shell in methane below the homopause.

Cravens et al. (2006) built on this work to show that the majority of Jupiter's disk emission was produced by reprocessed solar photons. They showed that differing atmospheric abundances with altitude lead to different albedos and different preferences between fluorescence and Thomson scattering for Venus, Mars (Cravens and Maurellis 2001), Jupiter and Saturn (Cravens et al. 2006). At Jupiter the preference remained towards elastic scattering.Bhardwaj et al. (2005, 2006); Branduardi-Raymont et al. (2007b) showed that the X-ray spectra from the equatorial regions on Jupiter replicated the solar X-ray spectra very well (e.g. Figure 1.15). Further, they showed that the solar X-ray light curves exhibit day-to-day variability that is very well correlated to the solar X-ray variability (as measured by the TIMED/SEE and GOES satellites). For instance, solar X-ray flares triggered corresponding brightening on the Jovian disk and the disk emission brightened/dimmed with

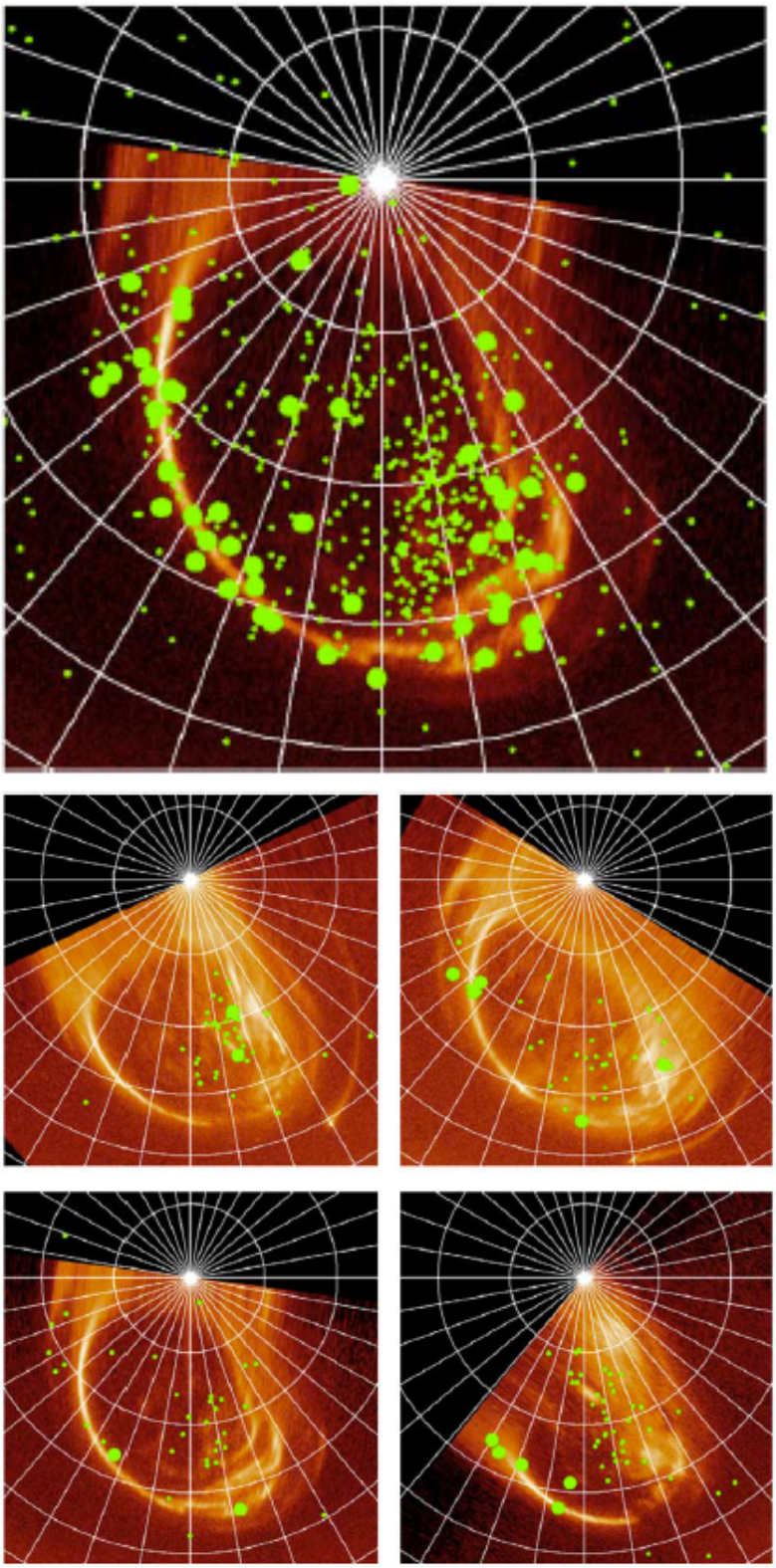

Figure 1.14: From Branduardi-Raymont et al. (2008): Top: Polar projection of one Hubble STIS FUV image of Jupiter's Northern aurora taken on 24 February 2003; overplotted are all the X-ray photons detected by the CXO during a Jupiter rotation simultaneous with the HST observation. Bottom: 4 Polar projections as in, but for X-ray photons collected by the CXO during individual orbits of HST; the X-ray events are overplotted on the first of several STIS exposures obtained during each HST orbit. Small green dots: photons with energies of 2 keV or less. Large green dots: photons with energies of 2 keV or greater. The 10° spaced grid is fixed in System III with 180° toward the bottom and 90° to the right.

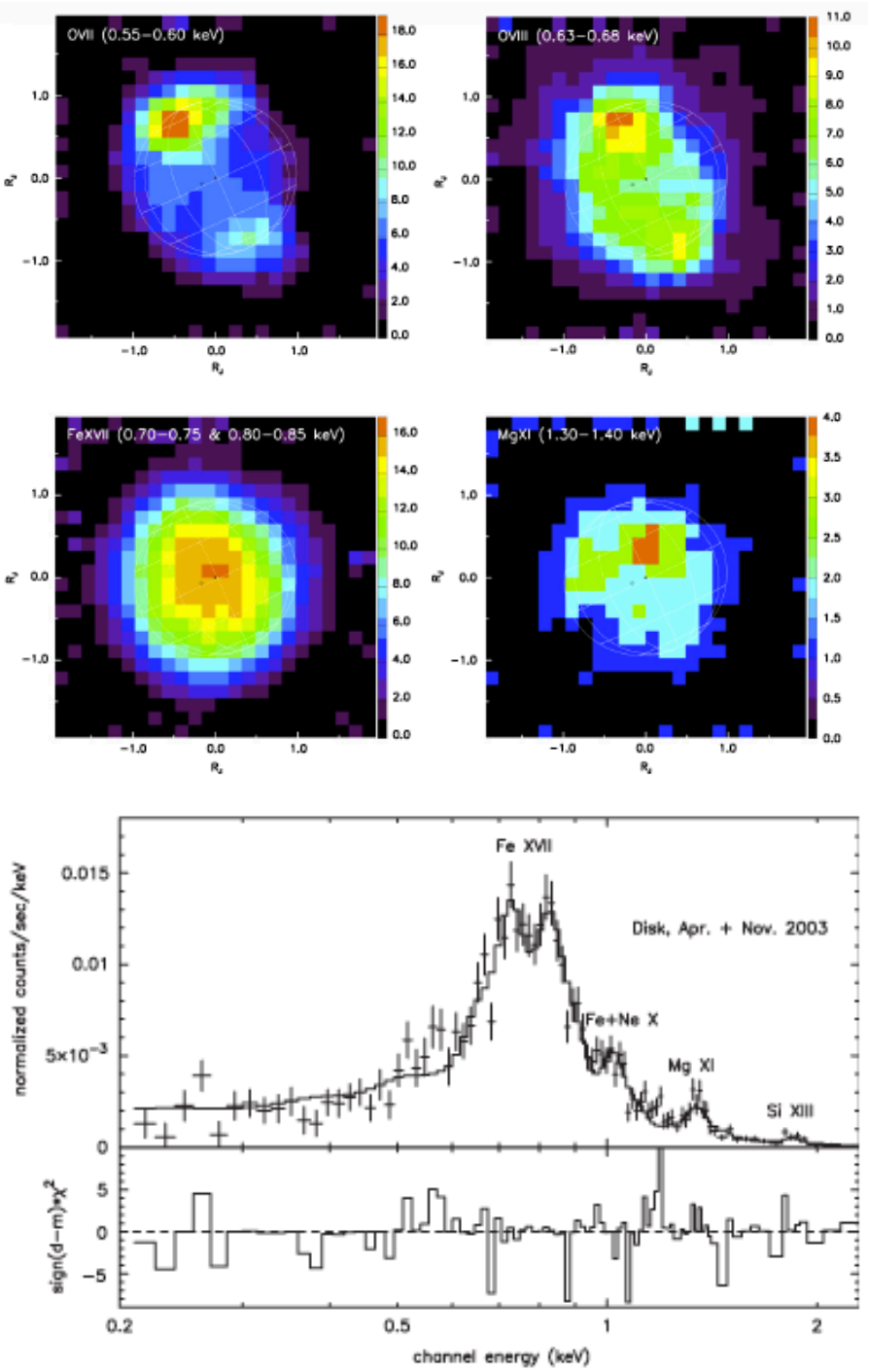

Figure 1.15: XMM-Newton EPIC images of Jupiter in different energy regimes and combined disk spectrum from Branduardi-Raymont et al. (2007b): Upper Four Panels: Smoothed XMM-Newton EPIC images of Jupiter in narrow spectral bands indicated on image. The colour scale bar is in units of counts. A graticule showing Jupiter's orientation with 30° intervals in latitude and longitude is overlaid. The circular mark indicates the subsolar-point; the sub-Earth point is at the center of the graticule. Lower: Jupiter's low-latitude disk spectrum (crosses) and best fit model (histogram) for the XMM-Newton EPIC observations in April and November 2003 combined. At the bottom the contribution to the χ^2 for each spectral bin is plotted. Labels indicate the locations of the emission features from Fe XVII at 0.7-0.8 keV and of the blend of Fe XVII, FeXXI and Ne X at 1 keV, all due to the coronal plasma spectral component. Additional line emission from Mg XI and Si XIII is also indicated.

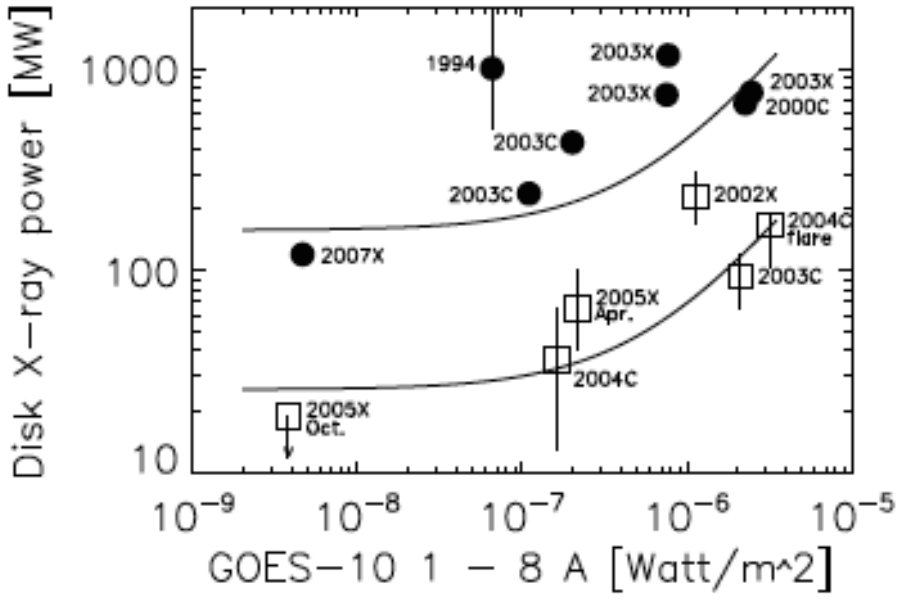

Figure 1.16: Jupiter and Saturn's disk X-ray flux against solar X-ray flux from Branduardi-Raymont et al. (2010): Saturn's (open squares) and Jupiter's (filled circles) disk 0.2-2.0 keV X-ray power plotted against the 1.5-12.4 keV solar X-ray flux measured by the GOES-10 satellite, for XMM-Newton (X), Chandra (C) and ROSAT (1994) observations. The continuous lines are linear square fits to each dataset.

corresponding solar X-ray variation throughout the solar cycle.

Careful studies of the Chandra data did reveal some small but statistically significant dependence on the surface magnetic field strength, suggesting that while fluoresced and scattered solar photons are the dominant disk emission source, there may be a secondary emission source in the form of precipitation from the radiation belts at low latitudes (Bhardwaj et al. 2006).

1.3.5.3 X-ray detection of the Galilean Satellites, IPT and Radiation Belts

Prior to the discovery of the X-ray hot spot with the observations in December 2000, Chandra ACIS observed Jupiter in November 1999. This revealed that both Io and Europa could be detected by their X-ray emissions, with luminosities of a few MW (Elsner et al. 2002) (see Fig. 1.17). The satellite spectra predominantly covered the band between 0.25-1.0 keV, which suggested that the X-ray emissions from the moons could be produced by the impact of iogenic magnetsopheric ions with the satellites surfaces. There were also hints

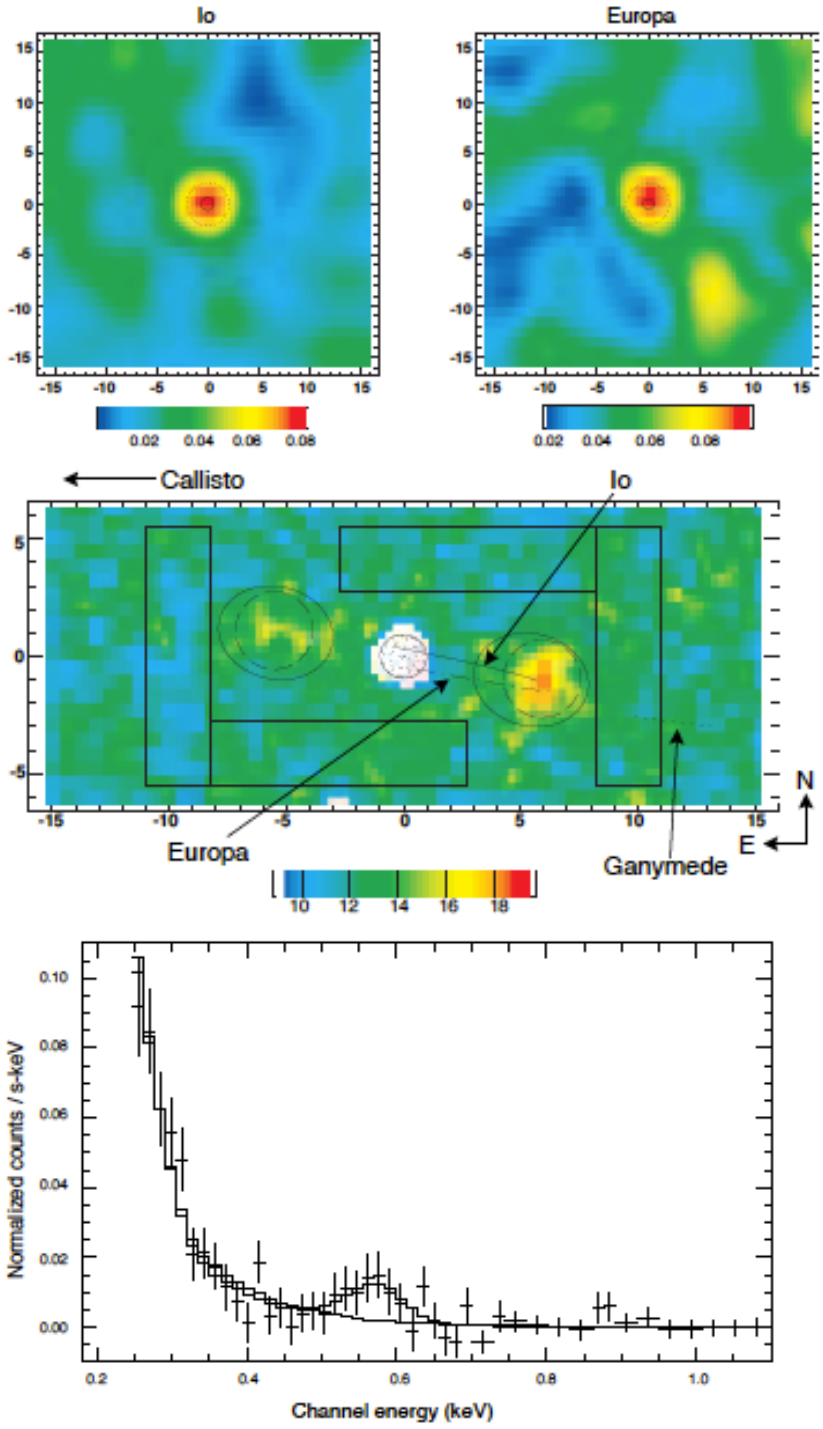

Figure 1.17: Chandra Detections of Jupiter's Moons Io and Europa and Image and Spectrum from the Io Plasma Torus from Elsner et al. (2002): Top: Smoothed ACIS images of Io and Europa (0.25-2 keV). The axes are labelled in arcsec (1" is roughly 2995 km). The scale bar is in counts. The solid circle shows the size of the satellite and the dotted circle the size of the detect cell. Middle: Smoothed HRC-I image of the IPT (Dec 18, 2000). The axes are labelled in units of R_J , and the scale bar is in counts. The paths traced by Io (solid line), Europa (dashed line), and Ganymede (dotted line) are marked on the image. Callisto is off the image to the dawn side. For this observation, Jupiter's equatorial radius corresponds to 23.9". The regions bounded by rectangles were used to determine background. The regions bounded by dashed circles or solid ellipses were defined as source regions. Bottom: The background subtracted ACIS IPT spectrum, normalized counts/s-keV vs channel energy in keV, for 0.25-1.0 keV, together with a power-law and power-law plus gaussian oxygen line model.

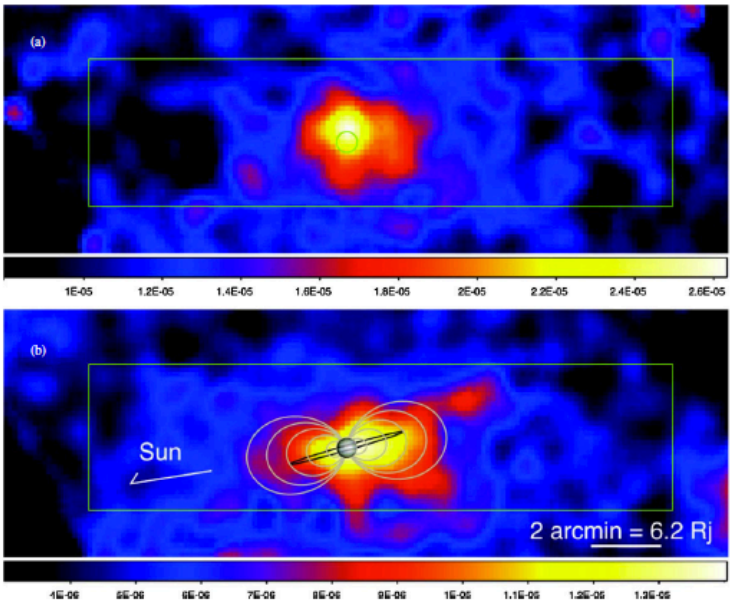

Figure 1.18: Suzaku Observation of the Jovian Radiation belt and/or Io Plasma Torus from Ezoe et al. (2010): Suzaku smoothed XIS images after correcting for the satellite orbital motion and Jupiter's ephemeris in the (a) 0.2-1 keV and (b) 1-5 keV bands. In panel (a), a circle indicates the expected position and size of Jupiter whose diameter is 39". In panel (b), gray lines indicate the equatorial crossing of magnetic field lines at 2, 4, 6, and 8 R_J. A black line is the path traced by Io. Image of Jupiter by Cassini is overlaid (Credit: JPL).

at the possible X-ray presence of Ganymede.

The December 2000 observations also revealed X-rays with luminosities of up ∼0.1 GW from the Io Plasma Torus (Elsner et al. (2002)- see Fig. 1.17). The spectrum from this was well fitted by a combination of a power law and an oxygen spectral line and was again predominantly in the soft X-ray region with energies between 0.2-1.0 keV. An observation of Jupiter by the Suzaku telescope in the energy range 1-5 keV revealed the possible presence of X-ray emission from the radiation belts and possibly a subsequent observation of X-rays from the IPT (Ezoe et al. (2010) see Fig. 1.18). Spectral modelling suggested that this was from solar photons Inverse Compton scattering off ∼10 MeV radiation belt electrons.

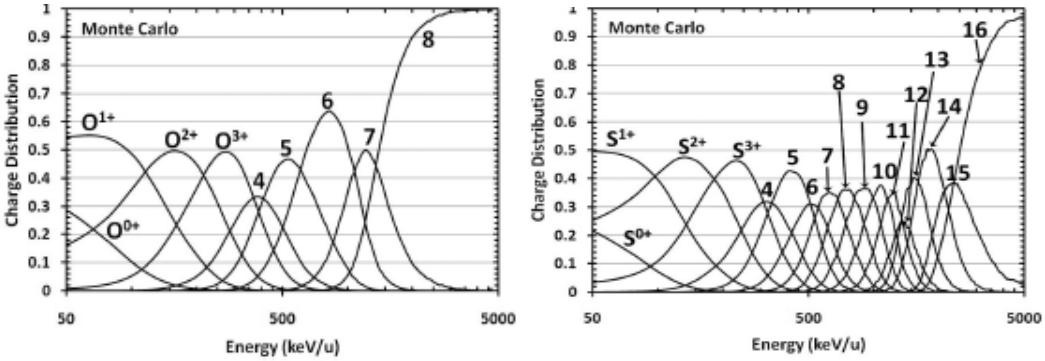

Figure 1.19: Charge Distributions of Precipitating Jovian Ions with Energy from Ozak et al. (2013): Monte Carlo simulations of the charge states attained for Oxygen (left) and Sulphur (right) depending on the initial energy of the ion prior to entering a molecular hydrogen atmosphere and beginning collisions. These are largely independent of whether the ion is initially singly or doubly charged.

1.3.6 Generating the X-ray Hot Spot Emissions - Particle Precipitation Studies

A combination of modelling and UV observations in the late 1980s suggested that the X-ray emission was likely to originate below the methane homopause layer (Waite et al. 1988; Horanyi et al. 1988). Below the homopause atmospheric gases share a common scale height, but above the homopause their scale height depends on their own molecular weight. This altitude would be transparent to the X-ray emission, but opaque to the associated UV emissions from precipitating sulphur and oxygen - explaining why the corresponding UV emissions were unobserved.

Following this work on low charge-states of oxygen, Cravens et al. (1995); Kharchenko et al. (1998); Liu and Schultz (1999, 2000) found that to produce the high charge-states required for X-ray emissions lines, while remaining consistent with the ion charge-state abundances in Jupiter's magnetosphere (Gehrels and Stone 1983), the auroral emissions would require precipitating S and O ions to have energies greater than 0.5 MeV/amu. The spectral observations have confirmed the presence of high charge state oxygen O^{6+} and O^{7+} and that the precipitating ions have these high energies (e.g. Branduardi-Raymont et al. (2007a)). These led to several subsequent Monte Carlo modelling efforts to better understand the precipitation emission and absorption (e.g. Kharchenko et al. (2006, 2008); Ozak et al. (2010, 2013)).

Charge exchange for Jupiter operates differently than for cometary charge exchange, since the thick Jovian atmosphere strongly modifies the ions properties as they penetrate. The ion energies are reduced by ion-atom collisions but their charge state increases (rising from $O^{1,2,3+}$ and $S^{1,2,3+}$ to $O^{6,7,8+}$ and $S^{11,12,13+}$), with the number of electrons stripped depending on the ion energies just prior to entering the atmosphere and to some extent this is independent of the initial charge state (e.g see Fig 1.19). Kharchenko et al. (1998, 2006, 2008) model how this ion population changes during its journey through the atmosphere by calculating the various charge-changing interactions that lead to charge-stripping or electron-capture with subsequent photon emission. They use a complex Monte Carlo model that includes cross-sections, collisional channels, and photon cascades for the ions to continuously apply the following processes (shown here for oxygen, but also applied to sulphur):

Charge Stripping:

$$O^{(q-1)+} + H_2 \rightarrow O^{q+} + H_2 + e^- \tag{1.20}$$

Charge Transfer:

$$O^{q+} + H_2 \rightarrow O^{(q-1)+*} + H_2^+ \tag{1.21}$$

X-ray Emission:

$$O^{(q-1)+*} \rightarrow O^{(q-1)+} + \gamma \tag{1.22}$$

Ionisation

$$O^{q+} + H_2 \rightarrow O^{q+} + H_2^+ + e^- \tag{1.23}$$

Excitation

$$O^{q+} + H_2 \rightarrow O^{q+} + H_2^* \tag{1.24}$$

This approach is quite different from fitting intensities for individual observed emission lines (e.g Elsner et al. (2005); Branduardi-Raymont et al.

(2007a)), since the lines generated by the Monte Carlo simulations accurately represent the intensity ratios required by charge exchange.

The Kharchenko et al. (2008) models find that ion excitation through collisions is negligible since at high energies ions will charge-strip and at low energies they will charge-exchange (see Figure 1.20 top left panel). This means that as they penetrate deeper into the atmosphere, and their energies degrade, they will charge strip first and then charge exchange after this. After a certain number of collisions, the charge states of ions will begin to reduce as their energies are sufficiently reduced such that charge exchange begins to dominate over charge stripping (see Figure 1.20 top right panel). The charge-state dominance (and associated X-ray emission) progresses monotonically for oxygen from O^{8+} to O^{7+} and so on, suggesting that with increasing numbers of collisions, and therefore increasing depth, the observed charge exchange lines will progress to lower charge-state lines. It may be expected therefore that higher charge state emissions will be observed at higher altitudes. However, for these Monte Carlo simulations, for Sulphur there seems to exist a threshold beyond which it becomes challenging to generate higher charge states (see Figure 1.20 lower left panel) because the charge stripping probability diminishes. For each spectral line Kharchenko et al. (2008) produce a likely yield of photons, which we include here in Table 1.4 for reference.

By comparing their theoretical spectra with observations Kharchenko et al. (2008) infer the initial particle energies and populations for the Northern and Southern polar regions. In doing this, they find that it is necessary to suppress the contribution from the otherwise dominant 0.561 keV O^{*6+} forbidden transition. While this line is the brightest feature for cometary and planetary charge exchange normally (Kharchenko and Dalgarno 2000; Kharchenko et al. 2003), it is a long-lived metastable state of O^{*6+}. For the case of acceleration into Jupiter's atmosphere ions may therefore undergo collisions that dissipate energy before they are able to relax and emit an X-ray photon. Quenching of the line by these collisions would be efficient for altitudes where the atmospheric density exceeds $10^{10} cm^3$ (below an altitude of 1200 km for Jupiter's atmosphere).

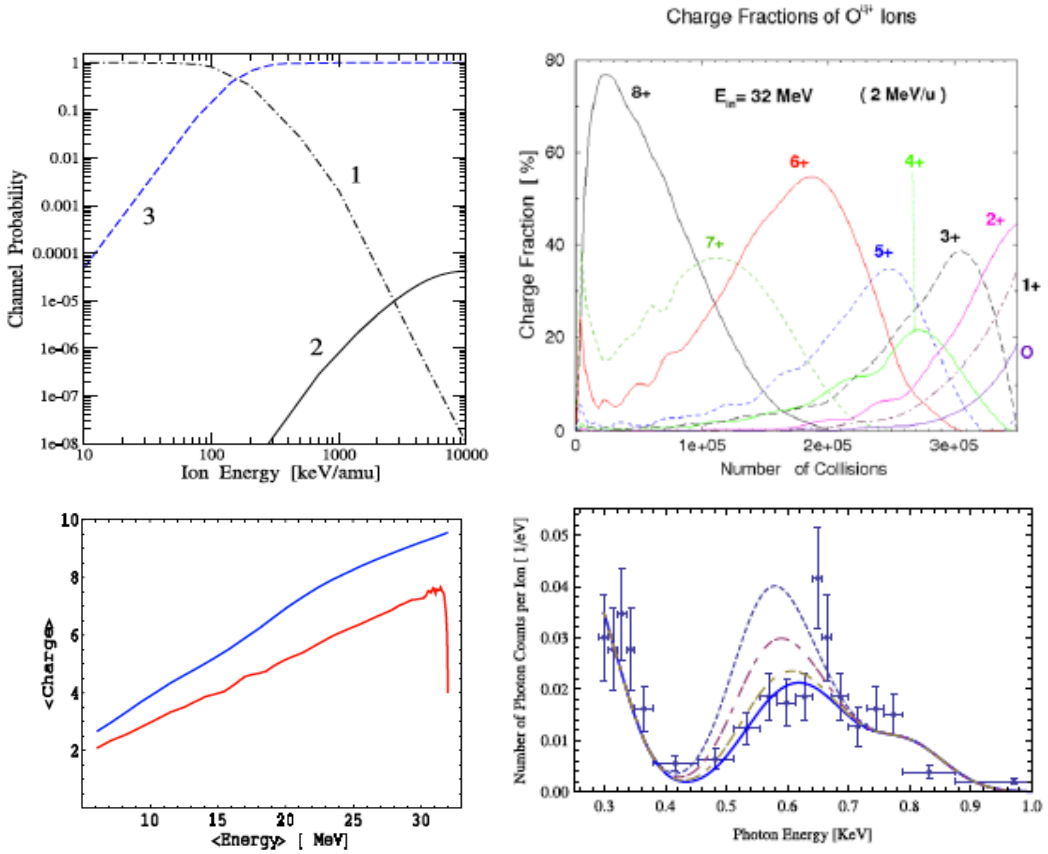

Figure 1.20: Monte Carlo Simulation Results for Jovian Magnetospheric Ions Precipitating into the Atmosphere from Kharchenko et al. (2008): Top Left: Probabilities for S^{14+} + H_2 collisions as functions of the kinetic energy per unit of nuclear mass. Curve 1 is the charge-exchange probability, curve 2 is the electron-stripping probability, and curve 3 is the probability of collisions that preserve the ion charge (including target ionisation, elastic, dissociation, and excitation collisions). Top Right: Population of the different charge states q = 0, 1, 2. . . 8 of the precipitating oxygen ions. The initial ion energy is E_in = 2 MeV/amu, and the initial charge is $q_in = 2$. N is the number of collisions since the beginning of precipitation. Lower left: The average charge of precipitating sulphur ions as a function of the average ion energy. The initial ion energy is $E_in = 32$ MeV (1 MeV/amu), and the initial charge is $q_in = 2$. The upper curve is the prediction of the equilibrium charge (EC) model, calculated with the updated values of cross-sections for collisions between S^{q+} ions and molecules of the H_2 gas. The lower curve shows the results of the Monte Carlo simulations. Lower Right: Observational (dots with error bars) and theoretical (solid line) Chandra spectra for the Jovian North pole. Theoretical spectra are normalised per single ion and computed for the ion flux composed of O^{q+} (79%) and S^{q+} (21%) ions. Average kinetic energies at the top of the Jovian atmosphere are 1.8 and 1.05 MeV/amu for O and S ions, respectively. In the spectrum, shown by the solid curve, the forbidden emission line $2^3S \rightarrow 1^1S$ of O^{*6+} at 561 eV is completely suppressed. Dashed lines show the charge-exchange X-ray spectra computed with collisional quenching efficiencies of 85%, 50%, and 0%. Without quenching collisions, the emission line of O^{*6+} at 561 eV dominates the theoretical spectrum between 500 and 600 eV and removes the agreement between observational and theoretical data. Quenching reduces the intensity of 561 eV line but does not influence other O*6+ emission lines such as the intercombination (569 eV) and resonance (574 eV) transitions.

Table 1.4: Table from Kharchenko et al. (2008) showing photon yields for two different possible energy regimes.

Line Energy (eV)	Yield for 1 MeV/amu	Yield for 2 MeV/amu	Ion
561	10.05	17.76	O6+
569	2.32	4.09	O6+
574	3.09	5.46	O6+
653	0.78	7.24	O7+
774	0.22	2.05	O7+
816	0.16	1.51	O7+
206.1	63.9	67.2	S6+
209.3	21.95	23.71	S7+
228.9	22.52	33.32	S8+
235	21.95	23.71	S7+
237.9	38.34	40.32	S6+
260.2	7.7	19.74	S9+
262.1	25.56	26.88	S6+
267.4	13.51	19.99	S8+
268.8	9	13.33	S8+
273.7	29.27	31.62	S7+
274.3	1.12	7.48	S10+
280.3	3.21	8.22	S9+
291.8	1.93	4.93	S9+
315.9	1.49	9.98	S10+
359	0.16	3.58	S11+
385.2	0.024	2.21	S12+
393.8	0.74	4.98	S10+
407.5	0.002	1.63	S13+
484.9	0.096	2.14	S11+
504.2	0.016	1.55	S12+
507.7	0.064	1.43	S11+
533.6	0.0072	0.66	S12+
538.9	0.0023	1.83	S13+
572.3	0.0007	0.61	S13+
2430	0	0.015	S14+
2447	0	0.004	S14+
2461	0	0.006	S14+

However, we note that the lack of this line in the Chandra ACIS Jovian spectra (where emission peaks at 0.6 keV) is at variance with the XMM-Newton spectra, where a line at 0.55-0.58 keV is dominant (Branduardi-Raymont et al. 2007a). Kharchenko et al. (2008) note though that the XMM-Newton 0.561 keV line (e.g. Branduardi-Raymont et al. (2007a)) is dimmer than would be expected from their Monte Carlo simulations. If quenching is occurring due to the limited time between collisions relative to the time scale for atomic relaxation, then this would also be true for any solar wind precipitation of O*6+, N*5+, and C*4+ ions, with quenching of helium-like forbidden carbon transitions occurring at higher altitudes than that of N*5+ and O*6+ ions. This would mean that rather than radiating the energy from these lines, they would contribute towards atmospheric heating.

The Monte Carlo simulations are able to reproduce the observed spectra (with a χ^2 of at least one more than the Elsner et al. (2005) and Branduardi-Raymont et al. (2007a) model fits) through the precipitation of 79% oxygen and 21% sulphur ions in the North and 85% and 15% in the South with average initial energies for O in the North (South) of 1.85 MeV/amu (1.75 MeV/amu) and for S of 1.05 MeV/amu (1.01 MeV/amu).

Ozak et al. (2010, 2013) extend the Monte Carlo models of Kharchenko et al. (2008); Hui et al. (2009, 2010) by including atmospheric effects such as depth dependence of the emission (e.g. opacity, air glow), more complete treatment of ionisation, secondary electron fluxes and the associated current systems. By including the atmospheric depth dependent effects (Fig. 1.21 Top Left) they can calculate the production of each charge state with depth (Fig. 1.21 Middle and Bottom Left) and account for the X-ray absorption by methane at lower altitudes (Fig. 1.21 Top Right).

They find that the height at which ions emit most of their X-rays is between 300-450 km. However, with increasing energy, the ions penetrate deeper and opacity effects become increasingly significant. This becomes relevant for O^{7+}, O^{6+} and S^{8+} ions with initial energies higher than 2, 1.2 and 1 MeV/amu respectively. For energies above 5 MeV/amu the atmosphere is opaque to all outgoing X-rays.

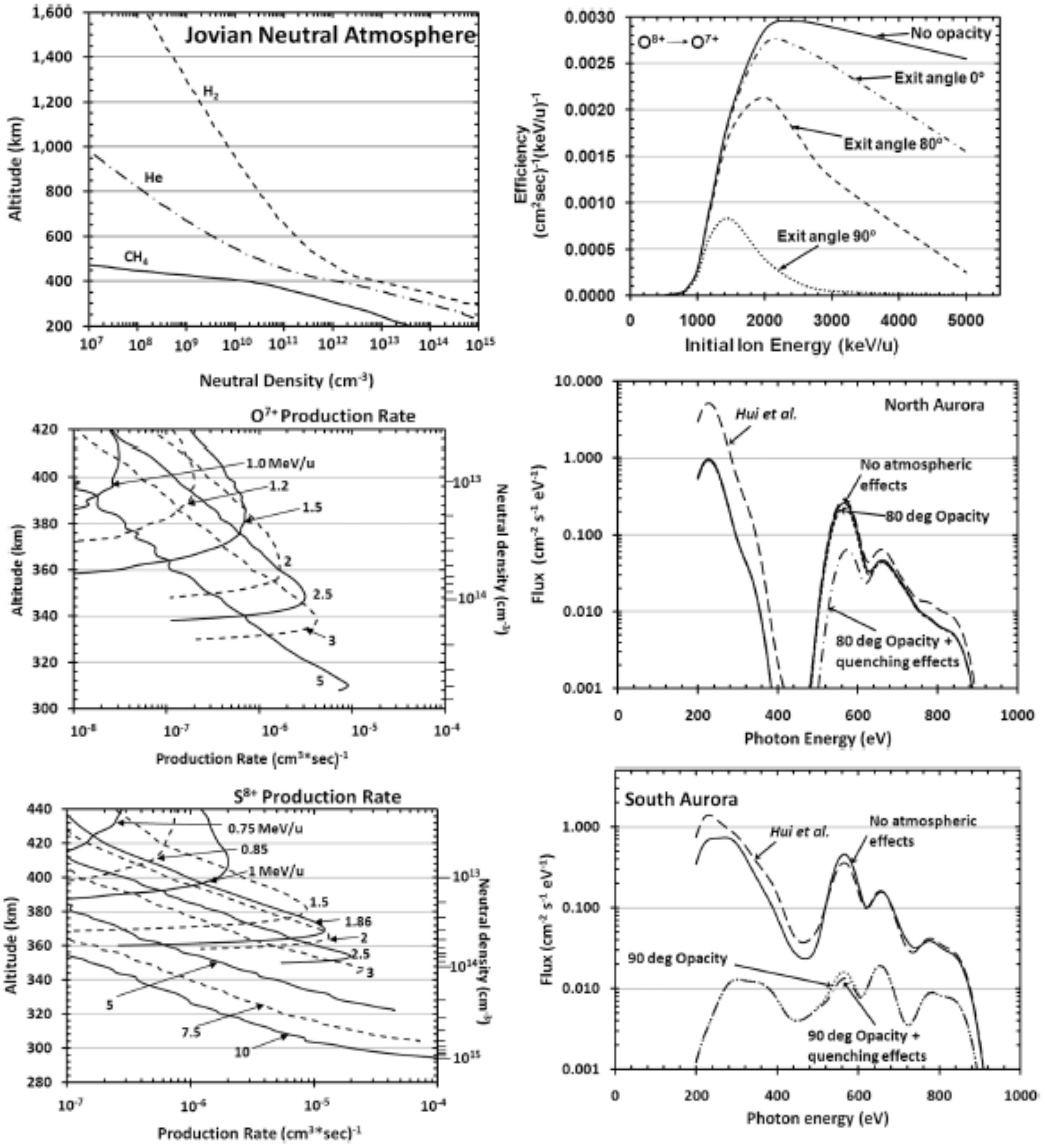

Figure 1.21: Monte Carlo simulation results of Jovian magnetospheric ions precipitating into the atmosphere, accounting for variations in atmosphere with depth from Ozak et al. (2010): Top Left: Jovian Neutral Atmosphere Profile for molecular hydrogen, helium and methane. Middle (Bottom) left: O^{7+} (S^{8+}) production rates with atmospheric depth of ion precipitation for ion energies of 1.0, 1.2, 1.5, 2.0, 2.5, 3.0, and 5.0 (0.75, 0.85, 1.0, 1.5, 2.0, 2.5, 3.0, 5.0, 7.5, and 10.0) MeV/amu as a function of altitude in km. The higher the energy of the ion population the more the higher charge state is produced at deeper altitudes. However, with altitude depth, absorption of subsequently emitted X-rays becomes increasingly important. The top right panel shows how atmospheric opacity affects emission from an excited O^{7+} ion depending on the precipitating ions initial energy. The solid line shows this efficiency without opacity effects, other line shows how opacity affects photons with different emission angles from the ions. Middle (bottom) right: Spectra calculated for the North (South) aurora by using Hui et al. (2010) as a proxy to the observational data. Initial energies considered for this calculation are 1.2 (2.0) MeV/amu for oxygen and 0.51 (1.86) MeV/u for sulfur. A sulphur to oxygen ratio of 204 (0.94) was taken. The long dashed curve shows Hui et al. (2010) modelled spectra as a comparison. The solid line shows the Ozak et al. (2010) model without any opacity or quenching effects. The small dashed line shows the current model with opacity effects. Note that it is almost overlapping the current model line (solid line). The dash-dotted line shows the current model with opacity and quenching effects.

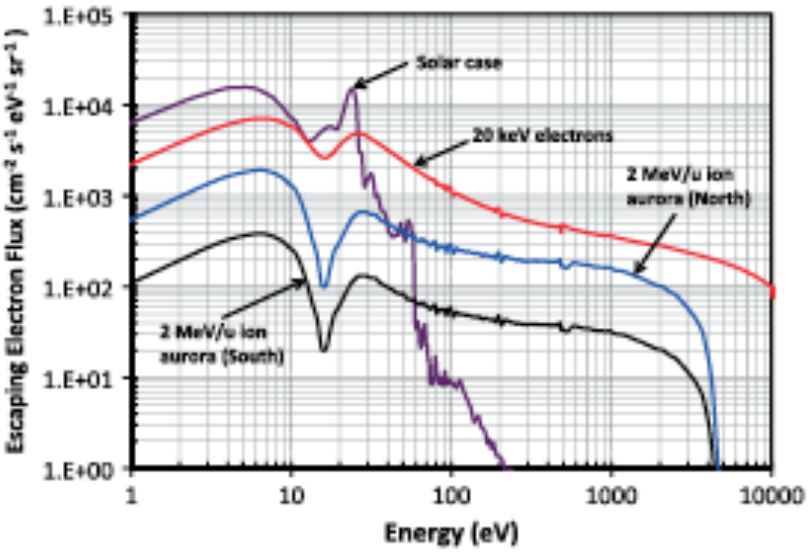

Figure 1.22: From Ozak et al. (2013): Escaping flux of electrons (i.e., upward electron fluxes at the top of the atmosphere, z = 3000 km) as a function of electron energy.

Ozak et al. (2010) utilise the 354 oxygen and sulphur X-ray emission lines calculated by Hui et al. (2010) along with the best model fits achieved by Hui et al. (2010), which they use as a proxy for the real Chandra Northern (Southern) auroral data. Using 1.2 (2) MeV/amu for oxygen and 0.51 (1.86) MeV/amu sulphur energies, they show that opacity effects are important above 1 MeV/amu and for exit angles with respect to the zenith greater than about 80. For instance, for the Southern X-ray aurora, which is often observed on the limb, opacity is particularly important, whereas the Northern hot spot is often viewed with more favourable viewing geometries, so opacity is less relevant (see Fig 1.21 middle and bottom right). This is particularly important for atmospheric depths within the methane layer where the soft X-ray photoabsorption cross section is large (Atreya et al. 1981; Yelle and Miller 2004).

Ozak et al. (2013) extend this work by also calculating the electron production rates from the ion precipitation (see Fig. 1.22). They find that those electrons produced by ionising collisions have bulk energies less than 100 eV. However, for electrons produced by ion charge-stripping the energies are much higher and these are typically produced in the direction of the ions motion. Most electrons are produced where collisions become most common, deeper

in the atmosphere where it is difficult for the electrons to escape. This may be relevant for the heating of the stratosphere for the co-located IR hot spot (see Chapter 3). Increasing the ion energy from 1 to 2 MeV only increases the number of escaping electrons from 1 to 1.5 electrons/cm^2/s. Ozak et al. (2013) close by noting that above the auroral acceleration region, NASA's Juno mission (completing first polar passes while this is being written) should be able to detect MeV electrons associated with these processes.

1.3.7 Summary of Jupiter's X-ray Emissions

Jupiter's X-ray emission divides into two components: an equatorial/disk component that is dominated by fluoresced and scattered solar photons (e.g. Cravens et al. (2006); Bhardwaj et al. (2005, 2006); Branduardi-Raymont et al. (2007b) and an auroral component. The auroral component further comprises two key features:

1. hard X-ray bremsstrahlung emission mostly co-located with the main UV oval emission, which is thus expected to be produced by the same precipitating electron population (Branduardi-Raymont et al. 2008, 2007a)
2. a soft X-ray hot spot, produced by charge exchange from precipitating ions that originates in regions that magnetically map beyond the main oval and thus into the outer magnetosphere (e.g. Gladstone et al. (2002); Elsner et al. (2005))

While we have discussed the X-ray emission mechanisms here what is less well understood is how Jupiter produces the 1-2 MeV/amu energies needed for magnetospheric ions to charge-strip sufficiently to generate the observed X-ray aurora. What physical process/es drive this? We will discuss in detail the possible acceleration mechanisms for the X-ray hot spot after first introducing the context of Jupiter's surrounding plasma environment (the solar wind) and Jupiter's magnetosphere itself. It is critical to have some familiarity with these features in order to understand the mechanisms that might be able to generate the high energies required for Jupiter's X-ray emissions.

1.4 The Solar Wind

> *"One can get a very good idea of the behaviour of a system if one has some feel for the character of the solution in different circumstances. "*
>
> — Richard Feynman

In order to investigate the possible driving of the solar wind on Jupiter's X-ray aurora, we provide a brief overview to the large-scale solar wind structures and dynamics that are relevant to this thesis.

The temperature of the low plasma β (magnetically-dominated) highly conductive solar corona increases with height, which generates a pressure-driven radial outflow of charged particles (Parker 1958), which become super-Alfvenic within 10 - 20 solar radii. This stream of continually ejected plasma, the solar wind, carries with it the coronal magnetic field which pervades the solar system as the interplanetary magnetic field (IMF) - sometimes called the heliospheric magnetic field. These charged particles are channeled by the IMF, which is anchored to the Sun's photosphere. This anchoring on the Sun means that as the Sun rotates, the radial solar wind flow generates an azimuthal component, B_ϕ which leads the IMF to trace out an Archimedean spiral (the 'Parker Spiral') as it propagates throughout the heliosphere. Distortions in the shape of the IMF are produced by changes in the solar wind flow. Some of the most significant transient changes in the solar wind flow (and connected changes in the IMF) are produced by interplanetary coronal mass ejections (ICMEs) and by the interaction of fast and slow solar wind streams in Corotating Interaction Regions (CIRs). Figure 1.23 shows a propagation from the Enlil model of the Solar Wind from the Sun through the heliosphere during solar maximum in 2014. This shows the Parker spiral and a variety of transient increases in density that are corotating through the heliosphere.

The shortest time-scales of the solar wind (up to tens of minutes) are dominated by waves and turbulence, while over timescales of centuries the solar activity cycle is also shown to reach grand maxima and minima. Both these shortest and longest timescales are beyond the scope of this work. Instead, we focus on timescale variations on the scales of hours to days, which are relevant for both large-scale compressions and expansions of the Jovian magnetosphere

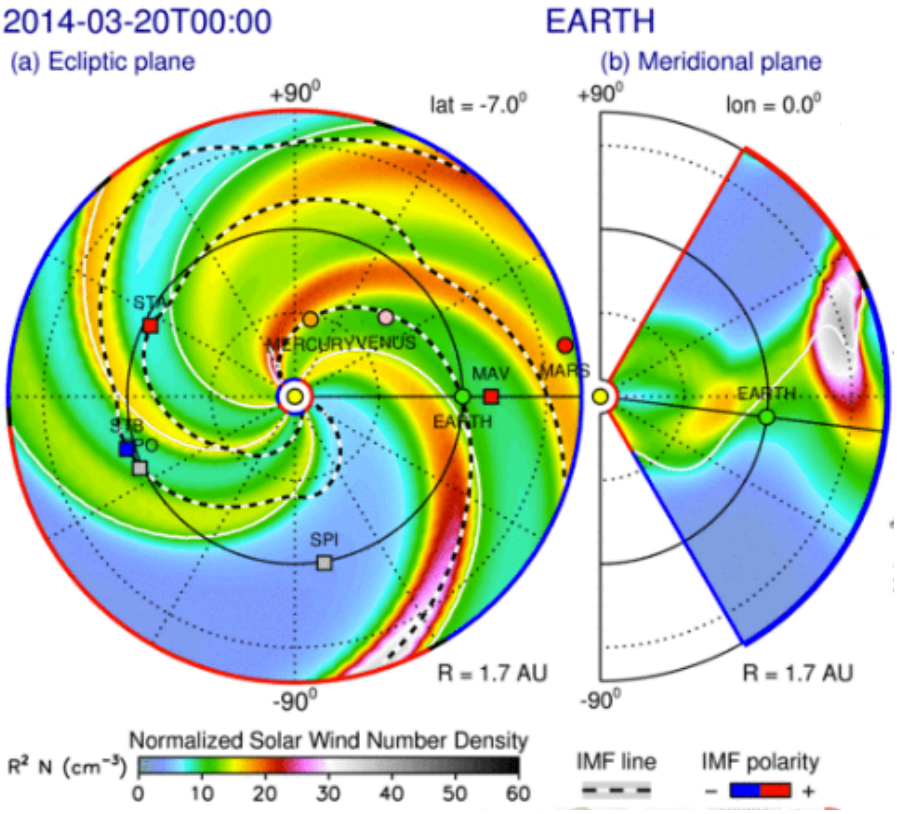

Figure 1.23: Left: The Wang-Sheeley-Arge Enlil solar wind propagation model, during solar maximum in March 2014. The Parker Spiral morphology can clearly be observed in the left hand panel which looks down onto the ecliptic, while the three dimensional structure of the heliospheric current sheet (coming out of the ecliptic in the meridional plane - right hand panel) can be seen separating the two differing polarities of the Sun's magnetic field shown in red and blue on the edge of the graphic. In this instance, Earth is about to encounter a strong density increase associated with a rotating feature and is in a region of negative IMF polarity.

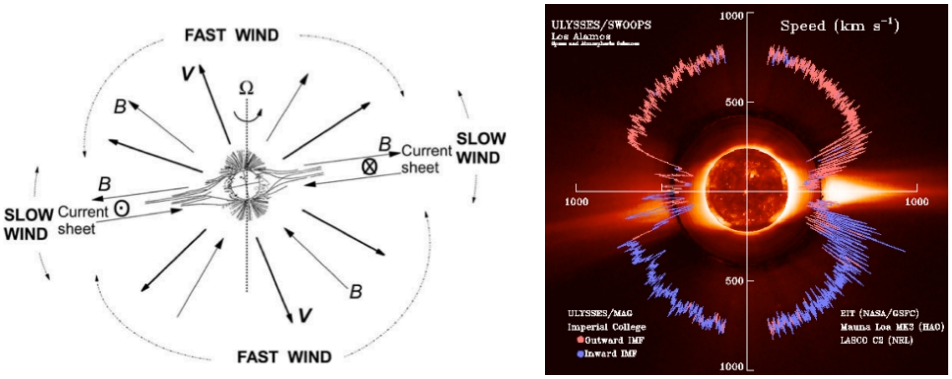

Figure 1.24: Left: Figure from Meyer-Vernet (2007) showing simplified picture of the large-scale structure of the solar wind near sunspot minimum, when the solar magnetic dipole makes a small angle with the spin axis (dotted line). The velocity and field lines are sketched in bold and thin lines respectively. Right: Graphic from ESA showing Polar overlay plot of SWOOPS solar wind speed data and EIT/LASCO/Mauna Loa images of the solar corona. This again shows slow solar wind at the equator from the streamer belt and fast solar wind towards the poles with the different magnetic field polarity of the Sun shown in red and blue.

(from ICMEs and CIRs). We note that each solar rotation (25.4-days or full synodic solar rotation, accounting for the motion of the planets relative to the Solar rotation, of 27.27 days) the IMF and solar wind will recur. We will also discuss 11-year solar cycle variation from low to high periods of solar activity and how this affects structures in the solar wind and solar X-ray output.

1.4.0.1 The Steady State Heliosphere

During solar minimum, the coronal magnetic field is closest to dipolar and the corona is well-structured. At the magnetic equator, there is a belt of dense bright coronal streamers. At higher latitudes, X-ray and EUV dark polar coronal holes dominate (e.g., Levine et al. (1977); Wang et al. (1996); Cranmer (2009)). Figure 1.24 shows how, at these times, the fast solar wind ($\sim$ 750 km/s) dominates the heliosphere originating from the open magnetic field lines in these coronal holes, while the slow solar wind (300 - 400 km/s) is ejected from the equatorial belts ($\sim 20^\circ$ latitude). The oppositely directed magnetic field from the Northern and Southern polar coronal holes, is separated by the heliospheric current sheet which is carried out by the equatorial slower solar wind and maintains the distinction between the different polarities of magnetic field throughout the heliosphere.

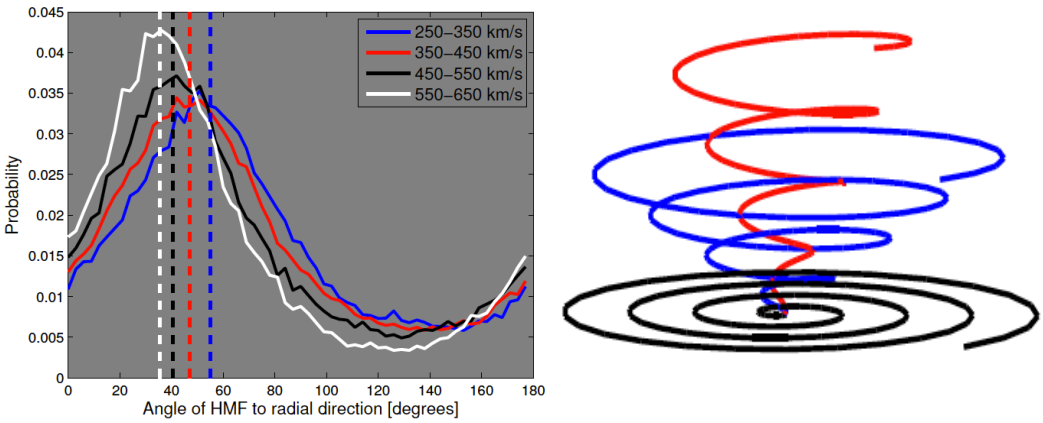

Figure 1.25: From Owens and Forsyth (2013): Left: Probability distribution functions for Interplanetary Magnetic Field (IMF) angle with the radial direction for different solar wind speeds, based on near-Earth measurements. Dashed lines highlight the Parker Spiral angles from the centre of each speed bin. Right: Parker Spiral angle between 0-25 AU for a solar wind speed of 450 km/s for heliographic latitudes of 0° (black), 30° (blue), and 60° (red).

If the solar wind flow is constant, then to conserve magnetic flux, the radial component of the IMF, B_R, must decrease with the inverse square of the distance from the Sun, R. This leads the azimuthal component of the IMF to exhibit a 1/R relationship (Owens and Forsyth (2013) and references therein). At Earth, this gives a dominant IMF angle to the radial of 45° for a typical solar wind of 400 km/s (e.g. Borovsky (2010)). However, as you progress radially to Jupiter this angle evolves to 90° (e.g. Ebert et al. (2010)) and the Parker spiral is shown to be a good explanation for the observed angle out to 8 AU (Burlaga et al. 1982; Thomas and Smith 1980). Moving to higher speed solar wind or higher latitudes leads to unwinding of the solar wind (e.g. Fig. 1.25).

1.4.0.2 Evolution of the Solar Wind with Solar Cycle

The Sun's magnetic field is generally dominated by its dipolar component, but as it progresses to solar maximum the quadrupole components begin to play a more significant role. Figure 1.26 shows the Ulysses measured development of the solar wind with solar cycle. During solar minimum this shows a well-organised dipolar structure with different polarity separated by the heliospheric current sheet. At solar maximum there appears to remain a clear distinction between two regions of polarity, still suggesting a dipolar structure,

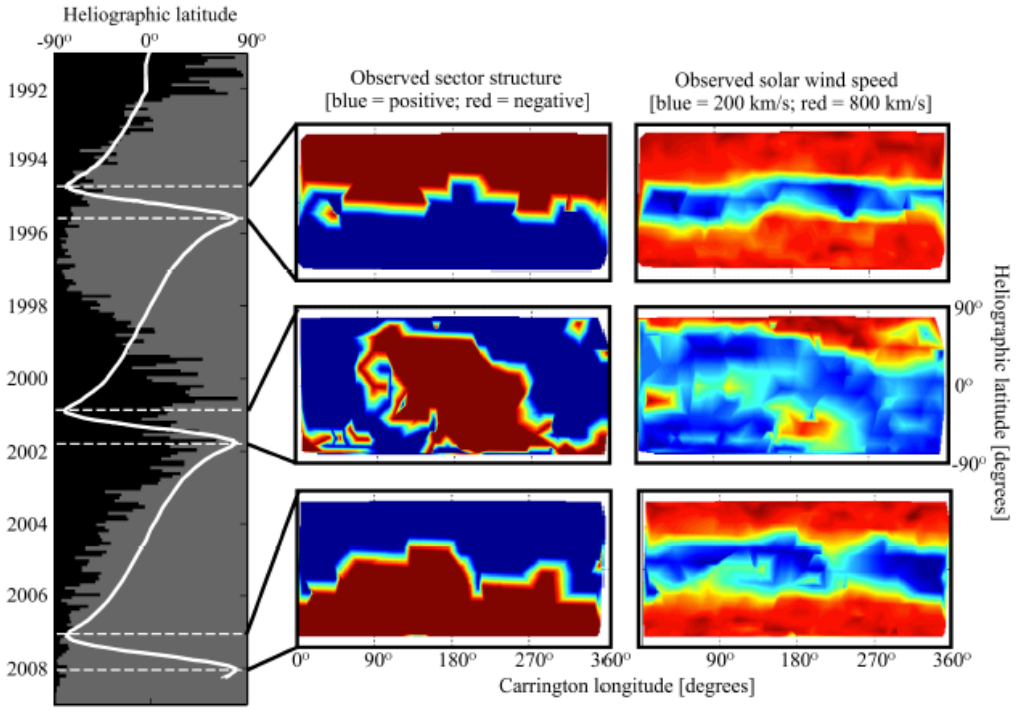

Figure 1.26: Figure from Owens and Forsyth (2013):A summary of the Ulysses observations. The white line in the left-hand panel shows the heliographic latitude of the spacecraft, overlaid on the sunspot number. The dashed line shows the 1 year timelines where Ulysses flew 'fast-latitude' trajectories from 80° S to 80° N. The centre and right-hand columns show latitude-longitude maps of Ulysses scan observations during the fast-latitude scans. The centre column shows magnetic field polarity, with blue/red indicating inward/outward field. The right-hand column shows solar wind speed, with blue through red showing 200 to 800 km s/1. Image adapted from Owens et al. (2011).

but with the dipolar angle tilted to the rotation axis (see central panels). However, this is contradicted by near Earth measurements, which suggest a more quadrupole-like structure at solar maximum (Owens and Forsyth (2013) and references therein). The right-hand column of this figure shows that during solar minimum, the fast solar wind dominates at the poles where the coronal holes are located, while the slow solar wind dominates the equatorial regions (e.g. Fig 1.24). However, during solar maximum, as magnetic polarities converge, streamer belts proliferate and the slow solar wind dominates much of the heliosphere.

During solar minimum the heliospheric current sheet (e.g. Fig 1.23) is constrained to the equator, so that, given a typical slight dipole-rotation axis tilt, solar systems bodies close to the ecliptic will experience alternating polarity

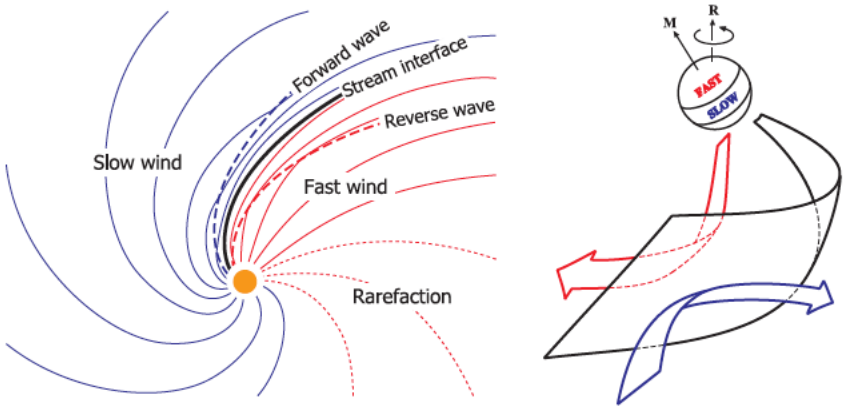

Figure 1.27: Figure and caption from Owens and Forsyth (2013):A sketch of a stream interaction region. Left: Looking down on the ecliptic plane. Magnetic field lines within fast (slow) wind, shown in red (blue), become aligned with the stream interface by the reverse (forward) wave. Right: a view from Earth. The magnetic axis, M, and therefore the wind speed belts, are inclined to the rotation axis, R. The point in the heliosphere at which fast wind is able to catch up to the slow wind ahead of it is the stream interface (SI), which forms a spiral front in the heliosphere, shown as the black-outlined curved surface. In the frame of reference of the SI, both fast and slow wind flow toward the SI. Fast (slow) wind, shown by the red (blue) arrow, is slowed (accelerated) and deflected along the SI in the direction counter to (along) solar rotation. Right panel adapted from Pizzo (1991).

during each solar rotation. As the solar cycle develops towards maximum, and quadrupole moments begin to dominate, the relationship between solar rotation phase and the polarity experienced by solar system bodies becomes more complex. The heliospheric current sheet is produced by the convergence of distinct polarities of open solar flux due to the (non-radial) expansion of coronal holes. As the solar cycle progresses and the open solar flux develops from a 2-polarity to a 4-polarity structure, more heliospheric current sheet crossings may be expected for solar system bodies. The two-sector structure is observed to recur at Earth every 27 days, in contrast the four-sector structure rotates more slowly and recurs every 28 days (Svalgaard and Wilcox 1975).

1.4.0.3 Co-rotating Interaction Regions

Figure 1.27 shows how the combination of warps in the streamer belt, the tilt-angle of the magnetic field to the rotation axis and the differing velocities of the two winds leads to features where the fast solar wind (red) catches up with the slow solar wind (blue). These features occur at fixed heliospheric longitudes that rotate with the Sun and are thus called Co-rotating Interaction Regions

(CIRs)(Smith and Wolfe 1976; Pizzo 1991; Gosling and Pizzo 1999; Crooker et al. 1999). CIRs are most common during the declining phase of the solar cycle when the dipole has a significant tilt to the rotation axis. The fast solar wind cannot overtake the slow wind or pass through the interaction region, instead the slow and fast solar wind are deflected in opposite directions along this boundary as shown in Fig. 1.27. This leads to periods of slow solar wind being caught up by fast solar wind which is then followed by a rarefaction where the slow wind is trailing behind the fast wind.

Within the interaction region itself, the magnetic field strength and plasma density are enhanced. However, the compression leads IMF within the region to lie parallel with the interaction region. The shocks that these CIRs generate can often lead to acceleration of energetic particles. Fig 1.28 highlights the sub-structures within a CIR along with the respective changes in solar wind parameters as a CIR arrives at a body. The first signature observed is the preceding rarefaction region with low temperature, solar wind speed, magnetic field intensity and flow angle, but with slightly heightened density. Then as the ambient slow solar wind (S) changes to the shocked accelerated slow solar wind (S') there is an increase in plasma temperature, density, magnetic field intensity and flow angle, while the wind speed is still characteristically slow. The transition to the region of highly shocked plasma at S' indicates the forward shock. This is characterised by steepening temperature, density, and field intensity as the fast solar wind increasingly collides and shocks the slow solar wind. Transitioning across the compression into the decelerated fast solar wind that is producing it (F'), the temperature increases again, the solar wind speed rises, the magnetic field intensity remains reasonably constant but dips slightly with the reduction in density due to the differing type of solar wind and the flow angle reverses with the differing solar wind direction along the interaction region. As the compression region passes, and we move across the reverse shock into a region of ambient fast solar wind (F) behind it, the solar wind speed increases further to the ambient level and the density, temperature and magnetic field continue to drop as we pass while the flow angle returns to the solar wind flow direction. This reverse shock is characterised by a

return to rarefaction conditions with density, temperature and field strength all decreasing.

With increasing distance from the Sun, it becomes more likely that the heliospheric current sheet is embedded within a CIR (Thomas and Smith 1981) and that across the CIR the polarity might be expected to change. CIRs are typically confined to 40° of the solar equator, about 10° greater than the 30° maximum latitude of the heliospheric current sheet, but the energetic protons and electrons produced by CIR shocks occur at much higher latitudes (Roelof et al. 1997). Eventually, CIRs and/or ICMEs (see next sub-section) begin to coalesce to form Merging Interaction Regions.

1.4.0.4 Interplanetary Coronal Mass Ejections

Interplanetary Coronal Mass Ejections (ICMEs) are vast eruptions of plasma and magnetic field from the Sun that propagate out into interplanetary space causing the largest deviations from the Parker spiral magnetic field (e.g. Gosling (1993); Schwenn (2006)). They also produce strong meridional (out-of-the-ecliptic) IMFs through both their intrinsic magnetic field and also by distorting the surrounding IMF (e.g. Jones et al. (2002)). While ICMEs are very diverse and thus not yet fully catalogued (e.g. Neugebauer and Goldstein (1997); Wimmer-Schweingruber et al. (2006)), their composition is normally similar to the hotter corona (e.g. Gloeckler et al. (1999); Lepri and Zurbuchen (2004)), while their density and pressure are typically less than the ambient solar wind. This suggests that ICMEs undergo greater expansion than the bulk solar wind (e.g. Cane and Richardson (2003)).

We note that Neugebauer and Goldstein (1997); Wimmer-Schweingruber et al. (2006) provide thorough reviews of ICME signatures. For the purposes of this thesis only the 30-50% of ICMEs that are magnetic clouds (Gosling 1990; Cane and Richardson 2003) will be discussed, since (at least for Earth) these are most relevant to magnetosphere-solar wind interactions. Magnetic Clouds are identifiable by their accompanying flux-rope-like structure which features large-scale smooth rotation in magnetic field direction and a decrease in small-scale field variance (Burlaga et al. 1981, 1982; Burlaga 1988; Lepping and

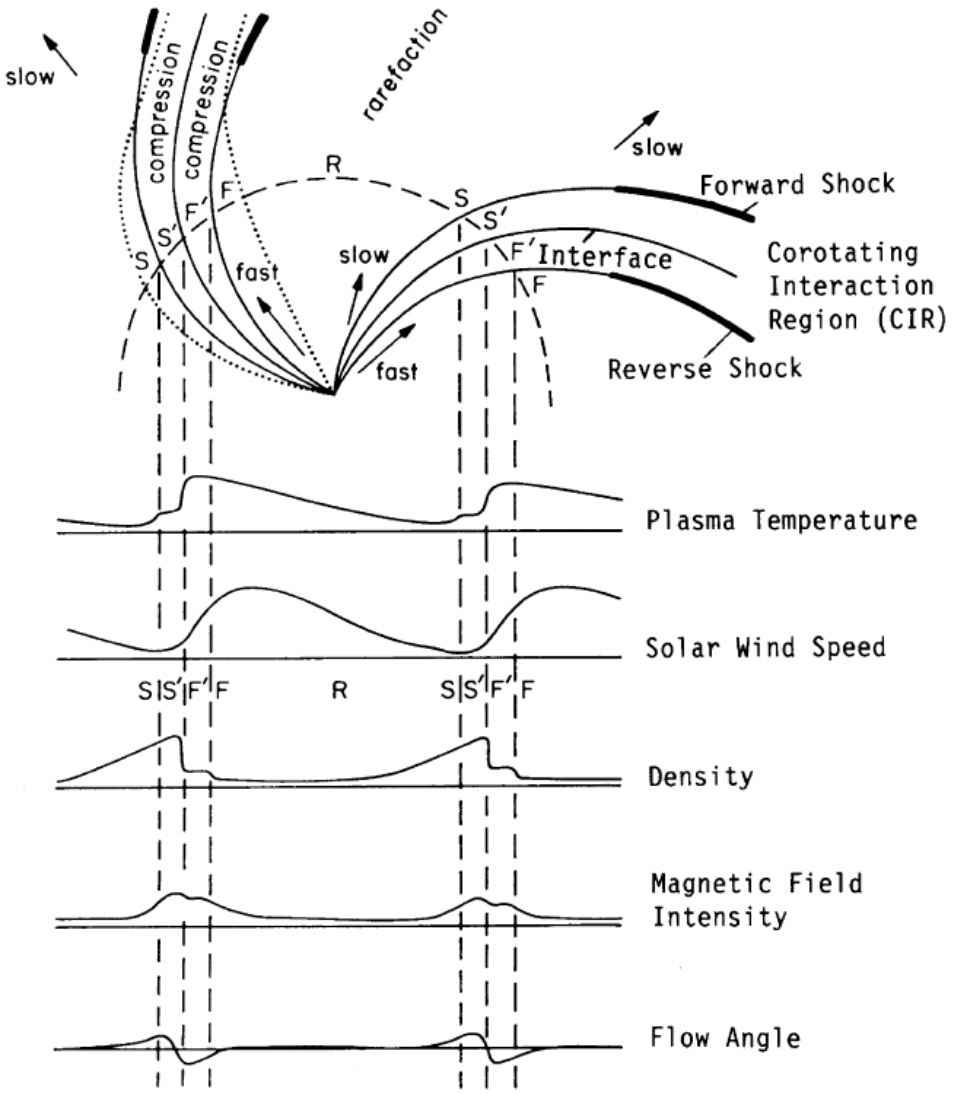

Figure 1.28: Figure and caption from Richardson et al. (1996) (after Belcher and Davis (1971)): Schematic showing the different features within a Corotating Interaction Region and how these connect with the observed solar wind parameters. S is the ambient, slow solar wind, S' is the compressed, accelerated, slow solar wind, F' is the compressed, decelerated, fast-stream plasma, and F is the ambient, undisturbed, fast-stream plasma, while R highlights the rarefaction regions between the fast solar wind and slow solar wind following it.

Burlaga 1990).

As with CIRs, ICMEs (and particularly fast ICMEs) generate large amplitude waves which often produce shock waves(Balogh et al. 1995). For ICMEs, this compressed solar wind that occurs between the shock and the leading edge of the ICME is called the 'sheath' and in many ways is similar to planetary magnetosheaths (Siscoe and Odstrcil 2008; Savani et al. 2011). For Earth, 25-50% of geomagnetic activity may relate to the strong magnetic fields produced in the sheaths of ICMEs (Owens et al. 2005; Richardson et al. 2001; Tsurutani et al. 1988).

As the sheath and its ICME propagate through the solar system, they will consume many solar wind structures in their path. As with CIRs, these structures will form compressed planes perpendicular to the leading edge of the ICME (Jones et al. 2002). Both the leading edge and the low shear, low plasma β field inside ICMEs provide preferential locations for solar wind magnetic reconnection (e.g. Gosling et al. (2007)).

While ICMEs and CIRs are distinguished by a number of characteristics, a few attributes may be important to interpreting their differing impacts on the Jovian system. ICMEs typically travel radially, meaning that to propagate conditions to Jupiter, a spacecraft would need to be within the angle of the ICME impact (see chapter 2 for further details), while, in contrast, a compression that corotates may be more easily inferred, without requiring strict opposition.

While CIRs and ICMEs will both act to compress the Jovian magnetosphere, their magnetic influence and the resulting dynamics may differ. While CIRs do include changes in IMF direction, this is not so pronounced as the complete IMF rotation that a flux-rope in a magnetic cloud ICME would introduce. Where a CIR impact may potentially only compress the magnetosphere, it is possible that an ICME may trigger new/different reconnection sites where solar wind and magnetospheric field lines have become anti-parallel.

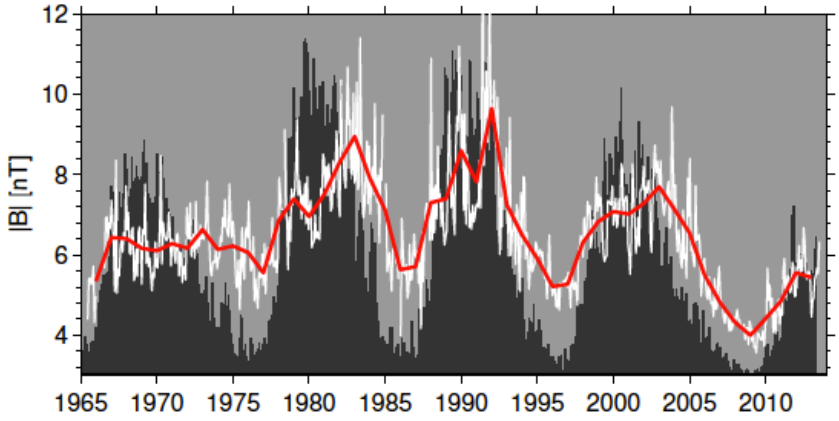

Figure 1.29: Figure and caption from Owens and Forsyth (2013): Carrington-rotation (solar rotation) averages (white) and annual averages (red) of the near-Earth IMF scalar magnetic field intensity from the OMNI dataset. The dark background shows the monthly sunspot number, scaled to fit the same axis.

1.4.0.5 Changes in the Solar wind with Solar Cycle

At solar minimum, the more dipolar field is well-organised with different polarity at each pole, where coronal holes are confined at this time. These differing polarities are divided by the heliospheric current sheet and helmet streamers at the equator. At this time, CMEs are less frequent and occur mainly at low latitudes (St Cyr et al. 2000).

However, with the evolution of the solar cycle the dipole magnetic field becomes more complex and more tilted to the rotational axis and consequently streamers and the heliospheric current sheet form at progressively higher latitudes until they reach all latitudes at solar maximum. With the poleward extension of these features, CMEs also become increasingly frequent at higher latitudes and generally a greater number of ICMEs occur in the ecliptic too. With these transients, the IMF progressively departs from an ideal Parker spiral.

As the solar cycle progresses towards solar maximum, not only do ICMEs become a more dominant part of the solar wind, but the coronal hole area becomes smaller, leading to less fast solar wind and a slow solar wind dominance. This leads to ICMEs becoming the dominant source of shocks in the solar system. Around this time, the Sun's polarity also reverses.

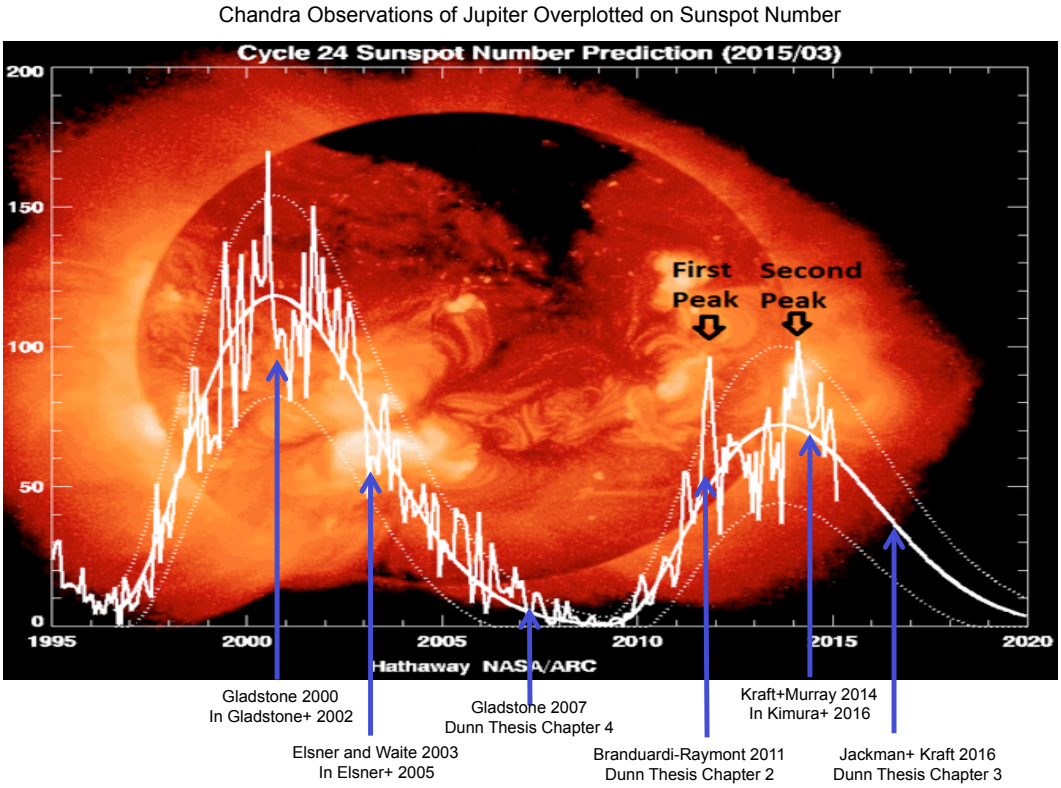

Figure 1.30: Times of Chandra Observations of Jupiter pre-2017 overlaid onto a Hathaway NASA/ARC graphic showing Sunspot number. The Upper name on each label indicates the PI of the campaign, while the lower name indicates the first publication that the observations were featured in.

Fig 1.29 is included to provide a reference point for the solar cycles of the Chandra and XMM-Newton era (from 1999 onwards) relative to their predecessors. It shows that the IMF intensity and open solar flux varies with solar cycle since 1965. While ICMEs are recognised to lead to short-term enhancements in IMF strength (Cane and Richardson 2003; Riley et al. 2006), the general trend of IMF intensity was shown to not be a direct result of measuring an increased number of ICMEs (Richardson et al. 2000). Fig 1.29 also highlights that the minimum from 2007-2009 featured the lowest magnetic field strength and open solar flux since 1965. The subsequent peak from 2013-2016 has been a markedly weak solar maximum comparable to the solar minimum of 1996.

Fig. 1.30 highlights the times of X-ray observations relative to the solar cycle revealing that there were X-ray campaigns in the deep solar minimum of 2007 and in the solar maxima of 2000-2003 and 2013-2016. These provide well distributed X-ray observations able to test relationships with the solar cycle. In this thesis, we present observations during solar maximum, solar maximum to declining phase and solar minimum in chapters 2, 3 and 4 respectively.

1.5 The Jovian Magnetosphere

> *"I understand what an equation means if I have a way of figuring out the characteristics of its solution without actually solving it"*
>
> — Paul Dirac

Given that it is interactions between Jupiter's magnetic field and associated/surrounding plasmas that will produce the Jovian X-ray aurora, it is important to understand the structures and dynamics that exist within the Jovian magnetosphere and ionosphere that might lead to the production of Jupiter's X-ray Aurora. Here, we will provide a brief orientation of the Jovian magnetosphere, ionosphere, non-X-ray auroral emissions and the possible processes that could produce the needed currents and voltages to produce Jupiter's X-ray aurora.

Gold (1959) originally defined a magnetosphere as "the region above the ionosphere in which the magnetic field of the Earth has a dominant control

	Earth	Saturn	Jupiter
Sun-Planet Distance (AU)	1	9.5	5.2
Orbital Period (years)	1	29.6	11.9
Equatorial Radius (1 bar level)	6378	60,268	71,492
Inclination (deg)	23.5	26.7	3.1
Main Atmospheric Constituents	N_2 O_2 O	H_2, H, He	H_2, H, He
Magnetic Field (T)	3.1 x 10^{-5}	2.2 x 10^{-5}	4.28 x 10^{-4}
Dipole Tilt Relative to Rotation Axis	+11.3°	0°	-9.6°
Spin Period (hrs)	24	10.6	9.9
Magnetic Moment (M_E, 7.9 x 10^{15} Tm^3)	1	600	20000
Plasma Source (kg/s)	5	12-250	260-1400
Plasma Source	Ionosphere & SW[a]	Enceladus	Io
Chapman Ferraro Radius	10 R_E	20 R_S	46 R_J
Observed Standoff Distance	8-12 R_E	22-27 R_S	63-92 R_J
Energy Source	SW	SW & Rotation	Rotation
Auroral Input (W)	10^{10}	$10^{11} - 10^{12}$	$10^{13} - 10^{14}$

Table 1.5: Comparison of Earth-Saturn-Jupiter from Bagenal et al. (2014). [a] SW - Solar Wind

over the motions of gas and fast charged particles". More broadly today, a magnetosphere is considered as the region around a body where the dynamics of charged particles are dominated by the intrinsic magnetic field of the given body.

Many have said that Jupiter is a planet of superlatives and the Jovian magnetosphere is no exception to this rule. First detected in 1954 via bursts of radio emission at decameter wavelengths (Burke and Franklin 1955), Jupiter's magnetic field was found to be particularly strong (surface field strengths up to 10s of Gauss) and tilted at almost 10° to the spin axis, with the opposite polarity to Earth's. Alongside these factors and Jupiter's rapid rotation (9.925 hours), the Galilean moon Io plays a fundamental role in producing Jupiter's vast magnetosphere - the largest structure within the heliosphere. In order to provide a reference point for the Jovian magnetosphere in the hierarchy of solar system magnetospheres, a few of the key differences between Earth, Saturn and Jupiter's magnetospheres are shown in Table 1.5 and Fig. 1.31.

The global configuration and dynamics of the Jovian magnetosphere have been explored in-situ by Pioneer 10 and 11, Voyager 1 and 2, Ulysses, Cassini, New Horizons and the Galileo spacecraft. At the time of writing this thesis,

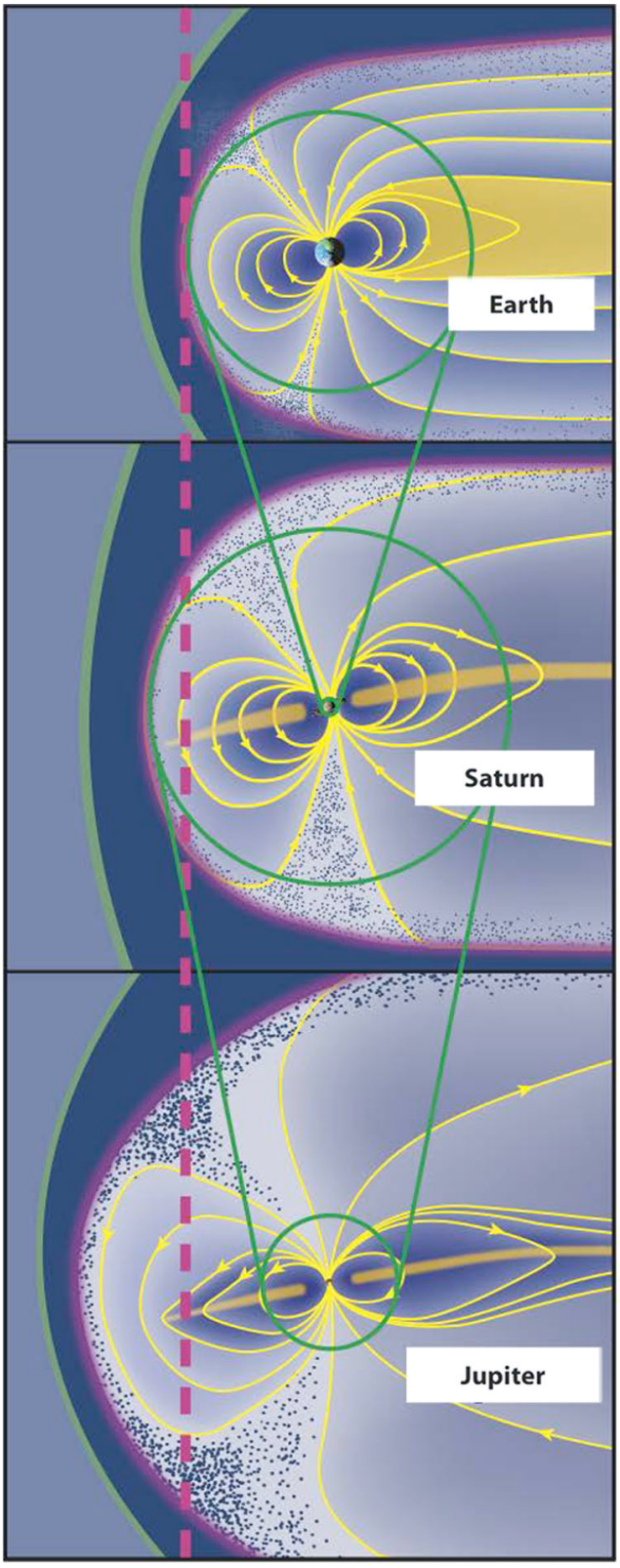

Figure 1.31: Figure and Caption from Bagenal et al. (2014): Comparison of the magnetospheres of Earth, Saturn and Jupiter. The green circles show how the magnetosphere of Earth scales to the planet Saturn and how the magnetosphere of Saturn scales to the inner 20% of Jupiter's magnetosphere. The dashed vertical line shows the scale of each magnetosphere for a pure dipole magnetic field with no internal plasma

Juno has just begun its exploration of the Jovian environment. The work presented here precedes released Juno results.

The combination of Jupiter's rapid rotation, strong magnetic field and internal plasma source (in the form of Io's volcanoes) produce many dynamics and structures in the Jovian magnetosphere. A general overview schematic of these features is shown in Fig. 1.32.

It was in 1979 with the Jupiter flyby of Voyager 1 that Io's extreme volcanic activity first became chronicled (Fig. 1.33 - Morabito et al. (1979)). Io's volcanoes eject more than 1000 kg of material every second. More than 260 kg/s (e.g. Bagenal et al. (2014)) of this predominantly SO_2 becomes dissociated and then ionised to provide electrons and ions (80% O^+ and S^{++}) that are trapped by the strong Jovian magnetic field. This plasma creates the giant toroidal loop of material that surrounds Jupiter as the Io Plasma Torus (IPT) at 5-10R_J (e.g. Bagenal (1994b)). Over timescales of weeks, flux tubes from this region interchange with those more radially distant to transport these ∼100 eV sulphur and oxygen ions and ∼5 eV electrons to the outer regions of the magnetosphere. As they are transported outwards they become heated. The exact cause of this heating remains unknown, but the plasma temperature increases to 10s of keV during this process (Bagenal et al. 2014). This provides a dense central plasma sheet of (∼100 eV heavy ions) and also a suprathermal population (greater than 1 keV) which dominates the plasma pressure at larger radial distances.

Closest to Jupiter are the highly energetic Jovian radiation belts which have been observed through synchrotron emissions produced by the ∼10 MeV particles occupying the region. These are shown in figure 1.34 and X-ray emissions from this region were reported by Ezoe et al. (2010), as previously discussed.

The magnetic field lines that the iogenic plasma is frozen onto are anchored to the Jovian ionosphere and thus rotate with the planet's rotation. This rapid rotation provides a strong centrifugal force that confines the plasma to the equator, generating a 'plasmadisk' and forcing the plasma radially outwards. This hot plasma swells the magnetosphere and the combination of the plasma

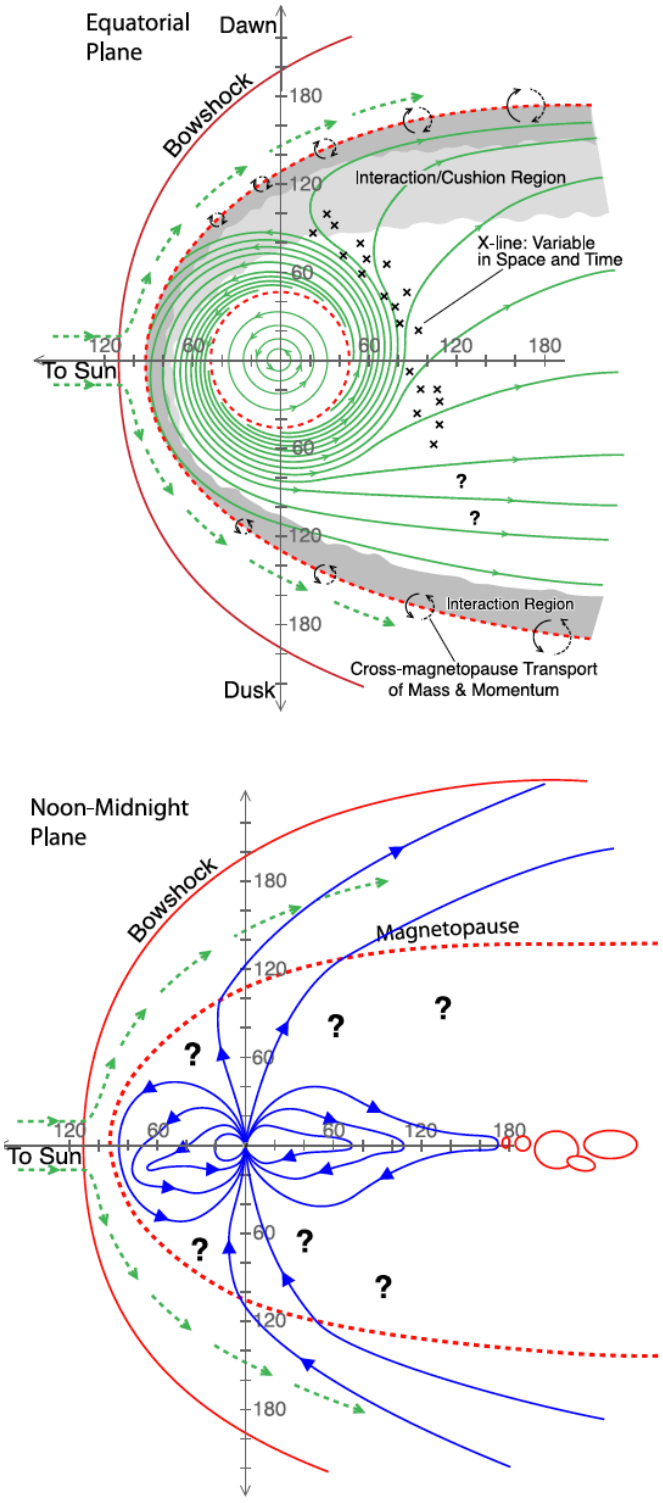

Figure 1.32: Figure and Caption from Bagenal et al. (2014): Magnetospheric structure and dynamics.While the equatorial plane (top) has been traversed multiple times and is well mapped, the polar region (see noon-midnight plane on bottom) has barely been explored and major questions remain. Blue lines show magnetic field, green lines indicate flows and red lines show boundaries between plasma regimes. On the top, the green lines indicate averaged motions of material: mostly corotating with the planet inside ∼50 RJ, outside of which the bulk of the plasma spirals outward, eventually being lost down the tail or through the magnetopause. To conserve magnetic flux through the equatorial plane, flux tubes that are largely empty must circulate inwards and return flux to the inner magnetosphere. (Based on Vasyliunas (1983); Delamere and Bagenal (2010c))

Figure 1.33: Voyager 1 photo of Io which allowed Morabito et al. (1979) to discover the first extraterrestrial volcanic eruption which can be seen from the curved bright extent on the left-hand limb of the image. Image courtesy NASA/JPL.

pressure (P_{Plasma}, Eqn: 1.25) and the magnetic pressure (P_B, Eqn: 1.26) produces a magnetosphere that is able to withstand the ram pressure of the solar wind (P_{SW}, Eqn: 1.27) to much larger distances than would be possible from the magnetic pressure of a dipole alone (as is the case for Earth - see Fig. 1.31 and Table 1.5).

$$P_{Plasma} = nk_BT \tag{1.25}$$

Where the plasma pressure, P_{Plasma}, is determined by the number density, n, temperature, T, and Boltzmann's constant, k_B.

$$P_B = \frac{B^2}{2\mu_0} \tag{1.26}$$

Where P_B is the magnetic pressure, B is the magnetic field and μ_0 is permeability of free space.

$$P_{SW} = \rho_{SW} v_{SW}^2 \tag{1.27}$$

Where P_{SW} is the ram pressure of the solar wind, v_{SW} is the velocity of

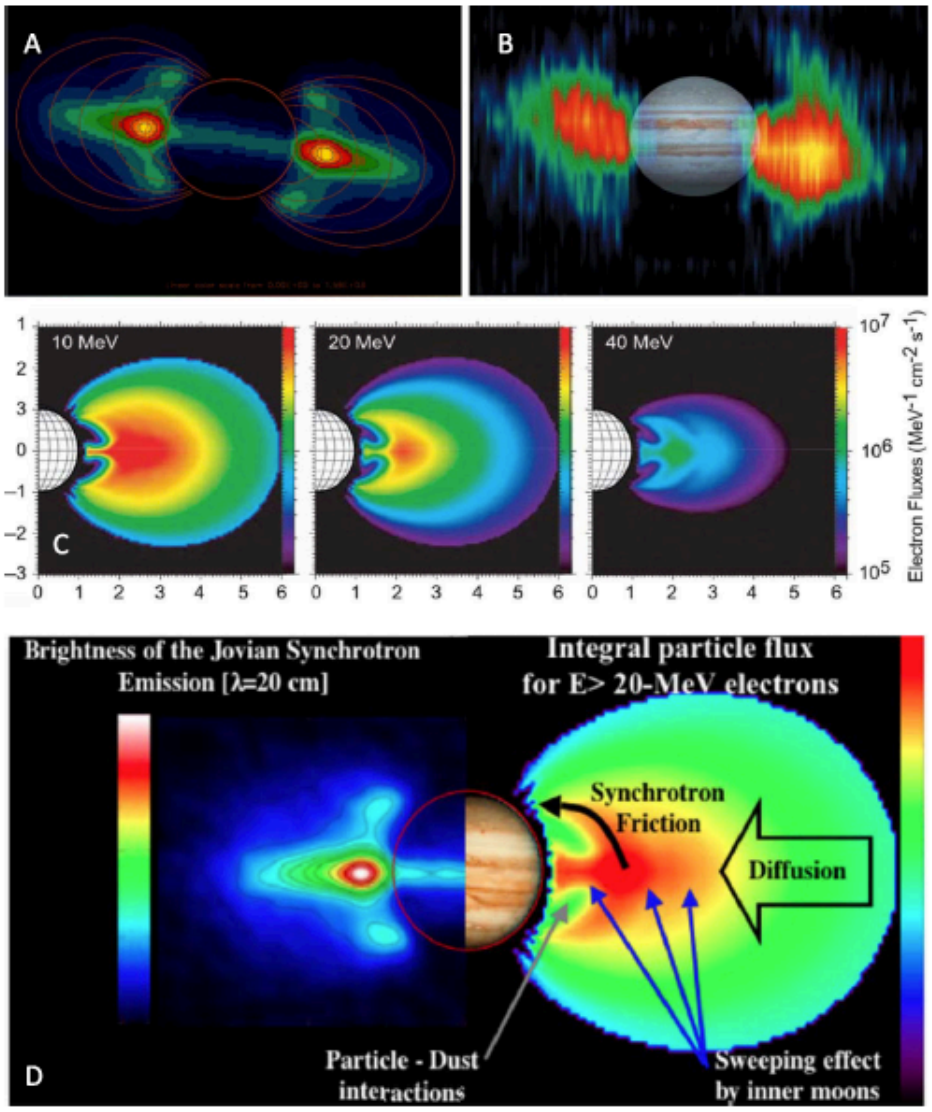

Figure 1.34: Collated in Bagenal et al. (2014) : Jupiter's synchrotron/radiation belts. A) 1400 MHz radio VLA observation of Jupiter B) 2.2 cm radio Cassini observation of Jupiter C) Models of omni-directional differential electron fluxes in a meridian plane for 10, 20 and 40 MeV. D) Schematic of electron transport, energisation, and loss processes that produce the spatial and spectral characteristics of the Jovian synchrotron emissions (Bolton et al. 2004; Santos-Costa and Bolton 2008)

the solar wind and ρ_{SW} is the density of the solar wind. $\rho_{SW} = m_p n_{SW}$ is dominated by the proton mass, m_p, and n_{SW} is therefore the proton number density.

Earth's magnetospheric standoff distance matches the 8-12 R_E expected from balance between the solar wind ram pressure (Eqn: 1.27) and the dipole magnetic pressure, (Eqn: 1.26) and - the Chapman Ferraro Radius. The standoff point for the Jovian Chapman-Ferraro radius of 46 R_J falls significantly short of the actual standoff distance because it does not account for the additional pressure from the hot plasma. This additional hot plasma pressure also makes the magnetosphere much more compressible with a more dramatic shift in magnetopause location than for the Earth. The Jovian standoff distance varies bimodally between 63 and 92 R_J (Joy et al. 2002) with solar wind compressions and rarefactions respectively (McComas et al. 2013, 2014).

This hot Jovian magnetospheric plasma has a high plasma β (Eqn: 1.28):

$$\beta = P_{Plasma}/P_B \tag{1.28}$$

so the plasma pressure dominates over the magnetic pressure and the magnetic field becomes stretched, which produces strong currents in the equatorial plasma disk. These stretched field lines come close together; to prevent oppositely directed field lines coming into contact a current sheet and associated plasma sheet must form. This equatorial magnetodisk rotates with the planet's magnetic field, which, given its 9.6 ° tilt to the rotation axis (e.g. Table 1.5), leads the magnetodisk to wobble up and down with respect to the planet's rotation equator. This disk is relatively thin in the dawn sector (2 R_J half thickness) and thicker on the dusk side (7.6 R_J half thickness) (Khurana et al. 2004).

While stretching of the magnetic flux tubes in the equatorial plane is associated with strong azimuthal currents in the plasma sheet (j_ψ), another current system pertinent for the aurora emission is also produced. From the middle magnetosphere outwards, Jovian magnetospheric plasma begins to drop below the corotation speed as it moves radially outwards and conserves angular

momentum. The equatorial plasma angular velocity and attached ionospheric magnetic flux tubes will eventually fall below the velocity of neutral particles in the planetary atmosphere, generating a differential velocity between the ionosphere and neutral atmosphere. This results in plasma-neutral collisions in the Pedersen conducting layer of the ionosphere which provides the needed torque to raise the ionosphere up to corotation velocities. The ionospheric Pedersen current (perpendicular to the magnetic field) balances the frictional torque with a jXB (cross product of the current,j, and magnetic field, B) force opposite to the planet's direction of rotation.

This ionospheric current systems is partnered by a field aligned current system ($j_{\parallel}$) flowing out of the ionosphere and into the plasma sheet (see Fig 1.35). This current system acts to impart angular momentum from the Jovian ionosphere into the equatorial plasma to maintain corotation with the planet (Cowley and Bunce 2001; Hill 2001). Upon reaching the current sheet it flows radially outwards (j_r) and generates a $j_r XB$ force which accelerates the magnetospheric plasma to also return it to corotation. It is this upward current system (outward from the planet), along which electrons flow down into the ionosphere that produces the bright UV main oval and hard X-ray oval. This novel concept relative to the Earth environment, shows that rapidly rotating bodies with an internal source of plasma can produce their own aurora through this process of corotation enforcement.

The field aligned current outward from the planet which then flows radially outwards through the disk to the outer magnetosphere and possibly the magnetopause (Cowley and Bunce 2001; Bunce et al. 2004; Kivelson et al. 2002; Cowley et al. 2005), must return to the ionosphere via another field aligned current at higher latitudes. It has been suggested that it is this returning (downward) current system that accelerates the ions to produce the X-ray aurora (see section 1.8 or Cravens et al. (2003)). Mauk and Saur (2007), suggested that instead/along with the downward (return) current flowing in the outer magnetosphere, downward currents might be interspersed with upward currents in the plasma sheet. In order for these interspersed currents to charge strip magnetospheric ions to produce X-rays they would also need to

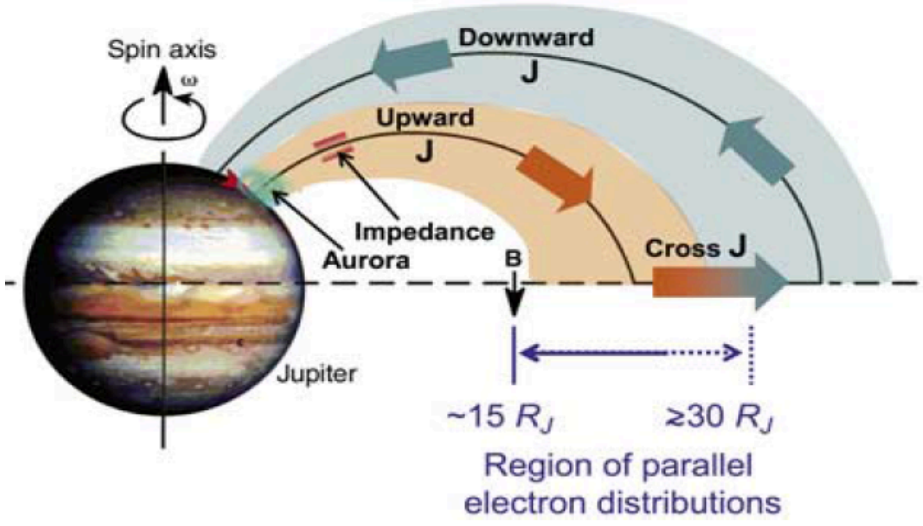

Figure 1.35: Schematic of Jupiter's Upward and Downward Current System from Mauk and Saur (2007). This shows the flow of an upward current system out of the planet, the subsequent radial flow which produces a J X B force (cross product of the current,j, and magnetic field, B) to accelerate plasma that would otherwise be sub-corotating back towards corotation, then a subsequent downward (returning) current system in the outer magnetosphere. Mauk and Saur (2007) suggest that there might be interspersed upward and downward currents within the upward current system.

provide high accelerations.

There is a local time variation in the location of corotation breakdown and the subsequent corotation enforcement current system. Mass-loading and loss (through the Vasyluinas cycle discussed later), is thought to be the source of this asymmetry which leads the corotation enforcement region to occur at $\sim 40 R_J$ in the dawn sector and 20-25R_J in the dusk sector. This local time variation in the upward current system leads to asymmetries in the auroral main emission. Mass-loading or loss triggered by Io or solar wind compressions/expansions can also move the corotation breakdown region.

Magnetospheric local time variations in the radial currents are thought to lead to strong local time asymmetries in the Jovian magnetic field (Khurana and Kivelson 1989a; Khurana 2001; Khurana and Schwarzl 2005). Fig. 1.36 shows the strong dawn-side bend-back (relative to the dusk-side magnetosphere).

Eventually, in the outer magnetosphere, the plasma begins to lag corotation and the field lines become stretched. Figure 1.32 shows the region where plasma lags corotation beyond $\sim 50 R_J$. In this region the radial outflow of the

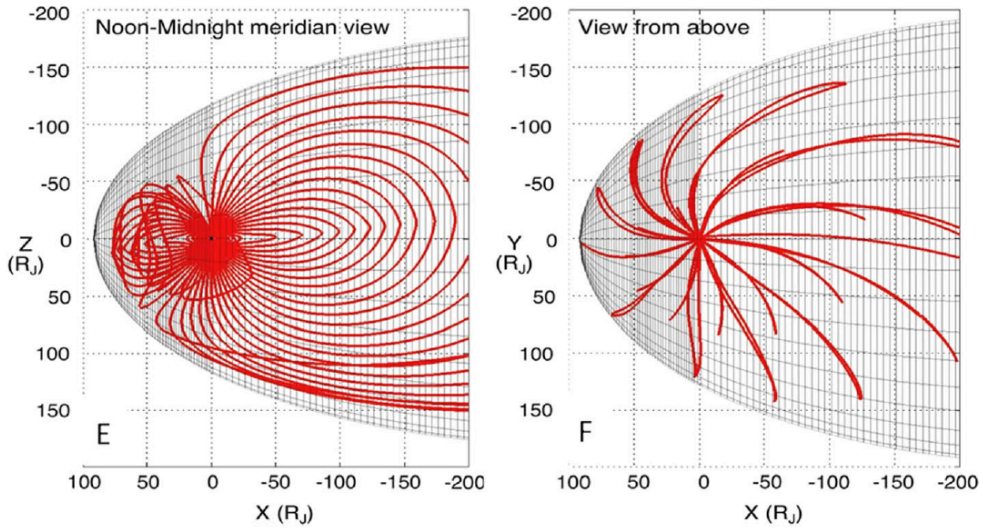

Figure 1.36: From Khurana and Schwarzl (2005): Three-dimensional magnetic field model including the VIP4 model for the interior field plus external magnetospheric currents. This reveals that radial currents produce strong asymmetries in the Jovian magnetic field including bend-back in the field lines in the dawn sector.

plasma becomes comparable to its azimuthal velocity and the plasma spirals outwards.

As the plasma rotates into the tail on the dusk side, the magnetic field lines become progressively more stretched by the equatorially confined dense plasma. Eventually, in a region in the dusk to night-side tail the current sheet that separates the field lines becomes particularly thin and oppositely directed field lines come into contact. A process of reconnection occurs and the stretched magnetic field lines can pinch off through the Vasyluinas Cycle (Vasyliunas 1983) (see Fig. 1.37). This releases plasmoids of magnetospheric plasma from closed magnetic field lines, ejecting them into the Jovian tail (as shown in the lower panel of Figure 1.32). This process of internally driven reconnection does not occur at Earth, but requires the internal plasma source and rapid rotation of planets like Jupiter and Saturn. This process may continue onto open field lines in a Dungey-like process (e.g. Cowley and Bunce (2003b)), where open flux advects across the poles of the planet and undertakes a second process of magnetic reconnection in the tail. However, the relative importance and rate of occurrence of a Jovian Dungey-like process remain debated (see section 1.6).

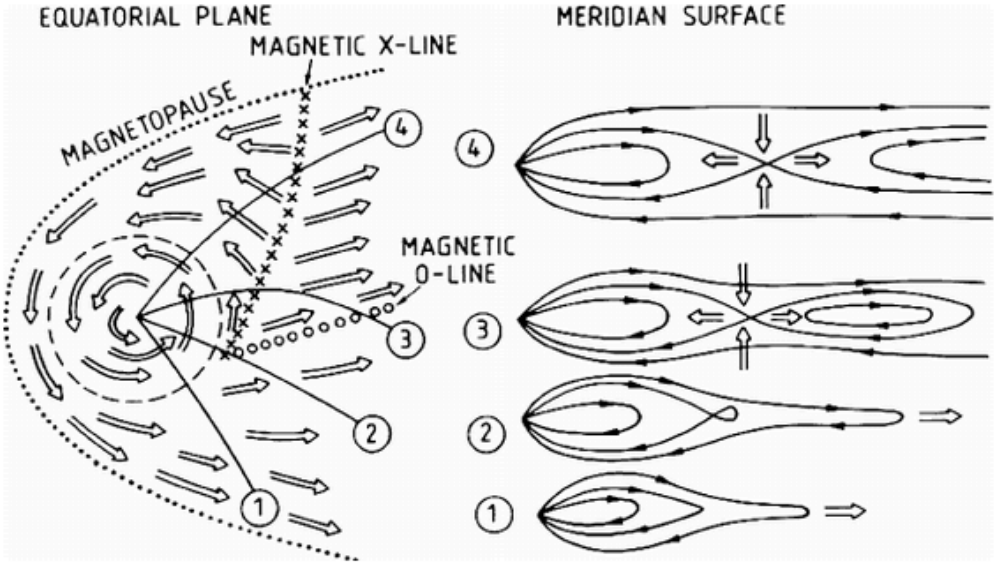

Figure 1.37: Schematic of Rotationally Driven Tail Reconnection from Vasyliunas (1983): The flow of magnetospheric plasma at Jupiter looking down onto the equatorial plane (left) and subsequent Jovian field configuration looking side-on in the meridian plane (right) with the expected subsequent release of a plasmoid caused by Jupiter's rapid rotation.

Once plasmoids have been ejected the empty flux tubes can rotate back into the dawn sector providing the more compressible dawn-side cushion region (Fig. 1.32). The plasma thickens on the dusk-side, expanding outwards to produce a more robust magnetopause boundary and stronger current systems. This heating and thickening may be produced by the rapid expansion of flux tubes in the afternoon-dusk sector, which may lead the second adiabatic invariant to no longer be conserved (Kivelson and Southwood 2005; Vogt et al. 2014). The conservation of the second adiabatic invariant, J, refers to conservation in the bounce frequency of a particle with mass, m, and parallel velocity $v_{\parallel}$ along a field line between two mirror points.

$$J = \oint m v_{\parallel} ds \tag{1.29}$$

For this not to be conserved the flux tubes must expand on a timescale shorter than that required for a charged particle to oscillate between the two mirror points and will result in a thermal anisotropy.

Plasmoids with scales of $\sim 25 R_J$ are observed to be ejected both tailward

and Sunward of Jupiter at radial distances of 70-120 R_J with a periodicity of 4 hours to 3 days (Krupp et al. 1998; Woch et al. 1998; Louarn et al. 1998; Kronberg et al. 2005, 2008; McComas and Bagenal 2007; McNutt et al. 2007; Hill et al. 2009; Vogt et al. 2010; Ge et al. 2010; Kasahara et al. 2013). Krupp et al. (1998); Woch et al. (1998) suggest that this periodic ejection is the product of the timescale for mass-loading, unloading and the snap-back of field lines, both radially towards the planet and azimuthally in the direction of planetary rotation. Louarn et al. (1998, 2000, 2001) showed that thickening and thinning of the disk (through loading and unloading of plasma) coincides with global disk perturbations of the IPT to 120 R_J on time scales of hours with Quasi-periodic (QP) variations of 3-10 days. In addition to these large-scale events, Bagenal (2007) suggest there could also be a diffusive 'drizzle' of plasma loss across highly-stretched field lines or quasi-steady release of small-scale plasmoids below the detection limits.

At distances of around 100 R_J the plasma becomes progressively less coupled to the ionosphere because the Alfvén travel time becomes so large. At 100 R_J, Bagenal et al. (2014) suggest that the one-way Alfvén travel time is about 100 minutes, meaning that during the propagation of a signal from the planet to the plasma sheet the ionosphere will rotate roughly 60° and the plasma sheet will rotate 30°.

1.6 Jupiter-Solar Wind Interactions

Having discussed the solar wind and Jupiter's magnetosphere as separate entities, we now broach the topic of how the largest structure in the heliosphere interacts with the plasma environment that surrounds it. What process dominates remains an open question, so here we will discuss in brief some of the possible interactions and discourse from the literature.

When the solar wind interacts with a magnetised object it produces a bow shock upstream of the object. Slightly downstream, behind the bow shock there is a magnetosheath of heated plasma that is deflected around the object. Downstream of the magnetosheath is the magnetopause, the boundary

Table 1.6: Table of Typical Solar Wind Parameters at Jupiter during the declining phase of the solar cycle 2003-2005 (Ebert et al. 2010; Bagenal et al. 2014): [a]These values are 1-hour averages of Ulysses data at heliocentric distances of 5.273 to 5.403 AU within 10° of Jupiter's inclination at the time.
[b]10th and 90th percentiles of the solar wind distribution
[c]Ratio of proton thermal pressure to magnetic field pressure
[d]Ratio of solar wind speed to Alfvén speed

	10 %[b]	Mean	Standard Deviation	Median	90 %[b]
Proton speed (km/s)	369	451	±71	438	557
Solar wind azimuthal deflection (deg)	-3.1	-0.3	±2.1	-0.2	2.0
Solar wind meridional deflection (deg)	-2.6	-0.16	±2.1	-0.16	2.1
Proton temperature (eV)	0.55	2.8	±3.8	1.4	6.8
Proton density (cm^{-3})	0.036	0.22	±0.27	0.13	0.50
Alpha particle composition (% by density)	2.6	3.1	±3.3	3.1	3.1
Dynamic pressure (nPa)	0.014	0.084	±0.11	0.045	0.20
B-field strength (nT)	0.18	0.69	±0.63	0.45	1.5
B-field azimuthal angle, B_t >0 (deg)	46	95	±35	98	137
B-field azimuthal angle, B_t <0 (deg)	-134	-81	±38	-79	-31
B-field meridional angle (deg)	-40.4	0.37	±31.1	0.49	40.8
Plasma β[c]	0.12	0.66	±1.6	0.38	1.2
Alfvén Mach Number[d] (Flow speed/Alfvénspeed)	7.4	17.7	±11.5	16	29

between the region dominated by the object's magnetic influence and that controlled by the surrounding plasma. The location of the magnetopause and the spatial extent of the magnetosphere is controlled by the balance between the internal magnetic and plasma pressure pushing outwards and the external ram pressure (in this case of the solar wind) pushing inwards. Downstream of the planet itself there is a magnetotail, in Jupiter's case this extends thousands of R_J downstream and has been observed at the orbit of Saturn.

As already discussed, the solar wind compresses and expands the Jovian magnetosphere to produce a bimodal distribution of magnetopause standoff distances between 63-92R_J (Joy et al. 2002; McComas et al. 2013, 2014).

Table 1.6 shows a statistical sample of the solar wind parameters at Jupiter as measured by Ulysses during the declining phase of the solar cycle in 2005 (Ebert et al. 2010). At Jupiter these solar wind parameters are far from

gaussian distributions, so for instance the density and consequently the dynamic pressure of the solar wind has a factor of 10 variation between the 10th and 90th percentile values. The magnetic field strength and consequently the plasma β also exhibit these factor of 10 variations. In contrast with this, the azimuthal and meridional flows of the solar wind are very small meaning that the solar wind flow is practically radial at Jupiter. Looking to the IMF, at Jupiter the azimuthal angle positions the Parker spiral at $\pm 90^\circ$ to the radial, but also changes direction multiple times during each solar rotation.

It is also important to consider the IMF angle out of the ecliptic (meridional), which may be considered important for reconnection, which prefers anti-parallel field lines. Relative to Jupiter's southward pointing magnetic field, the meridional IMF is dominantly at 0° with 10th and 90th percentiles only taking it as far as 40°. This may explain the low rates of steady, large-scale reconnection at Jupiter (Walker and Russell 1985; Desroche et al. 2012), since the IMF is rarely anti-parallel. Other important factors for reconnection include the plasma β which needs to suggest a magnetically-dominated (low β) environment to favour reconnection.

1.6.1 Competing Ideas

It has been noted that the corotation potential (376 MV) for Jupiter is far greater than the potential from the solar wind (0.5 MV), so the role of the solar wind may be minimal for Jupiter. Broadly, two scenarios exist for the dominant Jovian solar wind interaction:

1. Jupiter is an open magnetosphere: magnetic flux opened during reconnection with the solar wind at the dayside magnetopause is transported across the magnetospheric polar region into the tail followed by a returning planetward flow on the dawn-side of the tail (Cowley and Bunce 2003a; Badman and Cowley 2007). An open field region is often identified by: a) a change in plasma population, when previously-trapped magnetospheric plasma is lost to the interplanetary medium and magnetosheath plasma enters the magnetosphere, and b) the anti-sunward motion of open field lines. However, for Jupiter, long transport times due to the large scale of the Jovian magne-

tosphere have led the existence of an open field lines region to be disputed for Jupiter (Cowley et al. 2003; Badman and Cowley 2007; McComas and Bagenal 2007; Cowley et al. 2008; McComas and Bagenal 2008; Delamere and Bagenal 2010c). In 1992, Ulysses did appear to sample a region of Jupiter's magnetosphere analogous to Earth's polar cap (Simpson et al. 1992). In this region, the MeV particle fluxes were reduced (suggesting loss to the interplanetary medium). Alongside this, there were typical solar wind proton helium ratios, more isotropic distributions of MeV protons, loss of magnetospheric electrons and the presence of auroral hiss and anti-Sunward propagating ion flows (Bame et al. 1992; Simpson et al. 1992; Cowley et al. 1993; Stone et al. 1992). Perturbation in the magnetic field, suggested a field-aligned current at the boundary with a low ionospheric conductivity at the corresponding footprint (Cowley et al. 1993). However, the single spacecraft measurements were unable to constrain the extent of the region.

2. Jupiter is a closed magnetosphere: Jovian magnetic field lines do not remain connected to the IMF for timescales that are a significant fraction of the timescale required to transport magnetic flux across the pole and into the tail. Instead, magnetic flux is opened and closed intermittently in small-scale structures on the flanks of the magnetosphere (e.g. Delamere and Bagenal (2010c)) or through a second reconnection process shortly after it has opened (e.g. McComas and Bagenal (2007)). This would occur through processes like Kelvin Helmholtz instabilities in which a velocity shear drives viscous interactions between heavy, dense magnetospheric plasma and light, tenuous solar wind plasma (Delamere and Bagenal 2010c).

Outside of arguments of opened or closed magnetospheres, Kivelson and Southwood (2005) suggest a relationship between solar wind confinement of the magnetopause and the extent to which a Vasyluinas-like cycle is capable of ejecting material down the Jovian tail. They show that centrifugal instabilities in the outer magnetosphere can produce pressure anisotropies on the magnetic field. Force balance can be violated if the parallel pressure ($P_{\parallel}$) is greater than the combined magnetic pressure ($\frac{B^2}{\mu_0}$) and perpendicular pressure ($P_{\perp}$) - see

Eqn 1.30 .

$$P_{\parallel} > P_{\perp} + \frac{B^2}{\mu_0} \tag{1.30}$$

This leads to ballooning in the plasma sheet and where the magnetopause confines the plasma on the day side, the mass is forced down the tail. This is sometimes referred to as the 'firehose instability'. It leaves the plasma sheet thinned as it moves into the dawn sector across morning to noon, where the empty flux tubes are assimilated into the hot dusk plasma sheet.

1.6.1.1 The Presence of a Jovian Dungey Cycle

(Cowley et al. 2003) account for the outward moving, sub-corotation, hot Jovian plasma and Vasyluinas cycle in the outer magnetosphere to adapt a traditional Earth-like Dungey cycle to Jupiter. This results in a 'single-cell' Dungey cycle dominantly in the post-midnight to dawn sector, which explains well the observations of Stallard et al. (2001) of a strongly sub-corotating flow in the dawn-side polar aurora (e.g. see Fig. 1.55). Figure 1.38 shows schematically how the Dungey cycle would fit within the known magnetospheric dynamics of the Jovian system. Open field lines from the process flow from dusk to dawn, closing in the Dungey cycle tail reconnection site near the dawn magnetopause where they form a boundary layer. Here, Phillips et al. (1993); Krimigis et al. (1981) do indeed find the low plasma densities expected and Krimigis et al. (1981) identified a magnetospheric wind in this location.

This set of flows produces the distinction in auroral emissions and ionospheric flows shown in Figure 1.39, where as one moves progressively polewards the flows become sub-corotational. Depending on the drag of the ionosphere, this sub-corotation may be passed onto the neutral atmosphere. The Pedersen current structure produced by the flows generates a downward current system just inside the upward current system on the dawn edge which may explain the much thinner main oval emission always observed on this side. The empty flux tubes associated with the boundary layer formed by the Dungey cycle might also explain the dark region observed in the aurora.

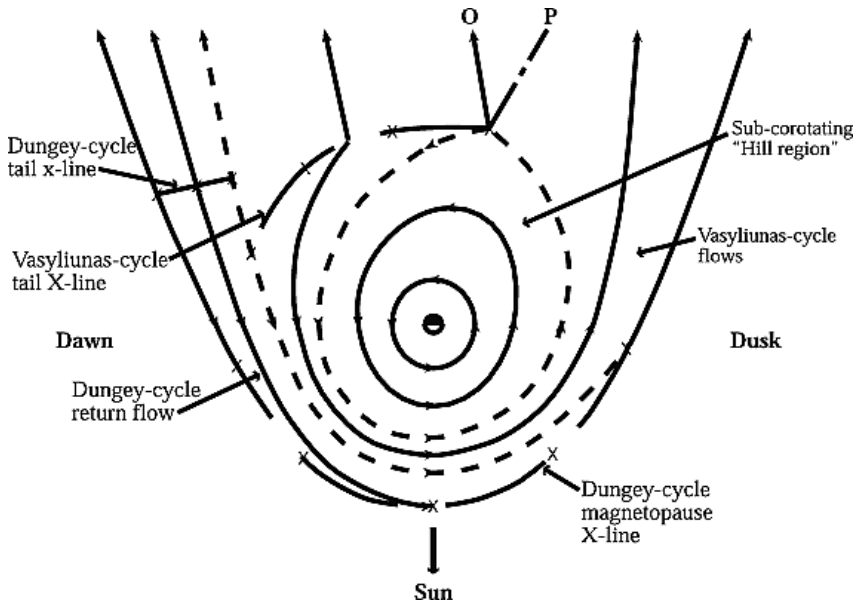

Figure 1.38: Schematic of Jupiter's Magnetosphere Showing a Possible 'Single-Cell' Dungey Cycle (Cowley et al. 2003): Sketch of the flows in the Jovian equatorial plane. The sub-corotating 'Hill region', represents the main part of the Jovian middle magnetosphere extending to distances of several tens of R_J. Outward from this is the region that is still driven by planetary rotation in which current sheet dynamics and reconnection occur via the Vasyliunas cycle (dashes and X's, labelled 'Vasyliunas-cycle tail X-line', where tail reconnection occurs). The O-type line of the plasmoid is a plasma streamline (marked by O), with the outer edge of the plasmoid shown by the dot-dashed line (marked P).

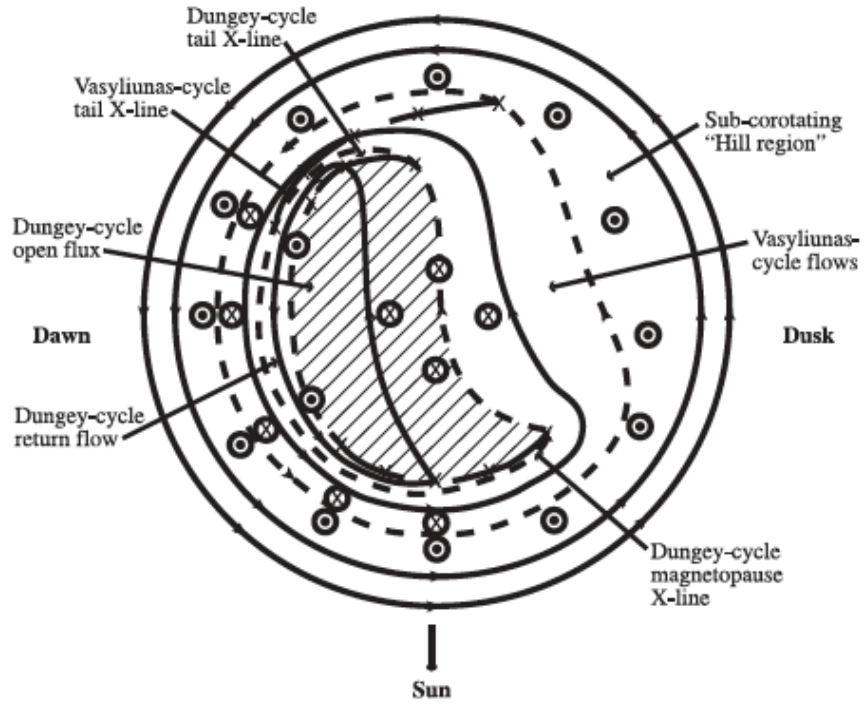

Figure 1.39: From Cowley et al. (2003): Sketch of the flows in the Northern Jovian Ionosphere.

Badman and Cowley (2007) build on this to suggest that while most magnetic flux circulates in the inner magnetosphere, during solar wind compressions from CIRs or ICMEs reconnection voltages of several MV occur. This heightened reconnection voltage leads to substantial Dungey cycle return flows with widths of $\sim$4 R_J inside the dawn-morning magnetopause. However, during solar wind rarefactions the flows may contribute less than 1 R_J of flowing material.

1.6.1.2 Absence of Dungey Return Flows and Possible Double Reconnection

In contrast with the suggested presence of a Dungey cycle, it has been noted that there is evidence of only small amounts of dayside reconnection at Jupiter, leading to a small Dungey reconnection potential compared with the planetary corotation potential (Walker and Russell 1985; Badman and Cowley 2007).

Further, the large time-scales required for open flux to convect across the pole and into the Jovian tail and then to return to the planet from the tail, led McComas and Bagenal (2007) to argue that a Dungey cycle would be unfeasible for Jupiter. Instead, they proposed that flux that opens at the dayside magnetopause must re-close through a second process of reconnection with the IMF and/or along the flanks before it reaches the tail (Figures 1.40 and 1.41). This results in little to no planetward Dungey return flow. In arguing against a return flow they note that it would take 3-4 days for open fields to penetrate the tail and during this time the solar wind would have dragged these field lines 1000s of R_J downstream, meaning that once this field line had undergone tail reconnection and closed, it would take 100s to 1000s of hours to return, during which Jupiter would have rotated 100s of times. This process of double reconnection or reconnection poleward of the terrestrial cusp has been observed at Earth (Lavraud et al. 2005; Song and Russell 1992). McComas and Bagenal (2007) suggest that the small Jovian polar cap and Voyager observations of the tail, which showed limited twisting and possible correlations with solar wind sector boundaries that would trigger the second reconnection process, also support their theory.

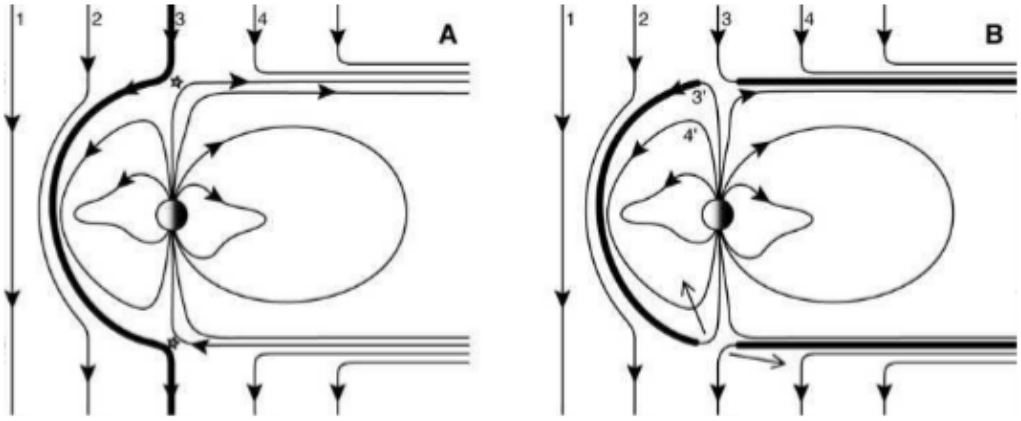

Figure 1.40: Schematic of Double Reconnection at Jupiter from McComas and Bagenal (2007): (a) A significantly southward IMF (1) drapes around the dayside magnetopause (2, 3) until it reconnects with an oppositely-directed planetary field (stars). (b) Flux tube 3 reconnects near the magnetopause near both north and south cusps, creating newly closed (3') and disconnected (3) flux tubes. (Note that Jupiter's intrinsic magnetic field is opposite that of the Earth's so erosion near the nose occurs preferentially for northward IMF instead of southward.) After reconnection, the short, newly closed flux tube is free to work its way back toward a more normal closed shape (4'), while the long, newly disconnected flux tube (4) is lost down the flanks of the tail

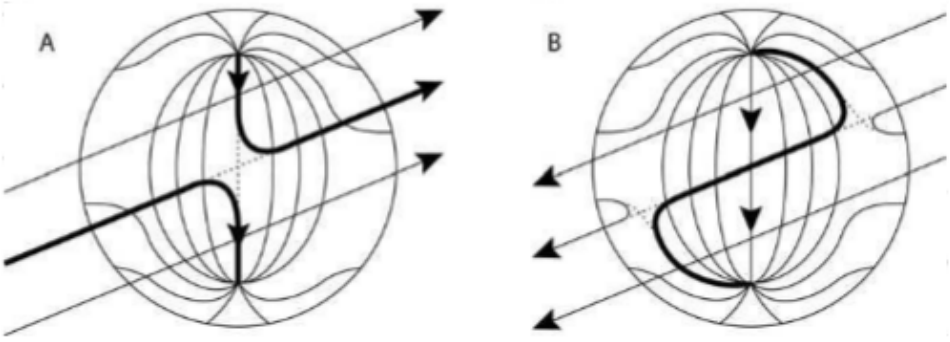

Figure 1.41: Schematic View of Jupiter's Magnetopause Nose from the Sun for Double Reconnection from McComas and Bagenal (2007): By 5 AU the IMF spiral (transverse) component is generally dominant and the sub-solar flow drapes the field around the lower latitude portions of the magnetosphere. (a) For outward sector IMF that are slightly northward, magnetic flux should be opened near the nose and pulled back (dark lines) over the top-right and bottom-left. (b) A change to inward sector IMF would produce reconnection of a single solar wind flux tube on both sides, re-close magnetic flux (dark line), and preferentially release disconnected flux tubes (U-shaped lines) down the top-right and bottom-left flanks for inward IMF sectors. Dashed lines indicate field topologies prior to reconnection. Similar reconnection topologies would be produced for inward sectors over the opposite quadrants.

1.6.1.3 Jovian Viscous Interactions with the Solar Wind

Cassini observations at Saturn have revealed extensive Kelvin Helmholtz structures (Masters et al. 2009; 2010; 2011a; 2011b; 2012; and Delamere et al. 2011;2013). Often for Jupiter, the high Alfven Mach number of the solar wind (see Table. 1.6) and the significant difference in plasma β across the magnetopause favour a suppression in reconnection (Masters et al. 2012; Desroche et al. 2012, 2013).

The location of the boundary between Jupiter's magnetosphere and the solar wind is determined by the balance between the dynamic pressure of the solar wind and the pressure from Jupiter's high plasma β magnetospheric plasma. This plasma-on-plasma environment will produce viscous interactions between the magnetospheric plasma and the solar wind plasma that wraps around the magnetosphere. Delamere and Bagenal (2010c) show that under these circumstances Kelvin Helmholtz Instabilities (KHI) or wave-induced transport processes can:

1. produce the required exchange of plasma across the boundary
2. create the observed magnetospheric dawn-dusk asymmetry
3. define the location of the reconnection X-line (through the balance of magnetospheric stress anti-sunward with the solar wind induced stress tailward) and therefore drive escape of plasma down the magnetotail
4. produce the observed polar aurora

For two fluids on either side of a shear flow boundary to be Kelvin Helmholtz unstable (prone to developing vortices) they must meet the following criteria:

$$[k.(v_1 - v_2)]^2 > \frac{n_1 + n_2}{\mu_0 m_0 n_1 n_2}[(k.B_1)^2 + (k.B_2)^2] \tag{1.31}$$

where k is the KHI wave vector, μ_0 is the permeability of free space, v is the velocity of each fluid, n is their number density, m_o is the ion mass, B is the magnetic field, and the indices 1 and 2 represent each of the fluids involved. The dependence on these parameters means that the compressed or

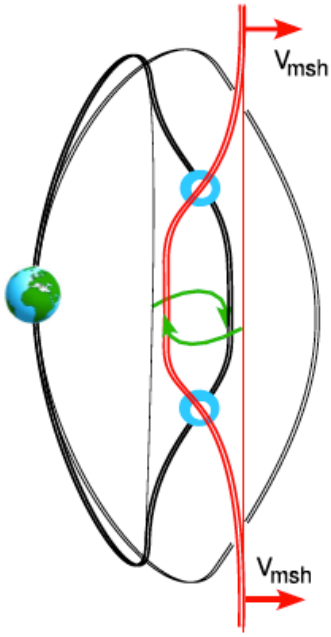

Figure 1.42: Schematic for Intermittent Reconnection from Kelvin Helmholtz Instabilities (Delamere and Bagenal (2010c) and references therein): The blue circles mark the location of reconnection at the boundary between magnetically connected KH stable (high latitude) and unstable regions (equatorial plane).

expanded state of the magnetosphere might significantly affect the stability, location and prevalence of KHI at Jupiter, since a compressed magnetosphere presents a higher magnetic field strength along the boundary, while an expanded magnetosphere is a higher plasma β medium (Delamere and Bagenal 2010c).

Historically, KHI were often thought of as distinct from magnetic reconnection. However, rather than being distinct, KHI can produce magnetic reconnection (Delamere and Bagenal (2010c) and references therein). Reconnection is often restricted for Alfvén Mach numbers (Ratio of solar wind speed to Alfvén speed) larger than one, however, KHI can compress the magnetopause to permit reconnection (Nakamura et al. 2006; Nykyri et al. 2006). Alternatively, KHI can produce magnetic field line topologies favourable to reconnection such as the twisted magnetic field line configuration shown in Figure 1.42 (Keller and Lysak 1999; Nykyri and Otto 2001). While there are regions associated with this figure that are KH stable and anchored in the ionosphere, there are other regions along the same flux tube that are KH unstable and can undergo reconnection. It is possible therefore for energetic particles

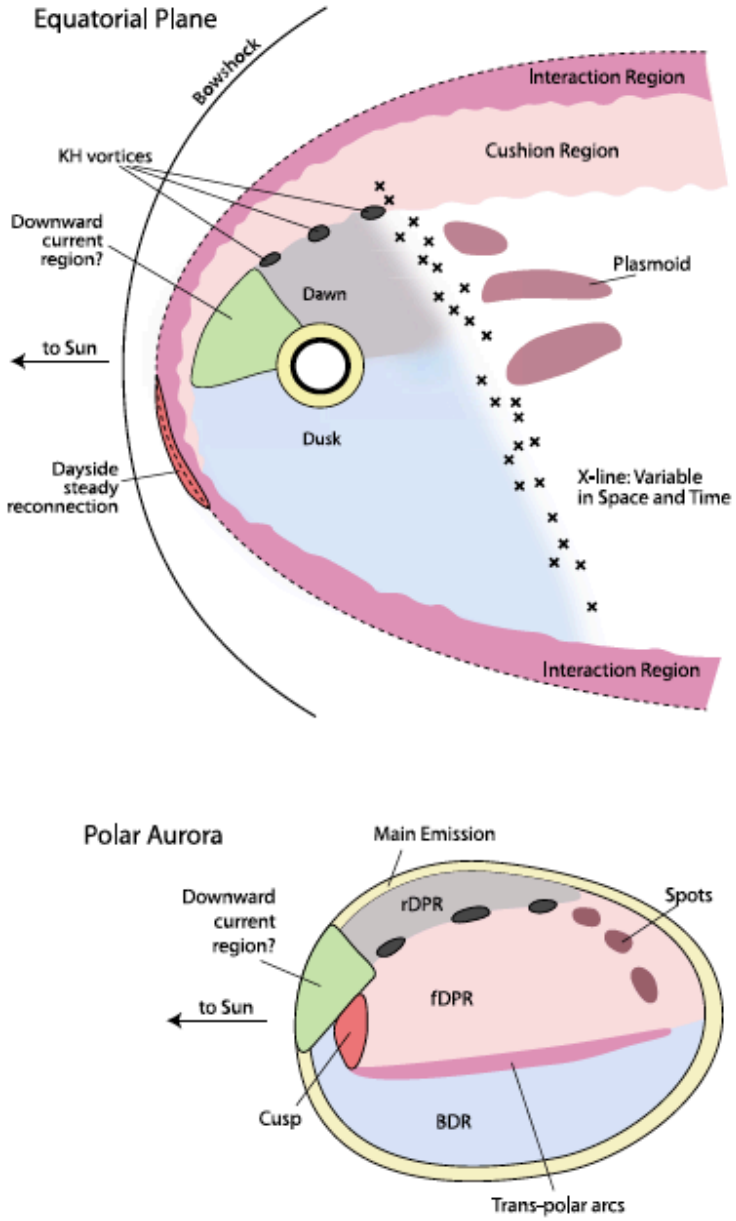

Figure 1.43: Schematic of the Magnetosphere and Polar Ionosphere with Auroral features produced by viscous interactions (Delamere and Bagenal 2010c): Illustration of aurora signatures associated with specific regions of the equatorial magnetosphere.The grey rotating DPR (rDPR) corresponds to the dawn corotational flows. The pink fixed DPR (fDPR) corresponds to the tailward flows in the interaction and cushion regions. The blue bright polar region (BPR) corresponds to the dusk sector where corotating ionospheric flows are decoupled from the subcorotating magnetospheric flows. The bright auroral emissions may be a signature of this decoupling.The transpolar arcs are likely associated with strong velocity shear at the interface between the fDPR and the BPR. Nightside spots suggest signatures of reconnection in the tail (plasmoids/spots) and shear-driven instabilities (black spots) between the rDPR and fDPR are suggested as a mechanism for the complex polar cap auroral forms. Cusp signatures are shown in red.

to be exchanged across the boundary several times in intermittent small-scale regions of open flux. Alternatively, solar wind driven compressional waves or many other types of instability might be able to transport mass, momentum or energy across the magnetopause (Johnson and Cheng 1997; Johnson et al. 2001; Delamere and Bagenal 2010c).

Of possible importance to the Jovian aurora, KH vortices are capable of generating strong intensifications in field aligned currents (Otto 2006, 2007, 2008). Figure 1.43 shows how Delamere and Bagenal (2010c) apply their model to the Jovian aurora in order to try to explain the observed emissions. They suggest that the stagnant flows in the dawn sector represented on the figure as the grey rotating dark polar region (rDPR) could be produced by dawn-side corotational flows, while the pink fixed dark polar region (fDPR) maps into the cushion region produced by solar wind induced drag. The blue bright polar region (BPR) corresponds to the dusk sector where corotating ionospheric flows are decoupled from the subcorotating magnetospheric flows. They further suggest that the transient transpolar arcs in this region are from velocity shears at the interface between the fDPR and the BPR. The cusp region with correspondingly small open flux is labelled in red.

Desroche et al. (2012) further explore the locations on an expanded magnetopause that could be KH unstable and/or susceptible to reconnection. Figure 1.44, suggests that the magnetopause is preferentially KH unstable on the dawn side, except when the magnetosphere is very polar flattened (bottom panels), when the dusk flank can also become unstable. Ma et al. (2015) show that for Saturn, while KHI are expected to first develop in the pre-noon sector, those that develop between 10 - 14h local time actually propagate across noon and into the dusk side where they are able to grow (see Fig. 1.45). Contrary to expectations, the strong shear flows on the dawn side actually inhibit KHI growth.

1.6.1.4 Locations Viable for Dayside Reconnection at Jupiter

Desroche et al. (2012) also show that the shear flows which permit KHI on the dawn flank also restrict traditional dayside reconnection there, but per-

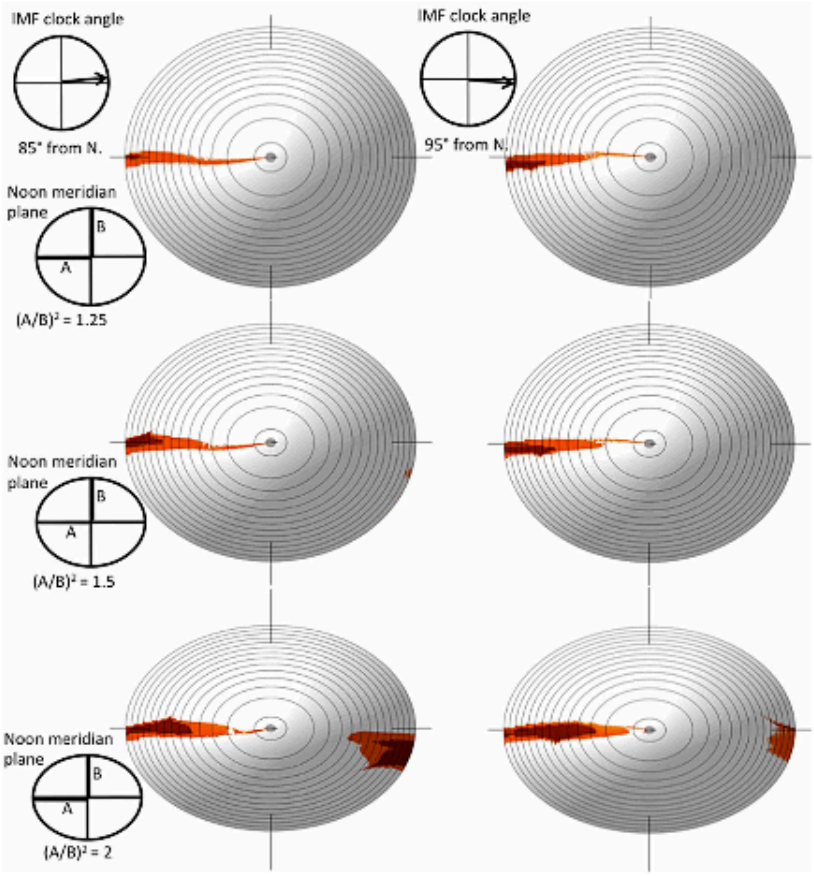

Figure 1.44: Locations that are Kelvin Helmholtz Unstable (prone to KHI development) for Jupiter's Magnetopause from Desroche et al. (2012): In all cases, the high shear flows create a dawn flank region that is KH unstable. In the case of the highly oblate magnetopause (bottom panel), the rotation of the magnetic field out of the equatorial plane allows for destabilization on the dusk flank as well. The destabilization is not significantly affected by changes in the IMF clock angle.

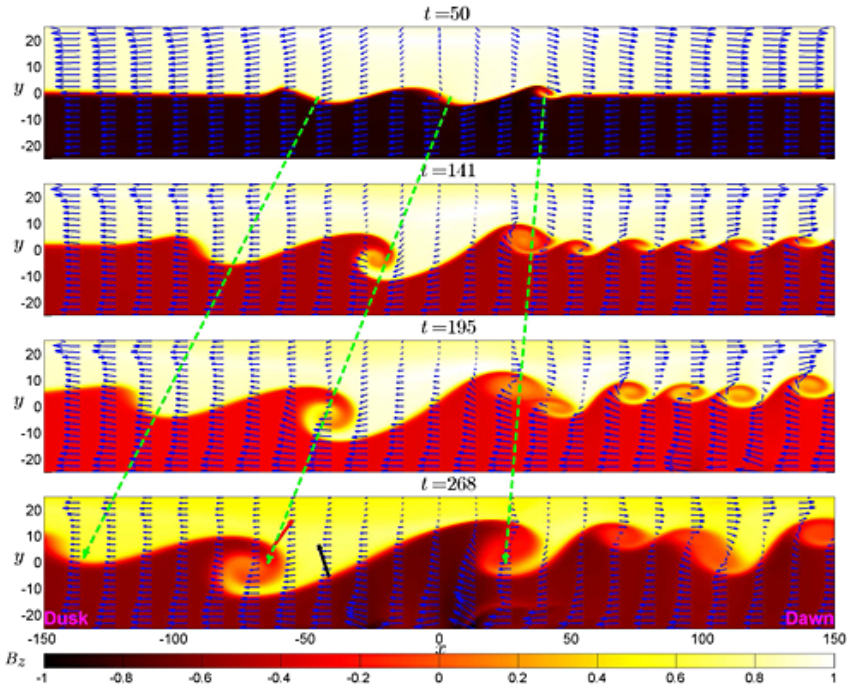

Figure 1.45: From Ma et al. (2015)): (from top to bottom) MHD simulation of KH waves propagating along the Saturn's magnetopause boundary at t=50, 141, 195, and 268, respectively. The color index presents the magnetic B_z component, and blue arrows are the bulk velocity in the xy plane. The black and red arrows represent the local normal directions in various locations along a Kelvin Helmholtz Instability.

mit it on the dusk flank (see Fig. 1.46). However, when the high plasma β environment that typically dominates the inside edge of Jupiter's expanded magnetosphere is accounted for, the possible reconnection locations shrink to Southern hemisphere dusk regions and Northern hemisphere dawn regions (see Fig. 1.47 for a β of 10).

1.7 The Jovian Aurora

Planetary aurorae permit the remote exploration of a planet's structure, composition, energy transport, temperature, plasma properties, atmosphere and magnetosphere. It seems unlikely that Jupiter's X-ray aurora exists in isolation from the well-studied Jovian Radio, UV and IR auroral emissions. In this section, we summarise relevant mechanisms, emissions and morphologies in these wavebands and begin to note possible connections with Jovian X-rays.

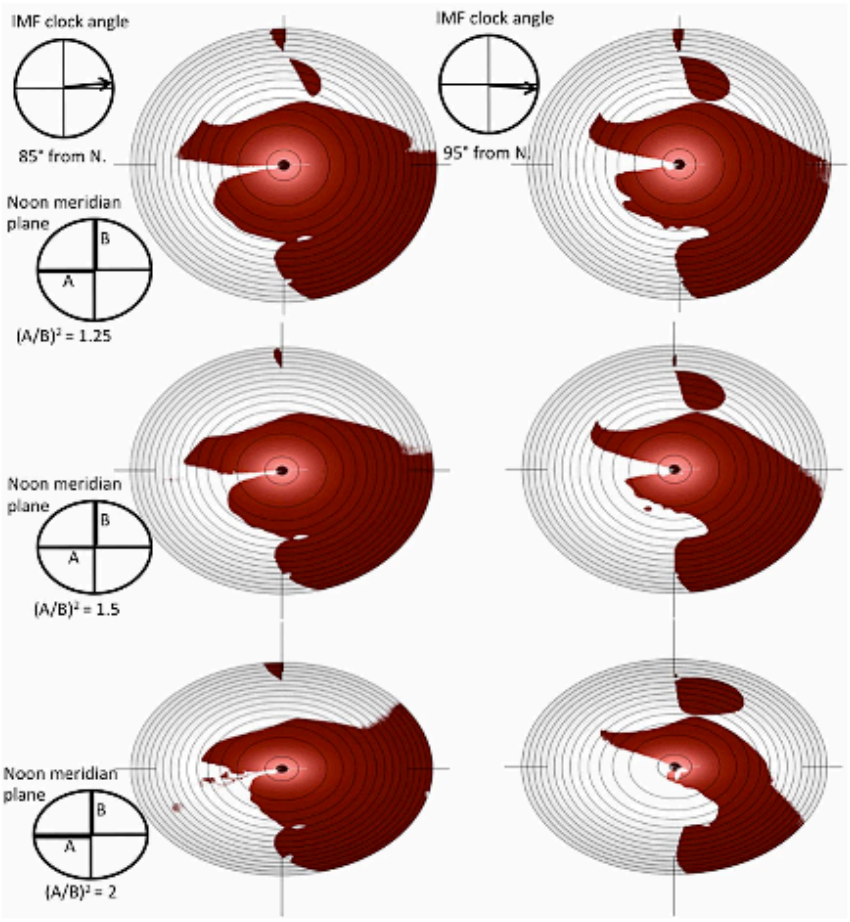

Figure 1.46: From Desroche et al. (2012): Region of the magnetopause viable for reconnection onset (indicated with red), based on the plasma shear speed. For regions where the plasma shear flow is greater than the Alfvén speed, reconnection is suppressed. Due to the large shear flows on the dawn flank, and low Alfvén speed in the plasma sheet, reconnection is suppressed on this flank. For the case of a northward component to the IMF, the dusk flank, with its antiparallel magnetic fields and low shear speeds is available for reconnection. When the IMF turns southward, reconnection begins to be suppressed on the dusk flank. As the asymmetry of the magnetopause increases, both the shear and rotation of the field on that flank increase, suppressing reconnection onset.

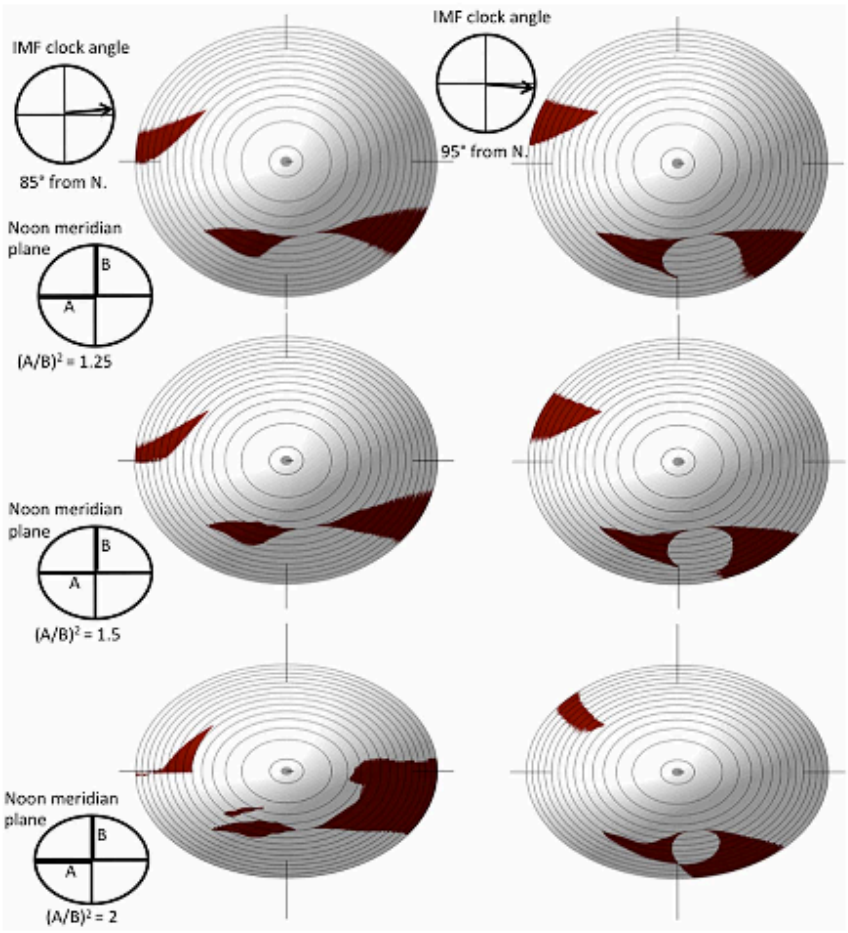

Figure 1.47: From Desroche et al. (2012): Region of the magnetopause viable for reconnection (red) with the magnetosphere $\beta = 10$. β in the magnetosheath is approximately unity. With this large difference in β between the sheath and magnetosphere, the onset of reconnection is mostly suppressed. The exceptions are the northern dawn flank, where the bent back field lines are antiparallel to the draped magnetosheath field, and the dusk flank, when the IMF has a component parallel to the planet's spin axis (and therefore antiparallel to the mostly dipolar magnetosphere field in this region).

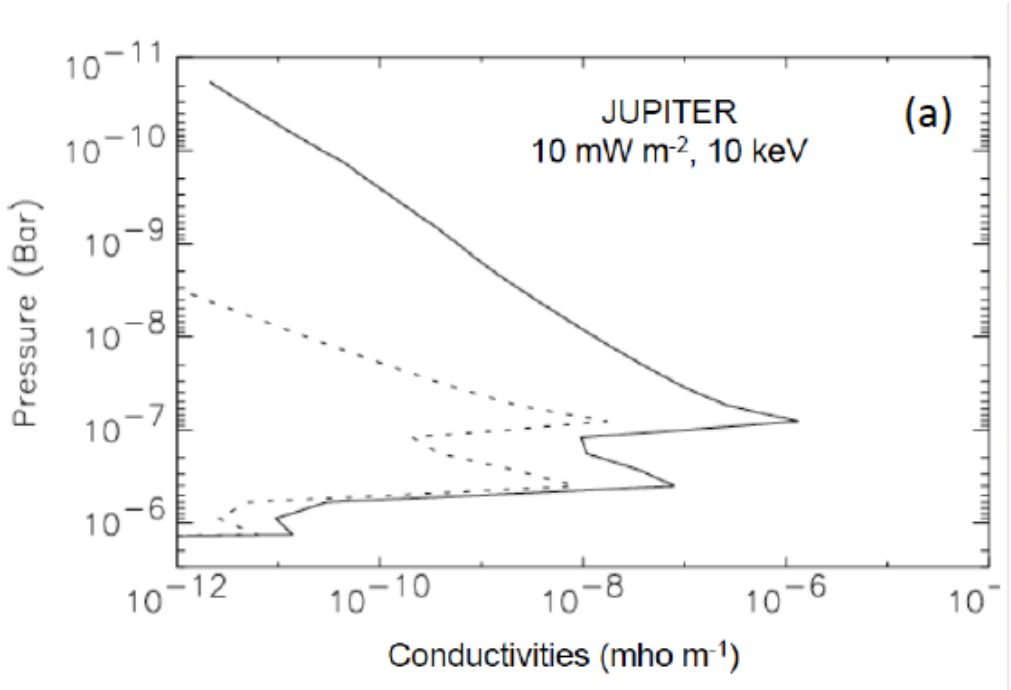

Figure 1.48: From Millward et al. (2002): Jovian Ionospheric Pedersen (solid line) and Hall (dashed lines) conductivities profiles as a function of pressure.

1.7.1 The Jovian Ionosphere

The ionosphere of a planet is the upper most region of the atmosphere, where photoionisation by solar X-rays/EUV and particle impacts (particularly at high latitudes) partially ionise the atmospheric atoms to form a plasma region. The Jovian atmosphere is predominated by H_2 with some He and atomic hydrogen present. By connecting this atmosphere with the magnetosphere, the ionosphere experiences, transfers and controls the exchange of particles, momentum and energy between these two otherwise distinct regions (e.g. Hill (1979, 2001); Cowley and Bunce (2001)).

While the ionosphere controls the coupling with the magnetosphere it is equally controlled by this, since the energy degradation of auroral particles increases ionospheric densities and electrical conductances (e.g. Millward et al. (2002); Hiraki and Tao (2008); Galand et al. (2011)). The ionospheric currents discussed previously, permit the closure of the magnetospheric current systems and require the ionospheric conductivity that is provided by this auroral precipitation. The conductivities in the ionosphere provide particle mobility for these current systems perpendicular to the magnetic field and parallel (Ped-

ersen) or perpendicular (Hall) to the ionospheric electric field. Currents in the Pedersen layer require mobility and production of the ions that carry the current, in a region where the ion gyrofrequency is similar to the ion-neutral collision frequency. For Jupiter, this is in the lower ionosphere, close to the homopause, where the ionosphere is dominated by molecular ions (Millward et al. 2002; Moore et al. 2010; Galand et al. 2011). Hall currents are carried by electrons in a thicker layer below the homopause, where chemistry with hydrocarbons is important (e.g. Galand et al. (2011); Kim and Fox (1994); Moses and Bass (2000)). Millward et al. (2002) showed that for Jupiter the Pedersen conductance increases with precipitating electron energy at least until 60 keV. At auroral latitudes, the conductances depend not only on particle precipitation, but also upon Jupiter's strong magnetic field strength, which controls the angular gyrogrequency. Since the Jovian X-ray aurora are concentrated around regions of high field strength, it is possible that the ionosopheric conductances are important to an understanding of the X-ray aurora.

1.7.2 Auroral Processes

Badman et al. (2015) define auroral emissions as: "the photo-manifestation of the interaction of energetic, extra-atmospheric particles with an atmosphere" (Clarke et al. 2004; Bhardwaj and Gladstone 2000; Galand and Chakrabarti 2002; Fox et al. 2008; Slanger et al. 2008; Badman et al. 2015)). Bagenal et al. (2014) describe a series of physical processes that generate auroral emissions and which they believe to be ubiquitous:

1. Electrical currents and voltages are produced with magnetospheric plasma.

2. These electrical currents are diverted along magnetic field lines towards the polar ionosphere.

3. Out of the equatorial plane, and particularly above the ionosphere, there is a low density of charge carriers which produces electric fields parallel to the magnetic field lines connecting the equatorial plasma to the ionosphere.

4. Charged particles are accelerated from these regions of parallel electric fields into the upper atmosphere and also out of the ionosphere and towards the magnetosphere.

5. Atoms and molecules in the ionosphere are excited, ionised or dissociated by the precipitation of charged particles, this also alters the ionospheric conductivity and results in subsequent photon emission.

6. The upward and downward going currents close in the ionosphere.

7. The neutral atmosphere is heated through collisions with current carriers.

At Earth, the systems that produce aurora can be broadly described by 3 categories: upward currents, downward currents and Alfvénic regions. A schematic and outline list of the observed physical properties can be seen in Figure 1.49 while in-situ observations of these signatures are shown in Figure 1.50. The relative importance of each of these systems for Jupiter's aurora remains to be seen.

Generally, there are considered to be two distinct auroral morphologies associated with these processes: diffuse aurora and discrete aurora. Diffuse aurorae have no observable internal structure and are produced when trapped magnetospheric particles are scattered into the loss cone by waves. Typically, these form broad regions of low intensity aurora. Discrete aurorae are structured and localised aurora, often in the form of bright arcs. They are typically produced when charged particles are accelerated along field aligned (Birkeland) currents (e.g. Hill (2004); Ray et al. (2010, 2012)).

1.7.3 Jovian Auroral Wavebands

As well as X-ray emission, Jupiter's aurora produces emissions in the radio, infrared, visible and UV wavebands. The visible auroral power is 2-3 orders

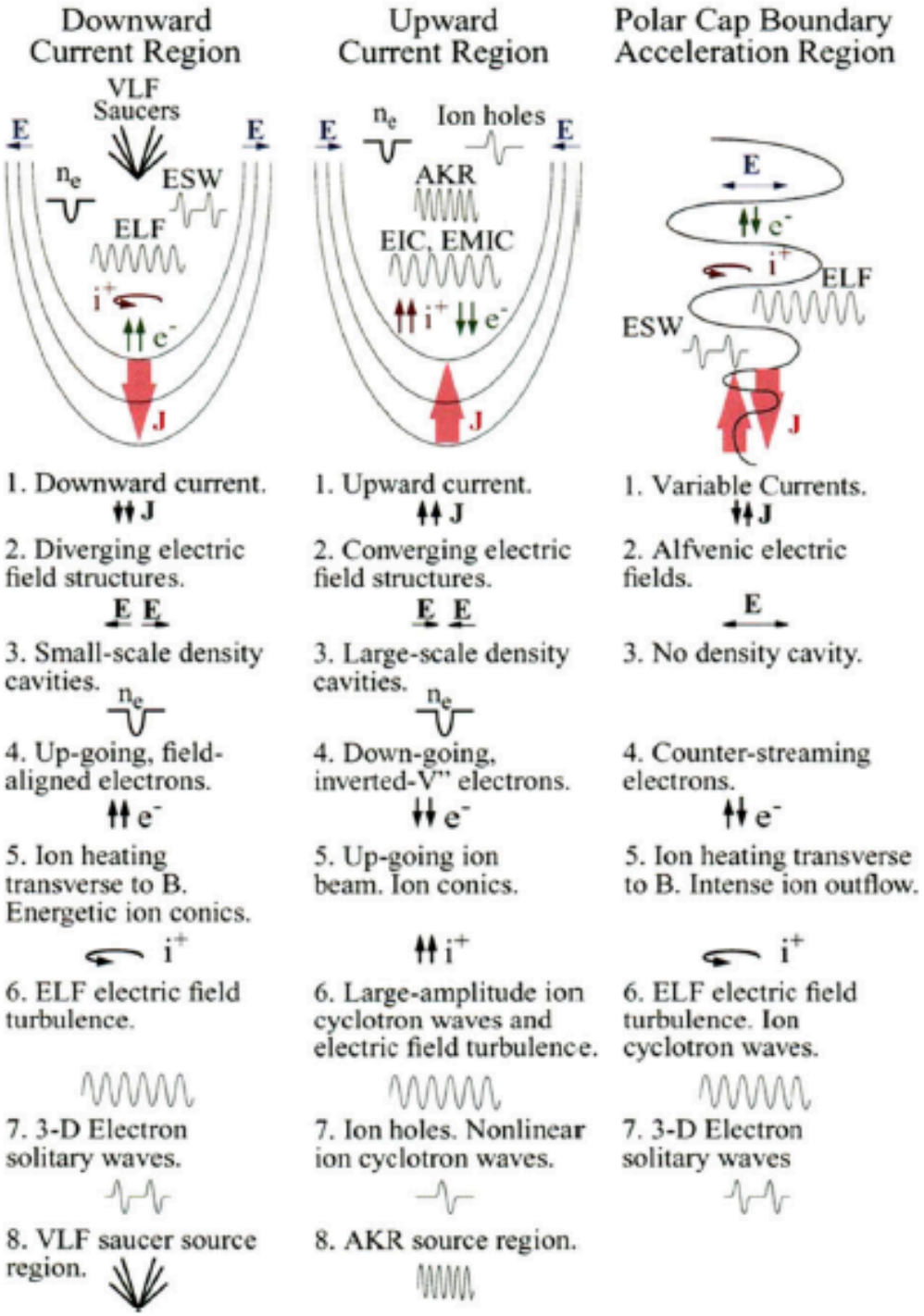

Figure 1.49: From Bagenal et al. (2014): The three types of auroral zones based on experience from Earth: upward currents, downward currents and Alfvénic regions. Adapted from Carlson et al. (1998)

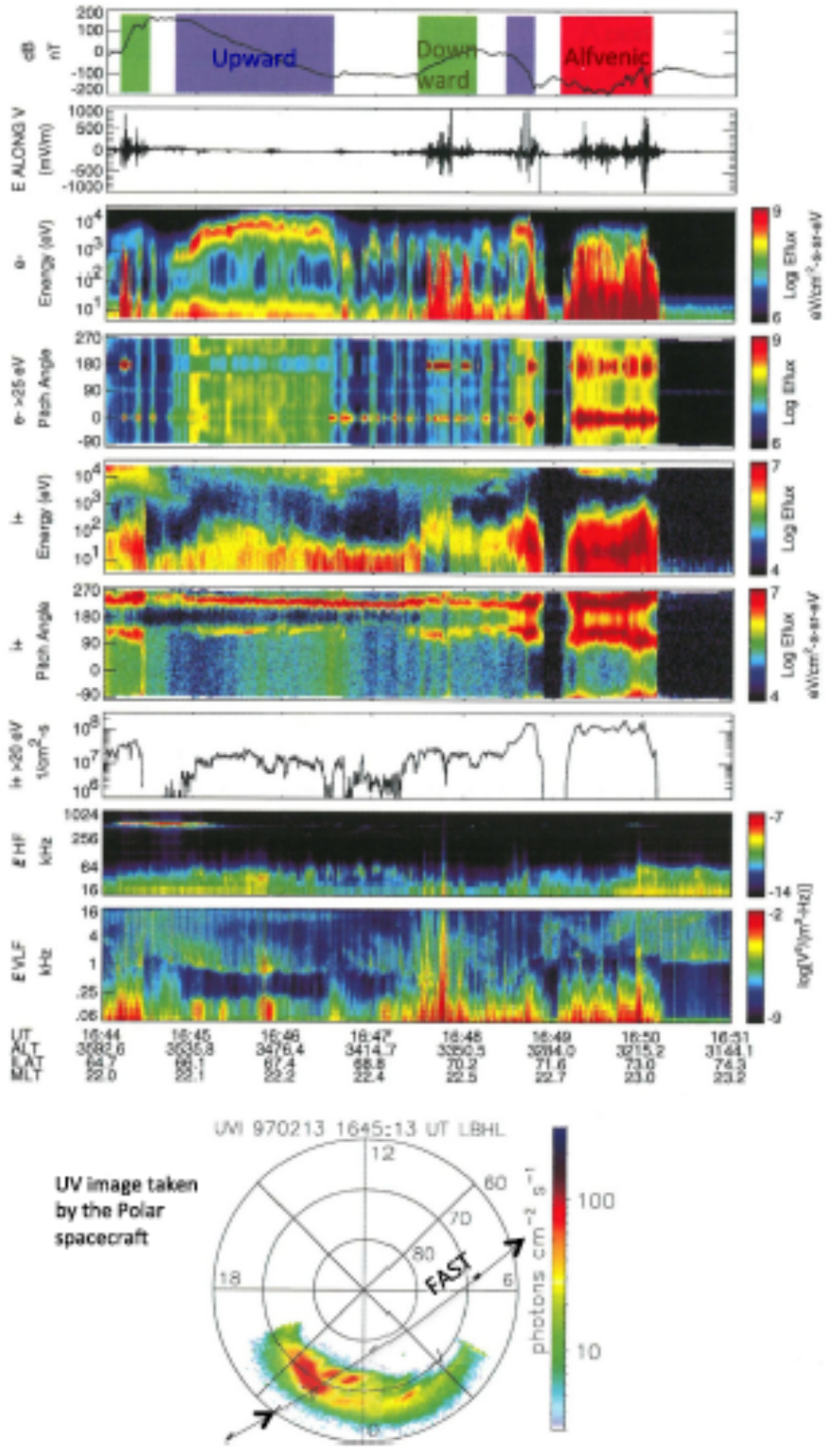

Figure 1.50: From Paschmann et al. (2012): FAST data obtained as the spacecraft passed through the 3 types of auroral coupling regions illustrated in Fig. 1.49. From the top the panels show first: magnetic field perturbations relative to Earth's reference field, with downward (green) field-aligned currents (FACs) and upward (blue) FACs and Alfvénic currents (red). Second: electric field fluctuations with electrostatic shock structures associated with the auroral acceleration region. Third: spectrogram of electron energies and densities ; Fourth: Electron Pitch Angle distribution; Fifth: spectrogram of ion energies and densities; Sixth: Ion pitch-angle distribution. Seventh: ion outflow. Eighth and Ninth: wave activity Tenth: UV auroral image from the Polar satellite with the FAST trajectory projected on top.

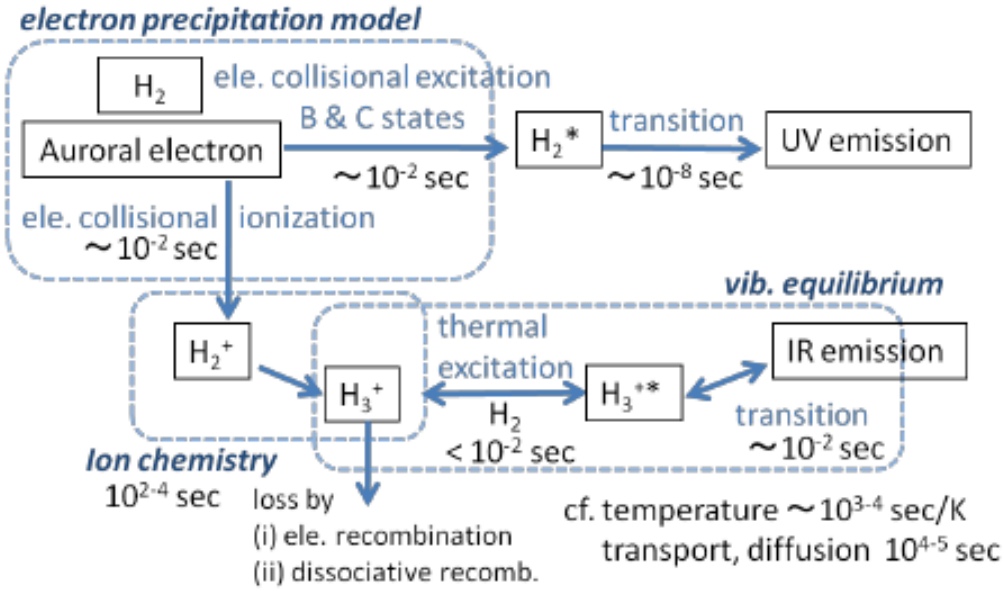

Figure 1.51: From Badman et al. (2015): Flowchart of UV and IR auroral emissions with the timescale for each process.

of magnitude less than the UV and IR and is difficult to distinguish from the reflected solar emission on the dayside, so we neglect this. Figure 1.51 outlines how the precipitation of auroral particles generate UV and IR photo-emissions for Jupiter.

Traditionally the Jovian aurora has been sub-categorised into 3 separate groups (see panel b Fig. 1.52) that vary independently in time and space:

1. The Main Emission
2. The Satellite Footprints
3. The Polar Emissions

However, it is possible that a fourth category should be added to this list: low latitude injections that occur transiently between the main emission and the satellite footprints (e.g. Mauk et al. (2002); Kimura et al. (2015)). Within each of the above categorisations there are further sub-divisions and the polar emissions are not all produced by the same process. In fact, it has been noted that Jupiter's aurora should always be referred to as a plural (auroras/aurorae) because the different morphologies, intensities, temporal signatures, spectra and expected origins of the auroral emissions are exceptionally diverse.

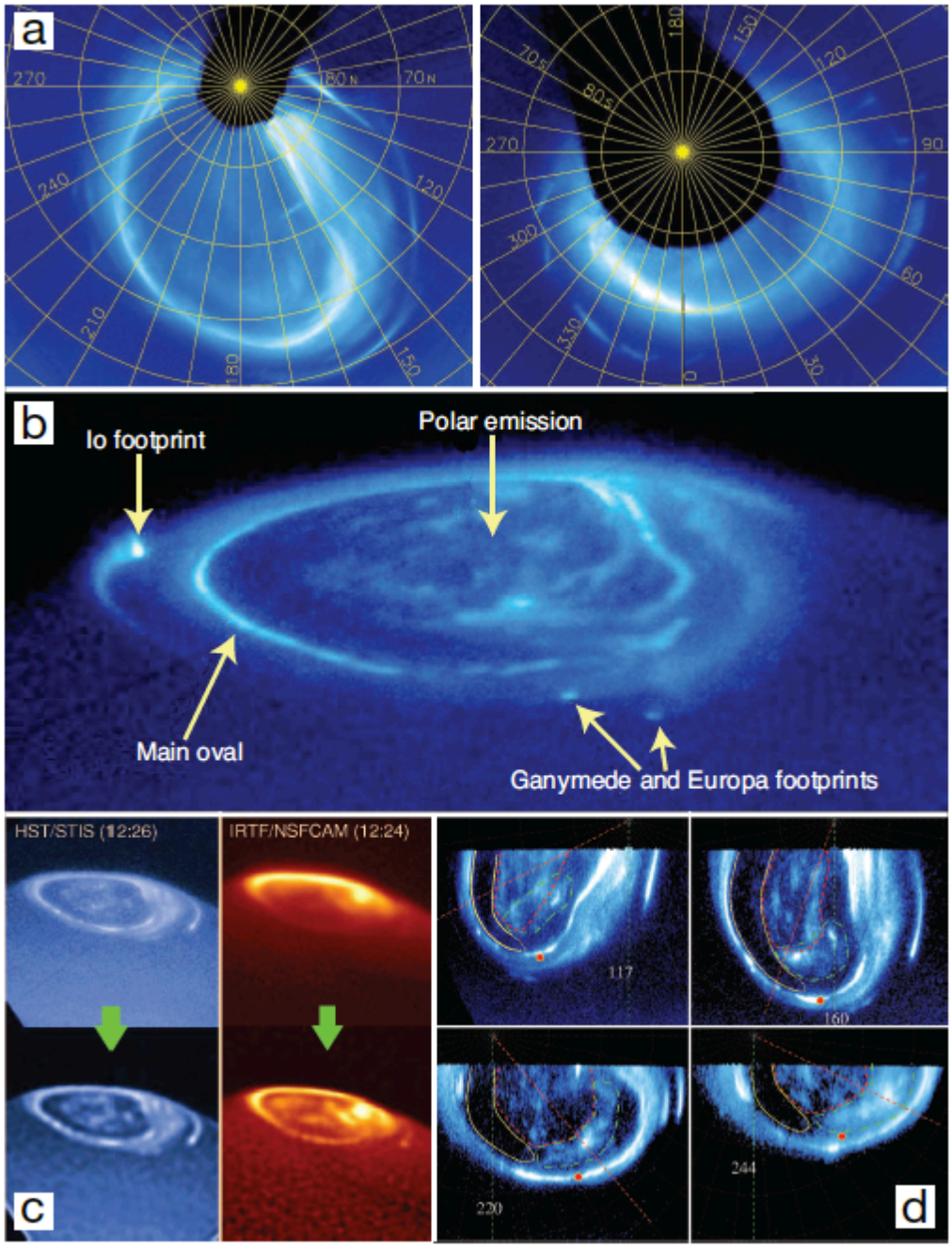

Figure 1.52: Jovian Aurora Overview from Clarke et al. (2004): Auroral images. a) Mean of all HST STIS images from Dec 2000 - Jan 2001 for the Northern (left) and Southern (right) polar regions. b) HST STIS UV image of the northern aurora with satellite footprints, the auroral oval and the polar emission indicated. c) Comparison of UV (left) and H_3^+ IR (right) images of Jupiter's aurora. Lower panels show the images after processing. d) Polar projections of Jupiter's aurora from STIS UV images.

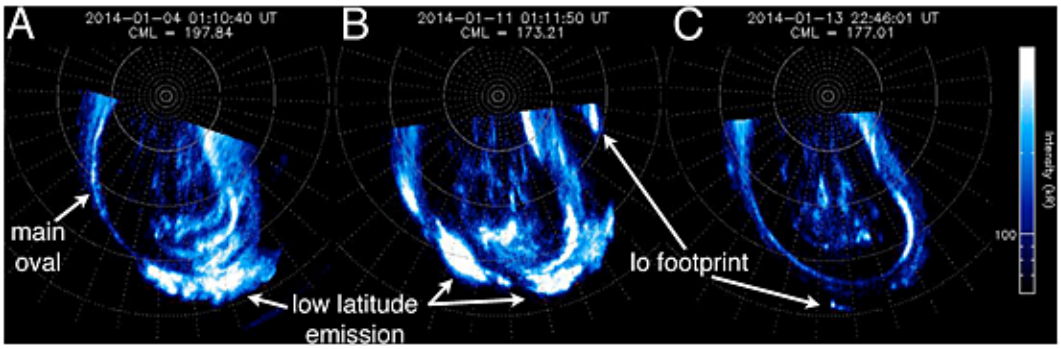

Figure 1.53: From Kimura et al. (2015): Polar projections of northern auroral emissions taken by HST/STIS with a spatial resolution of 0.08 arcsec (the pixel scale is 0.025 arcsec/pixel). (a) Image taken during a sudden brightening detected by Hisaki on day 4 2014. (b) image taken on day 11 during a sudden brightening. (c) An example auroral polar projection taken on day 13 when no sudden brightening was observed.

1.7.3.1 The Jovian Main Emission (Main Oval)

Approximately 70% of Jupiter's UV auroral emission ($10^{13} - 10^{14}$ W) is produced by the main oval. This is sometimes called 'the main emission' because in the North a magnetic anomaly warps its oval-like shape to produce a kidney bean morphology (Pallier and Prangé 2001; Grodent et al. 2008). These Northern and Southern UV main emissions are continuously present and consist of a narrow (100 - 500 km wide) bright oval (100 kR-1 MR, where 1 Rayleigh = $\frac{10^6}{4\pi} photons\ cm^{-2}s^{-1}sr^{-1}$ and can be converted to energy through 1 R = 3.71546 x $10^{-14}\lambda^{-1} erg\ s^{-1}cm^{-2}arcsec^{-2}$ where λ is in Angstroms) of emission at 15° magnetic co-latitude (e.g. Clarke et al. (2004)).

The dawn side of the oval sometimes thickens and brightens during dawn storm events (e.g. Gustin et al. (2006)) but is typically thinner than the dusk-side. The dusk oval is often thicker and splits into into multiple arc-like structures at higher latitudes (e.g. Fig. 1.52). Between the dawn and the dusk sides of the oval there is often a dark patch at noon, which has been suggested to be associated with a downward current region (Radioti et al. 2008a). It is worth noting that the differences between local time effects and System III effects for Jupiter's aurora are not well understood. Juno will help to address this by providing auroral images at never before seen local times including on the night side of the planet. For the purposes of this thesis, we refer to the dawn/dusk sides of the aurora as viewed from Earth.

The UV oval is produced by precipitating electrons with quiescent (dawn storm) energies of 30-200 keV ($\sim$ 500 keV) and energy fluxes of 2-30 mWm^{-2} (90mWm^{-2}) (Gustin et al. 2006). These precipitate along 100 kV potentials into the ionosphere along the $\sim$ 100 MA field aligned upward current system that enforces corotation in the middle magnetosphere between $\sim$20-40 R_J (McNutt Jr et al. 1979; Cowley and Bunce 2001; Hill 2001; Bunce and Cowley 2001; Khurana 2001; Bunce et al. 2002; Cowley and Bunce 2003a,b). The precipitation of high energy electrons in this region produces the hard X-ray aurora by bremsstrahlung emission. While the subsequent cooling of atmospheric H_3^+ generated by this current system produces the co-located IR oval (e.g. Fig. 1.52).

Rather than this being a solely upward current region, Mauk and Saur (2007) analysed in-situ data to find pairs of upward and downward currents in the plasma sheet, suggesting fine-structure within the upward current region. Saur et al. (2003) proposed that Jupiter's aurora could be generated by magnetic turbulence, given the pervasiveness of structuring over multiple scales (at Earth, this is equivalent to 'Alfvénic Aurora').

1.7.3.2 Variation in the Jovian UV Main Emission

The main oval is known to shift locations. Sometimes this occurs concurrently with a shift of the Ganymede footprint, which suggests that the shift is produced in the ionosphere and reflects a change in the ionosphere-magnetosphere mapping of the aurora. However, sometimes the oval will shift independently of the Ganymede footprint which could indicate either a change in the corotation enforcement region or an enhancement of the azimuthal current modifying the magnetic field mapping. This could be caused by an increase in the mass outflow rate from Io or changing solar wind conditions (e.g. Hill (2001); Nichols and Cowley (2003, 2004); Grodent et al. (2008); Tao et al. (2010); Nichols (2011); Ray et al. (2012); Bonfond et al. (2012); Hess et al. (2012)

Nichols et al. (2007, 2009a); Clarke et al. (2009) have reported that the main oval seems to brighten in response to solar wind pressure enhancements. This was contrary to expectations, since a solar wind compression may be

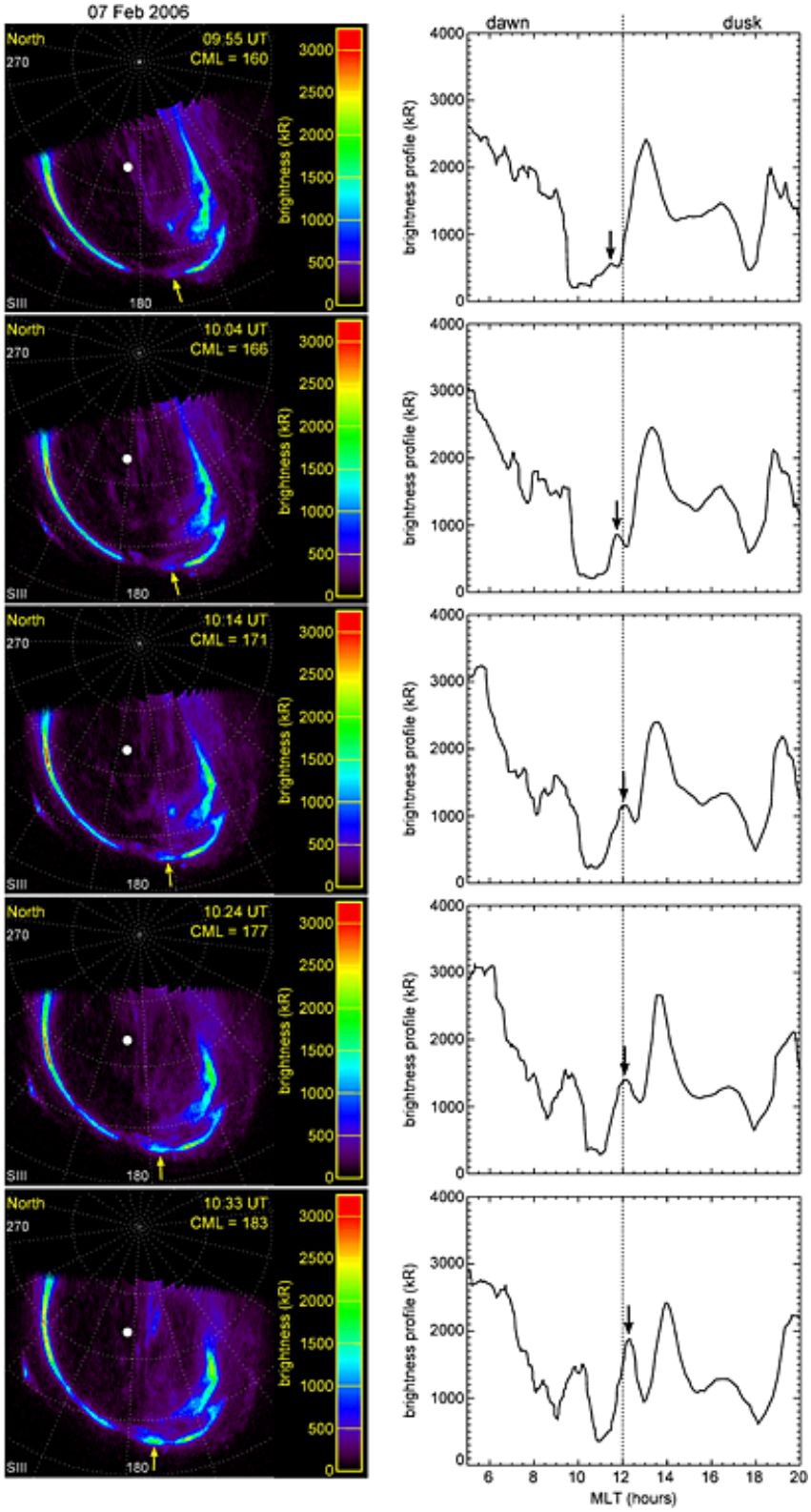

Figure 1.54: Transient Brightening on the Jovian Main Emission from Palmaerts et al. (2014): Left column: Sequence of five Jupiter North pole projections of HST-ACS auroral images from 7 Feb 2006. System III 180° meridian is toward the bottom of the plots. The observation sequence lasts 38 min and CML ranges from 160° - 183°. The white large dot indicates the morphological center of the main emission. Right Column: Profiles of the maximum brightness along the main emission corresponding to the projections. The brightness is given in kR (above the background) as a function of the magnetic local time derived from Vogt et al. (2011). The dotted line indicates magnetic noon. An arrow points to the localised peak which corresponds to a transient auroral feature in the main emission.

expected to increase the plasma angular velocity and reduce the requirement for a corotation enforcement current (Southwood and Kivelson 2001).

Badman et al. (2016) also report a possible connection between the main oval and solar wind conditions. They observe the oval shifting to lower latitudes and dimming by 70% from decreasing electron density or an order of magnitude drop in the source electron thermal energy. They suggest that this could either be explained by a) expansion of the magnetosphere during a solar wind rarefaction or b) increased inward transport of hot plasma and outward transport of cold plasma.

One other main UV emission feature that may be relevant for the X-rays is a transient small-scale structure that exhibits brightness enhancements near noon on timescales of a few tens of minutes. Palmaerts et al. (2014) who identified this feature, suggest that it could relate to shear flow from inward moving plasma close to noon (see Figure 1.54).

1.7.3.3 The Satellite Footprints

Equatorwards of the main oval are the footprints of the Galilean satellites Io, Europa and Ganymede. Io's footprint is brightest and features a tail region (e.g. Fig. 1.52 b). Callisto's footprint has not been observed, since it would overlap the brighter main oval emissions (Connerney et al. 1993; Clarke et al. 2002).

A satellite auroral footprint is produced because the moon's Keplerian orbit is slower than the velocity of the surrounding plasma, which is magnetically attached to the fast-rotating planet. This leads the moon to act as an obstacle to the plasma flow, perturbing the plasma and the magnetic field line that the plasma is attached to. This generates Alfvén waves which propagate along the magnetic field line to the planet and cause electron precipitation into the ionosphere to produce aurora (e.g. Kivelson (2004); Saur et al. (2004); Jia et al. (2010)). Alfvén waves travel at a velocity, v_A, dependent on the magnetic

field strength, B, and density, ρ, of the medium:

$$v_A = \frac{B}{\sqrt{\mu_0 \rho}} \tag{1.32}$$

The plasma between the Galilean satellites and Jupiter is dense, so the Alfvén travel time is longer than the time for plasma to flow past the moon. This creates a situation where there is not a persistent current system connecting the planet and moon, instead the interaction between the two bodies is governed by Alfvén waves that reflect between the IPT and Jupiter's ionosphere.

The auroral footprints of the satellites appear as spots (multiple spots in the cases of Io and Ganymede) and trails of enhanced emissions behind the footprint itself (e.g. Bonfond et al. (2008, 2013)). The Io footprint is produced at higher altitudes than the main emission by particles with a mean energy of ∼1-4 keV (Bonfond et al. 2008, 2009; Hess et al. 2007). The mechanism that produces the tail is disputed: Ergun et al. (2009) argues that it is from upward and downward currents which through low numbers of current-carrying electrons at high latitudes, limit the currents and produce parallel potential drops of ∼ keV energy (Hess et al. 2007). However, given that the altitude profile of both the main Io spot and the tail are similar, Bonfond et al. (2009) argue that that Alfvén waves produce both. A satellite footprint has not yet been detected in the X-ray emission.

1.7.3.4 The Polar Aurora

Almost 30 % of the Jovian UV auroral emission occurs poleward of the main oval, where there are a variety of highly variable auroral features. It has proven challenging to interpret these polar signatures because of the vast diversity of morphologies, their broad distributions in temporal and spatial scales and the uncertainty surrounding which polar regions connect with which outer magnetosphere (or possibly open) field lines. The X-ray emission is co-located with some of these UV polar features. However, only two studies so far (Elsner et al. 2005; Branduardi-Raymont et al. 2008) have begun to probe the UV-X-

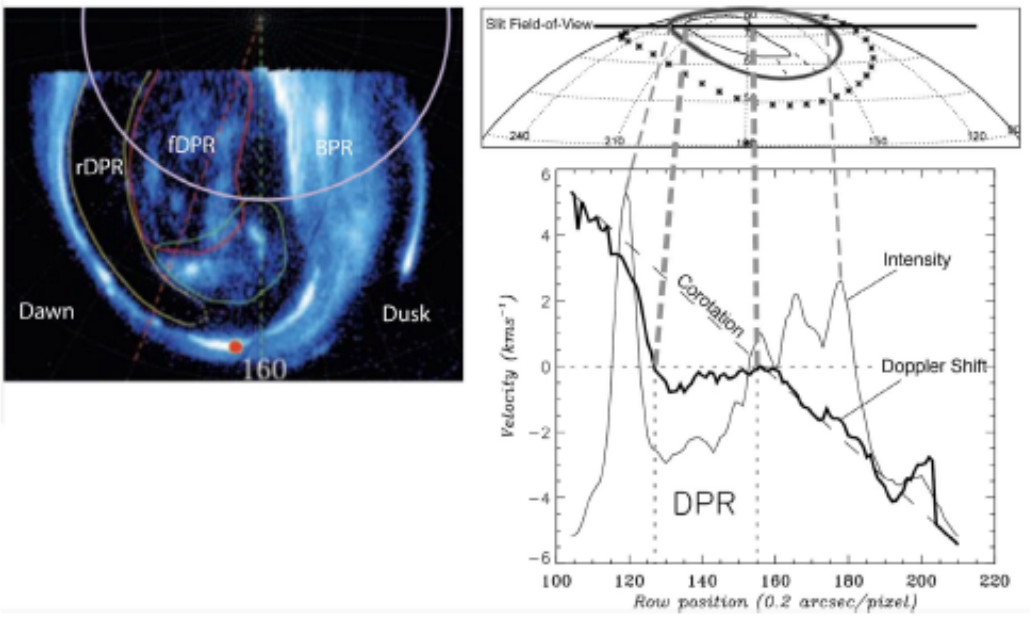

Figure 1.55: Figure and Caption from Delamere and Bagenal (2010c): Left: Polar projection of the northern UV auroral region showing the shape and position of the dark region (yellow contour), the swirl region (red contour), and the active region (green contour) as they appear at CML = 160° (green dashed line). Red dashed line: Longitude 180°. Red dot: Ganymede footprint at 15 R_J (Grodent et al. 2003a). Purple circle: latitude 74° , the projected location of the slit field of view of the data on the right. Top Right: Viewing geometry and (bottom right) Doppler shifted H_+^3 IR emission profile from Stallard et al. (2003), showing the stagnated flows in the dark polar region (DPR). This DPR corresponds to the swirl region on the UV image on the left. Both images illustrate the dawn-dusk asymmetry of the polar auroral emission intensity.

ray connection.

While pre-Juno, the current system that produces the Jovian main oval was thought to be well understood, the current system responsible for the polar aurora is not. Figure 1.39 shows the possible ionosphere-magnetosphere/open field line mappings of the polar regions, assuming that a Dungey cycle is present, while Figure 1.43 shows viscous interaction explanations for these features.

Figure 1.55 shows overarching structures in the polar aurora. The polar emissions occur in a split dark region on the dawn-side and a brighter more active region from noon to dusk, where ∼100 seconds flares (e.g. Fig. 1.56 and 1.57) and variable dusk and transpolar arcs occur (e.g. Fig. 1.59) (Waite et al. 2001; Bonfond et al. 2011, 2016; Nichols et al. 2009b; Grodent et al. 2003b). Swirls of emission are observed to occur poleward of these two regions, where IR observations show that the magnetospheric flow is inward towards the planet and Sunward (Fig. 1.55; Stallard et al. (2001, 2003)). Magnetospheric mapping suggests that the swirl region may contain open field lines (Vogt et al. 2011, 2015). However, up to 200 kR emissions occur in this region, requiring precipitating electrons with energies greater than 15.4 keV to ionise the existing H_2. It remains challenging to explain the existence of this population on open field lines, when downward currents with upward flowing electrons are expected for open field lines in the region (Cowley et al. 2003). Signatures related to closure of a large-scale Dungey cycle open field lines have not been identified in the Jovian aurora.

The bright flares in the active region at noon may relate to the boundary of the Jovian cusp (see Fig. 1.58) (Pallier and Prangé 2001, 2004; Waite et al. 2001; Bonfond et al. 2011). These flares have previously been reported to occur on timescales that would be expected for flux transfer events from reconnection (Walker and Russell 1985). They have also been shown to be concurrent with X-ray hot spot emissions (Elsner et al. 2005).

The dark region on the dawn side, is suggested to map to the empty and compressible dawn-side outer magnetosphere where the solar wind pressure will reduce the load on the ionosphere and where empty flux tubes from a

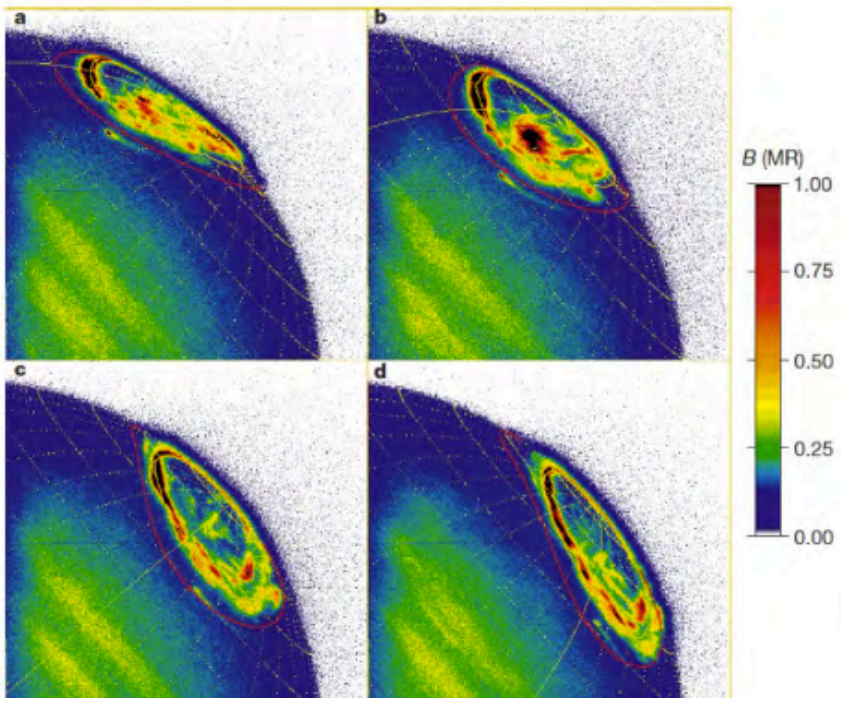

Figure 1.56: A Jovian UV Auroral Polar Flare from Waite et al. (2001): False-colour brightnesses are indicated in megarayleighs (MR). Waite et al. (2001) clipped the brightnesses above 1 MR to highlight fainter emissions. The exposures were made at a, 20:27:30-20:31:30; b, 21:04:50-21:08:50; c, 22:01:54-22:06:54; and d, 22:38:52-22:45:32 UT. A jovicentric graticule with 10° intervals is overlaid (with the 180° meridian in solid colour), along with L = 30 footprint and the L = 5.9 mapping of the Io torus.

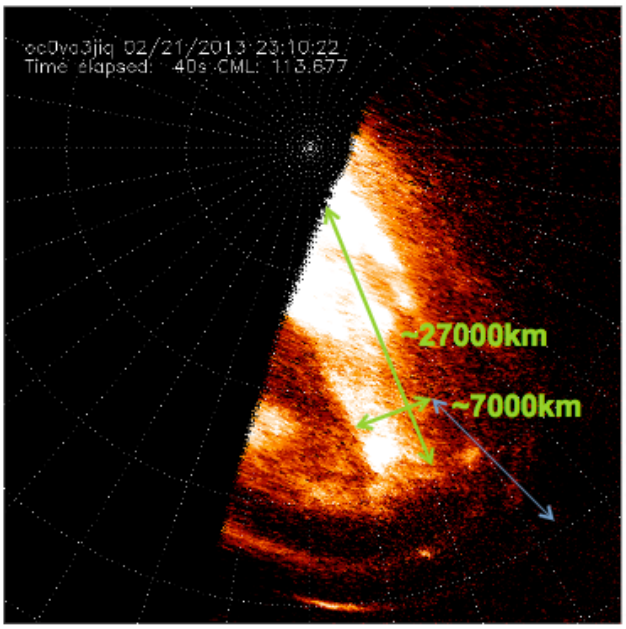

Figure 1.57: From Bonfond et al. (2016): A UV polar flare in the dusk sector.

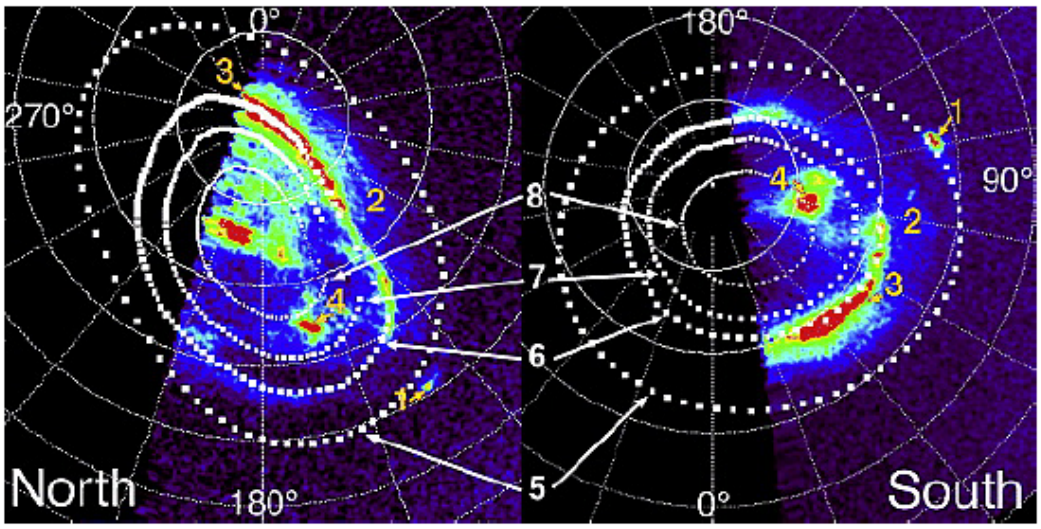

Figure 1.58: Figure from Pallier and Prangé (2004): Two consecutive colour-coded polar projected maps of Jupiter's aurora on 15 Aug 1999 using HST-STIS (1180 -1530 ÅFWHM). Dark blue: the faint solar reflected flux, light blue-green: moderate emissions including (2) the 'low-latitude belt', and red: brightest auroral features, (1) Io footprint, (3) main oval, (4) conjugate polar cusps. The dotted curve on top of (3) is the Pallier-Prange (PP) reference main oval (6). (7, 8) are inner reference ovals, and (5) is the VIP4 model Io footprint.

Dungey cycle could return. Arcs stretching from the Jovian dusk/night-side aurora to noon (Fig. 1.59 top four panels) have been likened to transpolar arcs at Earth. These may relate to lobe reconnection as at Earth (Nichols et al. 2009b; Fear et al. 2014) or velocity shears (Delamere and Bagenal 2010c).

In the magnetotail, beyond 50 R_J plasmoids are observed to be ejected by the Vasyluinas cycle (Woch et al. 2002; Kasahara et al. 2013; Vogt et al. 2010; Kronberg et al. 2005). In the dusk to dawn polar aurora sector, in a region mapping to more than 100 R_J, auroral signatures that may correspond to these plasmoids have been observed to last 10s of minutes and recur every 2-3 days (Grodent et al. 2003b, 2004; Radioti et al. 2008b, 2010, 2011) (see Fig. 1.59 lower panel). Alternatively, Delamere and Bagenal (2010c) suggest that these spots could be produced by Kelvin Helmholtz instabilities on the dawn flank. Gray et al. (2016) track a feature in a similar location and note that it exceeds the corotation speed and progresses radially inwards towards the main oval, suggesting that it is the signature of hot plasma injections following tail reconnection (see Fig. 1.60. They further connect the UV emissions with radio hectometric (HOM) and non-Io decametric (DAM) signatures that imply

a global magnetospheric disturbance may be associated with the reconnection and injection intervals of such events

1.7.3.5 UV Aurora and Colour Ratios

The Jovian UV aurora was discovered two years before the X-ray aurora, by Voyager 1 in 1979 and is mainly due to H Lymanα and H_2 Werner and Lyman bands with emitted wavelengths between 90 - 160 nm (e.g. Bhardwaj and Gladstone (2000)). UV auroral emissions at wavelengths of 123-130 nm are absorbed by hydrocarbons, while those between 155-162 nm are not. By using colour ratios between these two bands it is therefore possible to estimate the extent of hydrocarbon absorption. Given that the hydrocarbon layer is at lower altitudes, this allows the colour ratio to be used as a measure of penetration depth and therefore auroral particle energy (e.g. Livengood and Moos (1990); Harris et al. (1996); Gérard et al. (2002, 2003); Gustin et al. (2004)). These studies have shown that attenuation by hydrocarbons depends on intensity of the emission (Livengood and Moos 1990) and that mean electron energy from the colour ratio varies with auroral brightness (energy flux) and is in-line with Knight's theory of field aligned currents (Knight (1973); Gustin et al. (2004, 2016) - see Fig. 1.61).

1.7.4 IR Aurora

As shown in figure 1.62 auroral precipitation leads to both excited hydrogen and subsequent UV emission and also ionised hydrogen and subsequent IR emission. Below the homopause, H_3^+ dominates, since H^+ is lost twice as fast to reactions with hydrocarbons (Kim and Fox 1994; Moses and Bass 2000). H_3^+ is formed via chemical reactions with ionised molecular hydrogen, which subsequently thermalises with the neutral atmosphere and emits in the IR. There is a time-lag in response to auroral precipitation and a lifetime (at Jupiter: 4-40 seconds (Radioti et al. 2013)) associated with the ion and its subsequent emission meaning that the emission maps a life-time average of the auroral morphology.

The IR aurora feature the moon footprints, main emission and polar emis-

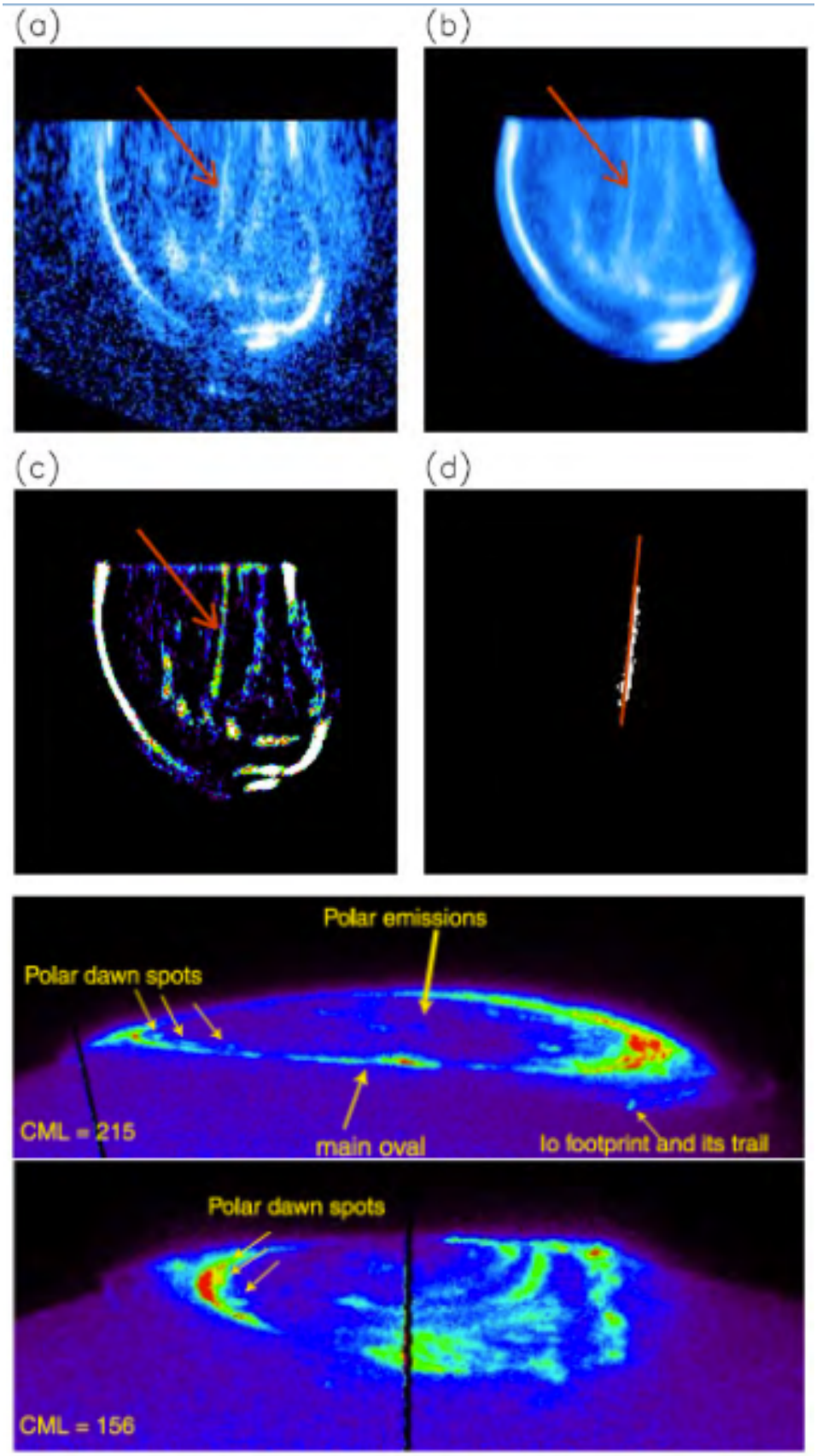

Figure 1.59: Top: Nichols et al. (2009b) identified a thin UV transpolar arc, which may relate to velocity shears (Delamere and Bagenal 2010c) or lobe reconnection (Nichols et al. 2009b). Bottom: Radioti et al. (2008b) identified polar spots in auroral regions that map to dawn. These have been suggested to be signatures of tail reconnection (Grodent et al. 2003b, 2004; Radioti et al. 2008b, 2010, 2011) or Kelvin Helmholtz along the dawn flank (Delamere and Bagenal 2010c).

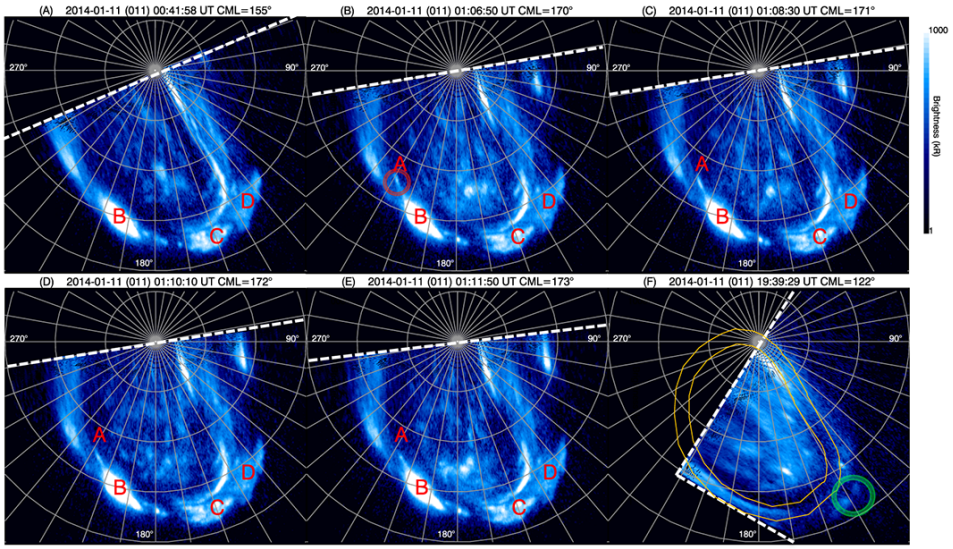

Figure 1.60: Equatorward Superrotation in a Dawn Spot from Gray et al. (2016): Six panels showing polar-projected HST 100s images of Jupiter's Northern FUV aurora on 11 Jan 2014 at (a) 00:41 UT, (b) 01:06 UT, (c) 01:08 UT, (d) 01:10 UT, (e) 01:11 UT, and (f) 19:39 UT. The log intensity scale saturates at 1000 kR. The dashed white line shows the edge of the field of view. The grey lines indicate a 10° by 10° Jovicentric latitude-system III longitude grid. 180 S3 longitude is toward the bottom. In a-e the superrotating polar spot (A or circled in b) catches up to the expanded main emission region (B) and two equatorward emissions (C and D). Yellow lines in f, taken 18 hrs after a, show the main emission boundaries, derived from the average over the 2014 campaign. Equatorward emissions circled in green are possible remnants of features C and D.

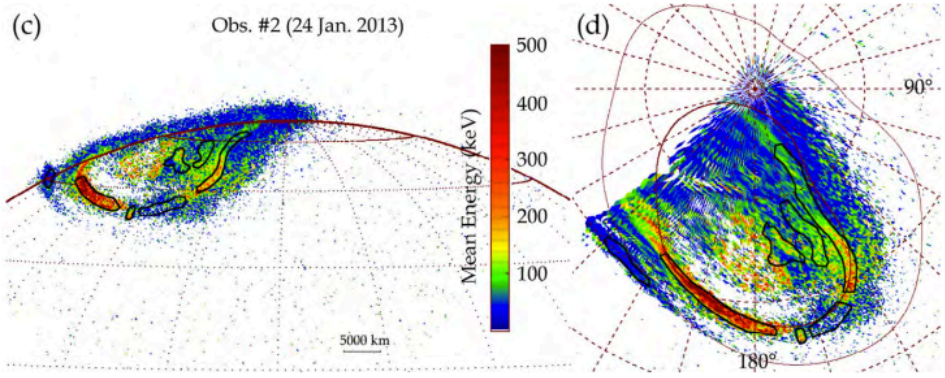

Figure 1.61: Jovian UV Aurora Colour Ratios from Gustin et al. (2016): Map of the precipitating electron mean energy for a STIS observations, in Earth-orbit view (left) and polar projected view (right). The two regions on the main emission are the most energetic (330 keV and 130 keV respectively), followed by the poleward flare emissions (70-90 keV).

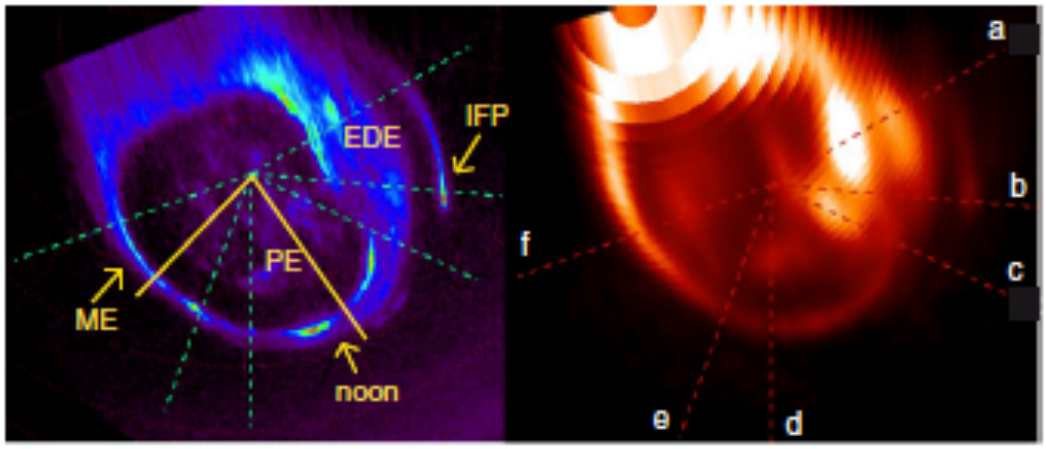

Figure 1.62: From Radioti et al. (2013): Simultaneous ultraviolet H and H_2 and infrared H_3^+ images of Jupiter's northern aurora obtained in 2004 (Clarke et al. 2004). The main oval, dark polar region, equator-ward emission, and Io footprint are all co-located in the infrared and the ultraviolet, but the polar emissions differ.

sions, which are all co-located with the UV emissions (Radioti et al. (2013) - see Fig. 1.62). However, the polar emissions, which include flares that occur on timescales of 2-3 minutes (Bonfond et al. 2011) for instantaneous UV emission, appear different for longer timescale H_3^+ emission. During these longer timescales, the H_3^+ can be transported horizontally within the thermosphere so that H_3^+ aurora provide an auroral image that is smeared in both time and space (Tao et al. 2013; Radioti et al. 2013).

There are a variety of valuable atmospheric and auroral characteristics that H_3^+ observations can trace, but which are beyond the scope of this study; these include: line of sight velocities through doppler shifts (see Fig. 1.55, e.g. Stallard et al. (2003)), the auroral energy deposition (e.g.O'donoghue et al. (2013)), atmospheric temperature (e.g.Achilleos et al. (1998); Stallard et al. (2001)) and cooling (e.g. Lamy et al. (2013)) and also the ionospheric conductivity (e.g. Tao et al. (2010)). See Badman et al. (2015) and references therein for a more complete review of these processes and findings.

1.7.5 Radio Emissions

The connection between the radio emissions and aurora is only partially understood, with some of these multi-waveband connections shown in Figure 1.63. Figure 1.64 shows a summary of the Jovian radio emissions from Zarka (1998,

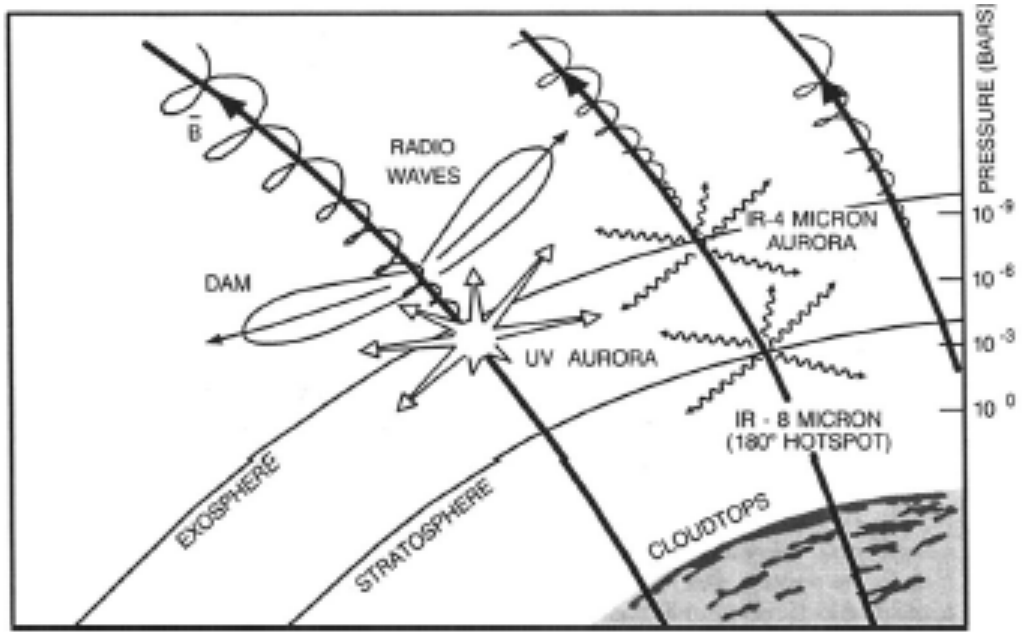

Figure 1.63: From Connerney (1992): Schematic illustration of charged particles spiralling along the magnetic field and the various emissions they generate as they approach the atmosphere in the north polar region

2000); Zarka et al. (2004). Radio emission from Jupiter occurs from ∼kHz to ∼10 MHz (see Fig. 1.64 panel B) of which only the decametric emissions (∼10 MHz) can be observed from Earth's surface.

Many of these emissions (particularly the Decametric and Hectometric emissons) are thought to be produced by the Cyclotron Maser Instability (CMI). CMI operates when the electron plasma frequency is much less than the electron gyrofrequency and if the electrons occupy an unstable loss cone, ring or shell distribution (Roux et al. 1993; Louarn and Le Quéau 1996; Delory et al. 1998; Ergun et al. 2000). This allows the production of resonant wave-particle interactions between non-maxwellian electrons gyrating around magnetic field lines and background radio waves. If these occur close to the electron gyrofrequency then the waves are amplified at the cost of the electron's perpendicular energy. Since the gyrofrequency depends on the magnetic field strength, the frequency of the emissions traces the altitude of the source above the ionosphere. Radio emissions can also trace the current system that generates the emission, since the morphology of the arcs of radio emission (see Fig. 1.64) suggests different observed beaming. For instance, transient

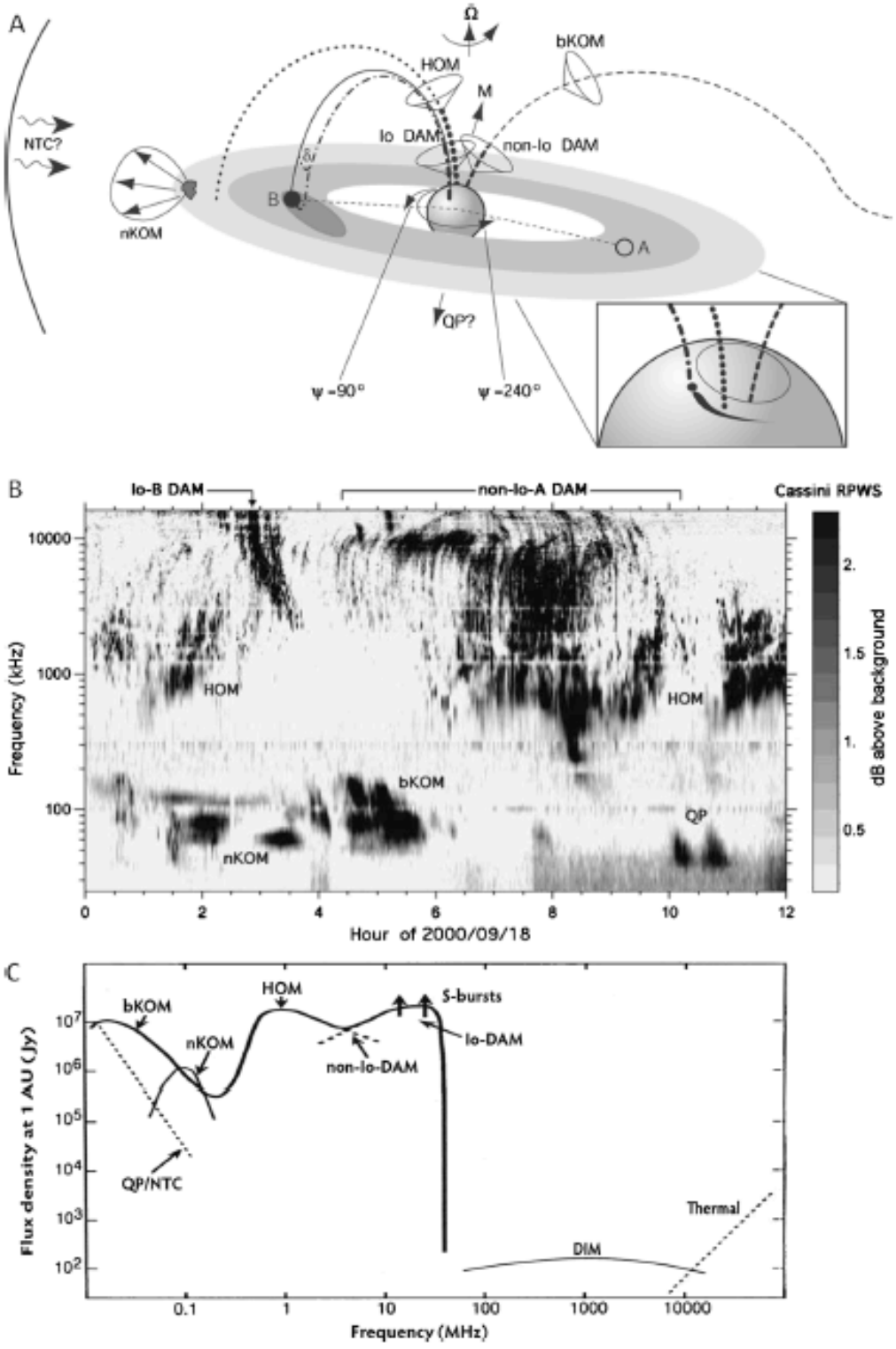

Figure 1.64: Figure collated in Bagenal et al. (2014) with the following caption: (A) Morphology of the types of Jovian radio emissions from Zarka (2000). (B) Frequency-time spectrogram of radio emissions obtained by Cassini when it flew past Jupiter in 2000 (from Zarka et al. (2001b,a). (C) Power of emissions (as received at Earth) for Jovian radio emissions versus frequency. The decimetric synchrotron emission (DIM) is over four orders of magnitude weaker than the high latitude emissions.

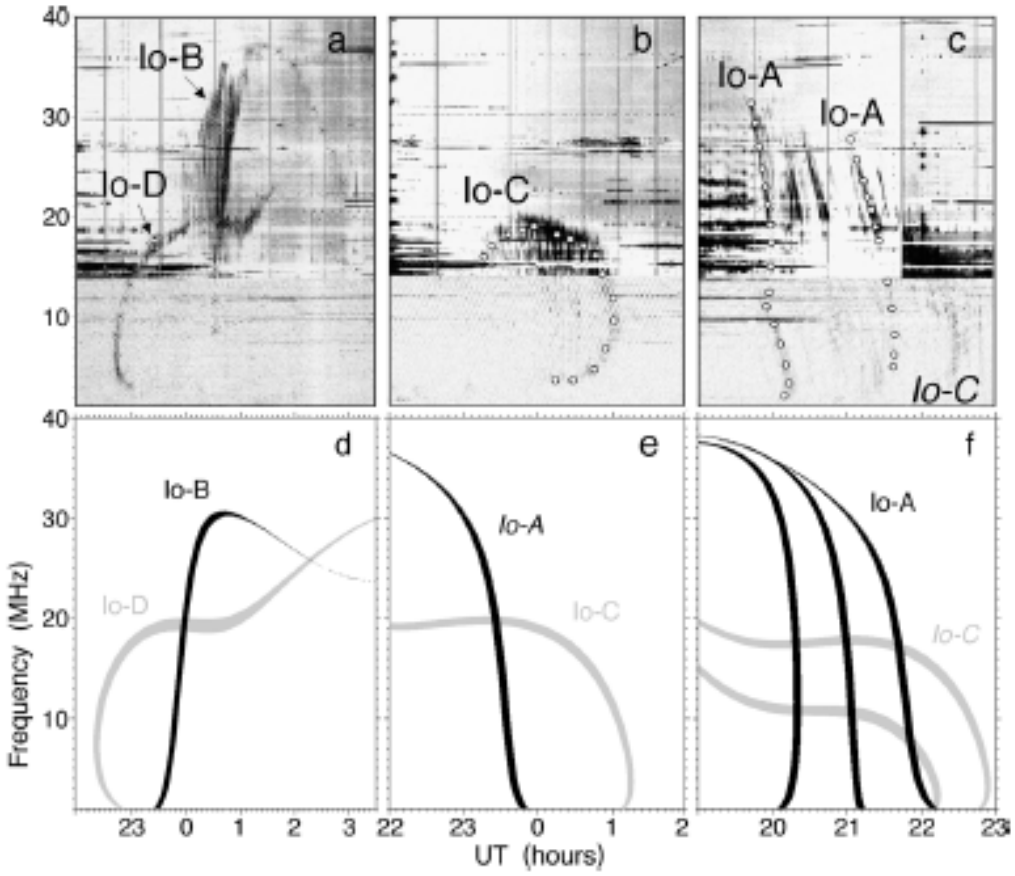

Figure 1.65: Figure collated in Bagenal et al. (2014) and references therein, with the following caption: Top (a, b, c) Dynamic spectra of typical Io-Jupiter arcs observed by Wind/Waves and the Nancay decameter array. The various symbols superimposed along the arcs were used to identify their line of maximum intensity in the frequency-time plane. Bottom (d, e, f) Dynamic spectra of Io-Jupiter emission for the same time intervals as above simulated using loss-cone cyclotron maser instability where the black arcs are generated in the northern hemisphere and grey arcs are in the south. From Hess et al. (2008, 2009).

currents generate loss-cone driven CMI with a changing emission angle, while auroral cavities produce a shell-driven emission with a constant emission angle (Badman et al. (2015) and references therein).

Studies of the Jovian radio emission have led them to be sub-divided into different categories. Here we briefly highlight the four that are relevant to the research presented here:

1. Io-Decametric Emission (Io-DAM) are produced by plasma disturbances generated by Io (see section of auroral satellite footprints) which accelerate electrons with unstable loss-cone distributions to generate the emission via CMI (e.g Hess et al. (2008, 2009)) (See Fig. 1.65).

2. Non-Io Decametric Emissions (Non-Io-DAM) appear to co-rotate, sug-

gesting an inner or middle magnetosphere origin. The distinctive curvatures of their arcs can be used to trace solar wind, with the presence of vertex-early and/or vertex-late morphology (see Fig 1.65 for example morphology) distinguishing between forward or reverse solar wind shocks that produce magnetospheric compression and expansion (e.g. Hess et al. (2012, 2014); Lamy et al. (2012)). They are also used to trace more general reconfigurations of the Jovian magnetodisk produced through mass loss (e.g. Gray et al. (2016)).

3. Hectometric (HOM) Emission occurs partially along field lines mapping to the extended IPT which could relate to inward moving empty flux tubes (Reiner et al. 1993; Hess et al. 2011). However, it may also have a higher latitude more radially distant component that may be the lower frequency counterparts to DAM arcs (Panchenko et al. 2013). Alongside Non-Io DAM, HOM bursts have been observed to be triggered by solar wind compressions (e.g. Gurnett et al. (2002)).

4. Quasi-periodic (QP) bursts with periods of the order of 20-40 minutes are thought to correspond to the most poleward auroral emissions (Hospodarsky et al. 2004; Kimura et al. 2010) and have been noted to have corresponding periodicity to the X-ray emissions (e.g. Gladstone et al. (2002); MacDowall et al. (1993)).

Other common radio emissions include: Auroral Broadband Kilometric Emission (bKOM) which is associated with the main auroral oval; Narrowband Kilometric Emission (nKOM) which is produced by plasma waves in the outer region of the Io Plasma Torus (Reiner et al. 1993); and Non-thermal Continuum emissions which may be produced at density gradients in the magnetopause (Kurth 1992) or could relate to lower frequency emissions associated with QP bursts.

The cones in panel A of Fig. 1.64 show the beamed nature of the bKOM, HOM and DAM emissions. This beam is only observable if the observer is able to look into the cone. This means that as the source rotates with the planet, even though it emits continuously, the cone will move into and out of view of the observer. This will result in observations of the radio emission at specific intervals and the morphology of the observed radio emission will directly de-

pend on the viewing of the cone. This means that while radio emissions bursts may have been triggered earlier, they will only be observable when the region rotates into view, which contributes a time-lag when attempting to connect them with the magnetospheric disturbances that generated them.

1.8 Proposed Drivers of the X-ray Aurora

Having introduced the Jovian magnetosphere, its multi-waveband aurora and the solar wind, we close the introduction by linking the preceding material with current ideas around the driving mechanisms that provide the significant energies required for Jupiter's X-ray Aurora. Having already discussed the link between the UV main oval corotation enforcement currents and the hard X-rays, here we focus on the X-ray hot spot.

Cravens et al. (2003) outline two possible models in which heavy ion precipitation could generate the observed hot spot X-ray fluxes:
1. Open Magnetic Field lines in Jupiter's cusp accelerate solar wind ions which subsequently produce X-rays through Solar Wind Charge Exchange (e.g. Cravens, 2002)
2. MV downward (return) Field Aligned Currents on closed magnetic field lines accelerate magnetospheric ions, which subsequently produce X-rays through charge exchange.

1.8.0.1 Direct Solar Wind Precipitation in the Cusp

The first scenario from Cravens et al. (2003) involves direct solar wind particle precipitation on open magnetic field lines that are attached to Jupiter's ionosphere at one end and the solar wind at the other end. Through density measurements of the magnetosheath, Cravens et al. (2003) calculate that the available abundances of high charge-state oxygen and carbon would require a potential drop of 200 kV and an inordinately large current of 1000 MA (ten times the upward current system (Bunce et al. 2004)) to produce sufficient particle fluxes for all of the observed X-ray emission. Alongside these accelerated high charge-state ions, there should also be a population of precipitating

protons and alpha particles, which would produce much larger UV emissions than are typically observed.

Since it is important for understanding the X-ray production system and any changes introduced by new observations, we follow Cravens et al. (2003) by walking-through these calculations and the application of the Knight relation below.

It is assumed that the solar wind ions are isotropic and not accelerated and that each produce N=2-3 X-ray photons. A solar wind heavy ion flux of f=10^{-3} times the density of protons in the solar wind, n_{SW}, is weighted by a factor of 2 to account for the fact that the magnetosheath is denser than the solar wind. A slow solar wind velocity, u_{SW}, of 400 km/s leads the calculation:

$$4\pi I = 2 n_{SW} u_{SW} f N \tag{1.33}$$

to produce a value of $10^5 cm^{-2} s{-}1$ = 0.1 R (we note that repeating the calculation with the 90% values from table 1.6 produces a value about an order of magnitude larger than the slow solar wind values). The observed X-ray $4\pi I$ values are 2-20 R (Gladstone et al. 2002), so without acceleration solar wind charge exchange emission could only account for 1-10 % of the observed emission. Alongside this heavy ion precipitation, there should be the accompanying precipitation from the 1000s of times more protons that exist in the sheath.

The authors further calculate that for an auroral area of 10^{14} m^2 and a photon energy of 0.3 keV, then the emission from solar wind charge exchange is around 50 MW. They quote that the observed auroral power is 1 GW (although Branduardi-Raymont et al. (2008) place the soft X-ray power at 230 MW). The authors acknowledge that little is known of the Jovian cusp, so they assume a terrestrial-like cusp and find that these numbers are consistent with the $\sim$ 10 MW auroral hiss detected during the Ulysses Jovian cusp encounter (Farrell et al. 1993).

If there were insufficient charge carriers to fulfil the current density required to 'complete the circuit', then the solar wind ions might experience a

parallel electric field along the magnetic field lines (Knight 1973) in the Jovian cusp. This would provide a potential drop and, by increasing the loss cone precipitation, would provide a higher flux of ions into the ionosphere (e.g. Lyons and Speiser (1982) for the terrestrial aurora).

Describing this in more detail: Cravens et al. (2003) assume that the adiabatic invariant conserving the magnetic moment, μ, holds true (Eqn: 1.34) and that the particle energy, ϵ is conserved (Eqn:1.35):

$$\mu = \frac{mv_{\perp}^2}{2B} \tag{1.34}$$

$$\epsilon = q\phi + \frac{1}{2}mv_{\parallel}^2 + \frac{1}{2}mv_{\perp}^2 \tag{1.35}$$

where $v_{\parallel}$ ($v_{\perp}$) is the velocity parallel (perpendicular) to the magnetic field line, B is the magnetic field strength, m is the particle mass, q the particle charge and ϕ the potential.

As a particle approaches a region of higher magnetic field strength the perpendicular velocity of the particle will increase (Eqn: 1.34) and to conserve energy the parallel velocity will decrease (Eqn:1.35). Particles with low pitch angles (those with velocities parallel to the field line) will escape through the loss cone and precipitate into the ionosphere as flux contributing to the current. Those with higher pitch angles (velocities close to perpendicular) will be repelled at the mirror point and bounce back along the field line. This means that as particles move from a region of low magnetic field strength (e.g. the Jovian plasma disk) to a region of high magnetic field strength (e.g. the polar ionosphere hot spot), they are more likely to be reflected and bounce back (not provide current) according to the magnetic mirror ratio:

$$r_{Bmirror} = \frac{B_{Max}}{B_{Min}} \tag{1.36}$$

In order to provide sufficient flux into the ionosphere, so that the current system can be maintained, a parallel electric field is formed. This electric field acts to increase the particle flux into the ionosphere by increasing the parallel

velocity (flux into the loss cone) of precipitating particles.

The ratio of the actual current density that this produces over the thermal current density that is otherwise available is a function of the parallel potential produced by the field and the magnetic mirror that would otherwise restrict the particle flux. The ratio of the accelerated flux that the electric field produces, F, to the initial thermal flux F_{th} (where $F_{th} = nu_{th}$ the density multiplied by the thermal velocity) is defined as the Knight factor, R_{Knight}, which depends, in turn, on the ratio of the kinetic energy gained, $K_{\parallel}$ by a particle due to the parallel potential drop $qV_{\parallel}$ (where q is the charge and $V_{\parallel}$ is the potential drop in volts) vs the thermal kinetic energy, K_{Th} which would otherwise have been available.

$$\frac{F}{F_{Th}} = R_{Knight} \approx \frac{K_{\parallel}}{K_{Th}} \tag{1.37}$$

If this mechanism existed above the ionosphere then the parallel potential drop would increase the flux of the precipitating particles. Based on the unaccelerated solar wind fluxes, an increase in the particle flux by a factor of 20-200 is needed, so Cravens et al. (2003) take a Knight factor of 100 and calculate that a 200 kV drop would be needed. However, the larger flux of solar wind protons should produce a UV aurora from doppler broadened Lyman α that exceeds that observed (except during UV polar flare events - Fig 1.56). The flow of these solar wind protons and ions alone (not including electrons) would generate very large currents of the order of 1000 MA. Cravens et al. (2003) close by saying that this could therefore not be the only mechanism responsible for generating the X-ray aurora, since the observed UV emissions are not sufficiently bright and the current system is infeasibly large.

Alongside Cravens et al. (2003), Bunce et al. (2004) also show that precipitation of magnetosheath electrons and protons does not match the observed UV emissions. Even given the order of magnitude increase in the current systems produced by the Bunce et al. (2004) model (described below) during a solar wind compression, the acceleration of magnetosheath plasma is incapable of explaining all of the UV emission in the region and instead acceleration is

required on both open and closed field lines.

As an aside, we note that the magnetic field strength over the Northern hot spot is 10-14 G, while over the Southern spot it is 10-12 G. There may therefore be a region in the Northern hot spot where the mirror ratio and subsequent parallel voltages are larger. This should lead to larger energy for ion precipitation in the North than the South, which contradicts the findings of the Ozak et al. (2010) and Hui et al. (2010) who find best-fit spectral models have higher energies in the South.

1.8.0.2 MV Downward Currents on Closed Field Lines

By again applying the Knight relation, Cravens et al. (2003) find that a much more likely scenario for X-ray generation is that large potential drops of ∼8 MV exist on downward field-aligned currents from the outer magnetosphere.

As discussed previously, beyond 20 R_J, Jupiter's magnetospheric plasma begins to drop below corotation velocities. Upward field aligned currents (outward from Jupiter) are produced to transfer planetary momentum to the magnetospheric plasma. Having flowed radially outward through the magnetosphere (and applied the accelerating JXB force), these currents return to the planet as downward field-aligned currents from the outer magnetosphere. This return current system poleward of the main oval would be carried by planetward precipitating ions and anti-planetward electrons.

In the outer magnetosphere there is a Sulphur to Oxygen ratio of about 1 with a typical temperature of 40 keV (Hamilton et al. 1981; Krimigis and Roelof 1983; Lanzerotti et al. 1992) and a typical charge-state that is singly or doubly ionised. To reach the needed energies of 1-2 MeV/amu in order to charge strip magnetospheric O^{++} to form the observed X-ray emissions from $O^{7+,8+}$, Cravens et al. (2003) calculate that a potential drop of 8 MV is needed somewhere between the outer magnetosphere and the ionosphere. This would produce 1-2 GW, ∼ 10 R X-ray emissions as observed in the hot spot (Gladstone et al. 2002).

One of the highlighted problems for a direct solar wind precipitation origin for the X-ray aurora is that it should produce bright UV emissions from

precipitating protons. The ratio between protons and heavy ions in the outer magnetosphere is an order of magnitude smaller than that for the solar wind and therefore the auroral emissions associated with Lyman α from these protons will be 10-70% the magnitude of the X-ray luminosity from precipitating heavy ions (Cravens et al. 2003). In addition, the more significant acceleration for the magnetospheric ions will mean that the protons penetrate deeper into the atmosphere and their subsequent UV emissions are more likely to be absorbed in the hydrocarbon layer.

By estimating the total charge flowing into the atmosphere from the heavy ions and protons, Cravens et al. (2003) calculate that the field aligned current associated with flowing ions would be 2 MA and would be 6 MA from the secondary electrons from charge-stripping. This would provide a total current of 8 MA. Ozak et al. (2013) update this by calculating total downward currents of 2 MA.

While Cravens et al. (2003) are able to explain well in this way the observed X-ray and UV auroral luminosities and brightnesses, they note that their mechanism does not directly explain the pulsating nature of the emissions.

However, their mechanism does connect the X-ray emissions with the QP radio and energetic particle emissions. MacDowall et al. (1993) observed 40 minute QP bursts of radio emission from keV - MeV electrons. These bursts seem to precede anti-planetward moving MeV electrons in the high-latitude dusk magnetosphere (Simpson et al. 1992; McKibben et al. 1993). Cravens et al. (2003) suggest that the pulsed precipitating ions produce pulsed MeV secondary electrons, which subsequently produce the observed radio bursts with similar periodicity to the X-ray emissions. Galileo observations may dispute this connection, since they did not detect MeV electron beams at 39 - 46 RJ (Williams et al. 1996), however, we show in chapter 2 that these Galileo observations may not have been sufficiently far from the planet.

Finally, Cravens et al. (2003) note that if the periodicity relates to bounce times or standing waves, this is more likely to occur on closed field lines than open field lines. Alternatively, it may relate to phenomena similar to terrestrial

substorms (Desch 1994). We also note that at Earth downward current regions are often more bursty and less quasi-static than their upward current partners (priv comms P. Delamere).

1.8.0.3 Vortical Flows from Pulsed Dayside Reconnection

While the Cravens et al. (2003) work was unable to provide a physical explanation for the presence of periodicity of the pulsations, Bunce et al. (2004) offer a scenario capable of explaining the luminosities/brightnesses and also the pulsations of the Jovian X-ray aurora. They propose that dayside reconnection would perturb Chapman-Ferraro Currents between the magnetopause and the ionosphere and that, under suitable solar wind conditions, the resulting current systems can sufficiently accelerate ions to produce the X-ray aurora. Given that reconnection often occurs in pulses, their model also explains the characteristic X-ray pulsations. At Earth, these pulsations regularly occur at the Alfven transit time, which from pole-to-pole at Jupiter is 30-50 minutes (Cowley and Bunce 2003b) - in line with the 45 minute pulsation rate seen in the Jovian X-ray aurora. However, they note that this is a longer timescale than was observed for Jovian Flux Transfer Events (FTEs) by Walker and Russell (1985) (the transfer of flux across the magnetopause during reconnection). To interpret the X-ray auroral signatures in the context of this model, here we qualitatively describe the models predictions.

In the region of the open-closed field line boundary, when a pulse of reconnection occurs, open field lines will be dragged poleward, while, more slowly, field lines either side are dragged equatorward. This produces a localised twin-vortex flow (e.g Siscoe and Huang (1985); Cowley and Lockwood (1992)). The newly opened field lines poleward of the boundary form the cusp, across which magnetosheath plasma can precipitate into the ionosphere.

Bunce et al. (2004) propose two models, one for low and one for high IMF strength. Using these models, they calculate how the twin vortical flows produced by day-side reconnection result in bi-polar (an upward and a downward) field aligned currents. For the low IMF model, this produces low voltages, with negligible X-ray emission and small spots of UV emission co-located with the

suspected open-closed field line boundary and UV cusp emission (e.g. Cowley et al. (2003); Pallier and Prangé (2004) - See Fig. 1.58 and 1.39). However, for high IMF strength, this forms intense arcs along the open-closed field line boundary and sufficient voltages to accelerate low charge-state ions to produce the observed X-ray emissions.

The resulting field aligned currents and electrostatic potentials that the reconnection induced vortices produce are shown in Figure 1.66 for times of solar wind rarefaction (upper two panels) and compression (lower two panels). The vortices divert the Chapman-Ferraro currents on the magnetopause downward along field lines in the Eastern vortex, across the ionosphere as a Pedersen current and then upward back to the magnetopause in the western vortex. This model therefore produces pairs of upward and downward field aligned currents between the ionosphere and the magnetopause at the open-closed field line boundary. It should be noted that this pair of upward and downward currents is not expected to occur across the entire open-closed boundary, instead it may be expected to occur on up to one third of the open-closed boundary at and beside the specific location where reconnection is occurring.

As with Cravens et al. (2003), Bunce et al. (2004) apply the Knight relation such that parallel electric fields and their associated field aligned potentials produce the required fluxes of charge carriers. They use known and expected magnetosphere and sheath populations to produce a set of observable results.

For solar wind rarefactions, this leads to UV brightnesses in the open field line region of 10 kR from upward currents and 10-100 kR from downward currents. In contrast, on the closed magnetosphere side the upward currents produce 100-400 kR and the downward currents produce 300 kR. These should produce adjacent bright spots or arcs of a few 1000 km length and a few 100 km width, separated by several 1000 km. In contrast with the UV, for solar wind rarefactions the X-ray emission is expected to be negligible, since precipitating magnetospheric O^{2+} do not gain sufficient energy to charge-strip and solar wind ion precipitation is only expected to produce 20 kW of X-ray

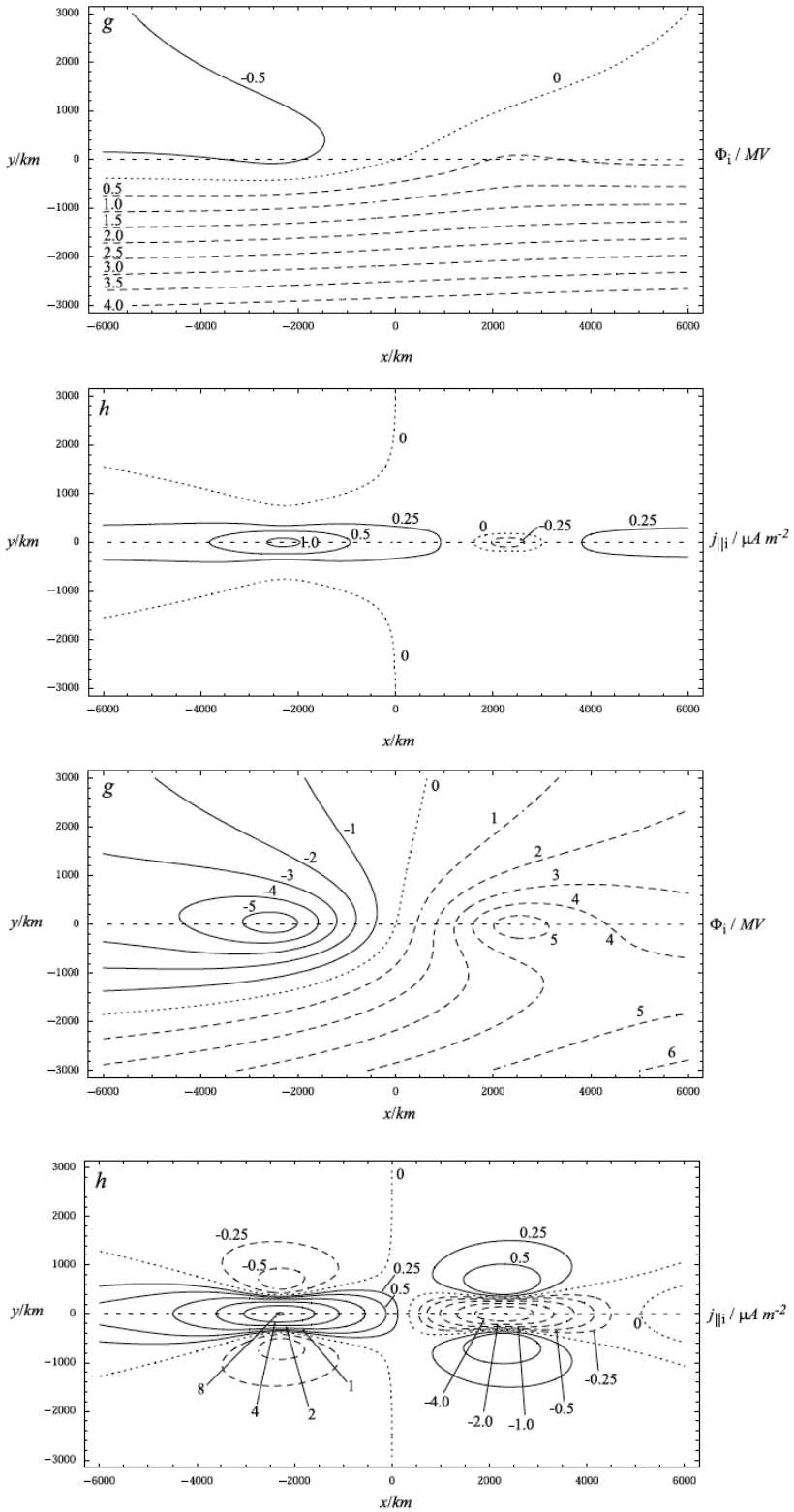

Figure 1.66: From Bunce et al. (2004): Production of vortical flows during pulsed reconnection for solar wind rarefaction (upper two panels) and compression (lower two panels) for electrostatic potential (1st and 3rd panels) and field aligned current density (2nd and 4th panels). East is in the positive x direction while poleward is in the positive y direction and the origin is at the centre of the reconnection site on the open-closed field line boundary (but not along all of it). For the electrostatic potential plots: the dotted line depicts zero electrostatic potential. The solid lines show contours of negative electrostatic potential. Contours are labeled in steps of 0.5 MV. For the field-aligned current density plots: Dotted lines indicate contours of zero field-aligned current density. Solid lines indicate the regions of upward directed field-aligned current density, while the dashed lines indicate the regions of downward directed field-aligned current density. Contours are labeled in units of μAm^2.

power.

For solar wind compressions the story is quite different. On the open field side of the boundary, the upward currents include 300-600 V regions, while the downward currents have 10-20 kV regions carried mostly by magnetosheath protons. This produces 100 kR emissions peaking at 2.5 MR. On the closed-magnetosphere side of this boundary the upward current region is expected to have 10-100 kV potentials, while the downward current region is expected to have 0.5-5 MV regions. This should generate an upward current region of 6000 km along the boundary and 350 km wide with more than 100 kR UV brightness. In the downward current region, the UV emissions from closed field lines should reach 30 MR in a 3000 km region that is 250 km wide. This leads to a predicted emission of 10 MR from an arc 10,000 km in length with a 'discernible break' between upward and downward field regions. Bunce et al. (2004) also note that during solar wind compressions, electrons accelerated through their model should produce X-rays through bremsstrahlung emission. Under these conditions X-ray emissions comparable to the Cravens et al. (2003) calculations with several GW of power should be observable on closed field lines while on open field lines the emissions should remain negligible at 1 MW.

This profound difference between open and closed field lines is produced by the significantly higher densities of particles in the magnetosheath and limiting currents, than in the magnetospheric population. This leads to smaller accelerating voltages and precipitating energy fluxes for open field lines. Elsner et al. (2005) comment that their observations of a UV-X-ray flare in 2003 match well to the Bunce et al. (2004) predictions. However, we note that auroral X-ray emissions are always observed, so the low IMF strength case from Bunce et al. (2004) may be too conservative or there may be additional X-ray generation mechanisms, as yet unidentified.

Having introduced the processes involved in X-ray emission, the historic observations of Jupiter and the solar wind and magnetospheric processes that have thus far been discussed for Jupiter and the ion acceleration needed for the Jovian X-ray aurora, we will now introduce the instrumentation used for the observation in this thesis and then present three new observation campaigns

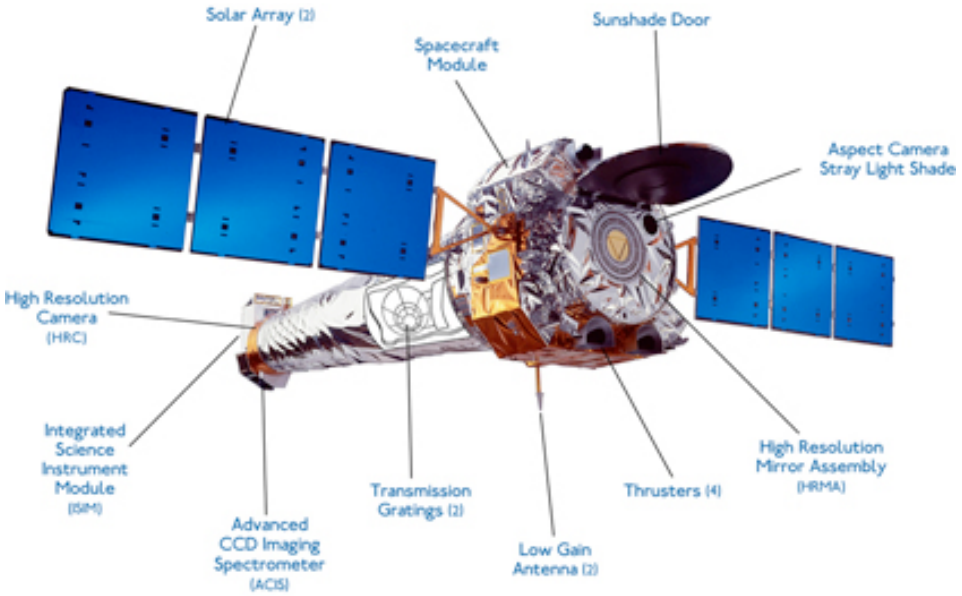

Figure 1.67: Schematic of the Chandra X-ray Observatory Key Components (from http://chandra.harvard.edu).

of Jupiter and their analysis.

1.9 The Chandra X-ray Observatory - Instrumentation

Named after Nobel prize winning astrophysicist Subrahmanyan Chandrasekhar, NASA's Chandra X-ray Observatory (CXO - see Fig. 1.67 (Weisskopf et al. 2000)) was launched on July 23, 1999. It has a highly elliptical orbit that lasts 64 hours 18 minutes and takes CXO one third of the way to the Moon (133,000 km) at apogee and 16,000 km from Earth at perigee. This provides continuous observations of up to 55 hours. The observatory carries four key scientific instruments: the Advanced CCD Imaging Spectrometer (ACIS - e.g. Garmire et al. (2003)), the High Resolution Camera (HRC - e.g. Murray et al. (2000)), the High Energy Transmission Grating (HETG - 0.4 - 10 keV) and the Low Energy Transmission Grating (LETG - 0.08 - 2 keV). Here, we focus on the two instruments used for Jupiter observations: ACIS and HRC.

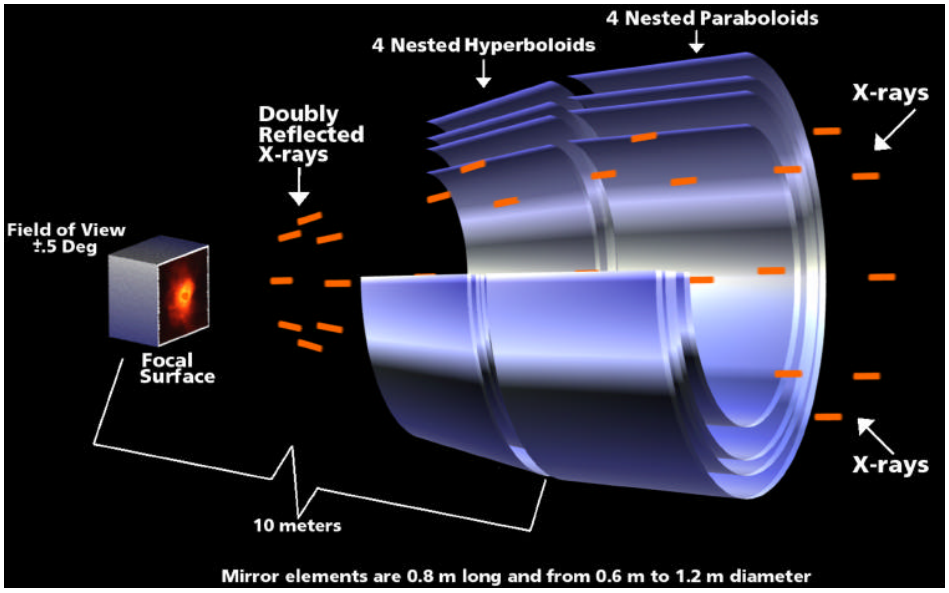

Figure 1.68: Chandra's paraboloid and hyperboloid mirrors utilise grazing incidences to guide X-rays into the focal plane detectors ACIS and HRC (from http://chandra.harvard.edu).

1.9.1 The Telescope System

If mirrors are not aligned nearly parallel with the incident direction of an X-ray photon, then the particle-like behaviour will lead X-rays to penetrate the mirrors and not be observed at the detector. X-ray photons therefore have to be 'guided' to the detectors through grazing impacts with the mirrors. Figure 1.68 shows the schematic for Chandra's mirrors which have a 10 metre focal length. The Integrated Science Instrument Module then controls whether it is HRC or ACIS that is placed into the focal plane to collect the X-rays.

1.9.2 Advanced CCD Imaging Spectrometer - ACIS

ACIS is an array of charged coupled devices (CCDs) capable of simultaneously providing high spatial and moderate spectral resolution (spectral resolution can be vastly improved by using ACIS with H/LETG) (e.g. Garmire et al. (2003); Weisskopf et al. (2000)). Each CCD pixel offers ~ 0.5" resolution. At launch, the combination of CCDs and mirrors provide an effective area (X-ray collection area) of 110 cm^2 at 0.5 keV. ACIS also offers different timing modes. The lowest temporal resolution is slightly over 3 seconds. Typically, the choice of mode offers a trade-off between spatial and timing resolution.

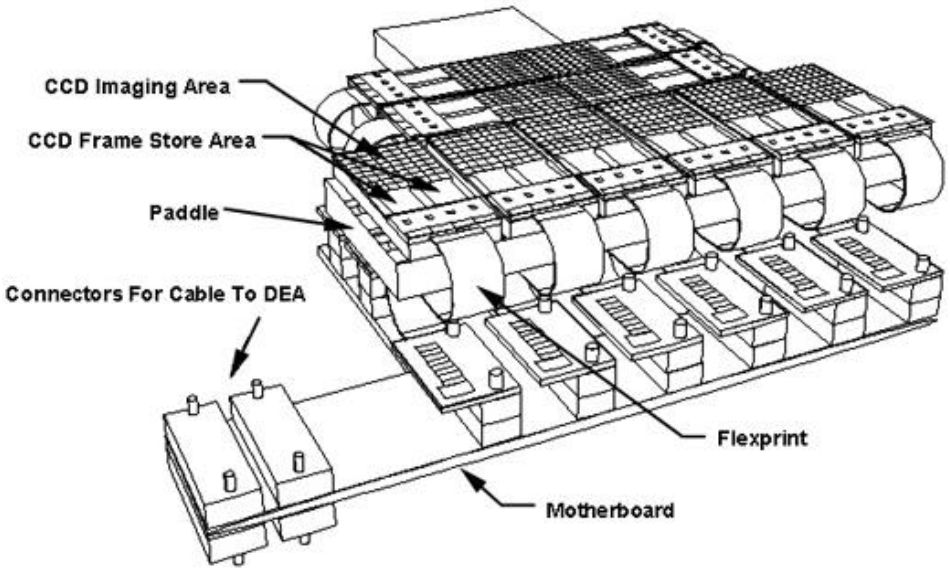

Figure 1.69: Schematic of Chandra's ACIS CCD instrument which provides both high spatial resolution and moderate spectral resolution. ACIS-I which is primarily used for imaging is the 2 x 2 CCD imaging area. ACIS-S which is used for imaging or read-out from the transmission grating instruments is shown as the line of 6 CCDs beneath ACIS-I (from http://chandra.harvard.edu).

ACIS consists of 10 planar 1024 by 1024 pixel CCDs split between:
ACIS-I: 4 chips in a 2 by 2 format for imaging, particularly permitting access to wide fields (16.9' x 16.9') (2 by 2 CCDs in fig 1.69)
ACIS-S: 6 chips in a 1 by 6 format used either for imaging (8.3' x 50.6') or for a H/LETG spectrum read-out (line of 6 CCDs in Fig. 1.69).

Two of the CCDs are back illuminated and provide access to lower energies and better energy resolution - these are preferable for Jupiter's dominantly soft X-ray emission. The other 8 CCDs are front illuminated and have suffered some radiation damage from terrestrial radiation belt protons, negatively impacting their energy resolution. Since noticing this, steps to protect the CCDs have been taken and consequently no further degradation has occurred. A correction to account for this degradation is available in the CIAO software package.

Upon impact of an X-ray a number of electrons proportional to the X-ray energy are released in the CCD and confined by an electric field. The energy resolution depends on the precision with which the quantity of charge (electrons) produced by a single photon is measured, which for ACIS involves

a read-out noise of less than 2 electrons RMS. After a 3.2 s exposure and 41ms read-out, the next exposure begins while, in parallel, the data is transferred from the frame store to a local processor which removes bias and identifies the position and amplitude (analogous to energy) of any 'events'. Any event recorded by the CCD is tested against a range of criteria based on its amplitude and the amplitude of a surrounding set of 3 x 3 or 5 x 5 pixels (depending on the telemetry mode selected) and assigned a 'grade'. This grade may lead to the event being rejected, since it may appear to be unphysical or non-X-ray related (e.g. a cosmic ray).

Since the CCDs are also sensitive to optical emissions, the Optical Blocking Filter is positioned between the mirror array and the CCD array of ACIS, to absorb optical light. It is believed that there is a 'red-leak' in the infrared I or J bands, which previously led to disregarding the 0.2-0.3 keV emissions from Jupiter.

Unfortunately, contaminant issues with the Optical Blocking Filter have led ACIS to no-longer be a viable option for observations of Jupiter. The optical blocking filter has continuously built up contamination from out-gassed carbon, oxygen and fluorine which have deposited onto its cold filter and significantly degrade the spectra between 0.277 - 1 keV - this issue has not occurred for the warmer HRC filters. There is some discussion of 'baking-off' the contaminant by temporarily raising the ACIS temperature to HRC temperatures (R. Kraft, priv comms), which, if successful would again make ACIS a relevant instrument for Jovian studies. However, this is unlikely to happen in the short-term since ACIS is still widely used for observing objects with a higher hard X-ray output.

1.9.3 Observing Jupiter with ACIS

For the Chandra ACIS observations of Jupiter, we had to re-grade the event lists (see chapter 2 and 4), so we briefly discuss the onboard grading process and the observation parameters. Prior to the start of the observation, bias frames are taken to record the amplitude of the charge in each pixel. The bias-subtraction for each event is conducted onboard of Chandra. The bias-

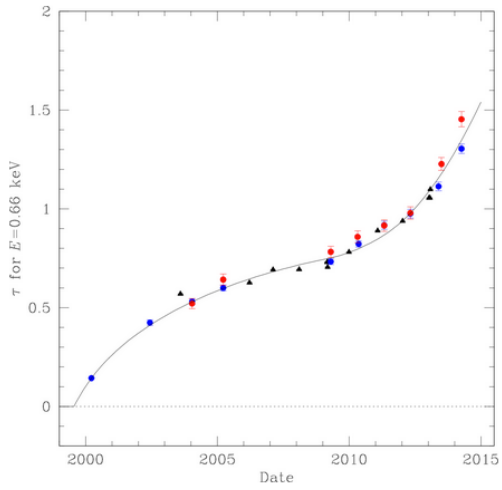

Figure 1.70: From Chandra Proposers' Observatory Guide : Optical depth of the contaminant versus time, showing increased obscuration with time for the X-ray sources: A1795 with ACIS-I (red); A1795 with ACIS-S (blue); E0102-72.3 with ACIS-S (black).

subtracted event list is then examined on-board and each event that exceeds a threshold is graded according to a set of 256 possible grades. The grade is assigned based on characteristics of the event such as: the distribution of different Pulse Height Amplitudes (a measure of the electron charge from the X-ray energy) on each pixel in the local 3 x 3 (or sometimes 5 x 5) group.

For Jupiter, ACIS events must be re-graded on the ground because light-leak through the filters from Jupiter's optically and IR-bright disk leads to a build up of charge across many CCD pixels in any 5 x 5 array. This would normally lead to the events being rejected as non-physical. However, to prevent this automatic rejection, for Jupiter observations the thresholds for what is classed as an event are raised onboard Chandra, so that the onboard processing doesn't reject the events before grading them. They are then graded onboard. However, the grading they are assigned onboard is incorrect since it accounts for the marginally raised amplitudes of every pixel from the light leak. We therefore re-assign grades using the algorithms designed by P. Ford (Priv Comms) in order to correct for the onboard grading (see chapter 2 and 4).

One can choose to operate ACIS in Timed Exposure (0.2-10 second exposures) or in Continuous Clocking Mode (at the cost of one spatial dimension) in which ACIS can operate with 3 ms timing resolution. For Jupiter, we used

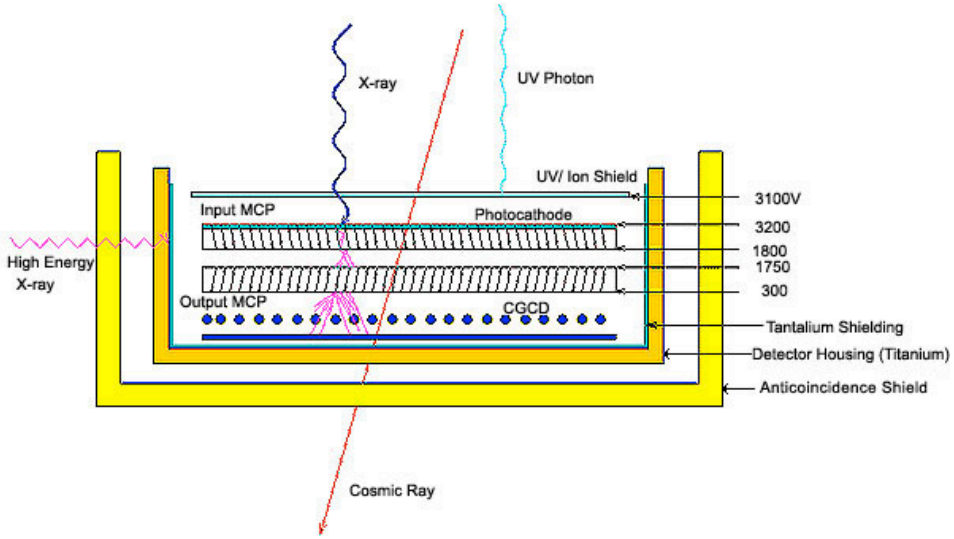

Figure 1.71: Schematic of Chandra's HRC instrument (from http://chandra.harvard.edu).

Timed Exposure, since we want two dimensional spatial positions for X-ray photons. In the observations reported here, 'Very Faint' Telemetry mode is chosen in order to return as much information on each individual event as possible. This applies certain limitations, such as losing 1-2% of good events and applying a 12 keV cut-off, but it is necessary for event-regrading on the ground. It also provides a grading based on 5 x 5 pixels which limits the number of spurious events from the OBF low energy light-leak. The bias frame for Jupiter should be taken without the planet in view to limit unreliability of the bias frame caused by light leak from the planet (e.g Elsner et al. (2005)).

1.9.4 High Resolution Camera

HRC (e.g. see Murray et al. (2000)) consists of two Micro-Channel Plates (MCP) detectors: HRC-I, which is optimised for imaging and has the largest field of view on Chandra (31x31'), and HRC-S which is used for LETG read-out (not supported for HETG read-out).

The structure for HRC is shown in Figure 1.71. Above the detector there is a shield to prevent entry from UV emission, ions and low energy electrons. The MCPs consist of a 10-cm square cluster of 69 million lead-oxide glass tubes (each 10 μm diameter and 1.2 mm long). Each set of tubes is tilted by an angle of 6° to improve the probability of interaction with an incident

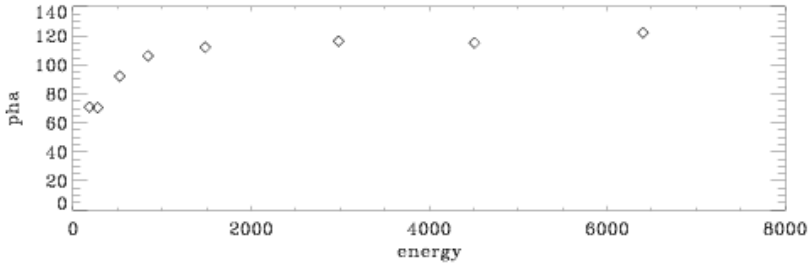

Figure 1.72: Schematic of Chandra HRC's PHA to energy relation (http://chandra.harvard.edu).

X-ray and the CsI-coating raises the photoemission. Voltages applied across the tubes then accelerate the electrons to produce a cascade of 10s of millions of electrons as the initially ejected electron collides with the tube to release further electrons ($\sim$ 2 x 10^7 electrons per X-ray photon). These electrons are detected through a grid of wires (or hybrid for HRC-S). The centroid of the charge cloud (a combination of a Gaussian and Lorentzian distribution) records the location of the original X-ray to 0.5 arc-second resolution (0.4 arc seconds is HRC's PSF, while 0.13 is from read-out). Non-X-ray events have broader charge clouds and so can often be identified and rejected from an event list through the shape of the cloud. HRC can achieve temporal resolution of as little as 16 msec.

The spectral resolution of the HRC is poor so spectral fitting is not viable. Pulse Height Amplitudes are returned with the data and it is possible to distinguish between hard and soft X-rays with this (see Fig 1.72), but the improved low-energy sensitiviy and the timing and spatial resolution of HRC are a trade-off for the higher spectral resolution that ACIS offers.

Jupiter typically blocks the cosmic X-ray background (e.g. Elsner et al. (2005)), so background subtraction is not applied (or rather is unapplied since it is often automatic for the software package 'XSPEC'). The X-ray background consists of the cosmic X-ray background; the charged particle, photon and neutron particle background (the particle background is typically at higher energies than those emitted by Jupiter, so we choose to disregard these Pulse Amplitudes); and read-out artefacts (e.g. trailing from bright sources that lead to charge build up on pixels during the short read-out time). It should

be noted that the background rates (from non-heliospheric cosmic ray charged particles) vary inversely with the solar cycle since a stronger solar magnetic field at solar maximum deflects and prevents charged particles from entering the heliosphere.

1.10 The XMM-Newton Observatory - Instrumentation

XMM-Newton was launched on December 10th 1999 and is named for its X-ray Multi-Mirror (XMM) assembly and Isaac Newton. It consists of three Wolter type-1 X-ray telescopes and a co-aligned 30-cm optical/UV telescope with a MCP pre-amplified CCD detector. While XMM-Newton offers simultaneous X-ray and optical/UV observations, we will focus only on the X-ray instruments. The X-ray cameras all lie in the focal plane of the three X-ray telescopes, which each feature 58 gold-coated concentric nested mirrors of 0.3-0.7 m diameter and 0.6 m length. This provides a total collecting area of 4300 cm^2 at 1.5 keV and a focal length of 7.5m (Jansen et al. 2001). As with Chandra, XMM-Newton also occupies a high-altitude elliptical orbit that lasts about 48 hours, and is capable of up to 40 hours of continuous observation in one orbit.

The key X-ray instruments for Jupiter observations are the European Photon Imaging Camera (EPIC) and the two Reflection Grating Spectrometers (RGS). EPIC consists of three CCD cameras that each have a 30' field of view and 0.15-12 keV operational energy range. They are based on:
a) two Metal Oxide Semi-conductors (MOS) CCD arrays with moderate spectral (E/$Delta$E $\sim$ 10-50) and spatial resolution (PSF with 5" FWHM) and high timing resolution of 1.5 ms (Turner et al. 2001)
b) an array of 12 pn CCDs which also possess moderate spatial (PSF with 6" FWHM) and spectral (E/$Delta$E $\sim$ 5-50) resolution and high time resolution of 0.03 ms (Strüder et al. 2001).

RGS 1 and 2 each provide high spectral resolution (E/ΔE $\sim$ 100-500) for the energy range 0.35 - 2.5 keV and highest time resolution of 15 ms

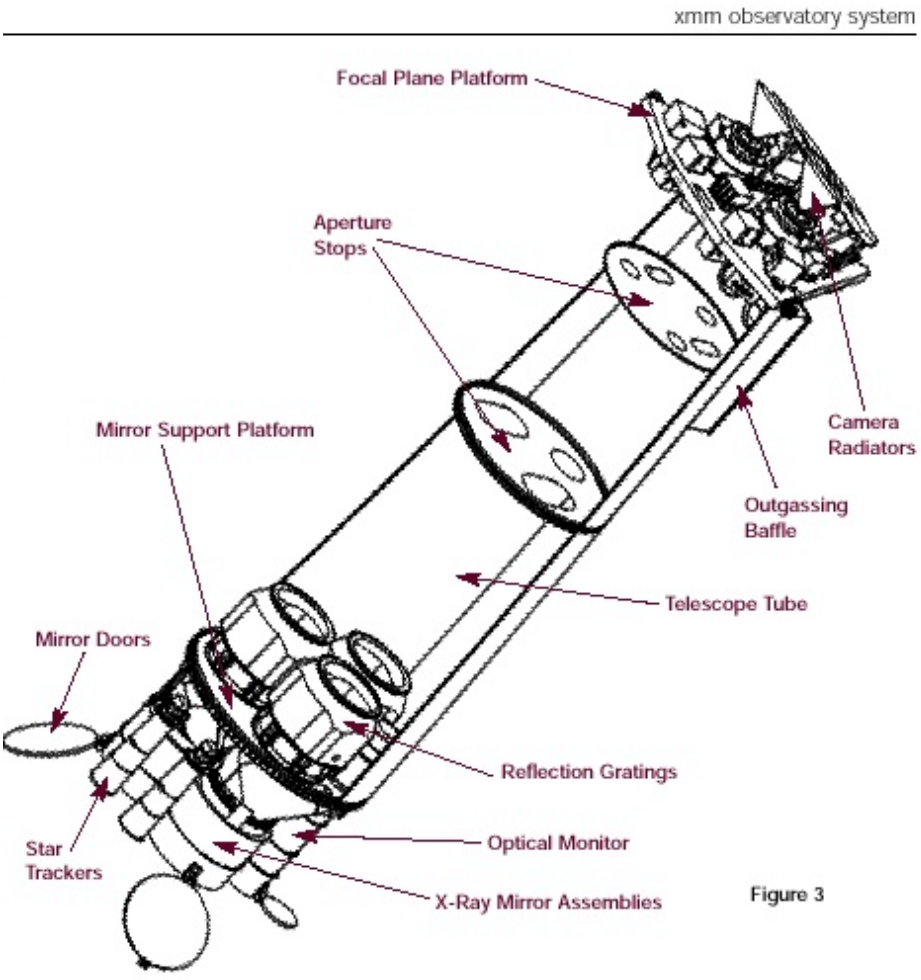

Figure 1.73: Schematic of XMM-Newton from the XMM-Newton Users Handbook.

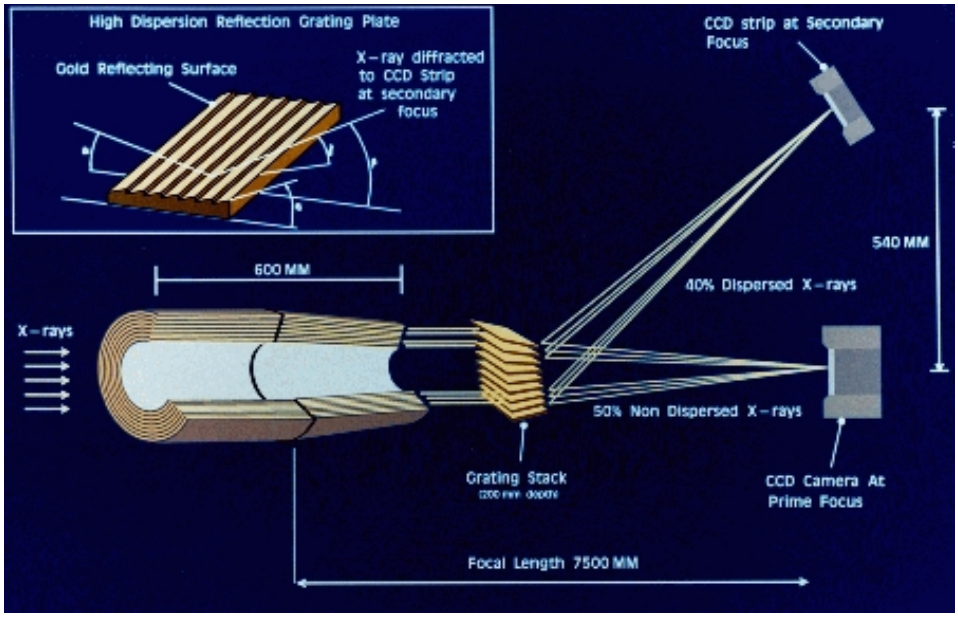

Figure 1.74: Schematic of XMM-Newton's mirror layout for the EPIC and RGS instruments (from the XMM-Newton Users Handbook).

(Den Herder et al. 2001). EPIC-MOS 1 and 2 share their telescopes with RGS 1 and 2 with a photon flux ratio split of approximately 50:50 (as seen in Fig. 1.74), while EPIC-pn receives the full photon flux.

Only the EPIC-pn instrument features in the research described here. EPIC-pn is based on a back illuminated CCD with enhanced soft X-ray response with respect to the MOS camperas and as with Chandra ACIS, when impacted by an X-ray photon it releases a number of electrons proportional to the incident photon energy. Strong electric fields in the detector prevent the electrons recombining with their silicon atoms and a voltage transfers them to readout nodes.

Observation modes permit full or partial frame imaging where respectively the whole CCD array is read out or only a specific chip is read out. Alternatively, higher time resolution can be achieved with EPIC-MOS or EPIC-pn by sacrificing a spatial dimension. However, given that we want both spatial dimensions for Jupiter, we used Full Frame imaging.

Chapter 2

The Impact of An ICME on Jupiter's X-ray Aurora

"You're asking me how a watch works, for now let's just keep an eye on the time. "

— Taylor Sheridan, *Sicario*

2.1 Abstract

Since the first in-situ observations in the 1970s, the nature of the relationship between Jupiter and the solar wind has been a topic of debate. Given that Jupiter's X-ray auroral hot spot is poleward of the UV main emission, its location is thought to map to regions beyond the middle magnetosphere and one might expect to observe changes in the auroral emissions with changes induced by the solar wind along this boundary. Systematically investigating the effect of changing solar wind parameters on the X-ray aurora is fundamental to examining what the interaction between Jupiter and the solar wind truly is. In this chapter, we begin this analysis with a case-study reporting the first Jupiter X-ray observations (PI: Branduardi-Raymont) planned to coincide with an Interplanetary Coronal Mass Ejection (ICME) arriving at the planet.

At the time when the ICME is predicted to arrive at Jupiter, we observe spatial, spectral and temporal changes in Jupiter's X-ray aurora, relative to an observation two days later, during less active solar wind conditions.

Bright emissions are triggered in regions normally void of X-rays and within 1.5 hours intense bursts of non-Io decametric radio emission are observed that are thought to be associated with ICME-driven compressions. We label this new emission region as the auroral enhancement region and treat analysis of it separately to the ever-present pulsating X-ray hot spot.

During the ICME arrival, the Northern hot spot, which may relate to cusp processes Bunce et al. (2004), expanded and exhibited periodic pulsations on two timescales: a 26-minute periodicity associated with precipitating sulphur ions and a 12-minute periodicity from a mixture of precipitating carbon/sulphur and oxygen ions. In the observation 2 days after the ICME, the dominant period was at a longer timescale of 42-minutes.

By comparing Vogt et al. (2011) Jovian mapping models with spectral analysis, we found that during ICME arrival at least two distinct ion populations, from Jupiter's dayside, produced the X-ray aurora. Aurorae mapping to magnetospheric field lines between 50-70R_J were dominated by emission from precipitating sulphur ions ($S^{7+,...,14+}$). Emissions mapping to more poleward closed field lines (70-120R_J) and to open field lines were generated by a mixture of precipitating oxygen ($O^{7+,8+}$) and sulphur/carbon ions, possibly implying some solar wind ion contribution.

We binned the X-ray events based on the timing of specific sub-solar longitudes ('noon times') and use these to identify how auroral developments relate to the evolution of the magnetosphere. Using the Vogt et al. (2011) model, we map the magnetospheric source and local time dependencies of the hot spot and auroral enhancement region. This indicates to what extent X-ray emission may be driven by the opening/closing of magnetic field lines, the location of the Sun relative to Jupiter's magnetosphere and the magnetosphere's auroral footprints.

We suggest that the best explanation for the X-ray hot spot is pulsed reconnection perturbing magnetospheric downward currents, as proposed by Bunce et al. (2004). The auroral enhancement region, outside of the hot spot, has different spectral, spatial and temporal characteristics to the hot

spot. By analysing these characteristics and the coincident radio emissions, we propose that the enhancement is driven directly by the ICME through Jovian magnetosphere compression, which may trigger radiation belt particles to scatter into the loss cone and/or a large-scale dayside reconnection event. However, we note that the unique characteristics of the auroral enhancement have not been observed before and so are less likely to be a typical/common behaviour for Jupiter and its X-ray aurora.

This results presented in this chapter have been published in the *Journal of Geophysical Research* with the citation Dunn, W. R., Branduardi-Raymont, G., Elsner, R. F., Vogt, M. F., Lamy, L. and Ford, P. G., Coates, A. J., Gladstone, G. R., Jackman, C. M., Nichols, J. D., Rae, I. J., Varsani, A., Kimura, T., Hansen, K. C., Jasinski, J. M., The impact of an ICME on the Jovian X-ray aurora. J. Geophys. Res. A Sp. Phys. 121, 2274-2307 (2016).

2.2 Introduction

2.2.1 The Impact of an ICME on Jupiter's Multi-waveband Aurora

While the impact of a southward-turning Interplanetary Magnetic Field and the pressure pulse induced by an Interplanetary Coronal Mass Ejection (ICME) on the Earth's aurora are known to produce auroral brightening (Elphinstone et al. 1996; Chua et al. 2001), the impact on Jupiter's larger, faster-rotating, internally mass-loaded magnetosphere remains a topic of debate.

Jupiter's auroral response to changes in solar wind pressure have begun to be catalogued in other wavebands (Barrow et al. 1986; Ladreiter and Leblanc 1989; Kaiser 1993; Prangé et al. 1993; Baron et al. 1996; Zarka 1998; Pryor et al. 2005; Nichols et al. 2007; Clarke et al. 2009; Nichols et al. 2009a; Hess et al. 2012, 2014) but X-ray emission is yet to be investigated in this manner. There have been few previous opportunities to connect X-ray observations of high-latitude precipitating ions with solar wind conditions. There has also been limited analysis of how the spatial morphology of X-ray features vary over time. In this research chapter, we analyse auroral spatial features, connect them with spectral features and compare their morphology and evolution over

time, in order to better understand how varying solar wind conditions might drive changes in the auroral X-ray emissions.

There are two key challenges associated with examining relationships between solar wind conditions and the Jovian aurora:
1. the timescales for the propagation of a solar wind-induced shock through the Jovian magnetosphere are not well-understood.
2. without in-situ measurements of the solar wind conditions close to Jupiter, we rely on propagation models to estimate the solar wind conditions upstream of Jupiter. The propagation of the solar wind beyond the inner heliosphere becomes increasingly complex, meaning that outside of certain limiting conditions (e.g: Jupiter in opposition) the uncertainty associated with propagation models can be of the order of days, making it difficult to precisely correlate solar activity with auroral intensification.

Another method for understanding varying solar wind conditions at Jupiter is to use emission signatures that have previously been associated with these events as a proxies. Gurnett et al. (2002) found that Jovian hectometric radio emission bursts (0.3-3MHz) coincided with maxima in solar wind density. Prangé et al. (2004) and Lamy et al. (2012) have used these enhancements in radio emission to trace the progress of ICME induced shocks through the solar system. Further, Echer et al. (2010); Hess et al. (2012, 2014) found that non-Io decametric radio emission bursts are correlated with periods of increased solar wind dynamic pressure and that their morphology could indicate compressions or expansions of the magnetosphere.

At the time of the observations reported here, there were no spacecraft directly upstream of Jupiter, so we utilised solar wind propagation models in order to try to identify the arrival time of an Interplanetary Coronal Mass Ejection (ICME). In order to try to validate the reliability of these solar wind propagations, we used radio emissions as a proxy for the arrival of this ICME.

Previously, it has been noted that brightening in X-ray emission may coincide with solar activity (Branduardi-Raymont et al. 2007a); however an extreme solar event such as an ICME was thought to provide the opportunity to better understand this connection. The two Chandra X-ray observations

reported here were organised by G. Branduardi-Raymont in order to begin to establish to what extent, if any, the solar wind drives Jupiter's X-ray aurora. The times of these observations were chosen to maximise the reliability of solar wind propagation models by observing when Jupiter was close to opposition, with the smallest possible Earth-Sun-Jupiter angle. Opposition occurred in October 2011, so a Chandra Target of Opportunity (TOO) proposal was submitted to observe Jupiter at the time when an ICME was predicted to arrive. In this chapter, we present the observed auroral changes at the time when propagation models and radio emissions suggest that an ICME arrived at Jupiter.

2.3 Tracking Solar Wind Conditions at Jupiter

2.3.1 Using the mSWiM Solar Wind Propagation Model

The 1.5-D MHD mSWiM model (http://mswim.engin.umich.edu/) (Zieger and Hansen 2008) was used to propagate measurements of solar wind parameters from 1 AU to Jupiter and to trigger the observations. Inspection of solar wind density, velocity and Interplanetary Magnetic Field (IMF) parameters (Figure 2.1) predicted the arrival of an ICME at Jupiter over the 2nd and 3rd of October 2011, Day of Year (DoY) 275-276 (figure 2.1). At this time, the Earth-Sun-Jupiter angle was $\sim$25° and Jupiter was $\sim$4.07AU from the Earth, so the propagation model offered a relatively low uncertainty of 10-15 hours and Jupiter was within the angular extent of the ICME (Robbrecht et al. 2009a,b). To account for this $\pm$ 10-15 hrs we smoothed the mSWiM propagations shown in Fig 2.1 over a 30 hour moving average.

For the mSWiM model, the most accurate parameter is solar wind velocity, followed by density and the tangential component of the magnetic field (B_T) (Zieger and Hansen 2008), which points toward the cross product of the solar rotation vector and the direction radially away from the Sun towards Jupiter. Inspecting the mSWiM model propagations of the solar wind reveals an increase in density (figure 2.1a) from 0.03 cm^{-3} on DoY 274.5 to a peak of 0.21 cm^{-3} on DoY 276.75. Density then decreases from this peak back

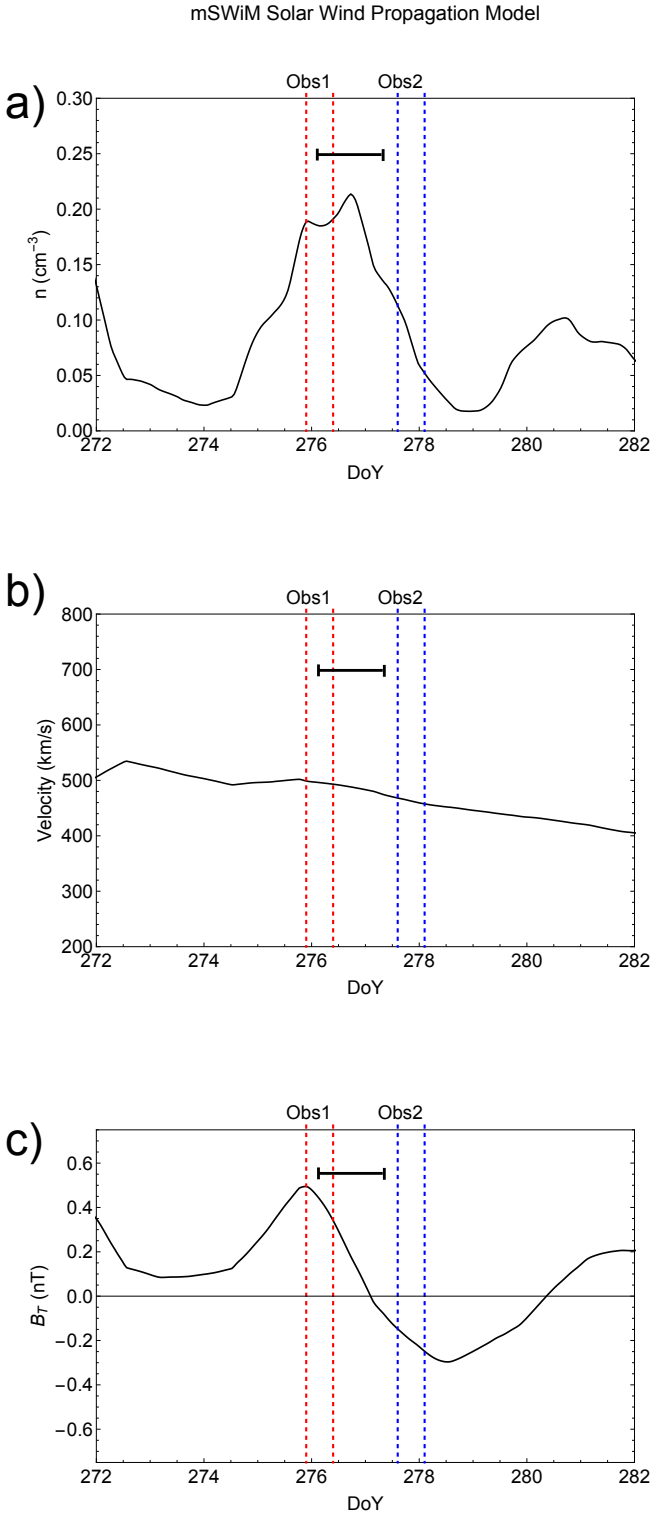

Figure 2.1: mSWiM propagation model (Zieger and Hansen 2008) at Jupiter on a given Day of Year in 2011. a) solar wind density, b) velocity and c) the B_T magnetic field component. Start/end times of the first and second Chandra X-ray observations are shown by dashed red and blue lines respectively. The ±10-15 hour uncertainty is indicated by the example error bar towards the top of each parameter plot.

to a minimum of 0.015 cm^{-3} on DoY 279.0. The median densities measured upstream of Jupiter by Pioneer 11, Voyager 1 and 2 were 0.13, 0.14 and 0.15 cm^{-3} respectively, so this solar wind density peak is a modest increase above previous values (Jackman and Arridge 2011). There is a modest increase in solar wind velocity during this time from 490 km/s on DoY 274.5 to 500 km/s on DoY 276.0 (figure2.1b), followed by a gradual decrease to 450 km/s by DoY 279.0. These solar wind velocities are similar to the median velocity upstream of Jupiter measured by Pioneer 11 (493 km/s), but represent an increase over the Voyager 1 and 2 median velocities (439 and 441 km/s respectively) (Jackman and Arridge 2011). The mSWiM predicted density and velocity are much closer to the mean from Pioneer 11, Voyager 1 and 2 upstream measurements (0.26, 0.23 and 0.25 cm^{-3} and 497, 446 and 448 km/s respectively), suggesting that the variations in solar wind conditions represent a rather modest ICME.

The B_T magnetic field plot suggests a rotation in the solar wind magnetic field, with the field oriented in the positive B_T direction from DoY 274.5 to 277 and a negative B_T direction from DoY 277 to 280, before returning to a positive orientation again (figure 2.1c). This variation in IMF along with the simultaneous increase in density and velocity, is consistent with an ICME with flux rope-like interior structure (Hanlon et al. 2004).

Looking at the time period prior to that in figure 2.1, the mSWiM model shows that a stronger ICME was incident at Jupiter from DoY 268 to 272 and the solar wind can be seen to be returning to non-ICME conditions from DoY 272.5. The predicted arrival of this preceding ICME is also accompanied by bursts of Jovian radio emission (Lamy et al. 2012). It is possible that this preceding ICME may also have driven changes in the Jovian magnetosphere, which are still observable in the X-ray observations reported here.

Lamy et al. (2012) conducted a series of multi-instrument, multi-planet radio observations during the same interval that the Chandra X-ray observations were conducted. Using ground-based observations, from the Nançay decameter array, and space-based observations, from WIND, STEREO A and B, Lamy et al. found that Jupiter displayed intensifications of auroral decametric to hectometric radio emissions close to 3 successive ICMEs, the second

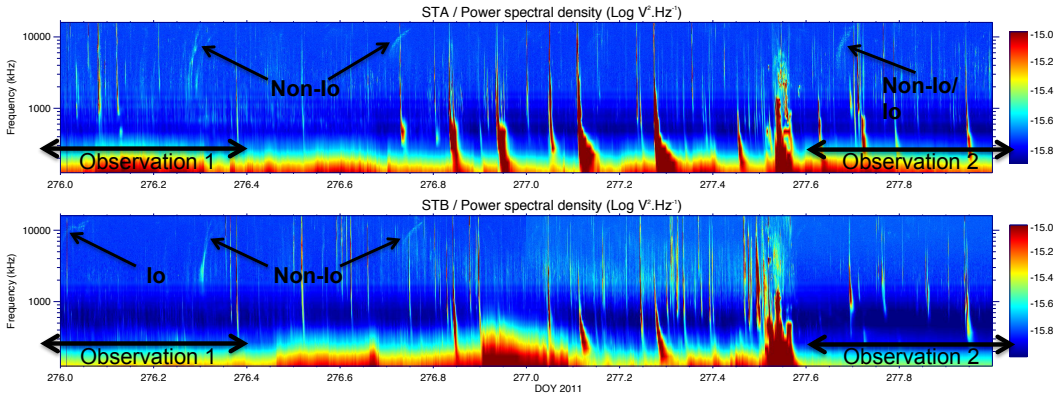

Figure 2.2: STEREO A (upper) and B (lower) Power Spectral Density plot of the radio emission, shifted for Jupiter-Earth light travel-time (UT-34 minutes). 'Non-Io' indicates bursts of non-Io decametric radio emission that suggest the arrival of a forward shock at Jupiter (Hess et al. 2012, 2014). 'Io' indicates Io decametric radio emission associated with activity from Io. The black horizontal arrows indicate the timings of the Chandra X-ray observations. The first non-Io decametric burst occurs 0.1 DoY before the end of the first Chandra observation, suggesting a forward shock arrived at Jupiter during the first X-ray observation. This plot was initially produced by L. Lamy with the minor adaptations by WD.

of which is investigated here. These enhancements driven by the solar wind activity were consistent with previous Galileo hectometric studies by (Gurnett et al. 2002) and also with decametric to hectometric observations from Galileo, Cassini and Nançay presented by (Hess et al. 2012, 2014).

2.3.2 Using Jovian Radio Emissions as a Proxy for Solar Wind Compressions

The radio observations obtained at the time of the Chandra observations (Figure 2.2) were shifted to account for light travel-time from Jupiter to Earth. Since non-Io decametric radio emission has been found to be correlated with solar wind pressure (Hess et al. 2012, 2014), investigating this radio emission helps to constrain the arrival time of the ICME-induced shock.

Non-Io decametric emission is arc-shaped in the time-frequency plane. The shape of the arc indicates which side of the magnetosphere it originates from. Vertex-early arcs indicate an emission source westward (Jovian dawn) of the observer (in the direction of Earth), while vertex late arcs suggest eastward (Jovian dusk) . Hess et al. (2012, 2014) showed that forward shocks (where increased solar wind pressure compresses the magnetosphere) are often followed

by emission from only one side of the magnetosphere. In contrast, reverse shocks (decreasing solar wind pressure and subsequent magnetospheric expansion) are often followed by emission from both sides of the magnetosphere (i.e: both vertex early and vertex late emissions would be observed). At DoY ∼276.3 and 276.7, STEREO A and B data showed two bursts of decametric emission with only vertex early morphology, which suggests incident solar wind forward shock/s. The first of these two bursts coincided with our first X-ray observation, occurring 2.5 hours (0.1DoY) before the end of the observation (see Figure 2.2). At ∼276.2 there is also a fainter burst of non-Io decametric emission.

Two additional radio bursts, which are less likely to be linked to solar wind compressions are also featured in the STEREO data:
1. a burst of Io-D decametric emission at DoY 276.0
2. an indistinguishable burst occurred one Io orbit (42 hours; 1.75 days) after the burst on DoY 276.0, at DoY 277.7, which may suggest Io is the source. However, it was only observed by STEREO B (where both spacecraft observed the other bursts) and was difficult to distinguish between Io and non-Io decametric emission.

If Io is not the source, then it may suggest that a magnetospheric disturbance has been maintained over 1 Jupiter rotation and that Jupiter‘s magnetosphere is therefore not completely quiet during the second observation. A corresponding auroral X-ray enhancement would go undetected for the burst on DoY 276.0 because the auroral footprints had not rotated into view at this time. It would also be very difficult to distinguish the burst on DoY 277.7, since the auroral footprint will have been on the limb of the Jovian disk at this time.

2.4 North Pole Projections

Using the technique applied in Gladstone et al. (2002), Elsner et al. (2005) and Branduardi-Raymont et al. (2008), time-tagged Chandra X-ray events were re-registered into Jupiter's System III (S3) spherical latitude-longitude

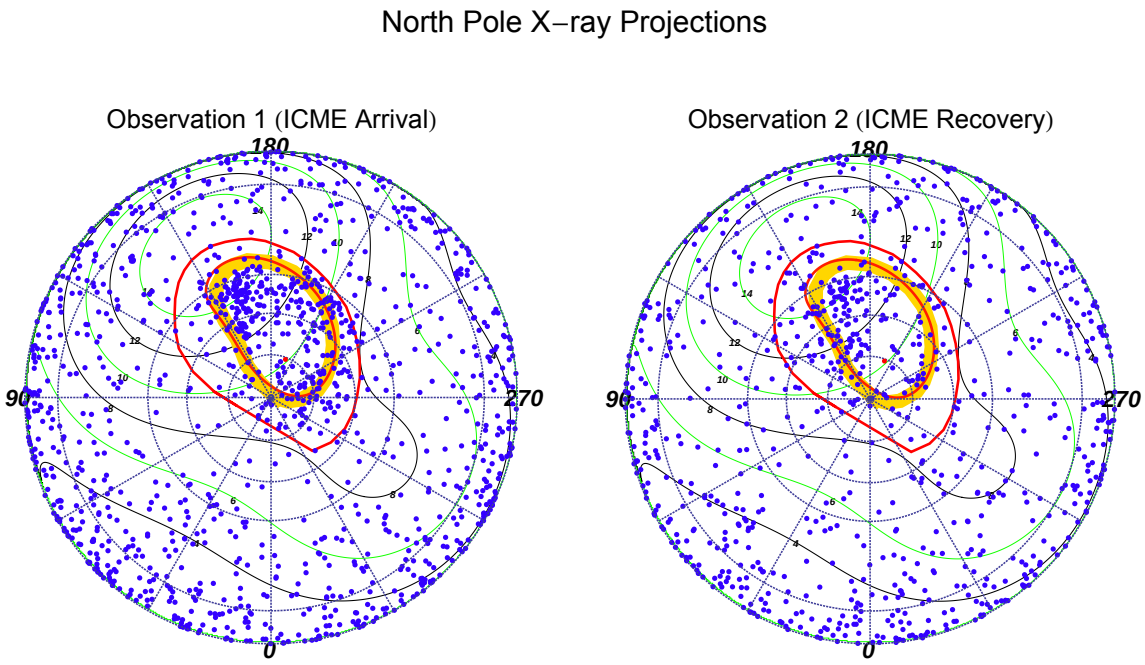

Figure 2.3: System III (S3) coordinate projections onto Jupiter's geographic North Pole (plot centre) for the first observation (left), during which the ICME arrived at Jupiter and the second observation (right), 1.2 days later. Lines of constant Jovian S3 longitude radiate outwards from the pole, increasing clockwise in increments of 30° from 0° at the bottom of the projection. Concentric dotted circles outwards from the pole represent lines of 80°, 70°, 60° and 30° latitude. The alternate green and black contours, indicate VIP4 model magnetic field strength in Gauss. The outer red oval is the Grodent et al. [2008] contour of Io's footprint (5.8R_J). The inner red contour is the footprint for the 30 R_J field line from Vogt et al. (2011) mapping using the Grodent et al. (2008) anomaly model. The thick orange contour is the average location of the UV main oval from two HST observation campaigns in 2007 (Nichols et al. 2009a). The projections show more X-ray events in the hot spot (160°-180° S3 longitude, 60°-70° latitude) during the first observation than the second. The events appear to spread from the hot spot into the region from 150°-160°. More clearly identifiable is the bright change in emission in the auroral enhancement quadrant (180°-270° S3 longitude, 55°-90° latitude). The distribution of this emission is not only enhanced in the main oval, but also poleward of this and at lower latitudes near Io's magnetic footprint.

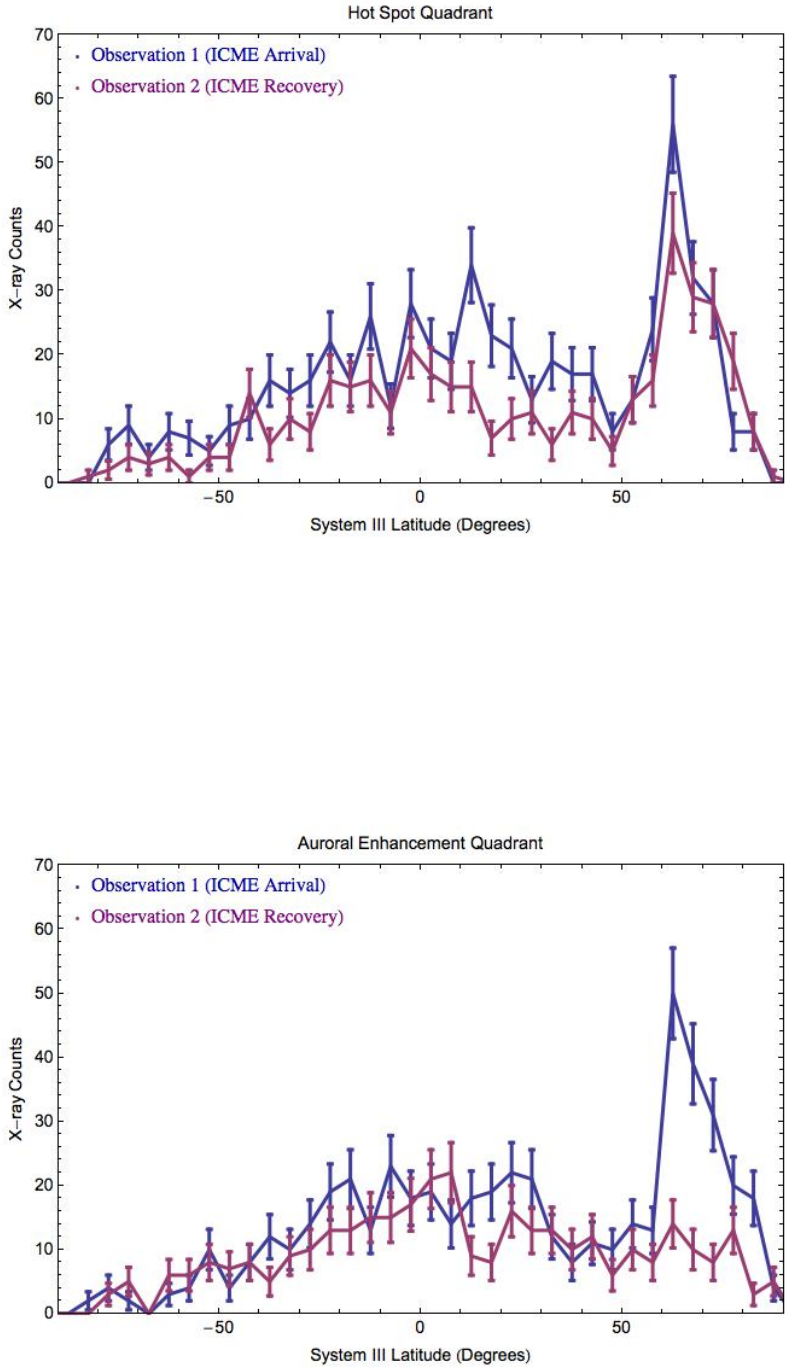

Figure 2.4: Number of events in 5° latitude bins during the first (blue) and second (red) observations. Upper plot: Hot Spot Quadrant with S3 longitudes 90° - 180°. Lower plot: Auroral Enhancement Quadrant with longitudes 180° - 270°. For the Auroral Enhancement Quadrant, emission above 60° latitude is up to 5 times brighter in the first observation than the second. Error bars are calculated from Poisson statistics. At the time of maximum visibility, each quadrant above 60° latitude had a projected area of $\sim$ 3% of the total observable Jovian disk.

coordinate system. These were then projected onto the poles to map the X-ray auroral distributions. A sky-projected disk of $1.01R_J$ was used for both observations. It should be noted that when re-registering to S3 coordinates, events emitted close to the limb of the Chandra-facing disk will have larger spatial uncertainties because of the increased obliquity of the planet's surface relative to the observer.

To identify the spatial distribution of auroral X-rays for the two observations, we present projections looking down onto the rotational North Pole of Jupiter. Figure 2.3 shows these projections for both observations. Figure 2.4 shows counts vs latitude plots to quantify the latitudinal concentrations of X-rays. During these observations the South Pole emission was obscured by the viewing geometry, so we focus on the North Pole projections.

We observed a range of differences in the spatial distribution of X-rays between the observations (figures 2.3 & 2.4). A surprising difference is a broad bright auroral enhancement in the first observation between 180°-270° longitude and above 60° latitude. The emission in this area is much dimmer in the second observation. This enhancement is significantly spatially separated from the hot spot (S3 Longitude: 160°-180°, Latitude 60°-70° (Gladstone et al. 2002; Elsner et al. 2005; Branduardi-Raymont et al. 2008)), where the brightest X-ray emission was previously observed. The region above 60° latitude and with longitudes 180°-270° features 201±14 X-ray counts in the first observation compared to 76±9 counts in the second.

Given the changing solar wind conditions throughout the observations and our lack of knowledge concerning the processes governing both the hot spot and this auroral enhancement region, we shall analyse the two separately. In this chapter, we refer to the 90°-180° longitude quadrant as the 'Hot Spot Quadrant' (HSQ) and to the quadrant between 180°-270° longitude as the 'Auroral Enhancement Quadrant' (AEQ). While there is potentially connected brightening across both quadrants, we note that the emissions between Io's footprint and the expected UV main oval location only occur in the auroral enhancement quadrant.

We look first at the HSQ. For both observations, the majority of the

auroral emission (above 60° latitude) occurs poleward of the 30R_J contour (the inner red oval on figure 2.3), indicating that the precipitating particles originate further from Jupiter than this. The whole region of the HSQ inside the 30R_J contour contains 113±11 counts in the first observation compared to 78±9 counts in the second. Previously (Gladstone et al. 2002; Elsner et al. 2005), the hot spot was defined as located between 160°-180° S3 longitude and 60°-70° latitude, where we find 52±7 counts in the first observation and 37±6 counts in the second observation. We find that the Hot Spot appears to spread out spatially in the first observation. The outer edge of the hot spot (at longitudes 150°-160° and latitudes 55°-60°) is where the greatest change occurs, with 55±7 X-ray counts in the first observation compared to 28±5 counts in the second. This changing emission occurs between the 30R_J contour and the hot spot, in the region where the poleward edge of the UV main oval was during the 2007 HST campaign (Nichols et al. 2009a). The second observation appears to have its events more concentrated into the spatially smaller region that was defined as the hot spot in previous publications. UV observations have shown that during solar wind compressions, the UV auroras brighten in the 'active region' close to this X-ray region (Grodent et al. 2003b; Nichols et al. 2007), where previous UV flares have been associated with X-rays(Elsner et al. 2005). It may also be of note that this region has previously been proposed as the cusp region (Bunce et al. 2004) and that the cusp is known to expand at Earth during magnetospheric compression. However, the location of Jupiter's cusp has not yet been confirmed. We note that, subsequent to this work, the 'expansion/contraction' of the hot spot was also reported in a longer observing campaign by Kimura et al. (2016).

For the Auroral Enhancement Quadrant, the first observation displays additional bright features with respect to the second. The difference is most evident in Figure 2.4, which shows the emission is up to a factor of 5 brighter across all latitude regions from 55°-85° during the first observation relative to the second. Additionally, Figure 2.4 shows that in the first observation the levels of emission observed in the AEQ are comparable to those in the same latitude range in the HSQ. Comparing the changes in counts for the HSQ and

AEQ could suggest that the HSQ is less sensitive to the ICME than the AEQ. Alternatively, it could suggest that the changes the ICME drives in the X-ray aurora develop with time or with varying solar wind parameters - as Jupiter rotates, the HSQ is visible first and the AEQ rotates into view slightly later (Figure 2.5). We also note that the location of the emissions equatorward of the main oval suggests origins in the inner magnetosphere, which would presumably require quite different drivers to those mapping beyond the main oval (and therefore beyond 30 R_J). Alternatively it may be that the compression changes the auroral mapping of regions.

One other aspect of note from the HSQ latitude-counts plot (Figure 2.4) is that there appears to be increased emission from the disk/equatorial region. This suggests the presence of increased solar X-ray flux, which is fluoresced and elastically scattered in the Jovian atmosphere. The occurrence of a solar flare at a time consistent with the increase is confirmed by inspection of GOES X-ray lightcurves (see 3.8 for further details). Analysis of the polar projections for discrete energy regimes (see 3.6 for further details) shows that the flare is not a significant contributing factor for the increased auroral emission, ensuring the validity of the changing auroral activity interpretation. We note that this Solar Flare is a distinct event from the ICME and directly introduces solar X-ray photons to the Jovian disk, where in contrast the ICME introduces a changing plasma population that may alter the magnetospheric dynamics and therefore the aurora.

2.5 Auroral X-ray Lightcurves

To generate the auroral X-ray lightcurves we extracted events above S3 latitudes of 60° in the polar projections (section 3) and placed them into 1-minute time bins, which were then smoothed with a 10-minute moving average. The lightcurves were shifted to account for Jupiter-Earth light travel time. During the first observation, the X-ray emission was brighter and more variable with multiple enhancements that contain twice as many counts as similar enhancements in the second observation. To distinguish between variation in emission

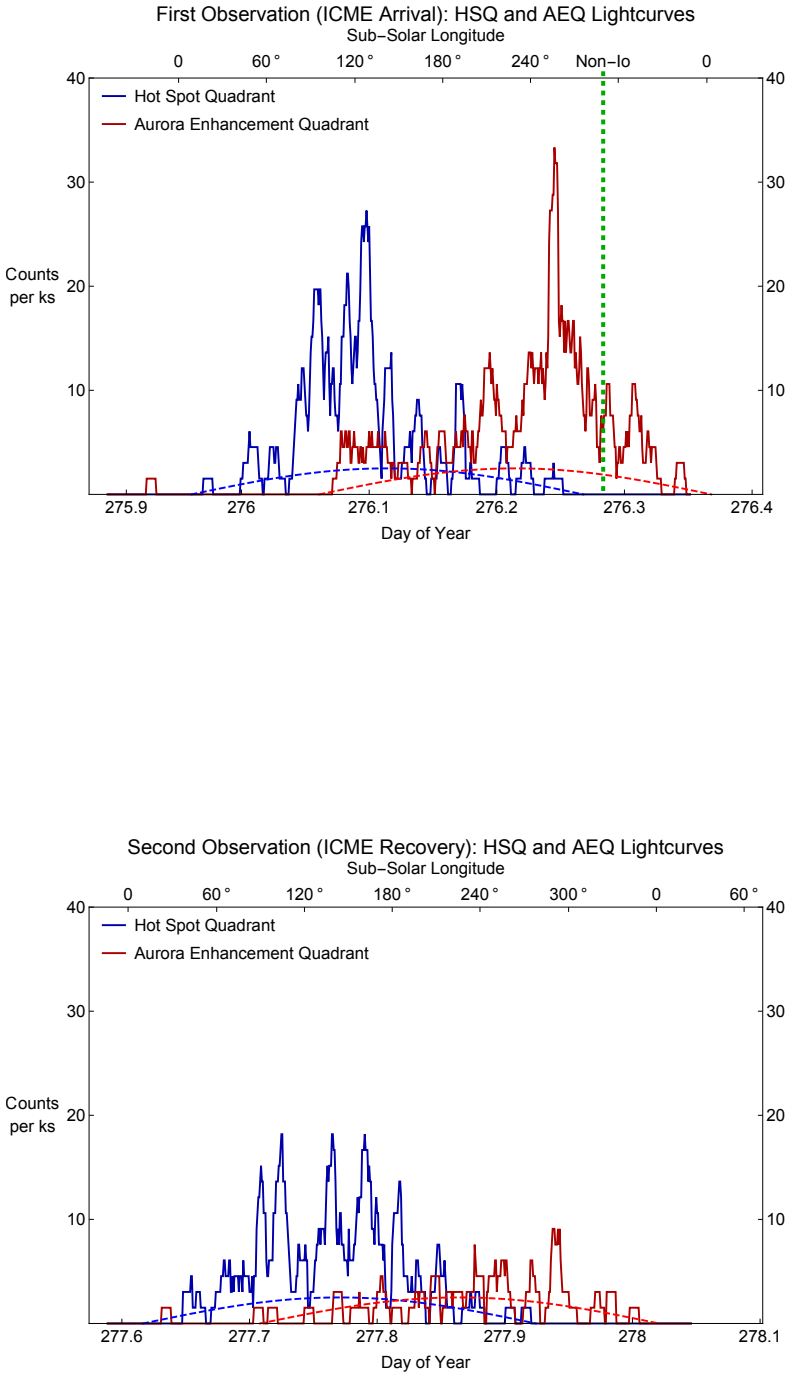

Figure 2.5: X-ray aurora lightcurves for the 1st (top) and 2nd (bottom) observation. Blue line: X-rays in the Hot Spot Quadrant (S3 longitude: 90-180°). Red line: X-rays in the Auroral Enhancement Quadrant (S3 longitude: 180-270°). The light curves were generated by placing events above 60° latitude in S3 coordinates into 1 minute bins and applying a 10 minute moving average smoothing. These were shifted to account for Jupiter-Earth light travel-time (UT - 34 minutes). The sub-solar longitude is indicated along the top of each plot. The green vertical dashed line indicates the onset of the brightest burst of non-Io decametric emission in the STEREO A data. The projected area of each quadrant (as a percentage of the total area of Jupiter) is indicated by the blue (HSQ) and red (AEQ) dashed lines. At the point of maximum visibility each quadrant above 60° latitude takes up $\sim 3\%$ of the observable Jovian disk.

from the HSQ and the AEQ, we produced separate lightcurves for each quadrant (figure 2.5). To help identify any local time dependencies we also indicate the sub-solar longitude (SSL).

Figure 2.5 shows that the first half of each observation was dominated by the hot spot. In the first observation, the hot spot became visible shortly before DoY 276.04 and 80° SSL and the counts increased by up to a factor of 6, from ∼4 counts/ks to peaks of 19-27 counts/ks. For the second observation, the hot spot appeared on the face before DoY 277.7 and the counts increased by up to a factor of 4.5, from 4 to 18 counts/ks.

The AEQ shows the most striking difference between the lightcurves. The second observation was generally quiet, with ∼3-5 counts/ks and a lone peak of 9 counts/ks at 277.93. In contrast, the first observation contained a prominent single peak of 33 counts/ks at DoY 276.24, which lasted 15-25 minutes and was higher than the peak emission from the hot spot. Prior to the peak, there was a gradual increase from DoY 276.2 to 276.22. After the peak there was an abrupt drop to 17 counts/ks and then a gradual decrease for 0.1 DoY afterwards, as the region rotated out of view. Throughout the whole first observation the AEQ was brighter, emitting 6 counts/ks, while in the second observation it emitted only 1-2 counts/ks.

The peak of the enhancement occurred 1-1.5 hours before the non-Io decametric radio burst at DoY ∼276.3 (indicated on figure 2.5 by the dashed line). We also note that the fainter burst of non-Io decametric emission at DoY 276.2 coincides well with the preceding peak on the AEQ auroral lightcurve, suggesting a further possible connection between X-ray emission and non-Io decametric emission. The previously recognised connections between non-Io decametric emission and forward shocks (Hess et al. 2012, 2014) suggests that the heightened X-ray emission is likely to be connected with the ICME.

We also detect periodicity in the raw timing data (i.e. non-smoothed) on the order of 10s of minutes for both observations, which is presented in section 2.7.

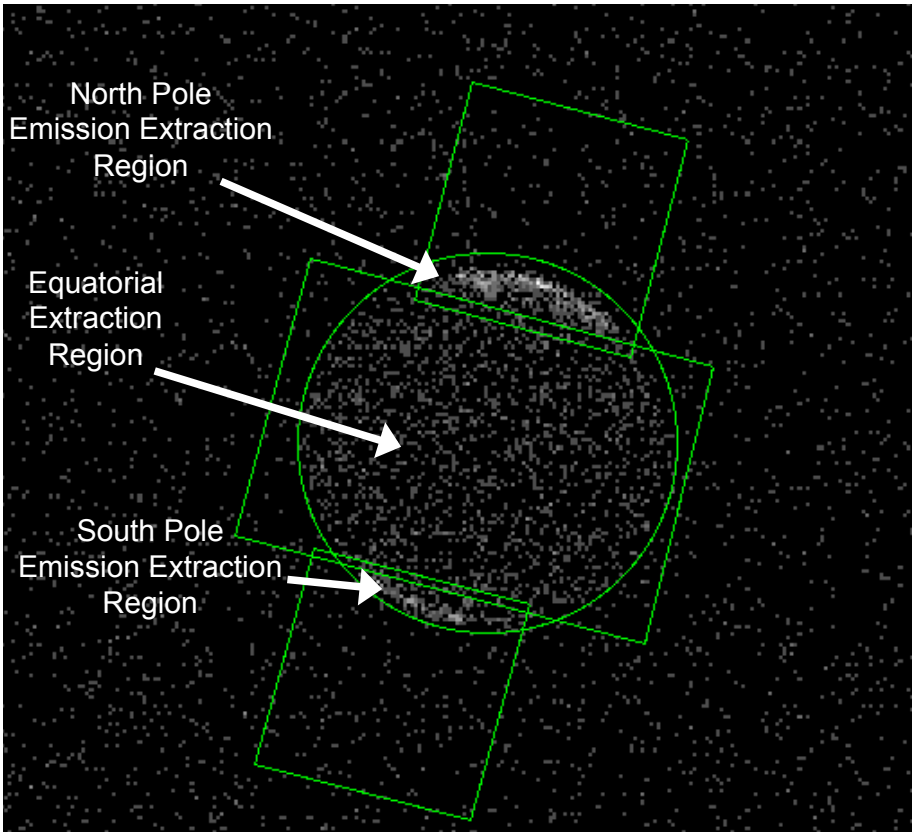

Figure 2.6: Regions used for spectra extraction. The northern aurora spectrum was extracted from the region of overlap between the top square and the circle. No emission outside of the combination of these two was included. The equatorial spectrum was extracted from the region of overlap between the middle rectangle and the circle. No emission outside of this overlap was included.

2.6 Auroral Spectra

2.6.1 Spectral Extraction and Modelling

For analysis of the Chandra spectra we divided Jupiter's observed disk emission into three sections: a Northern auroral zone, an equatorial region and a Southern auroral zone (see Fig. 2.6). Given the limited visibility of the Southern aurora, only the Northern aurora is presented here.

Using the CIAO software package (provided by the Chandra X-ray Center), we followed the standard procedures to extract spectra, which were then analysed using the XSPEC package (Arnaud 1996). We applied a correction to the effective area to account for the increased energy thresholds applied within ACIS to circumvent optical light leaks through the Optical Blocking Filters (see section 1.9.3). To do this, we corrected the response below 0.7 keV based

on fitting for the signal degradation to Supernova Remnant E0102-72.3. This provided a best fit curve of $f(x) = 1 - Y * (x - 0.7) * *2$ with $Y = 0.50$ and x = the energy of channel (this followed the degradation correcting algorithms produced by P. Ford).

We again treated the HSQ and AEQ separately. To do this, we separated each observation into two halves based on the time at which the emission from the hot spot dimmed (figure 2.5). The spectrum for the first (second) observation HSQ was produced at Jupiter from DoY 275.95 - 276.15 (277.6 - 277.8) UT, while the AEQ events occurred from DoY 276.15 - 276.35 (277.8 - 278) UT. The time intervals were selected to maximise exposure times of the given quadrant, while minimising contamination from the other. Figure 2.7 (left) compares the HSQ spectra, and figure 2.7 (right) those from the AEQ, for the two observations.

We fitted the spectra between 240-2000 eV, with a combination of lines with Full Width Half Maximum (FWHM) fixed at 20 eV. This produced two challenges. Firstly, the low count rates and large error bars produced unrealistically low reduced χ^2 values of 0.4-0.6 (for 105-111 degrees of freedom). Secondly, Chandra's spectral resolution and energy cutoff at $\sim$210 eV lead us to ignore the region from 210-250 eV, since the sharp drop in counts in this region inhibited good fitting. Table 2.1 and Figure 2.7 show the best fits.

2.6.2 Spectral Analysis

We first inspect the HSQ spectra (Figure 2.7a and 2.7b). Both observations featured a large peak between 250-350eV, which could be from sulphur and/or carbon ions.

Between 500-900 eV there were a range of oxygen lines. Both observations contained lines near 600 eV and between 700-730 eV, which are likely to be from OVII and possibly also OVIII transitions (e.g. Tables 1.2, 1.3, 1.4). The first observation showed an additional spectral line at $\sim$ 860 eV, which could have either been from O VIII transitions or evidence for solar X-ray scattering from the disk. While the best fit model contained only one line between 700-800 eV, at 730 eV, we were also able to obtain similar reduced χ^2 values by

1st Observation Hot Spot Quadrant – Reduced $\chi^2 \sim 0.45$ (105 Degrees of Freedom)

Best Fit Line, eV	Flux, Photons/cm^2/s	Known Ion Rest Frame Energies
310±10	5±1 x 10^{-4}	S VI-X (260-291;314;316 eV) or C V (299;304-308 eV)
595±20	1.5±0.5 x 10^{-5}	O VII (561;568;574 eV)
730±35	6.5±3 x 10^{-6}	O VII (698-713 eV) or O VIII (774 eV)
860±30	4.5±1.5 x 10^{-6}	O VIII (836 eV) or Solar Fe XVII (812;826 eV)
990±60	1.5±1 x 10^{-6}	Solar Ne X + Fe XXI (∼ 1000 eV)
1140±85	9±6 x 10^{-7}	Solar Ne X + Fe XXI (∼ 1000 eV)
1375±60	1±0.5 x 10^{-7}	Solar Mg XI (1350 eV)

2nd Observation Hot Spot Quadrant – Reduced $\chi^2 \sim 0.4$ (111 Degrees of Freedom)

Best Fit Line, eV	Flux, Photons/cm^2/s	Known Ion Rest Frame Energies
310±10	4.5±1 x 10^{-4}	S VI-X (260-291 eV) or C V (299;304-308 eV)
610±50	9±5 x 10^{-6}	O VII (561;568;574 eV) or O VIII (654 eV)
700±35	8.5±5.5 x 10^{-6}	O VII (698-713 eV)
925±25	4±1 x 10^{-6}	Solar Ne X + Fe XXI (∼ 1000 eV)

1st Observation Aurora Enhancement Quadrant – Reduced $\chi^2 \sim 0.6$ (109 Degrees of Freedom)

Best Fit Line, eV	Flux, Photons/cm^2/s	Known Ion Rest Frame Energies
305^{+10}_{-100}	3±2 x 10^{-4}	S VI-X (260-291 eV) or C V (299;304-308 eV)
390±60	4.5±3 x 10^{-5}	S IX- S XIV (336-348;380 eV) or C V-VI (354-378)
590±15	1.5±0.5 x 10^{-5}	O VII (561;568;574 eV)
775±20	7±2 x 10^{-6}	O VIII (774 eV)
915±65	1.5±2 x 10^{-6}	Solar Ne X + Fe XXI (∼ 1000 eV)

2nd Observation Aurora Enhancement Quadrant – Reduced $\chi^2 \sim 0.55$ (111 Degrees of Freedom)

Best Fit Line, eV	Flux, Photons/cm^2/s	Known Ion Rest Frame Energies
310±10	2±1 x 10^{-4}	S VI-X (260-291 eV) or C V (299;304-308 eV)
645±40	7±2.5 x 10^{-6}	O VII (665 eV) or O VIII (654 eV;698-713 eV)
875±60	2±1 x 10^{-6}	O VIII (836 eV) or Fe XXI + Ne X (∼1000 eV)
1095±65	1±0.5 x 10^{-6}	Solar Ne X + Fe XXI (∼1000 eV)

Table 2.1: Best fit parameters for the 0.24–2 keV spectra and closest known ion rest frame lines (Elsner et al. 2005; Kharchenko et al. 2008; Branduardi-Raymont et al. 2007a) Line half widths were held constant at 20 eV.

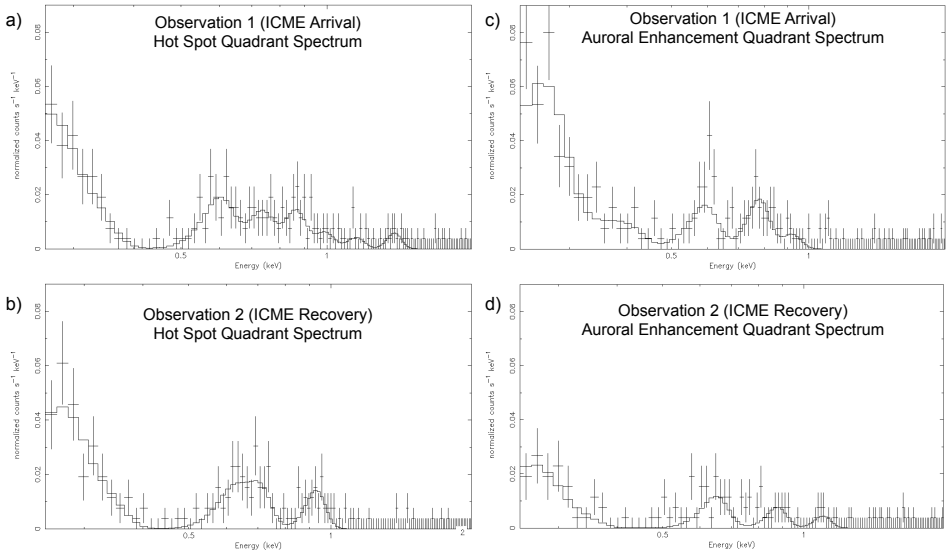

Figure 2.7: The Northern Auroral Zone spectra for the first (upper) and second observation (lower). The Hot Spot Quadrant spectra are on the left (a,b), while the Auroral Enhancement Quadrant are on the right (c,d). The data have been fitted with a combination of lines with half widths fixed at 20 eV.

fitting two lines at $\sim$ 700 eV (OVII) and $\sim$ 780 eV (OVIII), which may suggest the additional line at 860 eV was also an OVIII transition.

A solar X-ray flare reached Jupiter during the time covered by this spectrum (see 3.8) and may have imprinted solar lines onto the spectrum. The additional emission above 700 eV could have been from Fe XVII, Fe XXI or Ne X solar photons or a combination of solar photons and local oxygen. We also observed a Magnesium (Mg XI) line in the spectra near 1350 eV, which would be expected from a solar flare (Branduardi-Raymont et al. 2007b; Bhardwaj et al. 2005, 2006). However, we note that Haggerty et al. (2017), using Juno's high energy particle detector JEDI, detect transient precipitation of $\sim$MeV/amu magnesium. The X-ray detection of this may therefore verify that this is an auroral emission and may hint at varying driver processes or source populations for the Jovian aurora. These solar features are much less prominent in the AEQ and throughout the second observation.

For the AEQ, the difference between the spectra of the two observations is clear (Figure 2.7c and 2.7d). The first shows a prominent peak between 200-300eV that appears to be 3-4 times higher for the first observation than the second. We were unable to model this accurately because of the low

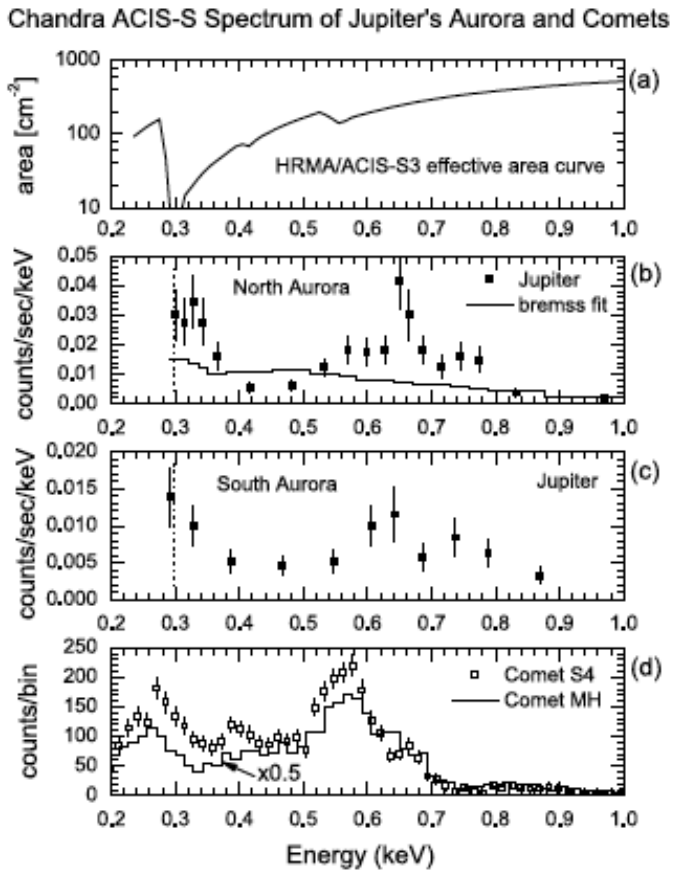

Figure 2.8: Figure from Elsner et al. (2005): (a) ACIS-S effective area versus energy in keV, including the effects of contamination on the optical blocking filter at the time of the observations. (b) and (c) Jovian auroral X-ray spectra between 300 eV and 1 keV of the north auroral region and the south auroral region for the first ACIS-S observation. The vertical dotted line at 0.3 keV shows the low-energy cutoff for the Jovian spectra. Each spectral point represents 10 measured events. The solid line in Figure 3b shows the best-fit thermal bremsstrahlung model to the measured northern auroral spectrum. This result demonstrates that bremsstrahlung in particular, and probably any reasonable continuum model alone, cannot account for the observed spectrum. The lower global count as well as number of events of the south auroral zone compared to the north are clearly visible. (d) Chandra ACIS-S spectrums of comets Linear S4 [S4] and McNaught-Hartley [MH]; note that the spectrum for comet MH is plotted after scaling by a factor of 0.5. Two noticeable features present in Jovian spectra but absent (or very much weaker) in the cometary spectra are located at around 0.65 keV and 0.75 keV.

energy cut-off and low spectral resolution, meaning that comparing fluxes and differentiating between sulphur and carbon was not possible. Between 300-500 eV there are additional transitions of carbon or sulphur which don't appear in the AEQ spectra or in the HSQ spectrum for the second observation.

The morphology of the AEQ spectrum between 380-700 eV is particularly interesting. The emission between 550-600 eV is mostly O VII and the line appeared to be asymmetric, with a sharp decline after 600 eV, which led the fit to underestimate the flux for this line in table 2.1. This steady increase followed by an abrupt decline may be expected because there are 3 prominent O VII lines between 561 - 574 eV (the He-like resonance, inter-combination and forbidden transitions). This region of the spectrum is similar to that of comets Linear S4 and McNaught-Hartley displayed by Elsner et al. (2005) and included here as figure 2.8. This similarity to cometary solar wind charge exchange spectra between 380-700 eV could suggest a solar wind origin for some of the precipitating ions.

The 775 eV line appeared to be a good match for the OVIII transition. GOES data (section 3.8) shows that the heightened solar X-ray flux from the first half of the observation was returning to normal at these times, so it is unlikely that solar photons caused the 700-900 eV morphology in this spectrum.

For the AEQ in the second observation, the spectrum is best fitted by a set of low flux sulphur/carbon and oxygen lines. Some of this emission may be contamination from the HSQ, which was still partially visible during these times.

2.7 Connecting Spatial and Spectral Features

In order to try to identify the precipitating ion species (i.e. carbon vs sulphur) in spite of the spectral resolution limitations of Chandra ACIS, we plotted the polar projected auroral emissions for different energy bands. By combining this with magnetic field mapping, we tried to establish the magnetospheric or solar wind origins for specific ion species. To do this, we binned X-rays

into four broad energy bins for: carbon/sulphur; oxygen; solar X-ray lines and Hard X-rays. We then plotted the polar projections for each energy range separately. The specific energy ranges were chosen based on a) the ease with which regions could be differentiated in the spectrum; b) the relevant spectral lines for different species (Elsner et al. 2005); c) Chandra's energy resolution limitations, d) by considering the solar X-ray lines from the equatorial region spectrum.

We considered the carbon or sulphur emission to be between ∼200-500eV. We included photons below 300eV because they were emitted almost exclusively from the auroral zone, with very little disk component (figure 2.10). The oxygen emission was defined by the band ∼500-800eV from spectral fitting of strong OVII and OVIII lines (Branduardi-Raymont et al. 2004, 2007a; Elsner et al. 2005). We considered the ∼800-1500eV emission to be from fluoresced or scattered solar photons because (as demonstrated by Bhardwaj et al. (2005, 2006); Branduardi-Raymont et al. (2007b) and figure 2.9) this energy range contains the peak of the disk spectrum. It should be noted that some O VIII lines from completely stripped oxygen (Elsner et al. 2005) also fall in this energy range and may contribute some of the observed auroral emission. Finally, we consider 1500-5000eV emission to be hard X-rays from precipitating electrons generating bremsstrahlung radiation (Branduardi-Raymont et al. 2007a, 2008).

Looking first to the polar projections of 200-500eV carbon/sulphur X-ray events (figure2.10a) we find that for both observations almost all emission originated in the aurora, with very little equatorial emission. This confirms that the changing emission in this part of the spectra was unrelated to solar flares. We find that carbon/sulphur is the source of the brightening on the edge of the hot spot, between 150°-160° S3 Longitude (see section 3 in this chapter). This emission lies in a region which during the 2007 HST observations (Nichols et al. 2009a) featured the poleward edge of the UV main oval, although we note that the main oval is known to shift in latitude.

In the AEQ, for the first observation we find a large number of carbon/sulphur events between the Io footprint (∼5.8R_J) and both the UV main

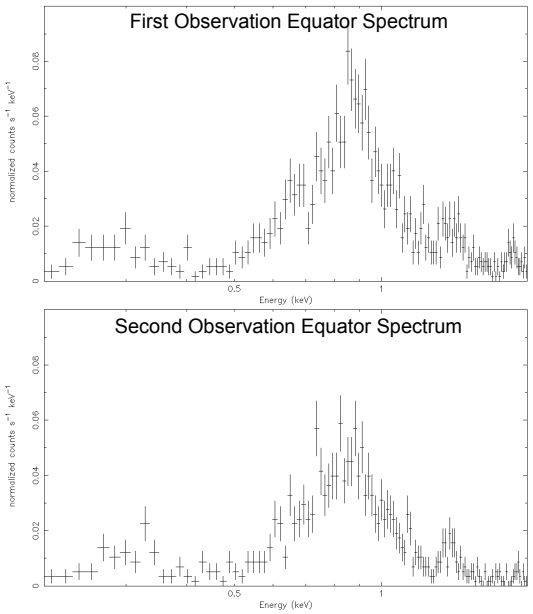

Figure 2.9: Spectra from Jupiter's Equator for the first (upper) and second (lower) observations. The brightening of the spectrum in the first observation from the solar flare is clearly identifiable.

oval and 30R_J contour. For the AEQ, we also find ion emission poleward of the 30R_J contour. This is unexpected, since previous observations showed that the majority of ion emission originated in the hot spot quadrant. Emission from carbon/sulphur in the AEQ is largely absent from the second observation.

For the 500-800eV oxygen emission (Figure 2.10b), events are also concentrated into the auroral zone. In the first observation, the events occur poleward of the 30R_J contour and the main oval reference contour in both the HSQ and AEQ, while in the second observation the auroral events are almost solely concentrated into the hot spot. Comparing the oxygen with the carbon/sulphur emission, we find that where there is some carbon/sulphur emission closer to the polar edge of the 30R_J contour, the oxygen emission generally originates poleward of this carbon/sulphur dominated emission region and appears to be more diffusely distributed across the entire polar region.

Figure 2.10c shows the 800-1500eV emission, dominated by solar photons, distributed across the disk and not concentrated into the aurora, as expected. The hard X-rays (figure 2.10d) cluster in two regions in parallel with the 30R_J contour in the first observation and are less prevalent in the second.

Figure 2.11 shows carbon/sulphur and oxygen latitude-count plots: the

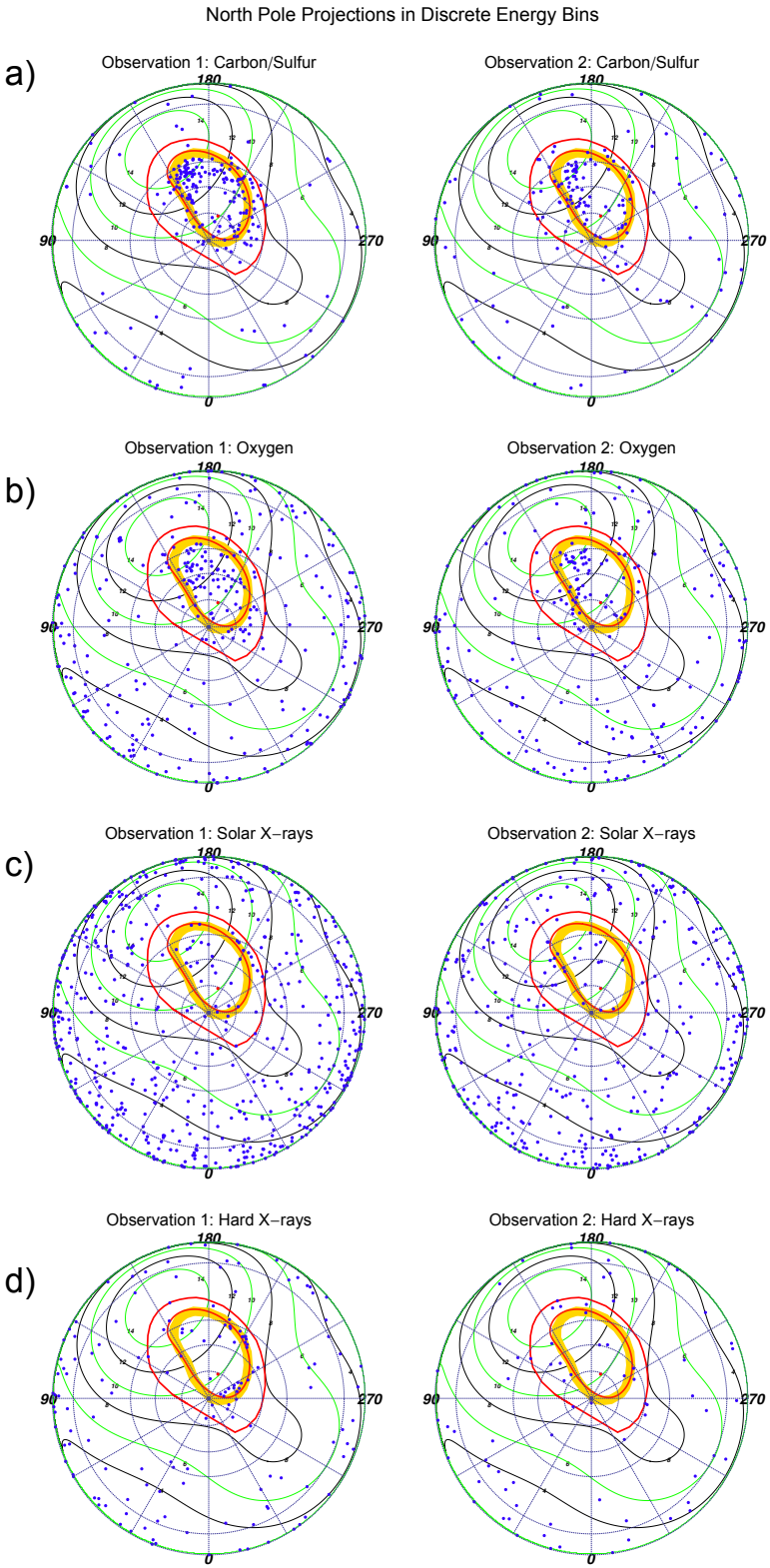

Figure 2.10: Comparisons of North Pole S3 projections for discrete energy ranges for the first (left) and second (right) observations. From top to bottom the energy ranges are: a) 200-500eV (carbon/sulphur ion lines), b) 500-800eV (oxygen ion lines), c) 800-1500eV (Dominated by fluoresced and scattered solar photons), d) 1500-5000eV (Hard X-ray bremsstrahlung radiation from electrons). For further plot details see figure 2.3.

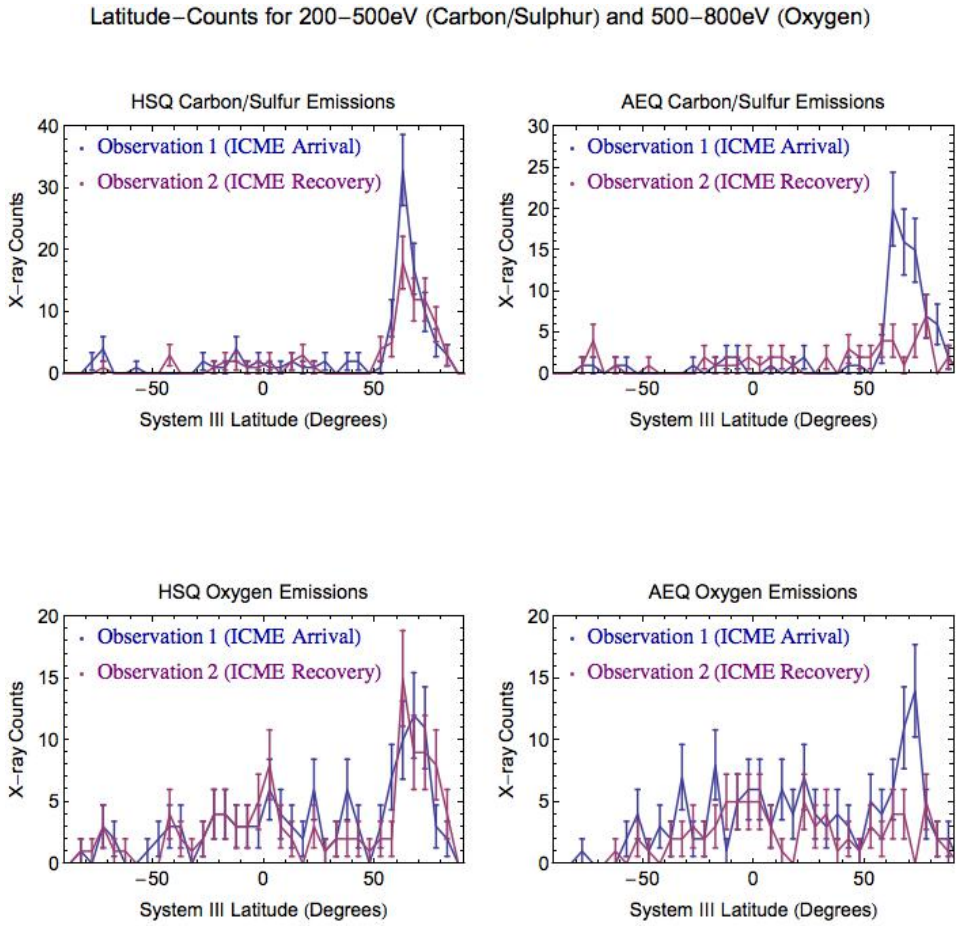

Figure 2.11: Latitude-counts plots for 5° latitude bins. Comparisons of the 200-500eV carbon/sulphur emission (upper 2 plots) or 500-800eV oxygen emission (lower 2 plots) between the first observation (blue line) and second observation (red line). The Hot Spot Quadrant (left) and Auroral Enhancement Quadrant (right) are treated separately. At the time of maximum visibility, each quadrant had a projected area of $\sim 3\%$ of the total observable Jovian disk.

change between observations in carbon/sulphur emission is similar in both quadrants, while oxygen emission stays almost constant in the HSQ, but changes by a factor of 3 in the AEQ. This differing behaviour and mapping for carbon/sulphur emission and oxygen emission may suggest different sources for each.

2.8 Timing Variation and Periodicity

Following the lead of Gladstone et al. (2002) and Elsner et al. (2005), we searched the observations for periodicities by selecting a circle in S3 coordinates centred on the hot spot (Radius: 6.5°, Centre: 67° latitude, 170° longitude - see Figure 2.12) and then fourier transformed this lightcurve to generate power spectral density (PSD) plots. We found that the area used by Gladstone et al. (2002) and Elsner et al. (2005) showed periodicity at two significant timescales during our first observation, at 12 and 26 minutes. The significance of the PSD peaks increased by expanding the circle to a radius of 8°, centred on 65° latitude and 163° S3 longitude. This larger region included more of the broad spatial spread of hot spot emission in the first observation, showing that the period was also present in the emission between the hot spot and 50 R_J contour. For the second observation, we found that the most statistically significant period occurred using the same S3 circle as Gladstone et al. (2002) and Elsner et al. (2005). The periodicities were apparent when the PSD was generated for all X-rays above 60° latitude in the quadrant, but the periods became more significant when the region selected was honed onto the hot spot.

To estimate the single-frequency probability of chance occurrence (PCO) for the detected periods, we used the statistical methods of Leahy et al [1983]. The results are shown as dotted horizontal lines on figures 2.13a, 2.13b, 2.13c and 2.13d. The lowest statistical significance and therefore highest PCO of 10^{-1} is at the bottom of the plot and the highest statistical significance and therefore lowest PCO of 10^{-6} is towards the top of the plot.

For the first observation, we found two strong periods (figure 2.13a). The

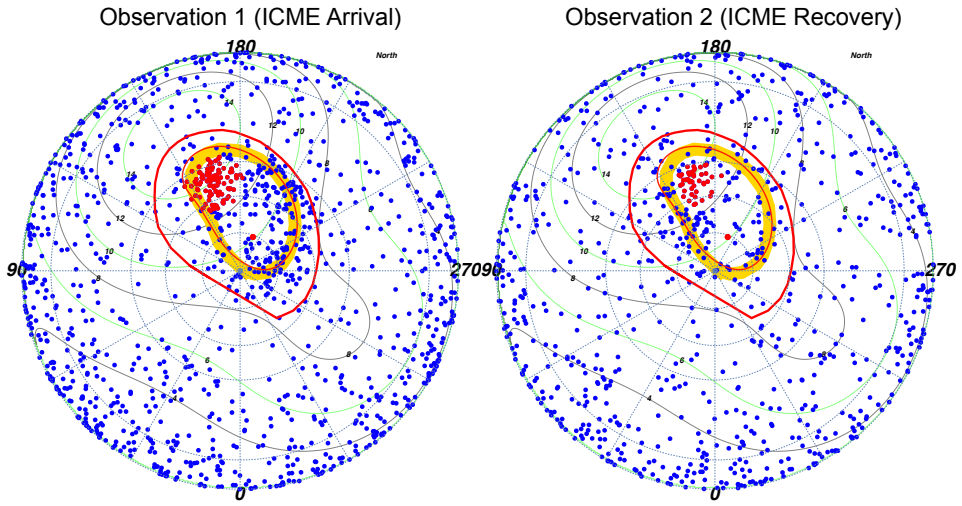

Figure 2.12: Polar projections indicating the events (red) which were used to generate the PSDs for the hot spot.

most prominent period occurred with a timescale of 26 minutes and a PCO of less than 10^{-6}. This is shorter and more significant than the Gladstone et al. [2002] period (∼45 min, 4 x 10^{-6}). The second period had a timescale of 12 minutes and a PCO of 10^{-5}. We tested a range of locations and sizes of regions encompassing the hot spot and found that these two periods dominated, although which of the peaks was most dominant did swap. The 26 minute peak was more dominant on the edge of the hot spot, where the carbon/sulphur particles were more concentrated than oxygen. The 12 minute period was more dominant above 70° latitude where the carbon/sulphur and oxygen is more evenly distributed.

Periodicities in the second observation were weaker than in the first (figure 2.13b). The most prominent period was at 42 minutes, with a PCO of 5 x 10^{-4}, not as significant as the period in the first observation or that reported by Gladstone et al. (2002). There was also indication of a shorter period of 19 minutes, but this was even lower in significance.

To determine whether one period was associated with one particle population, we used the same 8° radius region centred on 65° latitude and 163° S3 longitude and generated PSDs for discrete energy ranges. Figure 2.13c shows a prominent 26 minute period at high significance for the carbon/sulphur ions, with a PCO of 10^{-5}. It also shows a much weaker 12 minute period with a

PCO of 2 x 10^{-3}. Conversely, the oxygen emission (figure 2.13d) exhibited no 26 minute period and the strongest period was at 12 minutes with a PCO of 5 x 10^{-3}. This suggests that one dominant sulphur/carbon population produced the 26 minute period, while a second combined population of sulphur/carbon and oxygen generated the 12 minute period. For the second observation, the number of X-ray events was too low to provide reliable results when separating the carbon/sulphur and oxygen populations.

The two periods in the first observation could have been due to harmonics, although in this case it is challenging to explain how the period is divided between the two separate particle populations in this manner. This division by energy also suggests that they are unlikely to be from instrumental effects.

We also tested regions across the rest of the auroral zone and disk and found no other significant periods (see Figure 2.14). We sampled a range of smaller regions across the AEQ from low to high latitude and at varying longitudes and were still unable to detect a significant period in this region. Logistically, the periodicity may exist, but the paucity of events in any given region makes it difficult to detect. It also may be that the prolonged brightening of the auroral enhancement complicates this by 'washing-out' any period.

The paucity of hard X-rays from precipitating electrons also made it difficult to identify a significant period for them, although there is a suggestion of possible periodicity on 5-10 minute timescales with a PCO of 10^{-4}-10^{-3}.

2.9 Local Time Variation in the Hot Spot Morphology

The configuration of Jupiter's magnetosphere will evolve throughout the observations. As Jupiter rotates, a specific S3 longitude-latitude auroral position will map to changing magnetospheric local time sources. To identify how this rotation, and the associated change in local time, changes the X-ray aurora and to identify possible magnetospheric local time origins for features, we mapped the magnetosphere footprint configuration at distinct sub-solar longitudes (SSL). The SSL indicates which Jovian S3 longitude is directly facing the Sun at a given time - the location of noon.

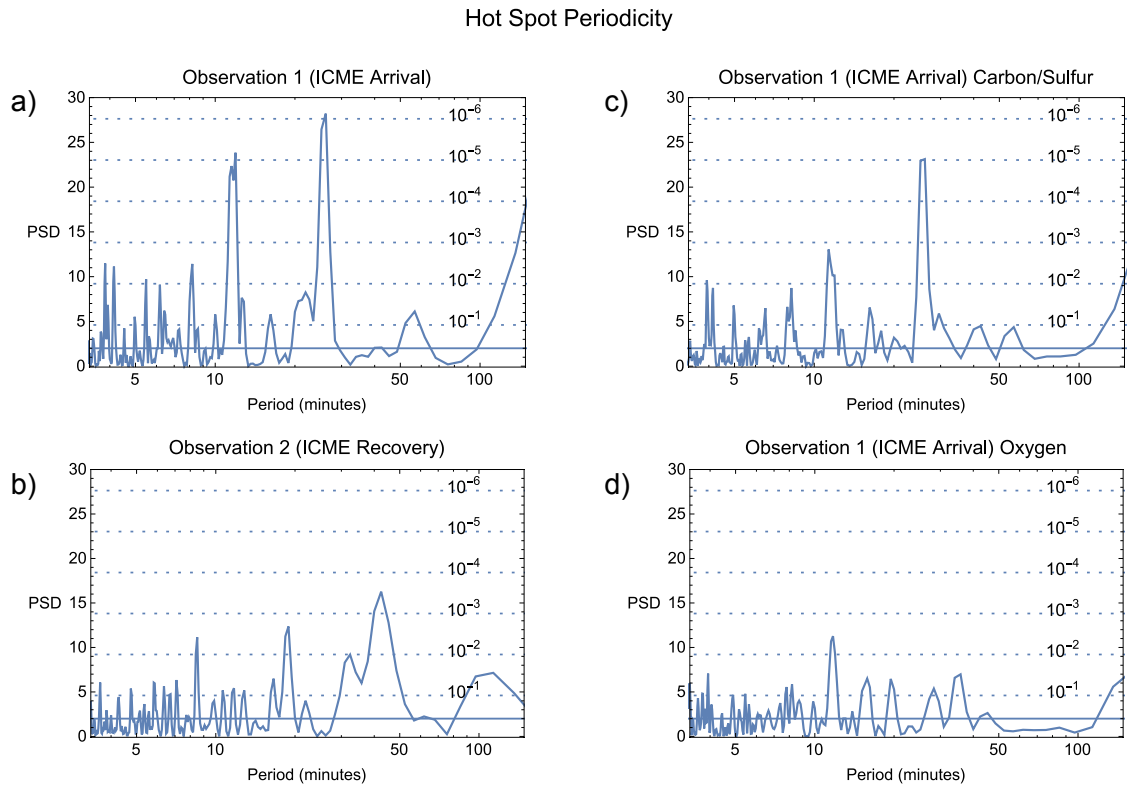

Figure 2.13: Power spectral density (PSD) plots showing periodicity in the hot spot: a) Observation 1 (ICME Arrival), b) Observation 2 (ICME Recovery), c) Observation 1 sulphur/carbon (200-500 eV) photons, d) Observation 1 oxygen (500-800 eV) photons. During the first observation two periods were detected at 12 and 26 minutes. The 26 minute peak was more significant than previously reported (e.g. Gladstone et al. (2002)). The second observation contains a less distinctive periodicity, with the most prominent period at 42 minutes. The hot spot region was found to be much broader during the first observation, so a different region was used for each PSD to maximise the significance of the periods and to utilise as much emission from the expanded hot spot as possible (see text for details). Carbon/sulphur emissions are dominated by the 26 minute period and also feature a less significant 12 minute period. The oxygen emissions feature no 26 minute, but do feature the less significant 12 minute period. When the two populations are combined the 12 minute period becomes much more significant. The dotted horizontal lines show single-frequency probabilities of chance occurrence (PCO) for the detected periods [Leahy et al. 1983]. The lowest statistical significance and therefore highest PCO of 10^{-1} is at the bottom of the plot and the highest statistical significance and therefore lowest PCO of 10^{-6} is towards the top of the plot.

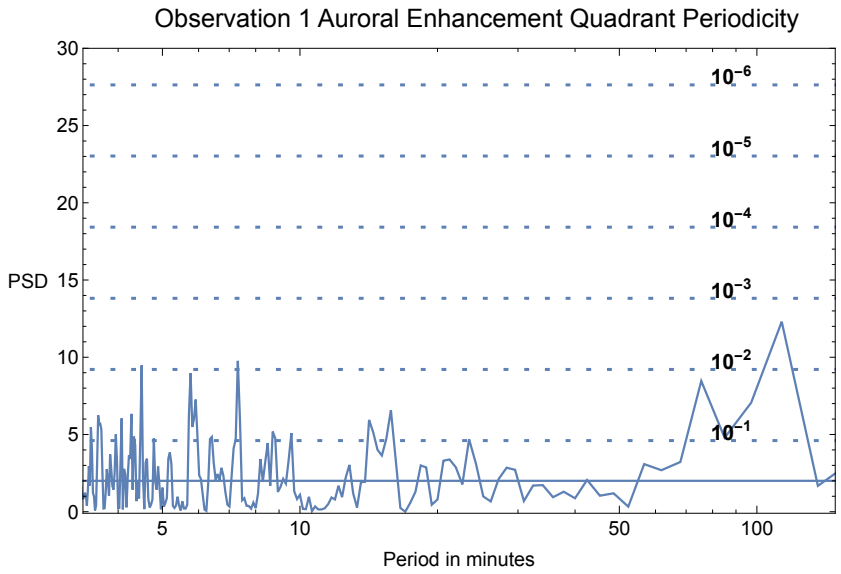

Figure 2.14: PSD generated from the events in the Auroral Enhancement Quadrant (Latitude: Above 60° Longitude: 180°-270°). No significant period is present.

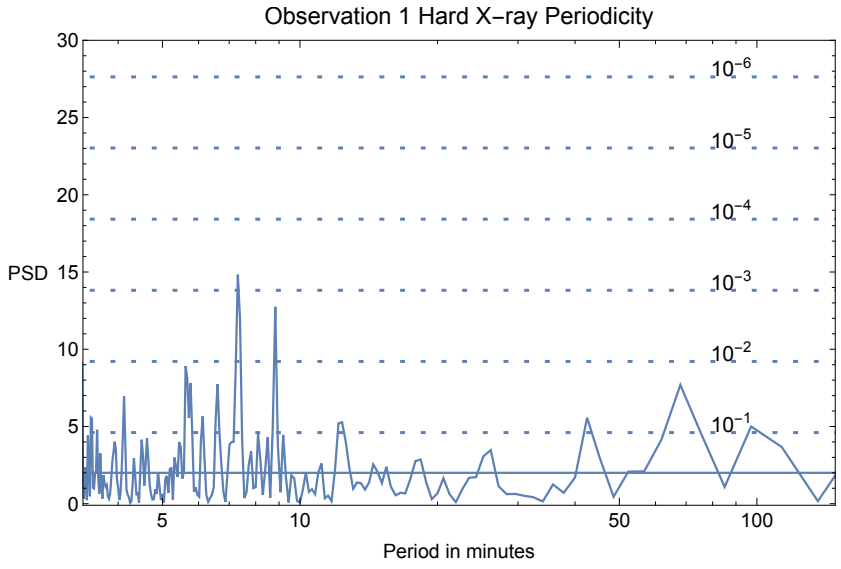

Figure 2.15: PSD generated from the hard X-ray events in the Auroral Enhancement Quadrant (Latitude: Above 60° Longitude: 180°-270°). There are hints at a 5-10 minute period.

To do this, we sub-divided each 11 hour observation into 50-minute time bins. For each time bin, we compared the S3 coordinates of auroral spatial and spectral features with their mapped source regions using the Jovian magnetosphere-ionosphere model mapping from Vogt et al. (2011, 2015).

This maps contours of constant radial distance from the magnetic equator to the ionosphere by ensuring that magnetic flux at the equator equals magnetic flux in the ionosphere. This enabled us to map ionospheric footprints to their equatorial magnetospheric origins up to 150 R_J from the planet, where the VIP4 model (Connerney et al. 1998) used for previous Jupiter X-ray observations was limited to 30 R_J (Gladstone et al. 2002; Elsner et al. 2005; Branduardi-Raymont et al. 2008). The Vogt model accounts for the bend-back of Jupiter's field lines, in order to identify their magnetospheric local time origins. For example, this would inform us that a specific ionospheric coordinate maps to a specific equatorial magnetospheric source (e.g. 50 R_J) and a specific magnetospheric local time (e.g. dawn).

Using NASA JPL Horizons ephemerides data, we chose the start and end times of 50 minute X-ray bins to coincide with 30° increments of SSL. X-rays emitted at times when the SSL was 15° - 45° were compared to the Vogt et al. (2011) mapping model at SSL 30° to identify the sources for these X-rays, and so on for each 30° SSL increment.

Joy et al. (2002) showed that the magnetopause location of Jupiter is bimodal. During periods of low solar wind dynamic pressure, the nose of the magnetopause standoff is expected to reach $\sim 92 R_J$ (an expanded magnetosphere), whilst for the high dynamic pressure periods, it will be as close as $\sim 63 R_J$ (a compressed magnetosphere). Vogt et al. (2011) account for these two different possible magnetopause standoff distances by moving the magnetopause location based on the measured distances of Joy et al. (2002).

The plotted projections in figures 2.16 – 2.18 show the expanded magnetosphere mapping of Vogt et al. (2011). The magnetopause is indicated by a thick purple contour. Jupiter's closed magnetic field lines map to latitudes equatorward of the magnetopause mapping. Towards noon (at the nose of the magnetopause), these closed field lines are shown as contours from 15 R_J (red

contour) to 95 R_J (green contour), in increments of 5 R_J. For the compressed magnetosphere (figure 2.19) closed field line contours at the nose of the magnetosphere extend only as far as 65 R_J (yellow contour). In the Jovian tail we mapped closed field contours up to 150 R_J. X-ray emission that maps to closed contours is likely to be produced by precipitating particles on closed field lines originating in Jupiter's magnetosphere. X-ray emission that maps poleward of the magnetopause, to the region absent of contours, is from precipitating particles that are more likely to be on open field lines.

Since Jupiter was close to opposition, the SSL and sub-observer longitude were only $\sim 6^\circ$ separated, so that the noon position on the planet was close to the centre of the observed disk. This means that counts originating near the limb of the Chandra-facing disk are easily identifiable on the time-binned projections and their larger uncertainties can be accounted for in the context of the magnetic footprint at that moment. Both the observation data and the mapping process contribute uncertainties.

Chandra's PSF of $\sim$ 0.5" in combination with a Jovian disk size of $\sim$40" means that X-ray photons emitted close to the centre of the observable disk have a positional uncertainty of the order of a few degrees in latitude and longitude. Closer to the edge of the disk, the obliquity of Jupiter leads this positional uncertainty to increase to $\sim$10s of degrees. Alongside these errors in the X-ray photon locations there are also errors in the mapping. Vogt et al. (2015) is dedicated to identifying and quantifying these mapping uncertainties, which they describe as occurring through a) the time averaged use of in-situ data, which will smooth out differing mapping for different solar wind conditions or for different mass-loading rates and b) through differences in the internal field model used. Differences in the internal field model leads to typical System III uncertainties in the footprint location of the order of a few degrees in latitude-longitude location (see Vogt et al. 2015), but can lead to positional uncertainties of up to 8 degrees in extreme cases. In support of the that we report here the active region, associated with X-ray and UV flares is generally found to have a similar mapping independent of models (Vogt et al. 2015). Further, Kimura et al. (2016) use the VIPAL model to map the

precipitating particle origins while in this chapter we use the Grodent Anomaly Model, but the results from both studies generally agree.

Analysing the SSL-binned polar projections with Vogt mapping revealed previously unreported relationships. Firstly, for both the expanded and compressed magnetospheres we find emission that mapped to the open field lines and also emission that mapped to the magnetosphere, suggesting that both may be sources for Jovian auroral X-rays. For the expanded model (figures 2.17 and 2.18) the majority of the emission originated on the magnetosphere side of the magnetopause, while for the compressed model (figure 2.19) the majority of emission originated on open field lines.

This may be particularly noteworthy for the ICME arrival observation. During this observation a compression may be expected to shift the magnetopause boundary from $\sim$92R$_J$ to $\sim$63R$_J$ (Joy et al. 2002). It is this region mapping to 60-90 R$_J$, across which the magnetopause would be compressed, which contained the hot spot expansion during the first observation and where we observed increased X-ray emission. The closeness of the emission to the magnetopause, our spatial uncertainties and our uncertainty in the choice of expanded or compressed magnetosphere inhibited us from precisely quantifying the relative importance of a solar wind vs a magnetospheric origin. The Vogt et al. (2011) models showed, however, that the majority of X-ray producing ions originate beyond 60 R$_J$.

Figures 2.17 and 2.18 also show, and particularly for the first observation, that emission clusters along the open-closed field line boundary and seems to move with SSL, suggesting a local time dependence and relationship with processes in this region. The emission seems to follow the nose of the magnetopause (noon) and the afternoon sector.

2.9.1 Noon-Binned Hot Spot Projections

For our observations, we considered the Hot Spot to be above 60° latitude and between S3 longitudes 150°-180°. We found for both observations that the hot spot had a strong local time dependence and emitted 78 of 100 X-rays (first observation) and 51 of 74 X-rays (second observation) around noon in

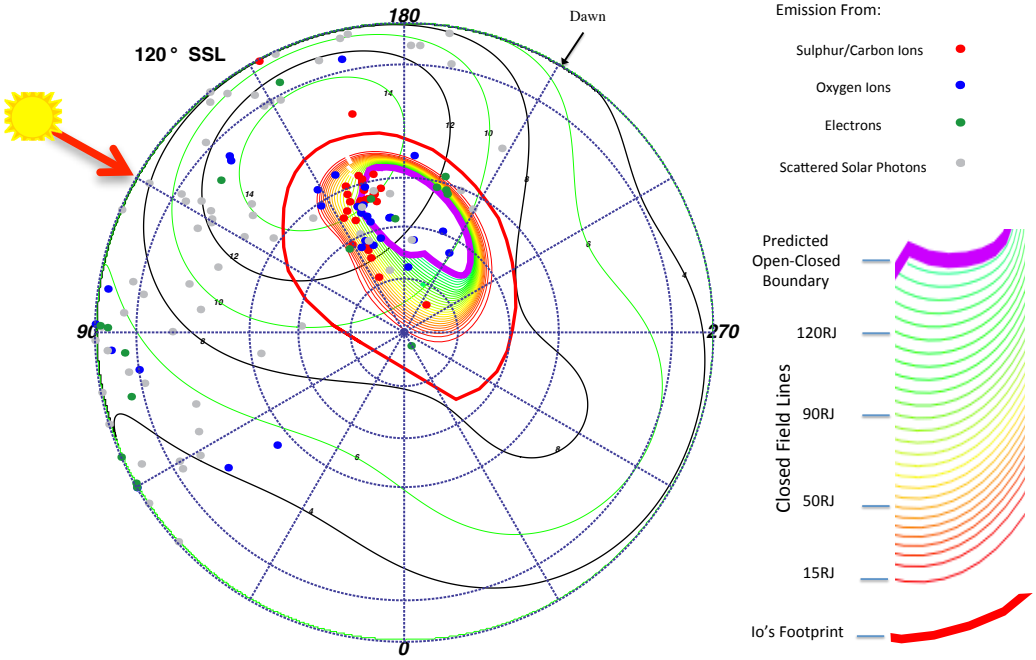

Figure 2.16: S3 Polar Projections showing X-ray emission coinciding with specific sub-solar longitudes (SSL). Each plot shows emission that occurred at times when the SSL was ±15° from the SSL stated (120° in this case). The Sun's direction (noon) lies along the red arrow, with dawn 90° clockwise from this and dusk 90° anti-clockwise. A Vogt et al. (2011) mapping using a Grodent Anomaly Model (Grodent et al. 2008), assuming an expanded magnetosphere, is plotted onto this polar projection. The plot shows closed field lines increasing in increments of 5R_J from the 15 R_J contour (red), through 50-80 R_J contours (yellow), to the last closed contour at the nose of an expanded magnetosphere 90 R_J (inner green contour). Green contours map to 95 - 150 R_J. The thick purple contour indicates the predicted open-closed field line boundary. Regions poleward of this and absent of contours indicate regions mapping to open field lines. Events occurring close to the noon position have uncertainties in their spatial position of ∼5° latitude-longitude, while those occurring closer to dawn or dusk originate on the limb and have uncertainties of ∼10°-20° latitude-longitude. Emission is colour coded: carbon/sulfur photons (red), oxygen photons (blue), solar X-rays photons (grey), Hard X-rays from electrons (green). carbon/sulfur emission can be found mostly on contours mapping to 50-90 R_J and also clustered in the open field line region. Oxygen emission is mostly on contours of 70-120 R_J and in open field line regions. The Hard X-rays from electrons can be found clustered on the dawn edge of the projection.

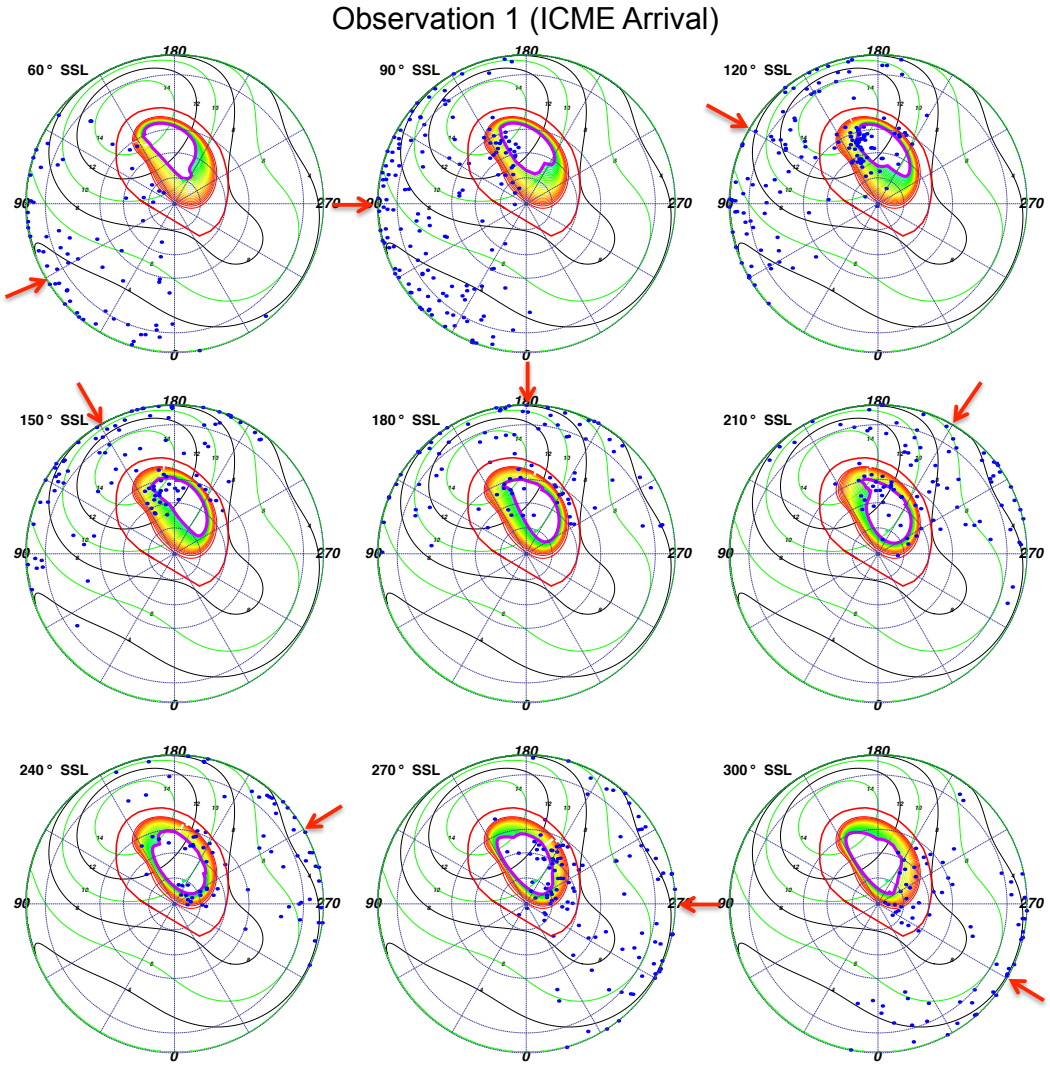

Figure 2.17: S3 Polar Projections of the first observation, binned based on sub-solar longitude (SSL). Vogt et al. (2011) expanded magnetosphere models are plotted onto the polar projections. Throughout the observation, emission appears to exhibit a local time dependence and following noon local time. The time-bins at 270° and 300° SSL show the auroral enhancement event. Each dot is an X-ray photon. For further plot details see figure 2.16.

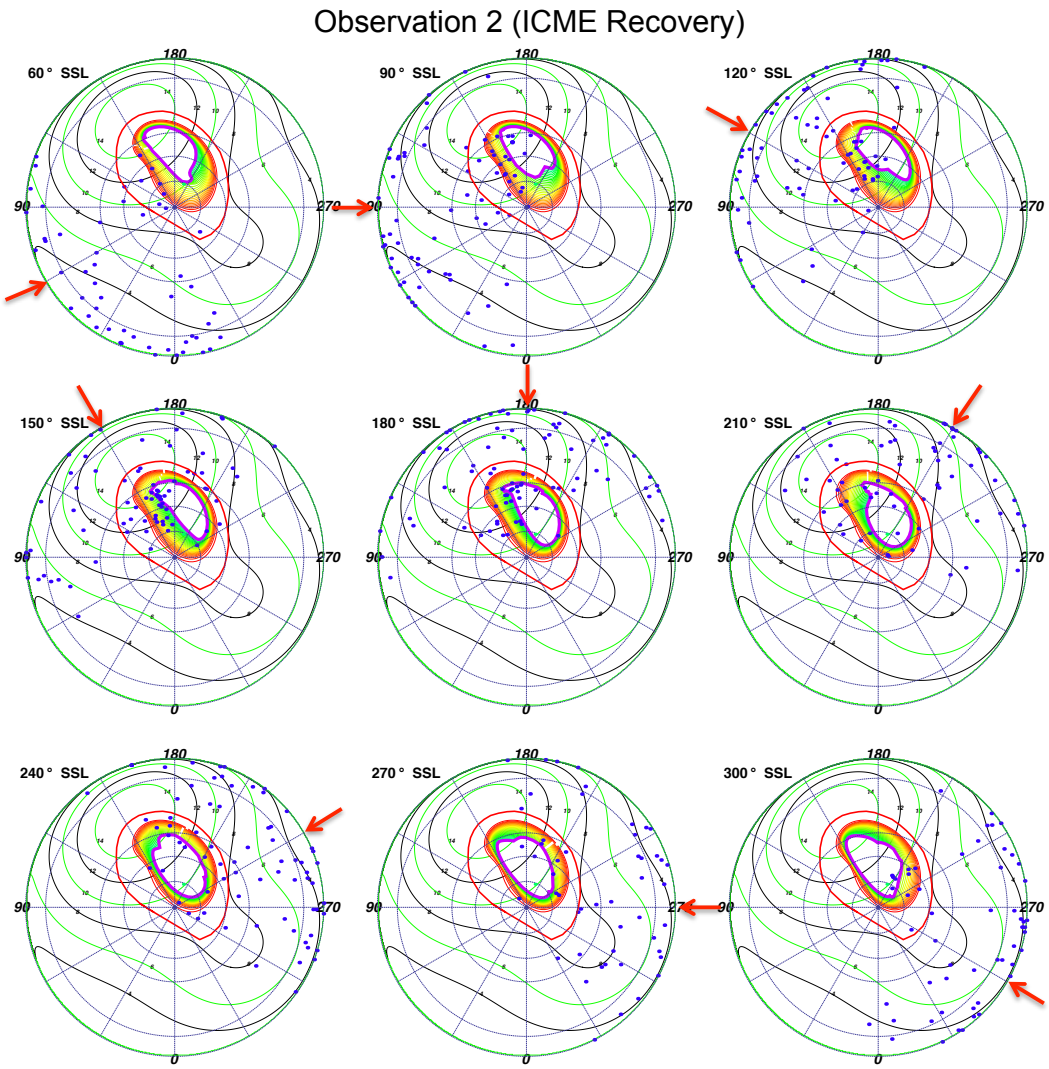

Figure 2.18: S3 Polar Projections of the second observation, binned based on sub-solar longitude (SSL), with Vogt et al. (2011) expanded magnetosphere models. Each dot is an X-ray photon. For further plot details see figure 2.16.

the region (165° SSL). After this time, the Hot Spot became dimmer, despite the region remaining observable on the Jovian disk for several hours after this. Analysing the footprints of the magnetic field leading up to 165° SSL (figure 2.20), we found that the majority of the hot spot emission originated on the day-side of Jupiter, with magnetospheric local times (MLT) between 10:30 and 18:00. Later in the observation, when the field lines that mapped to MLTs after 18:00 were still observable in the hot spot, we found significantly less emission from the region.

Having found that the Hot Spot emission occurred predominantly in the projections 90°-150° SSL (figure 2.17 and 2.18) (prior to mapping to MLTs of 18:00), we analysed these more closely. For the 90° SSL projection, the Hot Spot was close to the limb of the disk, so there was a large uncertainty of 10°-20° in the X-ray coordinates. Based on this, we focused our attention on projections of 120° and 150° SSL (figures 2.19 and 2.20), where the uncertainty was closer to 5° latitude-longitude.

Considering the first observation 120° SSL projection (figure 2.19 and 2.20), in the region of 150°-170° longitude and 55°-80° latitude, carbon or sulfur (red) emission and oxygen (blue) emission occurred along the field line contours. For the compressed magnetosphere, both carbon/sulfur and oxygen ions originated along the open edge of the open-closed field line boundary, while for the expanded magnetosphere the carbon/sulfur ions originated on closed field lines mapping to the outer magnetosphere. Accounting for spatial uncertainties, the carbon/sulfur events originated between 50-90 R_J (yellow-green contours) and on open field lines, while the oxygen ions originated poleward of this between 70-120 R_J (green contours) and also on open field lines. The emission was weaker in the second observation for this SSL projection (figure 2.20).

For the 150° SSL projection, both observations (figure 2.20) contained clustering of X-rays between 160-170° S3 longitude and 60-70° latitude from the afternoon-dusk flank of the magnetosphere (Vogt et al. 2011). Given that the time-binning is broad (50 minutes) across 30° SSL, it is uncertain whether these field lines were open or closed for most of this X-ray emission. Consid-

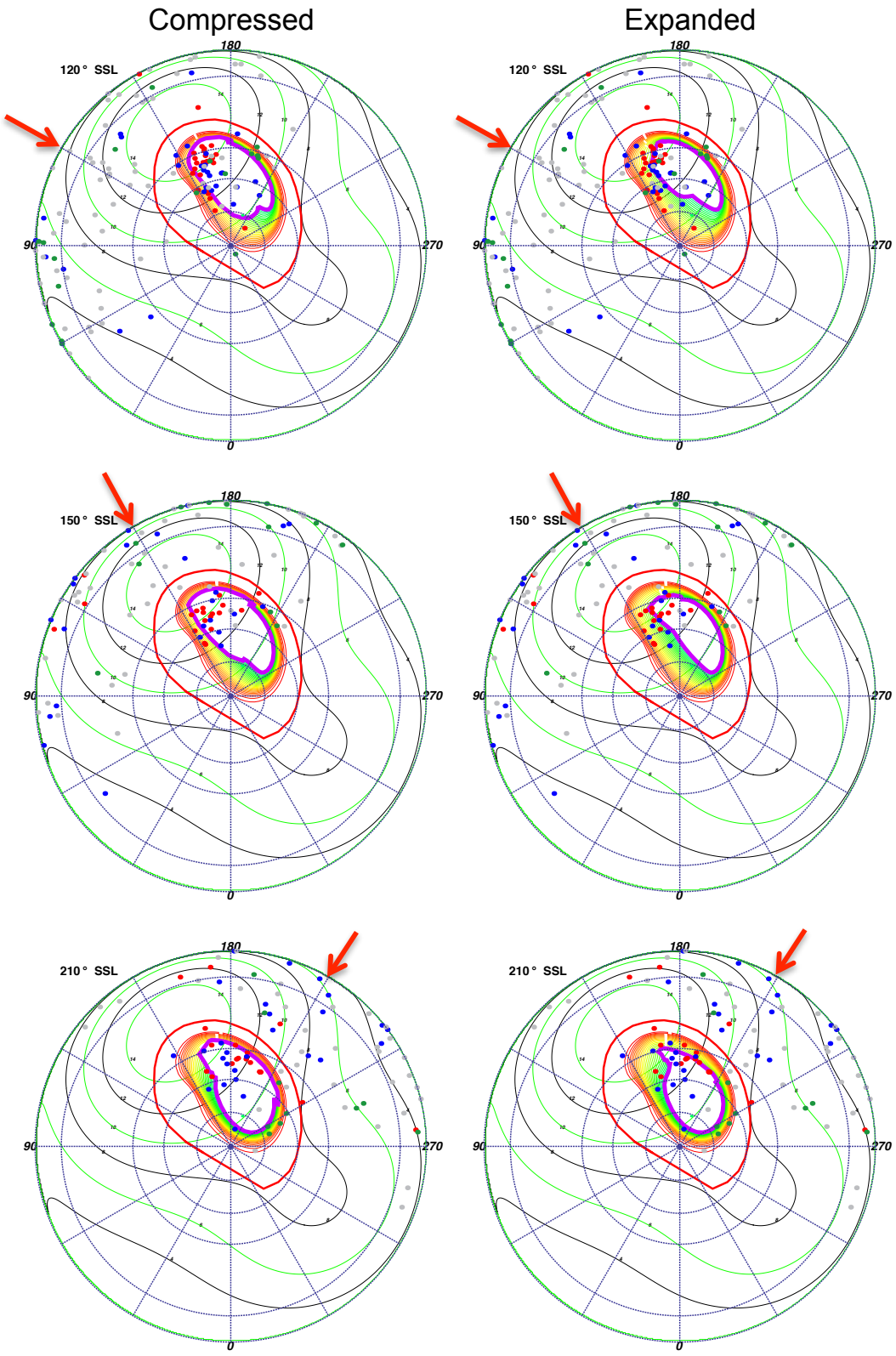

Figure 2.19: Sub-solar Longitude (SSL) binned polar projections comparing compressed (left) and expanded (right) magnetosphere models for the hot spot during the first observation. Projections for SSL of 120° (upper), 150°(middle) and 210° (lower) are shown. The models use Joy et al. (2002) measurements of the magnetopause distance. The compressed model uses a noon magnetopause at $63R_J$, while the expanded model, assumes a noon mangetopause at $92R_J$. The field lines increase in increments of $5R_J$ from the outer contour of $15R_J$ (red), to the final closed inner contour of 65 (yellow - left plots) or 95 (green-right plots). For colour coding and plot details see figure 2.16.

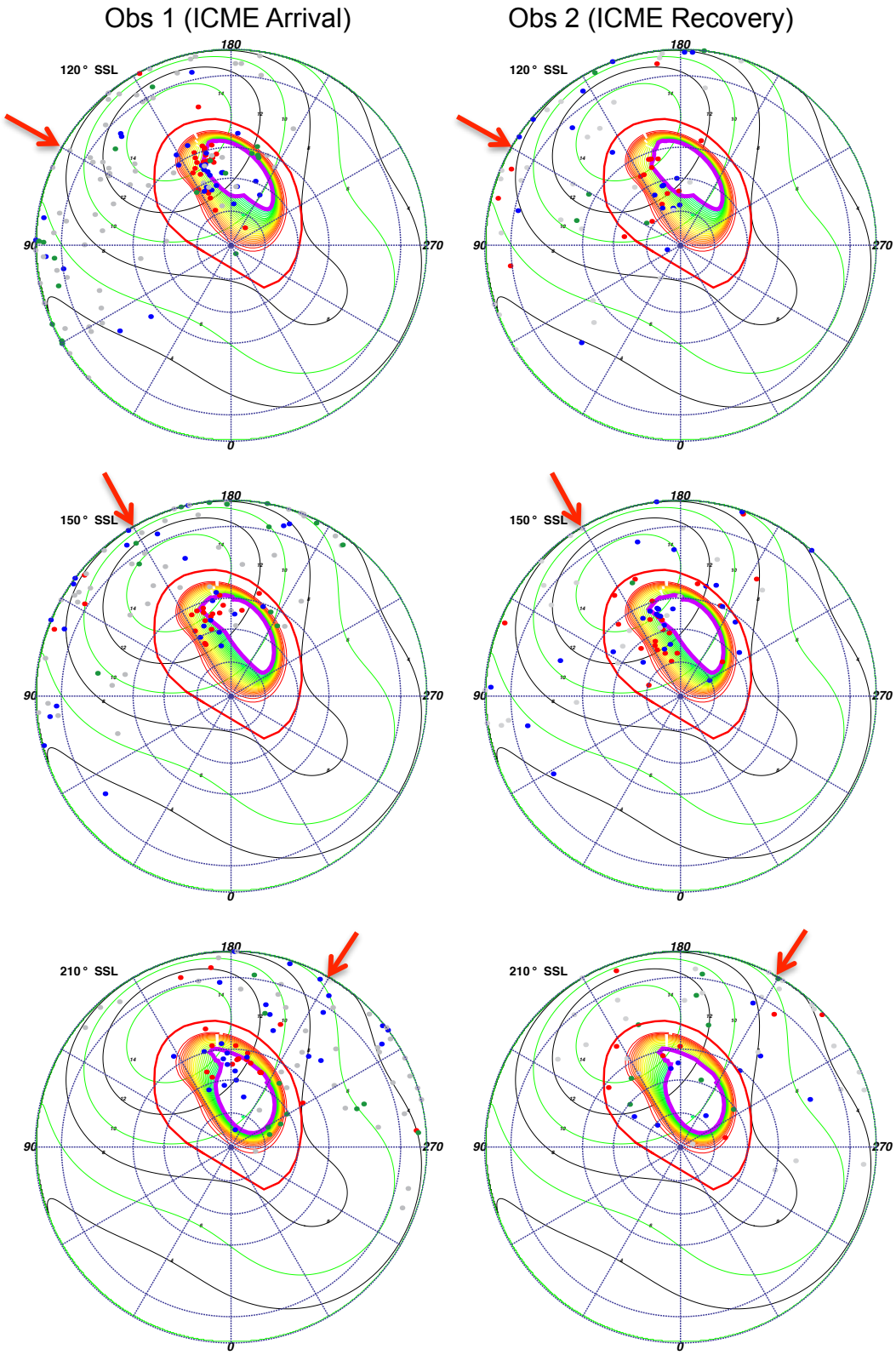

Figure 2.20: Sub-solar Longitude (SSL) binned polar projections for the hot spot for the first (left) and second (right) observation, using an expanded magnetosphere model for both. For colour coding and details see figure 2.16.

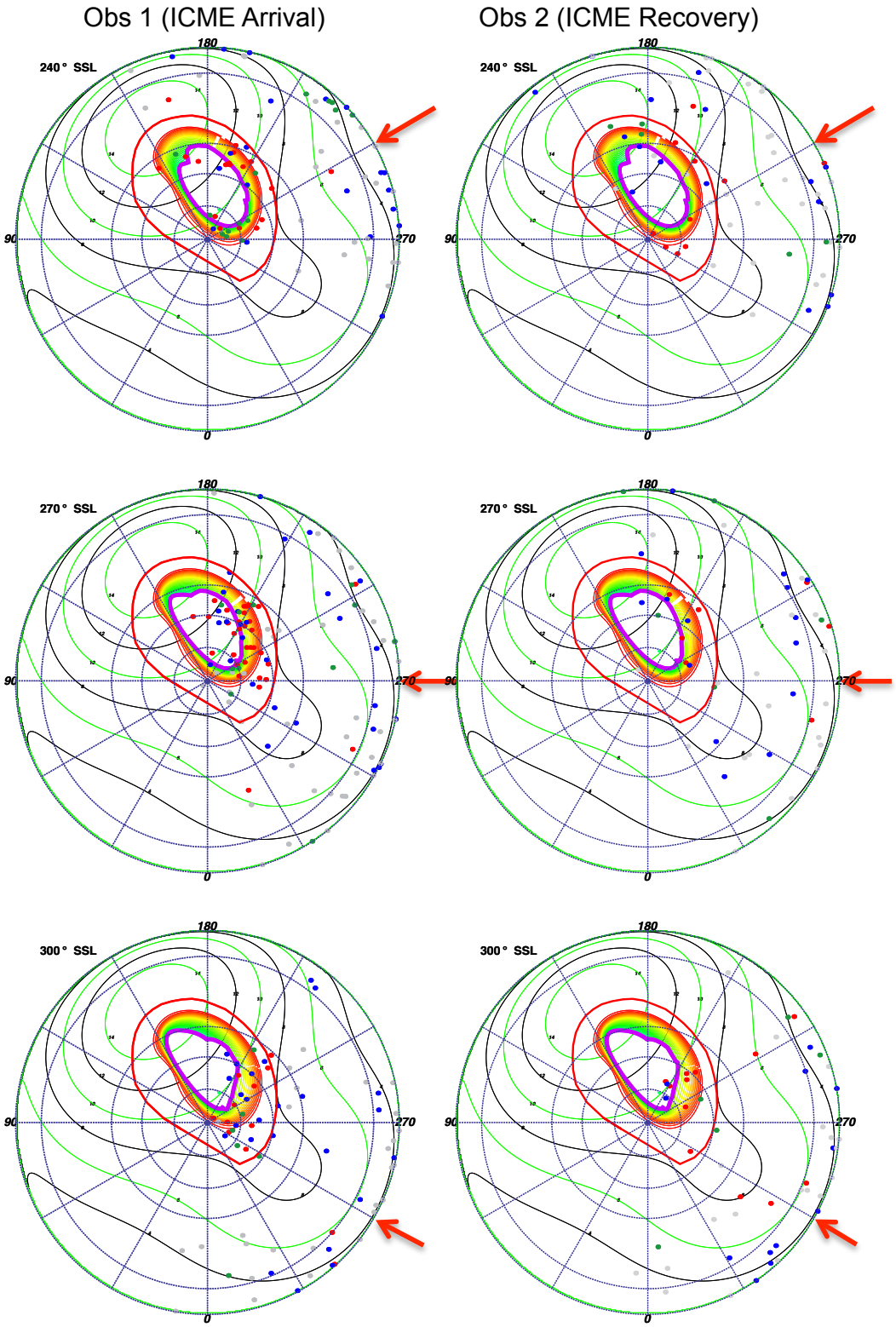

Figure 2.21: Sub-solar Longitude (SSL) binned polar projections for the auroral enhancement for the first (left) and second (right) observations, using the expanded magnetosphere model for both. The Auroral Enhancement occurs in the 270° SSL plot. For colour coding and plot details see figure 2.16.

ering uncertainties in the spatial location, this region would map either to the solar wind or closed field lines between 90-150 R_J. The similar source in both 120° and 150° SSL may suggest that the processes are persistent.

Finally, inspecting the 210° SSL projection (figure 2.20), we found that the Hot Spot contained very little emission, despite remaining on the observable disk. The emission appeared to have followed those field lines that mapped to MLT regions from 12:00-18:00 as Jupiter rotated and we found emission in both the outer magnetosphere and on open field lines in this area.

To reflect our spatial uncertainties, the timing spread of events and their broad spatial distribution in each region, we found a broad range of MLT sources for the emission. For the 120° and 150° SSL projection, most ion emission originated from magnetosphere locations with local times between 10:30-18:00. For the 210° SSL projection, events mapped to MLTs of 8:30-19:00 (figure 2.20). However, we note that none of these MLTs account for ion travel time from regions near the magnetopause to Jupiter's pole. During this time, the magnetosphere will rotate and so the origins for the particles may be at earlier MLTs than we have suggested. Without knowing the location of the energization region for the ions, it is difficult to quantify this time lag.

2.9.2 Noon-Binned Auroral Enhancement Projections

To identify the source/s and development of the auroral enhancement we focus on the 240°, 270° and 300° SSL projections (figure 2.21). Unfortunately, the auroral region had just begun to rotate out of view at this time, so a lot of the brightening occurred close to the limb of the disk, meaning that there were uncertainties of 10°-20° on the S3 coordinates of many X-rays.

The 270° SSL projection, when the auroral enhancement occurred, contained a broad spread of emission from closed lines in the outer magnetosphere and field lines that were open to the solar wind. This showed both oxygen and carbon/sulfur emission from the open field line region. The emission broadly mapped across the dayside of the planet between 06:00 to 16:00 MLT.

The 300° SSL projection had almost all the emission close to the limb, making it challenging to determine the location of the events because of the

S3 uncertainties. Carbon/sulfur and oxygen emission appeared to originate from the magnetosphere, from lower latitude regions than the 15 R_J footprint and from the open regions.

While we cautiously note that the counts were much lower for the hard X-ray emission from electrons (green), the hard X-rays appeared to cluster on the dawn side of the disk. This can be seen on the polar projections for SSLs 120°, 210° and 240° (figures 2.20 and 2.21). These regions mapped to MLTs 02:00-06:30hours. This is on the opposite side of the magnetosphere to the origin for the precipitating ions, but is consistent with the vertex-early dawn origin for the non-Io decametric emission that is observed coincident with the first observation and which is also produced by electrons.

2.10 Testing For Links to Solar Photons Scattered In Jupiter's Atmosphere

In order to determine whether many of the previously unexplored behaviours identified in this chapter could be related to the ICME influence, Io's radio burst or other magnetospheric factors, it is important to ensure that the observed changes are not simply due to variation in the emission from Jupiter's disk that is produced by increased solar X-ray flux.

During the October 2011 Chandra observations several solar flares occurred. These solar flare events are characterised by increased X-ray photon flux from the Sun, which leads to increased Jovian disk emission (Bhardwaj et al. 2005, 2006; Branduardi-Raymont et al. 2007b) because more X-rays are fluoresced and scattered in Jupiter‘s upper atmosphere.

In order to test whether any of the auroral brightening we observed (figure 2.5) could relate to the solar flares, we compare the solar X-ray flux across the observation with the Jovian auroral emissions. By doing this, we provide further evidence for the correlation between Jupiter's disk (and particularly equatorial) X-ray emission and solar emission (Bhardwaj et al. 2005, 2006; Branduardi-Raymont et al. 2007b).

Figure 2.22 shows the Sun's X-ray flux as recorded by the Solar X-ray

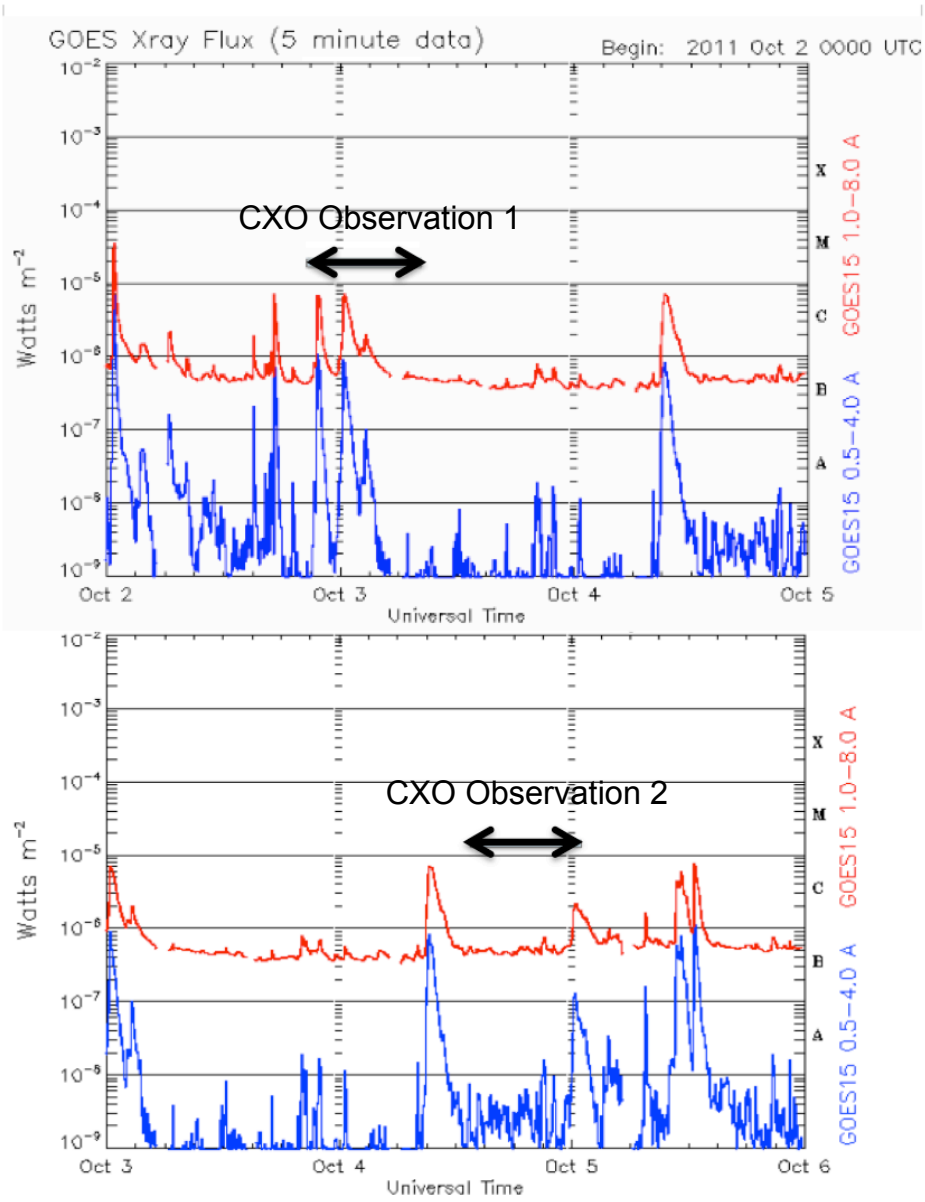

Figure 2.22: 5-minute binned X-ray flux from the Sun as recorded by the Solar X-ray Imager on the GOES spacecraft throughout the time period of our first (upper plot) and second (lower plot) Chandra X-ray observations. The black arrows indicate the timing of the respective X-ray observations and account for the difference in light travel time between the Sun and Earth and the Sun-Jupiter and Earth for solar X-rays fluoresced and scattered from Jupiter's disk.

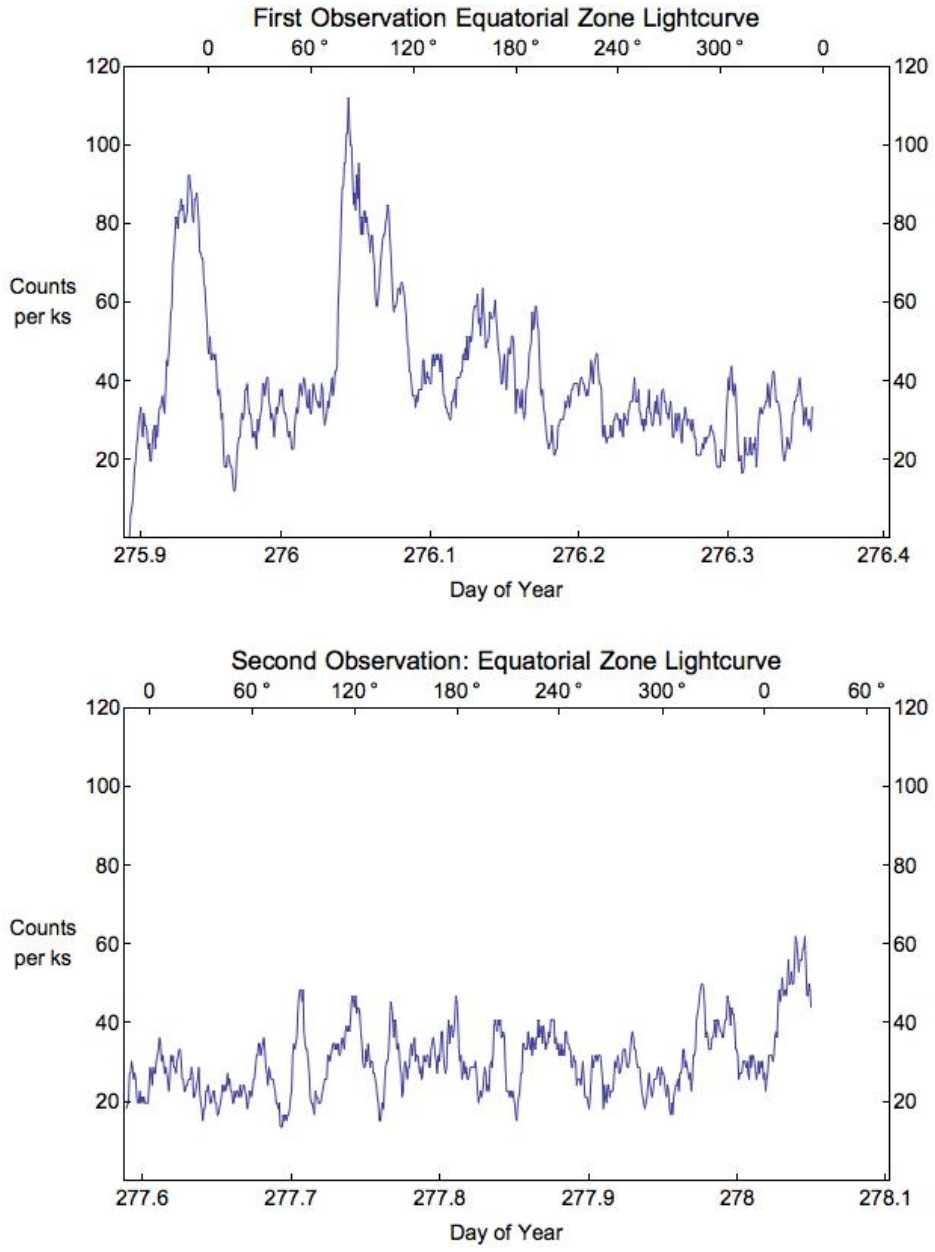

Figure 2.23: X-ray Equator Lightcurves with one minute binning for the first (upper) and second (lower) observations. The equatorial lightcurves use events between S3 latitudes of -60° and 60°. The lightcurve morphology appears to be a good a match for the GOES lightcurve in both cases.

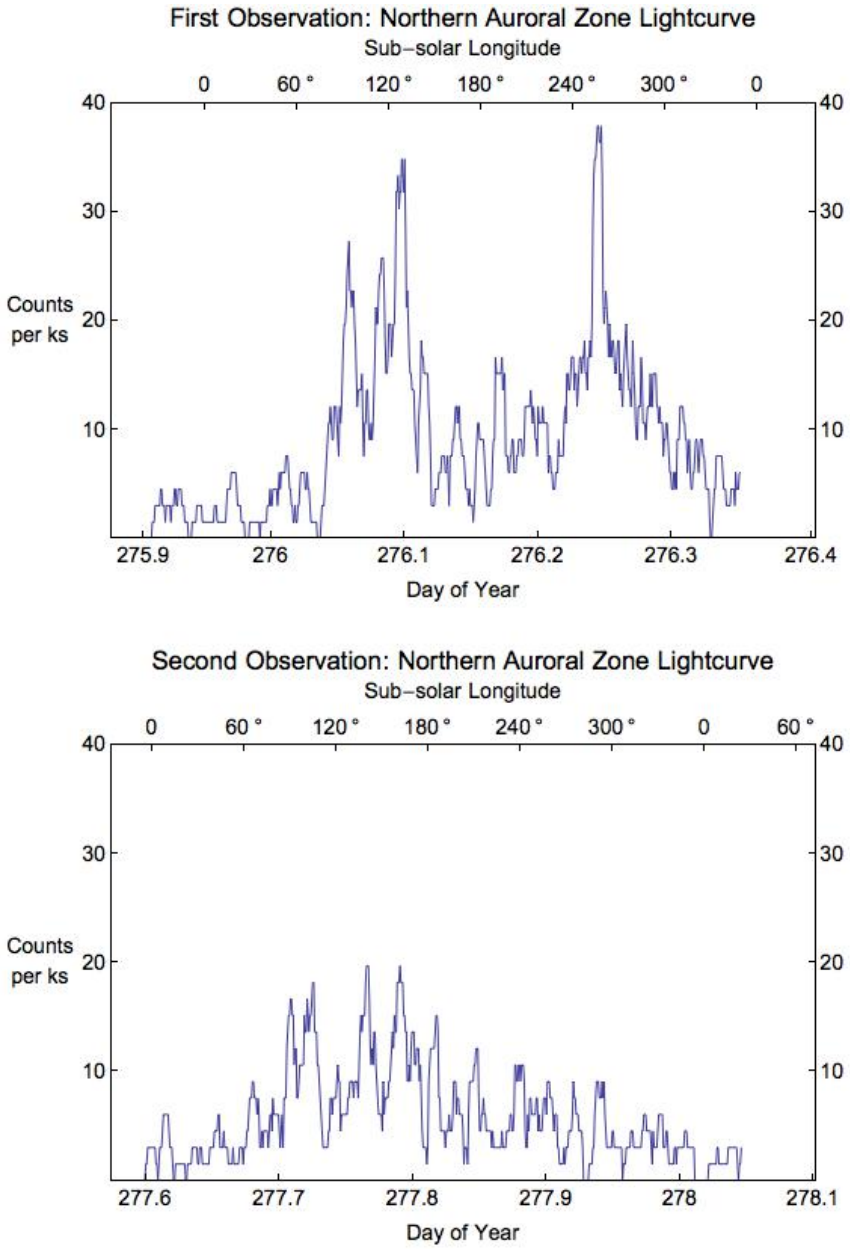

Figure 2.24: X-ray Aurora Lightcurves with one minute binning for the first (upper) and second (lower) observations. The auroral lightcurves use events above S3 latitudes of 60°. The lightcurve morphology is very unlike that of the equator or GOES lightcurves.

Imager (SXI) on the GOES spacecraft throughout the two Chandra X-ray observations of Jupiter in 2011. The black arrows plotted onto the figures indicate the times of the two Chandra observations, shifted to account for light travel time. Figure 2.22 shows that the X-ray flux of the Sun peaked three times during the first Chandra observation. The first two X-ray flux peaks correspond to an order of magnitude increase in Solar X-ray flux and the third peak corresponds to a half order of magnitude increase. During the second Chandra observation, there is only one half order of magnitude peak in the solar flux at the end of the observation.

Figure 2.23 shows the X-ray lightcurves for the equatorial zone on Jupiter (using latitudes: -60° - 60°) for each of the two observations. The equatorial lightcurve for the first observation features peaks, at the times when the flares observed by GOES SXI are expected to arrive at Jupiter. This shows that the disk emission replicates the GOES SXI data well, in strong support of the conclusions of Bhardwaj et al. (2005, 2006); Branduardi-Raymont et al. (2007b).

The equatorial lightcurves (Figure 2.23), which match the GOES SXI data well, feature very different morphology to the auroral lightcurves (Figure 2.24), which do not match the GOES SXI data. While the equatorial lightcurves (Figure 2.23) peak at the light-travel shifted times of the GOES lightcurves (Figure 2.22), the auroral lightcurves (Figure 2.24) do not vary with the first flare in a notable way. Unfortunately, at the time when the second solar flare arrived at Jupiter, the hot spot rotates into view on the disk. Disentangling the X-ray emission from the second solar flare from the increase in emission because of the hot spot visibility is challenging. However, the auroral zone associated with the hot spot continues to emit bright pulsations for more than an hour after the solar flare has dimmed from the equatorial zone. This supports an auroral origin for the majority of the additional emission observed in this region throughout the first observation. The solar flares may contribute a small fraction of the auroral emission, which may explain the appearance of common solar Fe XXI, Ne X and Mg XI lines in the hot spot spectrum (section 2.5).

There is no solar flare between DoY 276.2 - 276.4 and the equator has dimmed to a normal level by this point, meaning that solar flares are not responsible for Jupiter's auroral enhancement feature. For the second observation, the only solar flare occurs at the end of the observation and a corresponding factor 2 increase in the equatorial lightcurve is observed in the final hour of the observation. This appears to have minimal impact on the Northern Auroral zone lightcurve, again implying that the solar flares are not the main contributor to the variations we observe in the auroral emission.

Figure 2.9 highlights the increased brightness of Jupiter's disk spectrum, which is produced by the solar flares in the first observation relative to the non-solar flare spectrum of the Jovian disk in the second observation.

In support of a non-solar flare origin for the auroral behaviour, Figure 2.10 also showed that the sulphur/carbon and oxygen emissions are concentrated into the aurora and not distributed across the disk, showing that changes in solar photon flux are not responsible for the auroral changes we observe. If they were related, then we would not expect such distinct regional concentrations.

2.11 Summary of Results

We summarise results separately for the hot spot quadrant (S3 longitude: 90-180°) and the auroral enhancement quadrant (S3 longitude: 180-270°), since the spatial, spectral and temporal behaviours of each quadrant differ and the solar wind conditions may have been different for each (see figure 2.1).

2.11.1 Hot Spot Quadrant

- Spatial Emission: The change in emission in the hot spot is not as significant as in the AEQ (Figure 2.3). This increased emission spreads equatorward from the previously reported hot spot location (Gladstone et al. 2002; Elsner et al. 2005) up to the 50 R_J footprint. This gives the appearance of the hot spot having expanded for the first observation.

- Spectra: Both observations feature prominent 200-400 eV car-

bon/sulphur peaks and a prominent peak in the OVII spectral region between 550-620 eV. The first observation features either increased OVIII emission or increased solar photon emission.

- Energy Binned Polar Projections (figure 2.10): The 200-500 eV (carbon/sulphur) emission is mostly responsible for the increased emission between the normal hot spot location and the 50 R_J footprint in the first observation. Generally, 500-800 eV (oxygen) emission occurs poleward of this concentrated carbon/sulphur emission. We also find that the carbon/sulphur emission does not behave like the oxygen emission, with the carbon/sulphur emission brightness more enhanced than the oxygen emission for the expanded hot spot.

- PSDs: The first observation features 2 significant periods at 12 and 26 minutes - shorter timescales than previously reported (Gladstone et al. 2002). The second observation shows a less significant period of 42 minutes, closer to the 45 minute timescale of Gladstone et al. (2002). The 26 minute period is strong in carbon/sulphur emission in the hot spot, but not in oxygen emission. The 12 minute period is present for both carbon/sulphur and oxygen, but with much lower significance for each. When the two populations are combined the period becomes significant.

- SSL projections with Vogt et al. (2011) model mapping: 78% (first observation) and 69% (second observation) of hot spot emission occurs before noon in the region. This timing coincides with the region mapping to magnetospheric local times between 10:30-18:00 hours. Most of the carbon/sulphur emission originates in the outer magnetosphere between 50-90 R_J and on open field lines, while the oxygen emission originates further from Jupiter (70-120 R_J) or on open field lines (with identification of an open or closed origin depending on uncertainties in spatial resolution and choice of compressed/expanded magnetosphere

mapping). The expansion of the hot spot occurs on field lines mapping to the region where the magnetopause has been found to move during compression from 92 R_J to 63 R_J (Joy et al. 2002). The Vogt et al. (2011) model mapping showed that the majority of X-ray producing ions originate beyond 60 R_J.

2.11.2 Auroral Enhancement Quadrant

- Lightcurves: An auroral enhancement occurs during the first observation, the peak of which is ∼8 times brighter than for emission in the region during the second observation. This occurs 1-1.5 hours before a non-Io decametric radio burst, a previously recognised signature of ICME-induced forward shocks (Hess et al. 2012, 2014; Lamy et al. 2012).

- Spectra: The spectra from the first and second observation are different: there is an enhanced 200-400 eV carbon/sulphur double peak and a prominent peak in the OVII spectral region between 550-620 eV during the first observation. These peaks are much less prominent in the second observation. Between 380-700 eV the spectrum appears similar to cometary spectra from solar wind charge exchange (Elsner et al. 2005).

- Energy Binned Polar Projections: Both the 200-500eV (carbon/sulphur) and 500-800eV (oxygen) emissions are increased by a factor of at least 4 for both energy ranges in the first observation relative to the second. This is different to the hot spot emission, where carbon/sulphur is preferentially enhanced.

- Hard X-rays: The 1500-5000 eV (electron bremsstrahlung) emission is observed in clusters in the main oval region. It coincides with dawn on the surface and originates at MLT 02:00-06:30 hours. This is on the

opposite side of the magnetosphere to the source of the X-ray charge exchanging ions.

- PSDs: No significant periodicity was detected from the AEQ ion emission.

- SSL projections with Vogt et al. (2011) model mapping: The enhancements broadly map across the dayside of the planet between 06:00 to 16:00 MLT parallel with the open-closed boundary. The emission maps to open field lines and closed field lines in the outer magnetosphere and also to low latitude regions between Io's footprint and the 15 R_J contour.

2.12 Discussion

In the discussion, we attempt to address two questions: What are the source regions for Jupiter's X-ray aurora? What processes in these regions produce X-rays and how might these relate to the ICME?

The spectral, spatial and temporal differences between the hot spot and the auroral enhancement emission lead us to treat the two features separately. Our analysis of the periodicity, spectral and spatial origins of the emission suggests that both the hot spot and auroral enhancement each have multiple X-ray source regions.

Throughout the first observation, the Vogt et al. (2011) models showed that the majority of X-ray producing ions originate beyond 60 R_J. If we assume a compressed magnetosphere (with a stand-off distance at 63 R_J (Joy et al. 2002)), the open field lines contribute a large proportion of the emission, while for an expanded magnetosphere (with a stand-off distance at 92 R_J(Joy et al. 2002)), closed field lines are the dominant source.

2.12.1 The X-ray Hot Spot

2.12.1.1 Where is the Hot Spot Source?

While the auroral enhancement emission appeared to originate from several regions that map to different magnetospheric locations, the hot spot remained confined to a more limited region fixed in the planet's rotating frame. This spatial confinement permits more precise identification of possible sources for the precipitating ions that produce X-ray emission in this region.

The 200-500 eV sulphur and/or carbon emission features an additional component from lower latitudes than the 500-800 eV oxygen emission. If we assume an expanded magnetosphere, we find that most of the 200-500 eV emission maps to a region between the outer magnetosphere and the magnetopause, originating between 50-90 R_J (figure 2.19). This model suggests that most 200-500 eV emission is from precipitation of high charge state sulphur ions in the outer magnetosphere, as proposed by Cravens et al. [2003]. It also suggests that there may be some slight precipitation from open field lines and therefore possibly from carbon ions in the solar wind, but that this is a smaller proportion of the emission. However, in the case of a compressed magnetosphere, the emission is more evenly distributed between carbon ions in the solar wind and from sulphur ions from the outer edge of the magnetosphere (for a compressed magnetosphere this is 50-63 R_J at the stand-off point).

The observed strong 26 minute periodicity for these 200-500 eV X-rays suggests a sulphur source, since if the period originated in the solar wind we would expect to also observe oxygen exhibiting it (as the most abundant heavy ion in the solar wind). The absence of oxygen emission from the 26 minute period and spatial separation between these two species suggests that the lower latitude feature is from a dominant sulphur population, which does not include oxygen of a sufficiently high charge state. The 12 minute period increases in significance when oxygen is combined with carbon/sulphur, suggesting that there is a second population consisting of a mixture of both oxygen and carbon/sulphur. Alongside the periodicity, the spatial mapping suggests a different origin for each population: one solely sulphur population with 26

minute periodicity from 50-70 R_J; the other an oxygen + carbon/sulphur population from closer to the magnetopause and possibly from open field lines. Comparison of the two observations would seem to suggest that the lower latitude sulphur dominated population is more sensitive to changes in the solar wind conditions, since it is much more prevalent in the first observation.

Io injects both oxygen and sulphur into the Jovian magnetosphere, so if both X-ray-producing populations originate in the outer magnetosphere, there needs to be an explanation for why the 50-70 R_J region is dominated by sulphur emission and features less oxygen emission. Oxygen ions that produce X-rays have a higher ionisation energy than sulphur ions. For instance, O^{6+} requires 739 eV to become ionised (Drake 1988), while S^{6+}-S^{9+} only requires 281 - 447 eV (Biémont et al. 1999). This means that it is possible to have a magnetospheric region where there is sufficient energy for charge stripping and X-ray production from sulphur, but not from oxygen. Different energy regimes may be expected with distance from Jupiter through associated changes in density, currents and voltages through either pulsed dayside reconnection (Bunce et al. 2004), or outer magnetosphere field aligned potentials (Cravens et al. 2003).

It is also possible that quenching and opacity effects, as suggested by Kharchenko et al. (2008) and Ozak et al. (2010), may need to be considered to explain the spatial differences, since different energy regimes will also produce different atmospheric penetration and different observed signatures.

Figure 2.25 summarises the equatorial mapping of the sources for different precipitating particles generating the observed X-rays. In support of the work presented in this chapter, Kimura et al. [2016] recently identified similar sources for X-rays, suggesting that both closed field lines in the outer magnetosphere and open field lines beyond the magnetopause were possible X-ray sources.

The presence of both magnetospheric and cusp precipitation is not precluded by the findings of Cravens et al. (2003), Bunce et al. (2004) or Kharchenko et al. (2006, 2008). However, they suggest that cusp precipitation could only provide a significant source of emission during auroral UV flare-like conditions or heightened solar wind conditions and then the emission should

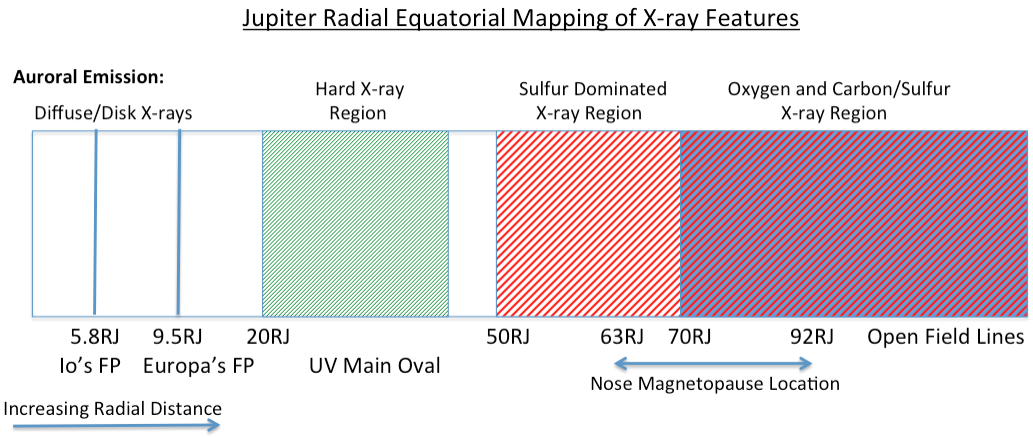

Figure 2.25: Summary of X-ray source mapping (not to scale) accounting for uncertainties in photon spatial mapping. The x-axis indicates the equatorial radial distance from Jupiter that the source regions map to. The different X-ray regions are indicated by the striped blocks: the Hard X-ray region (green), the region dominated by high charge state sulphur region (red) and the mixed high charge state carbon/sulphur and oxygen region (red and blue).

be less than the magnetospheric contribution. The mSWiM propagation and radio emissions show that solar wind densities increased at Jupiter during the first observation, suggesting that these heightened solar wind conditions may have been present. Cusp precipitation would include precipitation from protons, which are highly abundant in the solar wind and would be expected to generate bright polar UV flares (Cravens et al. 2003). Without coincident UV observations at the time of the X-ray observations reported here, it is difficult to identify levels of proton precipitation and therefore to further separate a solar wind or magnetosphere source for the higher latitude mixed population of high charge-state oxygen and carbon/sulphur.

The precise magnetospheric origins of each particle depends on not only the spatial uncertainties but also the internal field model used to initialise the Vogt et al. (2011) mapping. Vogt et al. (2015) analyse the differences in each model (VIP4 (Connerney et al. 1998), Grodent Anomaly Model(Grodent et al. 2008) and VIP Anomaly Longitude (Hess et al. 2011)) and highlight the differences between each. From a simple X-ray Hot Spot comparison, we found that the Grodent Anomaly Model we used in this work normally mapped X-rays closer to Jupiter. VIPAL and VIP4 often mapped emission beyond the magnetopause. When the Grodent Anomaly Model did map X-rays more

distantly than VIP4, then there was often less than a 10 R_J separation and local times were often 0.5-3 hours later than VIP4 or VIPAL.

2.12.1.2 What Process Drives the Hot Spot X-ray Emission?

We find that in both observations the ions that precipitate to produce the hot spot originate from locations between 10:30-18:30 on the dayside magnetosphere. Bonfond et al. (2011) map quasi-periodic auroral flares in the Far UV to the same region in Jupiter's magnetosphere at local times between 10:00 and 18:00 and note the similarity between these flares and flux transfer events observed by Pioneer and Voyager probes. They suggest possible connections between these UV and X-ray features and the Jovian cusp.

Combined with the dayside origin, the periodicities observed may also be an important clue to the mechanisms driving the emission. Using Ulysses, Marhavilas et al. (2001) found dual periods of 15 - 20 minutes and 40 minutes in energetic particles upstream from the Jovian bow shock. This may indicate a solar wind connection for emission. Ulysses also detected 20 minute and 40 minute periodicities in the dusk magnetosphere (Anagnostopoulos et al. 1998, 2001; Karanikola et al. 2004). Alternatively, the 12 minute period falls within the 10-20 minute timescale of Jovian global ultra-low-frequency oscillations (Khurana and Kivelson 1989b). High energy ions have also been previously observed to have periods within this range (Wilson and Dougherty 2000a). At Earth, Ultra Low Frequency waves are often associated with dayside reconnection (Prikryl et al. 1998) or with either compression from shock events or Kelvin Helmholtz instabilities (Dungey and Loughhead 1954; Chandrasekhar 1961; Kivelson and Russell 1995). It seems possible that one or more of these mechanisms may contribute to the detected hot spot periods in our observations.

Bunce et al. (2004) found that pulsed dayside reconnection perturbing outer magnetosphere field lines would generate arc-like emission and a ∼30-50 minute period, not dissimilar to the 26 minute period we observe. They also suggest that this is more likely to occur during high solar wind pressure, such as during our first observation. At this time, in support of a reconnection

origin, emission appears to cluster close to regions where reconnection could occur (figure 2.17). Desroche et al. (2012) found that reconnection was possible in the afternoon to dusk region based on plasma flow shear speeds and also plasma βs of 10 and 1, which may suggest the local time dependence of hot spot emission could be connected with this process.

If the 26 minute periodicity were to be related to bounce times on field aligned potentials instead, then it remains challenging to explain the shared 12 minute oxygen and carbon/sulphur period in this way. This is because the different masses of oxygen and sulphur/carbon would produce different bounce times for ions that originated in the same region. Their shared period may therefore favour a non-bounce time related mechanism for the 12 minute period in the first observation. We note that this 12 minute period is of the same order of magnitude as the Alfvèn wave transit times calculated by Bunce et al. (2004). If the periodicity does relate to the Alfvèn transit time, then the shift in period from 12 or 26 minutes to 42 minutes may make sense in the context of a shift in magnetopause distance because of solar wind induced compression/expansion of the magnetosphere.

For the second observation, when the solar wind was returning to pre-ICME conditions, emission still originates from the dayside of the planet but more prominently from locations in the magnetosphere closer to 15:00-18:00 MLT, along recently closed field lines (figure 2.20). Kimura et al. (2016) suggested that flow shear effects such as Kelvin Helmholtz instabilities (KHIs), also found at the magnetopauses of Saturn (Masters et al. 2010; Wilson et al. 2012) and Earth (Hasegawa et al. 2004), may be an important factor, and thus an explanation for the periodicity in the Jovian X-ray emission. KHIs are expected to develop on both the dawn and dusk flanks of the planet and are expected to become more substantial moving down the flanks, where the velocity shears are larger, as the magnetosphere and solar wind become progressively more rolled-up (Miura 1984; Nykyri et al. 2006). These structures could either inject solar wind particles directly into the magnetosphere, through small scale reconnection events (Fairfield et al. 2000; Nykyri and Otto 2001) or could facilitate the transport of momentum across the magnetopause boundary layer

(Miura 1984; Chen and Kivelson 1993), during the linear- phase prior to roll-up. Multiple current systems are generated by KHIs (Masters et al. 2010), which may provide the needed energisation source to create the high charge-state ions that can produce X-rays.

At Earth, Taylor et al. (2012) reported a dawn-dusk asymmetry in rolled-up vortices detection, with higher frequency on the post-noon dusk flank, while a previous study by Hasegawa et al. (2006) reported as many KHIs on either flank. Unlike Earth, the Jovian magnetosphere is populated by highly co-rotating plasma (Thomsen et al. 2010; Mauk et al. 2009), which contributes to a larger shear at the dawnside, where the corotation is sunward (Johnson et al. 2014a). As a result, this larger shear is expected to favour the generation of KHI on the dawnside rather than on the duskside (Desroche et al. 2012, 2013). However, based on the development timescale of KH vortices in relevance to Jovian orbital period, the structures at the dawn and dusk flanks may primarily originate from the same location (Johnson et al. 2014a), which could result in observation of rolled-up vortices at earlier MLTs.

KHIs similar to those at Earth are less able to explain the first observation emission that originates closer to the nose of the magnetosphere, near to noon MLT. Cowley et al. (2007), however, find that flow shear along the open-closed field line boundary would be important at Jupiter and capable of generating high latitude aurora. The shear increases when the magnetosphere is compressed due to increased angular velocity of the magnetospheric plasma, which could cause auroral emission to brighten (Nichols et al. 2009a), so it may be that flow shear is also relevant close to the nose.

The fact that the hot spot feature is localised (Elsner et al. 2005; Gladstone et al. 2002; Branduardi-Raymont et al. 2008) and restricted to limited longitudes of the Jovian pole is probably an important clue to its drivers. Magnetospheric processes capable of producing ~ 10 MeV downward precipitating ions only in this region must uniquely link with locations that the region maps to. A good explanation for this localisation may be that it connects to the magnetopause and therefore to KHIs or dayside reconnection. Alternatively, if it is produced by a high energy downward current region there must be an

explanation for the localisation of this.

The high energy electrons that generate the bremsstrahlung emission originate on the opposite side of the planet to the ion emission, in regions between 02:00-06:30 magnetospheric local time. At Earth, similar features are associated with whistler mode waves and the dawn chorus. The possible periodicity in the 5 - 10 minute range may be consistent with this explanation. Dawn storms at Jupiter have been observed in the UV on several prior occasions [e.g: Gustin et al. (2006); Clarke et al. (2009); Nichols et al. (2009a)] and may be capable of supplying sufficiently energetic electrons for X-ray brehmstrahlung emission. The hard X-ray emission from high energy electron precipitation also increased during the first observation. Brightening of the UV main emission has been observed to occur coincident with solar wind shocks [e.g:Nichols et al. (2009a)]. Simultaneous UV-X-ray observations would help to further constrain these connections between brightness variation in the UV main oval and increased hard X-ray emission from high energy electrons in this region. They would also help to identify global current systems, with UV highlighting upward currents (away from the planet) and X-rays from ions helping to identify downward currents (towards the planet).

2.12.2 The Auroral Enhancement

2.12.2.1 Where is the Auroral Enhancement Source?

In the quadrant from 180°-270° S3 longitude, we observed the largest change in auroral emission between the two observations, the bright auroral enhancement on Day of Year 276.25. The brightest peak of this event lasts ∼20 minutes, 2-4 times longer than the flare reported by Elsner et al. (2005).

Figure 2.3 and 2.17 show that the ion emission originates from a range of different latitudes and therefore maps to several closed and open field line regions, suggesting that, at this time, there may be several downward current regions on which the ions can precipitate. The precipitating particles also originate from a range of different magnetospheric local times across the dayside of Jupiter from dawn to close to dusk.

2.12.2.2 What Process Connected to the ICME Drives the Observed Auroral Enhancement?

The auroral enhancement occurs 1-1.5 hours prior to a bright non-Io decametric radio burst (figure 2.2), which has previously been found to relate to the impingement of a solar wind forward shock (Gurnett et al. 2002; Lamy et al. 2012; Hess et al. 2012, 2014). The mSWiM propagation also suggests the arrival of an ICME close to this time. The combination of this radio emission and the mSWiM predicted solar wind density peak leads us to believe that the bright X-ray auroral enhancement is driven directly by this ICME.

What process could be directly responsible for this X-ray brightening? The driver does not seem to be a continuation of the same process that produces the hot spot emission because the properties of the two emissions differ. The prominent differences between the AEQ and HSQ emissions include: a different population of precipitating particles (figures 2.7 and 2.11); the AEQ emission is spatially less localised than the hot spot emission (figures 2.3, 2.10, 2.11, 2.17, 2.18, 2.19, 2.20 and 2.21); the AEQ emission seems to increase temporally into an event lasting $\sim$ 20 minutes, with no significant periodicity in the ion emission (figures 2.5 and 2.13), while the hot spot emission exhibits clear pulsations.

The AEQ features also seem atypical when compared with other X-ray observations (Elsner et al. 2005; Gladstone et al. 2002; Branduardi-Raymont et al. 2008). While the hot spot may be driven by KHIs or pulses of dayside reconnection close to a downward current region, we suggest that the auroral enhancement is driven by a less common process that is directly associated with the changing solar wind parameters induced by the ICME. Inspecting the mSWiM propagation (Figure 2.1) implies that the driver relates to either increased solar wind density and/or changing Interplanetary Magnetic Field angle (as suggested by the rotation in B_T). We propose two possible drivers based on these changing solar wind parameters but note that they might not be independent drivers: 1) an ICME-induced compression event and/or 2) an-ICME induced instance of large-scale dayside reconnection.

Increased ram pressure from the heightened solar wind density (Figure

2.1a) could drive a Jovian magnetosphere compression. The Vogt et al. (2011) mapping shows X-ray emission from several regions inside the magnetosphere, suggesting that the ICME transfers energy into the magnetosphere, so that ions are sufficiently energetic for X-ray production. This also raises questions as to the location of the downward currents (on which the ions precipitate) at this time. Compression events have been suggested to drive changes in Jupiter's current system and therefore acceleration processes [Cowley et al. 2007; Cowley and Bunce 2003A; 2003B]. Adjustments to the location of downward currents, induced by the compression, may therefore explain the observed broad spatial spread of ion emission, which during the auroral enhancement is not restricted to the hot spot as it normally is. Alternatively, compression at other planets is known to lead high energy particles that are bouncing on field lines in the radiation belts to be scattered into the loss cone or to gyrate onto field lines that map to much higher latitudes (sometimes precipitating in the cusp). Similar scattering from the Jovian radiation belts and IPT could explain the broad range of latitudes and apparently impulse-like nature of the emission.

Alternatively, or in combination with a compression, a large-scale instance of dayside reconnection may explain the observations. Desroche et al. (2012) showed that dayside reconnection would be confined to local regions on the magnetopause for certain IMF orientations, but varying IMF angle could lead dayside reconnection to occur across a larger proportion of the magnetopause. Masters [2015] further shows for Saturn that changing IMF angle can lead to increased reconnection voltages and a larger spatial scale of magnetopause reconnection. This could result in increased injection of solar wind particles and energisation of a larger region of the outer magnetosphere plasma, explaining the observations of the larger spatial scale of emission and the observed change in the precipitating population from the spectra. The inverse of this mechanism may also help to explain reduced emission from the hot spot for some observations, since a less favourable IMF angle would suppress reconnection and therefore emission from the hot spot. Further comparison of Jupiter X-ray emission with upstream IMF measurements would help to investigate this

relationship.

The Vogt et al. (2011) mapping also lends weight to the argument that solar wind-magnetosphere coupling is at work during this interval. It is possible that the solar wind compression and/or possible associated dayside reconnection for favourable IMF direction can lead to an opening of magnetic flux on the dayside, and concurrent X-ray flaring. Cravens et al. (2003), addressing charge exchange, show that X-ray emissivity from solar wind particles depends on solar wind velocity and density, which is in-line with our observation of increased emission. We also found that the magnetospheric mapping suggests an open field line origin for at least some of the emission. This is supported by similarities between the AEQ spectrum and cometary spectra, which are known to be produced by solar wind charge exchange (from direct solar wind ion precipitation). However, we are cautious to note that the complex configuration of the Jovian magnetosphere may not be accurately represented by the Vogt et al. (2011) mapping model, so the magnetospheric mapping may not be fully reliable.

The low frequency of such ICME events, relative to the timescales of X-ray observations, may help to explain why these features have not been previously reported in the literature and why the second observation seems to have an AEQ that is again largely devoid of emission. We also note that such events may be confused with hot spot emission, if they occur at a time when the hot spot is in the observable quadrant, as opposed to this observation where the hot spot was rotating out of view when the auroral enhancement occurred.

While we suggest that the solar wind does drive several changes in Jupiter's X-ray aurora, we note that the importance of the solar wind as a driver of magnetospheric dynamics, and that the existence of Dungey cycle processes at Jupiter remain a subject of debate (McComas and Bagenal 2007, 2008; Cowley et al. 2008). In this instance, an alternative is that the AEQ emission may be an X-ray observation of a low latitude injection event (Mauk et al. 2002; Kimura et al. 2015). These auroral injection events could be the result of tail reconnection(e.g. for Saturn (Jackman et al. 2008; Bunce et al. 2005; Masters et al. 2011)) from solar wind compressions or from Io volcanism,

similar to those shown in the introduction (e.g. Kimura et al. 2015). This may connect with the observed radio signatures, since it implies a redistribution of plasma in the disk. The UV signatures associated with these are known to be very energetic, to map between the main oval and IPT and to last about 10 hours (priv comms. C. Tao and B. Bonfond). Further X-ray observations coincident with UV observations would help to determine if these are connected.

2.13 Conclusion

We report the first X-ray observation that was planned to coincide with an ICME arrival at Jupiter and find evidence for ICME-induced changes in the Northern X-ray aurora. We observe changes in the morphology, spectra and periodicity of the X-ray emission at this time. We particularly find an auroral enhancement by a factor 8, occurring 1-1.5 hours before a bright burst of non-Io decametric radio emission, often associated with the arrival of an ICME-induced fast forward shock (Hess et al. 2012, 2014; Lamy et al. 2012) and at a time when solar wind propagation models indeed predict an ICME arrival.

We have used Vogt et al. (2011) magnetospheric mapping to identify the origin of the X-ray emission. This mapping suggests that most auroral X-ray emission came from precipitating ions with origins beyond 60 R_J on both open and closed field lines. Spatial uncertainties and uncertainties as to whether the magnetosphere is compressed or expanded at this time inhibit us from quantifying from which side of the magnetopause the majority of emission originates. The region between 50-70R_J is dominated by 200-500 eV emission, which we attribute to precipitating high charge-state magnetospheric sulphur ions. At higher latitudes that map between 70-120 R_J and to open field lines there is a mixture of precipitating high charge-state carbon/sulphur and oxygen ions.

In the Hot Spot, the separate origins for ions of different species is supported by periodicity measurements. In the first observation we find a strong 26 minute period associated with the carbon/sulphur (200-500 eV) emission,

but not with the oxygen (500-800 eV) emission. We do, however, find a 12 minute period at a low level of significance in both the oxygen and carbon/sulphur emission. When the two populations are combined, the 12 minute period becomes significant. The periods of 12 and 26 minutes in the first observation are distinctly shorter than the 42 minute period we detect in the second observation, which is close to the 45 minute timescale found by Gladstone et al. (2002).

X-ray emission is concentrated in regions near to open field lines. On the basis of the magnetospheric local time of the source and the origin close to the magnetopause, alongside the periodicities and heightened solar wind conditions, we suggest that pulses of dayside reconnection (Bunce et al. 2004; Desroche et al. 2012) near a magnetospheric downward current region could be driving the X-ray hot spot emission. We also suggest that the spectral, spatial and temporal differences between the hot spot emission and auroral enhancement emission imply that they are not created by a continuation of the same process. Instead, we suggest that the auroral enhancement is directly driven by the ICME through either a compression event and/or a larger-scale instance of dayside reconnection than that producing the hot spot emission.

Other mechanisms in the outer magnetosphere, near the magnetopause, such as KHIs, may also have an important role in transferring momentum and energy in our observations, given that the Dungey cycle may well be less important for Jupiter than Earth (McComas and Bagenal 2007, 2008; Delamere and Bagenal 2010c; Johnson et al. 2014a).

We believe that the approach of applying Vogt et al. (2011) model mapping to energy-binned, sub-solar longitude-binned X-rays offers excellent possibilities for mapping the origins of the Jovian X-ray aurora and thus better understanding the Jovian outer magnetosphere and the processes occurring close to the magnetopause. Similar analysis on new and archival X-ray observations is required to determine whether the features observed in these observations persist and how they relate to systematic trends in solar wind conditions. Combining observations of this kind with the approach and arrival of the Juno spacecraft in 2016 will offer further opportunities to understand

the processes governing Jovian auroral X-rays.

Chapter 3

Independent Pulsations from Jupiter's Northern and Southern X-ray Auroras

3.1 Abstract

Auroral hot spots are observed across the Universe from brown dwarfs (Hallinan et al. 2015), X-ray pulsars (Ozel 2013), magnetars and planets. They mark the coupling between a surrounding plasma environment and an atmosphere. Within our own solar system, Jupiter possesses the only resolvable example of this large-scale energy transfer. Discovered in 2000, Jupiter's Northern auroral X-ray hot spot occupies the most poleward regions of the planet's aurora and pulses either periodically (Dunn et al. 2016; Gladstone et al. 2002) or irregularly (Branduardi-Raymont et al. 2007a; Elsner et al. 2005). X-ray emission line spectra demonstrate that Jupiter's Northern hot spot is produced by relativistic (∼MeV/amu) high charge-state oxygen, sulphur and/or carbon ions undergoing charge exchange (Branduardi-Raymont et al. 2007a; Elsner et al. 2005; Kharchenko et al. 2008; Cravens et al. 2003). While the Northern soft X-ray aurora has always been observed to be concentrated into a hot spot, 16 years of observations failed to reveal a similar feature in the South (Gladstone et al. 2002; Dunn et al. 2016; Branduardi-Raymont et al. 2008; Kimura et al. 2016). Here, we report for the first time the existence of a persistent Southern X-ray hot spot. Surprisingly however, this large-scale Southern auroral structure behaves independently of its Northern counterpart. Using XMM-Newton and Chandra X-ray campaigns from May-June 2016 and March 2007, we show

that Jupiter's Northern and Southern spots each exhibit different characteristics, including different periodic pulsations and uncorrelated changes in brightness between each spot. These observations challenge currently proposed X-ray generation mechanisms for Jupiter. They imply that highly energetic, non-conjugate magnetospheric processes sometimes drive the polar regions of Jupiter's dayside magnetosphere. Understanding the behaviour and drivers of Jupiter's pair of hot spots is critical to the use of X-rays as diagnostics of the wide-range of rapidly rotating extra-solar objects that exhibit these auroral phenomena.

This results presented in this chapter have been accepted for publication in *Nature Astronomy* with the citation W. R. Dunn, G. Branduardi-Raymont, L. C. Ray, C. M. Jackman, R. P. Kraft, R. F. Elsner, I. J. Rae, Z. Yao, M. F. Vogt, G. H. Jones, G. R. Gladstone, G. S. Orton, J. A. Sinclair, P. G. Ford, G. A. Graham, R. Caro-Carretero, A. J. Coates, The Independent Pulsations of Jupiter's Northern and Southern X-ray Auroras.

3.2 A Rare Viewing Geometry

The XMM-Newton and Chandra X-ray Observatories conducted 12 hour (1.2 Jupiter rotations) observations of Jupiter on 24th May (XMM and Chandra) and 1st June (Chandra) 2016 and a 5-hour observation (0.5 Jupiter rotations) on 3rd March 2007. The observation start and end times and associated Central Meridian Longitudes (CML) are listed in Table 3.1. At these times, Jupiter's tilt provided excellent visibility of both Jupiter's Northern and Southern polar aurorae. The combination of Chandra's HRC (2016) and ACIS (2007) and XMM-Newton's EPIC together provided high spatial and spectral resolution X-ray observations. The entire observable disk of Jupiter fits in the Chandra-HRC and XMM-Newton-EPIC field of view, so that in 2016 both instruments provided continuous coverage of the planet for more than one Jupiter rotation and could observe both Northern and Southern aurora regions, as they rotated into view.

For all previously published X-ray campaigns with Chandra (Table 3.2)

Obs Start - End	Instrument	CML Start	CML End	Duration
3 Mar 2007 07:47 - 12:50	CXO ACIS	289°	112°	183°
24 May 2016 10:05 - 22:23	XMM-Newton EPIC-PN	175°	297°	482°
24th May 2016 10:23 - 22:05	CXO HRC	185°	250°	425°
1st June 2016 11:32 - 23:16	CXO HRC	350°	56°	426°

Table 3.1: The observation start and end times and corresponding Central Meridian Longitude (CML) visibility for each observation.

Obs Date	Publication	N Pole Distance /°	Sub-Earth Lat /°	Visible Pole
Dec 2000	Gladstone et al. (2002)	23	0.2	North
Feb 2003	Elsner et al. (2005)	21	3.5	North
Oct 2011	Dunn et al. (2016)	23	3.9	North
April 2014	Kimura et al. (2016)	18	1.7	North
May 2007	This Work	-16	-3.3	South
May 2016	This Work	-17	-1.7	South

Table 3.2: Published Chandra X-ray Campaigns of Jupiter prior to 2016, showing: observation dates, first publication that the X-ray observations were presented in, North Pole Distance Angle at the time of the observations from NASA JPL Horizons (the Pole's angular distance from the sub-observer point (center of disk) at observation time), sub-Earth latitude and which geographic pole presents better visibility for each respective Earth-based observation.

the viewing geometry favoured observations of the Northern aurora. At these times, the sub-Earth latitudes of 0.2°-3.9° and North pole distance angles of 18°-23° obscured visibility of the geographic South Pole. However, during Summer 2016 and March 2007 the tilt of Jupiter relative to the X-ray instruments in Earth orbit allowed clear X-ray observations of Jupiter's Southern geographic pole (North pole angle of -17° and -16° respectively and Sub-Earth Latitude of -1.7° and -3.3° respectively). It is this viewing geometry, which is rare in the legacy X-ray observations of Jupiter, that permitted clear observations of the Southern X-ray hot spot.

We note that the Southern spot is rotating out of view when the Northern spot rotates into view, so that both spots can only be simultaneously observed in their entirety between CMLs 90°-120° and at these times there are still viewing geometry limitations from tilt and possible effects produced by the precipitation/emission-angle.

3.3 A Southern X-ray Hot Spot

3.3.1 2016

As said previously, both Chandra and XMM-Newton time-tag each X-ray photon, which, for Chandra HRC's high spatial resolution, allows Jupiter's X-ray emissions to be connected with the latitude and S3 longitude locations from which they originate. In Figure 3.1, we show projections of the locations of these X-ray emissions on Jupiter's poles. These reveal that both Jupiter's Northern and Southern X-ray auroral emissions are concentrated into hot spots that persistently occur in the same range of S3 latitude-longitude locations (Fig. 3.1 and 3.2). These X-ray hot spots both occur poleward of Jupiter's main UV auroral oval, which is known to be generated by corotation enforcement currents mapping to between 15 and 50 R_J10. The Southern spot (poleward of -67° latitude and between 30°-75° S3 longitude) occurs closer to its respective geographic pole than the Northern spot (60°-75° latitude and 155°-180° S3 longitude(Gladstone et al. 2002). This explains how, in previously published X-ray observations unfavourable viewing meant the Southern hot spot was obscured.

3.3.2 2007

Figure 3.2 shows a projection onto the South Pole from a Chandra ACIS observation on 3rd March 2007. As described in chapter 2, in order to analyse the ACIS data, we applied a correction to the effective area (Dunn et al. 2016; Elsner et al. 2005) to account for the increased energy thresholds applied within ACIS to circumvent optical light leaks through the optical blocking filters. This observation had a lower observer co-latitude (see Table 3.2), offering better visibility of the geographic South Pole than the 2016 campaign. Although the observations from the 2007 campaign were dimmer than those from 2016 and used a different instrument (Chandra ACIS instead of Chandra HRC), the polar projection shows that the X-rays are again concentrated into the Southern hot spot and that this occurs poleward of 70° latitude and between 30°-60° S3 longitude. Studies of eight X-ray observations of the Northern Spot

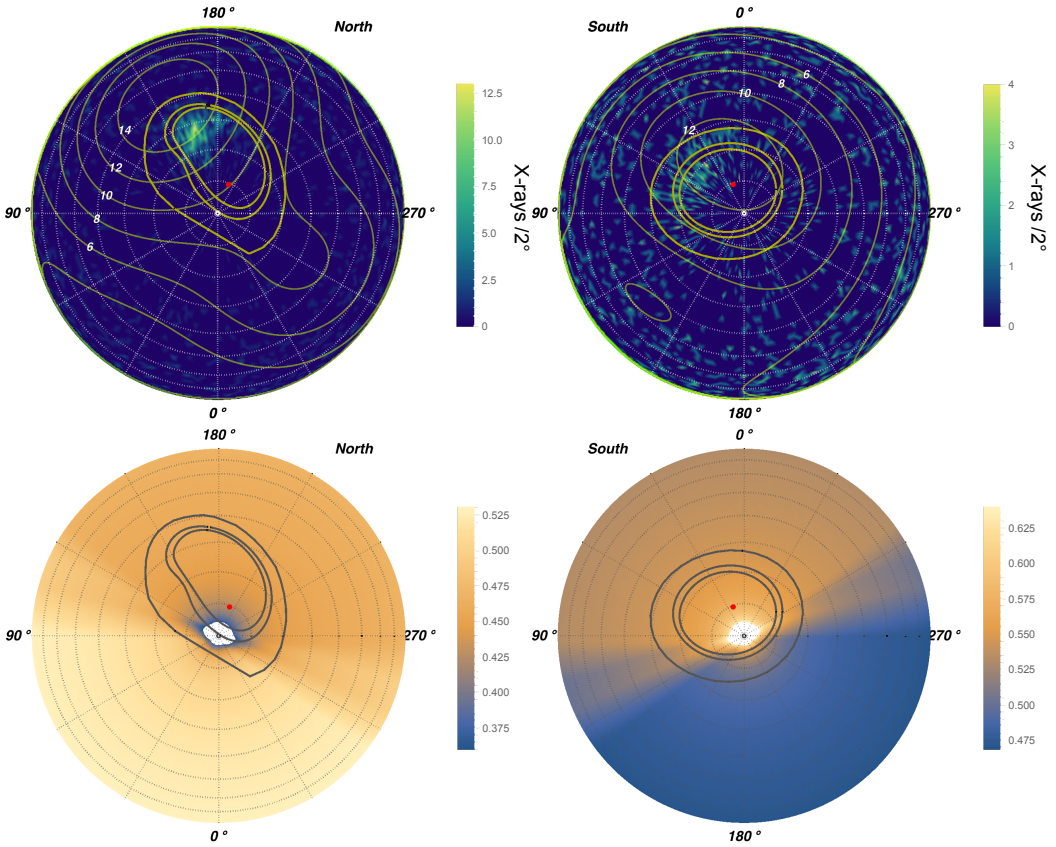

Figure 3.1: *Upper*: Projections centred on Jupiter's North (Left) and South (Right) poles. The projections combine 11-14hr X-ray observations of Jupiter on 24th May and 1st June 2016. Colours indicate the number of X-rays observed with the Chandra HRC in bins of 1.5° by 1.5° of S3 latitude-longitude. Dotted lines of longitude radiate from the pole, increasing clockwise (anti-clockwise) for the North (South) pole in increments of 30° from 0° at the bottom (top). Concentric dotted circles outward from the pole represent 80°, 70° and 60° latitude. Thin gold contours with white text labels indicate the VIP4 model magnetic field strength in Gauss (Connerney et al. 1998). Thick gold contours show the magnetic field ionospheric footprints of field lines intersecting the Jovigraphic equator at 5.9 R_J (Io's orbit), 15 R_J and 50 R_J from equator to pole respectively (Grodent et al. 2008; Vogt et al. 2011). The location of Jupiter's magnetic pole is given by the red dot. These projections reveal that the X-ray aurora is clustered into a hot spot at both poles. The Northern spot is between 155° and 180° longitude and 60° and 75° latitude, as previously observed (Gladstone et al. 2002; Dunn et al. 2016; Branduardi-Raymont et al. 2008; Kimura et al. 2016; Elsner et al. 2005). The Southern spot is longitudinally broader (30°-75°) and poleward of 67° latitude, located closer to the geographic pole. Projection effects lead regions of 1.5° latitude by 1.5° longitude near the poles to appear longer in latitude than in longitude, which leads to the streak-like morphology. This is an artifact of the projection and not a physical feature.
Lower: North (left) and South (right) polar projection exposure maps. The colour bar indicates the fraction of the total observing time during which each region was observed. These show that the clustering of X-rays in the hot spots is not due to additional observation time in these regions.

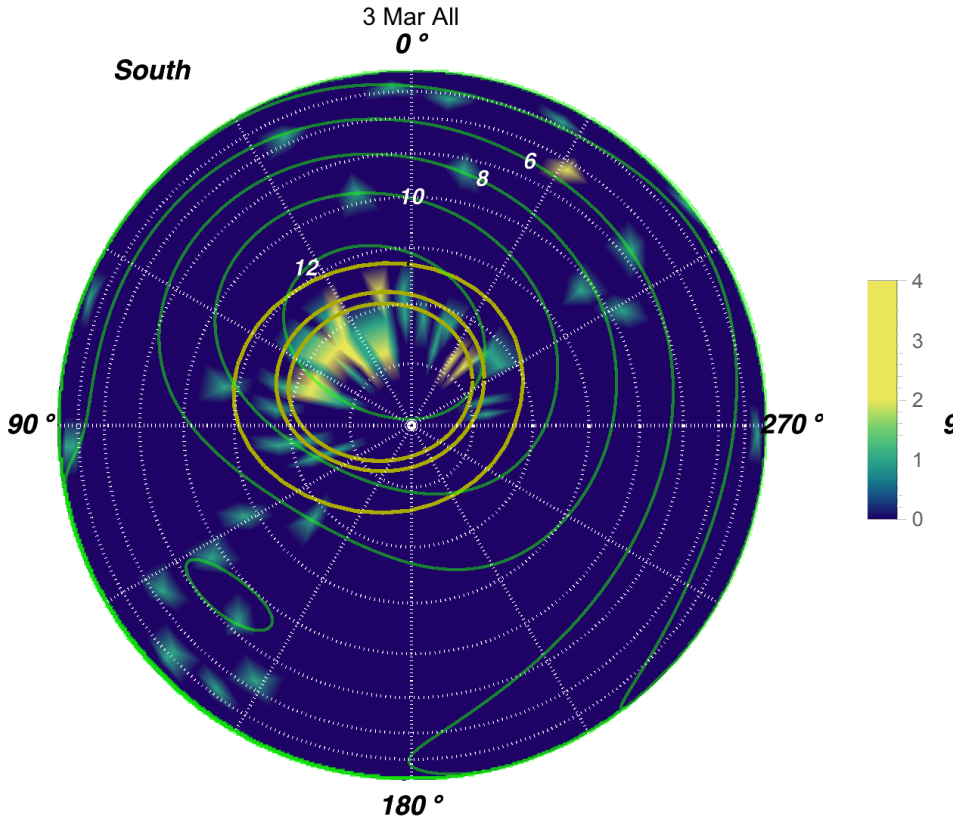

Figure 3.2: Projections centered on Jupiter's South pole from Chandra ACIS observations of Jupiter on 3rd March 2007. The colour bar indicates the number of X-rays in bins of 4° by 4° of S3 latitude-longitude. Dashed lines of longitude radiate from the pole, increasing anti-clockwise in increments of 30° from 0° at the top. Concentric dotted circles outward from the pole represent lines of latitude in increments of 10°. Thin gold contours with white text labels indicate the VIP4 (Connerney et al. 1998) model magnetic field strength in Gauss. Thick gold contours show the magnetic field ionospheric footprints of field lines intersecting the Jovigraphic equator at 5.9 R_J (Io's orbit), 15 R_J and 50 R_J (Grodent et al. 2008; Vogt et al. 2011) from equator to pole respectively. These projections reveal that the X-ray aurora is clustered into a hot spot between 30°-60° S3 Longitude and 70°-80° latitude.

have shown that from observation to observation the hot spot expands and contracts centered on a persistent location (Dunn et al. 2016; Kimura et al. 2016). This may suggest that while the Southern spot is centered on the same location in 2007 and 2016, it also expands and contracts from this location. Alternatively, the apparent expansion in the 2016 observations may be a projection effect produced by the slightly poorer visibility of the region during the 2016 observations relative to the 2007 observations.

Figure 3.3 quantifies the concentrations of X-rays shown in figures 3.1 and 3.2. In the 2016 and 2007 observations the Southern hot spot occurred in the same longitude range, suggesting that it is a persistent feature of the Southern X-ray aurora. We contrast the count concentrations in the auroral zones with emission from fluoresced and scattered solar photons in Jupiter's equatorial atmosphere. This demonstrates that the distributions are not produced by transient variations in the solar X-ray flux. If this were the case then the disk distributions might be expected to match the auroral distributions and they do not. We also plot error bars on the count measurements, highlighting the significance of the spots longitudinal concentrations relative to the more uniform equatorial emission.

3.4 Spectra of the Spots

Analysis of the hot spots XMM-Newton EPIC spectra show that the dominant emissions from both hot spots are from precipitating ions of $O^{7+,8+}$ and $S^{6+...14+}$ and/or $C^{5+,6+}$ and therefore relate to downward current regions (Cravens et al. 2003; Bunce et al. 2004).

We analysed the XMM-Newton EPIC-PN spectral data from May 24th 2016 to identify the source populations of the observed emissions. To do this, we applied the standard High Energy Astrophysics Packages including XMM-SAS and XSPEC. XMM-Newton has lower spatial resolution than Chandra. To circumvent this, we utilised the information from Chandra (from the overlapping interval) on the spatial locations of the spots with visibility information from NASA JPL Horizons ephemerides data to select times that corresponded

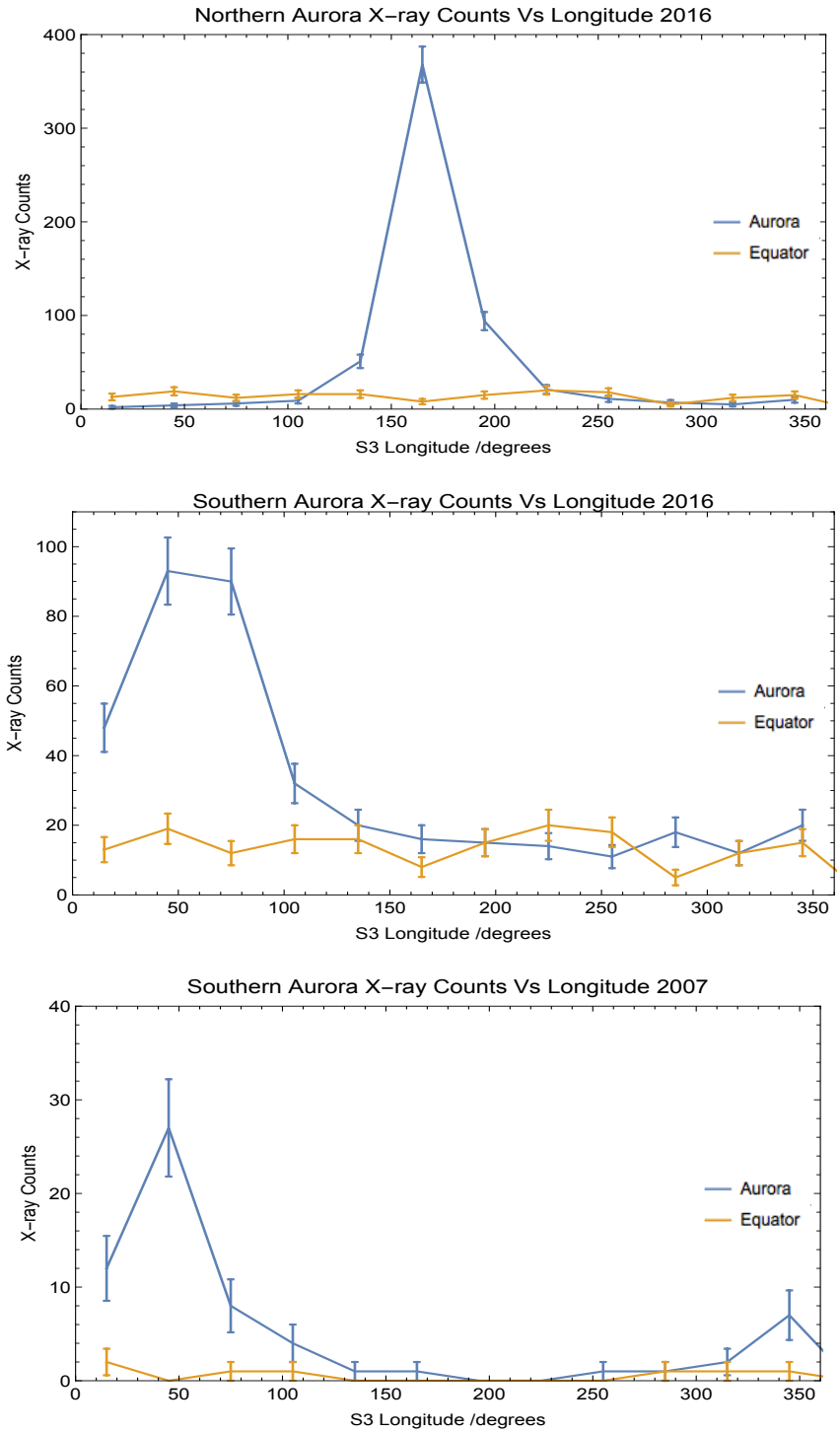

Figure 3.3: X-ray counts per 30° longitude from Jupiter's Northern and Southern aurora (blue), poleward of 60° and -60° latitude respectively, are contrasted with counts from a band at -3° to 3° latitude (gold), where solar X-rays fluoresce and are scattered from the Jovian atmosphere (Bhardwaj et al. 2005, 2006; Branduardi-Raymont et al. 2007b). Upper (Middle): 24th May and 1st June 2016 Northern (Southern) auroral emission combined. X-ray emission peaks in both auroral hot spots. Lower: Southern X-ray auroral emission from 3rd March 2007. Error bars are from Poisson statistics. 2016 data are from CXO HRC, while 2007 data are from CXO-ACIS. The auroral X-ray hot spot concentrations are unrelated to distributions in disk emission. We note that the disk emission was reduced for the 2007 observations because of a period of particularly dim X-ray emission from the Sun during solar minimum, which led to less incident photons that could fluoresce and scatter in Jupiter's atmosphere.

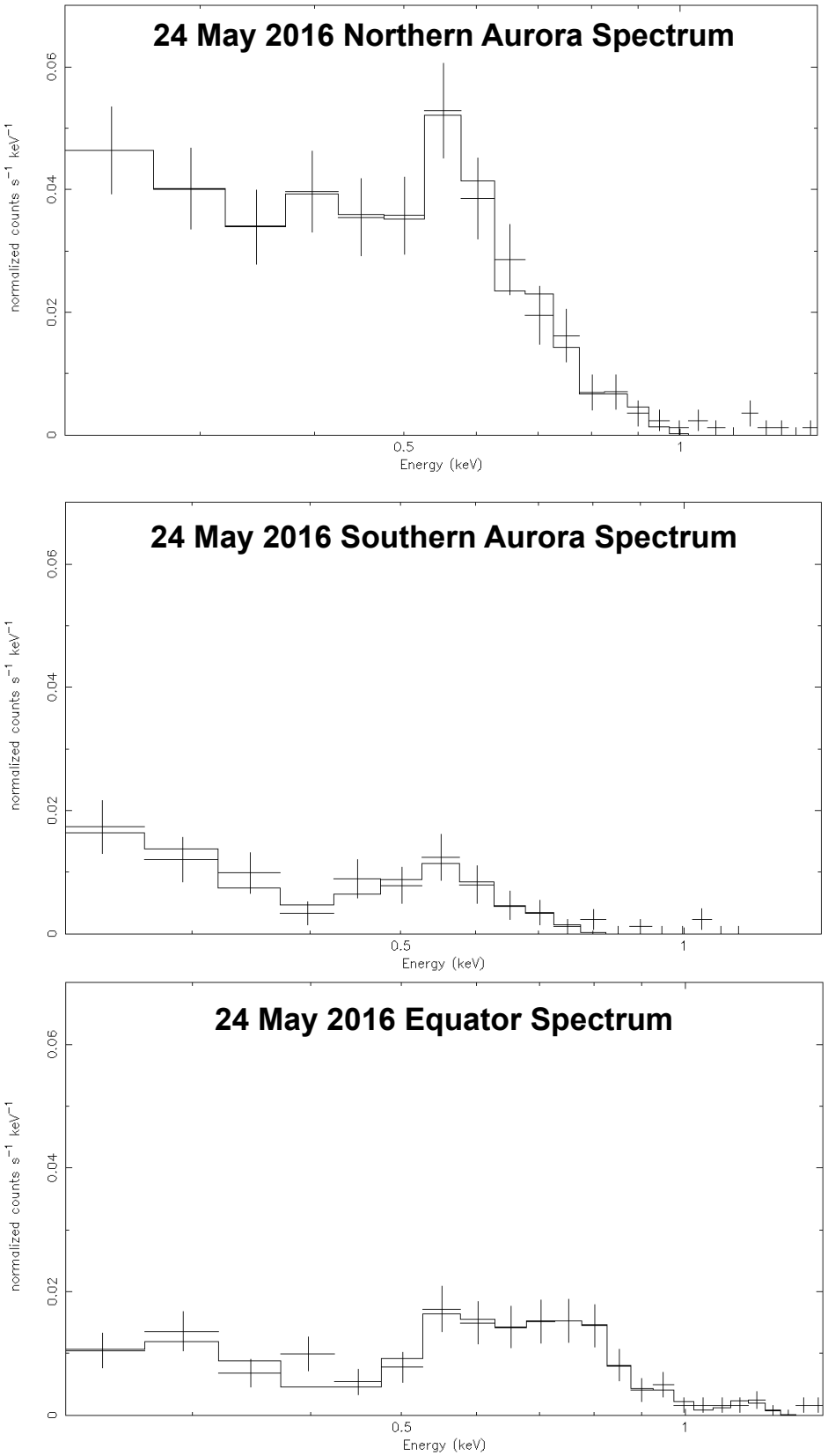

Figure 3.4: The Northern (upper) and Southern (middle) auroral and Jovian equatorial (lower) spectra. Best fit model lines are shown over-plotted onto the data from XMM-Newton's EPIC-PN instrument on May 24th 2016. Tables 3.3, 3.4 and 3.5 show the best fit model parameters respectively for each spectrum.

Line Energy (eV)	Flux (10^{-6} photons/cm^2/s)	Known Ion Rest Frame Energies
294^{+30}_{-60}	120^{+60}_{-50}	S VI-X (260-291,314,316 eV) and/or C V (299,304-308 eV)
430^{+30}_{-30}	20^{+10}_{-9}	C VI (435, 459 eV)
568^{+18}_{-18}	20^{+5}_{-5}	O VII (561, 568, 574 eV)
707^{+30}_{-40}	6^{+3}_{-2}	O VII (665,698,713 eV)
860^{+70}_{-40}	2^{+1}_{-1}	O VIII (817, 836 eV)

Table 3.3: Northern Aurora Best-Fit Model with reduced χ^2 of 0.7 (χ^2 of 7 for 12 Degrees of Freedom (DoF) and Null Hypothesis Probability of 0.9). Table shows best-fit model parameters and closest known ion rest frame lines (Elsner et al. 2005; Branduardi-Raymont et al. 2007a; Kharchenko et al. 2006, 2008) with line half widths held constant at 20 eV (Elsner et al. 2005). Quoted errors indicate the 90% confidence values. A slightly better fit could be attained with very low flux ($\sim 10^{-7}$) lines at 1040 eV and 1220 eV. However, the 90% confidence levels in the locations of these additional lines could not be attained due to the model fit being insensitive to the low fluxes of the lines. These additional lines are close to the Ne X and Fe XXI solar emission lines that are found on Jupiter's disk (Branduardi-Raymont et al. 2007b), so may indicate that any contamination from scattered solar photons is at a very low level.

Line Energy (eV)	Flux (10^{-6} photons/cm^2/s)	Known Ion Rest Frame Energies
301^{+30}_{-40}	60^{+30}_{-30}	S VI-X (260-291,314,316 eV) and/or C V (299,304-308 eV) S IX-XIV (336-348 eV)
470^{+70}_{-70}	2.5^{+3}_{-2}	C VI (435, 459 eV)
568^{+50}_{-50}	5^{+3}_{-3}	O VII (561, 568, 574 eV)
694^{+150}_{-150}	1.5^{+2}_{-1}	O VII (665,698,713 eV) and/or OVIII (654,774 eV)

Table 3.4: Southern Aurora Best-Fit Model with reduced χ^2 of 0.7 (χ^2 of 7 for 12 DoF and Null Hypothesis Probability of 0.9). Table shows best-fit model parameters and closest known ion rest frame lines (Elsner et al. 2005; Branduardi-Raymont et al. 2007a; Kharchenko et al. 2006, 2008) with line half widths held constant at 20 eV (Elsner et al. 2005). Quoted errors indicate the 90% confidence values. Quoted errors indicate the 90% confidence values for the best-fit model parameters. A slightly better fit could be attained with the listed line at 470 $^{+70}_{-70}$ eV. However, the signal to noise on this line led 90% confidence levels to be insensitive to this lines location.

Line Energy (eV)	Flux (10^{-6} photons/cm^2/s)	Known Ion Rest Frame Energies
320^{+50}_{-30}	30^{+20}_{-20}	S VI-X (260-291,314,316 eV)
		and/or C V (299, 304?308 eV)
570^{+20}_{-40}	7^{+2}_{-3}	O VII (561, 568, 574 eV)
690^{+50}_{-100}	4^{+2}_{-2}	O VII (665,698,713 eV)
		and/or OVIII (654,774 eV)
		and/or Fe XVI-FeXVIII (704-791 eV)
790^{+50}_{-30}	4^{+2}_{-2}	Fe XVII-Fe XIX (740-840 eV)
940^{+70}_{-50}	$0.9^{+0.6}_{-0.5}$	Fe XVIII-XIX, Ni XIX-XX,
		Ne VII-Ne X (890-1010 eV)
1154^{+50}_{-70}	$0.9^{+0.3}_{-0.3}$	Fe XVII-XXIV, Ni XXI,
		Na X (1083-1174 eV)
1390^{+50}_{-50}	$0.9^{+0.3}_{-0.3}$	Mg X-XI, Ne X (1330-1450 eV)

Table 3.5: Jupiter's Disk Emission Best-Fit Model with reduced χ^2 of 0.6 (χ^2 of 13 for 21 DoF and Null Hypothesis Probability of 0.9). Table shows best-fit model parameters and closest known ion rest frame lines (Elsner et al. 2005; Branduardi-Raymont et al. 2007a; Kharchenko et al. 2006, 2008; Phillips, K.J.H.; Leibacher, J.W.; Wolfson, C.J.; Parkinson, J.H.; Fawcett, B.C.; Kent, B.J.; Mason, H.E.; Acton, L.W.; Culhane, J.L.; Gabriel 1982) with line half widths held constant at 20 eV (Elsner et al. 2005). Quoted errors indicate the 90% confidence values for the best-fit model parameters. We also attempted to force fits with a line at 0.4 but these always led to worsening the reduced χ^2 by at least 0.5. Solar X-ray emission lines are found to be a good fit to the equatorial spectra.

to CML ranges when the hot spots were on Jupiter's observable disk. For XMM-Newton, for the North (South) we extracted hot spot spectra from times when the CML ranges were 60°-270° (300°-170°). The time intervals outside of these windows were checked to ensure that the X-ray emission was evenly distributed across Jupiter's entire disk and no significant auroral concentrations were lost. Given the dynamic nature of the hot spots, we only used the longest observation window and did not combine the shorter partial observation windows with this. This disregarding of times when the hot spot was unobservable is an alteration from previous spectral studies (Branduardi-Raymont et al. 2007a, 2004) that allowed us to minimise contamination from scattered solar photons and provided a more accurate calculation of X-ray emission rates from the aurora only.

Using the standard XMM-SAS package, we then selected the appropriate source regions for the Northern and Southern aurora from a planet-centered image and extracted the relevant spectral products (spectral data from source region, spectral data from background region, auxiliary response and redis-

tribution matrix files). To ensure there were sufficient counts to reliably fit models, we binned the data into 10-channel energy bins. Using the XSPEC modelling package, we then tested fits for a combination of different Gaussian lines and bremsstrahlung continuum to a non-background subtracted spectrum (Jupiter's disk blocks background emission (Elsner et al. 2005)).

To distinguish between auroral emission and potential contamination in the polar region from solar photons fluoresced/scattered in Jupiter's atmosphere, we also extracted the Equatorial emission by using the same time window as the auroral emissions. Given the low count rates, we used an equatorial spectrum that covered the times when either hot spot was observable (sub-observer longitude 300°-270°). Modelling of the Equatorial spectrum showed clearly distinctive features from the auroral emissions, indicating that the auroral spectra were dominated by a different emission process (i.e. not fluorescence and scattering of solar photons). Figure 3.4 and tables 3.3,3.4 and 3.5 show the spectra and best-fit models for the North, South and Equatorial best-fit models.

A bremsstrahlung continuum was found to not improve any fits for the Northern or Southern auroral emission, suggesting that both observed hot spots are dominated by spectral lines from precipitating ions.

It was challenging to directly compare the Northern and Southern aurora spectra due to the low count levels for the South, but both the North (Table 3.3) and South (Table 3.4) best-fit models feature a prominent and well-defined O VII line centred on 568 eV and a high flux line in the region where a range of sulphur and carbon lines are present. Both aurora best-fit models also include a line at 430-470 eV where there are known C VI lines. Interestingly, Carbon is much more abundant in the solar wind than in Jupiter's magnetosphere so this could suggest some direct solar wind precipitation. However, we note that the 90% confidence errors on the fluxes for this specific line are 50% of the measured flux for the North and more than this for the South. This 430-470 eV line coincides with the lowest data point between 200-900 eV on the equatorial spectrum, suggesting that it is not contamination from scattered solar photons, but is a part of the auroral spectrum. The equatorial spectrum

(Fig. 3.4) does hint at the presence of a line at 400 eV and we attempted to force model fits to this but these always led to worse fits and increased the reduced χ^2 by at least 0.5.

As with previous Jovian disk analysis (Branduardi-Raymont et al. 2007b), we could attain a good fit (reduced χ^2 of $\sim$0.7) to the equatorial spectrum from 500-1500 eV with a vmekal hot plasma model using solar abundances and kT $\sim$ 0.3 and flux of $\sim$ 9 x 10^{-7} photons $cm^{-2}s^{-1}$. To further compare with the auroral emission in Fig. 3.4, we show a spectral line fit with known solar spectrum lines (Phillips, K.J.H.; Leibacher, J.W.; Wolfson, C.J.; Parkinson, J.H.; Fawcett, B.C.; Kent, B.J.; Mason, H.E.; Acton, L.W.; Culhane, J.L.; Gabriel 1982) this demonstrates that the equatorial emission has a very different structure from the auroral one above 600 eV. If the observed and modelled auroral emissions were due to contamination, then one would not expect the auroral emissions to decrease at energies above 600 eV as they do.

3.5 Independent Temporal Behaviour in Each Spot

Figure 3.5 shows the complete Northern and Southern auroral lightcurves for the 24 May (Chandra and XMM-Newton) and 1 June (Chandra) 2016. For Chandra, the lightcurves from the Northern spot were produced by extracting X-rays from 155°-190° longitude and poleward of 60° latitude. For the South, the lightcurves were extracted from 20°-70° longitude and poleward of -60° latitude.

The lightcurves from XMM-Newton's EPIC contain more noise than the Chandra HRC lightcurves because EPIC's lower spatial resolution leads to additional contamination from fluoresced and scattered solar X-ray photons on Jupiter's disk. This limited spatial resolution also prevents lightcurves from being extracted based on System III coordinate locations. There are also different energy-dependent responses and effective areas for XMM-Newton's EPIC and Chandra's HRC and ACIS instruments, which may lead to differing lightcurve morphology for each instrument.

The lightcurves have been binned into 1-minute time bins and smoothed

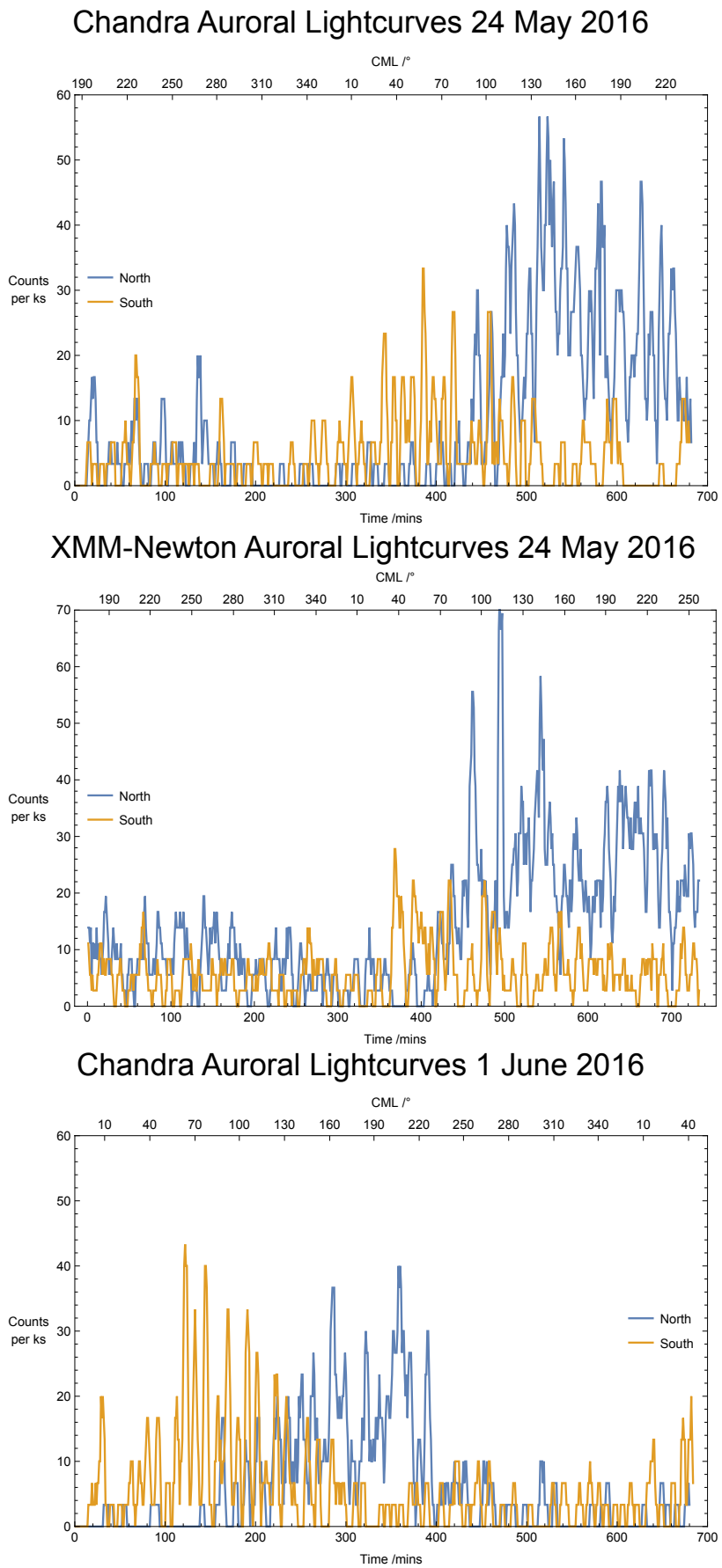

Figure 3.5: Lightcurves from the entire observation of Jupiter's North (blue) and South (gold) aurora from Chandra HRC on 24 May and 1 June 2016 (top and bottom) and XMM-Newton's EPIC-pn on 24 May 2016 (middle). CML is provided along the top of each plot. Time along the bottom is in minutes from the observation start time (see Table 3.1)

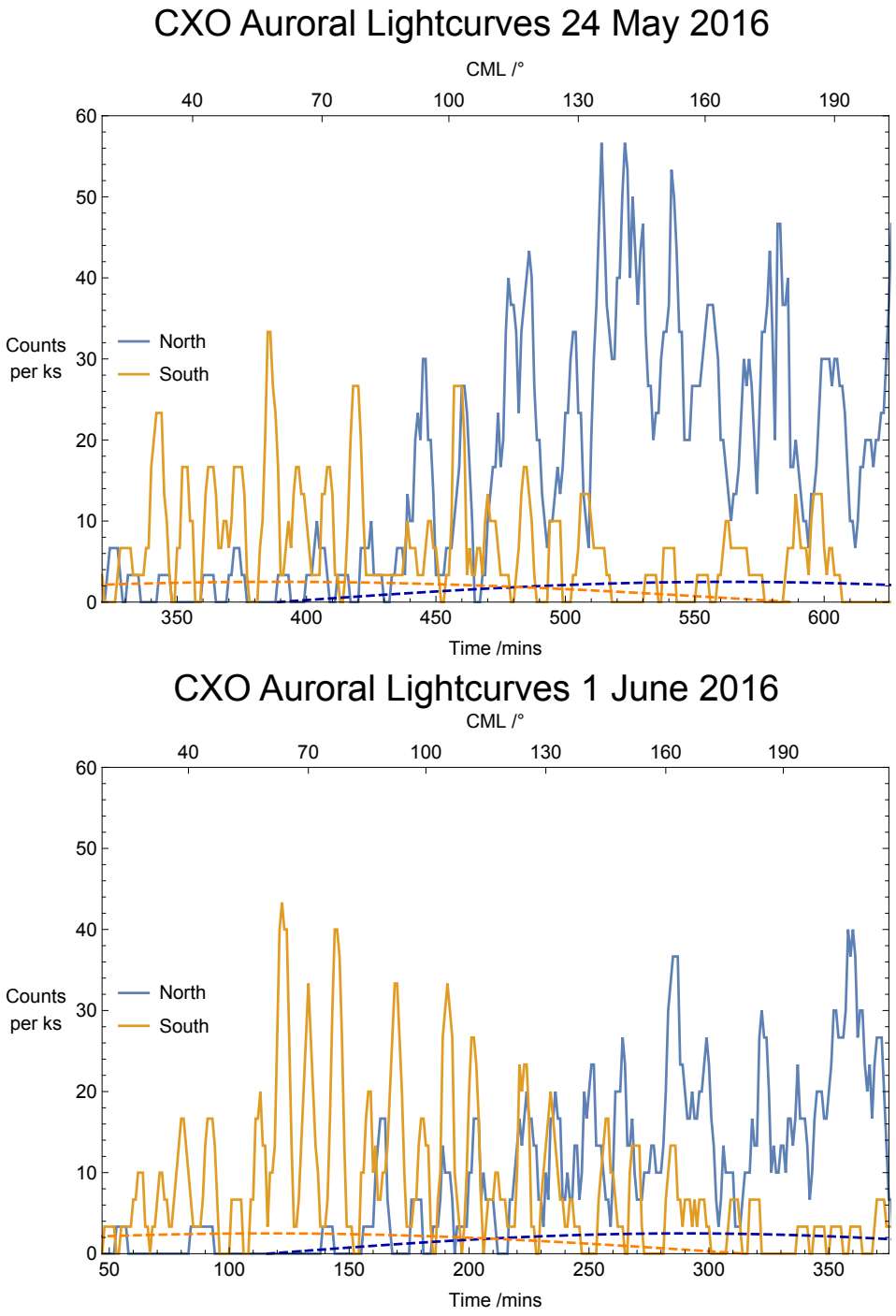

Figure 3.6: Chandra X-ray lightcurves from times when the Northern (blue) and Southern (gold) hot spots were both observable on 24th May 2016 (upper) and 1st June 2016 (lower). The visibility as a fraction of maximum visibility for the Northern (blue) or Southern (gold) hot spot is indicated by the dashed curves. Central Meridian Longitude is indicated across the top, while minutes from the observation start times (10:23 and 11:32 UT, respectively) are indicated on the x-axis. The lightcurves are 1-minute binned, with 6-minute moving-average smoothing.

over a 6 minute moving average window. These reveal the characteristic pulsations of each pole. Figure 3.6 show these lightcurves at times when both spots are on Jupiter's observable disk (∼CML 90°-120°). These lightcurves show that the X-ray spots sometimes pulse together (e.g. minute 460, 24 May), but also often pulse independently (e.g. minute 420-450 and 470-500 24 May). This means that knowledge of whether one hot spot brightens does not help to predict whether its counterpart also brightens.

The Northern X-ray spot has been observed to pulse either irregularly (Branduardi-Raymont et al. 2007a; Elsner et al. 2005; Kimura et al. 2016) or with regular periods of 12, 26 or 40-45 minutes (Gladstone et al. (2002) and Chapter 2). In order to provide quantitative estimates of the periodicities in each of the hot spots for these observations, a Fourier transform was performed on the raw unsmoothed time series to produce power spectral density (PSD) plots (Fig. 3.7). The XMM-Newton Southern (Northern) Power Spectral Densities were produced from Fourier transforms of the same time window as that used for Chandra - 300-500 minute (450-700 minute) unsmoothed data that produced the lightcurves (Fig. 3.5). We note that this is different from previous searches for periodicity in the XMM-Newton data, where the whole lightcurve has been used.

These PSDs show that on both 24th May and 1st June 2016 the Southern spot pulsed with statistically significant regular periods of 9-11-min. This is the first time a period has been observed to recur in subsequent X-ray observations and the first time a Jovian auroral period has been detected in XMM-Newton observations. A Northern 12-min periodicity in the X-ray brightness was previously observed during a magnetospheric compression (see Chapter 2). The recurrence of a 9-12 min and 40-45-min (Gladstone et al. (2002) and Chapter 2) period across multiple observations may suggest bimodal regular periodicity.

Surprisingly, while the 9-11 min Southern spot period is highly statistically significant in both observations (probability of chance occurrence (PCO) 10^{-5}-10^{-7}), the Northern spot pulsations show no significant 11-min period on 24th May and only a low- significance 12-min period (PCO 10^{-2}) on 1st June. The

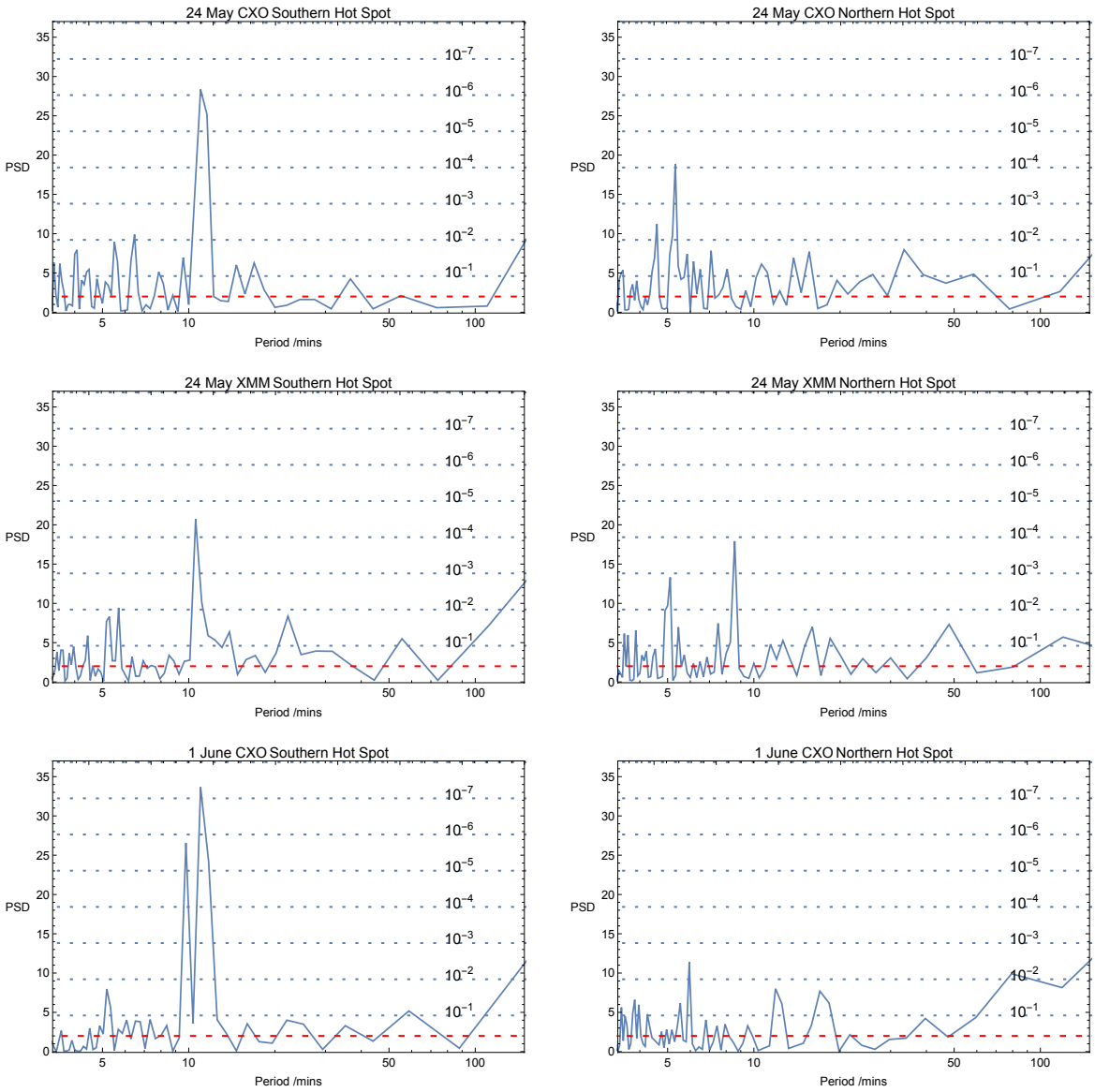

Figure 3.7: Power Spectral Density plots from fast Fourier transforms of unsmoothed X-ray lightcurves from the Southern (left) and Northern (right) X-ray hot spots in 2016. PSDs are shown from Chandra observations on 24th May (upper), simultaneous XMM-Newton observations on 24th May (middle) and from Chandra observations 1st June (lower). The dotted horizontal lines show single-frequency probabilities of chance occurrence (PCO) for the detected periods (Leahy et al. 1983). The lowest statistical significance and highest PCO of 10^{-1} is at the bottom of the plot. The dashed red line shows the value obtained if photons from a steady source were randomly distributed over the visibility period. Lightcurves were extracted from 20-70° longitude and poleward of -60° latitude for the South and from 155-180° longitude and poleward of 60° latitude for the Northern hot spot. For XMM, with poorer spatial resolution and therefore subject to increased contamination from the disk emission, the lightcurves are extracted from the same time window as the CXO observations.

Hot Spot	Date	Counts	Visibility Duration /ks	Counts /second
N	24 May 1st Visit	21 ± 5	5.5	0.004
N	24 May 2nd Visit	298 ± 17	14.3	0.021
N	1 June Only Visit	189 ± 14	16.5	0.011
S	24 May Only Visit	79 ± 9	17.9	0.004
S	1 June 1st Visit	111 ± 11	13.4	0.008
S	1 June 2nd Visit	18 ± 4	8.7	0.002

Table 3.6: Chandra X-ray hot spot counts extracted from the hot spot during each window when the hot spot could be observed. Each X-ray observation was longer than 1 full Jupiter rotation, so that the Northern or Southern hot spot was observed partially twice in each observation.

North does exhibit some lower significance (PCO greater than 10^{-4}) 5-8 min periods, but these are not consistent across hemispheres or instruments.

The periodicity is not the only characteristic that appears to behave independently for each spot during these observations. The lightcurves (Fig. 3.5 and 3.6) also show that the brightnesses of the two spots are uncorrelated. We observed 78±9 X-ray photons from the Southern spot during the first CXO observation and 111±11 X-ray photons during the second observation i.e. a ∼40% increase in X-ray emission. In contrast, we observed 298±17 X-rays from the Northern spot during the first observation, but only 189±14 X-rays during the second observation - emission decreased by ∼40%.

Given that each observation continuously covered 1.2 Jupiter rotations this meant that, for both observations, Jupiter's Northern and Southern hot spots were observed at least once, and the 24th May (1st June) observation partially observed Jupiter's Northern (Southern) hot spot a second time. To ensure that we did not artificially enhance the X-ray counts by including multiple visits to the same spot (two visits to the North on 24th May and two to the South on 1st June), in each observation we extracted counts only from the longest duration window of these two possible observing windows (see table 3.6 for complete counts).

To test the reliability of the results from the Northern and Southern X-ray hots spots, we contrasted them with lightcurves and PSDs from Jupiter's disk, where emissions are produced by solar photons that are fluoresced and scattered in Jupiter's atmosphere (Bhardwaj et al. 2005, 2006; Branduardi-

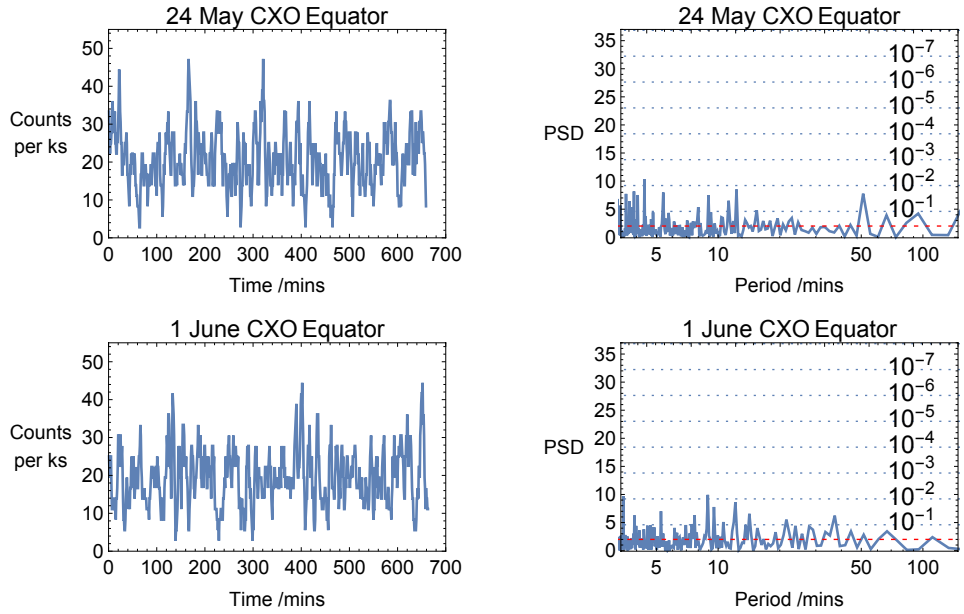

Figure 3.8: Lightcurves (left) and Power Spectral Density plots (right) from Jupiter's Equator on 24 May (top) and 1 June (bottom) 2016 from Chandra (CXO) High Resolution Camera.

Raymont et al. 2007b). Lightcurves and PSDs from the Jovian equator on 24 May (DoY 145) and 1 June (DoY 153) (Fig. 3.8) between -30° and 30° latitude demonstrate that the periodic behaviour is not present in the equatorial region and that there was not a significant variation in the solar X-ray output (e.g. from solar flares) during the observations (Bhardwaj et al. 2005, 2006; Branduardi-Raymont et al. 2007b; Dunn et al. 2016).

3.6 Mapping the Twin Spots

To more precisely identify the sources for these precipitating ions and the associated downward currents, as in Chapter 2, we use a flux equivalence mapping model(Vogt et al. 2011, 2015; Grodent et al. 2008; Connerney et al. 1998) to connect magnetic field lines in the ionosphere with the equatorial magnetosphere (using the Northern Grodent Anomaly (Grodent et al. 2008) and Southern VIP4 (Connerney et al. 1998) models). Our Northern distribution (Fig. 3.9) matches that shown previously (Chapter 2 and Kimura et al. (2016), with the precipitating ions originating beyond 60 Jupiter Radii (RJ) and between 10:00 and 19:00 Magnetospheric Local Time (MLT). The Southern spot

also maps beyond 60RJ, but is concentrated between 10:00 and 14:00 MLT and it then rotates out of view before we have the opportunity to observe it mapping to later MLTs. If, as with the Northern spot, Southern X-rays continue to be triggered when the spot maps along the afternoon-dusk flank, this emission would be unobservable from Earth, addressing why fewer X-rays are almost always observed from the South (Waite et al. 1994). This broader local time origin for the Northern spot may also explain the distinctive temporal signatures shown in Fig. 3.5, 3.6 and 3.7 since more sources regions/processes may be involved along the dusk flank.

As discussed previously, Jupiter's magnetopause has a typical subsolar standoff distance of 60-90RJ, depending on the solar wind dynamic pressure (Joy et al. 2002). The flux equivalence mapping (Vogt et al. 2011, 2015; Grodent et al. 2008; Connerney et al. 1998) is calculated using magnetic field observations averaged over all solar wind conditions so that emission mapping beyond 60R_J could indicate ions precipitating on closed field lines from the outer magnetosphere and/or field lines that are open to the solar wind, depending on solar wind conditions at the time. Of the X-rays in each spot, 30-60% of photons mapped to locations beyond the modelled expanded magnetopause location and are thus not shown on Fig 3.9.

3.7 Discussion and Possible Drivers

Currently, the favoured explanation for the Northern X-ray hot spot is that it is the signature of Jupiter's Northern cusp (Bunce et al. 2004; Elsner et al. 2005; Dunn et al. 2016; Kimura et al. 2016) i.e. the dayside region of the magnetosphere that is open to the solar wind. It might therefore follow that Jupiter's Southern spot locates Jupiter's Southern cusp. For fast solar wind, X-rays are proposed to be generated in this cusp region by vortical flows from pulsed reconnection at the dayside magnetopause (Bunce et al. 2004). As previously discussed, these flows alter the downward currents into the ionosphere and produce ∼MV field-aligned potential drops (Cravens et al. 2003). These potential drops can accelerate ∼2 keV O2+ ions (Bagenal 1994a) in the

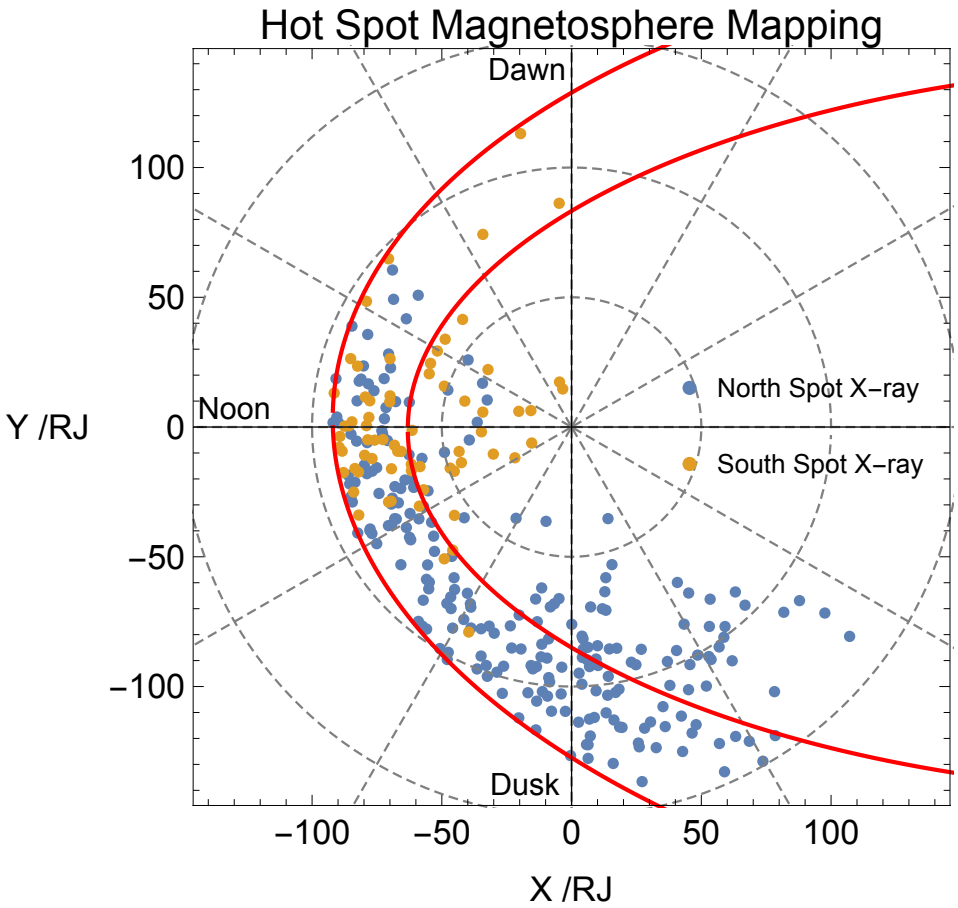

Figure 3.9: Mapping of Ionospheric X-ray photon emission to the equatorial magnetosphere source regions for the Northern (Blue) and Southern (Gold) hot spots. The solid red lines indicate Jupiter's magnetopause, for an expanded 92 RJ, standoff distance (outer contour) and compressed 63 RJ standoff distance (inner contour) (Joy et al. 2002). We also note that even for the statistical location of the expanded magnetopause, because of the substantial spatial extent of the hot spots, 30%-60% of X-rays mapped beyond the magnetopause, meaning that their origins cannot be identified by the model mapping and they are not plotted here.

outer magnetosphere to the 16-32 MeV (1-2 MeV/amu) needed for Jupiter's atmosphere to strip electrons and produce the observed O^{6+} X-ray K-shell line emissions (Branduardi-Raymont et al. 2007a; Cravens et al. 2003; Kharchenko et al. 2006, 2008). If reconnection pulses occur at Jupiter's 30-50 min Alfvén wave transit timescale it is suggested that this mechanism could also explain the 45-min X-ray periodicity (Bunce et al. 2004).

However, there are a varied set of challenges that need to be overcome in order for pulsed dayside reconnection to explain the generation of Jupiter's X-ray hot spots in the observations reported here: 1) the 9-12-min periodicity observed is on a shorter timescale than predicted (Bunce et al. 2004); 2) for subsolar point reconnection, both poles should pulse periodically in-phase (Bunce et al. 2004), but the dominant periodicity in the South does not also dominate the Northern lightcurves (Fig. 3.7) and North-South pulsations often appear to be independent of one another (Fig. 3.5 and 3.6) 3) the overall brightness of the Northern spot appears to be uncorrelated to the overall brightness of the Southern spot (Fig. 3.5 and 3.6 and Table 3.6) 4) a more general challenge to the proposed pulsed reconnection mechanism is that it explains X-ray emissions during fast solar wind conditions, but previously X-rays have also been observed during slow solar wind conditions (Chapter 2 and Kimura et al. (2016)). To address these challenges, here we propose adaptations and alternative mechanisms to explain the observed X-ray hot spot emissions during these observations.

Differing pulsation periods for each pole could be produced by orientations of the Interplanetary Magnetic Field that do not favour subsolar reconnection (Bunce et al. 2004). At Saturn, tension associated with east-west motion of field lines during off-equatorial reconnection can produce transient non-conjugate enhancements in UV polar auroral brightness by disrupting field-aligned currents in the respective poles (Meredith et al. 2013) (Figure and caption is included here in Fig. 3.10).

High-latitude anti-parallel reconnection may also provide non-conjugacy. Lobe reconnection has been debated (McComas and Bagenal 2007; Cowley et al. 2008; McComas and Bagenal 2008) as Jupiter's dominant solar-wind re-

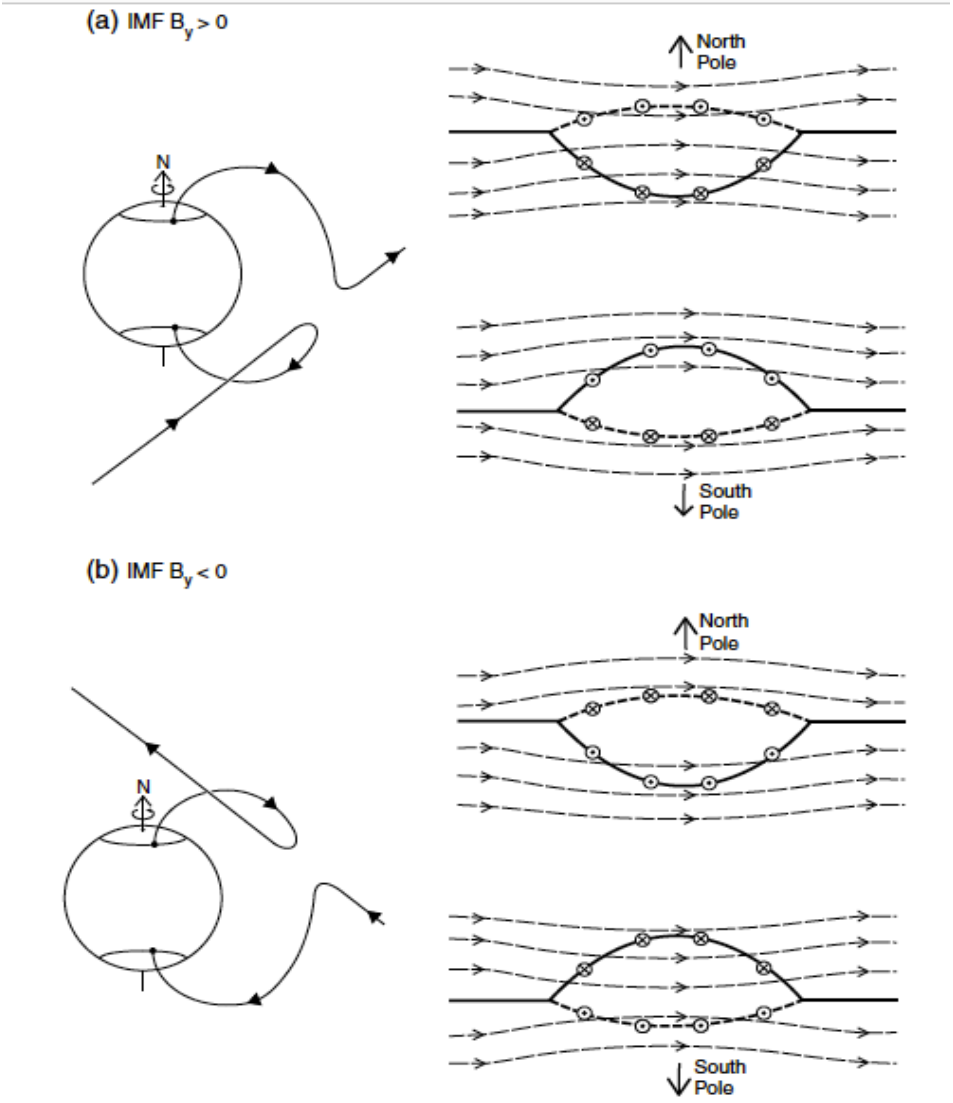

Figure 3.10: Figure from Meredith et al. (2013): Sketches illustrating the North-South asymmetries on newly opened flux tubes due to the presence of IMF B_y, where it shows the cases of (a) positive and (b) negative IMF B_y (and positive B_z). The sketches on the left in each panel show newly-opened field lines in the postnoon sector in each case, in views looking from the direction of the Sun, showing the senses of the field tension force associated with the east-west field. For near-antiparallel reconnection, the reconnection site is displaced into the southern hemisphere for positive B_y and into the northern hemisphere for negative B_y, as shown. The effects on the plasma flow and currents in the northern and southern ionospheres are sketched in the upper and lower diagrams on the right in each panel, respectively. The solid lines show the open-closed boundary in each hemisphere, displaced equatorward in the central region by the reconnection event forming the equatorward limit of the patches of new open flux, while the short dashed lines show the former boundary marking the poleward limit of the patches, perturbed poleward as they transfer into the polar cap. The arrowed long-dashed lines show plasma streamlines, while the circled dots and crosses show the regions of upward and downward field-aligned currents, respectively, on the boundary of the open patch.

connection process. This is predominantly because the planet's immense size, rapid rotation and internal plasma source lead to long relative timescales for return flows from an Earth-like Dungey cycle, and, under certain conditions, suppress dayside reconnection (Desroche et al. 2012). For high-latitude reconnection, reconnected/closing lobe field lines may travel equatorward across the cusp and into the dayside magnetosphere (Lockwood and Moen 1999; Fuselier et al. 2012). This could explain the large spatial extent of the X-ray spots. Asymmetric high-latitude reconnection can also produce a persistent reconnection site over one pole and a moving reconnection site over the other pole. This may explain the contrasting regular 9-11 min X-ray period in the South and irregular pulsations in the North. Sub-solar dayside reconnection can produce X-rays from high charge-state magnetosheath/solar wind ions on open field lines, but these emissions are calculated to be orders of magnitude fainter than the total X-ray brightness observed (Cravens et al. 2003; Bunce et al. 2004). However, certain topologies of high-latitude reconnection may offer additional acceleration mechanisms, since stretched or twisted lobe/open field lines closing and dipolarising in the outer magnetosphere could energise ions through Fermi acceleration.

Kelvin Helmholtz Instabilities (KHIs) are thought to occur at Jupiter's magnetopause (Johnson et al. 2014b; Delamere and Bagenal 2010a,b; Desroche et al. 2012), offering an alternative mechanism capable of explaining the periodic X-ray signatures (Dunn et al. 2016; Kimura et al. 2016). For Earth's magnetosphere, KHIs can trigger magnetopause fluctuations and excite compressional ULF magnetic field oscillations and field line resonances, driving standing Alfvn waves in the ionosphere (Rae et al. 2005; Mann et al. 2002). At Jupiter, ULF waves have been observed with 10-20 min periodicity (Khurana and Kivelson 1989c; Wilson and Dougherty 2000b), the lower bound of which matches our 9-12 min X-ray pulsations. The periodicity of ULF oscillations depends on the magnitude of the magnetospheric cavity, velocity shear and thickness of the interaction boundary. At Jupiter, the size of the magnetosphere varies bi-modally (Joy et al. 2002) between compressed and expanded states (respective standoff distances: 60-90RJ). This could explain

the bimodal 9-12-min and 40-45-min X-ray aurora periodicity. If the thickness of the magnetopause boundary and velocity shear were similar on 24th May and 1st June, then KHI-driven Alfvén waves could produce recurring periodicity. Moreover, KHI could generate different brightening in each pole by driving oppositely-directed field-aligned currents in each hemisphere through Ampere's law (see Fig. 3.11). KHIs remain to be fully explored at Jupiter, including the possibility of MeV/amu acceleration required for the observed X-ray signatures. However, wave-particle interactions, KHI-driven reconnection and/or modulation of current systems and their associated potential drops are all possible acceleration mechanisms.

The Southern X-ray spot rotates out of view while the Northern spot rotates into view, so that both are observable simultaneously only when they approach opposite limbs of Jupiter's observable disk. If the two spots are globally driven, then arguably the simplest explanation for the North-South differences is that magnetospheric conditions changed with time and damped the 11-min Southern period. Whether the differences are due to changes with time or due to differing polar dynamics, localised magnetic conditions at each pole may also play some part in ensuring MeV/amu ion acceleration is produced only in the hot spots and not in any other auroral region. For instance the Northern spot is located close to a region of surface magnetic field strength of 10-14 G, while the Southern spot occupies a region of 10-12 G. It may be that the differing magnetic field strength produces differing mirror points and differing voltages. Although this cannot explain the lack of correlation in brightening between the two, it may explain why the North is always brighter.

These findings also highlight possible multi-wavelength connections for Jupiter's aurora. UV polar auroral flares (Bonfond et al. 2011) sometimes coincide with X-ray brightenings (Elsner et al. 2005) and, like the X-ray pulsations, quasi-periodically brighten on timescales close to 10 minutes (Nichols et al. 2017) . It has been suggested (Nichols et al. 2017) that some of these UV pulsations may relate to tail reconnection, which could explain the duskward mapping for the X-ray emissions for the Northern hot spot. The mapping further suggests that additional X-ray generation processes connected with

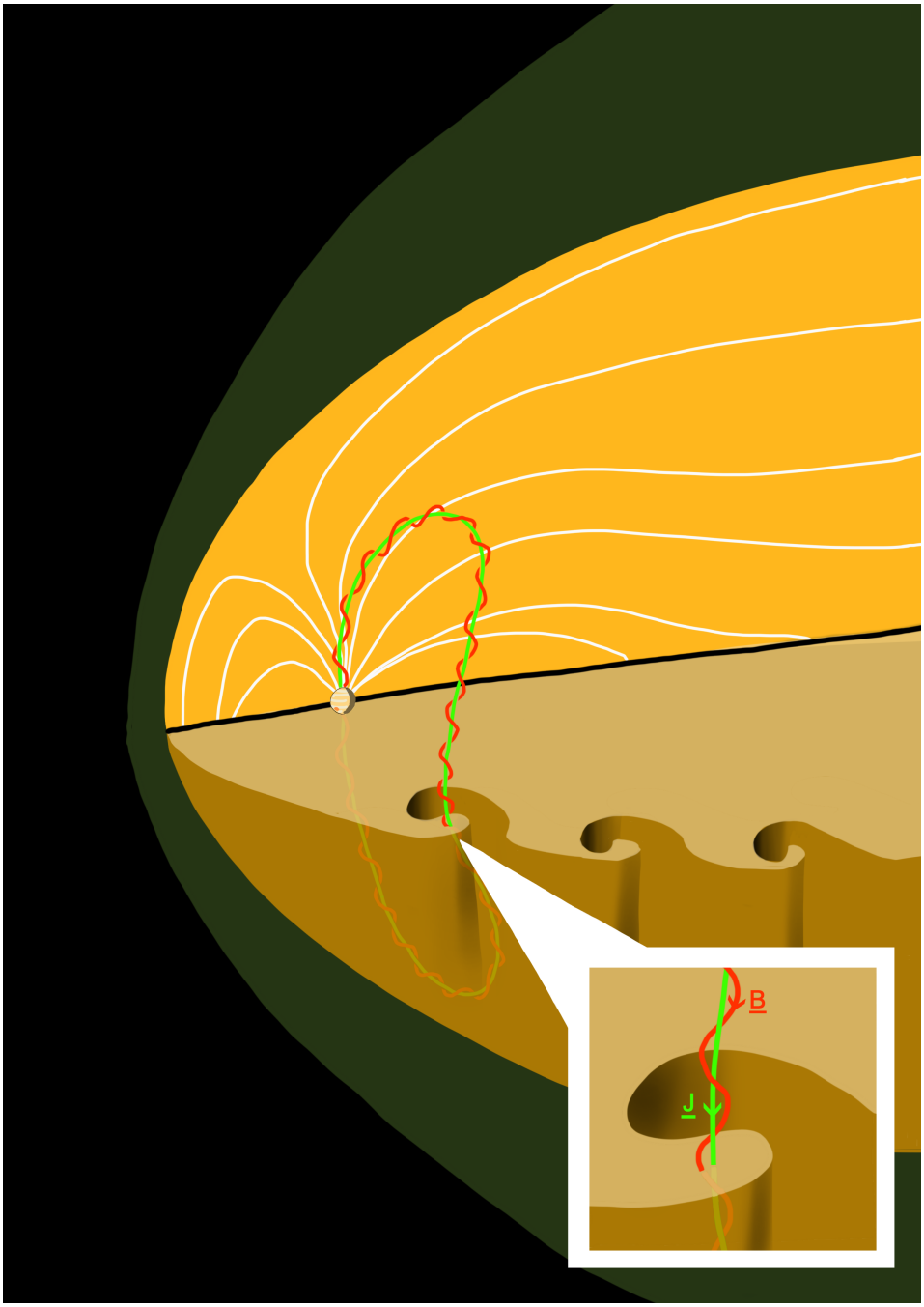

Figure 3.11: An illustration (Image Credit: G. Jones) of a possible source mechanism for the observed hot spot emissions. Kelvin Helmholtz Instabilities along the magnetopause could produce field line resonances that generate regular periodicity in the emissions. Further, these field line resonances could vary bi-modally with the compressed or expanded states of Jupiter's magnetosphere. These Kelvin Helmholtz instabilities may also generate non-conjugate North-South auroral signatures, since twisting of the magnetic field line (illustrated in red) can generate inter-hemispheric currents (green).

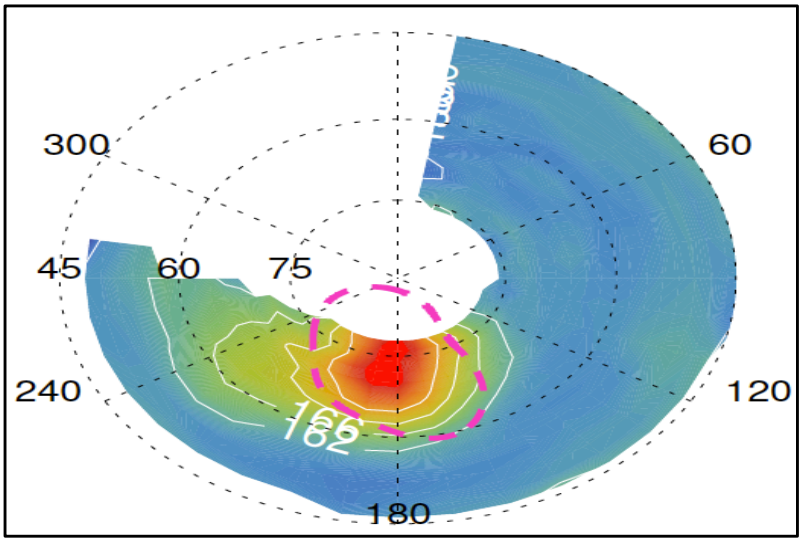

Figure 3.12: An IR hot spot in the methane layer of the atmosphere. Figure adapted from Sinclair et al. (2017).

the dusk-flank and tail would be unobservable for the South and therefore would not complicate the Southern temporal signatures. Bright infrared auroral hot spots are also co-located with the X-ray hot spots (Sinclair et al. 2017), which may suggest that the pulses of ∼MeV/amu ion precipitation, and their associated drivers, provide an important heating mechanism for Jupiter's stratosphere down to the 10-mbar pressure level (Sinclair et al. 2017) (see Fig. 3.12).

We note that both of the observations presented here were during solar wind compressions (see Nichols et al. 2017). This may lend some credence to the idea that the 9-13 minute period relates to a compressed magnetosphere. We also note that the 45 minute period detected during the December 2000 observation (Gladstone et al. 2002) was accompanied by upstream measurements from Cassini which suggest that the Jovian magnetosphere would have been in an expanded state (priv comms. A. Masters).

The independent behaviour of Jupiter's pair of X-ray hot spots during these observations raises fundamental questions about what processes at rapidly rotating magnetospheres produce these aurorae. For Jupiter, the precipitating ion spectral signatures suggest that the spots locate Jupiter's downward currents (Cravens et al. 2003) and may identify the Northern and South-

ern Cusps (Bunce et al. 2004). However, the observed distinctive behaviour could be indicative of non-equatorial reconnection, magnetopause-driven ULF waves, tail reconnection or local magnetic conditions at each polar region. Over the coming 2 years, X-ray observing campaigns in conjunction with NASA's Juno mission will offer the opportunity to determine whether the independent behaviour that we report here is commonplace or rare. Critically, such campaigns will help to identify the magnetospheric conditions and auroral processes that are able to generate Jupiter's highest-energy emissions and the seemingly independent behaviour of the Northern and Southern X-ray hot spots.

Chapter 4

Jupiter's X-ray Aurora During Solar Minimum

"The Universe doesn't owe you tidy conclusions."
— Ales Kot, *The Surface*

4.1 Abstract

The solar minimum from 2007-2009 is the deepest and longest of the space age. Here we present X-ray observations of Jupiter during February and March 2007, when the New Horizons spacecraft was approaching the planet and measuring the solar wind velocity. We find that the X-ray emission from Jupiter's equatorial regions is exceptionally dim relative to non-solar minimum X-ray observations. This is expected, since the low solar X-ray flux would produce lower levels of scattered or fluoresced X-rays. We also find that the X-ray aurora is generally dim, but brightens or dims by a factor of 2 from observation-to-observation.

During these 6 Chandra observations, New Horizons measured the approach of Corotating Interaction Regions, which resulted in the incidence of 3 solar wind compressions at Jupiter. One of these coincided with an X-ray observation (24-25 Feb). During this compression, the X-ray aurora brightened and, as observed previously during solar wind compressions (see Chapters 2 and 3), exhibited pulsations on a regular 9-13 minute timescale, suggesting that this is a characteristic timescale for the Jovian aurora during solar wind

compressions. At the time of this brightening, contemporaneous (not simultaneous) Hubble UV observations show that Jupiter had a bright polar dusk arc, which exhibited pulsations in the X-ray hot spot region on a similar timescale to those in the X-ray observation one Jupiter rotation later. When a UV dawn storm and bright polar dusk arc are present, the hard X-ray emission is brighter, shifted to higher latitudes and located near to/across the soft X-ray hot spot. Some of the UV emissions have morphology that is spot/patch-like and close to noon, while others are bifurcations from the arc that stretch into the darker polar cap. We suggest that these connect with the X-ray pulsations and that the spot/patch like short-timescale emissions are from the cusp on an expanded polar cap and thus occur at lower latitudes than normal. The bifurcations may represent opening/closing of flux on the magnetopause or in the tail or variations/turbulence in flow shears along the dusk outer magnetosphere.

The 24 Feb X-ray observation occurs 1 day after the arrival of a CIR, from which our analysis of the UV observations suggests there is a 3-4 day timescale of evolving auroral emissions. Observations on the 8th Feb, 10th Feb and 8th March all occur 3-5 days after the arrival of a shock and show different spectral, temporal and spatial characteristics. This could allow us to trace the development of the X-ray aurora during recovery and subsequent magnetospheric expansion. However, with limited HST observations at this time, only solar wind velocity data and with greater than 2 day uncertainties in propagation models, it is challenging to conclusively tie these to drivers. With additional observations during quiescent solar wind conditions, it might be possible to better interpret these results. The 3 March observation is during solar wind rarefaction and shows very dim UV and X-ray polar auroral emission. It provides the first simultaneous UV-X-ray observation of the Southern aurora, but this is not very informative due to the very low X-ray count rates at the time. For each observation we present polar projections and magnetosphere-ionosphere mapping for distinct precipitating species along with colour ratios. However, the dim auroral emissions at this time make it challenging to derive firm results from the colour ratios.

Finally, we note that the solar wind velocity is lower for the brightest X-ray observations and higher during the dimmer observations, suggesting that there may not be a direct positive correlation between Jovian auroral X-rays and solar wind velocity alone, as suggested in previous work. Instead, other parameters or the combination of parameters might need to be considered. We close by suggesting that the X-ray aurora is produced by both cusp processes and possibly also tail reconnection processes that are 'switched-on' by solar wind compressions. If this is true, then it may also be possible for mass-loading by Io to drive tail reconnection and produce X-ray auroral brightening independent of the solar wind.

4.2 Introduction

Dunn et al. (2016), Kimura et al. (2016) and Branduardi-Raymont et al. (2007a) all report relationships between solar wind parameters and Jupiter's X-ray aurora. Using XMM-Newton, Branduardi-Raymont et al. (2007a) found that hard and soft X-ray emission increased during a period of heightened solar wind conditions. Dunn et al. (2016) find significant changes in the auroral emissions during the arrival of an Interplanetary Coronal Mass Ejection (ICME) and Kimura et al. (2016) note correlations between solar wind parameters and the X-ray aurora.

However, Dunn et al. (2016) rely on only two observations to identify connections between Jupiter's X-ray emission and the solar wind, while Kimura et al. (2016) find a marginal solar wind correlation based on only one outlier datapoin (see Fig. 4.1). Further, the findings of these two works are contradictory. Kimura et al. (2016) suggest that the X-ray aurora is connected to solar wind velocity and not with the solar wind density/dynamic pressure (see Fig. 4.1). In contrast, Dunn et al. (2016) (see first research chapter) show that significant changes in X-ray emissions are connected with an increase in density and a rotation in the magnetic field, but with very little change in solar wind velocity. As shown in the thesis introduction, it is likely that these solar wind parameters are coupled, so it may not be possible to treat them

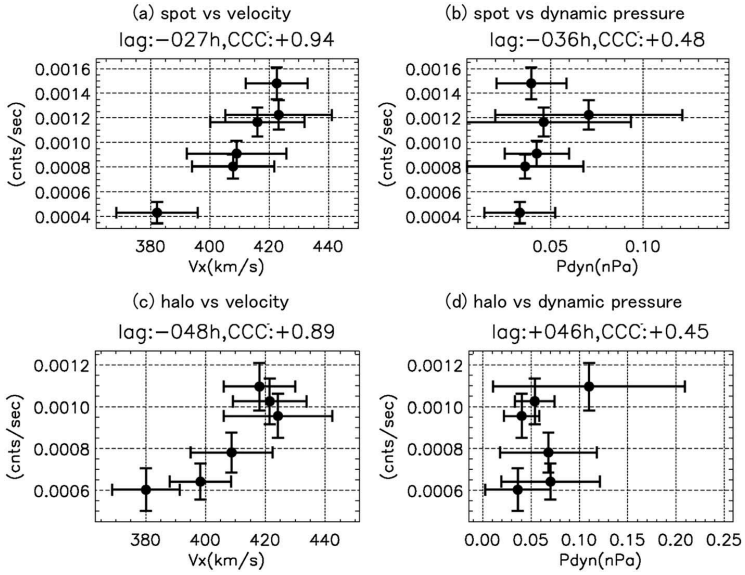

Figure 4.1: From Kimura et al. (2016): Scatterplots of the X-ray count rates and solar wind parameters. (a) The hot spot count rates as a function of solar wind velocity. The solar wind velocity is averaged over ±48 h from the count rate measurement time. The error bars in the velocity are standard deviations of the time series that span ±48 h from the count rate measurement time. The error bars in the count rate are estimated based on the photon statistics.

independently.

The challenge faced by Dunn et al. (2016) and Kimura et al. (2016) is that the observations occurred in the absence of upstream solar wind measurements, which forced both authors to utilise models that propagate solar wind conditions from measurements at 1 AU to Jupiter at 5 AU. These models have large uncertainties on the time at which solar wind conditions arrive at Jupiter (Dunn et al. (2016) ±10 - 15 hours, Kimura et al. (2016) ± 48 hours) making it difficult to correlate specific solar wind parameters to auroral variation. More importantly, these models can only propagate 1 of 3 spatial components of the solar wind magnetic field, while the possible occurrence and location of reconnection depends on all 3 IMF components, among other factors.

To address whether a connection with solar wind parameters exists, it is important to systematically relate solar wind conditions with X-ray aurora and preferably to do this while there are upstream measurements of Jupiter's solar wind conditions. In February and March 2007, NASA's New Horizons spacecraft was approaching Jupiter and conducting measurements of the solar

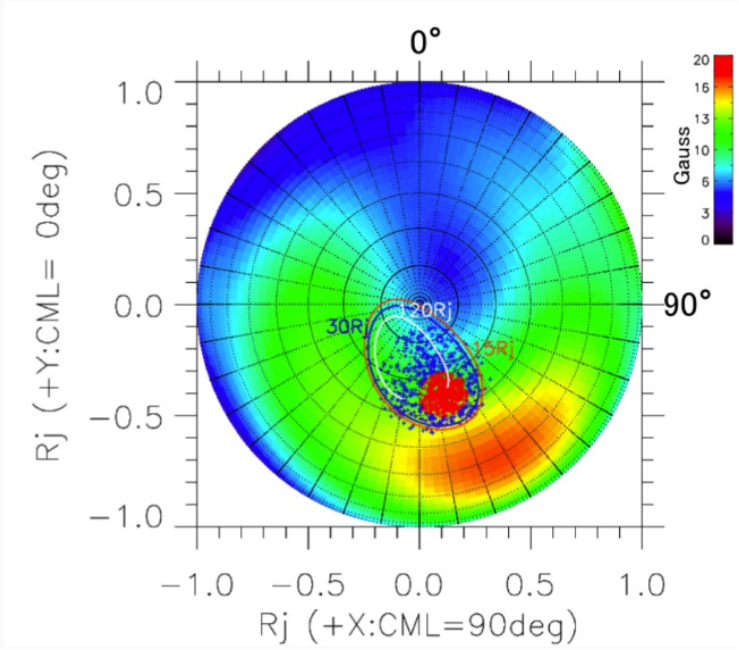

Figure 4.2: From Kimura et al. (2016): Polar Projection of X-ray photons in S3 coordinates from Chandra observations between 8-20 April 2014. The background coloured contours indicate the magnitude of the magnetic field strength provided by the VIPAL model (Hess et al., 2011). The x-axis is in the meridian plane at S3 longitude of 90°, and the y-axis is in the meridian plane of 0. The interval of the latitudinal grids is 10°. The orange, blue, and white lines indicate latitudes from which magnetic field lines map to radial distances of 15, 30, and 120 R_J in the equatorial magnetosphere, respectively. Red points indicate the 'core' region where the photon density is the highest. Blue points indicate the 'halo' region, where the photons are more sparse, surrounding the core region.

wind velocity. Around this time, there were 6 Chandra ACIS X-ray observations of Jupiter and XMM-Newton observations were coincident with four of these (included in the masters thesis of V. Carter-Cortez). In this chapter, we compare the upstream solar wind velocity measured by New Horizons SWAP instrument with the X-ray emissions.

Kimura et al. (2016) also studied the distribution of X-ray emission from the hot spot region during a campaign of 6 observations in 2014. They defined a central concentration of photons that is emitted from the hot spot, which they call the 'core' region (Fig. 4.2). They also define a more sparse distribution of emission surrounding the core which they call the 'halo' region.

Another way to constrain the processes driving Jupiter's aurora is through comparison of different wave-bands. The last simultaneous X-ray-Hubble Space Telescope (HST) observation in 2003 led to 2 discoveries: hard X-rays overlap the UV main emission (Branduardi-Raymont et al. 2008) and UV polar

Obs ID	Start - End Time	DoY	CML Start - End	NP Ang/Dist
7405	8 Feb 08:30:49 - 13:46:56	39	94°-286°	6/-16.1°
8216	10 Feb 19:54:26 - 11 Feb 01:21:10	41-42	88°-286°	5.9/-16.2°
8217	24 Feb 21:24:20 - 25 Feb 02:17:20	55-56	90°-267°	5/-16.9°
8219	3 Mar 07:42:32 - 13:02:32	62	286°-120°	4.7/-17.2°
8220	7 Mar 14:18:56 - 19:07:35	66	48°-223°	4.5/-17.4
8218	8 Mar 21:03:31 - 9 Mar 02:45:26	67-68	83°-290°	4.5/-17.5

Table 4.1: The observation start and end times and corresponding Central Meridian Longitude (CML) visibility for each Chandra ACIS observation in 2007.

flares coincide with X-rays (Elsner et al. 2005). Drivers for this UV region have been proposed (e.g. Bonfond et al. (2011); Nichols et al. (2017); Pallier and Prangé (2001)), so further UV-X-ray links help to constrain these physical drivers. Here, we present UV-X-ray comparisons based on UV observations conducted by HST in 2007 (e.g. Nichols et al. (2009a)).

4.3 Jupiter's X-ray Aurora in 2007

4.3.1 The Observations

During February and March 2007, Chandra's ACIS instrument conducted six X-ray observations of Jupiter. Table 4.1 shows the start/end times and CML coverage of each observation. At this time, Jupiter's sub-observer latitude was -3.31°(NASA JPL Horizons Ephemerides data) and the observation durations were shorter than those from 2011 and 2016 and only covered ~ 0.5 Jupiter rotations each. The first 3 observations and last observation provided similar viewing geometry - all favouring visibility of the Northern Hot Spot, with little coverage of the Southern spot. The observation on 3rd of March offered very limited coverage of the Northern spot, but excellent visibility of the southern spot (as discussed in the previous chapter). The observation on 7 March provided only moderate coverage of both regions. For all of these observations the previously discussed combination of red-leak through the ACIS Optical Blocking Filter and contaminant build-up had to be accounted for in the manner described in Chapter 2 and Elsner et al. (2005).

As shown previously, Chandra ACIS provides both spatial and spectral

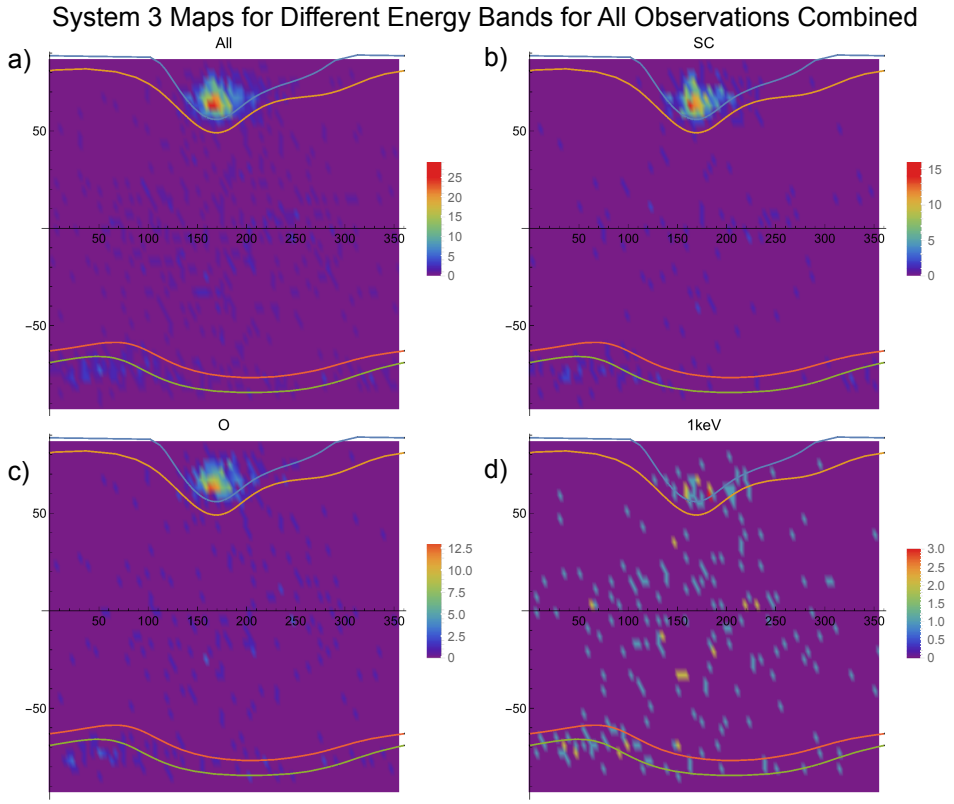

Figure 4.3: System III Maps of Jupiter's X-rays for a) all of the X-ray emission, b) X-rays with energies between 0.2-0.5 keV (sulphur/carbon emission), c) 0.5-0.9 keV (oxygen emission) and d) above 1 keV (hard X-ray bremsstrahlung from electron precipitation). The emissions in the equatorial regions are produced by fluoresced and scattered solar X-ray photons.

resolution, which allows us to compare the spatial locations of specific precipitating particle populations. The spatial and temporal resolution of Chandra allows emitted X-rays to be re-registered to System III latitude-longitude positions from which they originate. Figure 4.3 shows System III latitude-longitude maps of Jupiter's X-rays for distinct energy bands between 0.2-0.5 keV (sulphur/carbon emission), 0.5-0.9 keV (oxygen emission) and above 1 keV (hard X-ray bremsstrahlung from electron precipitation) for all of the 2007 observations combined. It should be noted that 4 of the 6 observations favour visibility of the Northern aurora, so the distinction between the brightness of the North and South is not accurately represented by these maps. The maps reveal that, as observed previously, the 0.2-1 keV X-ray emission is concentrated into a hot spot poleward of the UV main oval. The auroral hard X-rays from precipitating electrons are concentrated in the main oval region (between the contours), with a small number of events also in the hot spot.

4.3.2 Auroral Spectra

Following the method of Chapter 2, the X-ray spectra were extracted from the Northern and Southern aurora using CIAO and XSPEC software packages. Low levels of auroral counts made it challenging to model the spectra. Figure 4.4 shows the un-binned spectra, which retain the spectral details, while figure 4.5 shows spectra binned by a minimum of 10 counts per bin in order to fit spectral models. We do not show models for 3rd and 7th March because the counts were so low that models had more parameters than spectral data points. The spectra (Fig. 4.4, 4.5 and Tables 4.2 and 4.3) show a few key spectral differences across the campaign which we summarise here:

1. There appears to be a difference in behaviour between 0.2-0.4 keV (e.g. Fig. 4.4). An abrupt decrease at 0.3 keV for 10th of Feb (Fig. 4.4b) is contrasted by the more gradual decline that is observed for 8th and 24th Feb (Fig. 4.4c and f respectively), suggesting the presence of different sulphur and/or carbon lines. The general profile and intensity of this part of the spectra varies from observation to observation.

2. There appears to be a line between 0.43-0.5 keV that is present on the 10th

and 24th Feb and 8th March (Fig. 4.4b, c and f respectively), but is very dim (if present) on 8th Feb ((Fig. 4.4a). This line was also present in the 2016 observation, but was otherwise previously unreported.

3. 0.55-0.61 keV lines are always present with a peak between 0.02-0.04 counts per sec per keV.

4. There is significant variation in the lines between 0.62-0.9 keV, which seems to occur somewhat independently of the ∼0.56 keV emission. This seems surprising since any O^{7+} emitting between 0.62-0.8 keV would be expected to continue to charge exchange and also emit OVII lines at 0.55-0.61 keV, unless opacity prevented the subsequent OVII emission being observed. This may imply a distinct population of O^{6+} from a distinct energy regime.

5. The 24 Feb and 8 March observations (Fig. 4.4c and f respectively) have the brightest OVIII emission which implies that the aurora was more energetic at these times. At the same epochs the flux below 0.4 keV is also enhanced suggesting higher contributions of sulphur/carbon lines.

It is strange that the 2007 Chandra ACIS observations appear to record higher fluxes than the XMM-Newton observations from 2016 (see Table 4.3. However, we note that the Chandra fluxes are comparable to those reported by Elsner et al. (2005), while the XMM-Newton fluxes are comparable to those reported by Branduardi-Raymont et al. (2007a). The differences between the Chandra and XMM-Newton spectra are explored further in V. Carter-Cortez's 2017 Masters thesis (supervised by W. Dunn and G. Branduardi-Raymont) and a more detailed Chandra/XMM-Newton cross-calibration is forthcoming. Rather than focussing on the absolute values, we have therefore chosen to focus on the relative values here.

4.3.3 Polar Projections

Figure 4.6 shows projections of the X-ray photon locations on the Jovian Northern and Southern poles for all of the observations combined. These are divided by energy with 0.2-0.5 keV (sulphur/carbon emission) in red, 0.5-0.9 keV (oxygen emission) in blue, and above 1 keV (hard X-ray bremsstrahlung from electron precipitation) in yellow. The precipitating ions are located in

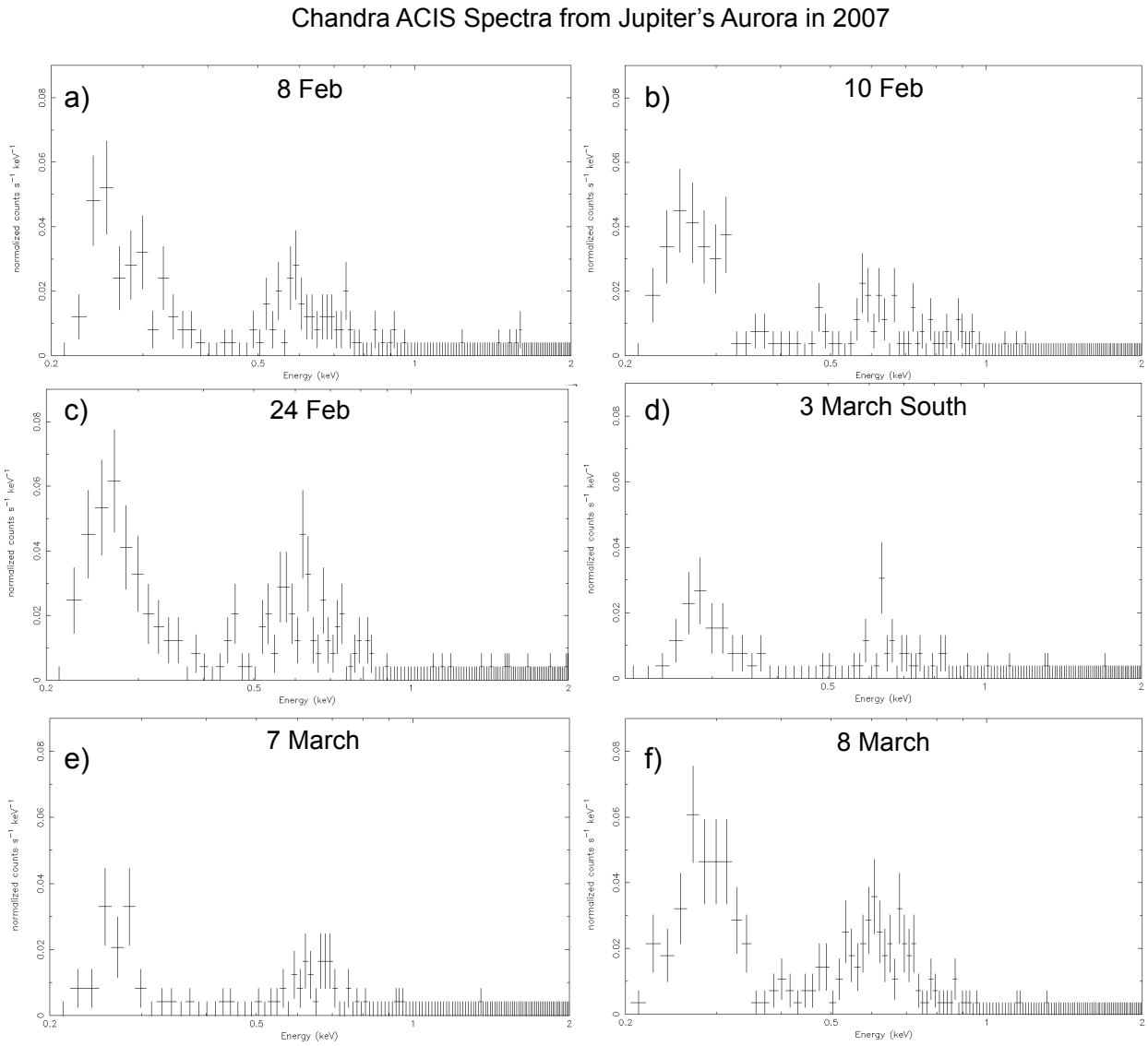

Figure 4.4: Un-binned Spectra from the Chandra ACIS observations of the Jovian Northern X-ray Aurora on 8, 10, 24 Feb and 7, 8 March 2007 and from the Southern X-ray aurora on 3 March.

Ion Source	8 Feb	10 Feb	24 Feb	8 March	XMM 24 May 2016
S/C	297^{+10}_{-10}	302^{+10}_{-10}	300^{+10}_{-70}	305^{+10}_{-10}	294^{+30}_{-60}
S/C	(351)	-	(340)	-	-
C?	-	-	456^{+40}_{-100}	485^{+50}_{-40}	430^{+30}_{-30}
OVII	585^{+20}_{-20}	580^{+20}_{-20}	598^{+20}_{-25}	592^{+30}_{-30}	568^{+18}_{-18}
OVIII	727^{+30}_{-20}	729^{+35}_{-25}	727^{+25}_{-25}	689^{+35}_{-20}	707^{+30}_{-40}
OVIII	-	933^{+25}_{-25}	(861)	871^{+25}_{-25}	860^{+70}_{-40}

Table 4.2: Northern Aurora Best-Fit Model line Energies in eV with reduced χ^2 of 0.2 - 0.7 for the various models. The model fits can be seen overplotted on the data in Fig. 4.5. Lines in the best fit model are shown with quoted errors indicating the 90% confidence values for the best-fit model parameters. Lines that were also good fits but were not in the best fit model are shown without errors and in parentheses, in order to differentiate them. Line widths were frozen at 20 eV.

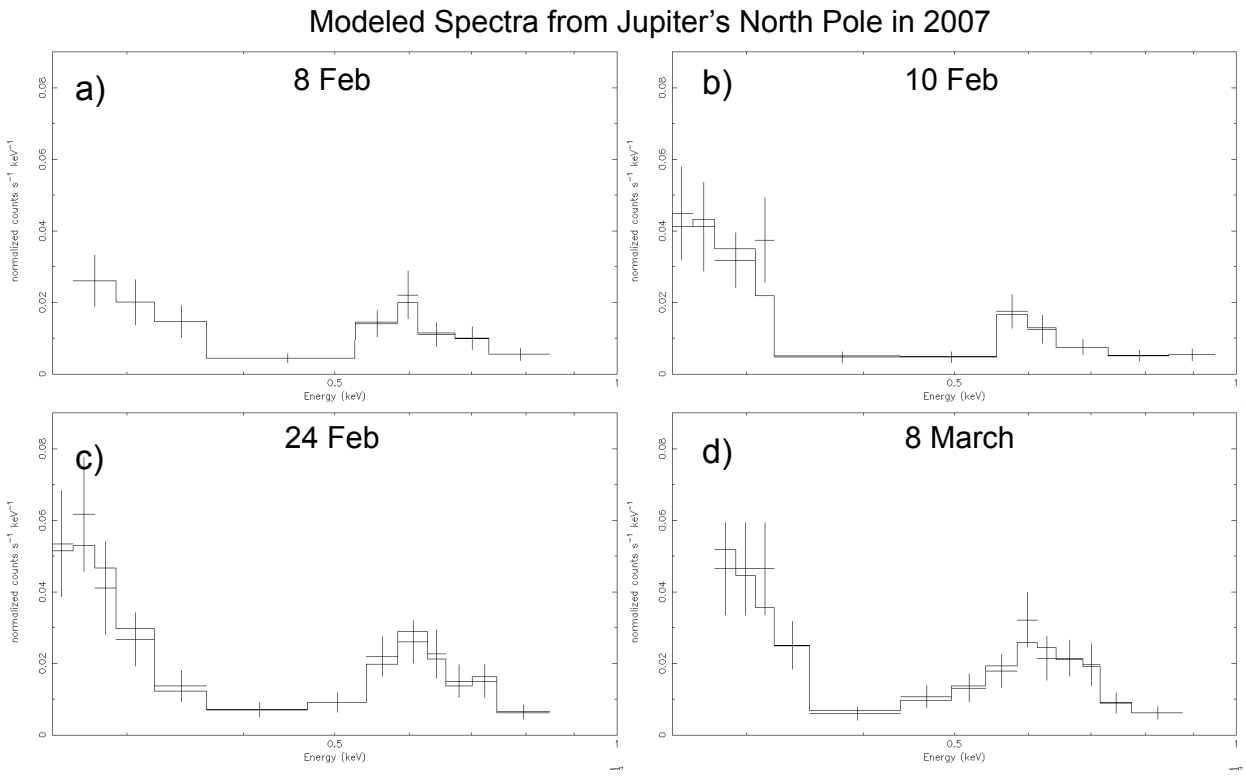

Figure 4.5: Modelled Spectra from the Chandra ACIS observations of the Jovian Northern Aurora in 2007. These spectra have been binned to ensure there are a minimum of 10 counts in each bin and thus have poorer spectral resolution than Fig 4.4. Best fit lines and fluxes for these models can be found in Tables 4.2 and 4.3.

Ion Source	8 Feb	10 Feb	24 Feb	8 March	XMM 24 May 2016
S/C	4400^{+1000}_{-2000}	5700^{+1000}_{-1000}	6600^{+1500}_{-4000}	8300^{+2000}_{-2000}	120^{+60}_{-50}
S/C	(550)	-	(850)	-	-
C?	-	-	50^{+100}_{-30}	30^{+20}_{-10}	20^{+10}_{-9}
OVII	50^{+20}_{-20}	40^{+15}_{-15}	60^{+30}_{-20}	50^{+20}_{-20}	20^{+5}_{-5}
OVIII	10^{+5}_{-5}	10^{+5}_{-5}	20^{+7}_{-7}	20^{+30}_{-10}	6^{+3}_{-2}
OVIII	-	3^{+2}_{-2}	(4)	5^{+2}_{-2}	2^{+1}_{-1}

Table 4.3: Northern Aurora Best-Fit Model line fluxes in 10^{-6} photons/cm^2/s with reduced χ^2 of 0.2 - 0.7 for the various models. The model fits can be seen overplotted on the data on Fig. 4.5. Lines that were also good fits but were not in the best fit model are shown without errors and in parentheses in order to differentiate them.

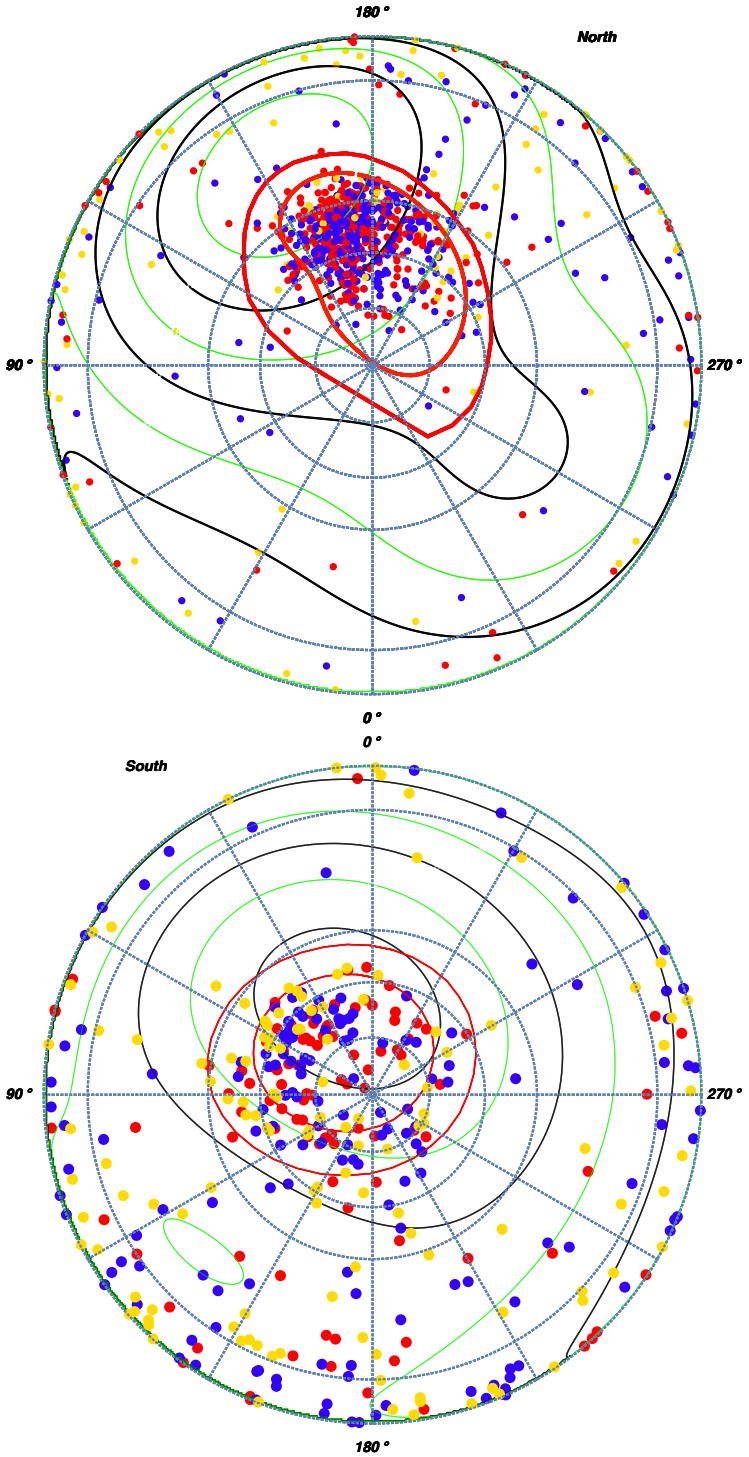

Figure 4.6: System III (S3) coordinate projections onto Jupiter's geographic North (Top) and South (Bottom) Poles for all observations combined. Photons of different energies are colour-coded so that 200-500 eV (sulphur/carbon emission) is in red, 500-900 eV (oxygen emission) is in blue and above 1 keV (hard X-ray bremsstrahlung from electron precipitation) is in yellow. Lines of constant Jovian S3 longitude radiate outwards from the North (South) pole, increasing clockwise (anti-clockwise) in increments of 30° from 0° at the bottom of the projection. Concentric dotted circles outwards from the pole represent lines of (-) 80°, (-) 70°, (-) 60° and (-) 30° latitude. The alternate green and black contours, indicate VIP4 model magnetic field strength in Gauss. The outer red oval is the Grodent et al. [2008] contour of Io's footprint (5.8R_J). The inner red contour is the footprint for the 30 R_J field line from Vogt et al. (2011) mapping using the Grodent et al. (2008) anomaly model - comparable to the expected UV main oval location. The size of the data points does not have any physical meaning.

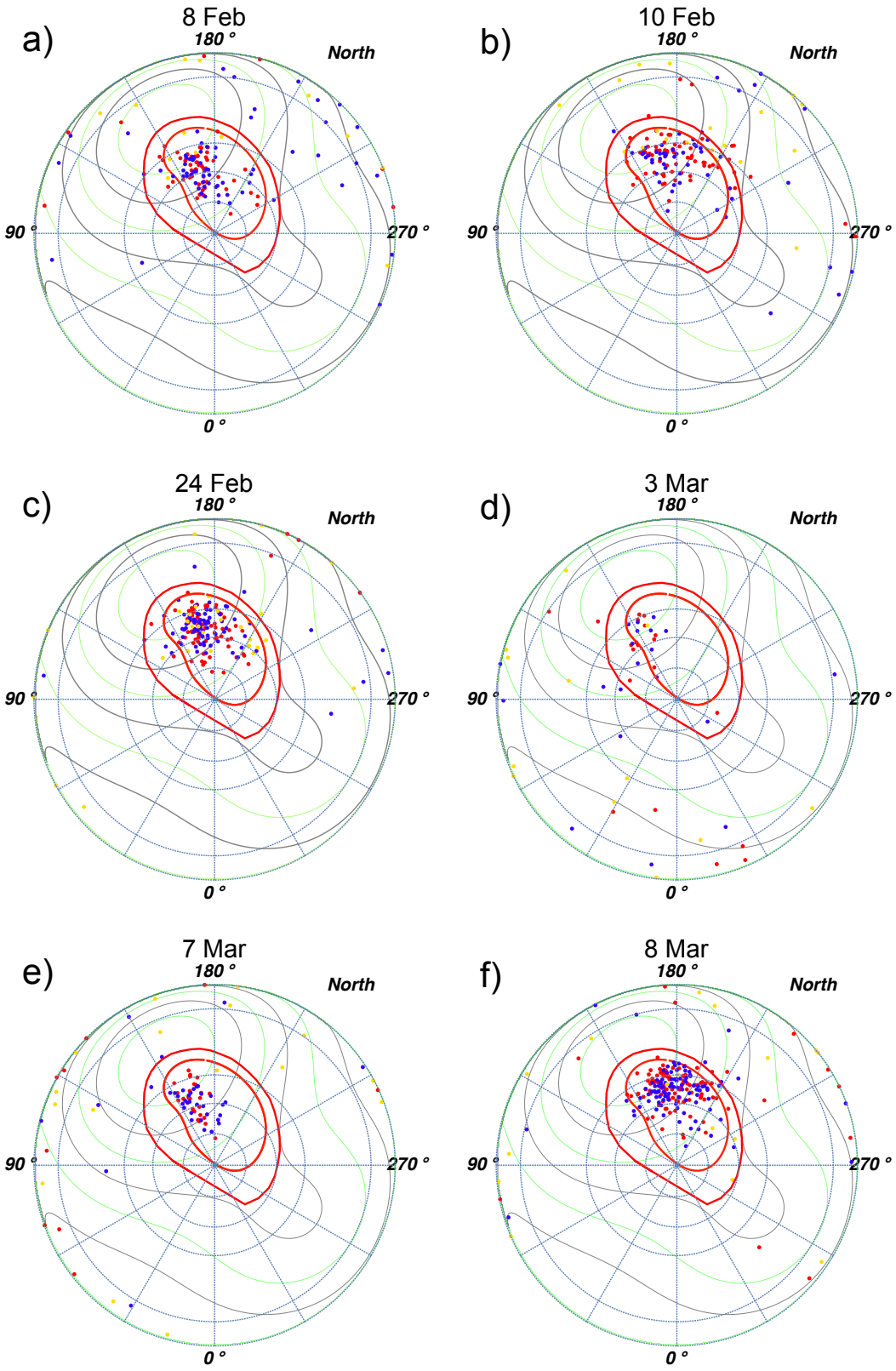

Figure 4.7: North Pole S3 projections for each observation. For further plot details see figure 4.6. The 3rd of March and 7th of March observations provided very limited visibility of the North auroral region and thus feature fewer X-rays.

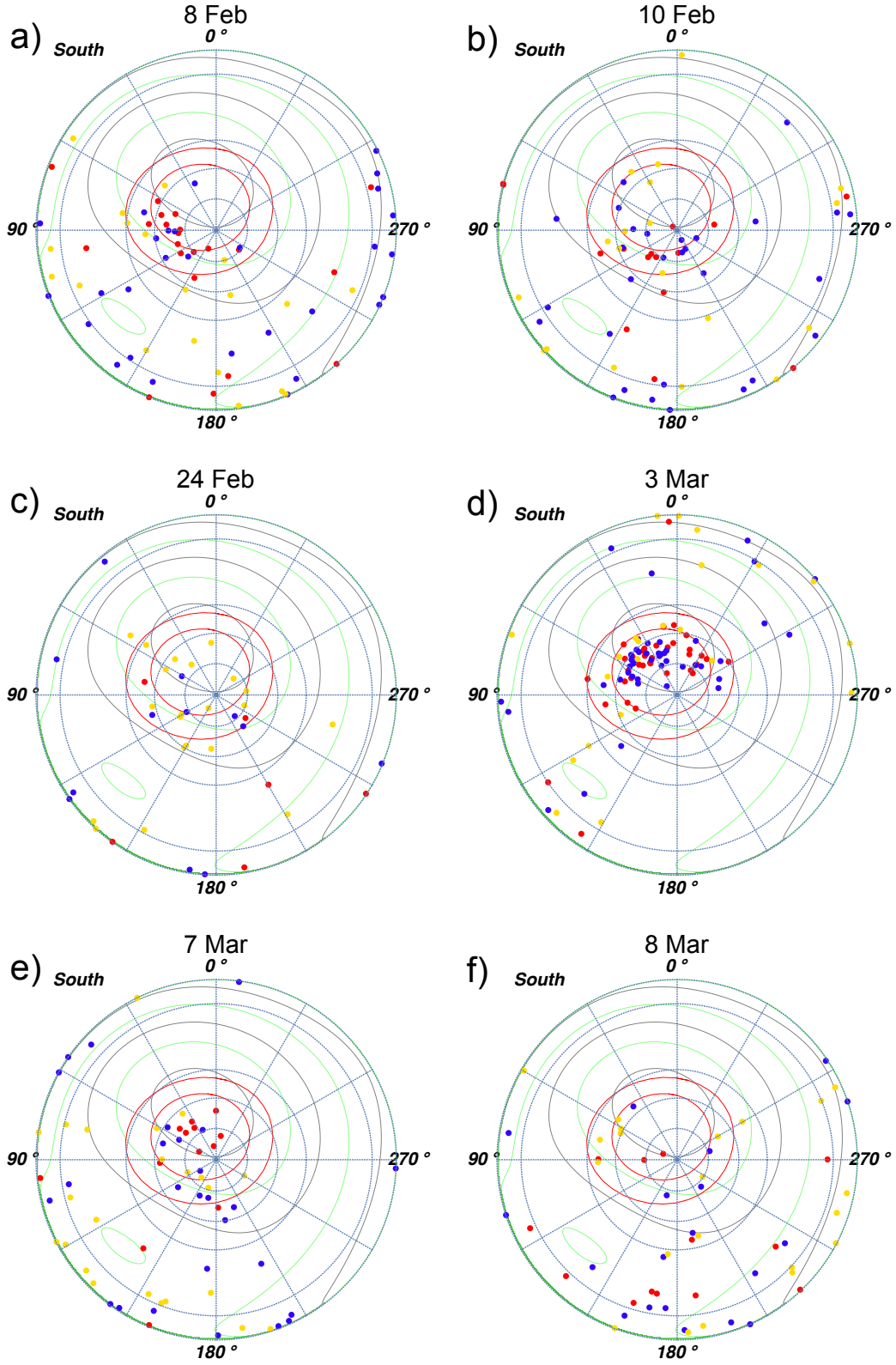

Figure 4.8: South Pole S3 projections for each observation. For further plot details see figure 4.6. All observations except the 3rd of March provided very limited visibility of the Southern auroral region and thus feature fewer X-rays.

the hot spot region poleward of the expected main oval.

Fig 4.6 shows the combined distribution from all of the observations together. We note that our distribution of a halo of emission around a core hot spot emission matches the distribution that was reported for observations in 2014 by Kimura et al. (2016). This may indicate that X-ray emission from the Northern hot spot can originate from a wide-range of polar locations.

Figures 4.7 and 4.8 show Northern and Southern polar projections for each observation revealing possible differences in the distribution from a concentrated hot spot (e.g. 8th Feb - Fig. 4.7a), to a more diffuse/patchy distribution (e.g. 10th Feb - Fig. 4.7b). For the 3rd and 7th of March, the Southern hot spot location matches that identified in 2016 (see previous chapter) and suggests that a Southern hard X-ray oval occurs equatorward of the Southern hot spot (Fig. 4.8d and e) - as is the case for the North (Branduardi-Raymont et al. 2008).

4.3.3.1 Polar Projected Density Maps

In order to provide a visualisation that might better identify possible morphology in the 2007 aurora, we produced 4°-binned density (herein referred to as 'heat map') polar projections for all of the X-ray emission and for each of the wavebands in turn (Fig. 4.9, 4.10, 4.11,4.12,4.13,4.14 and 4.15).

Looking first at the heat maps for all the observations combined (Fig. 4.9 and 4.10). The density maps suggest that the Northern hot spot is concentrated into a bright patch of emission between 60-70° latitude and between 155-175° S3 longitude. Poleward of the core hot spot, the X-ray emission stretches as a streak of emission that runs parallel with the main oval up to 80° latitude. This seems to stop at a fairly abrupt boundary a few degrees poleward of the 45 RJ contour. This polar extension is particularly clear in the energies associated with Sulphur/Carbon emission (Fig. 4.9b), but also exists in the oxygen emission energies (Fig. 4.9c). Rotating to higher longitudes from the core of the hot spot, there is a dim but extended patch of emission between 60-70° latitude that fades out as it progresses towards 210° longitude in the Sulphur/Carbon and Oxygen emission. As with the 2011 ob-

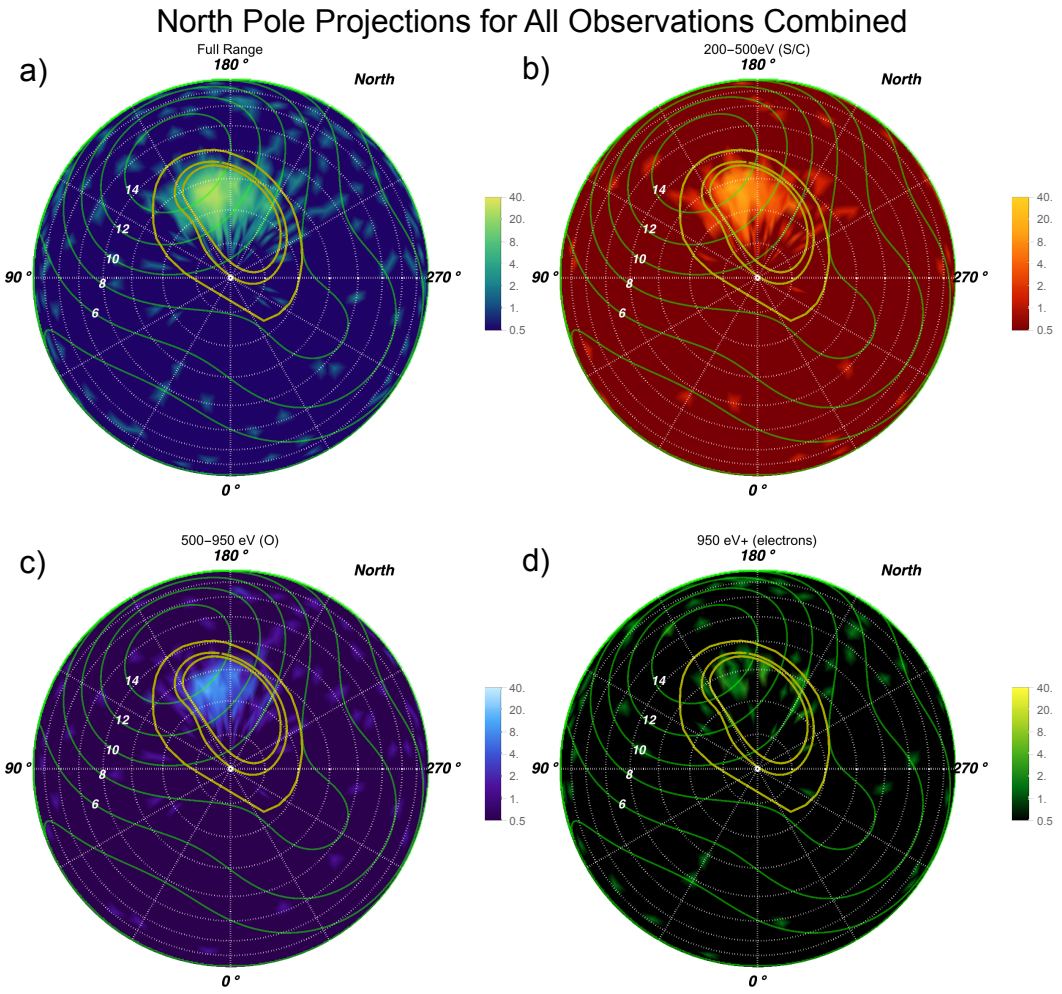

Figure 4.9: Projected heat maps centred on Jupiter's North pole from Chandra Advanced CCD Imaging Spectrometer (ACIS) observations. These show a) the full energy range in blue-green-yellow, b) 200-500 eV (sulphur/carbon emission) in red-yellow c) 500-900 eV (oxygen emission) in blue-white, and d) greater than 1 keV emission (hard X-ray bremsstrahlung from electron precipitation) in green-yellow. The logarithmic colour bar indicates the number of X-rays in bins of 4° by 4° of S3 latitude-longitude. Dashed lines of longitude radiate from the pole, increasing clockwise in increments of 30° from 0° at the bottom. Concentric dotted circles outward from the pole represent lines of latitude in increments of 10°. Thin green contours with white text labels indicate the VIP4 (Connerney et al. 1998) model magnetic field strength in Gauss. Thick gold contours show the magnetic field ionospheric footprints of field lines intersecting the Jovigraphic equator at 5.9 RJ (Io's orbit), 15 RJ and 45 RJ (Grodent et al. 2008; Vogt et al. 2011) from equator to pole respectively.

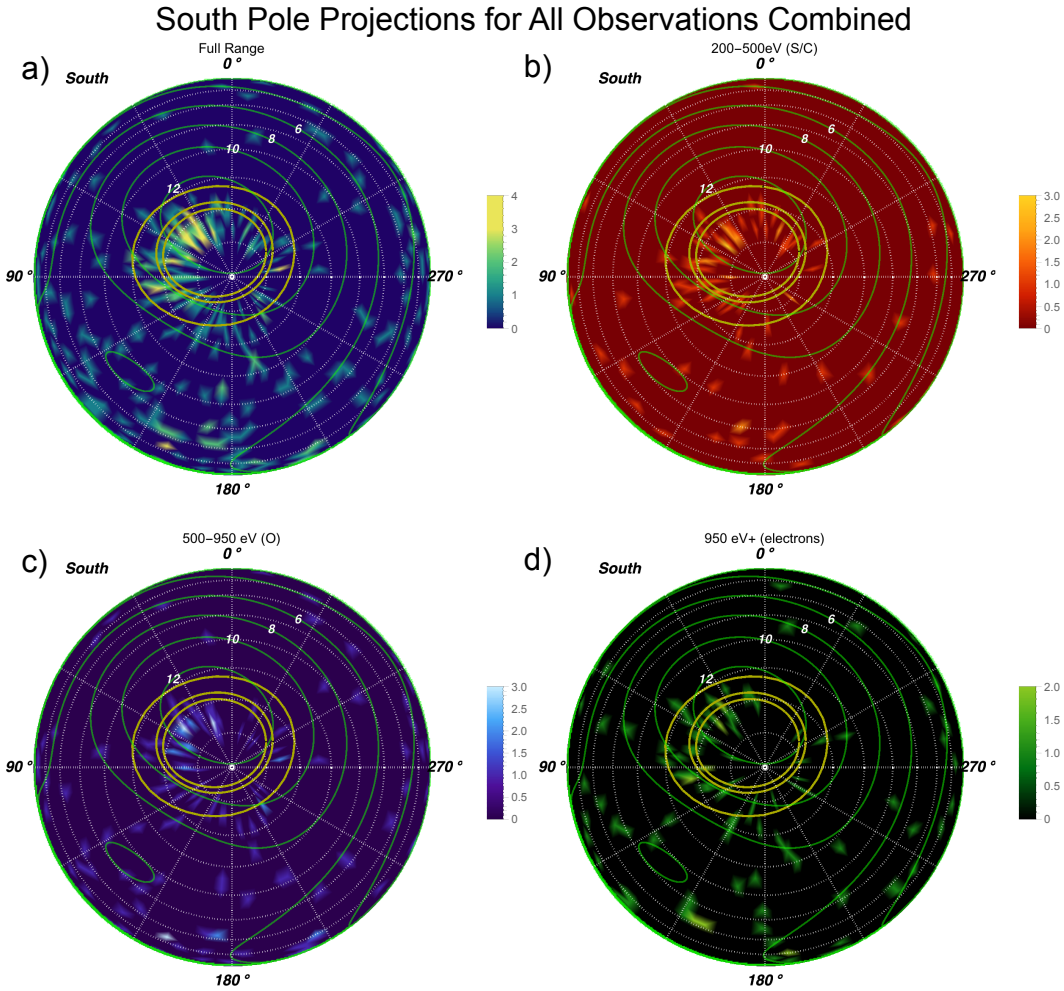

Figure 4.10: Projected heat maps centred on Jupiter's South pole from Chandra ACIS observations. These show a) the full energy range in blue-green-yellow, b) 200-500 eV (sulphur/carbon emission) in red-yellow, c) 500-900 eV (oxygen emission) in blue-white and d) greater than 1 keV emission (hard X-ray bremsstrahlung from electron precipitation) in green-yellow. The colour bar indicates the number of X-rays in bins of 4° by 4° of S3 latitude-longitude. Dashed lines of longitude radiate from the pole, increasing anti-clockwise in increments of 30° from 0° at the top. For further details see Fig. 4.9.

servations presented in Chapter 2, equatorward of the hot spot emission, the Sulphur/Carbon emission appears to stretch to lower latitudes, closer to (but still polewards of) the main oval than the oxygen emission.

Dim patches of ion emission also stretch below the main oval and across Io's footprint, but these are much less concentrated than the emission poleward of the oval and may be produced by projecting high obliquity regions on to the poles.

For the North, the soft X-rays are concentrated into the region where the surface field strength is 12-14 G. This region will mirror more particles and require the Knight relation to provide higher electric fields and subsequent potential drops in order to provide the needed particle fluxes into the ionosphere. These larger potential drops will provide more acceleration.

Fig. 4.9d shows that the hard X-rays again appear along the main oval as found by Branduardi-Raymont et al. (2008). There is also a bright patch of hard X-ray emission co-located with the hot spot, which was emitted during the Feb 24 observation and we will return to this shortly.

The distribution for the South (Fig. 4.10) matches that shown in the previous chapter for the 2016 observations. The core of the hot spot occurs between 30-75° longitude and between 70-80° latitude. This emission is mostly produced by precipitating ions. The hard X-ray emission lines up well with the expected main oval location between 15-45 RJ (Fig. 4.10d). There is some scatter of ion emission close to the main oval from 90-150°, however we note that this region was observed for 4-5 times as long as the region from 0-60° and that any X-rays from inside of the oval would occur on the limb of the disk for all but the 3rd and 7th of March observations. It would therefore be expected to have more scatter.

We assess each observation in turn (Fig. 4.11) to identify different X-ray hot spot behaviour.

4.3.3.2 8th Feb Northern Aurora Morphology

Feb 8th observation has emission evenly distributed across both the core region and the poleward extension of this, with sulphur/carbon ions and oxygen ions

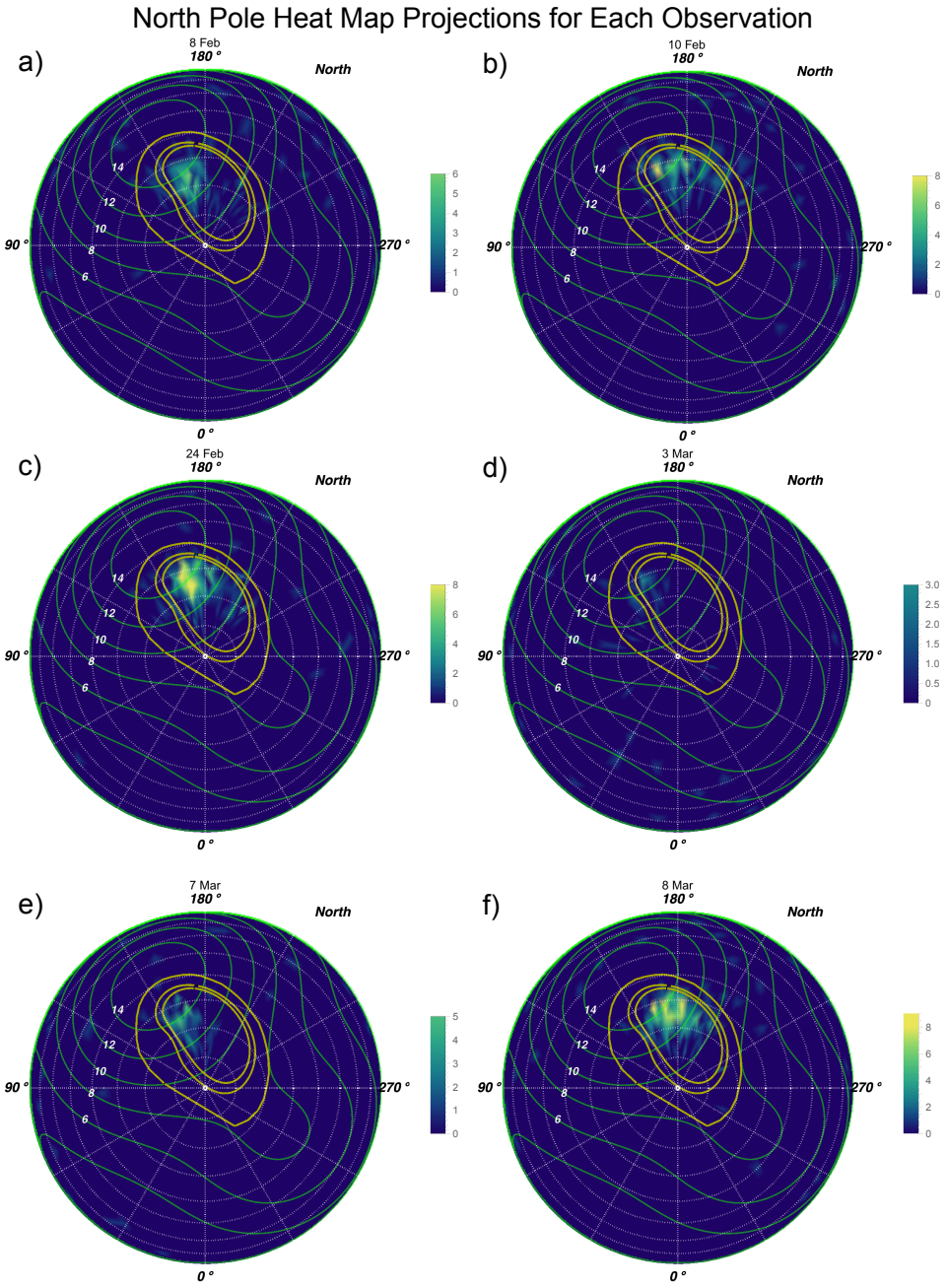

Figure 4.11: Projected heat maps centred on Jupiter's North pole from Chandra ACIS for each observation for the full energy range. All projections are scaled to saturate at 8 counts. For further details see Fig. 4.9.

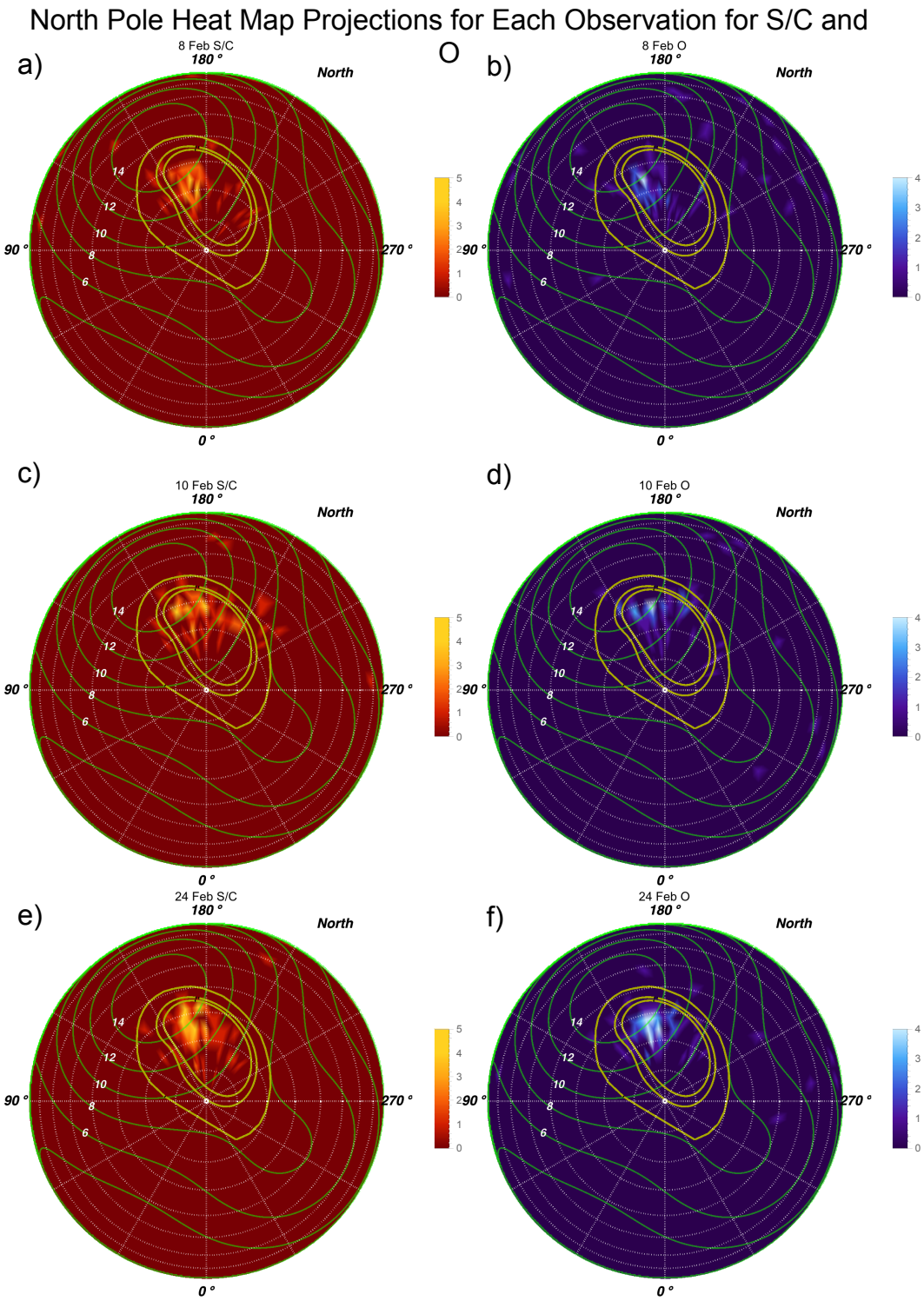

Figure 4.12: Projected heat maps centred on Jupiter's North pole from Chandra ACIS, comparing the 200-500 eV emission from sulphur/carbon ions (left) with the 500-900 eV emission from oxygen ions (right) for the February 2007 observations, with both scaled to saturate at 5 counts. For further details see Fig. 4.9.

both contributing equally to this dim even-spread of emission (Fig. 4.11a and 4.12a and b). Hard X-ray emission on the 8th of February was very low so, for brevity, is not plotted.

4.3.3.3 10th Feb Northern Aurora Morphology

Despite the average number of counts per second being similar to Feb 8th (and a similar observation duration), the Feb 10th observation has quite a different distribution of emission (Fig. 4.11b and 4.12c and d). The emission appears to occur in more distinct patches/streaks that occur up to 210° longitude. A dim arc of hard X-ray emission overlaps the expected main oval location (Fig. 4.14a and b).

4.3.3.4 24th Feb Northern Aurora Morphology

The 24th Feb observation is one of the brightest of the campaign and this higher intensity appears to originate from a latitudinally extended bright ion-produced region from 56-72° and centred on 165° longitude (Fig. 4.11c). This region extends down to very close to the main oval contours, with bright patches both along the inside of the expected oval and between 65-72°. Interestingly, there are several hard X-rays that appear co-located and poleward of some of the 200-500 eV hot spot emission in this region (Fig. 4.14c and d). Hard X-rays between 180-270° longitude overlap the location of an expanded arc of main UV oval emission with intensity greater than 500 kR, that was observed 10 hours prior to this (shown later in Fig. 4.29). The poleward dusk arc of UV emission may also explain the hard X-rays in the hot spot region. We note that this was the brightest hard X-ray emission observed during the campaign.

4.3.3.5 3rd and 7th March Northern Aurora Morphology

The 3rd of March observation (Fig. 4.11d) provided very little coverage of the Northern aurora. The 7th of March (Fig. 4.11e) provided slightly more suggesting that, like the 8th of Feb (Fig. 4.11a), an even distribution of emission in a streak/arc parallel with the main oval. However it is difficult

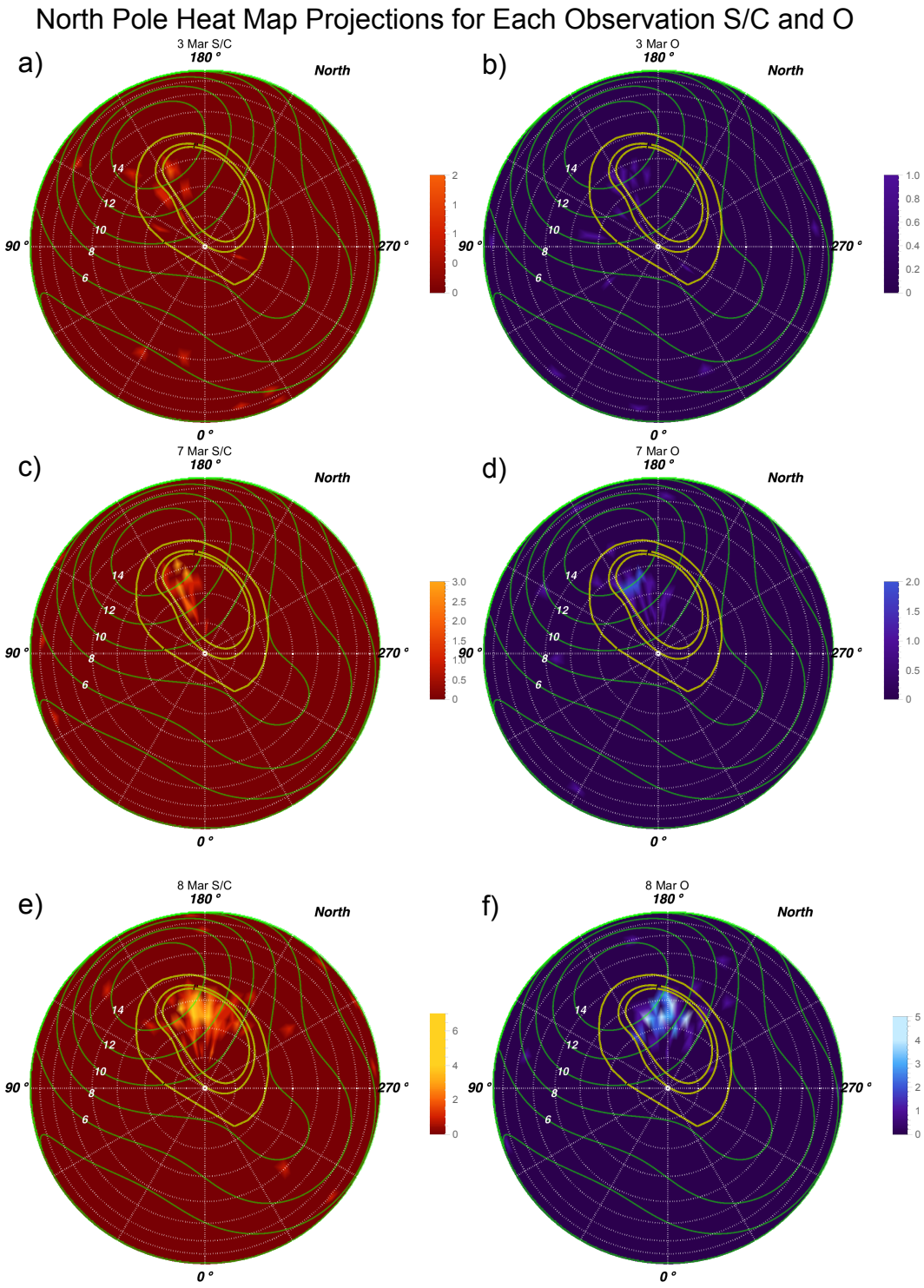

Figure 4.13: Projected heat maps centred on Jupiter's North pole from Chandra ACIS, comparing the 200-500 eV emission from sulphur/carbon ions (left) with the 500-900 eV emission from oxygen ions (right) for the March 2007 observations, with both scaled to saturate at 5 counts. For further details see Fig. 4.9.

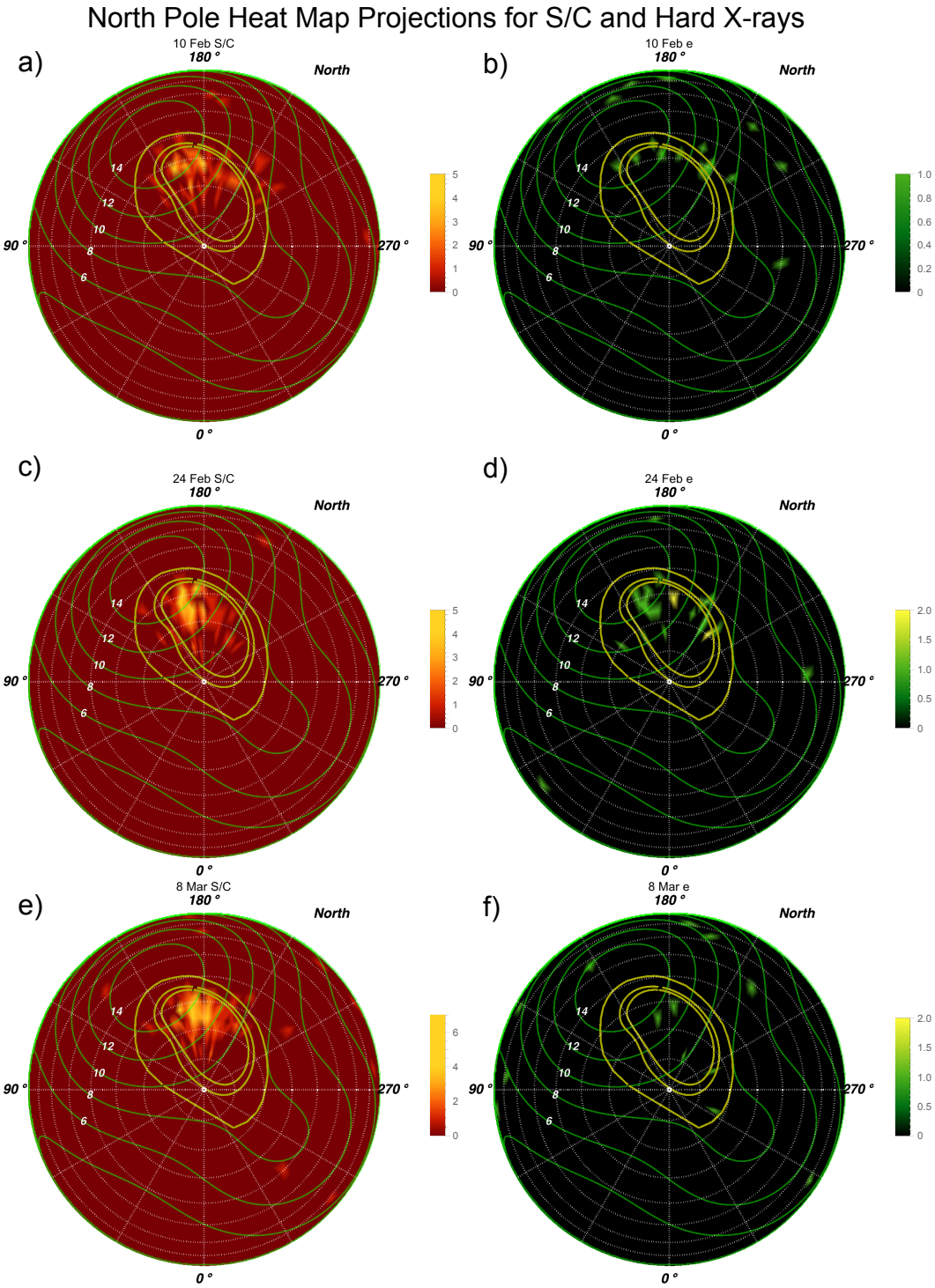

Figure 4.14: Projected heat maps centred on Jupiter's North pole from Chandra ACIS, comparing the 200-500 eV emission from sulphur/carbon ions (left) with the greater than 1 keV emission (right) from electrons for observations on the 8th Feb (a and b), 24th Feb (c and d) and 8th March (e and f) 2007. 200-500 eV is scaled to saturate at 5, while greater than 1 keV saturates at 2. For further details see Fig. 4.9.

to tell whether this distribution is due to the limited visibility window and consequent limited count rates.

4.3.3.6 8th March Northern Aurora Morphology

The 8th of March observation shows that the hard X-ray emission is very dim (Fig. 4.14e and f), while the soft X-ray emission is very bright. This suggests that, as reported by Branduardi-Raymont et al. (2004), there is independence in the soft X-ray and hard X-ray drivers. There is emission stretching from the most Northerly observable regions ($\sim 80°$) to the inner edge of the main oval, with the emission appearing to be concentrated into a hot spot core that extends to 200° longitude.

4.3.3.7 3rd March Southern Aurora Morphology

As previously discussed, for the 3rd March Southern Aurora (Fig. 4.15) the ion emission is poleward of the main oval and mostly concentrated into the region between 20-75° longitude and between -70 and -80° latitude. The Hard X-rays appear to occur equatorward of this along the expected main oval location.

4.3.3.8 Summary of Northern Aurora Morphology

The 8 Feb, 24 Feb and 7 March Northern aurora distributions appear qualitatively similar with emission more constrained in parallel with the dusk-side of the main oval (e.g Fig 4.11a, c, e). The 10 Feb and 8 March Northern aurora observations are more patchy and extend to higher longitudes (e.g Fig 4.11b and f). It is possible that this shows two distinct types of X-ray aurora behaviour, since as discussed later these observations are expected to represent different phases of a solar wind compression.

4.3.3.9 Exploring X-ray Colour Ratios

Given the very low counts in the observations, we only compare the lower energy 200-500 eV sulphur/carbon emissions with the higher energy 500 - 900 eV oxygen emissions. Given more photons, it might be possible to explore the

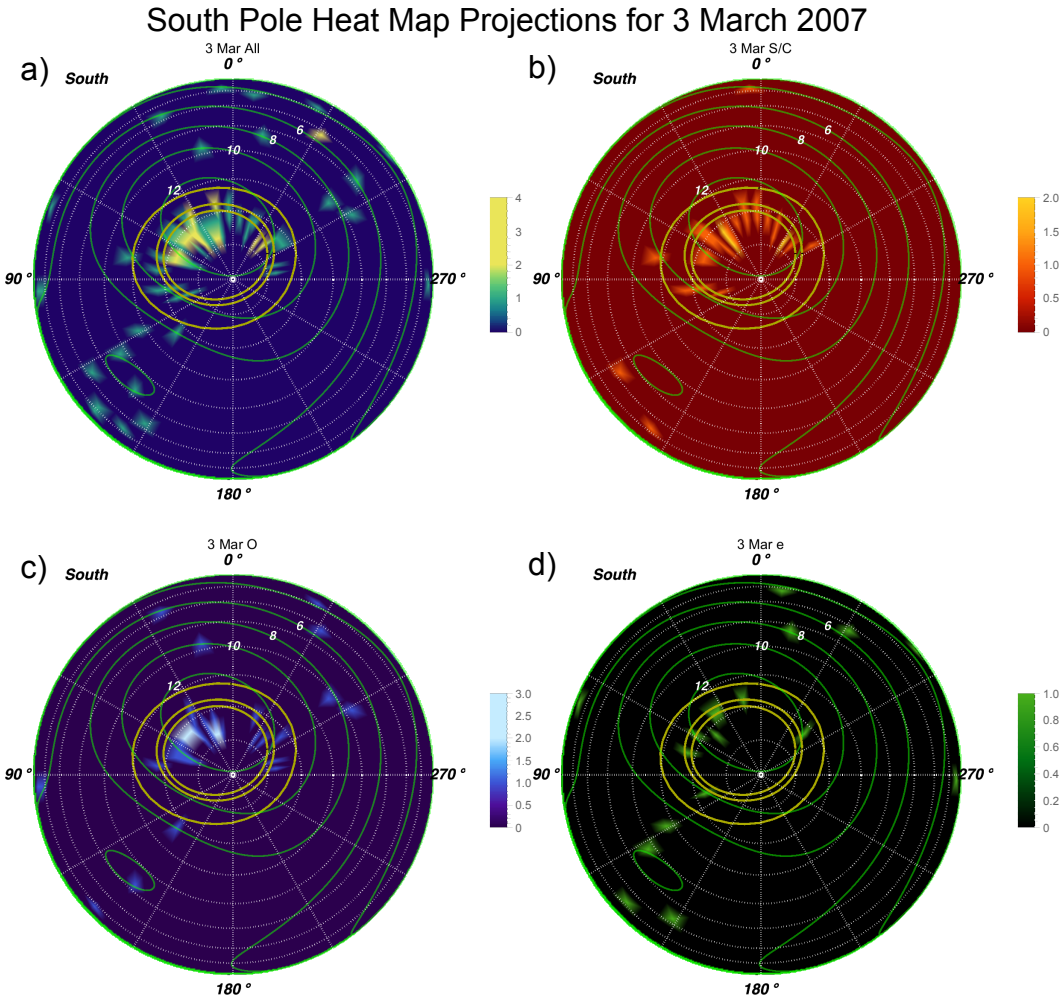

Figure 4.15: Projected heat maps centred on Jupiter's South pole from Chandra ACIS for the 3rd of March 2007. These show a) the full energy range in blue-green-yellow, b) 200-500 eV (sulphur/carbon emission) in red-yellow, c) 500-900 eV (oxygen emission) in blue-white and d) greater than 1 keV emission (hard X-ray bremsstrahlung from electron precipitation) in green-yellow (lower right). The colour bar indicates the number of X-rays in bins of 4° by 4° of S3 latitude-longitude and is saturated at 2. For further details see Fig. 4.10.

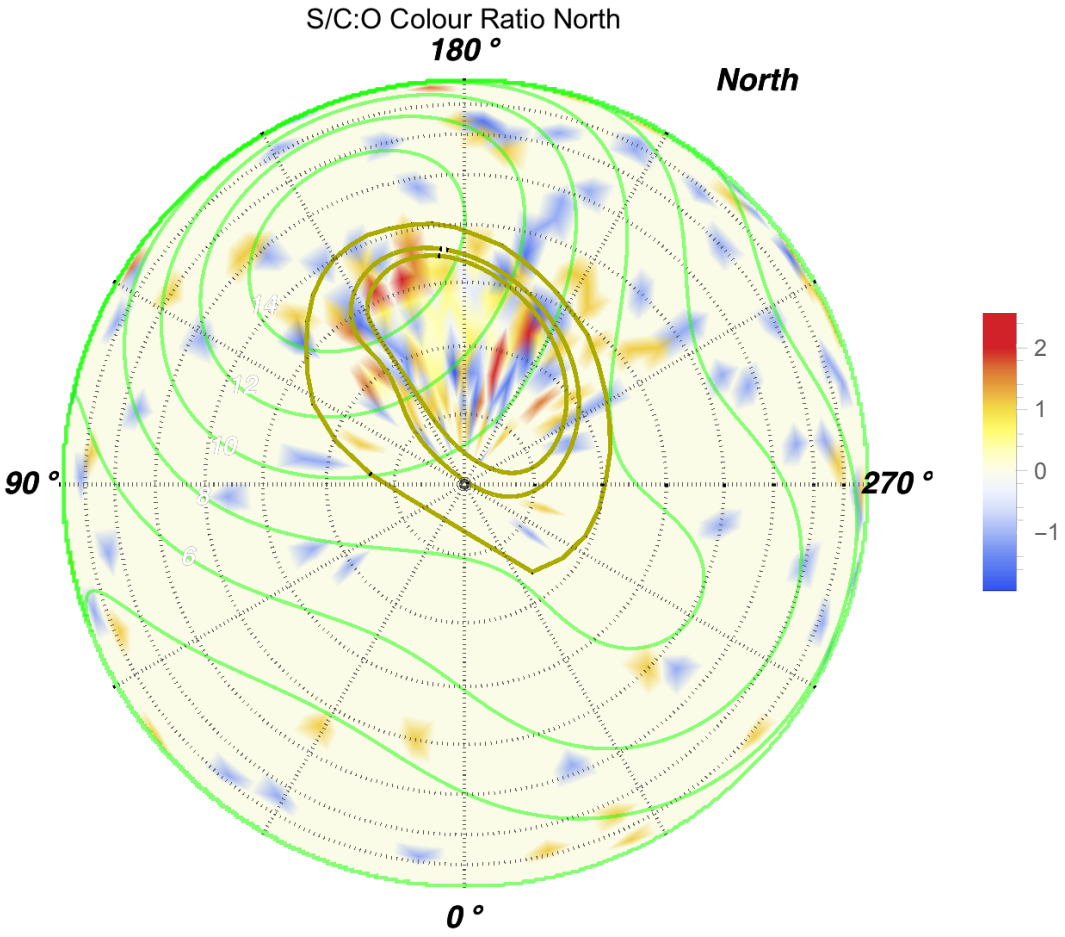

Figure 4.16: Polar Projected Colour Ratio of 200-500 eV sulphur/carbon ion emission with 500-900 eV oxygen emission for 4° by 4° bins. The colour scale shows the log of the ratio with more red indicating that 200-500 eV emission was enhanced relative to 500-900 eV emission and more blue indicating a 500-900 eV enhancement. The different contours are described in Fig. 4.9.

relationship between OVII and OVIII in order to try to identify polar regions with different energisation mechanisms/acceleration.

Fig. 4.16 shows this colour ratio for all of the observations combined. Equator-wards of the main oval the different coloured patches of colour ratio are the product of the low levels of counts in these regions and are blue from the harder disk spectrum (e.g. Fig. 4.9) so we focus only on the regions poleward of this. Fig. 4.16 shows that emission from the core of the hot spot is reasonably evenly distributed between sulphur/carbon and oxygen emissions, with a ratio close to 1. Between the main oval and the region of 60° latitude and 150-175° longitude is the region with the highest absolute colour ratio, where the emission appears to be dominated by 200-500 eV emission sulphur/carbon emission, suggesting a region of lower acceleration, where oxygen does not receive sufficient acceleration for the required charge states for X-ray emission. Alternatively, this may suggest a region where oxygen precipitates too deeply and opacity effects dominate. This is the same region that appeared to be dominated by 200-500 eV emission in the 2011 observations (Dunn et al. 2016). This is also true for the region between 60-80° latitude and ∼200° longitude. In the core of the hot spot the colour ratio is lower and there appears to be either a more equal distribution of each or a stochastic preference for oxygen or sulphur/carbon emission. However, we are cautious not to over interpret these maps, since there are low numbers of auroral X-ray photons in these observations.

4.3.4 Mapping Different Spectral Bands

As with the 2011 and 2016 observations, we applied the model mapping of Vogt et al. (2011, 2015) to identify the possible source regions for the distinct energy bands used previously. Fig. 4.18 shows these distributions for the Northern and Southern aurora. The North featured very low levels of hard X-ray emission throughout the campaign. Generally this was concentrated along the main oval, but the Feb 24 observations also featured this in the hot spot region. The ion emission occurs mainly between the statistical magnetopause locations (Joy et al. 2002) from noon to dusk and into the dusk tail where

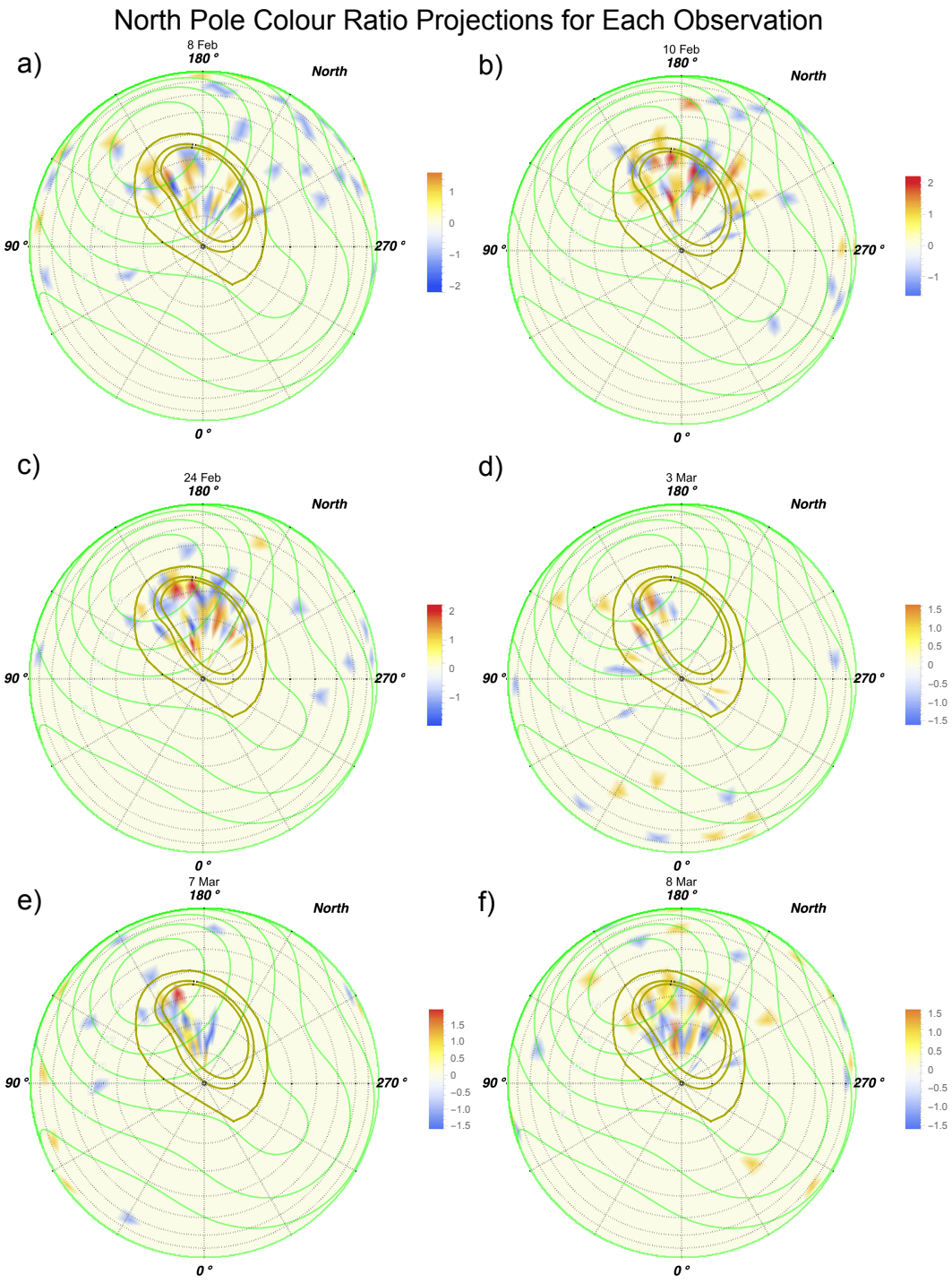

Figure 4.17: Polar Projected Colour Ratio of 200-500 eV sulphur/carbon ion emission with 500-900 eV oxygen emission for each observation for 4° by 4° bins for all observations combined. The colour scale shows the log of the ratio with more red indicating that 200-500 eV emission was enhanced relative to 500-900 eV emission and more blue indicating a 500-900 eV enhancement. The different contours are described in Fig. 4.9.

Obs Date	Total Mapped	Magnetosphere	Poleward	Equatorward
8 Feb North	113	65 (57%)	37 (33%)	11 (10%)
10 Feb North	122	55 (45%)	46 (38%)	21 (17%)
24 Feb North	175	90 (51%)	73 (42%)	12 (7%)
7 March North	60	43 (72%)	14 (23%)	3 (5%)
8 March North	178	68 (38%)	101 (57%)	9 (5%)
3 March South	81	45 (56%)	21 (26%)	15 (19%)

Table 4.4: Mapping of the auroral X-rays for each 2007 observation separately. Mapping model from Vogt et al. (2011, 2015), using a Grodent et al. (2008) model for the North and a VIP4 model for the South (Connerney et al. 1998). The percentages in brackets indicate what percentage of the auroral emission maps to locations: within the magnetosphere, poleward of the closed field line mapping and equatorward of locations that the auroral magnetic mapping is capable of identifying.

velocity shears drive current systems and Vasyluinas reconnection may occur. As found for the 2016 data the Southern spot maps much more uniquely to the noon and slightly post-noon magnetopause. This also shows a strong concentration of hard X-rays in the main oval region.

The Vogt et al. (2011, 2015) magnetic field mapping is only able to map the equatorial magnetosphere locations of places in the ionosphere that are on closed field lines. Poleward of the closed field lines (beyond the purple line on Fig. 2.16) are regions that may map to 'open field lines'. We cautiously note that it remains unclear whether Jupiter has any open field lines and whether these instead map to Jupiter's lobe and distant (1000s RJ) tail. We therefore refer to events that Vogt et al. (2011, 2015) map to open field lines as 'poleward' of the mapping to avoid over interpretation. There are also regions equatorward of the auroral zone, where the mapping is not able to connect regions with closed field lines. X-rays occurring in ionospheric locations on the footrprints of closed field lines are shown in Figures 4.18 and 4.19. Any X-ray events that occur poleward or equatorward of the mapping limits cannot be shown on Figures 4.18 and 4.19, since their source is unclear, but they are recorded in Tables 4.4 and 4.5.

As with previous work (Dunn et al. 2016; Kimura et al. 2016), we find that only $\sim 50\%$ of emission maps to closed field lines within the magnetosphere. Tables 4.4 and 4.5 show the number of counts and percentages of emission that map to: closed field lines within the magnetosphere; locations poleward of the

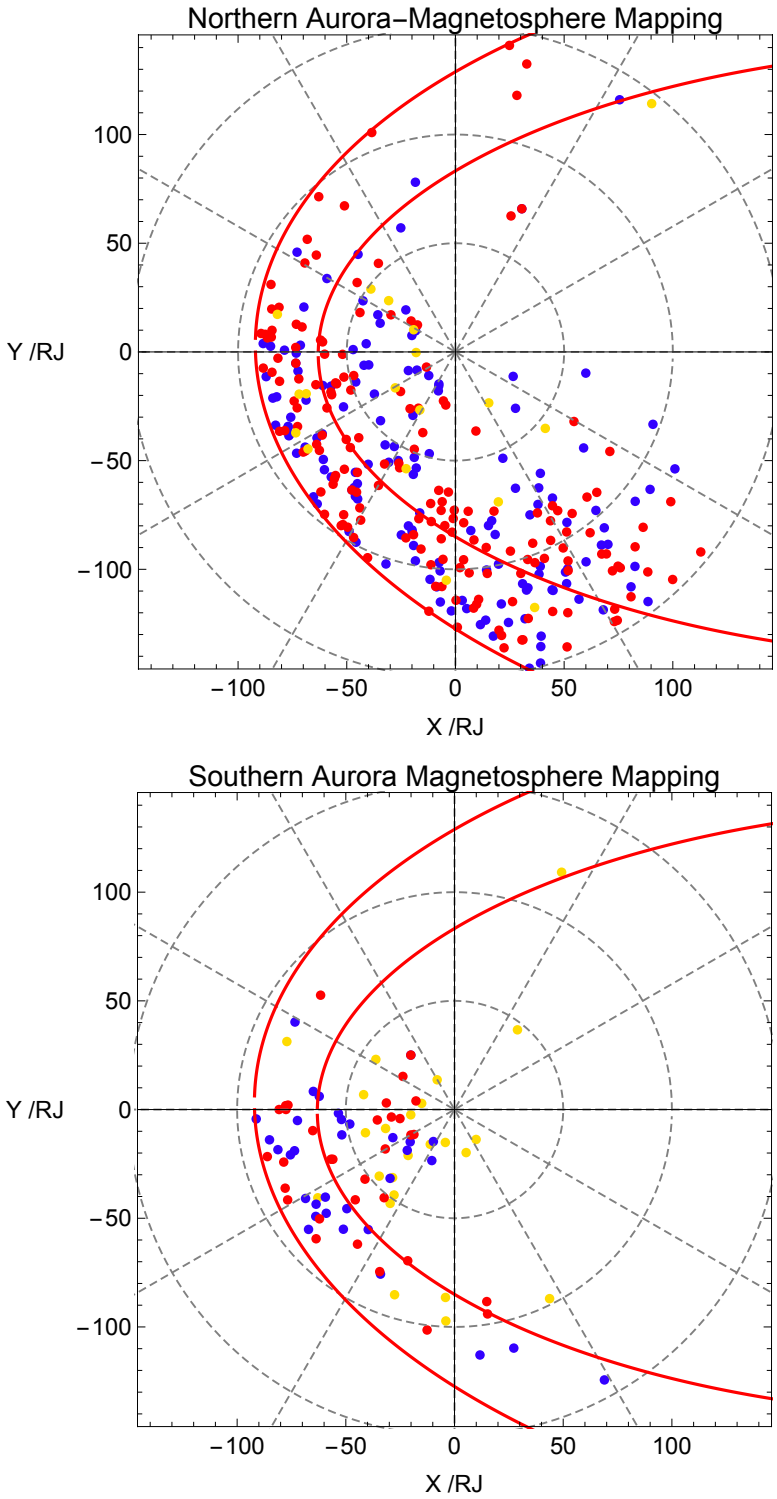

Figure 4.18: Ionosphere-Magnetosphere magnetic field mapping of X-ray photons for the Northern (Upper) and Southern (Lower) auroral zones. Mapping model from Vogt et al. (2011, 2015), using a Grodent et al. (2008) model for the North and a VIP4 model for the South (Connerney et al. 1998). The solid red lines indicate Jupiter's magnetopause, for an expanded 92 RJ, standoff distance (outer contour) and compressed 63 RJ standoff distance (inner contour) (Joy et al. 2002). We also note that even for the statistical location of the expanded magnetopause, because of the substantial spatial extent of the hot spots, 30%-60% of X-rays footprints map beyond the magnetopause, meaning that their origins cannot be identified by the model mapping and they are not plotted here. X-rays are colour coded as previously, with 200-500 eV (sulphur/carbon ions) emission in red, 500-900 eV (oxygen ions) emission in blue and 1 keV + (electron) emission in yellow.

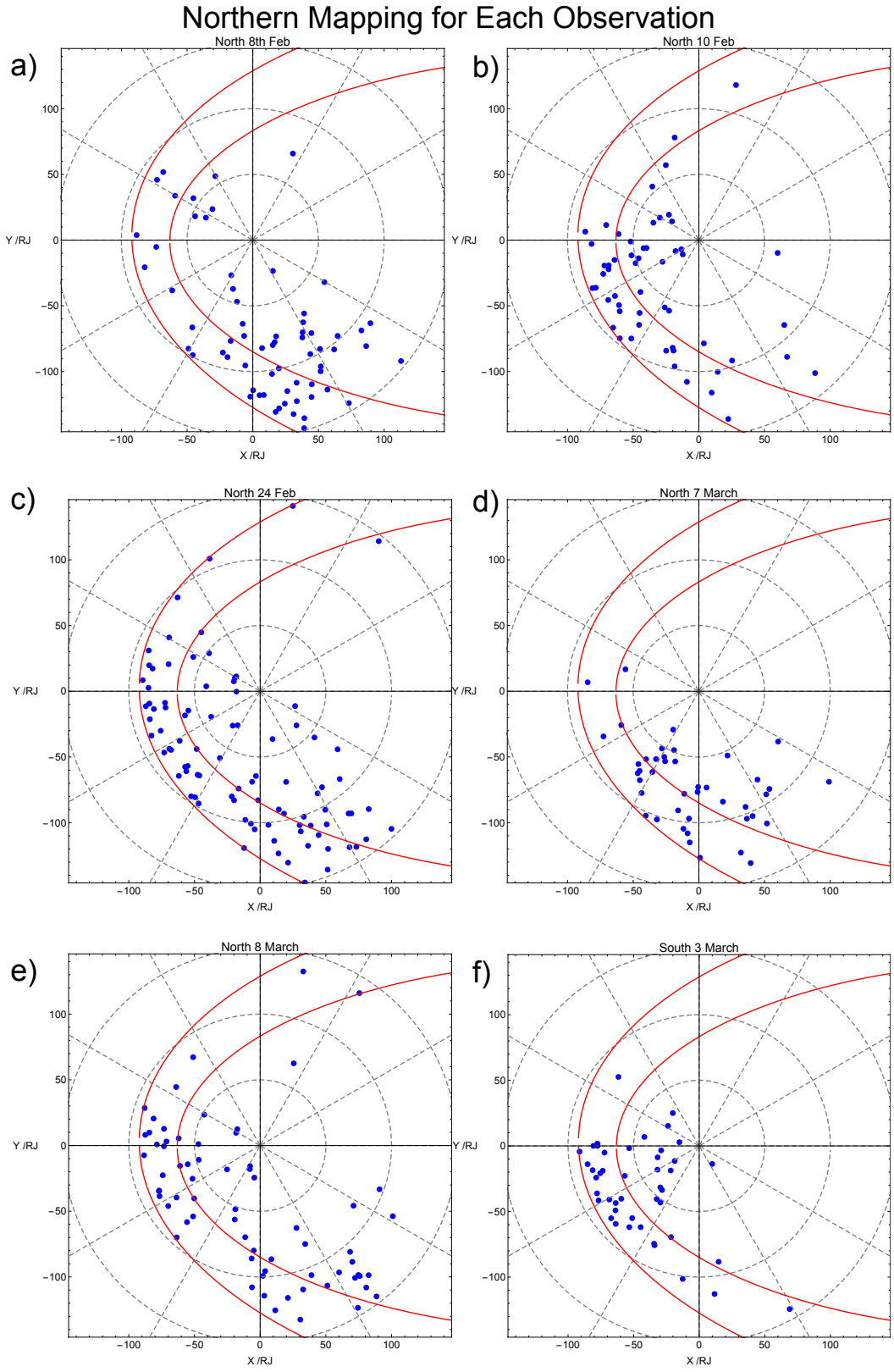

Figure 4.19: Ionosphere-Magnetosphere magnetic field mapping of X-ray photons for the Northern aurora on a) 8 Feb, b) 10 Feb, c) 24 Feb, d) 7 March and e) 8 March and f) Southern aurora for the 3rd March. Mapping model from Vogt et al. (2011, 2015), using a Grodent et al. (2008) model for the North and a VIP4 model for the South (Connerney et al. 1998).

Energy Band	Total Mapped	Magnetosphere	Poleward	Equatorward
All Energies North	670	331 (49%)	268 (40%)	71 (11%)
200-500 eV North	334	170 (51%)	133 (40%)	31 (9%)
500-900 eV North	300	144 (48%)	127 (42%)	29 (10%)
More than 1 keV North	44	19 (43%)	13 (30%)	12 (27%)
All Energies South	209	90 (43 %)	35 (17%)	84 (40%)
200-500 eV South	72	33 (46%)	17 (24%)	22 (30%)
500-900 eV South	78	33 (42%)	15 (19%)	30 (38%)
More than 1 keV South	57	25 (44%)	3 (5%)	29 (51%)

Table 4.5: Mapping of the Auroral X-rays by Waveband for all of the 2007 observatons combined. Mapping model from Vogt et al. (2011, 2015), using a Grodent et al. (2008) model for the North and a VIP4 model for the South (Connerney et al. 1998). The percentages in brackets indicate what percentage of the auroral emission maps to locations: within the magnetosphere, poleward of the closed field line mapping and equatorward of locations that the auroral magnetic mapping is capable of identifying.

mapping limits in the ionosphere; and locations equatorward of the mapping limits in the ionosphere. The location of an open-closed field line boundary at Jupiter is not well understood, so we do not treat this as a method for identifying the origins of the emissions. Instead, we use it to indicate the extent of their poleward emissions relative to other regions and thus as a method for quantifying the auroral morphology. (Bonfond et al. 2017) have found that the UV region with the highest colour ratio (deepest precipitation) maps to locations that the Vogt et al. (2011) mapping suggests are 'open field lines'. X-ray aurora that is occurring poleward of the Vogt et al. (2011) mapping limits, may also be connected with this high energy region, where particles precipitate deeply.

For the North much of the emission maps either to the outer magnetosphere (as shown in Fig. 4.18 and 4.19) or poleward of the ionospheric limits of the model. Table 4.4 shows that for all observations except the 10th of Feb less than 10% maps to regions equatorward of the auroral zone. The ion emissions are almost exclusively from high latitude regions with $\sim 10\%$ of emission occurring equatorward of the auroral zone. For the hard X-rays there is an equal percentage of emission poleward and equatorward of the auroral zone. The equatorward emissions are likely to be fluoresced or scattered solar photons.

For the South the most reliable observation is the 3rd of March, which

features a similar quantity of emission mapping to the magnetosphere, but with slightly less emission poleward and slightly more equatorward, relative to the other observations. The Southern values that combine all of the observations for the different wavebands are biased towards locations equatorwards of the auroral zone because of the limited visibility of the Southern aurora.

4.3.5 Temporal Relationships

Figure 4.20 shows the complete Northern and Southern auroral lightcurves for each observation. The lightcurves were produced by extracting X-rays from poleward of 60° latitude. As previously, the lightcurves have been binned into 1-minute time bins and smoothed over a 6 minute moving average window and thus disguise any periodic pulsations at timescales shorter than 6 minutes.

The lightcurve for Feb 10th (Fig. 4.20b) reveals why the auroral morphology may consist of distinct patches that are widely-distributed across longitude (e.g. Fig. 4.12c and d), since the pulses feature a ∼30° rotation in CML between each of them and occur from a CML of 115° until a CML of 240°. In contrast, most of the emission on Feb 8th (Fig. 4.20a) is emitted before a CML of 200° at which point the hot spot emission becomes much dimmer for the rest of the observation. This distribution is similar to 7th of March (Fig. 4.13 c and f), when, through virtue of the observation timing, the emission stops being observed at approximately this time, which is consistent with the two having a similar auroral morphology. The 24th Feb and 8th of March observations are the two brightest (Fig. 4.20a) and feature several bright peaks. The peaks for Feb 24th are well-organised into regular 9-13 minute pulsations, while those on 8th March are far less pulsed.

As previously (see preceding two chapters for details) we produced power spectral densities (Fig. 4.21) for these lightcurves. Interestingly there is a 5 min period on both 8 and 24 Feb (Fig. 4.21a and c). and in addition there is a 9-13 min period on 24 Feb, which had been observed already in 2011 and 2016, during times of solar wind compression.

We attempted to split the lightcurves into their constituent energy bands, but due to the low levels of auroral emission in these observations, it is chal-

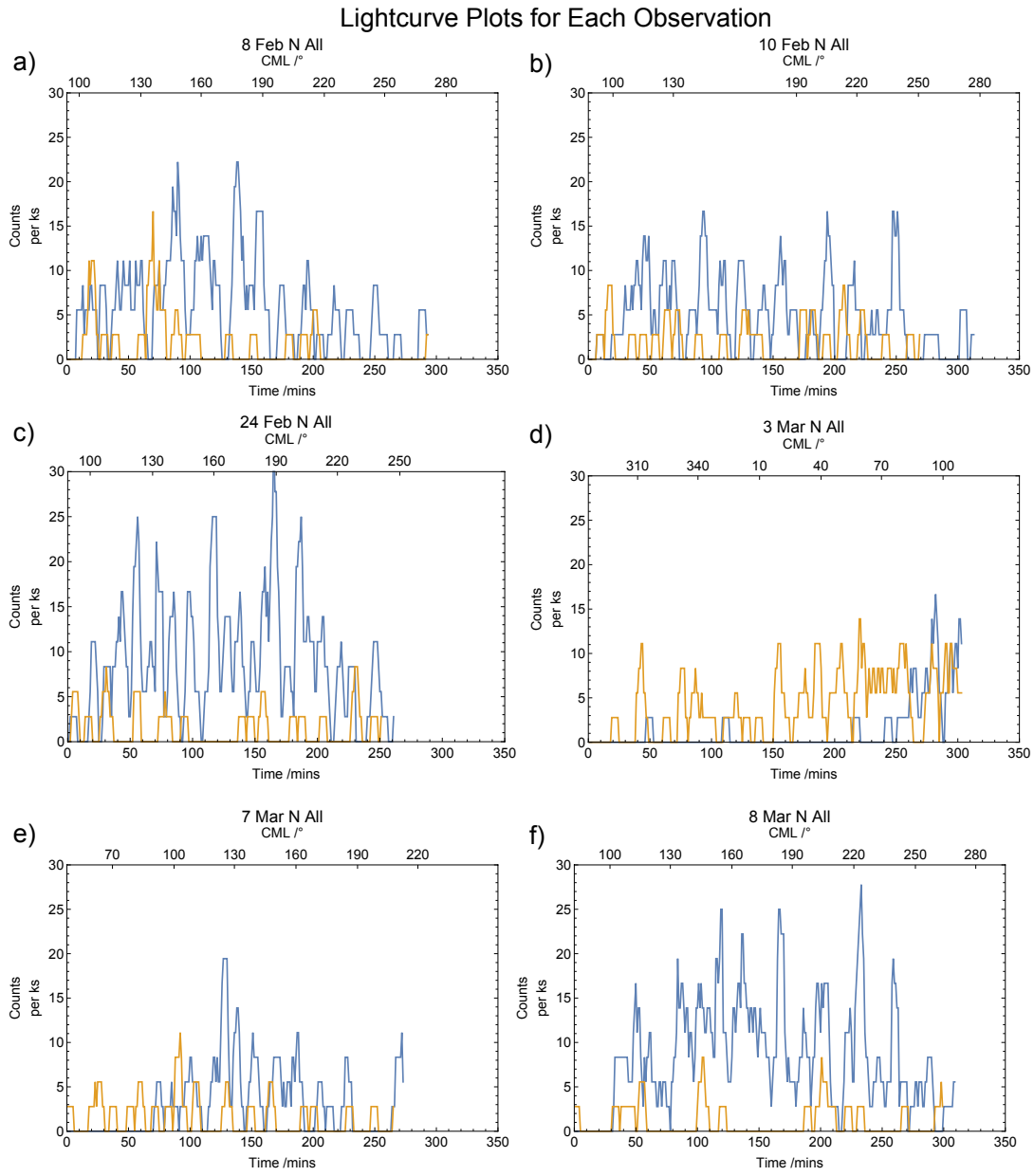

Figure 4.20: Chandra ACIS X-ray lightcurves from the Northern (blue) and Southern (gold) aurora for each observation. Central Meridian Longitude is indicated across the top, while minutes from the observation start times (Table 4.1) are indicated on the x-axis. The lightcurves are 1-minute binned, with 6-minute moving-average smoothing and thus disguise any periodic pulsations at timescales shorter than 6 minutes.

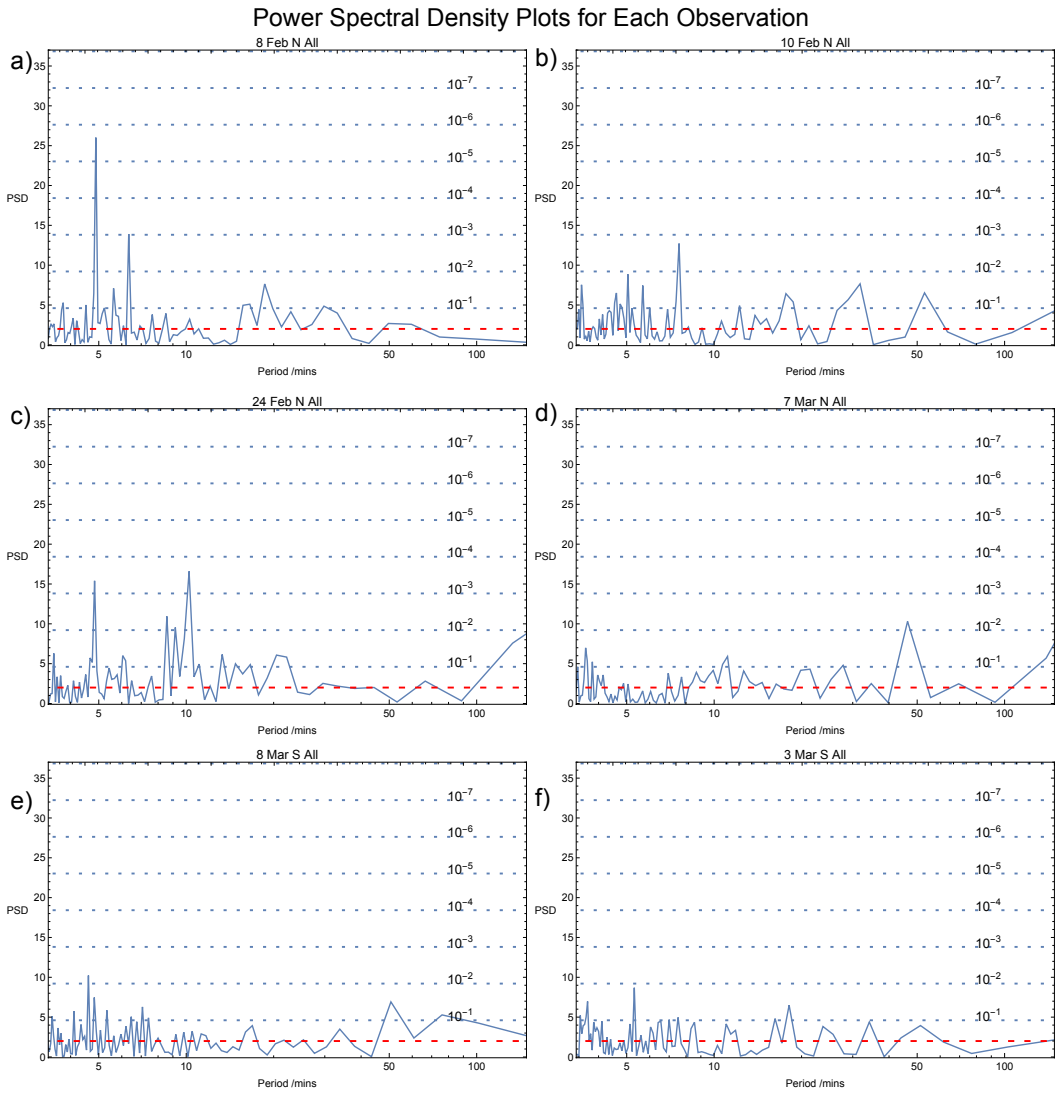

Figure 4.21: Power Spectral Density plots from fast Fourier transforms of X-ray lightcurves from the Northern X-ray aurora on a) 8th Feb, b) 10th Feb, c) 24th Feb, d) 7th March, e) 8th March and f) from the Southern X-ray aurora on 3rd of March. The dotted horizontal lines show single-frequency probabilities of chance occurrence (PCO) for the detected periods (Leahy et al. 1983). The lowest statistical significance and highest PCO of 10^{-1} is at the bottom of the plot. The dashed red line shows the value obtained if photons from a steady source were randomly distributed over the visibility period.

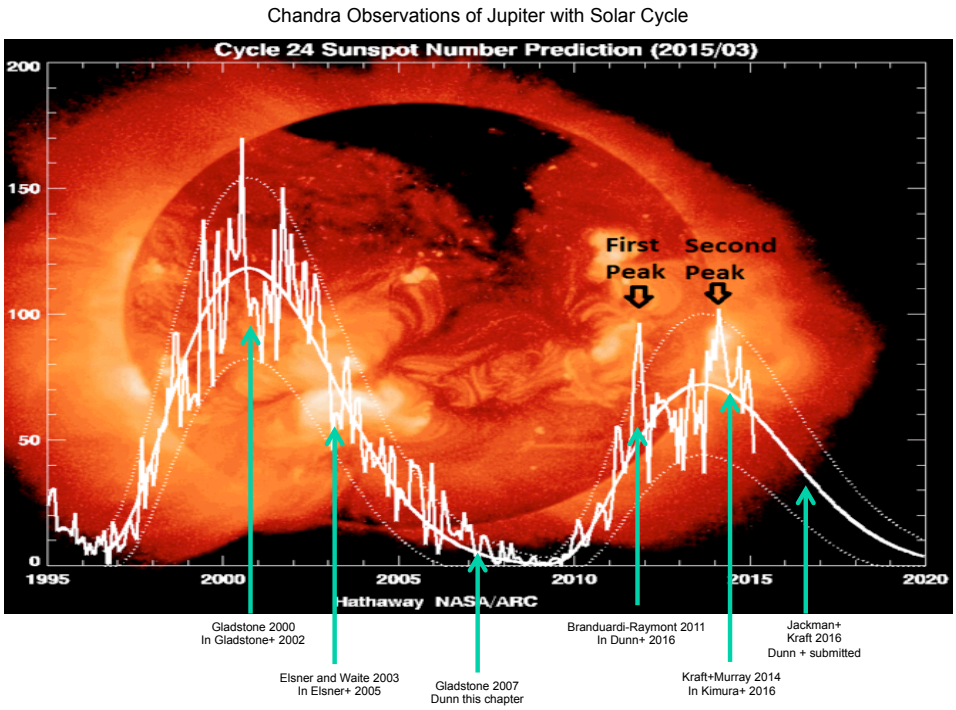

Figure 4.22: Times of Chandra Observations of Jupiter pre-2017 overlaid onto a Hathaway NASA/ARC graphic showing Sunspot number. The Upper name on each label indicates the PI of the campaign, while the lower name indicates the first publication that the observations were featured in.

lenging to tell anything statistically significant from this and thus to explore any persistence in the distinct sulphur/carbon and oxygen timing relationships reported in chapter 2. We note that given a sufficiently bright observation, this may provide a method for distinguishing between different auroral drivers.

4.4 Comparison with Solar Wind Conditions from New Horizons

Fig. 4.22 shows the times of all pre-2017 Chandra Jupiter observations plotted over a graph of sunspot number. These highlight that the observations taken in 2007 were during the lowest point in the solar cycle of any Chandra observations of the planet. The low levels of X-ray output from the Sun during solar minimum explain the low levels of emission from Jupiter's disk in these observations relative to other campaigns. It also may offer some explanation for why the 2 Chandra X-ray observations in October 2011 featured a total

number of Northern auroral X-rays very similar to the total number from all 6 2007 observations. This may suggest a long term relationship between solar wind activity and the Jovian X-ray aurora.

During February 2007, NASA's New Horizons spacecraft was approaching Jupiter and conducting measurements of the solar wind velocity upstream of the planet. On February 26th, New Horizons entered Jupiter's magnetosphere and ceased to provide information on the solar wind conditions upstream. This means that for half of the observations we have information on the solar wind velocity upstream of Jupiter. In order to maximise the use of this information, we: a) inspect the New Horizons data for features that recur over the time span of a solar rotation in order to predict the recurrence of compressions/expansions, b) propagate solar wind conditions from instruments at 1AU to Jupiter using the mSWiM model (Zieger and Hansen (2008)) and Chihiro Tao's solar wind propagation model (Tao, priv comms) and validate them with the results of (a).

4.4.1 Interpreting the New Horizons In-Situ Data

Figure 4.23 shows the peak of the solar wind velocity distribution upstream of Jupiter on a given day of year (R. Ebert, D. McComas, H. Elliott, priv comms) as measured by the New Horizons SWAP instrument. We have added labels to this to indicate structures that may be of interest.

A1-B1-C1 shows a transition from slow solar wind (A) across an abrupt discontinuity into solar wind which is ~ 100 km/s faster (B) to even faster solar wind (C). We interpret this to be a co-rotating interaction region, where slow solar wind (A) is caught-up by fast solar wind, which is consequently slowed at a shock (B). When this shocked fast wind passes New Horizons, SWAP then measures the fast but not-shocked solar wind (C). This then transitions to slow wind across a rarefaction (C-D). More details can be found in the thesis introduction solar wind section.

Since these features rotate with the Sun, they are expected to recur a solar rotation apart (25-27 days). 23 days after A1-B1-C1, similar features are observed again at A2-B2-C2, where slow solar wind abruptly transitions

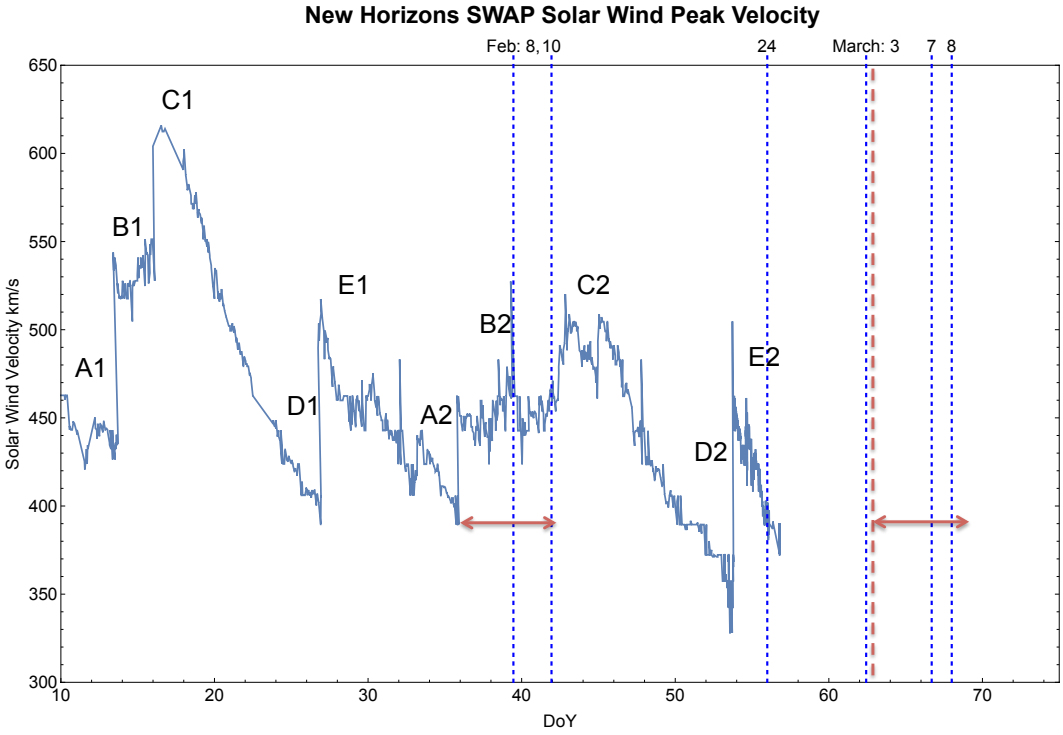

Figure 4.23: Peak of the solar wind velocity distribution upstream of Jupiter on a given day of year as measured by the New Horizons SWAP instrument (R. Ebert, D. McComas, H. Elliott, priv comms). A and D show times of low solar wind velocity prior to an abrupt change, with the associated numbers indicating that they are approximately a solar rotation apart. B shows a region of faster solar wind, that we suggest is shocked from a CIR and is slower than the subsequent faster solar wind at C. E could indicate the arrival of a CIR or a heliospheric current sheet crossing. The dashed blue vertical lines indicate the mid-points of X-ray observations. The dashed red vertical line indicates approximately one solar rotation after the abrupt change at B2. Red arrows indicate the possible duration time of the compression.

to faster solar wind. The peak on DoY 39.5 corresponds to a 26 day time lag from B1, so it is clear that this feature is spatially or temporally evolving because the peak velocity significantly reduced for B2-C2 (by ~ 120 km/s) with a more prolonged compression at B2 than B1 and an earlier abrupt change to faster solar wind (23 days rather than 25-27).

D1-E1 and D2-E2 also show a repeating discontinuity from slower to faster solar wind that is one solar rotation apart. This shock feature does not show A-B-C's characteristic transition from shocked to unshocked fast wind making it more challenging to categorise. We suggest that it could be a CIR or a heliospheric current sheet crossing, which at this stage in the solar cycle and this distance from the Sun, could be embedded within a CIR (see thesis introduction).

While there is not a consistent time lag between A1-B1-C1/A2-B2-C2 ($\sim$23 days apart) and D1-E1/D2-E2 ($\sim$27 days apart), A2-B2-C2 has a comparable speed to D-E so it may be expected to recur with a similar 27 day interval. This would lead it to return on DoY 62-63 (March 3rd-4th). Having identified features that are rotating with the Sun, we further explore the nature of these with solar wind propagation models.

4.4.2 Solar Wind Propagations

Solar wind propagation models are particularly unreliable at the time of these Chandra observations ($\pm$48hours). During this interval, Jupiter was still 3-4 months from opposition (5th June 2007) and the Sun-Earth-Jupiter angle varied from 60-90° while the Sun-Jupiter-Earth angle was $\sim$10°. This means that Earth-orbit spacecraft were observing solar wind conditions $\sim$90° heliospheric longitude from Jupiter and that radially moving ICMEs that Jupiter may have experienced are unlikely to have also impacted Earth. Hence we utilise this information very cautiously, with the expectation that rotating features are better predicted than ICMEs.

Figure 4.24 shows that there is reasonable agreement between the mSWiM and Tao solar wind propagation models. The Tao model only provides propagations from March 2007 because of unreliability in the model prior to this.

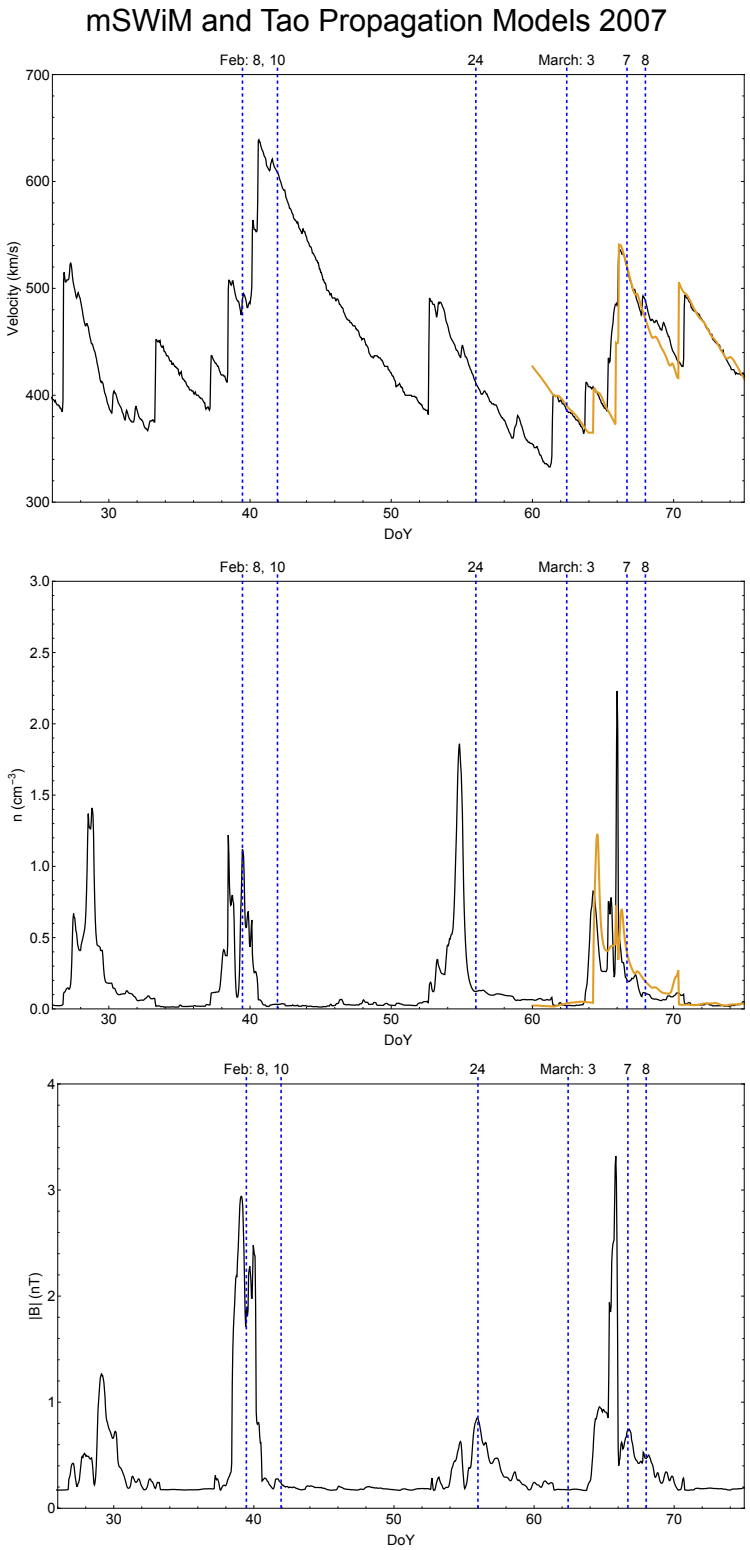

Figure 4.24: mSWiM (black) and Tao (gold) propagation models (Zieger and Hansen 2008) at Jupiter on a given Day of Year in 2007 for solar wind velocity (upper), density (middle) and magnetic field magnitude (lower). Mid-times of the Chandra observations are indicated by the blue-dashed lines with the start times of those observations listed at the top of the plot.

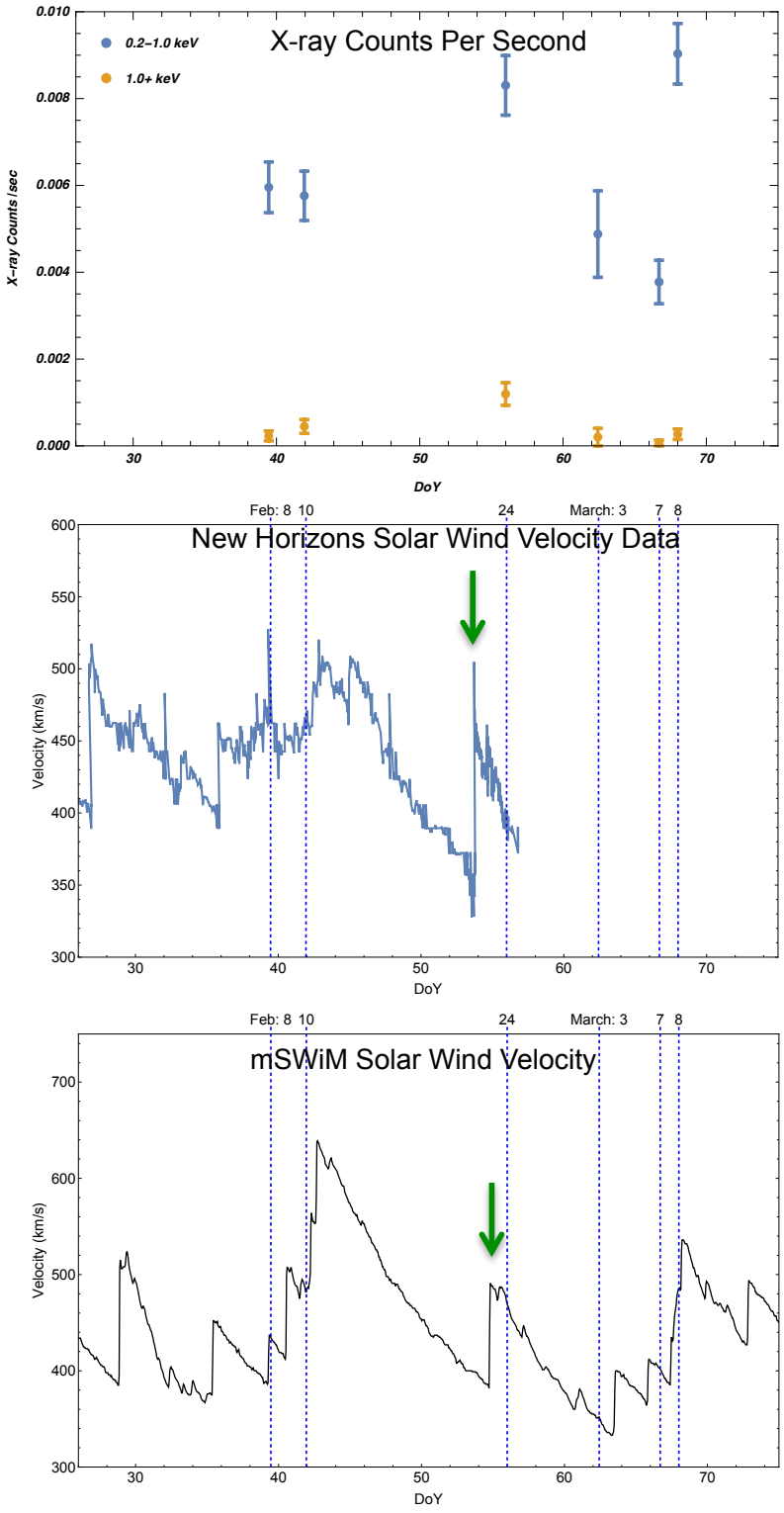

Figure 4.25: Upper: Northern aurora X-ray counts per second for the soft X-rays and Hard X-rays for each observation. Middle: New Horizons Solar Wind Peak Velocity propagated to Jupiter. New Horizons data provided by R. Ebert, D. McComas and H. Elliott. Lower: Shifted mSWiM solar wind velocity propagation to bring it inline with the New Horizons data. Combining these observations with the information in Fig. 4.24 shows that a CIR rotates over Jupiter on DoY 29 then again on DoY 54 and another CIR rotates over Jupiter on DoY 42.5 and again on DoY 68. Green arrows indicate the peak used to align the propagation models and New Horizons SWAP data.

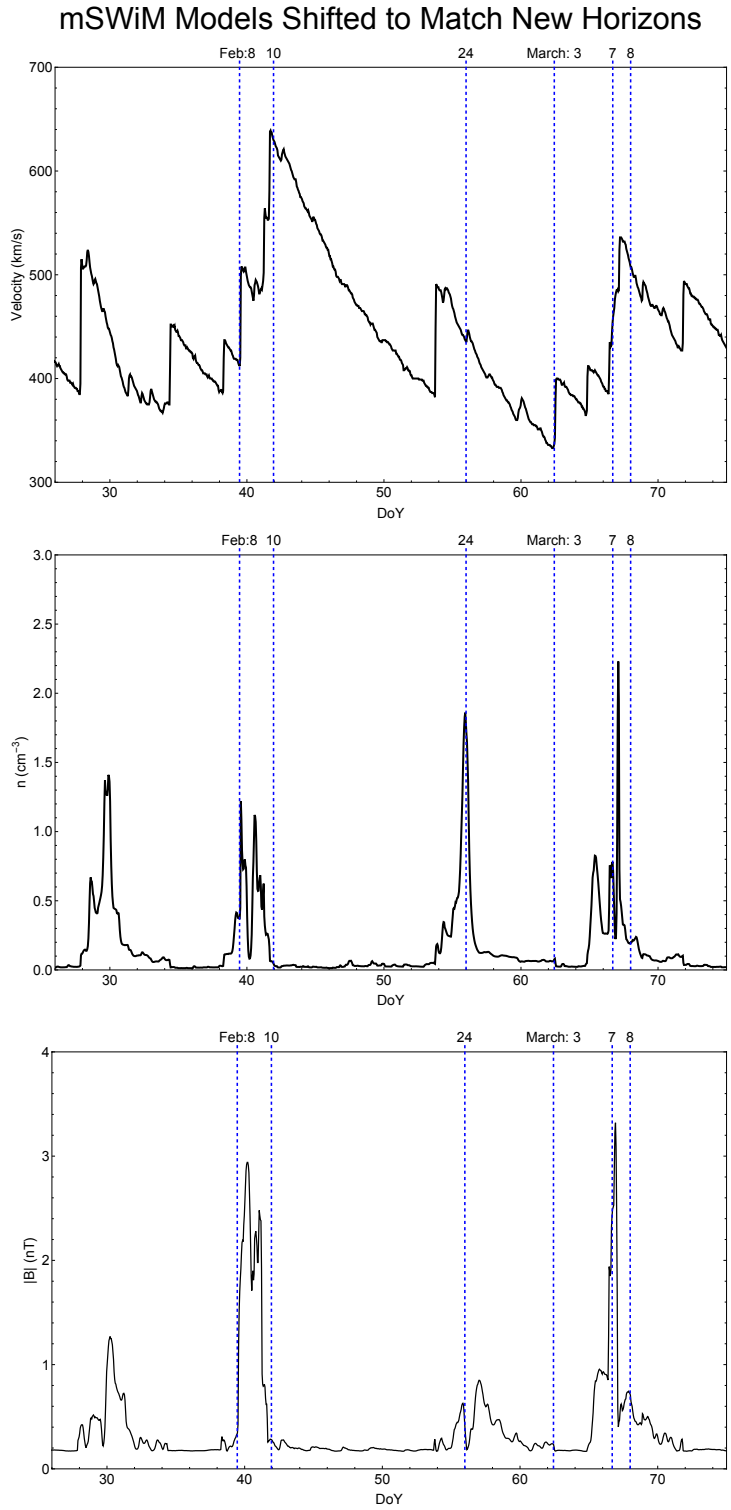

Figure 4.26: mSWiM propagation model (Zieger and Hansen 2008) at Jupiter on a given Day of Year in 2007 for solar wind velocity (upper), density (middle) and magnetic field magnitude (lower). These values have been shifted by 1.1 days with the perceived arrival time of solar wind compressions from New Horizons. We note though that there are still up to 1 day differences between the New Horizons conditions and those predicted by the solar wind propagation model. Mid-times of the Chandra observations are indicated by the blue-dashed lines with the start days of those observations listed at the top of the plot.

However, comparison between the propagation models and the New Horizons solar wind velocity data (Compare middle panel on Fig. 4.25 with top panel on Fig. 4.24), suggests that the models are shifted relative to the New Horizons data. Nichols et al. (2009a) found that a 2.1 day shift was required to account for the in-situ data, but that this 2.1 day shift was not consistent throughout the HST campaign. We note the significant differences in the height of the predicted and measured solar wind velocity between DoY 42 and 52, which better replicate the shape of the distribution of A1-B1-C1 than they do of A2-B2-C2. We use the peak on $\sim$ DoY 53.5 as the reference point from which to shift the solar wind propagations (see green arrow on Fig 4.25). This results in a -1.1 day shift in the mSWiM model relative to the New Horizons measurements (See bottom panel on Fig. 4.25). This provides a reasonable alignment between the model and the measured values. We plot these shifted propagations in Figure4.26, but note that between DoY 30-40 they appear to be $\sim$1 day removed from the observed structures in the New Horizons data. Consequently, a similar 1 day uncertainty may also need to be considered for the observations in March.

These models support the New Horizons interpretation of two repeating CIRs represented by repeating solar wind velocity discontinuities, solar wind density peaks and IMF magnitude peaks. The discontinuity in solar wind velocity that indicates a solar wind shock on DoY $\sim$27 and $\sim$53 (Fig. 4.25) is accompanied by an increase in density and magnetic field strength. Because these occur $\sim$26 days (a solar rotation) apart and feature similar morphology we suggest that they are a Corotating Interaction Region (see thesis introduction for more details). Similarly the solar wind density and magnetic field increase on DoY $\sim$39 recurs on DoY $\sim$65. The Chandra observation on the 10th of Feb occurs one solar rotation prior to the one on 7th of March, meaning that we might expect those observations to experience similar solar wind conditions. Unfortunately the 7th of March observation had limited CML coverage of both aurorae, so it is difficult to draw direct comparisons.

However, the timing of the compressions suggests that the observations on Feb 8th, 10th and 24th and March 7th and 8th were all either during

a solar wind compression or during the post-compression expansion of the magnetosphere and thus might provide different phases of the X-ray aurora during a solar wind shock. On the 3rd of March the solar wind conditions appear to suggest a deep rarefaction, which may explain the very dim auroral emissions at this time.

4.5 Comparison with HST UV Aurora

In order to enrich our understanding of the drivers of Jupiter's aurora it is important to attempt to systematically understand how the different auroral wavebands are connected. This also combines the advantages of distinct wavebands, while mitigating their weaknesses. For example, X-ray observations provide hours of continuous time-tagged coverage of the high energy emissions from both poles, but provide limited counting statistics and poorer spatial resolution than HST. In contrast, the HST UV observations are photon-rich, but can only observe for up to 1 hour intervals and must concentrate on only one pole at any one time. The two wavebands therefore provide highly complementary observations.

Alongside the X-ray campaign of 2007 (DoY: 39, 41-42, 55-56, 62, 66, 67-68) , there was also an extensive Hubble Space Telescope campaign over DoY 51-70, which used the Advanced Camera for Surveys Solar Blind Channel. This UV campaign consisted of 907 (580) images of the Northern (Southern) Aurora, taken in groups of 15 images spanning $\sim$1 hour, with most exposures lasting 100 s (Nichols et al. 2009a). This observation campaign was first discussed in Nichols et al. (2009a) and the images shown here are from videos provided by J. Nichols (priv. comms).

4.5.1 Phases of UV Auroral Morphology Produced by a CIR

Before comparing the UV and X-ray emissions, we first utilise the UV coverage to add further interpretation to the solar wind conditions at this time. The New Horizons data predicts the arrival of solar wind compression D2-E2 on 23 Feb (DoY 54). By shifting CIR A2-B2-C2 by one solar rotation we also

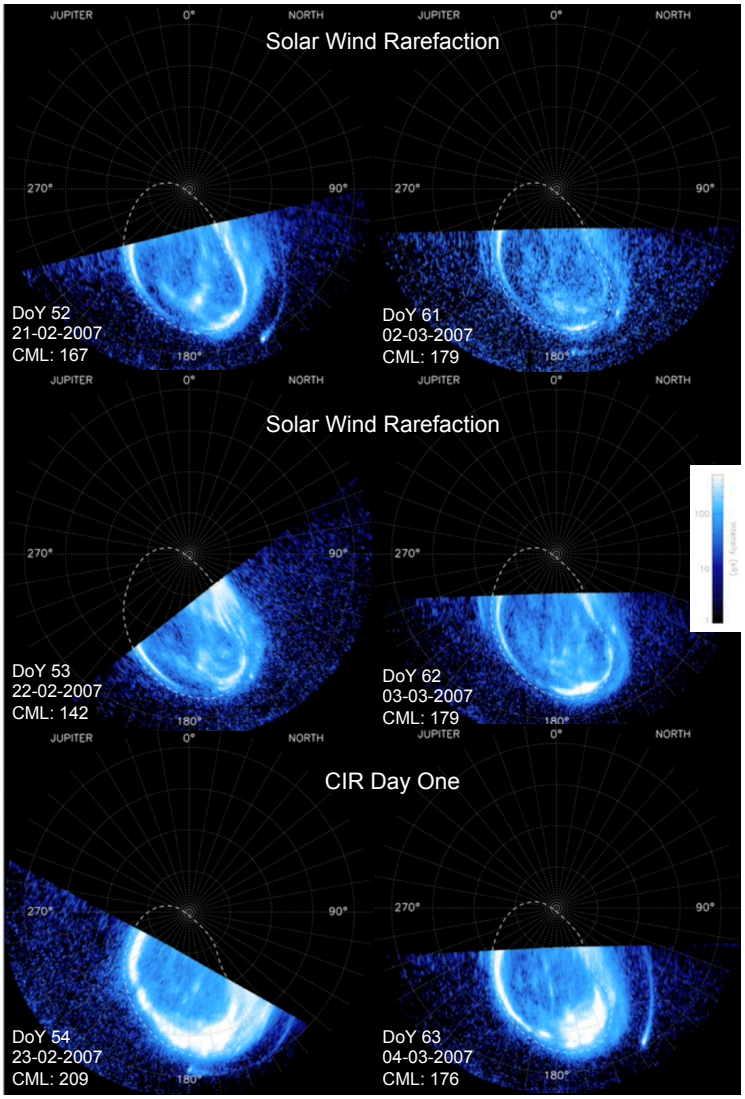

Figure 4.27: A series of UV Auroral Images as close to a CML of 180° as possible, which show the auroral morphology during solar wind rarefaction and then at the arrival of a CIR induced shock for two separate shock intervals. Each image is a $\sim$ 2 minute exposure. Images provided by J. Nichols (priv. comms) and entire HST campaign discussed in Nichols et al. (2009a).

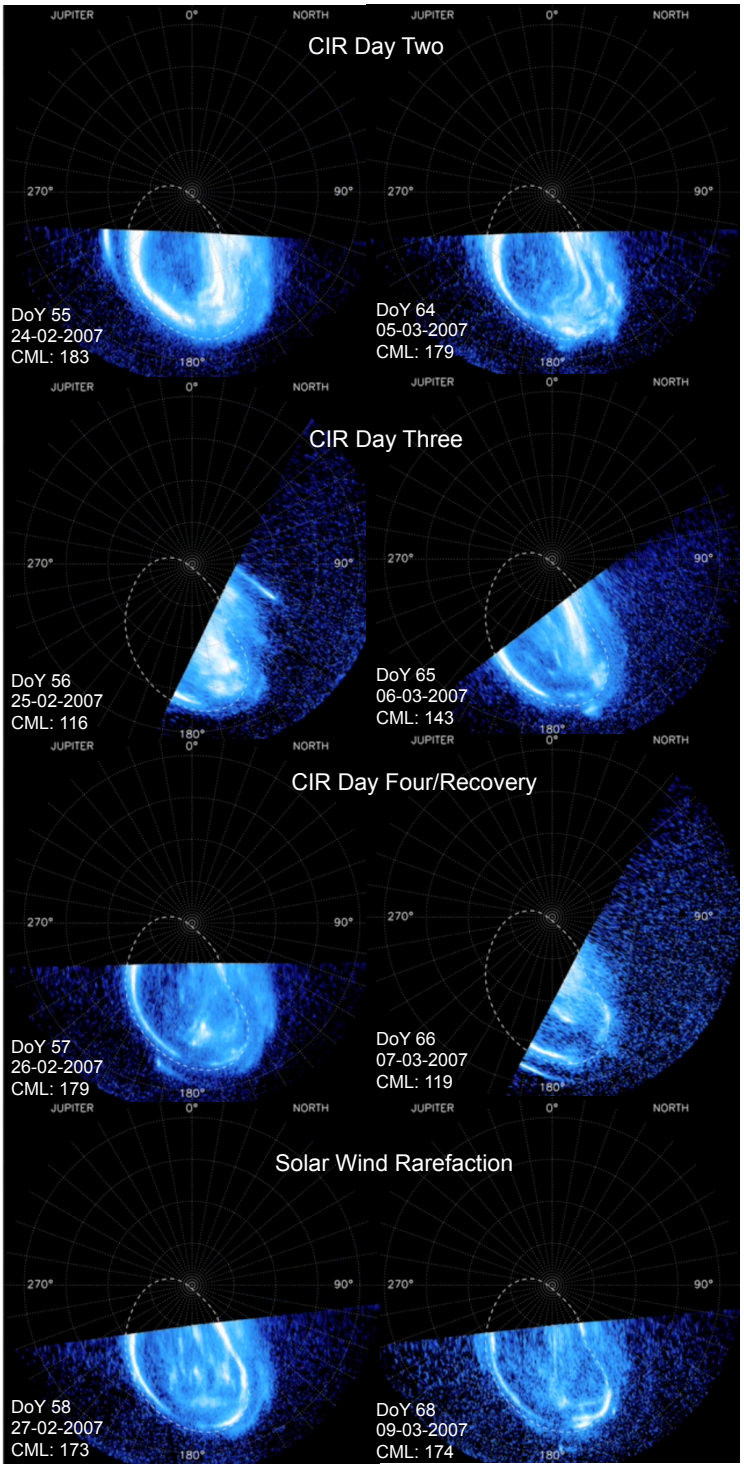

Figure 4.28: A series of UV Auroral Images as close to a CML of 180° as possible, which show the evolution of auroral morphology throughout a CIR. Images provided by J. Nichols (priv. comms) and entire HST campaign discussed in Nichols et al. (2009a).

expect a subsequent shock, A3-B3-C3, on 3-5 March (DoY 62-64). The shifted solar wind propagations also predict the shock arrival on 5 March with a 2-day uncertainty.

Between the 22nd to the 23rd of February, when the solar wind shock D2-E2 arrived, the UV aurora changed morphology dramatically. A similar change in morphology is also observed on 4 March with the expected arrival of A3-B3-C3.

Assuming that the shocks D2-E2 and A3-B3-C3 impacted Jupiter at this time, we place the UV auroral observations from this time interval in phase with the shock arrival. This allows us to directly compare the consistent changes in the aurora with the shock arrival, in order to better understand how the UV aurora develops with the shock. We show this comparison in figures 4.27 and 4.28, where we directly compare the changing UV aurora emissions with the development of the solar wind compressions D2-E2 and A3-B3-C3. Here, we briefly describe how the UV aurora develops over the course of the compression.

Pre-CIR (21-22 Feb and 2-3 March): The main oval is thin and occurs along the dashed reference contour defined by J. Nichols, which represents its average location from the observation campaign (Nichols et al. 2009a). There are intermittent 'swirls' of emission in the high latitude swirl region and bright flashes/flares from the Pallier and Prange (2004) cusp.

CIR arrival (23 Feb and 4 March): The main oval significantly thickens and moves poleward on the dawn side. From noon-dusk an additional oval disconnected from the main oval is found at higher latitudes. This polar dusk arc emits bright pulses 20-30 minutes apart. On 4 March the cusp region is still observed as a bright spot.

CIR +1 day (24 Feb and 5 March): the thick polar dusk arc that formed at the time of arrival appears to have split into multiple arcs in the dusk sector. These arcs exhibit bright pulsations and poleward bifurcations from the dusk sector (see Fig 4.29). These pulses often occur at noon local time at the ends of the dusk arc, and could be interpreted as occurring equatorward of the arc,

while the bifurcations occur on the polar cap side of the arc.

CIR +2 days (25 Feb, 6 March): The CML coverage makes it challenging to interpret whether there is still a pulsing dusk arc for 25 Feb or whether it is large polar flares. For 6 Mar there are no longer discrete arcs just one thick and pulsing arc.

CIR +3 days/subsequent solar wind rarefaction (26-27 Feb, 7-9 March): The main oval dims and returns at lower latitudes. The polar emissions are limited to bright flares that occur in the 'cusp' region, with swirls again poleward of this. The poor CML coverage on the 7 March makes it challenging to know whether the polar emissions are still flaring, but there appears to be some continued pulsing at very high latitudes close to the nightside.

We now attempt to interpret the magnetospheric processes that are induced by the compression and produce the recurring signatures described above.

4.5.2 Interpreting the Magnetospheric Processes Associated with the UV Auroral Signatures

The following explanation for the observed behaviour developed during conversations with S. Badman and R. Gray. When the CIR arrives the formation of the second oval poleward of the main oval from noon-dusk is likely to suggest velocity shears (e.g. Cowley et al. 2007) and the cusp brightening may suggest increased reconnection in line with Bunce et al. (2004).

Figure 4.30 utilises the Vogt et al. (2011; 2015) ionosphere-magnetosphere mapping in order to interpret the signatures observed. This shows that the equatorward pulses connect to the noon magnetopause, whereas the dusk arc and bifurcations connect to the dusk magnetopause and open field lines respectively. The small difference in ionospheric location compared to the large difference in magnetospheric mapping is because the field lines near the dusk flank magnetopause are significantly bent towards the tail (see thesis introduction).

This suggests that the pulsing bifurcations in the dusk oval may represent: a) signatures of rolled up Kelvin Helmholtz along the boundary, b) opened

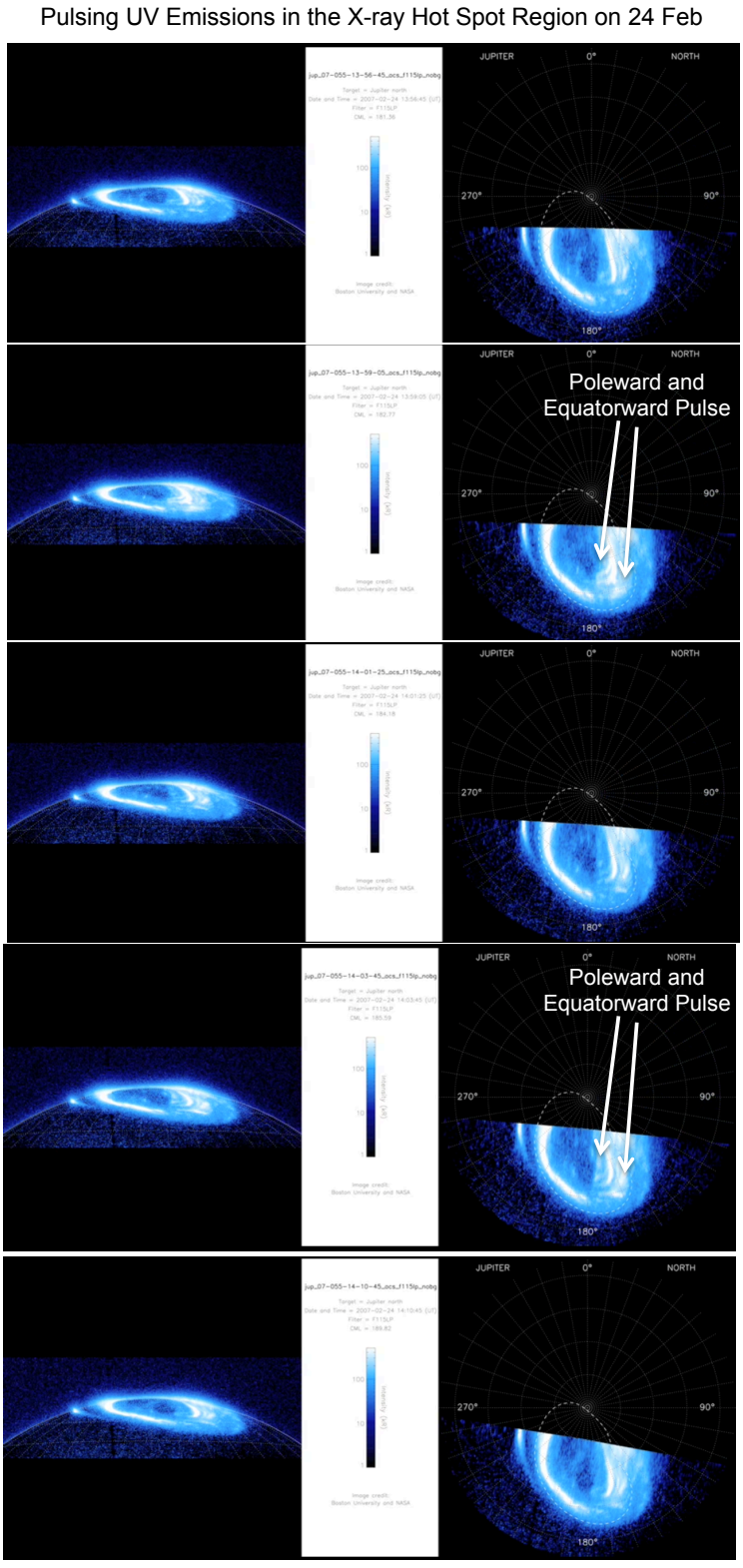

Figure 4.29: Hubble ACS UV images of Jupiter (left) and polar projections (right) from 2007 courtesy of J. Nichols. Pulsing UV Polar Aurora on the same day, but not at the same time, as the X-ray observation on Feb 24th. These observations were taken 1 Jupiter rotation prior to the X-ray observations shown previously in this chapter. An arc of emission on the dusk flank is periodically accompanied by a pulses of emission poleward and equatorward. The polar pulses sometimes appear to be bifurcations in the arc that stretch into the polar cap. Here we show a simultaneous pulse of poleward and equatorward emission followed by another 5 minutes later. During the contemporaneous X-ray observation, the X-ray hot spot appeared to have expanded equatorward and the hard X-ray emissions match the location of the UV main oval here - i.e. the hard X-rays are shifted to be co-located with the pulsing soft X-ray hot spot.

flux being convected across the polar cap, c) tail reconnection signatures (e.g. Nichols et al. (2017), or d) turbulence in velocity shears as plasma moves from noon to dusk. We propose that the flaring at noon that surprisingly appears to be equatorward of the polar dusk oval is actually the signature of the cusp. We argue that there is no longer an auroral signature associated with the cusp's previous location, but during compression the signature of the cusp should be at its brightest (e.g Bunce et al. (2004)). The cusp's new location at lower latitudes is a consequence of the polar cap having expanded with the associated solar wind compression. Alternatively, the processes that producing the pulsing feature at high latitudes need to have shifted to locations deeper inside the magnetosphere and still close to noon.

Given that the shock that appears on 4 March is a rotating feature in the solar wind that is predicted by the models to have also occurred 26-27 days earlier, this shock is also likely to have arrived at Jupiter around the 5th of Feb. Given that the UV auroral response is shown to last 3-5 days, then the X-ray observations on Feb 8th and 10th would have occurred towards the end of the compression or subsequent to it, during solar wind expansion. This is in-line with the 3.5 day separation between the abrupt discontinuity in the New Horizons data on 5th Feb (DoY 36) and the first X-ray observation of the campaign on 8 Feb (DoY 39). However, there is also a sharp spike in solar wind velocity on DoY 39, which may also indicate the presence of a shock. Without further in-situ data it is difficult to determine.

4.5.3 Interpreting the X-ray observations in the Context of the Solar Wind Conditions

We present each of the observations in the order in which they experience a solar wind shock, starting with the observation closest to the shock arrival and ending in rarefied solar wind conditions.

The Feb 24th observation occurs when New Horizons was closest to Jupiter and therefore the solar wind conditions are those that are best constrained. This observation occurs shortly ($\sim$ 1.5 days) after an abrupt change in velocity at the same time as the solar wind density is predicted to peak by the propa-

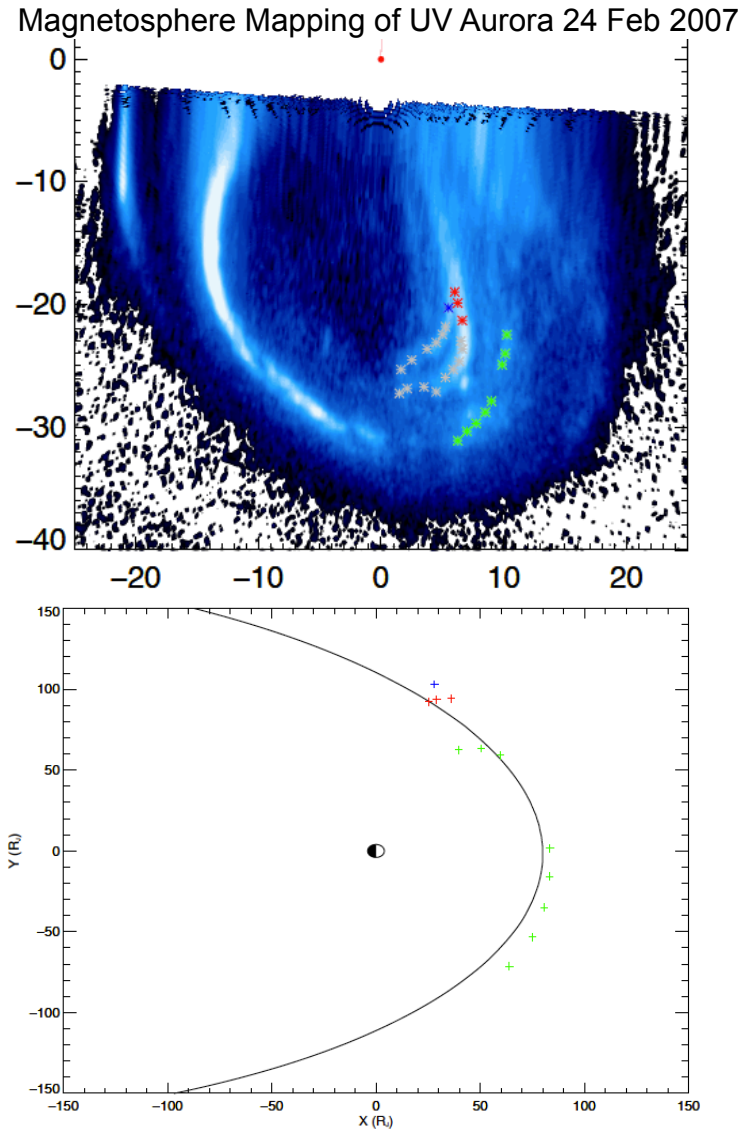

Figure 4.30: From Gray (priv comms): Ionosphere-Magnetosphere mapping for bifurcations and noon local time pulses in the UV polar aurora.

gation models (Fig 4.26). All 4 X-ray observations (Feb 24 2007, Oct 2 2011, 24 May 2016, 1 June 2016) that occur within 2 days of solar wind compression, including this one, feature 9-13 minute pulsations. This suggests that during solar wind compressions, a 9-13 minute pulsation period is a characteristic timescale for either wave activity, resonance or transit time between the poles and the magnetopause. If the X-ray emission is associated with the cusp as suggested by Bunce et al. (2004), Elsner et al. (2005) and Dunn et al. (2016), then the apparent motion of the cusp to lower latitudes that is observed in the UV observations would match the equatorward expansion of the hot spot at this time and would suggest that the changing hot spot morphology is caused by polar cap expansion during the solar wind density peak and height of solar wind compression. Applying the Joy et al. (2002) magnetopause model to the mSWiM density and New Horizons solar wind velocity gives a magnetopause stand-off point of $\sim$60 R_J for the 24-25 Feb.

The solar wind velocity for the 24 Feb observation is 50 km/s lower than for the 2 observations on Feb 8th and 10th and yet on the 24th Feb observation the X-ray aurora was much brighter. This contradicts the findings of Kimura et al. (2016) that the X-ray hot spot brightness is positively correlated with solar wind velocity.

The 8th Feb, 10th Feb and 8th March observations are more difficult to interpret because there is far less agreement between the solar wind propagation (Fig. 4.26) and the New Horizons upstream data and it is clear the shock that they experience is evolving.

The 8 March observation has less regular but comparably bright X-ray pulsations to the 24 Feb. The solar wind propagations and the UV observations suggest that the shocks direct influence on the aurora ends during or shortly after this observation. The solar wind propagations suggest that the density peak occurs during this period without HST observations, but during the 8 March Chandra observation. There appears to be a change in the X-ray lightcurve behaviour during the observation at 160 min (175° CML), which may reflect the changing nature of the magnetosphere and explain the challenges in modelling the unusual XMM spectra at this time (V. Carter-

Cortez, priv comms). It may therefore be that the brightening in the soft X-ray emission is a response to this density peak, while the mass-loss from the tail reconnection induced by the preceding solar wind compression produced low middle magnetosphere plasma densities and the observed dim UV/hard X-ray main oval. Alternatively, maybe the X-ray aurora is bright during periods of magnetospheric expansion or brightens due to other factors unrelated to the solar wind.

Based on the New Horizons measurements, the 8 Feb observation occurs 3.5 days after the compression began. The CIR phases of the UV aurora may suggest that the 8th Feb is towards the end of the auroral response and the low levels of hard X-ray emission at this time may support this. However, the solar wind propagations suggest that the third largest of the density enhancements occurred during this observation and the occurrence of a regular 5 minute period and similar auroral morphology on 8 Feb and 24 Feb may support this.

The New Horizons data indicate that the solar wind transitions to unshocked fast solar wind during the 10 Feb observation and is therefore less dense which presumably leads to magnetospheric expansion. At this time, the soft and hard X-ray aurora is dim, but has morphology similar to the 8 March observation which is also between the end of a compression and subsequent rarefaction. The low levels of hard X-ray emission may also suggest that a dusk polar arc or dawn storm is no longer present.

The 3 March Southern aurora observation was very dim in comparison to the 2016 observations and the New Horizons SWAP data, solar wind propagations and UV auroral emissions all suggest that this was during solar wind rarefaction. This may therefore represent the quiescent state of Jupiter's Southern X-ray aurora in the absence of a solar wind induced shock.

4.5.4 UV-X-ray Comparisons

Figures 4.31 shows how the different components of the UV auroras varied during the Feb-March 2007 campaign. Only one of the UV observations was simultaneous with the X-ray observations, this was the Southern Auroral observation on the 3rd of March. The Feb 24th X-ray observation featured one

HST visit one Jupiter rotation either side of the X-ray observation, but unfortunately none that were simultaneous. The 7th March X-ray observation is preceded by 1 day by a HST observation and one day after the 8th March X-ray observation there was another HST visit. The Feb 8th and 10th X-ray observations were conducted before the HST campaign began.

4.5.5 24 - 25 Feb

The UV main oval and high latitude emission is bright in both the 24 and 25 Feb observations (Fig. 4.29 and 4.31) that bracket the X-ray observation. On 24 Feb the emission from the UV polar aurora features a bright polar dusk arc. One Jupiter rotation later, the X-ray observation occurred. The Feb 24th observation is the only 2007 X-ray observation with a bright hard X-ray component. Some of this hard X-ray emission appears to occur across the hot spot in the location of the polar dusk arc. The rest appears to be co-located with the thickened dawn storm arc of the main oval.

Initially it had appeared surprising that this hard X-ray emission (from electrons) appears to be roughly co-located with soft X-ray emissions (from ions). However, we observe the UV emission to pulse both poleward and equatorward of this dusk arc with a $\sim$ 5 minute gap between two pulses (Fig. 4.29). The soft X-rays appear to also feature characteristic pulsations at 5 and 10 minute periods in the observation one Jupiter rotation after the UV pulsations are observed in this region. We therefore suggest that the X-ray emissions relate the UV pulsations and polar dusk arc bifurcations. We suggest that these are produced by events along the open-closed boundary, which has expanded due to the expansion of the polar cap during compression, but that they may also relate to KHI, Tail Reconnection.

Figure 4.33 shows that one Jupiter rotation after the X-ray observations, the UV polar aurora remains highly active, suggesting that the auroral behaviour during the X-ray observation may be comparable to the HST observations either side of it.

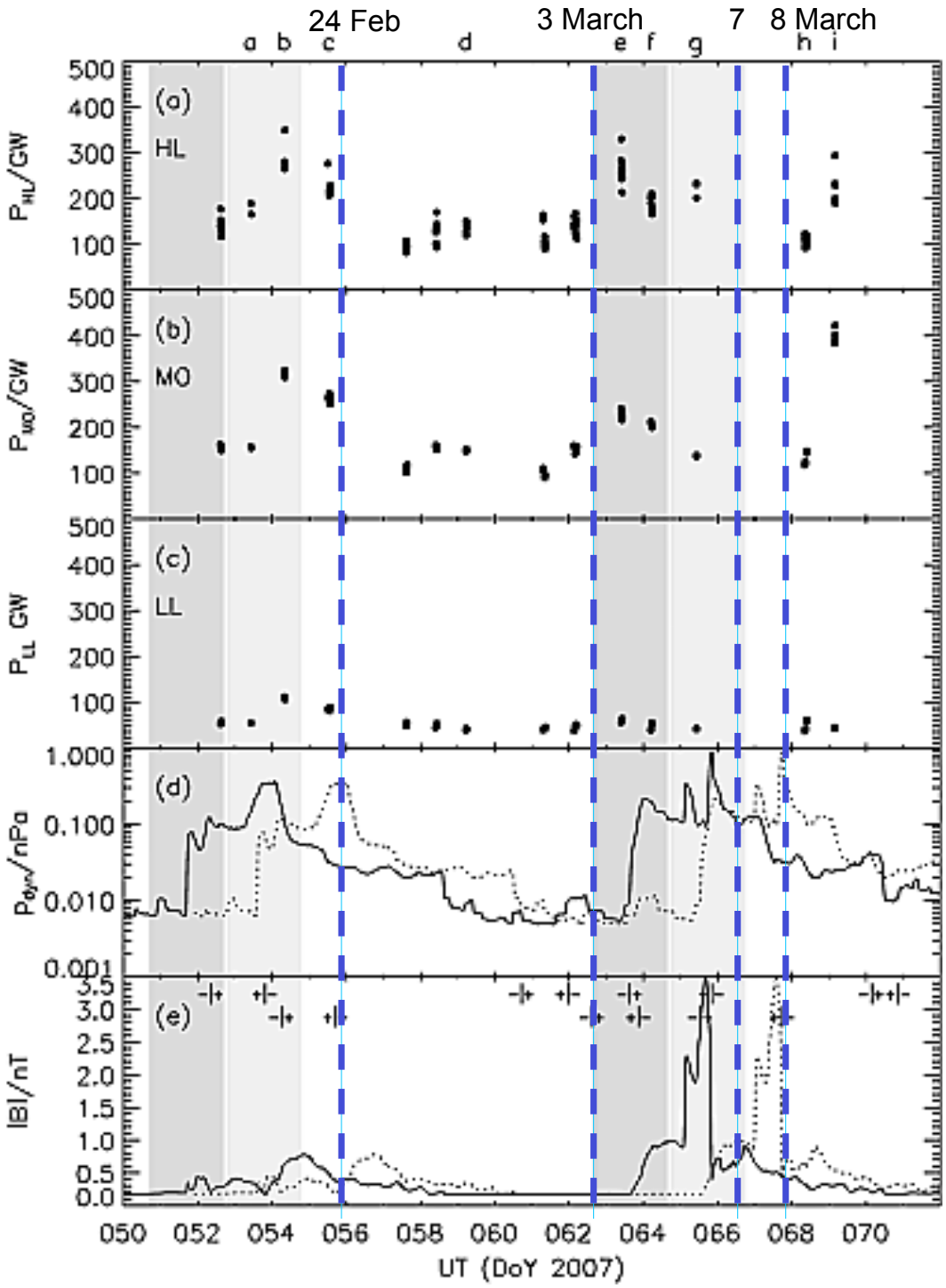

Figure 4.31: Adapted from Nichols et al. (2009a): Power emitted from the different auroral regions defined in Figure 4.32, along with the modelled solar wind conditions for the first HST campaign in Feb-March 2007. Specifically, we show (a) the power emitted from the high-latitude region ('PHL'), (b) the power emitted from the main oval region ('PMO'), (c) the power emitted from the low-latitude region ('PLL'), d) the solar wind dynamic pressure, and (e) the interplanetary magnetic field (IMF) magnitude $|B|$. The individual points in a-c represent the powers obtained for each image. The solid lines in the magnetohydrodynamic (MHD) model (d and e) show the original model timings, while the dotted lines show the timings shifted by +2.1 days. The dark grey regions show the estimated arrival time of the forward shocks within 1 standard deviation uncertainty of the MHD model timings, and the light grey regions are similar but for the shifted timings. Also shown in e are the estimated locations of the sector boundaries, along with the sign of B_T either side. The original timing is on top, while the shifted timing is below. Overlaid on the figure are blue dashed lines to indicate the times of X-ray observations.

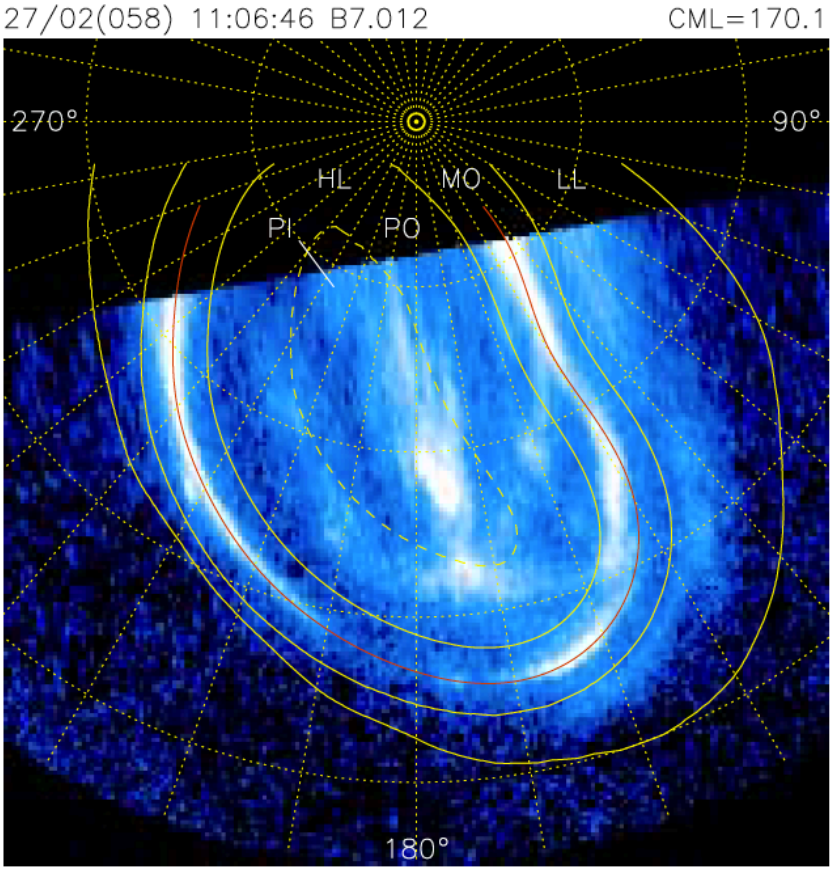

Figure 4.32: Figure from Nichols et al. (2009a): A typical projected Hubble Space Telescope (HST) image of Jupiter's auroras, obtained on 27 February 2007. The simulated view is from above the north pole, and the image is displayed with a log colour scale saturated at 500 kR. The red line shows the reference main oval as given by the locations in Table 1. The solid yellow lines show the boundaries between the high-latitude region, the main oval, and the low-latitude emission. The dashed yellow line indicates the boundary between the polar inner and polar outer regions. The yellow points indicate a 10° by 10° planetocentric latitude - SIII longitude grid. The image is oriented such that SIII longitude 180° is directed toward the bottom.

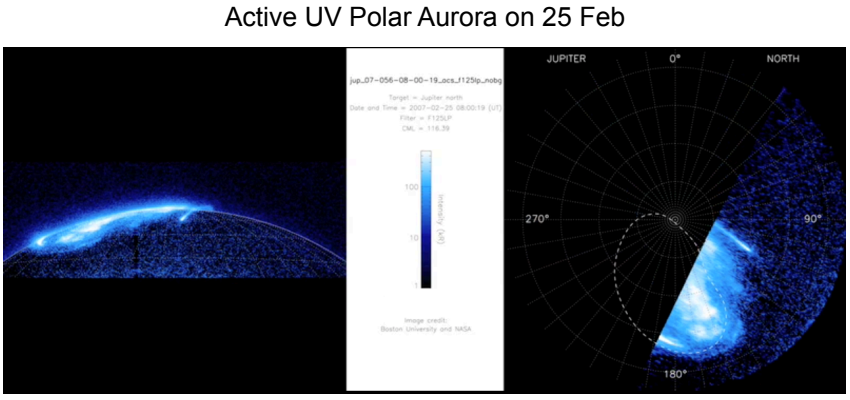

Figure 4.33: Hubble ACS UV images of Jupiter (left) and polar projection (right) on 25 Feb 2007 (J. Nichols, priv comms).

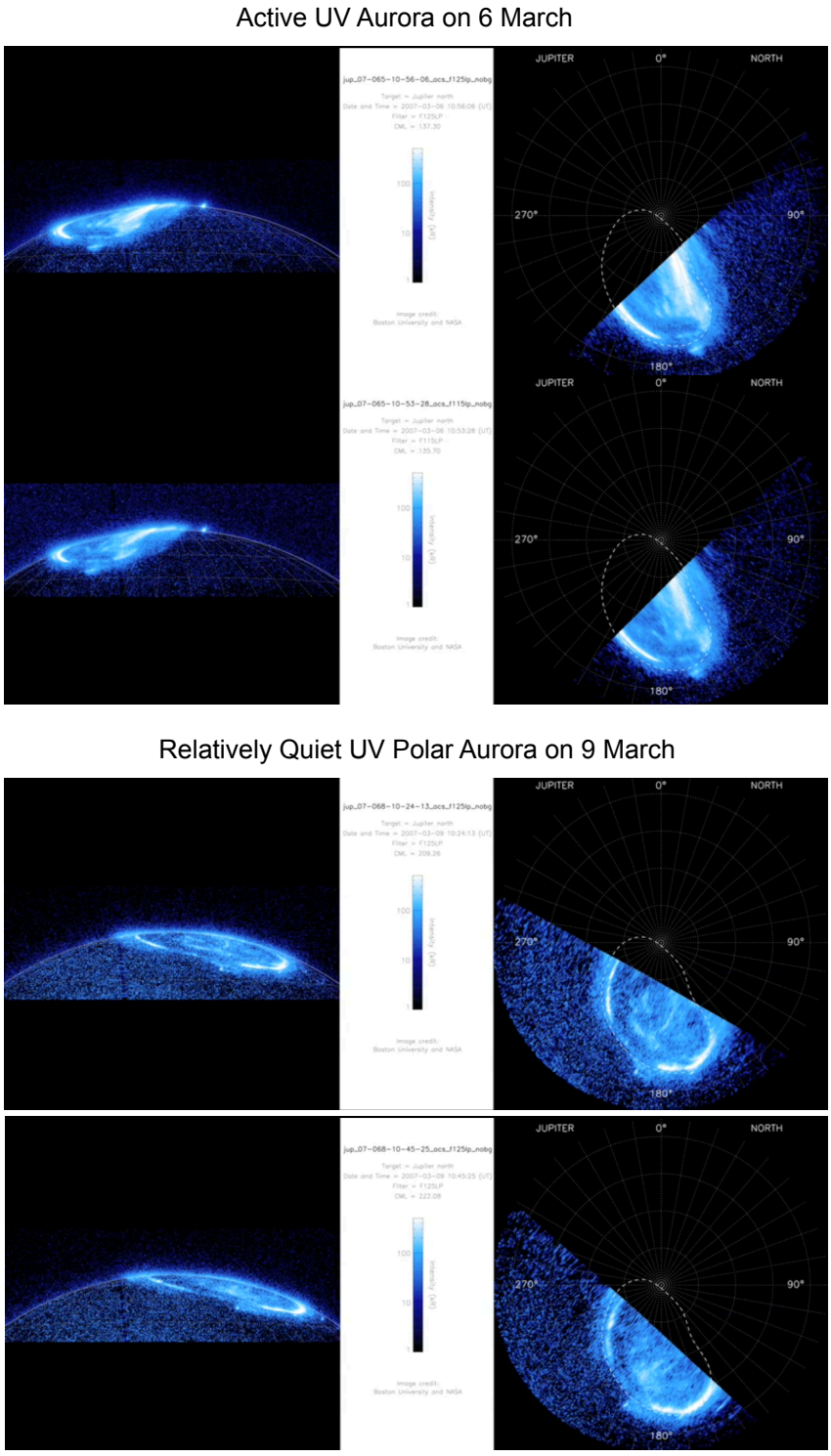

Figure 4.34: Hubble ACS UV images of Jupiter (left) and polar projection (right) on 6 (upper) and 9 (lower) of March 2007 (J. Nichols, priv comms). The UV aurora features a bright dusk arc on the 6 March (upper) prior to the 7 and 8 March X-ray observations, but this has dissipated by 9 March (lower). There are suggestions of a transpolar arc on 9 March.

4.5.6 8 - 9 March

In contrast with the Feb 24-25 observations, the hard X-ray emission on 8-9th March is very dim and the UV main oval is correspondingly dim on both the 7th and 9th of March HST observations (Fig. 4.31). However, the soft X-ray emission from the region poleward of this is the brightest of the campaign and appears similar to the 24 Feb observation. Two days prior to this (see Fig. 4.31 and 4.34) the polar UV emissions were also bright and active, however, the UV observation closest to the X-ray observation one Jupiter rotation later on the 9th of March shows much dimmer polar emission. Given that none of these observations were simultaneous, it is difficult to know whether it is possible to have relatively bright X-ray aurora, while there is dim UV aurora. We note that the mSWiM model predicts that the density peaks between the UV observations, so any corresponding change in the UV emission may have been missed by the Hubble observations.

Alternatively, we have already suggested (Chapter 2) that high latitude reconnection may produce some of the timing signatures observed in the 2016 X-ray observations. A possible signature associated with this process is auroral transpolar arcs (e.g. Nichols et al. (2009b)). There appears to be a transpolar arc stretching from noon to midnight present in the UV aurora on the 9th March (see Fig 4.28 and also 4.34 to trace the local time persistence of this feature), suggesting that solar wind and magnetospheric conditions might favour this process at this time. The 8th March X-ray aurora also seems to have intermittent poleward streaks with similar morphology (e.g. 4.13) to the UV transpolar arcs.

4.5.7 3 March

The 3rd of March observation occurs during an extended period of low power UV emissions (Fig. 4.31) and the Southern X-ray aurora is also very dim at this time relative to the 2016 observations (although we note that different instruments were used for each - ACIS vs HRC). This observation is also predicted to be coincident with a deep solar wind rarefaction approximately

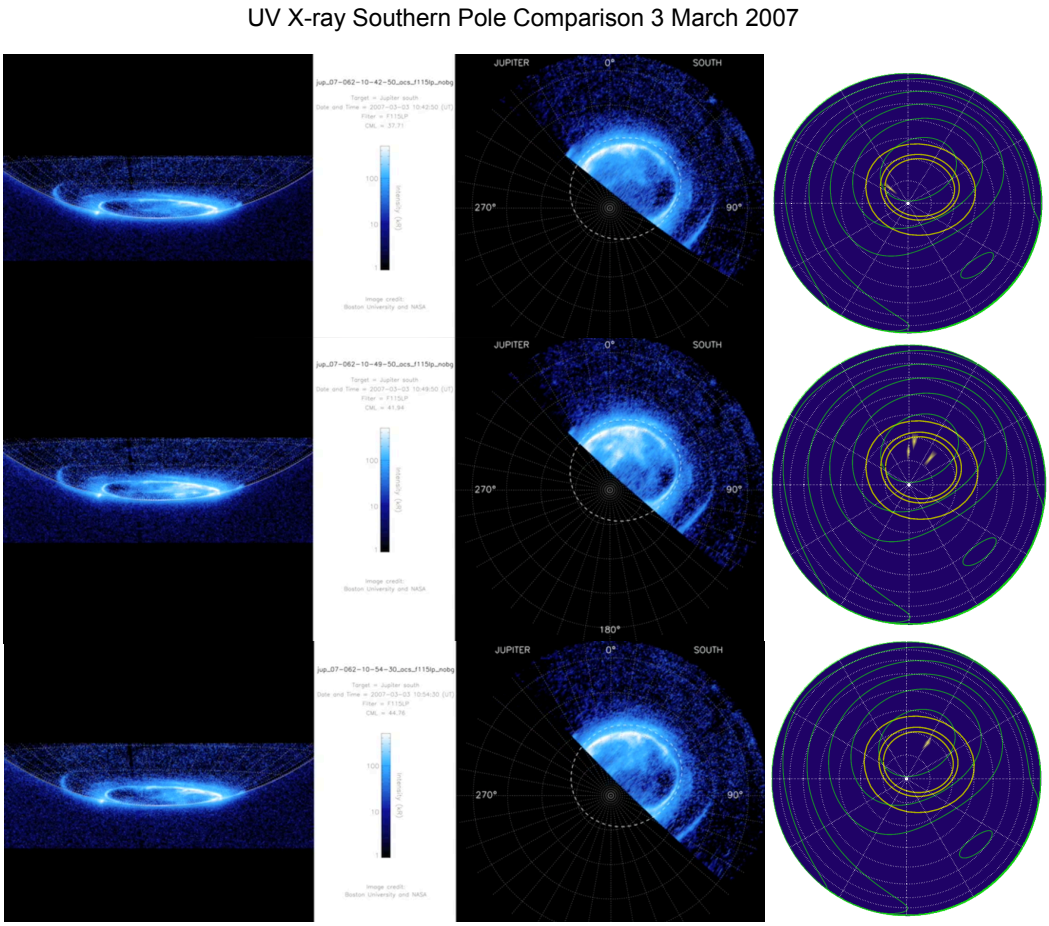

Figure 4.35: Simultaneous UV and X-ray Observation of Jupiter's South Pole on 3 March 2007. HST images provided by J. Nichols (priv comms). UV images of Jupiter's Southern hemisphere (left), UV South Pole Projections (centre), X-ray South Pole Projections (right). Top:10:42:29 - 10: 47:29 (pre-marginal brightening); Middle: 10:47:30 - 10:52:10 (during marginal brightening); Lower: 10:54:30-10:59:30 (post- marginal brightening).

one day prior to the shock associated with a recurring CIR.

On the 3rd of March there were simultaneous UV and X-ray observations. Simultaneous times spans: 08:52 - 09:36 (Chandra observation minute: 69 - 113), 10:23 - 11:06 (Chandra observation minute: 160 - 203) and 12:00 - 12:42 (Chandra observation minute: 257 - 299). However, the Southern X-ray hot spot emission is especially dim throughout this whole observation. Here we show an example of a 'peak activity time' when 3 X-ray events were detected simultaneous with 3 UV polar emissions that saturate the 500 kR colour bar. We contrast these marginally brighter X-ray and UV emissions from 10:47:30 - 10:52:10 with dimmer X-ray and UV emissions from 10:42:29 - 10: 47:29 (pre-flare) and 10:54:30-10:59:30 (post-flare). We stress that these are very low signal observations and well within the Poisson errors, but note that Jupiter blocks background X-ray emission and the ACIS instrument produces very little spurious internal background, so these three X-rays are expected to be genuine events. The X-ray brightening during a UV flare reported in Elsner et al. (2005) consisted of 7 X-ray events. However, further simultaneous observations are needed during times when the aurorae are bright and times when they are dim, in order to systematically constrain whether there is a connection between the UV kR intensity and X-ray emissions (e.g. a threshold UV intensity that also results in X-rays).

4.6 Conclusion

We present X-ray observations of Jupiter during solar minimum in February and March 2007. We find that the equatorial and auroral emission is dimmer than in previous campaigns. We compare the observations with New Horizons solar wind measurements upstream of Jupiter and a contemporaneous Hubble Space Telescope UV campaign.

One day after a solar wind shock, on February 24th, the Jovian soft and hard X-ray aurorae brighten and the hot spot pulses with a 5 and 9-13 minute period, as has been observed during other solar wind compressions (see previous two chapters). During this interval (but not simultaneously), a dawn

storm forms in the UV main oval and a newly-formed dusk polar arc pulses at a similar rate to the X-ray emissions. This is the only 2007 observation with significant hard X-ray emission and these hard X-rays appear co-located with the UV dawn storm and dusk polar arc. Soft X-ray emission from the hot spot appears to occur co-located or possibly both slightly equatorward and poleward of the dusk polar arc.

We propose that the pulsing UV and X-ray hot spot emission at the noon-end of the dusk arc is from a shifted cusp on an expanded polar cap, during solar wind compression. Poleward and duskward of this, we report the identification of pulsing bifurcations in the dusk arc, which also occur with similar regularity to the X-ray hot spot pulsations. These may relate to a second driver process such as Kelvin Helmholtz Instabilities or tail reconnection, which would both be triggered by solar wind conditions.

The other observations (8th and 10th Feb, 7th and 8th March) occur 3-5 days after the arrival of a solar wind compression. They all have very dim hard X-ray emission, but the hot spot behaviour varies significantly spectrally, temporally and spatially. This may suggest that the response of the hard X-rays is shorter lived, since it is observed on 24 Feb 2007 and 2 Oct 2011 within 2 days of shock arrival, but has dimmed within 3-5 days of the shock arrival for the other observations. The rarer brightening of the hard X-ray emission, that we observe on 24 Feb 2007 and 2 Oct 2011, may be a direct tracer of solar wind compressions, while the soft X-ray hot spot response seems more complex and requires further investigation. This means that while the soft and hard X-ray emissions appear to be independent, analysing their combined response can provide important clues to the state and dynamics of the magnetosphere.

We also study the timescale for the UV auroral response to shocks, which suggests that the overall morphological response tends to last 3-4 days. Comparing this timescale to those of the 8th Feb, 10th Feb, 7th March and 8th March X-ray observations, which occurred 3-5 days after compression, means that it is challenging to determine whether the X-ray behaviours are connected with either the final day of a solar wind compression or a subsequent magnetospheric expansion or neither. The 8th March observation lightcurve,

morphology and spectra seem to suggest that there is a transition in auroral behaviour during the observation.

In contrast with Kimura et al. (2016), we do not find a correlation between solar wind velocity and X-ray emissions. The X-ray auroral emissions are brightest during the lowest solar wind velocity and dimmest during faster solar wind, but the difference in solar wind speed is small ($\sim$ 50 km/s). The dimmest X-ray observation occur during a deep solar wind rarefaction on 3 March. At this time there were simultaneous HST and Chandra observations for $\sim$120 minutes. However, given the very dim X-ray emission at this time, it is challenging to draw conclusions that are significant against the Poisson errors, although we do observe a 2 minute exposure when the X-ray emission brightened alongside a UV polar aurora brightening.

The observations reported here build important steps towards understanding the relationship between the X-ray aurora and both solar wind conditions and UV emissions. However, more observations during solar wind rarefaction or connected with solar wind conditions would help to further complete this narrative and determine whether and how X-ray observations trace the internally and externally driven dynamics of the Jovian magnetosphere.

Chapter 5

Conclusions and Future Work

"What man, laid on his back counting stars, ever thought about a number?"

— Don Draper, *Mad Men*

5.1 Conclusion

It is almost 40 years since the discovery of Jupiter's X-ray emissions. In this thesis, we analysed X-ray observations of the planet spanning the last decade (2007-2016) which occurred under a variety of solar and solar wind conditions.

We utilise the most capable current ionosphere-magnetosphere mapping (Vogt et al. 2011, 2015) to show that the MeV/amu ions that produce Jupiter's Northern and Southern X-ray hot spots appear to originate beyond 50 R_J and close to or beyond the noon-dusk magnetopause. Given this source location, it may be expected that the X-ray aurora would be modulated by changes in solar wind conditions, which can compress/expand the magnetosphere and trigger processes such as dayside and/or tail reconnection, along with the development of Kelvin Helmholtz instabilities and compressional waves.

We find that during solar wind compressions in 2007, 2011 and 2016 the Jovian soft X-ray aurora brightened and exhibited characteristic pulsations with a regular 9-13 minute interval. The observations in 2007 seem to suggest that Brightening of the hard X-ray emission accompanies dawn storm features and/or dusk polar arcs in the UV emission and lasts up to two days. Typically a hot spot X-ray aurora pulsation brightens for 1-2 minutes and then

dims for the characteristic inter-pulse timescale (e.g. 9 minutes) before brightening again. However, a more prolonged non-pulsing brightening of emission is observed during an ICME in a region distinct from the hot spot and is accompanied by bursts of Non-Io decametric emission.

The observations in 2007 and 2011 show that brightening is often associated with an expansion of the hot spot to lower latitudes. Studies of the spatial location and pulsations of different energy emissions along with colour ratios show that the lowest latitude emission is produced by high charge-state sulphur, while at higher latitudes oxygen and sulphur/carbon contribute the emission. This may be because sulphur can access X-ray-producing charge-states with a lower energy threshold than oxygen requires. It also suggests stratification of energy in the downward currents that produce the X-ray emission. Observations from March 3 2007, during solar wind rarefaction show that the X-ray aurora appears to be dimmer at these times, but there is also some suggestion that the soft X-ray aurora can brighten outside of times of compression with the pulsation rate of emission having a longer interval at these times.

We find that Jupiter's Northern and Southern X-ray hot spots appear to sometimes behave independently with different pulsation rates at each pole and uncorrelated brightening from pole to pole. We note that their mapping is different, with the Northern emissions originating from noon to dusk and the Southern emissions mostly mapping to noon. In order to explain the high energy emissions, spatial locations, characteristic pulsations and solar wind and multi-waveband relationships that we report in this thesis, we propose the following possible drivers for the X-ray aurora:

1. The North and South X-ray hot spots are produced by cusp processes in-line or slightly adapted from Bunce et al. (2004). To explain the independent behaviour these processes may need to occur away from the sub-solar point or possibly at high latitudes (e.g. McComas and Bagenal (2007)).

2. In addition to the cusp, the Northern hot spot maps to the dusk sector,

which may be associated with tail reconnection. The viewing geometry may prevent this from being observed in the South. The combination of cusp and tail pulsations would produce a more complex lightcurve for the North, while for the South, the observed lightcurve would be more regular because it only consists of ions that travel from the noon magnetopause. This would also explain the brightening during solar wind compressions. Tail reconnection associated X-ray emissions would 'switch on' with solar wind compressions, causing the observed X-ray brightening and 'expanded hot spot' (actually constituting two sources in the North: tail and cusp). It has been suggested that the UV dusk polar arcs connect with tail reconnection (Nichols et al. 2017) and we find here that X-ray brightening occurs when the dusk polar arcs form and with a similar pulsation rate.

3. Kelvin Helmholtz Instabilities (KHI) that form in the pre-noon sector (e.g. Ma et al. (2015)), and grow along the dusk flank, generate field line resonances. The characteristic period associated with these resonances depends on the field line. For regions further from noon, this may produce increasingly long timescales, which would explain the more complex Northern lightcurve. This can also generate intermittent reconnection and uni-directional currents (through field line twisting) which may explain differing hemispheric brightnesses. The scales of the KHI depend on the magnetic field strength, density and velocity of the plasmas on either side of the magnetopause and thus vary with solar wind conditions.

4. Alternative wave-particle interactions that propagate to different altitudes for each pole might also play a role.

We have already begun work that tries to distinguish between these drivers, but this is beyond the scope of this thesis. In the future work section, we will highlight how X-ray observations that are conjugate with Juno and other waveband observational campaigns will help to build the needed multi-waveband, plasma and magnetic field detail required to finally identify how

Jupiter generates its X-ray aurora.

5.2 Future Work

> *"We are little people on a little planet with tiny brains who can go so deep and understand what happens... It's astonishing that there are any laws of nature at all. That they are describable by mathematics. That mathematics is a tool that humans can understand. That the laws of nature can be written on a page. It's the greatest of all mysteries. There is a strong sense that we are hearing nature talk to us."*
>
> — Savas Dimopulos, *Particle Fever*

The scope for future work on the Jovian X-ray emissions is vast. In the long-term (beyond 2028), we expect ATHENA and Lynx to usher in paradigm shifts in our understanding of planetary X-rays. The outstanding collecting area and energy resolution of ATHENA will easily resolve the different sulphur and carbon spectral lines of the Jovian aurora along with any other species that may be present, while the excellent sensitivity and Chandra-like spatial resolution of Lynx will provide auroral images and videos akin to those that HST provides for the UV, conclusively revealing sub-structures within the hot spot (such as a distinct cusp and tail reconnection region) and revealing a whole new domain of auroral X-rays.

However, to focus this section on ATHENA and Lynx, would be a gross injustice to the vast potential and possibility that the current generation of instruments offer. The discoveries from Chandra and XMM-Newton have barely begun and there are years of potential science within their legacy and future observations. Beyond the existing X-ray observatories, it is an incredibly exciting time to be in the field, with the Juno mission offering potentially once in a lifetime, unprecedented in-situ access to the auroral regions.

Vast is the volume of potential science that is yet to be done. To try to elucidate the potential body of work available, while providing practicable steps along the path, here we briefly discuss four diverse and distinct research projects: 1. Joining Juno in Exploring the Jovian Magnetosphere

2. Multi-waveband Auroral Observing Campaigns

3. X-ray Identification of the Surface Composition of Io and Europa

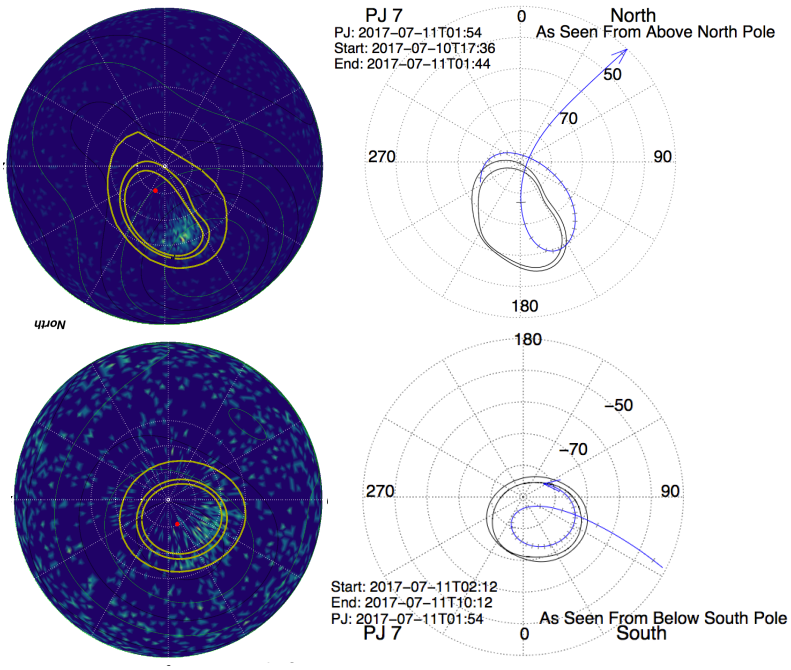

Figure 5.1: Left: Polar projections of Jupiter's Northern (upper) and Southern (lower) X-ray Emissions from June 1 2016. Right: Polar projections indicating Juno's orbital trajectory during perijove 7 (blue arrow) for the Northern (upper) and Southern (lower) pole. Juno trajectory plots are from http://lasp.colorado.edu/home/mop/missions/juno/trajectory-information/

4. Deriving Physical Parameters Applicable to X-ray Observations of Exoplanets

Alongside these projects, there may well be further serendipitous findings that also help to advance our understanding of Jupiter. There is also a variety of new analysis techniques presented in this thesis that would be well supported by additional data or further exploration (e.g. distinguishing the pulsation locations based on their mapping in chapter 2; expanding colour ratios in chapter 3 for higher signal observations; exploring the solar wind relationships in the legacy observations etc.).

5.2.1 Joining Juno in Exploring the Jovian Magnetosphere

5.2.1.1 The Aurora

November 2016 provided the first of a series of unprecedented opportunities to explore the mechanisms that produce Jupiter's auroral X-rays. The Juno

spacecraft undertook its first perijove pass over the poles of Jupiter with the full complement of scientific instruments conducting 4π insitu plasma and magnetic field measurements. Since this moment, Juno has undertaken a perijove pass every 53.5 days. However, Juno does not have an X-ray instrument on board. In order to gain deeper/clearer insight into the relative importance of different physical drivers for the X-ray emissions, we must therefore compare X-ray observations from Earth with the in-situ measurements. To do this, G. R. Gladstone scheduled a Chandra campaign and we scheduled an XMM-Newton campaign to coincide with perijove passes. Of the perijove passes, perhaps the most promising is perijove 7 on July 10-12th 2017, when Juno flew directly over both the Northern and Southern X-ray hot spot regions (see Fig 5.1). At this time, we scheduled a continuous 40 hour XMM-Newton observation. Figure 5.2 shows the lightcurves from the Northern and Southern X-ray aurora during the Juno perijove, with the auroral pulsations clearly transitioning from one rotation to the next. We note that this is very preliminary work and needs much more careful analysis.

Conducting conjugate X-ray observations with the Juno spacecraft measurements presents a huge array of possible opportunities for understanding the driver processes that produce the Jovian X-ray aurora. For example, by comparing ion velocities from line broadening in the RGS spectra with precipitating ion energies from Juno's JEDI instrument, we might be able to quantify and identify the acceleration process that produces Jupiter's X-rays. Equally, by correlating variability in Jupiter's X-ray spectra with Juno's plasma and magnetic field measurements of the auroral zone, we will gain unparalleled insights into what conditions and particles produce Jupiter's X-ray aurora.

5.2.1.2 Identifying the driver

Visibility constraints will limit the number of opportunities to observe Jupiter's X-rays while Juno is passing over the poles. To try to maximise the learning from these passes, it will be important to expand the current modelling work. The current Monte Carlo simulations (e.g. Kharchenko et al. 2008) have done a spectacular job of identifying the energies required and

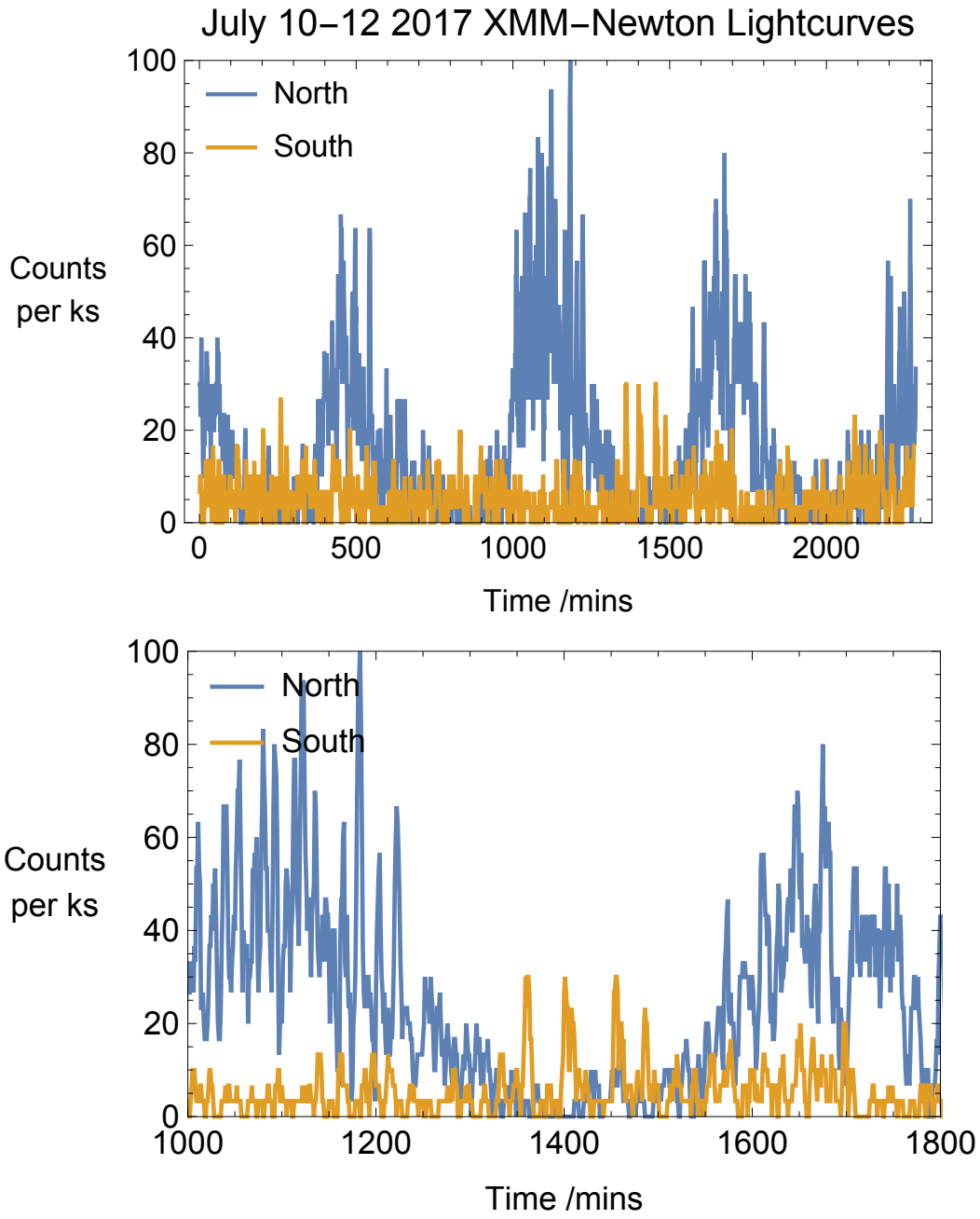

Figure 5.2: Top: Complete XMM-Newton Lightcurves for Northern and Southern Aurora from July 10th-12th 2017, during which Juno undertook Perijove 7. Lower: Zoomed version of lightcurve to highlight changing pulsation rate and brightness from one rotation to the next.

atmospheric processes that produce the X-ray aurora (e.g. Ozak et al. 2010). However, the spectral fits that they achieve are significantly worse than those achieved by arbitrarily fitting spectral lines. This is likely because the models over-simplify the current systems and magnetospheric processes that produce the emissions. For instance, they often assume that the precipitating particles all undergo the same acceleration. However, this contradicts both the theory and the data.

Bunce et al. (2004) show that the voltages may be expected to vary with distance from the vortices (see Section 1.8.0.3). This may suggest that the precipitating particle populations do not all experience the same acceleration. Cravens et al. (2003) shows that precipitating ions will experience a voltage dependent upon the magnetic mirror ratio they precipitate through. Dunn et al. (2016) show that the precipitating ions move across a region of 10 - 14 G. It may therefore not be reasonable to assume a single acceleration for the entire population, since the differing surface field strengths will produce different mirror ratios and differing voltage associated with each. This brings with it added complications of differing opacity and quenching effects from the starting spatial and temporal location of the ions (see the Introduction or Ozak et al. 2010, 2013 for further details).

While 'arbitrarily fitting spectral lines' may not make sense from a standard charge exchange model perspective, the variety of potentials and subsequent penetration depths may lead this to be necessary in the short term. In the longer term, Juno will offer unprecedented access to these particle populations. In concert with X-ray observations of doppler broadening, this will start to constrain the dominant acceleration mechanisms.

5.2.1.3 Upstream Solar Wind Measurements

Prior to orbital insertion, Juno also sampled the solar wind conditions upstream of Jupiter. We scheduled the observations in May and June 2016 (Chapter 3) to utilise this unique opportunity. We have already commented that the observations in which the 9-13 minute period is observed (Feb 24 2007, Oct 2 2011, May 24 2016, June 1 2016) all occur within 3 days of a

solar wind compression arriving. However, unlike the New Horizons SWAP instrument, Juno offers not only solar wind velocity, but also density and IMF parameters. This provides unprecedented access to the upstream solar wind conditions during Chandra and XMM-Newton X-ray observations of Jupiter, which will greatly help with interpretation of the auroral emissions. Figure 5.3 shows the Juno solar wind measurements from Nichols et al (2017) with the X-ray observation times overplotted. At the time of writing this chapter, the Juno upstream solar wind measurements were not publicly available, but are due for release, so in the near future it should be possible to conduct a similar study for the ∼40 hours of time-tagged X-ray observations that occurred during this time. Alongside predictions for magnetopause processes derived from the upstream solar wind data and the variations in the Northern and Southern X-ray aurora at this time, it may be possible to eliminate some of the possible drivers suggested in Chapter 3. We are also in the process of building collaborations with the Juno team, which will hopefully prove highly complementary.

Alongside the plasma and magnetic field measurements, Juno has radio, UV and IR instruments, which in concert with X-ray observations will help to provide the first truly multi-wavelength observations of Jupiter.

5.2.2 Multi-waveband Auroral Observing Campaigns

The results of Elsner et al. (2005) and Branduardi-Raymont et al. (2008) showcase the value of simultaneous multi-waveband observations. The strengths of each waveband can be amplified, while the weaknesses are mitigated by the complementary waveband. For instance, X-rays cannot boast the richness of photons offered by the Hubble Space Telescope UV observations. However, HST UV observations typically last less than an hour and focus on only one pole, while the orbit of Chandra and XMM-Newton X-ray observatories allows observations for 10s of hours and along with simultaneous viewing of the entire Jovian disk (including both aurorae). By utilising systematic comparisons of both wavebands it will be possible to build a deeper understanding of how the signatures of each waveband relate e.g. the short-term

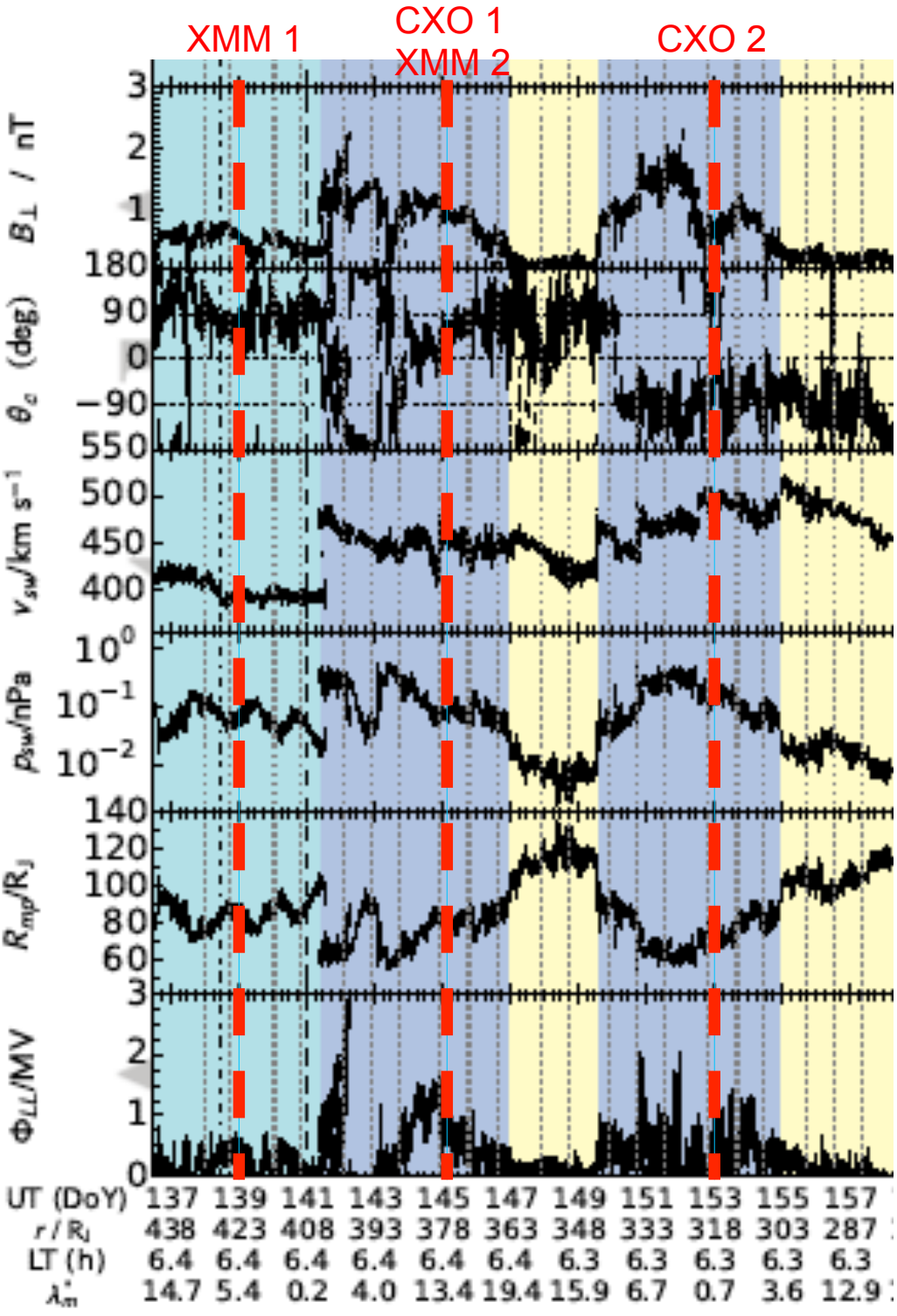

Figure 5.3: Adapted from Nichols et al. (2017): Plot showing interplanetary data versus UT at the ionosphere. In order from top to bottom a) $B_\perp$ in nT; b) IMF clock angle θ_c in degrees along with horizontal dotted lines at 0° and ±90° (c) v_{sw} in km/s (d) solar wind ram pressure, p_{sw} in nPa; (e) the magnetopause standoff distance R_{mp} in R_J (Joy et al. 2002) and (f) the potential reconnection voltage in MV (Nichols et al. 2006). Vertical grey dotted lines indicate the times of HST observations, in red are the X-ray observations (each 10-14 hours). Also shown by the vertical dashed and dash-dotted lines are times of an observed eruption on Io and sodium nebula enhancement, respectively. The colours indicate different interplanetary conditions: shallow (deep) solar wind rarefactions are in cyan (yellow) while compressions are in blue.

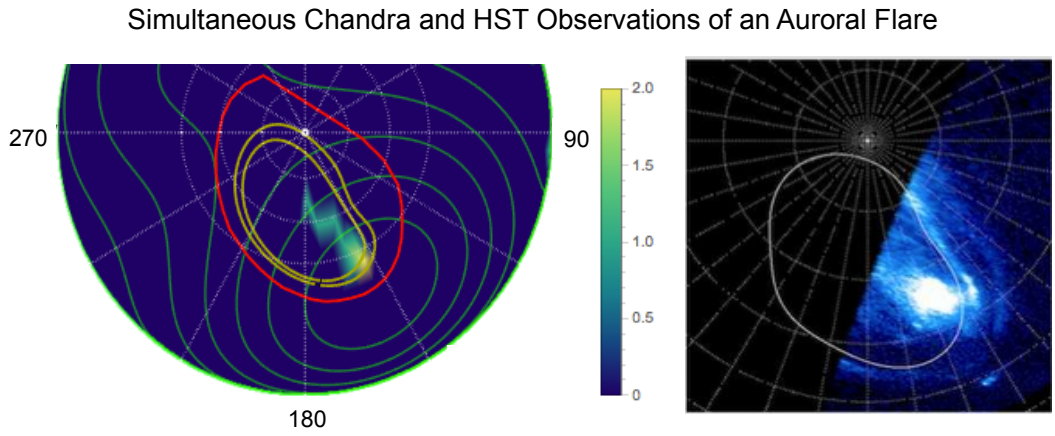

Figure 5.4: Preliminary North Pole Projections from Chandra and HST observations of an Auroral Flare (HST observations from - priv comms J. Nichols; Z. Yao; D. Grodent).

spatial morphology of the X-ray emissions and the long-term and global variability of the UV emissions. This will broaden the scope of both wavebands for exploration of the global magnetospheric dynamics of the Jovian system.

While Chapter 4 showed some UV-X-ray comparisons, only one of these was simultaneous and it was during a period of very dim auroral activity. To build on this work and to also provide a catalogue of coincident observations, where possible, we have scheduled X-ray observations from our campaigns over the last two years to coincide with HST campaigns that were organised by J. Nichols and D. Grodent. At the time of writing this thesis, we had scheduled X-ray observations (Campaign PI 2016: Kraft and Jackman; Dunn; 2017: Jackman; Dunn) to coincide with more than 15 HST observations ($\sim$ 10 hours of total coincidence) and we still have a significant observation budget remaining for 2018, which we will continue to try to schedule with other wavebands.

Figure 5.4 shows very preliminary comparisons of simultaneous (within the same minute) X-ray-UV observations of an auroral flare that occurred during the 2016-2017 campaigns. We very cautiously note that the X-rays have been smoothed to large bin sizes of (5° x 5°), since the coordinate transforms and polar projections need further tests; we also note that the emission occurred when the hot spot was on the limb of the planet, which leads to larger uncertainties in the projected coordinates. During the 5 minutes leading up

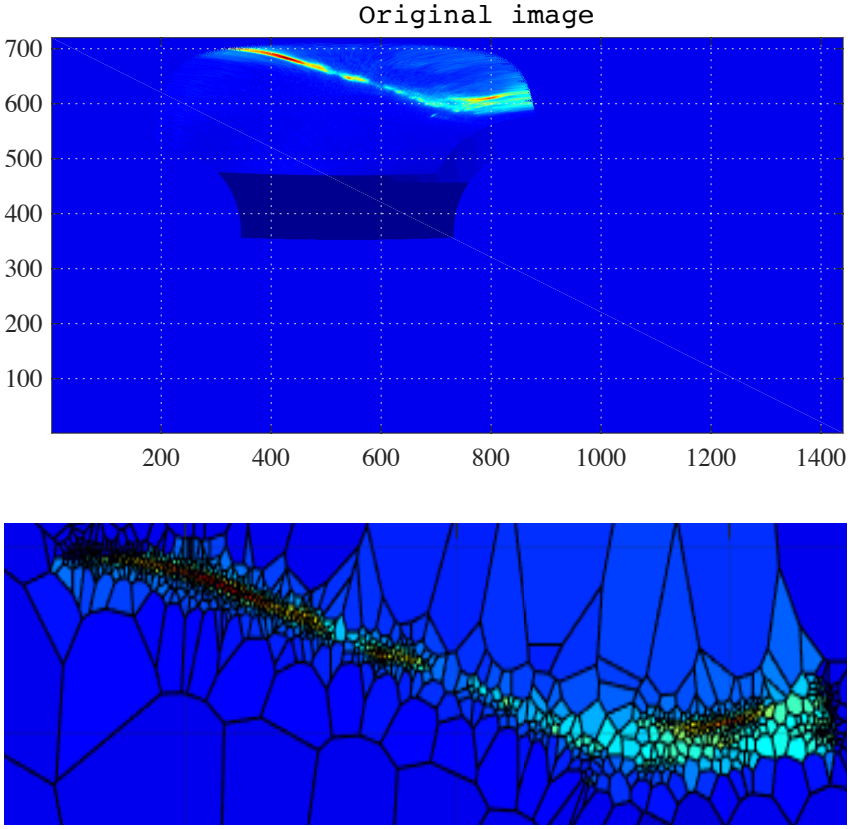

Figure 5.5: The VOISE algorithm produced by Guio et al. (2009) is capable of statistically distinguishing different intensities and length scales of features in an image. Here we have applied the VOISE algorithm to a HST image of the Northern Jovian aurora (original image (upper) provided by R. Gray, priv comms). VOISE identifies a variety of substructures within the aurora (lower). These can subsequently be studied in detail through the output data files.

to and following the flare the X-ray emission was consistently at 1 count or less per minute from the aurora.

It is important to move beyond auroral phenomenology to identifying the underlying physics behind the observed signatures, however, before that is possible one must robustly connect the phenomena. To do this, we intend to use the VOISE algorithm (Guio et al. 2009) to categorise the phenomena observed.

In figure 5.5 we have applied the VOISE algorithm to a HST UV observation. This algorithm statistically evaluates the intensities and length scales of auroral emissions. This can be applied to systematically identify if there are specific UV intensities, length scales or morphologies that connect with X-ray emissions. This will help to systematically evaluate the UV morpholo-

gies/intensities/length scales that are correlated with X-ray emissions. In turn, this may allow short duration but more frequent UV observations to provide clues as to the presence of X-ray emissions, while long duration, but rarer X-ray observations can suggest the development of the UV emissions. We note that in the example shown in figure 5.5 we are testing for small scale variations in the intensity, but the algorithm provides plenty of flexibility for different chosen parameters and different structure identifications (see Guio et al. 2009 for more details).

Beyond the closest waveband relative of the X-rays, there are also IR and radio observations. We have scheduled two coincident XMM-Newton-IRTF Texes observations (with IRTF observation PI: J. Sinclair) during the Summer of 2017, in order to try to identify connections between the IR hot spot and X-ray hot spot.

We also note that a statistical study of X-ray lightcurve brightness and DAM radio emissions may now be possible since the 2007, 2011, 2016 and 2017 X-ray campaigns are all simultaneous with Nancay, STEREO and Juno observations of the radio emissions.

5.2.3 X-ray Identification of the Surface Composition of Io and Europa

As shown in the introduction, X-ray emissions have been detected from Io and Europa (Elsner et al. (2002)). However, beyond this initial detection of the satellites and the Io Plasma Torus, little further work has been undertaken to determine what new information on these bodies can be gleaned from the many subsequent X-ray observations. X-ray fluorescence provides a powerful tool for identifying the composition of the atmospheres and surfaces of the satellites. On Europa, where questions of habitability hinge on the ice and sub-surface ocean composition, this could be a particularly valuable tool. The X-ray emission from the satellites is expected to be created by the impact of magnetospheric plasma with the satellite surface (Elsner et al. 2002; Kraft, priv comms), with the subsequent fluorescence providing signatures of the surface composition. The goal for the project is therefore to produce the best

signal to noise ratio possible for the spectrum, in order to gain insights into the surface composition. Ideally, XMM-Newton's higher spectral resolution and effective area would be applied to the task, however, the size of the Galilean satellites is less than two arc seconds, which is far less than the spatial resolution of XMM's EPIC instruments (5-6"). Studies will therefore rely more heavily on Chandra or require thorough checks for the presence of background X-ray sources in the XMM-Newton observations.

Since the initial detection of the satellites, Chandra ACIS (HRC) has conducted more than 270 ks (500 ks) of observations of Jupiter. Each Jupiter observation has a sufficiently large field of view so that it could include the satellites (e.g. Fig. 5.6). Slightly more than 10 counts were found in each detector cell for each moon during the $\sim$ 80 ks observation in 1999 (Elsner et al. 2002) with 10% of counts provided by the background. Assuming that this rate persists, it may be possible to bring the total number of counts to more than 50-60 counts per detector cell. For reference, the Jovian Northern auroral spectra from each observation in the 2007 campaign had between 90-180 counts.

As discussed previously, degradation in the ACIS OBF, means it is currently unable to provide access to low energy regimes (below 1 keV), however, depending on the energy of the fluorescence lines for the moons, this low energy cut-off may not be relevant for these studies. This raises the possibility of further observing campaigns in order to increase the spectral counts and identify the surface composition, which for Europa would provide important constraints for astrobiology discussions.

Alongside the 270 ks of ACIS data, there are also 500 ks of HRC data. While this does not provide the needed energy resolution, it may help to provide an indication of variability in the satellite emissions. This in turn might help to identify factors, such as to what extent the flow direction of the magnetospheric plasma (relative to the observed satellite face) matters or to what extent solar fluorescence contributes. These factors may help to inform X-ray observation proposals (i.e. triggering TOOs when Io is known to have contributed more plasma to the torus or scheduling observations at times when

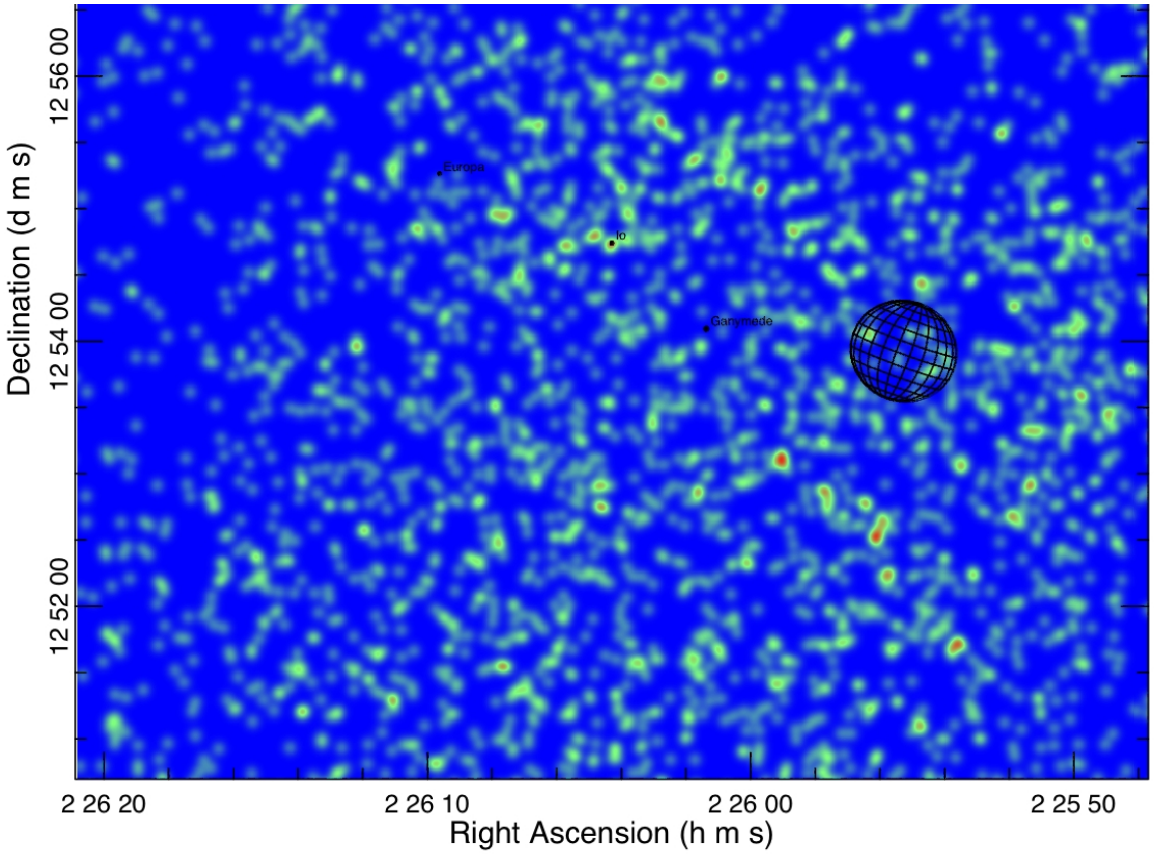

Figure 5.6: Provided by P. Ford (priv comms): Processed Chandra ACIS image of Io during the Oct 2nd 2011 observation of Jupiter (see Chapter 2). This has been reframed and processed to focus on Io, so blurs and removes emission from other bodies.

the observable face of the moon has the plasma flowing onto it).

These studies may also allow X-ray observations to provide a proxy for the magnetospheric plasma conditions, which could help to support ESA's JUICE and NASA's Europa mission in the longer term.

5.2.4 Deriving Physical Parameters Applicable to X-ray Observations of Exoplanets

The exploration of exoplanetary systems with the X-ray waveband is a young field in which X-rays are typically utilised to explore stellar-driven atmospheric loss of exoplanets, star-planet interactions and planetary transit studies (for more information see Branduardi-Raymont et al., in press (of which I am the second author) and references therein). Despite this rapidly growing body of work, application of knowledge of X-ray emission from bodies within our own solar system is rare. For instance, Marin and Grosso (2017) recently assessed the feasibility of detection of X-ray emissions from the atmosphere of exoplanet HD 189733b, but did not utilise any knowledge of solar system X-ray emission to do this.

By considering the known ratio between the Jovian disk power and the solar output (e.g. Branduardi-Raymont et al. 2010) and then scaling this for the $2\pi r^2$ relationship of flux with distance to simulate moving Jupiter to 0.03 AU (the star-planet distance for HD189733b), it is possible to attain a similar order of magnitude scale to that found by Marin and Grosso (2017) (Branduardi-Raymont et al., in press).

The goal of this project is to build on the preliminary work conducted in Branduardi-Raymont et al. (in press) to calculate the instrument sensitivity required to detect when a star occults an exoplanet (see fig 5.7 Winn (2010)). To do this we assume that the ability to identify the transit depends on the X-ray flux ratio between the star and the planet and suggest the following step-by-step analysis:

1. Do spectral fitting of the Jovian disk for all the archival observations of Jupiter and calculate the X-ray flux across the solar cycle.

2. While accounting for the distance between Jupiter and the Sun for each

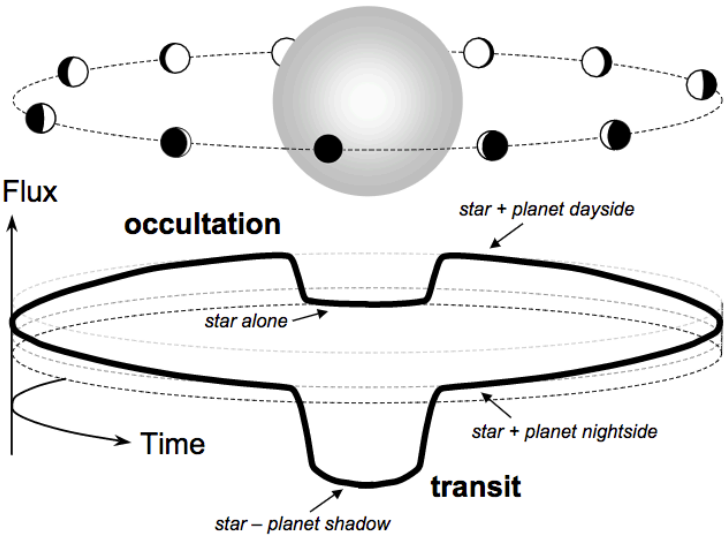

Figure 5.7: From Winn et al. (2010): Illustration of transits and occultations. Only the combined flux of the star and planet is observed. During a transit, the flux drops because the planet blocks a fraction of the starlight. Then the flux rises as the planet's dayside comes into view. The flux drops again when the planet is occulted by the star.

observation, compare the Jovian flux measurements from the disk with simultaneous GOES observations of the Sun to determine the ratio of solar flux to Jovian flux. It may also be possible to distinguish the florescence components (e.g. from Carbon in the methane layer) from the elastically scattered emission.

3. Scale this emission through the $2\pi r^2$ relationship to identify how the X-ray emission from a Jupiter-like planet changes with star-planet distance. Plot the ratio of Jupiter/Solar X-ray flux with star-planet distance.

4. Repeat ratio plots for different wavebands to test whether for a Sun-like star and Jupiter-like planet there is an ideal waveband for maximising the ratio.

5. Scale Jupiter's radius to a maximum, based on the largest known exoplanet. Identify to what extent the exoplanet's size is important in the ratio.

6. Utilise the atmospheric albedo and fluorescence methods of Cravens et al. (2006) and Cravens and Maurellis (2001) to understand how the differing atmospheric composition might lead to differing contributions from X-ray fluorescence or X-ray elastic scattering. For example, Venus' emission is dominated by fluorescence, whereas for the H_2 atmospheres of Jupiter and Saturn,

elastic scattering is more important. When accounting for the waveband optimisation of the ratio, to what extent is the planet's dominant emission mechanism important?

7. Study a range of stellar spectra to understand the differing spectral lines and whether this improves the ratio or changes the preferred waveband for secondary transit identification.

8. Compare this ratio with current and future instrument sensitivities. Check the exoplanet catalogue for any systems that, based on this analysis, might be sufficiently bright to be detected against their host star.

Here we have assumed that the exoplanets X-ray auroral emission is minimal and does not decrease with star-planet distance. However, the previous work presented in this thesis does seem to suggest that the Jovian X-ray aurora exhibits some solar wind relationship. Closer to the star, the density, velocity and IMF will increase, which will all drive changes in the exoplanets magnetosphere. This may increase the X-ray auroral output and make an X-ray exoplanet detection more likely. However, there are far more variables in the auroral emissions, so we take the cautious approach of only considering disk emission.

X-ray studies of planetary bodies remain a relatively young field, with a large number of exciting and interesting prospects on the horizon. Key amongst these are the collaborations with the Juno spacecraft and other observation campaigns. This will revolutionise our understanding of the Jovian aurora and particularly the X-ray emissions. The coming years are therefore a hugely exciting time to be studying this topic, with a great deal of potential science to be explored.

"Didn't that go fast?"
"Of course it did, we were having too much fun"
— Neil Gaiman, *Sandman*

Chapter 6

An Occupation-Driven Physics Curriculum

"Change requires more than righteous anger. It requires a programme and it requires organising."

— Barack Obama

"Most people think of things that are and ask 'Why?' Instead, dream of things that never were, and ask why not?"

— George Bernard Shaw, *Back to Methuselah*

"By defining our goal more clearly, by making it seem more manageable and less remote, we help all people to see it, to draw hope from it and to move irresistibly towards it."

— John F. Kennedy, *Quest for Peace*

6.1 Abstract

I have always believed that part of 'doing science' is sharing that passion for science with others. Consequently, almost every second of my spare time throughout the PhD has been consumed by either science outreach or science education work. In order for this PhD thesis to be an accurate reflection of my last four years of scientific endeavour, it seems appropriate to include a brief segment of this work, even though it was undertaken in parallel with the Jovian aurora research, I often found that it was a symbiotic relationship between the two. Science education is sort of a contradiction. In school you

learn about all the things we know, but really that's a misnomer, because being a scientist is about discovering those things that we don't know. It is this scientific adventure into the unknown that I fear we are losing in school education. Throughout the education equality and science outreach projects for Spacelink, Institute of Physics, Brilliant Club, Twinkle, MSSL, the Lord Mayor of London's Office, the Institute of Physics and others, the portion of the project reported in this chapter seemed one of the more appropriate as a body of research work suitable for a PhD thesis.

As part of the Institute of Physics National Curriculum committee, we explored and made recommendations on many aspects of the National Curriculum. As part of this, D. Sandford-Smith, from the Gatsby Foundation, and I undertook a project to investigate aspects of the pre-16 curriculum that are directly linked to occupational careers. D. Sandford-Smith provided much of the background information presented here, while the analysis from section 6.4 onwards is my contribution.

In this chapter, we use labour market data to justify the place of many aspects of the physics curriculum by virtue of their widespread importance in occupational professions across the UK economy. Using this labour market data, we first identify the UK graduate and vocational occupations that involve physics and find that more than 4 million people in the UK require at least GCSE physics knowledge in order to conduct their day-to-day work. Of these 4 million, 2.3 million are in 'non-graduate' or 'vocational' occupations. Since these vocational occupations often fall from the foreground when a physics curriculum is designed, they are the focus of this work. We investigate the skills and physics subject expertise that is required to undertake the most common non-academic occupations that utilise physics. From this, we identify a list of content that are required in the National Curriculum in order to facilitate these roles in the UK economy. We stress that the curriculum topics that we identify are not a self-contained curriculum and that a physics curriculum should include the complete range of topics outlined in the Institute of Physics papers on the topic (in press). This work instead provides a component of the curriculum that is necessary for the prosperity of the UK's

non-academic/vocatonal sector.

6.2 Introduction

The natural sciences hold a privileged position within the English curriculum. Science is a core subject alongside English and Mathematics; meaning that it is taught, in some form, to all pupils aged 5-16 . This contrasts with most other subjects, which pupils can drop at the age of 14, including: art and design, music, dance, drama and media arts, design and technology, geography, history and modern foreign languages .

The UK National Curriculum (2015) describes the following aims for science:

1. develop scientific knowledge and conceptual understanding through the specific disciplines of biology, chemistry and physics
2. develop understanding of the nature, processes and methods of science through different types of science enquiries that help them to answer scientific questions about the world around them
3. equip with the scientific knowledge required to understand the uses and implications of science, today and for the future.

However, none of these aims explain to a 15-year-old why physics will be sufficiently important in their future or why physics is compulsory, but they are allowed to give up history.

In Beyond 2000 (nuffieldfoundation.org/sites/default/files/Beyond%202000.pdf), the Nuffield Foundation examined the successes and failures of science education and what areas of science education were needed by young people today. They concluded that too often the design of the science curriculum was driven by the needs of the small majority who would continue to study science to the highest levels and that too little thought was given to those who would stop studying academic science after age 16.

In the early 2000's there was an increased uptake of applied science qualifications at Key Stage (KS) 4 (education from 14-16 years old). These qualifi-

cations gained popularity because they were considered equivalent to GCSEs in school league tables, but relied on the assessment of coursework rather than GCSE exams. They were often considered to be an alternative that was for weaker students. While these applied science qualifications were defined as vocational, it is unclear whether they were valued by employers (D. Sandford-Smith, priv comms). Their contribution to league tables was later dropped. Donnelly (2009) particularly noted "Schools do not generally see these qualifications as strongly vocational, in the sense of preparing students directly for scientific employment, but rather as a form of science curriculum and pedagogy with a distinctive character and appeal."

It is important to note that the contexts used for 'applied science' were designed by scientists or technicians engaged in the academic use of science (e.g. a scientific researcher) as opposed to the vocational application of science (e.g. an electrician). However, one of the key reasons that science holds a privileged position in the curriculum is because it is applied in a broad range of occupations beyond the actual practice of scientific discovery. We therefore begin this work by exploring what occupations physics is actively used in (particularly for vocational occupations) and therefore what is the impact on the UK economy of a rigorous and well-rounded physics education.

To identify those members of the population using physics as part of their daily work, we consider labour market information (LMI). In the UK, labour market statistics are collected and coded using Standard Industrial Classifications (SIC) and Standard Occupational Classifications (SOC). The SOC systems provide information on how many people work in a particular type of occupation and what the typical salaries and levels of education are within that occupation. SOC is a nested hierarchical classification system, which contains the following 9 major groups:

1: MANAGERS, DIRECTORS AND SENIOR OFFICIALS
2: PROFESSIONAL OCCUPATIONS
3: ASSOCIATE PROFESSIONAL AND TECHNICAL OCCUPATIONS
4: ADMINISTRATIVE AND SECRETARIAL OCCUPATIONS
5: SKILLED TRADES OCCUPATIONS

6: CARING, LEISURE AND OTHER SERVICE OCCUPATIONS

7: SALES AND CUSTOMER SERVICE OCCUPATIONS

8: PROCESS, PLANT AND MACHINE OPERATIVES

9: ELEMENTARY OCCUPATIONS

Nested within these groups are are 4-digit unit groups, with each digit implying an additional level of granularity. For example, a professional physicist (e.g. someone working as a physicist rather than someone with a physics degree) would be included within the unit code for a physical scientist. The following illustrates how the unit code 2113 for a physical scientist is derived.

2: PROFESSIONAL OCCUPATIONS

21: SCIENCE, RESEARCH, ENGINEERING AND TECHNOLOGY PROFESSIONALS

211: NATURAL AND SOCIAL SCIENCE PROFESSIONALS

2113: PHYSICAL SCIENTISTS

Searching Labour Market Information based on this SOC code would produce the description shown in Figure 6.1.

6.3 Occupations Utilising Physics

Office of National Statistics (ONS) data from August 2015 showed that 30,000 physical scientists were employed within the UK, out of a total of slightly less than 31 million employed. Although, many professions use physics beyond only Physical Scientists. We filtered this data to include roles that required GCSE physics knowledge and divided it by roles that required at least an undergraduate degree (not necessarily in physics) and those that did not require an undergraduate degree.

Table 6.1 shows, in order of number of people employed in each role, the 'graduate' occupations that actively apply physics that is beyond GCSE. 1.7 million people ($\sim$5% of the working population) working in the UK fit this description. Table 6.2 shows the occupations the 'non-graduate'/vocational occupations that require the application of GCSE physics. A total of 2.3 million UK vocational workers fit this description.

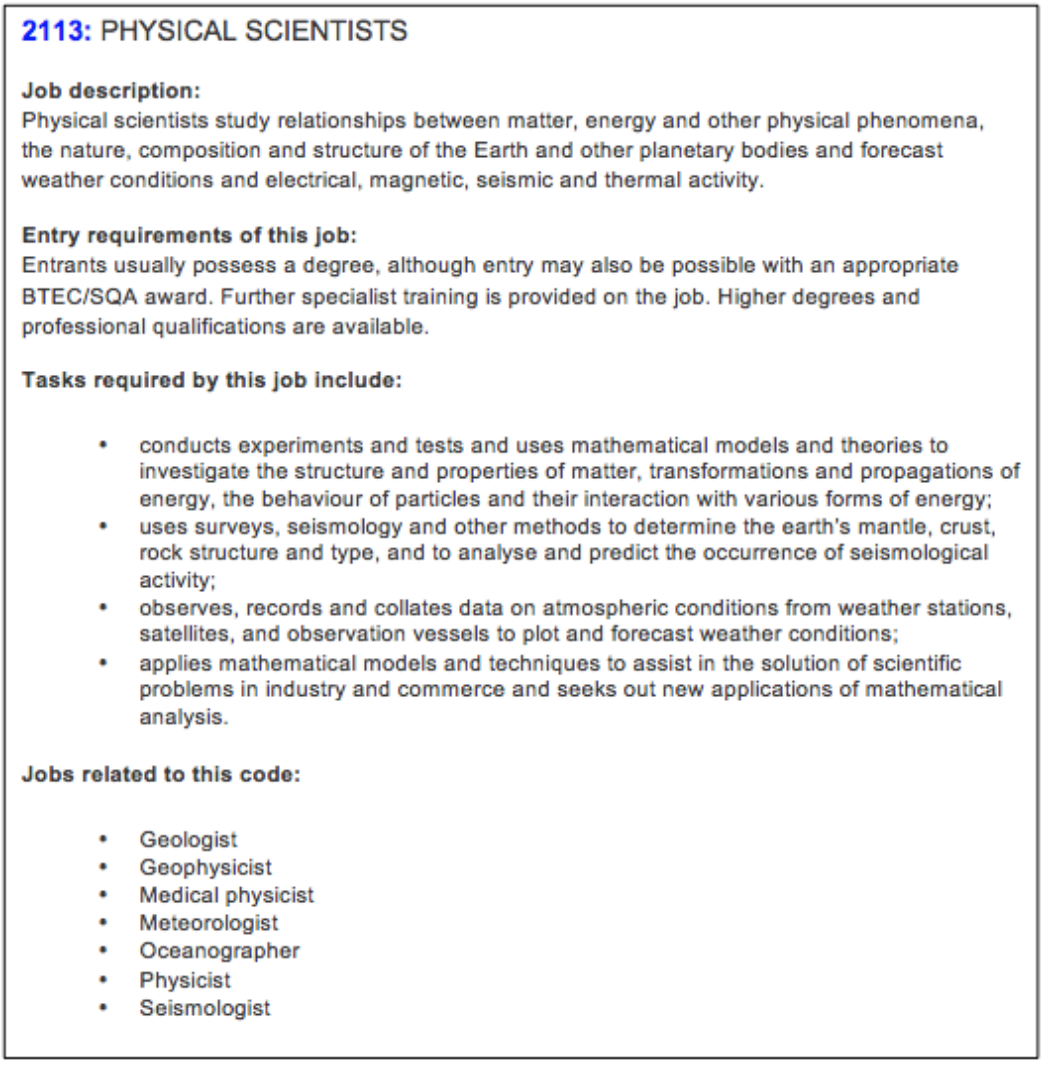

2113: PHYSICAL SCIENTISTS

Job description:
Physical scientists study relationships between matter, energy and other physical phenomena, the nature, composition and structure of the Earth and other planetary bodies and forecast weather conditions and electrical, magnetic, seismic and thermal activity.

Entry requirements of this job:
Entrants usually possess a degree, although entry may also be possible with an appropriate BTEC/SQA award. Further specialist training is provided on the job. Higher degrees and professional qualifications are available.

Tasks required by this job include:

- conducts experiments and tests and uses mathematical models and theories to investigate the structure and properties of matter, transformations and propagations of energy, the behaviour of particles and their interaction with various forms of energy;
- uses surveys, seismology and other methods to determine the earth's mantle, crust, rock structure and type, and to analyse and predict the occurrence of seismological activity;
- observes, records and collates data on atmospheric conditions from weather stations, satellites, and observation vessels to plot and forecast weather conditions;
- applies mathematical models and techniques to assist in the solution of scientific problems in industry and commerce and seeks out new applications of mathematical analysis.

Jobs related to this code:

- Geologist
- Geophysicist
- Medical physicist
- Meteorologist
- Oceanographer
- Physicist
- Seismologist

Figure 6.1: Labour Market SOC code information for a Physical Scientist.

Table 6.1: Table showing Office of National Statistics (ONS) data on those that use physics knowledge beyond GCSE within graduate roles.
[1] All in employment includes full and part time workers [2] n.e.c is 'not elsewhere classified' and represents occupations that are not large enough to have a SOC code of their own [3] There will also be physicists within the 167,000 Higher Education professionals and 458,000 Secondary education teaching professionals, who are not included here.

Occupation	Total in employment (000s)
2136 Programmers & software development professionals	289
2133 IT specialist managers	202
2139 IT and telecommunications professionals n.e.c.2	187
2135 IT business analysts, architects and systems designers	102
2112 Biological scientists and biochemists	100
2129 Engineering professionals n.e.c. 2	95
2126 Design and development engineers	93
2134 IT project and programme managers	79
2121 Civil engineers	76
2137 Web design & development professionals	70
2127 Production and process engineers	66
2122 Mechanical engineers	66
2150 Research and development managers	41
2123 Electrical engineers	39
2119 Natural and social science professionals n.e.c. 2	37
2142 Environment professionals	36
2124 Electronics engineers	31
2113 Physical scientists	30
2217 Medical radiographers	29
2111 Chemical scientists	29
2214 Ophthalmic opticians	13

Table 6.2: Table showing Office of National Statistics (ONS) data on those that use physics knowledge beyond GCSE within non-graduate occupations.
[3] All in employment includes full and part time workers [4] n.e.c is 'not elsewhere classified' and represents occupations that are not large enough to have a SOC code of their own

Occupation	Total employment (000s)
5241 Electricians and electrical fitters	257
5231 Vehicle technicians, mechanics and electricians	198
5223 Metal working production and maintenance fitters	188
5314 Plumbers and heating and ventilating engineers	172
8111 Food, drink and tobacco process operatives	159
3131 IT operations technicians	89
5249 Electrical and electronic trades n.e.c.4	87
3417 Photographers, audio-visual & broadcasting operators	83
3132 IT user support technicians	76
5215 Welding trades	73
3113 Engineering technicians	71
3111 Laboratory technicians	68
5242 Telecommunications engineers	63
8114 Chemical and related process operatives	45
5250 Skilled metal, electrical and electronic trades supervisors	45
5221 Metal machining setters and setter-operators	44
8125 Metal working machine operatives	44
3218 Medical and dental technicians	40
5245 IT engineers	40
3119 Science, engineering and production technicians n.e.c.4	33
3122 Draughtspersons	31
5232 Vehicle body builders and repairers	29
5235 Aircraft maintenance and related trades	28
3114 Building and civil engineering technicians	26
3116 Planning, process and production technicians	25
3112 Electrical and electronics technicians	23
8121 Paper and wood machine operatives	23
3121 Architectural and town planning technicians	22
8116 Plastics process operatives	21
3115 Quality assurance technicians	21
5224 Precision instrument makers and repairers	20
5234 Vehicle paint technicians	16
5222 Tool makers, tool fitters and markers-out	16
5244 TV, video and audio engineers	15

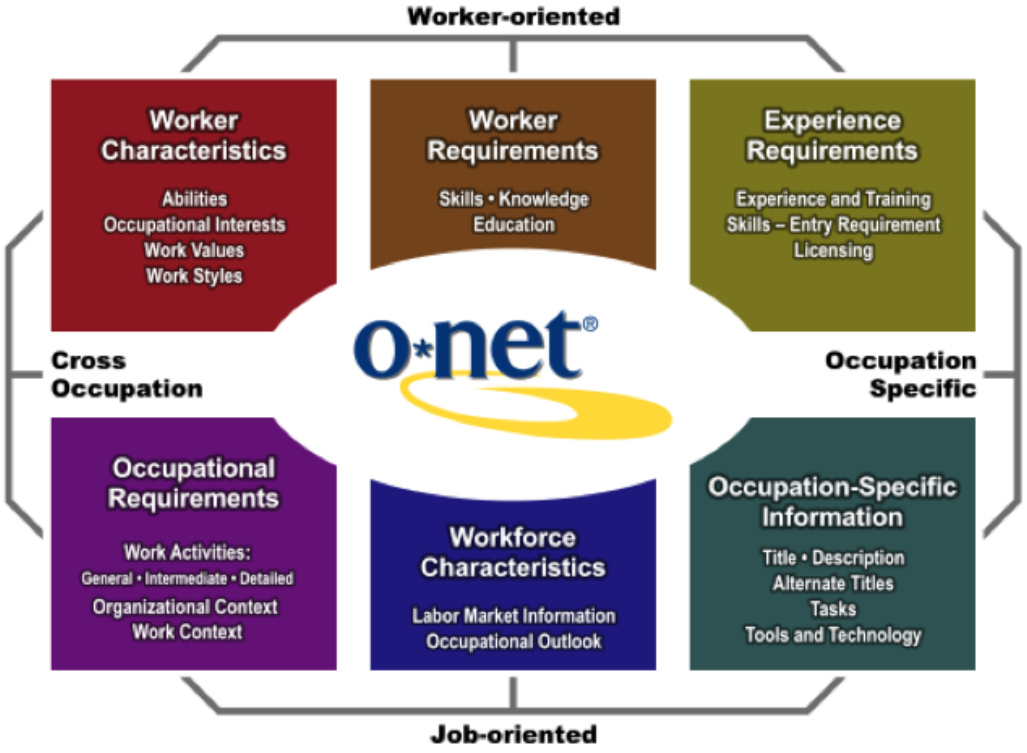

Figure 6.2: The dimensions of occupation that are available through O*NET: http://www.onetcenter.org/content.html

Beyond highlighting that a knowledge of physics is required to undertake these roles, the UK labour market information tells us very little about the detailed physics knowledge utilised in each role. In order to derive this information we used the American O*NET occupational information database. Figure 6.2 shows the occupational dimensions and information that can be accessed through the O*NET database.

6.4 Method for Identifying Curriculum Content

By analysing O*Net's Occupation-Specific data (Fig. 6.2), we extracted the physics knowledge that is required by any of the occupations in Table 6.2 that provide employment to more than 30,000 people (the number of UK physical scientists (Table 6.1)). From this list of day-to-day tasks, we identified a selection of physics curriculum topics that were critical for the success of the UK's vocational workforce.

Figure 6.3 shows an example output for a profession on the O*Net

Summary Report for:
47-2111.00 - Electricians

Bright Outlook
green

Install, maintain, and repair electrical wiring, equipment, and fixtures. Ensure that work is in accordance with relevant codes. May install or service street lights, intercom systems, or electrical control systems.

Sample of reported job titles: Chief Electrician; Control Electrician; Electrician; Industrial Electrician; Inside Wireman; Journeyman Electrician; Journeyman Wireman; Maintenance Electrician; Mechanical Trades Specialist, Electrician; Qualified Craft Worker, Electrician (QCW, Electrician)

View report: Summary | Details | Custom

Tasks | Tools & Technology | Knowledge | Skills | Abilities | Work Activities | Detailed Work Activities | Work Context | Job Zone | Education | Credentials | Interests | Work Styles | Work Values | Related Occupations | Wages & Employment | Job Openings | Additional Information

Tasks
5 of 21 displayed

- Plan layout and installation of electrical wiring, equipment, or fixtures, based on job specifications and local codes.
- Connect wires to circuit breakers, transformers, or other components.
- Test electrical systems or continuity of circuits in electrical wiring, equipment, or fixtures, using testing devices, such as ohmmeters, voltmeters, or oscilloscopes, to ensure compatibility and safety of system.
- Use a variety of tools or equipment, such as power construction equipment, measuring devices, power tools, and testing equipment, such as oscilloscopes, ammeters, or test lamps.
- Inspect electrical systems, equipment, or components to identify hazards, defects, or the need for adjustment or repair, and to ensure compliance with codes.

back to top

Tools & Technology
10 of 122 displayed

Tools used in this occupation:

- **Cable reels** — Single reel cable trailers; Wheeled wire dispensers; Wire dollies; Wire hand caddies
- **Stripping tools** — Cable jacket strippers; Self-adjusting insulation strippers; Universal stripping tools; Wire strippers
- **Voltage or current meters** — Non-contact voltage detectors; Test lamps; Volt tick meters; Voltmeters
- **Wire lug crimping tool** — Ratchet crimper kits; Terminal crimpers; Wire crimpers; Wire crimping tools
- **Wire or cable cutter** — Cable cutters; High-leverage cable cutters; Insulated cable cutters; Utility cable cutters

Technology used in this occupation:

- **Analytical or scientific software** — Construction Master Pro software; Electrosoft FlashWorks; Elite Software Inpoint; SoftEmpire Electrical Calculations
- **Computer aided design CAD software** — One Mile Up Panel Planner; SmartDraw software
- **Data base user interface and query software** — Insight Direct ServiceCEO; Resolve service management software; Sage 300 Construction and Real Estate; Shafer Service Systems software
- **Spreadsheet software** — Microsoft Excel
- **Word processing software** — Microsoft Word; Socrates Contractor's Library

back to top

Knowledge
5 of 11 displayed

- **Building and Construction** — Knowledge of materials, methods, and the tools involved in the construction or repair of houses, buildings, or other structures such as highways and roads.
- **Mechanical** — Knowledge of machines and tools, including their designs, uses, repair, and maintenance.

Figure 6.3: Example profession output from the O*Net database

database. Some professions from the UK ONS were listed with different titles or multiple professions on the O*Net database. Where this was the case, we compared "job description", "entry requirements", "tasks" and "related job titles" from the ONS information, with the more detailed descriptions provided on O*Net. We would disregard roles where the descriptions did not align despite similar naming conventions. For example, a 'related job title' for the ONS NQF level 3 role under 'SOC 5241: Electrician' is 'Electrical engineer', however, the detailed O*Net description for an 'Electrical Engineer' shows that 93% of those undertaking the role have at least a bachelors degree, so in this instance we considered this O*Net data to refer to a graduate engineering role, which would be inappropriate for the purposes of this study focussed on vocational occupations.

There was not always a clear one-to-one mapping from ONS SOC codes to O*Net entries. For example, 'Vehicle technicians, mechanics and electricians' from the ONS data mapped to O*Net entries of 'Automotive Master Mechanics', 'Automotive Specialty Technician' and 'Electronic Equipment installers and Repairers, Motor Vehicles'. Given that the curriculum content that we identify is collated from all the vocational roles that contribute employment of more than 30,000 people, the precise ONS-O*Net mapping should make little difference to the final curriculum content list (the complete mapping and frequency of content occurrence can be seen in the appendix). We mapped the 22 ONS Vocational Roles to 65 Vocational Roles on O*Net.

Having identified the ONS-O*Net mapping, we then analysed the O*Net database entries, which describe the work undertaken by professionals using a variety of attributes categorised as: 'Tasks', 'Tools and Technology', 'Knowledge', 'Skills', 'Abilities', 'Work Activities'.

In the context of identifying GCSE curriculum content, 'Tasks' was the most detailed and therefore useful field: An example Electrician Task from O*Net is "Test electrical systems or continuity of circuits in electrical wiring, equipment, or fixtures, using testing devices, such as ohmmeters, voltmeters, or oscilloscopes, to ensure compatibility and safety of system."

In contrast, those attributes defined as 'Skills', 'Abilities' and 'Knowledge'

were very general in their descriptions and were therefore challenging to relate to specific curriculum content. However, they are attributes that one would hope a 16 year old might have begun to cultivate during their compulsory physics education.

An example Electrician 'Skills' O*Net entry is: "Critical Thinking – Using logic and reasoning to identify the strengths and weaknesses of alternative solutions, conclusions or approaches to problems."

An example Electrician 'Abilities' O*Net entry is: "Problem Sensitivity – The ability to tell when something is wrong or is likely to go wrong. It does not involve solving the problem, only recognizing there is a problem."

An example Electrician 'Knowledge' O*Net entry is: "Physics – Knowledge and prediction of physical principles, laws, their interrelationships, and applications to understanding fluid, material, and atmospheric dynamics, and mechanical, electrical, atomic and sub- atomic structures and processes."

We exported all related "tasks" associated with the selected vocational occupations from O*Net. We then applied classroom experience and curriculum knowledge, in order to remove "tasks" that did not seem directly relevant to physics, while ensuring that we did not bias ourselves through knowledge of the existing curriculum.

For example, for an electrician we used some tasks: "Plan layout and installation of electrical wiring, equipment, or fixtures" "Connect wires to circuit breakers, transformers, or other components." "Assemble, install, test, or maintain electrical or electronic wiring, equipment, appliances etc." But chose to disregard: "Construct or fabricate parts, using hand tools, according to specifications."

This reduced $\sim$1400 tasks to $\sim$70 from which a set of curriculum content could be identified. The complete list of tasks, with indications as to whether they were considered appropriate for the physics curriculum or not is available upon request and not included here for brevity. Of particular interest, we note that we disregarded tasks that related to computer programming because we felt that they would be more suitable for a computer science/IT curriculum than a physics curriculum. The rigours and complexity of cutting-edge physics

make programming a fundamental part of almost every academic physicist's day-to-day role. Based on this study, it is possible that a more symbiotic relationship between physics and computer science may be appropriate for a modern physics curriculum.

6.5 Identified Curriculum Content List

We collated and summarised the tasks to produce the list of content below and the potential scope for numbers of workers that utilise the knowledge. For brevity we do not include definitions of each topic, but note that these can be found in the syllabus for most GCSE physics curriculum and are also available in the IoP National Curriculum recommendations document (in press). We grouped the variety of curriculum content by convenient overarching topics: Radiation/Light, Interaction Between Objects, Work and Heat, Properties/Quantities, Laws of Motion, Inside Atoms, Electricity and Magnetism, Energy Conservation/Dissipation and Renewable Energy Sources. Below we provide the content areas that fit within each of these overarching headings and the vocational occupations that the content is relevant for along with the potential maximum number of people that might utilise it. We also highlight key applications that arose multiple times. For renewable energy sources, this topic was often needed for a smaller number of roles within an overarching job type, so we do not list the related roles here. We do note though that it was always one of the fastest growing roles - meaning that this may be of particular importance for future-proofing the UK workforce.

6.5.1 Radiation/Light

Required by: Automotive Mechanics, Electricians, Electronics Technicians, Photographers and Audio-Visual Technicians, Telecommunications Technicians and Installers (Employment Impact: 668,000 people)

Curriculum Content:

- Electromagnetic Spectrum (e.g: understanding the different wavebands

and the application of each for different purposes)

- Transmission of Light (e.g. fibre optics)
- Properties of Light and Waves (e.g. signals, amplitudes, amplifiers)

6.5.2 Interaction Between Objects

Required by: Automotive Mechanics/Technicians, Plumbers, Food etc. Baking/Drying, Lab Technicians, Construction/Building Inspectors, Telecommunications Technicians and Installers (Employment Impact: 660,000 people)

Curriculum Content:

- Forces, Interaction at Surfaces and Pressure (e.g. hydraulics, pistons, plumbing)

6.5.3 Work and Heat

Required by: Automotive Mechanics/Technicians, Plumbers, Food etc. Baking/Drying, Welders, Metal workers, Mechanical/Electrical Technicians, Lab Technicians, Construction/Building Inspectors, Fire Inspectors (Employment Impact: 1,063,000)

Curriculum Content:

- Heating various liquids, solids, substances
- Application of heat/work and effects of heat/work
- Insulation and Conductance

6.5.4 Properties/Quantities

Required by: Electricians, Automotive Mechanics/Technicians, Plumbers, Food etc. Baking/Drying, Welders, Mechanical/Electrical Technicians, Construction/Building Inspectors, Fire Inspectors (Employment Impact:

1,063,000)

Curriculum Content:

- Charge, Voltage, Current, Resistance
- Elasticity
- Pressure in fluids
- Stress at a Surface

6.5.5 Laws of Motion

Required by: Automotive Mechanics/Technicians, Construction/Building Inspectors (Employment Impact: 245,000)

Curriculum Content:

- Horizontal motion (e.g. automobiles)
- Vertical motion (e.g. lifts).

6.5.6 Inside Atoms

Required by: Health and Safety Officer (Employment Impact: 47,000 people)

Curriculum Content:

- Radioactive Material (e.g: safe disposal)

6.5.7 Electricity and Magnetism

Required by: Electricians, Automotive Mechanics/Technicians, Plumbers, IT Support, Mechanical/Electronics/Electrical Technicians, Audio-Visual Technicians, Network Support Specialist, Welders, Medical/Clinical Lab technician, Construction/Building Inspectors, Fire Inspectors, Telecommunications

line installer, Electronic Assembler (Employment Impact: 1,305,000)

Curriculum Content:

- Constructing circuits
- Circuit Breakers and Transformers
- Using and measuring the quantities from Ohmmeters, Voltmeters, Oscilloscopes
- Power supplies
- Electronic Theory
- Resistance
- Amplifiers and signal-related
- Insulation and Conductance

6.5.8 Energy Conservation/Dissipation

Required by: Automotive Mechanics/Technicians, Heating Engineer, Electrical Engineers, Construction/Building Inspectors (Employment Impact: 504,000)

Curriculum Content:

- Energy efficiency
- Conservation
- Dissipation
- Consumption

6.5.9 Renewable Energy Sources

Curriculum Content:

- Solar/photovoltaic energy
- Wind turbines
- General Renewable Energy and Sustainability

6.6 Limitations and Possible Extensions of the Study

Our study does not provide a comprehensive, self-contained physics curriculum, since that would necessarily require inputs from those who continue to use physics in non-vocational roles as well (e.g. professional scientists or graduate engineers). Instead we begin to derive a component of the curriculum that is valuable for vocational occupations. Although we note that this should be used in conjunction with other studies and not exclusively.

For this study, we chose to use absolute employment numbers as a metric of the widespread importance of a vocational role to the UK economy at this moment in time. However, employment growth may be a better indicator of the vocational roles that we should have included. An employment growth based curriculum may provide more future-proofed and forward thinking content, relevant for the occupations of the next generation. We also did not divide roles by gender, but this would have been possible and should probably be explored in order to support efforts to address the extremely poor A-level physics gender split (80:20 Male:Female).

6.7 Conclusions

We have conducted a preliminary analysis of labour market information in order to begin to explore the curriculum content needed to meet the physics requirements of the UK workforce. Our analysis of the labour market suggests that a knowledge of physics at GCSE level is important in more than 4 million UK jobs. We connect the 2.3 million vocational roles in the UK that utilise physics with the physics knowledge that they require in order to undertake that role. Here, we provide an overview list of the curriculum content needed; a detailed breakdown is available upon request but is not included in this thesis

for brevity. Our analysis suggests that the content of GCSE physics may not need to change significantly but the results serve to underline the importance of several areas of curriculum content within a classroom education.

Acknowledgements

"Eighteen and stupid happens to everyone, I guess. If you survive it, it's probably half luck and half having the right people in your life"
— Joe hill, *Locke and Key*

I have been exceptionally fortunate to be surrounded by such an amazing group of family and friends. At a full table, it is the absences that are most conspicuous. During my PhD, four people who were particularly important to me became forever absent from that table. I dedicate this thesis to them.

My grandparents, John and Margaret Broughton, provided me with incredible support. The hundreds in attendance at their funerals speaks volumes of the impact that they had on anyone who had the privilege of meeting them. May we all have some fraction of that impact and mean as much to so many.

Trevor's enthusiasm for education was infectious. It is is undoubtedly the conversations with him that I had from childhood to only a few months ago that drove and sustained my deep passion for equal education opportunities for all. I would not have pursued the launch of the 'PhD Inspired' programme with such persistence and ambition without his wisdom, advice and inspiration. Without 'PhD Inspired', I may never have undertaken this PhD and cemented my passion for scientific research.

I also dedicate this PhD to my once housemate and even earlier accomplice in so much teenage mis-adventure - Ed. His unwavering moral compass and constant source of stubbornness and competition gave me the firmest logical, holistic and strategic foundations. Without him I would have lived life very differently. When your group loses someone who, through symbiosis, played such a huge role in your formative years, that chapter finally closes. Until that moment, you always believe you can (and often do) return to being the people

you were at that previous point in your life. That chapter is now closed. We can't ever return to it and it will now have to remain forever nostalgia and memory. I am fiercely proud that I was able to call myself Ed's friend. The inclusion of the final chapter is for him and Trevor. As with Ed, it is stubbornly included as contributing to science education is something that I feel sociologically compelled to do, and as with him, I have ignored the many that may have told me not to include it. As with Trevor, it represents a tiny fraction of my deep passion that all pupils should receive an exceptional education regardless of their background.

I would not be who I am and it is unlikely that I would have undertaken this PhD without John Broughton, Margaret Broughton, Trevor Howe and Edward Hughes. The world is a dimmer place without the light that they brought to it. This work is dedicated to them.

I have many many many people that I need to acknowledge/thank. There are things that the English language (or at least my mastery of it) is incapable of and these acknowledgements are one of those instances and will understate the contributions of others or the esteem I hold for those involved.

Firstly, Graziella Branduardi-Raymont and Andrew Coates have been the greatest supervisors that I could have asked for. Both have been endlessly supportive and patient with both my scientific stupidity and my penchant for outreach/education. Graziella is a constant inspiration and my passion for Jupiter's X-rays is entirely built upon the foundations that she laid.

Licia Ray was part-supervisor, but more friend throughout my PhD. She had a profound impact upon my writing, critical analysis and science from the moment she joined MSSL and, outside of my supervisors, had the biggest impact on my academic progression. She has also been a fantastic friend, although I will forever try to forget the car journey stories about her ovaries. Without Licia, we would not have been awarded so much time for X-ray campaigns and the legacy of Juno-XMM-Newton observations would not be nearly as extensive. Chapter 3 may not have had data without her inputs. Jonny Rae has also been endlessly generous with his time and wisdom, particularly in the nature of academia as a whole. I have learnt huge volumes from him.

Zhonghua Yao's embodiment of plasma physics is something that I will forever envy, along with his excellent appreciation of beer. Geraint Jones has also provided constant support, encouragement and wisdom. Without Caitriona Jackman, Jan-Uwe Ness, Nick Achilleos and Ralph Kraft's support, I would not have the chance to continue to pursue this research that I enjoy so much, so I am also hugely grateful to each of them. Adam Masters and Jaf Yates have been great friends and have provided phenomenal advice throughout. Pre-MSSL, David Kipping sparked my passion for research. He was an unparalleled masters supervisor and I'll forever be in his debt for rekindling my love of science.

Beyond academia, I have enjoyed every second of my time at MSSL and that is because that quirky Surrey mansion has somehow collected some of the most interesting, kind and fun people that I have ever met. Jamie, you made the transition to MSSL seamless. From day one, I enjoyed every minute there. I'm not sure how I survived without daily journeys in the Dragon accompanied by Pink Floyd and Dire Straits. Nadine always enriched the journeys to the lab with stories that cannot be mentioned here for fear that they would offend sensibilities. Ravi, Nadine, Andy, Joe, Ed, and Jacqueline provided the greatest pre/post conference travel partners. Ravi and Jacqueline, I will continue to try to imbue your ethics. Georgie, knowing you has made me a better person. One day I will beat you in a quiz... You accomplished more with the MSSL Space Week than I ever dreamed possible. And when I thought that I had seen the pinnacle of the programme Ollie, you and Georgie, ran a week that clearly had a profound and long-lasting impact on every pupil involved. I can no longer claim it as my legacy, since it is so much more both of yours. I hope you are both immensely proud of your accomplishments in it. The residents of 108: Annie, Yudish, Kim, Marianna, Leonardo, Roger and Sam, who have either provided endless stimulating conversation, music, comics, wisdom, intellect, croquet and quizzes. I woke up in the morning looking forward to a day in the office. Allan and Magnus, I forgive you both for the daggers in my back that were 'Wee Willy Dunce'. May you never feel such betrayal.

Right, on to those who over the last decade have become a family to me

and whose support and friendship have got me to this point. These thanks go, in no particular order, to: Ben, wise beyond his years, but I'll never admit to how often he is right, for the years of Springsteen and Meatloaf lip syncing. Shereif is probably the greatest man I'll ever know. There are not enough superlatives in the English language for him. Josh and Dan, without whom my life would have been lacking in so much mischief (and Megan would not have had someone to blame it on). For over a decade of mischief together from post-ULO visits to Roxy to post-grad pubs. I was very lucky to meet you both in first year. George, it is rare in life to meet someone who is so easy to speak to about any topic. You are profoundly good, profoundly funny and profoundly clever. Tom you are wise, kind and the best of board game competitors. Sam, possessor of the worlds smallest nipples and provider of never a dull moment. Deej for introducing me to real beer, real conversation and for all the visits to Kev's place. Oh, and for adopting Louis as his own. Komal, for having an excellent birth date that allowed us to share countless fun times in so many places! Vav for surprising me with his recent lefty conversion and making me believe we're all capable of change no matter how ingrained we once were. Emily for having someone to spend hours of conversation righting the world's wrongs. Kirthika, for a decade of constant goodness, a passion for so many different things in the world and for so many fantastic conversations of the future. Jack for boundless energy whenever it is needed, for taking the path less travelled, including that time you tried to tattoo yourself with an adapted biro. Mary for kindness, wisdom and for having someone with whom to share a passion for physics education. Jake, for your incredible ability to do physics no matter how horrendous our hangovers. Oli and Raphy for some of the most memorable meals and for so much laughter. To Space Boy and Blues Mouse: For sharing in a love of comics, great music, theatre, dance and all things space, no matter how late/early the hour. I hope we build many a science-arts collaboration to come.

My family: My Dad's entrepreneurship is something that I have clearly inherited alongside his shunning of societal career norms and constant pursuit of his dreams are traits without which I would not have pursued science. While

he may have finished his book a month before me, I like to think that we were in the race until the end. My Mum is the most caring person I know. She is endlessly patient, supportive and deeply kind and I could not ask for better parents, to help me to reach the point where I was able to undertake (and get through) a PhD. To James, Jon, Liam and Sam - one brother by blood and three by friendship and experiences. I am the sum of all of our years together and you each inspire me in different ways.

Finally, to the person who provides me with a constant source of inspiration every day and to whom, for more than a decade, I have been thankful for every day I get to spend with her - to Megan Nee I dedicate this thesis. For forcing me to explore the world and to crystallise every moment in time. For being irrepressibly fun. For having more will-power than I ever imagined possible and "for being an utter babe all the time" (M. Nee, priv comms). 99.99999% of anything I ever accomplish is because of her. Megan, you are the reason that I cherish every moment that I live on this pale blue dot.

Bibliography

Achilleos, N., Miller, S., Tennyson, J., Aylward, A., Mueller-Wodarg, I. and Rees, D. (1998), JIM: A time-dependent, three-dimensional model of Jupiter's thermosphere and ionosphere, *Journal of Geophysical Research: Planets* **103**(E9), 20089–20112.

Anagnostopoulos, G., Balogh, A., Marhavilas, P., Rigas, A., Sarris, E. and Trochoutsos, P. (1998), Quasi-periodic behavior of ion events and wave activity upstream from Jupiter's Bow Shock: Ulysses' observations, *Geophysical research letters* **25**(9), 1533–1536.

Anagnostopoulos, G., Karanikola, I. and Marhavilas, P. (2001), Large-scale energetic particle layers in the high latitude Jovian magnetosphere, *Planetary and Space Science* **49**(10), 1049–1065.

Arnaud, K. (1996), XSPEC: The first ten years, *in Astronomical Data Analysis Software and Systems V*, Vol. 101, p.17.

Atreya, S., Donahue, T. and Festou, M. (1981), Jupiter-Structure and composition of the upper atmosphere, *The Astrophysical Journal* **247**, L43–L47.

Badman, S., Bonfond, B., Fujimoto, M., Gray, R., Kasaba, Y., Kasahara, S., Kimura, T., Melin, H., Nichols, J. D., Steffl, A. et al. (2016), Weakening of Jupiter's main auroral emission during January 2014, *Geophysical Research Letters* **43**(3), 988–997.

Badman, S. and Cowley, S. (2007), Significance of Dungey-cycle flows in Jupiter's and Saturn's magnetospheres, and their identification on closed equatorial field lines, *in Annales Geophysicae*, Vol. 25, pp.941–951.

Badman, S. V., Branduardi-Raymont, G., Galand, M., Hess, S. L., Krupp, N., Lamy, L., Melin, H. and Tao, C. (2015), Auroral processes at the giant planets: Energy deposition, emission mechanisms, morphology and spectra, *Space Science Reviews* **187**(1-4), 99–179.

Bagenal, F. (1994a), Empirical model of the Io plasma torus: Voyager measurements, *Journal of Geophysical Research* **99**(A6), 11043.

Bagenal, F. (1994b), Empirical model of the Io plasma torus: Voyager measurements, *Journal of Geophysical Research: Space Physics* **99**(A6), 11043–11062.

Bagenal, F. (2007), The magnetosphere of Jupiter: Coupling the equator to the poles, *Journal of Atmospheric and Solar-Terrestrial Physics* **69**(3), 387–402.

Bagenal, F., Adriani, A., Allegrini, F., Bolton, S., Bonfond, B., Bunce, E., Connerney, J., Cowley, S., Ebert, R., Gladstone, G. et al. (2014), Magnetospheric science objectives of the Juno mission, *Space Science Reviews* pp.1–69.

Balogh, A., Gonzalez-Esparza, J., Forsyth, R., Burton, M., Goldstein, B., Smith, E. and Bame, S. (1995), Interplanetary shock waves: Ulysses observations in and out of the ecliptic plane, *Space Science Reviews* **72**(1), 171–180.

Bame, S. J., Barraclough, B. L., Feldman, W. C., Gisler, G. R., Gosling, J. T., McComas, D. J., Phillips, J. L., Thomsen, M. F., Goldstein, B. E. and Neugebauer, M. (1992), Jupiter?s magnetosphere: Plasma description from the Ulysses flyby, *Science* **257**(5076), 1539–1543.

Barbosa, D. (1992), Heavy ion dynamics and auroral arc formation in the Jovian magnetosphere, *Advances in Space Research* **12**(8), 7–13.

Baron, R., Owen, T., Connerney, J., Satoh, T. and Harrington, J. (1996), Solar wind control of Jupiter's H+ 3 auroras, *Icarus* **120**(2), 437–442.

Barrow, C., Genova, F. and Desch, M. (1986), Solar wind control of Jupiter's decametric radio emission, *Astronomy and Astrophysics* **165**, 244–250.

Belcher, J. and Davis, L. (1971), Large-amplitude Alfvén waves in the interplanetary medium, 2, *Journal of Geophysical Research* **76**(16), 3534–3563.

Bhardwaj, A., Branduardi-Raymont, G., Elsner, R. F., Gladstone, G. R., Ramsay, G., Rodriguez, P., Soria, R., Waite, J. and Cravens, T. E. (2005), Solar control on Jupiter's equatorial X-ray emissions: 26–29 November 2003 XMM-Newton observation, *Geophysical Research Letters* **32**(3).

Bhardwaj, A., Elsner, R. F., Gladstone, G. R., Waite, J. H., Branduardi-Raymont, G., Cravens, T. E. and Ford, P. G. (2006), Low-to middle-latitude X-ray emission from Jupiter, *Journal of Geophysical Research: Space Physics (1978–2012)* **111**(A11).

Bhardwaj, A. and Gladstone, G. R. (2000), Auroral emissions of the giant planets, *Reviews of Geophysics* **38**(3), 295–353.

Biémont, E., Frémat, Y. and Quinet, P. (1999), Ionization potentials of atoms and ions from lithium to tin (Z= 50), *Atomic Data and Nuclear Data Tables* **71**(1), 117–146.

Bolton, S. J., Thorne, R. M., Bourdarie, S., de Pater, I. and Mauk, B. (2004), Jupiter?s inner radiation belts, *Jupiter: The Planet, Satellites, and Magnetosphere* p.671.

Bonfond, B., Gladstone, G., Grodent, D., Greathouse, T., Versteeg, M., Hue, V., Davis, M., Vogt, M., Gérard, J.-C., Radioti, A. et al. (2017), Morphology of the UV aurorae Jupiter during Juno's first perijove observations, *Geophysical Research Letters* .

Bonfond, B., Grodent, D., Badman, S. V., Gérard, J.-C. and Radioti, A. (2016), Dynamics of the flares in the active polar region of Jupiter, *Geophysical Research Letters* **43**(23).

Bonfond, B., Grodent, D., Gérard, J.-C., Radioti, A., Dols, V., Delamere, P. and Clarke, J. (2009), The Io UV footprint: Location, inter-spot distances

and tail vertical extent, *Journal of Geophysical Research: Space Physics* **114**(A7).

Bonfond, B., Grodent, D., Gérard, J.-C., Radioti, A., Saur, J. and Jacobsen, S. (2008), UV Io footprint leading spot: A key feature for understanding the UV Io footprint multiplicity?, *Geophysical Research Letters* **35**(5).

Bonfond, B., Grodent, D., Gérard, J.-C., Stallard, T., Clarke, J. T., Yoneda, M., Radioti, A. and Gustin, J. (2012), Auroral evidence of Io's control over the magnetosphere of Jupiter, *Geophysical Research Letters* **39**(1).

Bonfond, B., Hess, S., Bagenal, F., Gérard, J.-C., Grodent, D., Radioti, A., Gustin, J. and Clarke, J. T. (2013), The multiple spots of the Ganymede auroral footprint, *Geophysical Research Letters* **40**(19), 4977–4981.

Bonfond, B., Vogt, M., Gérard, J.-C., Grodent, D., Radioti, A. and Coumans, V. (2011), Quasi-periodic polar flares at Jupiter: A signature of pulsed dayside reconnections?, *Geophysical Research Letters* **38**(2).

Borovsky, J. E. (2010), On the variations of the solar wind magnetic field about the Parker spiral direction, *Journal of Geophysical Research: Space Physics* **115**(A9).

Bowyer, S., Byram, E., Chubb, T. and Friedman, H. (1964), X-ray Sources in the Galaxy, *Nature* **201**(4926), 1307–1308.

Branduardi-Raymont, G., Bhardwaj, A., Elsner, R., Gladstone, G., Ramsay, G., Rodriguez, P., Soria, R., Waite, J., Cravens, T. et al. (2007a), A study of Jupiter's aurorae with XMM-Newton, *Astronomy & Astrophysics* **463**(2), 761–774.

Branduardi-Raymont, G., Bhardwaj, A., Elsner, R., Gladstone, G., Ramsay, G., Rodriguez, P., Soria, R., Waite, J. and Cravens, T. (2007b), Latest results on Jovian disk X-rays from XMM-Newton, *Planetary and Space Science* **55**(9), 1126–1134.

Branduardi-Raymont, G., Bhardwaj, A., Elsner, R. and Rodriguez, P. (2010),

X-rays from Saturn: a study with XMM-Newton and Chandra over the years 2002–05, *Astronomy & Astrophysics* **510**, A73.

Branduardi-Raymont, G., Elsner, R. F., Galand, M., Grodent, D., Cravens, T., Ford, P., Gladstone, G. and Waite, J. (2008), Spectral morphology of the X-ray emission from Jupiter's aurorae, *Journal of Geophysical Research: Space Physics (1978–2012)* **113**(A2).

Branduardi-Raymont, G., Elsner, R., Gladstone, G., Ramsay, G., Rodriguez, P., Soria, R. and Waite Jr, J. (2004), First observation of Jupiter by XMM-Newton, *Astronomy & Astrophysics* **424**(1), 331–337.

Bunce, E., Cowley, S. and Yeoman, T. (2004), Jovian cusp processes: Implications for the polar aurora, *Journal of Geophysical Research: Space Physics (1978–2012)* **109**(A9).

Bunce, E., Cowley, S., Wright, D., Coates, A., Dougherty, M., Krupp, N., Kurth, W. and Rymer, A. (2005), In situ observations of a solar wind compression-induced hot plasma injection in Saturn's tail, *Geophysical research letters* **32**(20).

Bunce, E., Hanlon, P. and Cowley, S. (2002), A simple empirical model of the equatorial radial field in Jupiter's middle magnetosphere, based on spacecraft fly-by and Galileo orbiter data, *Planetary and Space Science* **50**(7), 789–806.

Bunce, E. and Cowley, S. (2001), Divergence of the equatorial current in the dawn sector of Jupiter's magnetosphere: analysis of Pioneer and Voyager magnetic field data, *Planetary and Space Science* **49**(10), 1089–1113.

Burke, B. and Franklin, K. (1955), Observations of a variable radio source associated with the planet Jupiter, *Journal of Geophysical Research* **60**(2), 213–217.

Burlaga, L. (1988), Magnetic clouds and force-free fields with constant alpha, *Journal of Geophysical Research: Space Physics* **93**(A7), 7217–7224.

Burlaga, L., Lepping, R., Behannon, K., Klein, L. and Neubauer, F. (1982), Large-scale variations in the IMF: Voyager 1 and 2 observations between 1 and 5 AU, *J. Geophys. Res* **87**, 4345.

Burlaga, L., Sittler, E., Mariani, F. and Schwenn, R. (1981), Magnetic loop behind an interplanetary shock: Voyager, Helios, and IMP 8 observations, *Journal of Geophysical Research: Space Physics* **86**(A8), 6673–6684.

Cane, H. and Richardson, I. (2003), Interplanetary coronal mass ejections in the near-Earth solar wind during 1996–2002, *Journal of Geophysical Research: Space Physics* **108**(A4).

Carlson, C., Pfaff, R., and Watzin, J. (1998), The fast auroral snapshot (FAST) mission, *Geophysical research letters* **25**(12), 2013–2016.

Chandrasekhar, S. (1961), *Hydrodynamic and Hydrodynamic stability*, OUP.

Chen, S.-H. and Kivelson, M. (1993), On nonsinusoidal waves at the Earth? s magnetopause, *Geophysical research letters* **20**(23), 2699–2702.

Chua, D., Parks, G., Brittnacher, M., Peria, W., Germany, G., Spann, J. and Carlson, C. (2001), Energy characteristics of auroral electron precipitation: A comparison of substorms and pressure pulse related auroral activity, *Journal of Geophysical Research: Space Physics (1978–2012)* **106**(A4), 5945–5956.

Clarke, J., Ajello, J., Ballester, G., Jaffel, L. B., Connerney, J., Gérard, J.-C., Gladstone, G., Grodent, D., Pryor, W., Trauger, J. et al. (2002), Ultraviolet emissions from the magnetic footprints of Io, Ganymede and Europa on Jupiter, *Nature* **415**(6875), 997–1000.

Clarke, J., Nichols, J., Gérard, J.-C., Grodent, D., Hansen, K., Kurth, W., Gladstone, G., Duval, J., Wannawichian, S., Bunce, E. et al. (2009), Response of Jupiter's and Saturn's auroral activity to the solar wind, *Journal of Geophysical Research: Space Physics (1978–2012)* **114**(A5).

Clarke, J. T., Grodent, D., Cowley, S. W., Bunce, E. J., Zarka, P., Connerney,

J. E. and Satoh, T. (2004), Jupiter's aurora, *Jupiter. The planet, satellites and magnetosphere* **1**, 639–670.

Connerney, J. (1992), Doing more with Jupiter´ s magnetic field.

Connerney, J., Acuna, M., Ness, N. and Satoh, T. (1998), New models of Jupiter's magnetic field constrained by the Io flux tube footprint, *Journal of Geophysical Research: Space Physics (1978–2012)* **103**(A6), 11929–11939.

Connerney, J., Baron, R., Satoh, T. and Owen, T. (1993), Images of excited H3+ at the foot of the Io flux tube in Jupiter's atmosphere, *in Bulletin of the American Astronomical Society*, Vol. 25, p.1082.

Cowley, S., Alexeev, I., Belenkaya, E., Bunce, E., Cottis, C., Kalegaev, V., Nichols, J. D., Prangé, R. and Wilson, F. (2005), A simple axisymmetric model of magnetosphere-ionosphere coupling currents in Jupiter's polar ionosphere, *Journal of Geophysical Research: Space Physics* **110**(A11).

Cowley, S., Badman, S. V., Imber, S. and Milan, S. (2008), Comment on Jupiter: A fundamentally different magnetospheric interaction with the solar wind? by DJ McComas and F. Bagenal, *Geophysical Research Letters* **35**(10).

Cowley, S., Balogh, A., Dougherty, M., Edwards, T., Forsyth, R., Hynds, R. and Staines, K. (1993), Ulysses observations of anti-sunward flow on Jovian polar cap field lines, *Planetary and space science* **41**(11-12), 987–998.

Cowley, S., Bunce, E., Stallard, T. and Miller, S. (2003), Jupiter's polar ionospheric flows: Theoretical interpretation, *Geophysical research letters* **30**(5).

Cowley, S. and Bunce, E. (2001), Origin of the main auroral oval in Jupiter's coupled magnetosphere–ionosphere system, *Planetary and Space Science* **49**(10), 1067–1088.

Cowley, S. and Bunce, E. (2003a), Modulation of Jovian middle magnetosphere currents and auroral precipitation by solar wind-induced compressions and expansions of the magnetosphere: initial response and steady state, *Planetary and Space Science* **51**(1), 31–56.

Cowley, S. and Bunce, E. (2003b), Modulation of Jupiter's main auroral oval emissions by solar wind induced expansions and compressions of the magnetosphere, *Planetary and Space Science* **51**(1), 57–79.

Cowley, S. and Lockwood, M. (1992), Excitation and decay of solar wind-driven flows in the magnetosphere-ionophere system, *in Annales geophysicae*, Vol. 10, Copernicus, pp.103–115.

Cowley, S., Nichols, J. and Andrews, D. (2007), Modulation of Jupiter's plasma flow, polar currents, and auroral precipitation by solar wind-induced compressions and expansions of the magnetosphere: a simple theoretical model, *in Annales Geophysicae*, Vol. 25, pp.1433–1463.

Cranmer, S. R. (2009), Coronal holes, *Living Reviews in Solar Physics* **6**(1), 3.

Cravens, T. (1997), Comet Hyakutake x-ray source: Charge transfer of solar wind heavy ions, *Geophysical research letters* **24**(1), 105–108.

Cravens, T., Clark, J., Bhardwaj, A., Elsner, R., Waite, J., Maurellis, A., Gladstone, G. and Branduardi-Raymont, G. (2006), X-ray emission from the outer planets: Albedo for scattering and fluorescence of solar X rays, *Journal of Geophysical Research: Space Physics (1978–2012)* **111**(A7).

Cravens, T. E. and Maurellis, A. N. (2001), X-ray emission from scattering and fluorescence of solar X-rays at Venus and Mars, *Geophysical research letters* **28**(15), 3043–3046.

Cravens, T. and Ozak, N. (2012), Auroral ion precipitation and acceleration at the outer planets, *Auroral Phenomenology and Magnetospheric Processes: Earth And Other Planets* pp.287–294.

Cravens, T., Howell, E., Waite, J. and Gladstone, G. (1995), Auroral oxygen precipitation at Jupiter, *Journal of Geophysical Research: Space Physics (1978–2012)* **100**(A9), 17153–17161.

Cravens, T., Waite, J., Gombosi, T., Lugaz, N., Gladstone, G., Mauk, B. and MacDowall, R. (2003), Implications of Jovian X-ray emission for

magnetosphere-ionosphere coupling, *Journal of Geophysical Research: Space Physics (1978–2012)* **108**(A12).

Crooker, N., Gosling, J., Bothmer, V., Forsyth, R., Gazis, P., Hewish, A., Horbury, T., Intriligator, D., Jokipii, J., Kóta, J. et al. (1999), CIR morphology, turbulence, discontinuities, and energetic particles, *in Corotating Interaction Regions*, Springer, pp.179–220.

Culhane, J. L. and Sanford, P. W. (1981), X-ray Astronomy, *New York, Charles Scribner's Sons, 1981. 192 p.* .

Delamere, P. A. and Bagenal, F. (2010a), Solar wind interaction with Jupiter's magnetosphere, *Journal of Geophysical Research: Space Physics* **115**(10), 1–20.

Delamere, P. A. and Bagenal, F. (2010b), Solar wind interaction with Jupiter's magnetosphere, *Journal of Geophysical Research: Space Physics* **115**(10), 1–20.

Delamere, P. and Bagenal, F. (2010c), Solar wind interaction with Jupiter's magnetosphere, *Journal of Geophysical Research: Space Physics (1978–2012)* **115**(A10).

Delory, G., Ergun, R., Carlson, C., Muschietti, L., Chaston, C., Peria, W., McFadden, J. and Strangeway, R. (1998), FAST observations of electron distributions within AKR source regions, *Geophysical Research Letters* **25**(12), 2069–2072.

Den Herder, J., Brinkman, A., Kahn, S., Branduardi-Raymont, G., Thomsen, K., Aarts, H., Audard, M., Bixler, J., den Boggende, A., Cottam, J. et al. (2001), The reflection grating spectrometer on board XMM-Newton, *Astronomy & Astrophysics* **365**(1), L7–L17.

Dennerl, K. (2002), Discovery of X–rays from Mars with Chandra, *Astronomy & Astrophysics* **394**(3), 1119–1128.

Dennerl, K. (2009), X-rays from nonmagnetic planets, *Advances in Geosciences* **15**, 53–74.

Dennerl, K. (2010), Charge transfer reactions, *Space Science Reviews* **157**(1-4), 57–91.

Dennerl, K., Burwitz, V., Englhauser, J., Lisse, C. and Wolk, S. (2002), Discovery of X–rays from Venus with Chandra, *Astronomy & Astrophysics* **386**(1), 319–330.

Dennerl, K., Lisse, C., Bhardwaj, A., Burwitz, V., Englhauser, J., Gunell, H., Holmström, M., Jansen, F., Kharchenko, V. and Rodríguez-Pascual, P. (2006), First observation of Mars with XMM-Newton-High resolution X-ray spectroscopy with RGS, *Astronomy & Astrophysics* **451**(2), 709–722.

Desch, M. D. (1994), Jupiter radio bursts and particle acceleration, *in International Astronomical Union Colloquium*, Vol. 142, Cambridge University Press, pp.541–546.

Desroche, M., Bagenal, F., Delamere, P. and Erkaev, N. (2012), Conditions at the expanded Jovian magnetopause and implications for the solar wind interaction, *Journal of Geophysical Research: Space Physics (1978–2012)* **117**(A7).

Desroche, M., Bagenal, F., Delamere, P. and Erkaev, N. (2013), Conditions at the magnetopause of Saturn and implications for the solar wind interaction, *Journal of Geophysical Research: Space Physics* **118**(6), 3087–3095.

Donnelly, J. (2009), An invisible revolution, *Applied Science in the 14-19 curriculum: A report to the Nuffield Foundation* .

Drake, G. (1988), Theoretical energies for the n= 1 and 2 states of the helium isoelectronic sequence up to Z= 100, *Canadian journal of physics* **66**(7), 586–611.

Dungey, J. and Loughhead, R. (1954), Twisted magnetic fields in conducting fluids, *Australian Journal of Physics* **7**(1), 5–13.

Dunn, W. R., Branduardi-Raymont, G., Elsner, R. F., Vogt, M. F., Lamy, L., Ford, P. G., Coates, A. J., Gladstone, G. R., Jackman, C. M., Nichols,

J. D., Rae, I. J., Varsani, A., Kimura, T., Hansen, K. C. and Jasinski, J. M. (2016), The impact of an ICME on the Jovian X-ray aurora, *Journal of Geophysical Research A: Space Physics* **121**(3), 2274–2307.

Ebert, R., McComas, D., Bagenal, F. and Elliott, H. (2010), Location, structure, and motion of Jupiter's dusk magnetospheric boundary from 1625 to 2550 RJ, *Journal of Geophysical Research: Space Physics* **115**(A12).

Echer, E., Zarka, P., Gonzalez, W., Morioka, A. and Denis, L. (2010), Solar wind effects on Jupiter non-Io DAM emissions during Ulysses distant encounter (2003–2004), *Astronomy & Astrophysics* **519**, A84.

Edwards, P. J. and McCracken, K. (1967), Upper limits to the hard X-ray flux from the quiet Sun and Jupiter, *Journal of Geophysical Research* **72**(7), 1809–1812.

Elphinstone, R., Murphree, J. and Cogger, L. (1996), What is a global auroral substorm?, *Reviews of Geophysics* **34**(2), 169–232.

Elsner, R. F., Gladstone, G. R., Waite, J. H., Crary, F. J., Howell, R. R., Johnson, R. E., Ford, P. G., Metzger, A. E., Hurley, K. C., Feigelson, E. D. et al. (2002), Discovery of soft X-ray emission from Io, Europa, and the Io plasma torus, *The Astrophysical Journal* **572**(2), 1077.

Elsner, R. F., Lugaz, N., Waite, J., Cravens, T., Gladstone, G., Ford, P., Grodent, D., Bhardwaj, A., MacDowall, R., Desch, M. et al. (2005), Simultaneous Chandra X ray, Hubble Space Telescope ultraviolet, and Ulysses radio observations of Jupiter's aurora, *Journal of Geophysical Research: Space Physics (1978–2012)* **110**(A1).

Ergun, R., Carlson, C., McFadden, J., Delory, G., Strangeway, R. and Pritchett, P. (2000), Electron-cyclotron maser driven by charged-particle acceleration from magnetic field-aligned electric fields, *The Astrophysical Journal* **538**(1), 456.

Ergun, R., Ray, L., Delamere, P., Bagenal, F., Dols, V. and Su, Y.-J. (2009),

Generation of parallel electric fields in the Jupiter–Io torus wake region, *Journal of Geophysical Research: Space Physics* **114**(A5).

Ezoe, Y., Ishikawa, K., Ohashi, T., Miyoshi, Y., Terada, N., Uchiyama, Y. and Negoro, H. (2010), Discovery of diffuse hard X-ray emission around Jupiter with Suzaku, *The Astrophysical Journal Letters* **709**(2), L178.

Fairfield, D., Otto, A., Mukai, T., Kokubun, S., Lepping, R., Steinberg, J., Lazarus, A. and Yamamoto, T. (2000), Geotail observations of the Kelvin-Helmholtz instability at the equatorial magnetotail boundary for parallel northward fields, *Journal of Geophysical Research: Space Physics (1978–2012)* **105**(A9), 21159–21173.

Farrell, W., MacDowall, R., Desch, M., Kaiser, M., Stone, R., Kellogg, P., Lin, N., Cornilleau-Wehrlin, N., Canu, P., Bame, S. et al. (1993), Ulysses observations of auroral hiss at high Jovian latitudes, *Geophysical research letters* **20**(20), 2259–2262.

Fear, R., Milan, S., Maggiolo, R., Fazakerley, A., Dandouras, I. and Mende, S. (2014), Direct observation of closed magnetic flux trapped in the high-latitude magnetosphere, *Science* **346**(6216), 1506–1510.

Fisher, P. C., Clark, D. B., Meyerott, A. J. and Smith, K. L. (1964), Upper limit to Jupiter's X-ray flux on September 30, 1962, *Nature* **204**(4962), 982–983.

Fox, J. L., Galand, M. I. and Johnson, R. E. (2008), Energy deposition in planetary atmospheres by charged particles and solar photons, *Space science reviews* **139**(1-4), 3–62.

Fuselier, S. A., Trattner, K. J., Petrinec, S. M. and Lavraud, B. (2012), Day-side magnetic topology at the Earth's magnetopause for northward IMF, *Journal of Geophysical Research: Space Physics* **117**(8), 1–14.

Galand, M. and Chakrabarti, S. (2002), Auroral processes in the solar system, *Atmospheres in the Solar System: comparative aeronomy* pp.55–76.

Galand, M., Moore, L., Mueller-Wodarg, I., Mendillo, M. and Miller, S. (2011), Response of Saturn's auroral ionosphere to electron precipitation: Electron density, electron temperature, and electrical conductivity, *Journal of Geophysical Research: Space Physics* **116**(A9).

Garmire, G. P., Bautz, M. W., Ford, P. G., Nousek, J. A. and Ricker, G. R. (2003), Advanced CCD imaging spectrometer (ACIS) instrument on the Chandra X-ray Observatory, *in X-Ray and Gamma-Ray Telescopes and Instruments for Astronomy*, Vol. 4851, International Society for Optics and Photonics, pp.28–45.

Ge, Y., Russell, C. and Khurana, K. (2010), Reconnection sites in Jupiter?s magnetotail and relation to Jovian auroras, *Planetary and Space Science* **58**(11), 1455–1469.

Gehrels, N. and Stone, E. (1983), Energetic oxygen and sulfur ions in the Jovian magnetosphere and their contribution to the auroral excitation, *Journal of Geophysical Research: Space Physics* **88**(A7), 5537–5550.

Gérard, J.-C., Gustin, J., Grodent, D., Clarke, J. and Grard, A. (2003), Spectral observations of transient features in the FUV Jovian polar aurora, *Journal of Geophysical Research: Space Physics* **108**(A8).

Gérard, J.-C., Gustin, J., Grodent, D., Delamere, P. and Clarke, J. (2002), Excitation of the FUV Io tail on Jupiter: Characterization of the electron precipitation, *Journal of Geophysical Research: Space Physics* **107**(A11).

Giacconi, R., Gursky, H., Paolini, F. R. and Rossi, B. B. (1962), Evidence for X rays from sources outside the solar system, *Physical Review Letters* **9**(11), 439.

Gladstone, G. R., Waite, J. H. and Lewis, W. S. (1998), Secular and local time dependence of Jovian X ray emissions, *Journal of Geophysical Research: Planets (1991–2012)* **103**(E9), 20083–20088.

Gladstone, G., Waite, J., Grodent, D., Lewis, W., Crary, F., Elsner, R. F.,

Weisskopf, M., Majeed, T., Jahn, J.-M., Bhardwaj, A. et al. (2002), A pulsating auroral X-ray hot spot on Jupiter, *Nature* **415**(6875), 1000–1003.

Gloeckler, G., Fisk, L., Hefti, S., Schwadron, N., Zurbuchen, T., Ipavich, F., Geiss, J., Bochsler, P. and Wimmer-Schweingruber, R. (1999), Unusual composition of the solar wind in the 2–3 May 1998 CME observed with SWICS on ACE, *Geophysical research letters* **26**(2), 157–160.

Gold, T. (1959), Plasma and magnetic fields in the solar system, *Journal of Geophysical Research* **64**(11), 1665–1674.

Gosling, J., Eriksson, S., McComas, D., Phan, T. and Skoug, R. (2007), Multiple magnetic reconnection sites associated with a coronal mass ejection in the solar wind, *Journal of Geophysical Research: Space Physics* **112**(A8).

Gosling, J. and Pizzo, V. (1999), Formation and evolution of corotating interaction regions and their three dimensional structure, *in Corotating Interaction Regions*, Springer, pp.21–52.

Gosling, J. T. (1990), Coronal mass ejections and magnetic flux ropes in interplanetary space, *Physics of Magnetic Flux Ropes* pp.343–364.

Gosling, J. T. (1993), The solar flare myth, *J. Geophys. Res.* **98**, 18,937?18,950.

Grader, R., Hill, R. and Seward, F. (1968), X-ray airglow in the daytime sky, *Journal of Geophysical Research* **73**(22), 7149–7153.

Gray, R., Badman, S. V., Bonfond, B., Kimura, T., Misawa, H., Nichols, J., Vogt, M. and Ray, L. (2016), Auroral evidence of radial transport at Jupiter during January 2014, *Journal of Geophysical Research: Space Physics* **121**(10), 9972–9984.

Grodent, D., Bonfond, B., Gérard, J.-C., Radioti, A., Gustin, J., Clarke, J. T., Nichols, J. and Connerney, J. E. (2008), Auroral evidence of a localized magnetic anomaly in Jupiter's northern hemisphere, *Journal of Geophysical Research: Space Physics (1978–2012)* **113**(A9).

Grodent, D., Clarke, J., Kim, J., Waite, J. and Cowley, S. (2003a), Jupiter's main auroral oval observed with HST-STIS, *Journal of Geophysical Research: Space Physics* **108**(A11).

Grodent, D., Clarke, J., Waite, J., Cowley, S., Gérard, J.-C. and Kim, J. (2003b), Jupiter's polar auroral emissions, *Journal of Geophysical Research: Space Physics (1978–2012)* **108**(A10).

Grodent, D., Gérard, J.-C., Clarke, J., Gladstone, G. and Waite, J. (2004), A possible auroral signature of a magnetotail reconnection process on Jupiter, *Journal of Geophysical Research: Space Physics (1978–2012)* **109**(A5).

Gurnett, D., Kurth, W., Hospodarsky, G., Persoon, A., Zarka, P., Lecacheux, A., Bolton, S., Desch, M., Farrell, W., Kaiser, M. et al. (2002), Control of Jupiter's radio emission and aurorae by the solar wind, *Nature* **415**(6875), 985–987.

Gustin, J., Cowley, S. W. H., Grard, J.-C., Gladstone, G. R., Grodent, D. and Clarke, J. T. (2006), Characteristics of Jovian morning bright FUV aurora from Hubble Space Telescope/Space Telescope Imaging Spectrograph imaging and spectral observations, *Journal of Geophysical Research: Space Physics* **111**(A9), n/a–n/a. A09220.

Gustin, J., Gérard, J.-C., Grodent, D., Cowley, S., Clarke, J. and Grard, A. (2004), Energy-flux relationship in the FUV Jovian aurora deduced from HST-STIS spectral observations, *Journal of Geophysical Research: Space Physics* **109**(A10).

Gustin, J., Grodent, D., Ray, L., Bonfond, B., Bunce, E., Nichols, J. and Ozak, N. (2016), Characteristics of north jovian aurora from STIS FUV spectral images, *Icarus* **268**, 215–241.

Hallinan, G., Littlefair, S. P., Cotter, G., Bourke, S., Harding, L. K., Pineda, J. S., Butler, R. P., Golden, a., Basri, G., Doyle, J. G., Kao, M. M., Berdyugina, S. V., Kuznetsov, a., Rupen, M. P. and Antonova, a. (2015), Magnetospherically driven optical and radio aurorae at the end of the stellar main sequence, *Nature* **523**(7562), 568–571.

Hamilton, D., Gloeckler, G., Krimigis, S. and Lanzerotti, L. (1981), Composition of nonthermal ions in the Jovian magnetosphere, *Journal of Geophysical Research: Space Physics* **86**(A10), 8301–8318.

Hanlon, P., Dougherty, M., Krupp, N., Hansen, K., Crary, F., Young, D. and Tóth, G. (2004), Dual spacecraft observations of a compression event within the Jovian magnetosphere: Signatures of externally triggered supercorotation?, *Journal of Geophysical Research: Space Physics (1978–2012)* **109**(A9).

Harris, W., Clarke, J. T., McGrath, M. A. and Ballester, G. E. (1996), Analysis of jovian auroral H Ly-α emission (1981–1991), *Icarus* **123**(2), 350–365.

Hasegawa, H., Fujimoto, M., Phan, T.-D., Reme, H., Balogh, A., Dunlop, M., Hashimoto, C. and TanDokoro, R. (2004), Transport of solar wind into Earth's magnetosphere through rolled-up Kelvin–Helmholtz vortices, *Nature* **430**(7001), 755–758.

Hasegawa, H., Fujimoto, M., Takagi, K., Saito, Y., Mukai, T. and Rème, H. (2006), Single-spacecraft detection of rolled-up Kelvin-Helmholtz vortices at the flank magnetopause, *Journal of Geophysical Research: Space Physics (1978–2012)* **111**(A9).

Haymes, R., Ellis, D. and Fishman, G. (1968), Upper limits to the hard X-ray fluxes from Mars, Venus, and Jupiter, *Journal of Geophysical Research* **73**(3), 867–870.

Hess, S., Bonfond, B., Zarka, P. and Grodent, D. (2011), Model of the Jovian magnetic field topology constrained by the Io auroral emissions, *Journal of Geophysical Research: Space Physics (1978–2012)* **116**(A5).

Hess, S., Cecconi, B. and Zarka, P. (2008), Modeling of Io-Jupiter decameter arcs, emission beaming and energy source, *Geophysical Research Letters* **35**(13).

Hess, S., Echer, E. and Zarka, P. (2012), Solar wind pressure effects on Jupiter

decametric radio emissions independent of Io, *Planetary and Space Science* **70**(1), 114–125.

Hess, S., Echer, E., Zarka, P., Lamy, L. and Delamere, P. (2014), Multi-instrument study of the Jovian radio emissions triggered by solar wind shocks and inferred magnetospheric subcorotation rates, *Planetary and Space Science* **99**, 136–148.

Hess, S., Zarka, P. and Mottez, F. (2007), Io–Jupiter interaction, millisecond bursts and field-aligned potentials, *Planetary and Space Science* **55**(1), 89–99.

Hess, S., Zarka, P., Mottez, F. and Ryabov, V. (2009), Electric potential jumps in the Io-Jupiter flux tube, *Planetary and Space Science* **57**(1), 23–33.

Hill, M. E., Haggerty, D. K., McNutt, R. L. and Paranicas, C. P. (2009), Energetic particle evidence for magnetic filaments in Jupiter's magnetotail, *Journal of Geophysical Research: Space Physics* **114**(A11).

Hill, T. (1979), Inertial limit on corotation, *Journal of Geophysical Research: Space Physics* **84**(A11), 6554–6558.

Hill, T. (2001), The Jovian auroral oval, *Journal of Geophysical Research: Space Physics (1978–2012)* **106**(A5), 8101–8107.

Hill, T. (2004), Auroral structures at Jupiter and Earth, *Advances in Space Research* **33**(11), 2021–2029.

Hiraki, Y. and Tao, C. (2008), Parameterization of ionization rate by auroral electron precipitation in Jupiter, *in Annales geophysicae: atmospheres, hydrospheres and space sciences*, Vol. 26, p.77.

Horanyi, M., Cravens, T. and Waite, J. H. (1988), The precipitation of energetic heavy ions into the upper atmosphere of Jupiter, *Journal of Geophysical Research: Space Physics* **93**(A7), 7251–7271.

Hospodarsky, G., Kurth, W., Cecconi, B., Gurnett, D., Kaiser, M., Desch, M. and Zarka, P. (2004), Simultaneous observations of Jovian quasi-periodic

radio emissions by the Galileo and Cassini spacecraft, *Journal of Geophysical Research: Space Physics* **109**(A9).

Hui, Y., Schultz, D. R., Kharchenko, V. A., Bhardwaj, A., Branduardi-Raymont, G., Stancil, P. C., Cravens, T. E., Lisse, C. M. and Dalgarno, A. (2010), Comparative analysis and variability of the Jovian X-ray spectra detected by the Chandra and XMM-Newton observatories, *Journal of Geophysical Research: Space Physics (1978–2012)* **115**(A7).

Hui, Y., Schultz, D. R., Kharchenko, V. A., Stancil, P. C., Cravens, T. E., Lisse, C. M. and Dalgarno, A. (2009), The ion-induced charge-exchange X-ray emission of the Jovian Auroras: Magnetospheric or solar wind origin?, *The Astrophysical Journal Letters* **702**(2), L158.

Hurley, K. C. (1972), Search for X rays from the planet Jupiter, *Journal of Geophysical Research* **77**(1), 46–53.

Hurley, K. C. (1975), Upper limits to Jovian X-ray emission from the Uhuru satellite, *in The magnetospheres of the earth and Jupiter*, Springer, pp.241–244.

Jackman, C., Arridge, C., Krupp, N., Bunce, E., Mitchell, D., McAndrews, H., Dougherty, M., Russell, C., Achilleos, N., Jones, G. et al. (2008), A multi-instrument view of tail reconnection at Saturn, *Journal of Geophysical Research: Space Physics (1978–2012)* **113**(A11).

Jackman, C. and Arridge, C. (2011), Solar cycle effects on the dynamics of Jupiter's and Saturn's magnetospheres, *Solar Physics* **274**(1-2), 481–502.

Jackson, J. D. (1999), *Classical Electrodynamics John Wiley & Sons*, Inc., New York,.

Jansen, F., Lumb, D., Altieri, B., Clavel, J., Ehle, M., Erd, C., Gabriel, C., Guainazzi, M., Gondoin, P., Much, R. et al. (2001), XMM-Newton observatory-I. The spacecraft and operations, *Astronomy & Astrophysics* **365**(1), L1–L6.

Jia, X., Kivelson, M. G., Khurana, K. K. and Walker, R. J. (2010), Magnetic fields of the satellites of Jupiter and Saturn, *Space science reviews* **152**(1-4), 271–305.

Johnson, J. R., Cheng, C. and Song, P. (2001), Signatures of mode conversion and kinetic Alfvén waves at the magnetopause, *Geophysical research letters* **28**(2), 227–230.

Johnson, J. R. and Cheng, C. (1997), Kinetic Alfvén waves and plasma transport at the magnetopause, *Geophysical research letters* **24**(11), 1423–1426.

Johnson, J. R., Wing, S. and Delamere, P. A. (2014a), Kelvin Helmholtz instability in planetary magnetospheres, *Space Science Reviews* **184**(1-4), 1–31.

Johnson, J. R., Wing, S. and Delamere, P. A. (2014b), Kelvin Helmholtz Instability in Planetary Magnetospheres, *Space Science Reviews* **184**(1-4), 1–31.

Jones, G., Rees, A., Balogh, A. and Forsyth, R. (2002), The draping of heliospheric magnetic fields upstream of coronal mass ejecta, *Geophysical research letters* **29**(11).

Joy, S., Kivelson, M., Walker, R., Khurana, K., Russell, C. and Ogino, T. (2002), Probabilistic models of the Jovian magnetopause and bow shock locations, *Journal of Geophysical Research: Space Physics (1978–2012)* **107**(A10), SMP–17.

Kaiser, M. (1993), Time-variable magnetospheric radio emissions from Jupiter, *Journal of Geophysical Research: Planets (1991–2012)* **98**(E10), 18757–18765.

Karanikola, I., Athanasiou, M., Anagnostopoulos, G., Pavlos, G. and Preka-Papadema, P. (2004), Quasi-periodic emissions (15–80min) from the poles of Jupiter as a principal source of the large-scale high-latitude magnetopause boundary layer of energetic particle, *Planetary and Space Science* **52**(5), 543–559.

Kasahara, S., Kronberg, E., Kimura, T., Tao, C., Badman, S., Masters, A., Retinò, A., Krupp, N. and Fujimoto, M. (2013), Asymmetric distribution of reconnection jet fronts in the Jovian nightside magnetosphere, *Journal of Geophysical Research: Space Physics* **118**(1), 375–384.

Keller, K. A. and Lysak, R. L. (1999), A two-dimensional simulation of the Kelvin-Helmholtz instability with magnetic shear, *Journal of Geophysical Research: Space Physics* **104**(A11), 25097–25103.

Kharchenko, V., Bhardwaj, A., Dalgarno, A., Schultz, D. R. and Stancil, P. C. (2008), Modeling spectra of the north and south Jovian X-ray auroras, *Journal of Geophysical Research: Space Physics (1978–2012)* **113**(A8).

Kharchenko, V., Dalgarno, A., Schultz, D. and Stancil, P. (2006), Ion emission spectra in the Jovian X-ray aurora, *Geophysical research letters* **33**(11).

Kharchenko, V. and Dalgarno, A. (2000), Spectra of cometary X rays induced by solar wind ions, *Journal of Geophysical Research: Space Physics (1978–2012)* **105**(A8), 18351–18359.

Kharchenko, V., Liu, W. and Dalgarno, A. (1998), X ray and EUV emission spectra of oxygen ions precipitating into the Jovian atmosphere, *Journal of Geophysical Research: Space Physics (1978–2012)* **103**(A11), 26687–26698.

Kharchenko, V., Rigazio, M., Dalgarno, A. and Krasnopolsky, V. (2003), Charge abundances of the solar wind ions inferred from cometary X-ray spectra, *The Astrophysical Journal Letters* **585**(1), L73.

Khurana, K. K. (2001), Influence of solar wind on Jupiter's magnetosphere deduced from currents in the equatorial plane, *Journal of Geophysical Research: Space Physics* **106**(A11), 25999–26016.

Khurana, K. K. and Kivelson, M. G. (1989a), On Jovian plasma sheet structure, *Journal of Geophysical Research: Space Physics* **94**(A9), 11791–11803.

Khurana, K. K. and Kivelson, M. G. (1989b), Ultralow frequency MHD waves in Jupiter's middle magnetosphere, *Journal of Geophysical Research: Space Physics (1978–2012)* **94**(A5), 5241–5254.

Khurana, K. K. and Kivelson, M. G. (1989c), Ultralow frequency MHD waves in Jupiter's middle magnetosphere, *Journal of Geophysical Research* **94**(A5), 5241.

Khurana, K. K. and Schwarzl, H. K. (2005), Global structure of Jupiter's magnetospheric current sheet, *Journal of Geophysical Research: Space Physics* **110**(A7).

Khurana, K. K., Kivelson, M. G., Vasyliunas, V. M., Krupp, N., Woch, J., Lagg, A., Mauk, B. H. and Kurth, W. S. (2004), The configuration of Jupiter?s magnetosphere, *Jupiter: The planet, satellites and magnetosphere* **1**, 593–616.

Kim, Y. and Fox, J. L. (1994), The chemistry of hydrocarbon ions in the Jovian ionosphere, *Icarus* **112**(2), 310–325.

Kimura, T., Badman, S., Tao, C., Yoshioka, K., Murakami, G., Yamazaki, A., Tsuchiya, F., Bonfond, B., Steffl, A., Masters, A. et al. (2015), Transient internally driven aurora at Jupiter discovered by Hisaki and the Hubble Space Telescope, *Geophysical Research Letters* **42**(6), 1662–1668.

Kimura, T., Kraft, R. P., Elsner, R. F., Branduardi-Raymont, G., Gladstone, G. R., Tao, C., Yoshioka, K., Murakami, G., Yamazaki, A., Tsuchiya, F., Vogt, M. F., Masters, A., Hasegawa, H., Badman, S. V., Roediger, E., Ezoe, Y., Dunn, W. R., Yoshikawa, I., Fujimoto, M. and Murray, S. S. (2016), Jupiter's X-ray and EUV auroras monitored by Chandra, XMM-Newton, and Hisaki satellite, *Journal of Geophysical Research: Space Physics* **121**(3), 2308–2320.

Kimura, T., Tsuchiya, F., Misawa, H., Morioka, A. and Nozawa, H. (2010), Occurrence statistics and ray tracing study of Jovian quasiperiodic radio bursts observed from low latitudes, *Journal of Geophysical Research: Space Physics* **115**(A5).

Kirsch, E., Krimigis, S., Kohl, J. and Keath, E. (1981), Upper limits for X-ray and energetic neutral particle emission from Jupiter: Voyager-1 results, *Geophysical Research Letters* **8**(2), 169–172.

Kivelson, M. G. (2004), Moon–magnetosphere interactions: a tutorial, *Advances in Space Research* **33**(11), 2061–2077.

Kivelson, M. G. and Russell, C. T. (1995), *Introduction to space physics*, Cambridge university press.

Kivelson, M. G., Khurana, K. K. and Walker, R. J. (2002), Sheared magnetic field structure in Jupiter's dusk magnetosphere: Implications for return currents, *Journal of Geophysical Research: Space Physics* **107**(A7).

Kivelson, M. and Southwood, D. (2005), Dynamical consequences of two modes of centrifugal instability in Jupiter's outer magnetosphere, *Journal of Geophysical Research: Space Physics* **110**(A12).

Knight, S. (1973), Parallel electric fields, *Planetary and Space Science* **21**(5), 741–750.

Krasnopolsky, V. A. (2002), Mars' upper atmosphere and ionosphere at low, medium, and high solar activities: Implications for evolution of water, *Journal of Geophysical Research: Planets* **107**(E12).

Krimigis, S., Carbary, J., Keath, E., Bostrom, C., Axford, W., Gloeckler, G., Lanzerotti, L. and Armstrong, T. (1981), Characteristics of hot plasma in the Jovian magnetosphere: Results from the Voyager spacecraft, *Journal of Geophysical Research: Space Physics* **86**(A10), 8227–8257.

Krimigis, S. and Roelof, E. (1983), Low-energy particle population, *Physics of the Jovian Magnetosphere* pp.106–156.

Kronberg, E. A., Woch, J., Krupp, N., Lagg, A., Daly, P. W. and Korth, A. (2008), Comparison of periodic substorms at Jupiter and Earth, *Journal of Geophysical Research: Space Physics* **113**(A4).

Kronberg, E., Woch, J., Krupp, N., Lagg, A., Khurana, K. and Glassmeier, K.-H. (2005), Mass release at Jupiter: Substorm-like processes in the Jovian magnetotail, *Journal of Geophysical Research: Space Physics* **110**(A3).

Krupp, N., Woch, J., Lagg, A., Wilken, B., Livi, S. and Williams, D. (1998), Energetic particle bursts in the predawn Jovian magnetotail, *Geophysical research letters* **25**(8), 1249–1252.

Kurth, W. (1992), Comparative observations of plasma waves at the outer planets, *Advances in Space Research* **12**(8), 83–90.

Ladreiter, H. and Leblanc, Y. (1989), Jovian hectometric radiation-Beaming, source extension, and solar wind control, *Astronomy and Astrophysics* **226**, 297–310.

Lamy, L., Prangé, R., Hansen, K., Clarke, J., Zarka, P., Cecconi, B., Aboudarham, J., André, N., Branduardi-Raymont, G., Gladstone, R. et al. (2012), Earth-based detection of Uranus' aurorae, *Geophysical Research Letters* **39**(7).

Lamy, L., Prangé, R., Pryor, W., Gustin, J., Badman, S., Melin, H., Stallard, T., Mitchell, D. and Brandt, P. (2013), Multispectral simultaneous diagnosis of Saturn's aurorae throughout a planetary rotation, *Journal of Geophysical Research: Space Physics* **118**(8), 4817–4843.

Lanzerotti, L., Armstrong, T., Gold, R., Anderson, K., Krimigis, S., Lin, R., Pick, M., Roelof, E., Sarris, E., Simnett, G. et al. (1992), The hot plasma environment at Jupiter- Ulysses results, *Science* **257**(5076), 1518–1524.

Lavraud, B., Thomsen, M., Taylor, M., Wang, Y., Phan, T., Schwartz, S., Elphic, R., Fazakerley, A., Reme, H. and Balogh, A. (2005), Characteristics of the magnetosheath electron boundary layer under northward interplanetary magnetic field: Implications for high-latitude reconnection, *Journal of Geophysical Research: Space Physics* **110**(A6).

Leahy, D., Darbro, W., Elsner, R., Weisskopf, M., Kahn, S., Sutherland, P. and Grindlay, J. (1983), On searches for pulsed emission with application to four globular cluster X-ray sources-NGC 1851, 6441, 6624, and 6712, *The Astrophysical Journal* **266**, 160–170.

Lepping, R.P., J. J. and Burlaga, L. (1990), Magnetic Field Structure of Interplanetary Magnetic Clouds at 1 AU, *J. Geophys. Res.* **95**, 11,957–11,965.

Lepri, S. and Zurbuchen, T. (2004), Iron charge state distributions as an indicator of hot ICMEs: Possible sources and temporal and spatial variations during solar maximum, *Journal of Geophysical Research: Space Physics* **109**(A1).

Levine, R. H., Altschuler, M. D. and Harvey, J. W. (1977), Solar sources of the interplanetary magnetic field and solar wind, *Journal of geophysical research* **82**(7), 1061–1065.

Lisse, C., Christian, D., Dennerl, K., Meech, K., Petre, R., Weaver, H. and Wolk, S. (2001), Charge exchange-induced X-ray emission from Comet C/1999 S4 (LINEAR), *Science* **292**(5520), 1343–1348.

Lisse, C., Dennerl, K., Englhauser, J., Harden, M., Marshall, F., Mumma, M., Petre, R., Pye, J., Ricketts, M., Schmitt, J. et al. (1996), Discovery of X-ray and extreme ultraviolet emission from comet C/Hyakutake 1996 B2, *Science* **274**(5285), 205–209.

Liu, W. and Schultz, D. (1999), Jovian X-ray aurora and energetic oxygen ion precipitation, *The Astrophysical Journal* **526**(1), 538.

Liu, W. and Schultz, D. (2000), Ultraviolet emission from oxygen precipitating into Jovian aurora, *The Astrophysical Journal* **530**(1), 500.

Livengood, T. and Moos, H. (1990), Jupiter's north and south polar aurorae with IUE data, *Geophysical Research Letters* **17**(12), 2265–2268.

Lockwood, M. and Moen, J. (1999), Reconfiguration and closure of lobe flux by reconnection during northward IMF: possible evidence for signatures in cusp/cleft auroral emissions, *Annales Geophysicae* **17**(8), 996–1011.

Longair, M. S. (2011), *High energy astrophysics*, Cambridge university press.

Louarn, P. and Le Quéau, D. (1996), Generation of the auroral kilometric radiation in plasma cavities?II. The cyclotron maser instability in small size sources, *Planetary and space science* **44**(3), 211–224.

Louarn, P., Mauk, B., Kivelson, M., Kurth, W., Roux, A., Zimmer, C., Gurnett, D. and Williams, D. (2001), A multi-instrument study of a Jovian magnetospheric disturbance, *Journal of Geophysical Research: Space Physics* **106**(A12), 29883–29898.

Louarn, P., Roux, A., Perraut, S., Kurth, W. and Gurnett, D. (1998), A study of the large-scale dynamics of the Jovian magnetosphere using the Galileo Plasma Wave Experiment, *Geophysical research letters* **25**(15), 2905–2908.

Louarn, P., Roux, A., Perraut, S., Kurth, W. S. and Gurnett, D. A. (2000), A study of the Jovian ?energetic magnetospheric events? observed by Galileo: role in the radial plasma transport, *Journal of Geophysical Research: Space Physics* **105**(A6), 13073–13088.

Lyons, L. and Speiser, T. (1982), Evidence for current sheet acceleration in the geomagnetic tail, *Journal of Geophysical Research: Space Physics* **87**(A4), 2276–2286.

Ma, X., Stauffer, B., Delamere, P. and Otto, A. (2015), Asymmetric Kelvin-Helmholtz propagation at Saturn's dayside magnetopause, *Journal of Geophysical Research: Space Physics* **120**(3), 1867–1875.

MacDowall, R., Kaiser, M., Desch, M., Farrell, W., Hess, R. and Stone, R. (1993), Quasiperiodic Jovian radio bursts: Observations from the Ulysses radio and plasma wave experiment, *Planetary and space science* **41**(11), 1059–1072.

Mann, I. R., Voronkov, I., Dunlop, M., Donovan, E., Yeoman, T. K., Milling, D. K., Wild, J., Kauristie, K., Amm, O., Bale, S. D., Balogh, A., Viljanen, A. and Opgenoorth, H. J. (2002), Coordinated ground-based and Cluster observations of large amplitude global magnetospheric oscillations during a fast solar wind speed interval, *Annales Geophysicae* pp.405–426.

Marhavilas, P., Anagnostopoulos, G. and Sarris, E. (2001), Periodic signals in Ulysses? energetic particle events upstream and downstream from the Jovian bow shock, *Planetary and Space Science* **49**(10), 1031–1047.

Massie, H. and Robins, M. O. (1986), *History of British space science*, Cambridge University Press.

Masters, A., Achilleos, N., Kivelson, M. G., Sergis, N., Dougherty, M. K., Thomsen, M. F., Arridge, C. S., Krimigis, S. M., McAndrews, H. J., Kanani, S. J., Krupp, N. and Coates, A. J. (2010), Cassini observations of a Kelvin-Helmholtz vortex in Saturn's outer magnetosphere, *Journal of Geophysical Research: Space Physics* **115**(A7), n/a–n/a. A07225.

Masters, A., Eastwood, J., Swisdak, M., Thomsen, M., Russell, C., Sergis, N., Crary, F., Dougherty, M., Coates, A. J. and Krimigis, S. (2012), The importance of plasma β conditions for magnetic reconnection at Saturn's magnetopause, *Geophysical Research Letters* **39**(8).

Masters, A., Thomsen, M., Badman, S., Arridge, C. S., Young, D., Coates, A. J. and Dougherty, M. (2011), Supercorotating return flow from reconnection in Saturn's magnetotail, *Geophysical Research Letters* **38**(3).

Mauk, B., Clarke, J., Grodent, D., Waite, J., Paranicas, C. and Williams, D. (2002), Transient aurora on Jupiter from injections of magnetospheric electrons, *Nature* **415**(6875), 1003–1005.

Mauk, B. H. and Saur, J. (2007), Equatorial electron beams and auroral structuring at Jupiter, *Journal of Geophysical Research: Space Physics* **112**(A10).

Mauk, B., Hamilton, D., Hill, T., Hospodarsky, G., Johnson, R., Paranicas, C., Roussos, E., Russell, C., Shemansky, D., Sittler Jr, E. et al. (2009), Fundamental plasma processes in Saturn's magnetosphere, *in Saturn from Cassini-Huygens*, Springer, pp.281–331.

Maurellis, A. N., Cravens, T. E., Gladstone, G. R., Waite, J. H. and Acton, L. W. (2000), Jovian X-ray emission from solar X-ray scattering, *Geophysical research letters* **27**(9), 1339–1342.

McComas, D., Alexander, N., Allegrini, F., Bagenal, F., Beebe, C., Clark, G., Crary, F., Desai, M., De Los Santos, A., Demkee, D. et al. (2013), The

Jovian auroral distributions experiment (JADE) on the Juno Mission to Jupiter, *Space Science Reviews* pp.1–97.

McComas, D., Bagenal, F. and Ebert, R. (2014), Bimodal size of Jupiter's magnetosphere, *Journal of Geophysical Research: Space Physics* **119**(3), 1523–1529.

McComas, D. and Bagenal, F. (2007), Jupiter: A fundamentally different magnetospheric interaction with the solar wind, *Geophysical Research Letters* **34**(20).

McComas, D. and Bagenal, F. (2008), Reply to comment by SWH Cowley et al. on ?Jupiter: a fundamentally different magnetospheric interaction with the solar wind?, *Geophysical Research Letters* **35**(10).

McKibben, R., Simpson, J. and Zhang, M. (1993), Impulsive bursts of relativistic electrons discovered during Ulysses' traversal of Jupiter's dusk-side magnetosphere, *Planetary and space science* **41**(11), 1041–1058.

McNutt Jr, R., Belcher, J., Sullivan, J., Bagenal, F. and Bridge, H. (1979), Departure from rigid co-rotation of plasma in Jupiter's dayside magnetosphere, *Nature* **280**, 803.

McNutt, R., Haggerty, D., Hill, M., Krimigis, S., Livi, S., Ho, G., Gurnee, R., Mauk, B., Mitchell, D., Roelof, E. et al. (2007), Energetic particles in the Jovian magnetotail, *Science* **318**(5848), 220–222.

Meredith, C. J., Cowley, S. W. H., Hansen, K. C., Nichols, J. D. and Yeoman, T. K. (2013), Simultaneous conjugate observations of small-scale structures in Saturn's dayside ultraviolet auroras: Implications for physical origins, *Journal of Geophysical Research: Space Physics* **118**(5), 2244–2266.

Metzger, A. E., Gilman, D. A., Luthey, J. L., Hurley, K. C., Schnopper, H. W., Seward, F. D. and Sullivan, J. D. (1983), The detection of X rays from Jupiter, *Journal of Geophysical Research: Space Physics (1978–2012)* **88**(A10), 7731–7741.

Meyer-Vernet, N. (2007), *Basics of the solar wind*, Cambridge University Press.

Millward, G., Miller, S., Stallard, T., Aylward, A. D. and Achilleos, N. (2002), On the dynamics of the Jovian ionosphere and thermosphere: III. The modelling of auroral conductivity, *Icarus* **160**(1), 95–107.

Miura, A. (1984), Anomalous transport by magnetohydrodynamic Kelvin-Helmholtz instabilities in the solar wind-magnetosphere interaction.

Moore, L., Mueller-Wodarg, I., Galand, M., Kliore, A. and Mendillo, M. (2010), Latitudinal variations in Saturn's ionosphere: Cassini measurements and model comparisons, *Journal of Geophysical Research: Space Physics* **115**(A11).

Morabito, L., Synnott, S., Kupferman, P. and Collins, S. A. (1979), Discovery of currently active extraterrestrial volcanism, *Science* **204**(4396), 972–972.

Moses, J. I. and Bass, S. F. (2000), The effects of external material on the chemistry and structure of Saturn's ionosphere, *Journal of Geophysical Research: Planets* **105**(E3), 7013–7052.

Murray, S. S., Austin, G. K., Chappell, J. H., Gomes, J. J., Kenter, A. T., Kraft, R. P., Meehan, G. R., Zombeck, M. V., Fraser, G. W. and Serio, S. (2000), In-flight performance of the Chandra high-resolution camera, *in Proc. SPIE*, Vol. 4012, pp.68–80.

Nakamura, R., Baumjohann, W., Asano, Y., Runov, A., Balogh, A., Owen, C., Fazakerley, A., Fujimoto, M., Klecker, B. and Reme, H. (2006), Dynamics of thin current sheets associated with magnetotail reconnection, *Journal of Geophysical Research: Space Physics* **111**(A11).

Neugebauer, M. and Goldstein, R. (1997), *Particle and field signatures of coronal mass ejections in the solar wind*, Wiley Online Library.

Nichols, J., Bunce, E., Clarke, J. T., Cowley, S., Gérard, J.-C., Grodent, D. and Pryor, W. R. (2007), Response of Jupiter's UV auroras to interplanetary

conditions as observed by the Hubble Space Telescope during the Cassini flyby campaign, *Journal of Geophysical Research: Space Physics (1978–2012)* **112**(A2).

Nichols, J., Clarke, J., Gérard, J.-C., Grodent, D. and Hansen, K. (2009a), Variation of different components of Jupiter's auroral emission, *Journal of Geophysical Research: Space Physics (1978–2012)* **114**(A6).

Nichols, J., Clarke, J., Gérard, J.-C. and Grodent, D. (2009b), Observations of Jovian polar auroral filaments, *Geophysical Research Letters* **36**(8).

Nichols, J. D. (2011), Magnetosphere-ionosphere coupling in Jupiter's middle magnetosphere: Computations including a self-consistent current sheet magnetic field model, *Journal of Geophysical Research: Space Physics (1978–2012)* **116**(A10).

Nichols, J. D., Badman, S. V., Bagenal, F., Bolton, S. J., Bonfond, B., Bunce, E. J., Clarke, J. T., Connerney, J. E. P., Cowley, S. W. H., Ebert, R. W., Fujimoto, M., Gérard, J.-C., Gladstone, G. R., Grodent, D., Kimura, T., Kurth, W. S., Mauk, B. H., Murakami, G., McComas, D. J., Orton, G. S., Radioti, A., Stallard, T. S., Tao, C., Valek, P. W., Wilson, R. J., Yamazaki, A. and Yoshikawa, I. (2017), Response of Jupiter's auroras to conditions in the interplanetary medium as measured by the Hubble Space Telescope and Juno, *Geophysical Research Letters* .

Nichols, J. and Cowley, S. (2003), Magnetosphere-ionosphere coupling currents in Jupiter's middle magnetosphere: Dependence on the effective ionospheric Pedersen conductivity and iogenic plasma mass outflow rate, *in Annales Geophysicae*, Vol. 21, pp.1419–1441.

Nichols, J. and Cowley, S. (2004), Magnetosphere-ionosphere coupling currents in Jupiter's middle magnetosphere: Effect of precipitation-induced enhancement of the ionospheric Pedersen conductivity, *in Annales Geophysicae*, Vol. 22, pp.1799–1827.

Nykyri, K. and Otto, A. (2001), Plasma transport at the magnetospheric

boundary due to reconnection in Kelvin-Helmholtz vortices, *Geophys. Res. Lett* **28**(18), 3565–3568.

Nykyri, K., Otto, A., Lavraud, B., Mouikis, C., Kistler, L., Balogh, A. and Reme, H. (2006), Cluster observations of reconnection due to the Kelvin-Helmholtz instability at the dawnside magnetospheric flank, *in Annales Geophysicae*, Vol. 24, pp.2619–2643.

O'donoghue, J., Stallard, T., Melin, H., Jones, G., Cowley, S., Miller, S., Baines, K. and Blake, J. (2013), The domination of Saturn's low latitude ionosphere by ringrain', *arXiv preprint arXiv:1310.7293* .

Otto, A. (2006), Mass transport at the magnetospheric flanks associated with three-dimensional Kelvin-Helmholtz modes, *in AGU Fall Meeting Abstracts*.

Otto, A. (2007), Plasma entry and Kelvin-Helmholtz modes at the flanks of the magnetosphere, *in AGU Fall Meeting Abstracts*.

Otto, A. (2008), Three-dimensional simulation of Kelvin-Helmholtz modes at the magnetospheric boundary, *in AGU Spring Meeting Abstracts*.

Owens, M. J., Cargill, P., Pagel, C., Siscoe, G. and Crooker, N. (2005), Characteristic magnetic field and speed properties of interplanetary coronal mass ejections and their sheath regions, *Journal of Geophysical Research: Space Physics* **110**(A1).

Owens, M. J., Crooker, N. and Lockwood, M. (2011), How is open solar magnetic flux lost over the solar cycle?, *Journal of Geophysical Research: Space Physics* **116**(A4).

Owens, M. J. and Forsyth, R. J. (2013), The heliospheric magnetic field, *Living Reviews in Solar Physics* **10**(1), 5.

Ozak, N., Cravens, T. and Schultz, D. (2013), Auroral ion precipitation at Jupiter: Predictions for Juno, *Geophysical Research Letters* **40**(16), 4144–4148.

Ozak, N., Schultz, D. R., Cravens, T., Kharchenko, V. and Hui, Y.-W. (2010), Auroral X-ray emission at Jupiter: Depth effects, *Journal of Geophysical Research: Space Physics (1978–2012)* **115**(A11).

Ozel, F. (2013), Surface emission from neutron stars and implications for the physics of their interiors., *Reports on progress in physics. Physical Society (Great Britain)* **76**(1), 016901.

Pallier, L. and Prangé, R. (2001), More about the structure of the high latitude Jovian aurorae, *Planetary and Space Science* **49**(10), 1159–1173.

Pallier, L. and Prangé, R. (2004), Detection of the southern counterpart of the Jovian northern polar cusp: Shared properties, *Geophysical research letters* **31**(6).

Palmaerts, B., Radioti, A., Grodent, D., Chané, E. and Bonfond, B. (2014), Transient small-scale structure in the main auroral emission at Jupiter, *Journal of Geophysical Research: Space Physics* **119**(12), 9931–9938.

Panchenko, M., Rucker, H. and Farrell, W. (2013), Periodic bursts of Jovian non-Io decametric radio emission, *Planetary and space science* **77**, 3–11.

Parker, E. N. (1958), Dynamics of the interplanetary gas and magnetic fields., *The Astrophysical Journal* **128**, 664.

Paschmann, G., Haaland, S. and Treumann, R. (2012), *Auroral plasma physics*, Vol. 15, Springer Science & Business Media.

Phillips, J., Bame, S., Barraclough, B., McComas, D., Forsyth, R., Canu, P. and Kellogg, P. (1993), Ulysses plasma electron observations in the Jovian magnetosphere, *Planetary and space science* **41**(11-12), 877–892.

Phillips, K.J.H.; Leibacher, J.W.; Wolfson, C.J.; Parkinson, J.H.; Fawcett, B.C.; Kent, B.J.; Mason, H.E.; Acton, L.W.; Culhane, J.L.; Gabriel, A. (1982), No Title, *ASTROPHYS J* **256**(2), 774 – 787.

Pizzo, V. (1991), The evolution of corotating stream fronts near the ecliptic plane in the inner solar system: 2. Three-dimensional tilted-dipole fronts, *Journal of Geophysical Research: Space Physics* **96**(A4), 5405–5420.

Prangé, R., Pallier, L., Hansen, K. C., Howard, R., Vourlidas, A., Courtin, R. and Parkinson, C. (2004), An interplanetary shock traced by planetary auroral storms from the Sun to Saturn, *Nature* **432**(7013), 78–81.

Prangé, R., Zarka, P., Ballester, G., Livengood, T., Denis, L., Carr, T., Reyes, F., Bame, S. and Moos, H. (1993), Correlated variations of UV and radio emissions during an outstanding Jovian auroral event, *Journal of Geophysical Research: Planets (1991–2012)* **98**(E10), 18779–18791.

Prikryl, P., Greenwald, R., Sofko, G., Villain, J., Ziesolleck, C. and Friis-Christensen, E. (1998), Solar-wind-driven pulsed magnetic reconnection at the dayside magnetopause, Pc5 compressional oscillations, and field line resonances, *Journal of Geophysical Research: Space Physics (1978–2012)* **103**(A8), 17307–17322.

Pryor, W. R., Stewart, A. I. F., Esposito, L. W., McClintock, W. E., Colwell, J. E., Jouchoux, A. J., Steffl, A. J., Shemansky, D. E., Ajello, J. M., West, R. A. et al. (2005), Cassini UVIS observations of Jupiter's auroral variability, *Icarus* **178**(2), 312–326.

Radioti, A., Gérard, J.-C., Grodent, D., Bonfond, B., Krupp, N. and Woch, J. (2008a), Discontinuity in Jupiter's main auroral oval, *Journal of Geophysical Research: Space Physics* **113**(A1).

Radioti, A., Grodent, D., Gérard, J.-C., Bonfond, B. and Clarke, J. (2008b), Auroral polar dawn spots: Signatures of internally driven reconnection processes at Jupiter's magnetotail, *Geophysical Research Letters* **35**(3).

Radioti, A., Grodent, D., Gérard, J.-C. and Bonfond, B. (2010), Auroral signatures of flow bursts released during magnetotail reconnection at Jupiter, *Journal of Geophysical Research: Space Physics* **115**(A7).

Radioti, A., Grodent, D., Gérard, J.-C., Vogt, M., Lystrup, M. and Bonfond, B. (2011), Nightside reconnection at Jupiter: Auroral and magnetic field observations from 26 July 1998, *Journal of Geophysical Research: Space Physics* **116**(A3).

Radioti, A., Lystrup, M., Bonfond, B., Grodent, D. and Gérard, J.-C. (2013), Jupiter's aurora in ultraviolet and infrared: Simultaneous observations with the Hubble Space Telescope and the NASA Infrared Telescope Facility, *Journal of Geophysical Research: Space Physics* **118**(5), 2286–2295.

Rae, I. J., Donovan, E. F., Mann, I. R., Fenrich, F. R., Watt, C. E. J., Milling, D. K., Lester, M., Lavraud, B., Wild, J. A., Singer, H. J., Rème, H. and Balogh, A. (2005), Evolution and characteristics of global Pc5 ULF waves during a high solar wind speed interval, *Journal of Geophysical Research: Space Physics* **110**(A12), 1–16.

Ray, L., Ergun, R., Delamere, P. and Bagenal, F. (2010), Magnetosphere-ionosphere coupling at Jupiter: Effect of field-aligned potentials on angular momentum transport, *Journal of Geophysical Research: Space Physics* **115**(A9).

Ray, L., Ergun, R., Delamere, P. and Bagenal, F. (2012), Magnetosphere-ionosphere coupling at Jupiter: A parameter space study, *Journal of Geophysical Research: Space Physics* **117**(A1).

Reiner, M., Fainberg, J., Stone, R., Kaiser, M., Desch, M., Manning, R., Zarka, P. and Pedersen, B.-M. (1993), Source characteristics of Jovian narrowband kilometric radio emissions, *Journal of Geophysical Research: Planets* **98**(E7), 13163–13176.

Richardson, I., Cliver, E. and Cane, H. (2000), Sources of geomagnetic activity over the solar cycle: Relative importance of coronal mass ejections, high-speed streams, and slow solar wind, *Journal of Geophysical Research: Space Physics* **105**(A8), 18203–18213.

Richardson, I., Cliver, E. and Cane, H. (2001), Sources of geomagnetic storms for solar minimum and maximum conditions during 1972–2000, *Geophysical Research Letters* **28**(13), 2569–2572.

Richardson, I., Wibberenz, G. and Cane, H. (1996), The relationship between recurring cosmic ray depressions and corotating solar wind streams at? 1

AU: IMP 8 and Helios 1 and 2 anticoincidence guard rate observations, *Journal of Geophysical Research: Space Physics* **101**(A6), 13483–13496.

Riley, P., Schatzman, C., Cane, H., Richardson, I. and Gopalswamy, N. (2006), On the rates of coronal mass ejections: Remote solar and in situ observations, *The Astrophysical Journal* **647**(1), 648.

Robbrecht, E., Berghmans, D. and Van der Linden, R. (2009a), Automated LASCO CME catalog for solar cycle 23: are CMEs scale invariant?, *The Astrophysical Journal* **691**(2), 1222.

Robbrecht, E., Patsourakos, S. and Vourlidas, A. (2009b), No trace left behind: STEREO observation of a coronal mass ejection without low coronal signatures, *The Astrophysical Journal* **701**(1), 283.

Roelof, E., Simnett, G., Decker, R., Lanzerotti, L., Maclennan, C., Armstrong, T. and Gold, R. (1997), Reappearance of recurrent low-energy particle events at Ulysses/HI-SCALE in the northern heliosphere, *Journal of Geophysical Research: Space Physics* **102**(A6), 11251–11262.

Roux, A., Hilgers, A., Feraudy, H. d., Le Queau, D., Louarn, P., Perraut, S., Bahnsen, A., Jespersen, M., Ungstrup, E. and Andre, M. (1993), Auroral kilometric radiation sources: In situ and remote observations from Viking, *Journal of Geophysical Research: Space Physics* **98**(A7), 11657–11670.

Santos-Costa, D. and Bolton, S. J. (2008), Discussing the processes constraining the Jovian synchrotron radio emission's features, *Planetary and Space Science* **56**(3), 326–345.

Saur, J., Neubauer, F. M., Connerney, J., Zarka, P. and Kivelson, M. G. (2004), Plasma interaction of Io with its plasma torus, *Jupiter: The Planet, Satellites and Magnetosphere* **1**, 537–560.

Saur, J., Pouquet, A. and Matthaeus, W. H. (2003), An acceleration mechanism for the generation of the main auroral oval on Jupiter, *Geophysical research letters* **30**(5).

Savani, N., Owens, M., Rouillard, A., Forsyth, R., Kusano, K., Shiota, D., Kataoka, R., Jian, L. and Bothmer, V. (2011), Evolution of coronal mass ejection morphology with increasing heliocentric distance. II. In situ observations, *The Astrophysical Journal* **732**(2), 117.

Schwenn, R. (2006), Space weather: The solar perspective, *Living Reviews in Solar Physics* **3**(1), 2.

Simpson, J., Anglin, J., Balogh, A., Bercovitch, M., Bouman, J., Budzinski, E., Burrows, J., Carvell, R., Connell, J., Ducros, R. et al. (1992), The Ulysses cosmic ray and solar particle investigation, *Astronomy and Astrophysics Supplement Series* **92**, 365–399.

Sinclair, J., Orton, G., Greathouse, T., Fletcher, L., Tao, C., Gladstone, G., Adriani, A., Dunn, W., Moses, J., Hue, V. et al. (2017), Independent evolution of stratospheric temperatures in Jupiter's northern and southern auroral regions from 2014 to 2016, *Geophysical Research Letters* **44**(11), 5345–5354.

Siscoe, G. and Huang, T. (1985), Polar cap inflation and deflation, *Journal of Geophysical Research: Space Physics* **90**(A1), 543–547.

Siscoe, G. and Odstrcil, D. (2008), Ways in which ICME sheaths differ from magnetosheaths, *Journal of Geophysical Research: Space Physics* **113**(A9).

Slanger, T., Cravens, T., Crovisier, J., Miller, S. and Strobel, D. (2008), Photoemission phenomena in the solar system, *Space science reviews* **139**(1-4), 267–310.

Smith, E. J. and Wolfe, J. H. (1976), Observations of interaction regions and corotating shocks between one and five AU: Pioneers 10 and 11, *Geophysical Research Letters* **3**(3), 137–140.

Song, P. and Russell, C. (1992), Model of the formation of the low-latitude boundary layer for strongly northward interplanetary magnetic field, *Journal of Geophysical Research: Space Physics* **97**(A2), 1411–1420.

Southwood, D. and Kivelson, M. (2001), A new perspective concerning the

influence of the solar wind on the Jovian magnetosphere, *Journal of Geophysical Research: Space Physics (1978–2012)* **106**(A4), 6123–6130.

St Cyr, O., Howard, R., Sheeley, N., Plunkett, S., Michels, D., Paswaters, S., Koomen, M., Simnett, G., Thompson, B., Gurman, J. et al. (2000), Properties of coronal mass ejections: SOHO LASCO observations from January 1996 to June 1998, *Journal of Geophysical Research: Space Physics* **105**(A8), 18169–18185.

Stallard, T., Miller, S., Cowley, S. and Bunce, E. (2003), Jupiter's polar ionospheric flows: Measured intensity and velocity variations poleward of the main auroral oval, *Geophysical research letters* **30**(5).

Stallard, T., Miller, S., Millward, G. and Joseph, R. D. (2001), On the dynamics of the Jovian ionosphere and thermosphere: I. The measurement of ion winds, *Icarus* **154**(2), 475–491.

Stone, R., Pedersen, B., Harvey, C., Canu, P., Cornilleau-Wehrlin, N., Desch, M., De Villedary, C., Fainberg, J., Farrell, W., Goetz, K. et al. (1992), Ulysses radio and plasma wave observations in the Jupiter environment, *Science* **257**(5076), 1524–1531.

Strüder, L., Briel, U., Dennerl, K., Hartmann, R., Kendziorra, E., Meidinger, N., Pfeffermann, E., Reppin, C., Aschenbach, B., Bornemann, W. et al. (2001), The European photon imaging camera on XMM-Newton: the pn-CCD camera, *Astronomy & Astrophysics* **365**(1), L18–L26.

Svalgaard, L. and Wilcox, J. M. (1975), Long term evolution of solar sector structure, *Solar Physics* **41**(2), 461–475.

Tao, C., Badman, S. V. and Fujimoto, M. (2013), Characteristic time scales of Uv and Ir auroral emissions at Jupiter and Saturn and their possible observable effects, *in Proc. of the 12th Symposium on Planetary Science*.

Tao, C., Fujiwara, H. and Kasaba, Y. (2010), Jovian magnetosphere–ionosphere current system characterized by diurnal variation of ionospheric conductance, *Planetary and Space Science* **58**(3), 351–364.

Taylor, M., Hasegawa, H., Lavraud, B., Phan, T., Escoubet, C., Dunlop, M., Bogdanova, Y., Borg, A., Volwerk, M., Berchem, J. et al. (2012), Spatial distribution of rolled up Kelvin-Helmholtz vortices at Earth's dayside and flank magnetopause, *in Annales Geophysicae*, Vol. 30, pp.1025–1035.

Thomas, B. T. and Smith, E. J. (1980), The Parker spiral configuration of the interplanetary magnetic field between 1 and 8.5 AU, *Journal of Geophysical Research: Space Physics* **85**(A12), 6861–6867.

Thomas, B. T. and Smith, E. J. (1981), The structure and dynamics of the heliospheric current sheet, *Journal of Geophysical Research: Space Physics* **86**(A13), 11105–11110.

Thomsen, M., Reisenfeld, D., Delapp, D., Tokar, R., Young, D., Crary, F., Sittler, E., McGraw, M. and Williams, J. (2010), Survey of ion plasma parameters in Saturn's magnetosphere, *Journal of Geophysical Research: Space Physics (1978–2012)* **115**(A10).

Tsurutani, B. T., Gonzalez, W. D., Tang, F., Akasofu, S. I. and Smith, E. J. (1988), Origin of interplanetary southward magnetic fields responsible for major magnetic storms near solar maximum (1978–1979), *Journal of Geophysical Research: Space Physics* **93**(A8), 8519–8531.

Turner, M. J., Abbey, A., Arnaud, M., Balasini, M., Barbera, M., Belsole, E., Bennie, P., Bernard, J., Bignami, G., Boer, M. et al. (2001), The European photon imaging camera on XMM-Newton: the MOS cameras, *Astronomy & Astrophysics* **365**(1), L27–L35.

Vasyliunas, V. (1983), Plasma distribution and flow, *Physics of the Jovian magnetosphere* pp.395–453.

Vesecky, J. F., Culhane, J. and Hawkins, F. (1975), Upper limits for X-ray emission from Jupiter as measured from the Copernicus satellite, *in The magnetospheres of the earth and Jupiter*, Springer, pp.245–251.

Vogt, M. F., Bunce, E. J., Kivelson, M. G., Khurana, K. K., Walker, R. J., Radioti, A., Bonfond, B. and Grodent, D. (2015), Magnetosphere-ionosphere

mapping at Jupiter: Quantifying the effects of using different internal field models, *Journal of Geophysical Research: Space Physics* .

Vogt, M. F., Kivelson, M. G., Khurana, K. K., Joy, S. P. and Walker, R. J. (2010), Reconnection and flows in the Jovian magnetotail as inferred from magnetometer observations, *Journal of Geophysical Research: Space Physics* **115**(A6).

Vogt, M. F., Kivelson, M. G., Khurana, K. K., Walker, R. J., Ashour-Abdalla, M. and Bunce, E. J. (2014), Simulating the effect of centrifugal forces in Jupiter's magnetosphere, *Journal of Geophysical Research: Space Physics* **119**(3), 1925–1950.

Vogt, M. F., Kivelson, M. G., Khurana, K. K., Walker, R. J., Bonfond, B., Grodent, D. and Radioti, A. (2011), Improved mapping of Jupiter's auroral features to magnetospheric sources, *Journal of Geophysical Research: Space Physics (1978–2012)* **116**(A3).

Waite, J., Bagenal, F., Seward, F., Na, C., Gladstone, G., Cravens, T., Hurley, K., Clarke, J., Elsner, R. and Stern, S. (1994), ROSAT observations of the Jupiter aurora, *Journal of Geophysical Research: Space Physics (1978–2012)* **99**(A8), 14799–14809.

Waite, J., Boice, D., Hurley, K., Stern, S. and Sommer, M. (1992), Jovian bremsstrahlung X rays: A Ulysses prediction, *Geophysical research letters* **19**(2), 83–86.

Waite, J., Gladstone, G., Franke, K., Lewis, W., Fabian, A., Brandt, W., Na, C., Haberl, F., Clarke, J., Hurley, K. et al. (1995), ROSAT observations of X-ray emissions from Jupiter during the impact of comet Shoemaker-Levy 9, *SCIENCE-NEW YORK THEN WASHINGTON*- pp.1598–1598.

Waite, J., Gladstone, G., Lewis, W., Drossart, P., Cravens, T., Maurellis, A., Mauk, B. and Miller, S. (1997), Equatorial X-ray emissions: Implications for Jupiter's high exospheric temperatures, *Science* **276**(5309), 104–108.

Waite, J., Gladstone, G., Lewis, W., Goldstein, R., McComas, D., Riley, P., Walker, R., Robertson, P., Desai, S., Clarke, J. et al. (2001), An auroral flare at Jupiter, *Nature* **410**(6830), 787–789.

Waite, J. H., Clarke, J., Cravens, T. and Hammond, C. (1988), The Jovian aurora: electron or ion precipitation?, *Journal of Geophysical Research: Space Physics* **93**(A7), 7244–7250.

Walker, R. J. and Russell, C. T. (1985), Flux transfer events at the Jovian magnetopause, *Journal of Geophysical Research: Space Physics* **90**(A8), 7397–7404.

Wang, Y.-M., Hawley, S. H. and Sheeley Jr, N. R. (1996), The magnetic nature of coronal holes, *Science* **271**(5248), 464.

Wargelin, B., Beiersdorfer, P. and Brown, G. (2008), EBIT charge-exchange measurements and astrophysical applications, *Canadian Journal of Physics* **86**(1), 151–169.

Weisskopf, M. C., Tananbaum, H. D., Van Speybroeck, L. P. and O'Dell, S. L. (2000), Chandra X-ray Observatory (CXO): overview, *Arxiv preprint astro-ph/0004127* .

Williams, D., Mauk, B., McEntire, R., Roelof, E., Armstrong, T., Wilken, B., Roederer, J., Krimigis, S., Fritz, T. and Lanzerotti, L. (1996), Electron beams and ion composition measured at lo and in its torus, *Science* **274**, 401–403.

Wilson, R. and Dougherty, M. (2000a), Evidence provided by Galileo of ultra low frequency waves within Jupiter's middle magnetosphere, *Geophysical research letters* **27**(6), 835–838.

Wilson, R. J., Delamere, P. A., Bagenal, F. and Masters, A. (2012), Kelvin-Helmholtz instability at Saturn's magnetopause: Cassini ion data analysis, *Journal of Geophysical Research: Space Physics* **117**(A3), n/a–n/a. A03212.

Wilson, R. J. and Dougherty, M. K. (2000b), Evidence provided by galileo of

ultra low frequency waves within Jupiter's middle magnetosphere, *Geophysical Research Letters* **27**(6), 835–838.

Wimmer-Schweingruber, R., Crooker, N., Balogh, A., Bothmer, V., Forsyth, R., Gazis, P., Gosling, J., Horbury, T., Kilchenmann, A., Richardson, I. et al. (2006), Understanding interplanetary coronal mass ejection signatures, *Space Science Reviews* **123**(1-3), 177–216.

Woch, J., Krupp, N. and Lagg, A. (2002), Particle bursts in the Jovian magnetosphere: Evidence for a near-Jupiter neutral line, *Geophysical research letters* **29**(7), 42–1.

Woch, J., Krupp, N., Lagg, A., Wilken, B., Livi, S. and Williams, D. (1998), Quasi-periodic modulations of the Jovian magnetotail, *Geophysical research letters* **25**(8), 1253–1256.

Yelle, R. and Miller, S. (2004), *Jupiter?s thermosphere and ionosphere*, Vol. 185, Cambridge University Press.

Zarka, P. (1998), Auroral radio emissions at the outer planets: Observations and theories, *Journal of Geophysical Research: Planets (1991–2012)* **103**(E9), 20159–20194.

Zarka, P. (2000), Radio emissions from the planets and their moons, *Radio Astronomy at Long Wavelengths* pp.167–178.

Zarka, P., Cecconi, B. and Kurth, W. (2004), Jupiter's low-frequency radio spectrum from Cassini/Radio and Plasma Wave Science (RPWS) absolute flux density measurements, *Journal of Geophysical Research: Space Physics* **109**(A9).

Zarka, P., Queinnec, J. and Crary, F. J. (2001a), Low-frequency limit of Jovian radio emissions and implications on source locations and Io plasma wake, *Planetary and Space Science* **49**(10), 1137–1149.

Zarka, P., Treumann, R. A., Ryabov, B. P. and Ryabov, V. B. (2001b), Magnetically-driven planetary radio emissions and application to extraso-

lar planets, *in Physics of Space: Growth Points and Problems*, Springer, pp.293–300.

Zieger, B. and Hansen, K. C. (2008), Statistical validation of a solar wind propagation model from 1 to 10 AU, *Journal of Geophysical Research: Space Physics (1978–2012)* **113**(A8).